Università degli Studi di Ferrara

Ph.D. in Chemical Sciences

XXXVIII cycle

Development of new technologies, components and systems for Energy conversion and use

University of Ferrara

Department of Chemical, Pharmaceutical and Agricultural Sciences

SDS CHIM/02

2023 – 2025

Candidate Edoardo Barcaro

Supervisor Prof. Jusef Hassoun

Coordinator Prof. Alessandro Massi

List of Acronyms

AM Active Material

AC Amorphous Carbon

ACN Acetonitrile

CPE Composite Polymer Electrolyte

CV Cyclic Voltammetry

DEGDME diethylene glycol dimethyl ether

DME 1,2-dimethoxyethane

DOL 1,3-dioxolane

DSC Differential Scan Calorimetry

EIS Electrochemical Impedance Spectroscopy

EC Ethylene Carbonate

Eq Equation

ESV Electrochemical Stability Window

EV Electric Vehicles

DEC Diethyl Carbonate

FEC Fluoroethylene Carbonate

FLG Few-Layer Graphene (E2)

GDL Gas Diffusion Layer

GHG Greenhouse gases

LFP $LiFePO_4$

LiTFSI Lithium bis(Trifuloromethanesulfonyl)Imide

LIB Lithium-ion Battery

LiPS Lithium polysulfides

NIB Sodium ion Battery

NLLS Non-Linear Least Squares

NMC $LiNi_{1/3}Mn_{1/3}Co_{1/3}O_2$

NMP N-Methyl-2-Pyrrolidinione

OCV Open Circuit Voltage

OER Oxygen Evolution Reaction

ORR Oxygen Reduction Reaction

PEGDME Polyethylene Glycol Dimethyl Ether

PV PhotoVoltaic

PVdF Polyvinylidene Fluoride

RT Room Temperature

SEI Solid Electrolyte Interphase

SEM Scanning Electron Microscopy

SHE Standard Hydrogen Electrode

SPC super P carbon (E1)

TEGDME Tetra Ethylene Glycol Dimethyl Ether

TGA Thermo-Gravimetric Analysis

TEM Trasmission Electron Microscopy

VTF Vogel-Tammann-Fulcher

XRD X-Ray Diffraction

List of Equation and Mathematical relationships

- ***Randles-Sevick***[1,2]

$$I_p = 0.4463\ zFAC_{ion}(zFvD/RT)^{0.5} \qquad \textbf{Eq (1)}$$

I_p is the peak current related to the potential signals, z is the number of exchanged electrons, F is the Faraday constant (96,485 C mol^{-1}), A is the electrode geometric area, C is the estimated concentration of ion^+ in the electrode volume (mol dm^{-3}), v is the CV scan rate (mV s^{-1}), R is gas constant (8.31451 J mol^{-1} K^{-1}), and T is the room temperature (298 K).

- ***Arrhenius***[3]

$$k = Ae^{-Ea/KbT} \qquad \textbf{Eq (2)}$$

where k is the slope of the Arrhenius plot, A is a pre-exponential factor, E_a is the activation energy for ion motion (eV), k_b is the Boltzmann constant (8.52×10^{-5} eV K^{-1}), and T is the temperature (K).

- ***Conductivity***

$$\sigma = \frac{l}{R_b \times A} \qquad \textbf{Eq (3)}$$

where σ is the ionic conductivity (S cm^{-1}), R_b is the bulk resistance of the electrolyte (derived from the fitting), l is the O-ring thickness and A is its internal area.

- ***Vogel-Tammann-Fulcher*** *(VTF)*[4]

$$\sigma(T) = \sigma_\infty \exp\left(-\frac{E_a}{k_B(T - T_0)}\right) \qquad \textbf{Eq (4)}$$

where T_0 (K) is the temperature of zero-configurational entropy, typically 30 K lower than the glass transition one T_g (K). The other parameters are the ionic conductivity at infinite temperature σ_∞ (S cm^{-1}), the activation energy for Li^+ ion conduction E_a (eV), and the Boltzmann constant k_B (8.62×10^{-5} eV K^{-1}).

- ***Transference Number*** *(Bruce-Vincent-Evans Method)*[5]

$$t_+ = \frac{i_{ss}}{i_0} \times \frac{(\Delta V - R_0 i_0)}{(\Delta V - R_{ss} i_{ss})} \qquad \textbf{Eq (5)}$$

i_0 and i_{ss} represent the initial and steady-state current values, respectively; ΔV is the applied voltage; and R_0 and R_{ss} are the interfacial resistance values before and after cell polarization, respectively, as determined through fitting of the impedance spectra (read below for fitting details).

Impedance spectra fitting

All the Nyquist plots recorded by EIS were fitted through non-linear least-squares (NLLS) method with the aid of the Boukamp software. Only fits with a chi-square (χ^2) below 10^{-4} were considered acceptable for analysis.[6,7] Each equivalent circuit model adopted is discussed in the respective Experimental and Results section.

For the sake of compactness, EIS dispersions on which NLLS analyses by the equivalent circuit method have been applied are not always reported. Whenever not recalled directly in the Thesis, the reader is invited to check for further information in the published research papers.

References

(1) *Randles, J. E. B. Trans. Faraday Soc. 1948, 44, 327–338.*
(2) *Ševčík, A. Collect. Czech. Chem. Commun. 1948, 13, 349–377.*
(3) *Laidler, K. J. J.Chem. Educ. 1984, 61 (6), 494.*
(4) *Diederichsen K., Buss H., McCloskey B., Macromol. 2017, 50, 3831–3840.*
(5) *Evans, J.; Vincent, C. A.; Bruce, P. G. 1987, 28 (13), 2324−2328.*
(6) *B. Boukamp, Solid State Ion, 1986, 18-19, 136.*
(7) *B. Boukamp, Solid State Ion, 1986, 20, 31.*

Index

Each subchapter reports its own References and Figures lists. Tables are indicated progressively (for instance, the third table of subchapter 2.2 is indicated as Table 2.2.3. List of Acronyms and List of Equation are reported behind this page.

#Number indicates the presentation of published Research outcomes.

Aim of the Thesis

State of art and perspective of electrochemical energy storage

The production and management of energy is the only alternative for human society to guarantee both technological progress for the entire population and the preservation of the Earth's resources for future generations. This challenge requires the integration of different technologies, in which electrochemistry plays a fundamental role because it allows the use of chemical or electrochemical energy vectors with the highest efficiency, as opposed to mechanical, thermal or gravitational systems. In this optic, an intense pursuit is fundamental of high performance, safe, and easily manufacturable electrochemical energy storage. The sustainable formulation of innovative electrodes and safe, non-toxic, possibly solid-state, electrolytes and components has to be targeted, with careful attention to their potential recycling/reuse, in order to reduce the impact of electrochemical technologies, also in terms of critical raw materials, and to reduce their carbon footprint. The world's total energy consumption has surpassed 14 Gtoe (tonne of oil equivalent) in 2021, most of which comes from the burning of fossil fuels; these are coal, natural gas and crude oil.[(a)] For electricity production, our planet still boasts amounts of coal and natural gas that can fulfil the needs of human society for many hundreds of years. Therefore, the problem is not a shortage of fossil fuels, but rather environmental damage because of their combustion.

The unlimited source of energy for powering our planet is the sun, and another important source of sustainable energy is wind. Indeed, in recent years, impressive advancements have been achieved in developing wind turbines and technologies for harvesting solar energy and converting it to electricity or energy vectors, either via solar-thermal,[(b)] photo-voltaic (PV),[(c)] or photo-electrochemical approaches.[(d)] The PV is used widely, and the practical use of PV energy generation includes batteries charging, residential power uses and space technology. Moreover, PV system is scalable, from the household (kW range) to large-scale plants (GW range). Indeed, power generation from PV systems is highly dependent on the natural factors and the location of the PV plant, thus the related power supply may be affected by various issues including supply-demand imbalance and voltage

variation.[e] In this scenario, rechargeable batteries may represent a viable choice to mitigate the inconstancy of PV systems, thank to efficient energy storage that can allow load-levelling applications.[f]

However, great efforts are still required to reach the energy density standards necessary to efficiently support PV power plants and, at the same time, promote electrical propulsion for sustainable mobility, which attributes a fundamental role to the research on new generation energy storage systems. The common denominator to previously indicated applications is the requirement for efficient safety content, prolonged cycle life and the use of cheap and environmentally friendly materials. Nowadays, Li-ion batteries represent the most mature electrochemical energy storage technology; these systems provide an energy density exceeding 250 Wh kg^{-1} and power most of the portable electronics and electric vehicles (EVs). Nevertheless, the use of toxic metals such as cobalt and the employment of flammable electrolytes represent a major issue of these devices that may limit the optimization of the power grids and EVs technology.[g] Lithium-sulfur (Li-S) batteries, which rely on the multi-electron conversion process between Li and S that may lead to a practical energy density higher than 450 Wh kg^{-1} thank to the theoretical specific capacity of 1675 mAh gS-1.[h] Sulfur is cheap and abundant, and its insulating nature can be strongly mitigated using carbon substrates, such as nanotubes, nanospheres and graphene, that increase the electrical conductivity of the cathode and limit the dissolution of the polysulfides intermediates formed in the discharge process.[i] However, relevant concerns are associated to the use of lithium due to its limited availability and polluting extraction process. Thus, thanks to the widespread availability and low price of sodium, sodium-sulfur (Na-S) batteries may become the future energy storage system for smart electric grids that integrate renewable energy sources. A conversion electrochemical process like that of Li-S batteries powers these new generation devices, despite issues related to Na anode protection, battery cycle life and satisfactory energy density are far from solution. Following this thread, a crucial role in the applicability of these systems is played by the electrolyte: the choice is dictated from the electrodes employed, the cut-off voltage upon charge/discharge, environmental compatibility, and price. Moreover, high flash point, fast ions transport, wide electrochemical stability window and thermal

stability are required to guarantee high performance of the battery. Glyme-based solutions employing $CH_3(OCH_2CH_2)_nOCH_3$ solvents and various additives exhibit low flammability, negligible toxicity, and great stability towards alkaline-metals polysulfides, which make them attractive candidates for practical application in Li-S and Na-S batteries.[(i)]

The expected results of the PhD program include the optimization of alternative configurations of sulfur cathodes benefiting from enhanced sulfur loading, efficient current collector support, low content of inactive components, and the characterization of novel formulations of non-flammable and stable glyme-based electrolytes for Li-S and Na-S batteries. Particular focus has been devoted to the development of negative electrode having comparable electrochemical proprieties with respect to commercial graphite and/or hard carbon for Lithium-ion and Sodium-ion systems, which are expected to enhance the energy density in full-cell configuration. Polymeric separators based on PEO and PEGDME were extensively studied in order to enhance their interfacial contact. The enhancement of crucial parameters with respect to the state of the art such as energy density, cost, environmental compatibility, and safety content is the main goal of the research.

References

(a) https://yearbook.enerdata.net/total-energy/world-consumption-statistics.html

(b) R. Shinnar, F. Citro, *Technol. Soc.* **2007**, *29*, 261.

(c) R. C. Chiechi, R. W. A. Havenith, J. C. Hummelen, L. J. A. Koster, M. A. Loi, *Mater. Today* **2013**, *16*, 281.

(d) M. Grätzel, *Nature* **2001**, *414*, 338.

(e) C. Zhang, Y.-L. Wei, P.-F. Cao, M.-C. Lin, *Renew. Sustain. Energy Rev.* **2018**, *82*, 3091.

(f) S. Maddukuri, D. Malka, M. S. Chae, Y. Elias, S. Luski, D. Aurbach, *Electrochim. Acta* **2020**, *354*, 136771.

(g) J.-M. Tarascon, *Nat. Chem.* **2010**, *2*, 510.

(h) X. Ji, L. F. Nazar, *J. Mater. Chem.* **2010**, *20*, 9821.

(i) D. Di Lecce, V. Marangon, H.-G. Jung, Y. Tominaga, S. Greenbaum, J. Hassoun, *Green Chem.* **2022**, *24*, 1021.

Chapter 1.

Lithium-ion and Lithium-ion-Sulfur

1.1 Background

Electrochemical energy storage has been instrumental for the technological evolution of human societies in the 20th century and still plays an important role nowadays. In this introductory chapter, we briefly introduce definitions and examinate the most relevant topics of electrochemical energy storage associated with the battery field. As the global energy landscape rapidly transforms, energy storage is taking on an increasingly central role. Energy storage systems are becoming key enablers of renewable energy integration, grid stability, electrification, and energy autonomy. In Europe, the transition to a decarbonized energy system is inseparable from the broader goals of energy independence, climate neutrality, and economic stability. The present Li-ion battery (LIB) has been optimized during the last three decades of research to become the largest produced electrochemical system beyond Pb-based accumulator, finding application in various crucial fields, allowing the clean-energy transition thanks to its adoption in crucial fields such as electric-vehicle (EV) and energy storage from renewable sources. On the other hand, the forecasted growing demand for lithium-ion systems is currently posing serious concerns regarding core-elements and components availability in the long term. In this scenario, the necessity for efficient and complementary energy storage based on more abundant elements has triggered the improvement of rechargeable batteries. The fast-pace evolving energy demand requires complementary technologies to alleviate dependency from lithium-ion batteries in terms of various aspects, including materials distribution, toxicity, and performances. Boasted by energy densities greater than those of supercapacitors and power densities greater than those of fuel cells, batteries have performance characteristics to be used in a wide array of applications.[1, 2]

A battery is a closed system device that is comprised of one or more individual electrochemical cells. In this work, the terms "battery" and "cell" are used interchangeably. Batteries release electrical energy through redox reactions that occur at the cell electrodes. In general, batteries consist of a cathode where the reduction reaction takes place during discharge, an anode where the oxidation reaction takes place during discharge, an ion-shuttling electrolyte, and a separator that is electrically insulating but ionically permeable. The first rechargeable energy storage system based on two intercalation electrodes relying on transition

metals was developed by B. Scrosati, who successfully combined a wolframium oxide anode with a titanium sulfide cathode in December 1979 to obtain the first lithium-ion full-cell, proposed conceptually from M. Armand in the same timeframe.[3, 4] In the following decades this new technology attracted more and more research interest, until the actual commercialization of the first LIB in 1991, which was awarded in 2019 by the Nobel Prize in Chemistry assigned to M. S. Whittingham, J. B. Goodenough and A. Yoshino.[5] The widespread adoption of the LIB ramped up thank to the substitution of the lithium metal. [4] Lithium, despite being characterized by considerable theoretical specific capacity and the lowest standard reduction potential (namely 3860 mAh g^{-1} and -3.04 V *vs.* standard hydrogen electrode (SHE), respectively), is unstably reactive in presence of water and can forms dendritic structures on its surface due to uneven lithium plating upon repeated cycling that culminate in short-circuits and thermal runaways. Practically, a lithium-ion battery exploits a graphite anode (C_6) and a $LiCoO_2$ cathode, resulting in a specific energy of about 200 Wh kg^{-1}.[6] In this setup, the electrodes are soaked from an electrolyte based on a carbonate solvent and a lithium salt (**Figure 1**) which operates the exchange of Li^+ ions in according with reaction 1.1.1 [7,8]

$$C_6 + LiCoO_2 \rightleftarrows Li_xC_6 + Li_{1-x}CoO_2 \quad (1.1.1)$$

where x is the fraction of Li^+ ions that (de)intercalate in the electrodes structures (usually is about 0.6 due to practical limitations such as active material instability). On the other hand, the graphite/$LiCoO_2$ battery has been enhanced during the years by replacing the cathode, due to the poor thermal stability of the $Li_{1-x}CoO_2$ phase, the intrinsic toxicity of Co, and most importantly thanks to the discovery and development of new active material such as olivine and layered-based cathodes structure. [1, 9, 10]

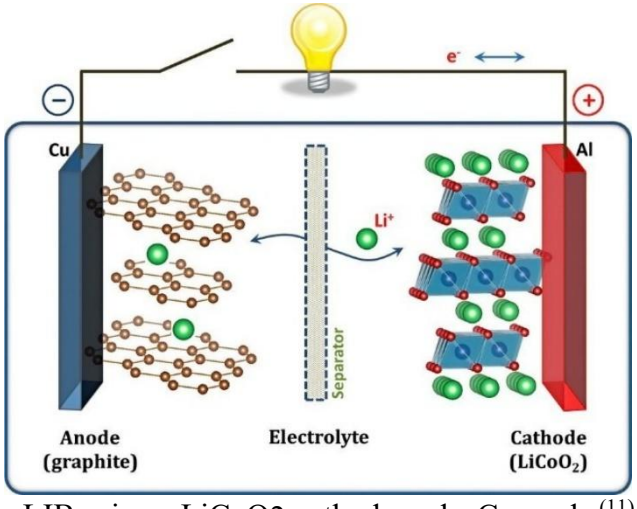

Figure 1. Scheme of a LIB using a LiCoO2 cathode and a C_6 anode.[11]

On the other hand, the results achieved by the lithium-ion technology led to an energy density of about 250 Wh kg^{-1}, which may be insufficient for the competitivity of the LIB technologies with other traditional systems in the case of automotive. However, the massive exploitation of carbon fuels and consequent emission of greenhouse gases (GHG) posed in recent years the urgency to develop more efficient and sustainable energy systems beyond the lithium-ion battery to facilitate the instauration of a carbon-neutral society, relying on equally distributed and easily accessible energy. One of the most appealing devices that will represent a step forward with respect to the lithium-ion technology is the lithium-sulfur (Li-S) battery, which conceptually operates through the reversible multi-electron conversion process between sulfur and lithium, centered within 2.3-2.1 V that leads to the final product Li_2S,[9, 10] as reported by reaction 1.1.2:

$$S_8 + 16Li^+ + 16e^- \rightleftarrows 8Li_2S \qquad (1.1.2)$$

One of the key advantages of the Li-S battery with respect to the lithium-ion one, which (de)intercalates only a limited fraction of Li^+ ions (x) in the layered electrodes structures ($0 < x < 1$) is represented by the exchange of multiple charges per mole of active material.[9, 10] The Li-S electrochemical conversion process allows a theoretical energy density of 3730 Wh kg^{-1} referring to sulfur mass.[12, 13] The reaction reported in reaction 1.1.2 actually evolves through a multi-step process involving the formation of lithium polysulfides (LiPS) intermediates (Li_2S_x, $2 \leq x \leq 8$) at different potential values as schematized in **Figure 2**. These LiPS can migrate through the electrolyte solution, delivering a continuous "shuttle" mechanism (**Figure 3**) that causes loss of active material, poor coulombic efficiency, and electrodes degradation.[14]

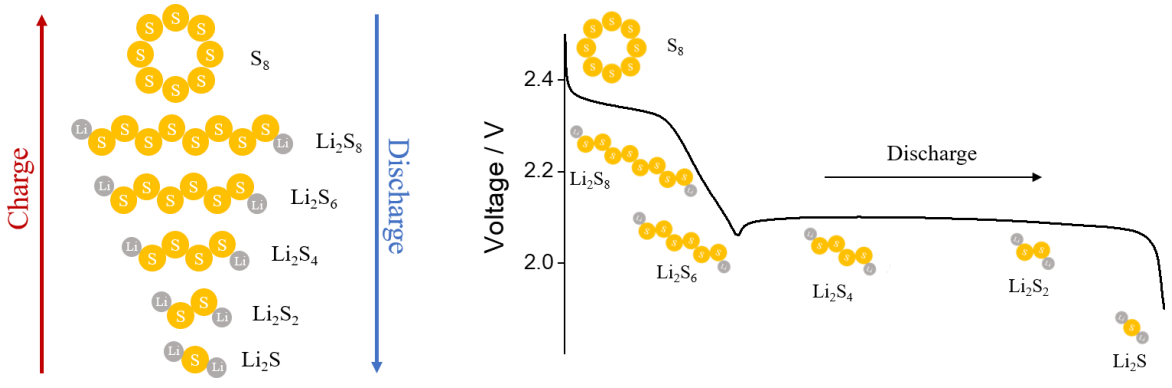

Figure 2. Graphical scheme of the species involved in the Li-S battery electrochemical conversion process and their evolution through the discharge step.[12]

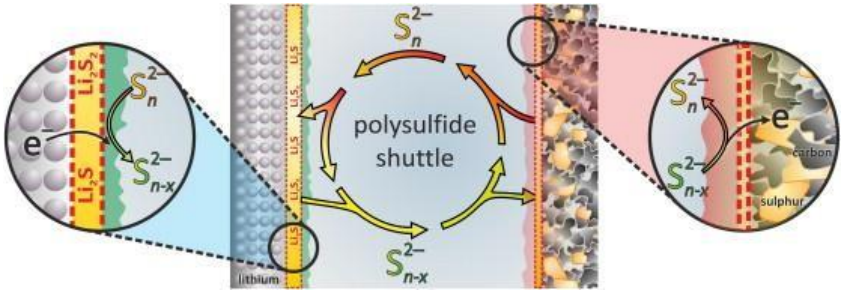

Figure 3. Representation of the polysulfides parasitic "shuttle" mechanism in a Li-S battery.[13]

Further issues affecting the Li-S battery are represented by the insulant character of sulfur and by the safety hazards deriving from the use of the lithium metal anode. In order to overcome these shortcomings, various strategies were proposed to safely and efficiently exploit the energetic conversion process of the Li-S battery, such as the enhancement of the sulfur electrode conductivity and the concomitant retention and entrapment of the polysulfide intermediates at the cathode side through the addition of carbonaceous additives. Alternative approaches consist in the development of suitable electrolyte configurations, either liquid or solid.[14] The next sections will go-through some suitable approaches to achieve sulfur-based batteries of practical interests.

References

(1) S. Whittingham, Chem. Rev., 2004, 104, 10, 4271.
(2) N. Armaroli, V. Balzani, En. & Env. Sci., 2001, 4, 3193.
(3) M. Lazzari, B. Scrosati, J. Electrochem. Soc., 1980, 127, 773
(4) B. Scrosati, J. Electrochem. Soc., 1992, 139, 2776
(5) J.-L. Brédas, J. M. Buriak, F. Caruso, K.-S. Choi, B. A. Korgel, M. R. Palacín, K. Persson, E. Reichmanis, F. Schüth, R. Seshadri, M. D. Ward, Chem. Mater. 2019, 31, 8577.
(6) D. Lin, Y. Liu, Y. Cui, Nat. Nanotechnol. 2017, 12, 194.
(7) K. M. Abraham, J. Phys. Chem. Lett. 2015, 6, 830.
(8) L. Croguennec, M. R. Palacin, J. Am. Chem. Soc. 2015, 137, 3140.
(9) B. Scrosati, J. Hassoun, Y.-K. Sun, Energy Environ. Sci. 2011, 4, 3287.
(10) J. B. Goodenough, K.-S. Park, J. Am. Chem. Soc. 2013, 135, 1167.
(11) P. Rozier, J. M. Tarascon, J. Electrochem. Soc. 2015, 162, A2490.
(12) R. Van Noorden, Nature 2014, 507, 26.
(13) M. R. Busche, P. Adelhelm, H. Sommer, H. Schneider, K. Leitner, J. Janek, J. Power Sources 2014, 259, 289.
(14) A. Manthiram, Y. Fu, S.-H. Chung, C. Zu, Y.-S. Su, Chem. Rev. 2014, 114, 11751.

1.2 The role of current collectors for lithium-sulfur battery

The insulating character of sulfur is one of the numerous challenges posed by these devices. The addition of conductive carbons to the sulfur cathode revealed remarkable improvements of the cycling behavior of the Li-S batteries due to a favorable combination between the enhancement of the electrode conductivity and the storing of active material in the porous structures of the carbon frames, which mitigates the dissolution of lithium polysulfides into the electrolyte (**Figure 1**).[14,15]

Following this trend, suitable cathodes based on encapsulation of sulfur were obtained by exploiting hollow carbons, that provide large internal volume allowing high sulfur loading and alleviating volume changes of the active material,[16,17] as well as hierarchical porous carbons which combine different porosities.[18-20]

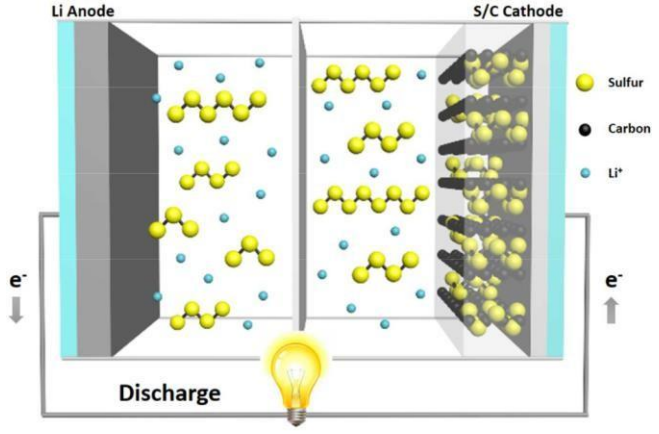

Figure 1. Graphical scheme of a Li-S battery employing a sulfur-carbon composite as cathode.[21]

Suitable carbon additives were also identified in nanotubes,[22,23] nanosheets,[24] nanospherules,[25] and other morphologies,[26,27] as well as in carbons doped with heteroatoms such as N, B, or S which provide additional polysulfide-retaining functional groups.[28-30] The inclusion of either metal or metal-oxide centers in the cathode formulation was recently proposed to strongly enhance the charge transfer kinetics and, possibly, catalyze the polysulfides conversion thank to the increased affinity between them and the electrode surface.[31-33] An additional advantage of this strategy resides in the higher conductivity of metals with respect to carbon, which may allow the use of a lower amount of inactive material and boost the practical energy density of the cell. The performance of a sulfur

cathode is heavily influenced by the electrode support. Aluminum (Al) is the substrate of choice for the high voltage-operating cathodes in LIB and sulfur electrodes due to its low reduction potential. However, recent studies suggested the substitution of Al with a porous carbon paper, namely a gas diffusion layer (GDL), due to its more suitable characteristics. GDL benefits from a macroporous texture with respect to conventional aluminum (**Figure 2**) that homogeneously accommodates the active material particles, leading to enhanced ionic and electronic conductivity, as well as to better electrode wettability.[34] Thus, the sulfur electrodes employing GDL showed improved cyclability with enhanced kinetics and higher delivered capacity values than the respective ones using Al.[34]

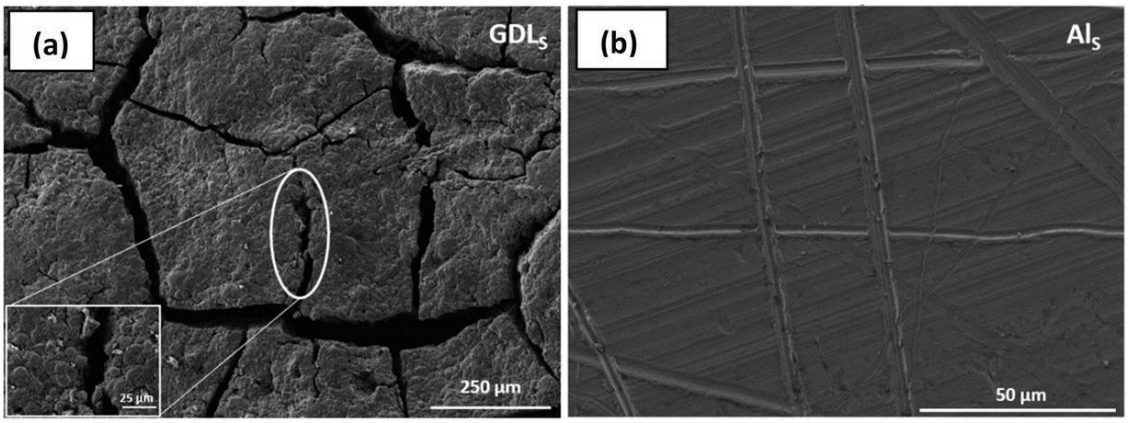

Figure 2. Images captured by scanning electron microscope (SEM) of **(a)** GDL and **(b)** Al current collectors.[34]

Hence, fibrous carbon-cloth supports such as GDL allow the infiltration of the amorphous sulfur upon charge, thus leading to improved conductivity of the cathode and an overall enhancement of the cell electrochemical performance. This unique feature represented a relevant advantage of GDLs compared to conventional metallic cathode supports such as aluminum, which allow only partial sulfur utilization due to a characteristic flat surface. Despite the silver linings associated with GDL-like supports, their excessive thickness (> 400 µm) compared to aluminum (~ 15 µm) can drastically affect the cell volumetric energy density and avoid an actual application in practical energy storage systems. Therefore, casting conductive and porous carbon coatings on aluminum substrates may represent a fair compromise between efficient sulfur utilization and appropriate thickness of the cathode. In particular, the use of FLG produced by exfoliation of graphite by wet-jet mill (WJM) process appeared an interesting strategy for enhancing Li- S performance.[26,27] Multi-walled carbon nanotubes (MWCNTs) have been often included in the sulfur cathode due to their excellent conductivity and macro-porosity provided by the

characteristic interwoven structure.[14] The latter can allow electrolyte swelling, sulfur accommodation, polysulfides restrain, and compensation of the volume changes of the cathode during cycling.

The effects of cycling on the cathode microstructure have been investigated in literature work by performing X-ray CT scans in a field of view of about 330 µm (**Figure 3**).[35] These measurements provide a three-dimensional map of the various phases in the electrode which are identified by differences in X-ray attenuation, thus enabling the detection of morphological features at the microscale with a voxel size smaller than 180 nm. **Figure 3** shows the X-ray imaging of cathode samples before (panels a–c) and after 1 (panels d–f) and 100 galvanostatic cycles in conventional glyme-based electrolyte (panels g–I, see next section for dedicated discussion regarding the electrolyte choice). The left-hand side panels (**Figure 3a, d, g**) report sections of the electrodes represented in grayscale, where the brightness reflects the local density of the specimen. The large Au aggregates can be detected as continuous bright spots (**Figure 4 a, d, g**), whilst sulfur appears as gray particles with moderate density. Besides, X-ray imaging reveals that the carbon-cloth support and the carbon-binder domain of the composite electrode film have lower density than sulfur, as suggested by the brightness scale of the images. Four domains are identified by analyzing the grayscale histogram of the CT reconstructions, and image segmentation is performed by processing the 3D datasets. **Figure 4(b, e, h)** shows the segmented images of the electrode and depict (i) highly attenuating gold in magenta, (ii) moderately attenuating sulfur in yellow, (iii) lowly attenuating carbon cloth and carbon-binder domain in gray, and (iv) exterior/pores in black.[35]

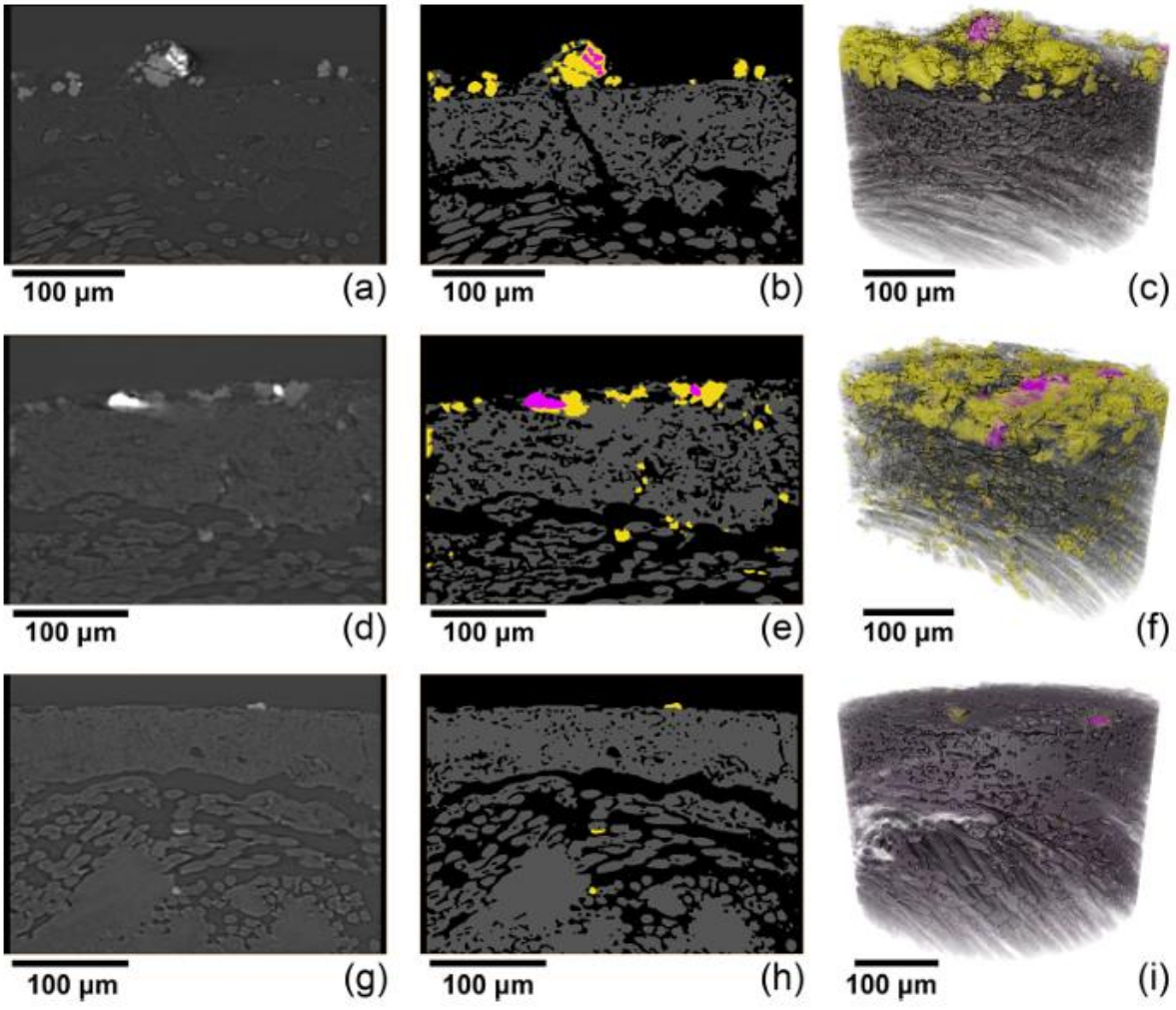

Figure 3. X-ray CT imaging at the microscale of S:Au **(a–c)** before and after **(d–f)** 1 and **(g–i)** 100 cycles at a 1C rate (1675 mA g_S^{-1}). In detail: **(a, d, g)** cross-sectional slices extracted in a plane parallel to the rotation axis (*Z* axis) and orthogonal to the electrode plane (beam attenuation represented through a grayscale), **(b, e, h)** corresponding four-phase segmented slices (Au: magenta, S: yellow, C/PVdF/C-cloth: gray; exterior: black), and **(c, f, i)** four-phase segmented volume rendering (Au: magenta, S: yellow, C/PVdF/C-cloth: gray; exterior: not represented). See reference for details regarding the Experimental setup.[35]

X-ray CT imaging in Figure 4 demonstrates that increase in electrode loading and decrease in current rate only slightly affect the characteristic features of microstructural rearrangements associated with electrochemical activation of the cell upon a discharge/charge cycle. The figure shows cross-sectional slices visualized employing a grayscale (**Figure 4a, d**) with corresponding segmentation **(Figure 4b, e)** as well as segmented volume renderings of the samples in the field of view of the tomographic scan (**Figure 4c, f**), referred to pristine and cycled electrodes. Gold aggregates exhibit significant attenuation of the beam, thereby forming bright spots (**Figure 4a, b**). Instead, sulfur, carbon-cloth, and carbon-binder domain are visualized as gray regions of different brightness due to the significantly higher X-ray transmittance. The comparison between

Figure 4 and **Figure 3(a–f)**, using the same color map for visualization, suggests similar depletion of sulfur along with its migration within the current collector pores by cycling. The low current rate and the increased loading likely boost the massive sulfur phase migration from the electrode surface to the bulk.[35] Thus, it's clear that sulfur utilization upon cycling relies on the catholyte reaction (i.e. liquid LiPS). This aspect appeared to us fundamental to rationalize and open new research lines toward the development of new current collectors for the purpose of enhancing the conversion reaction of the Li-S battery.

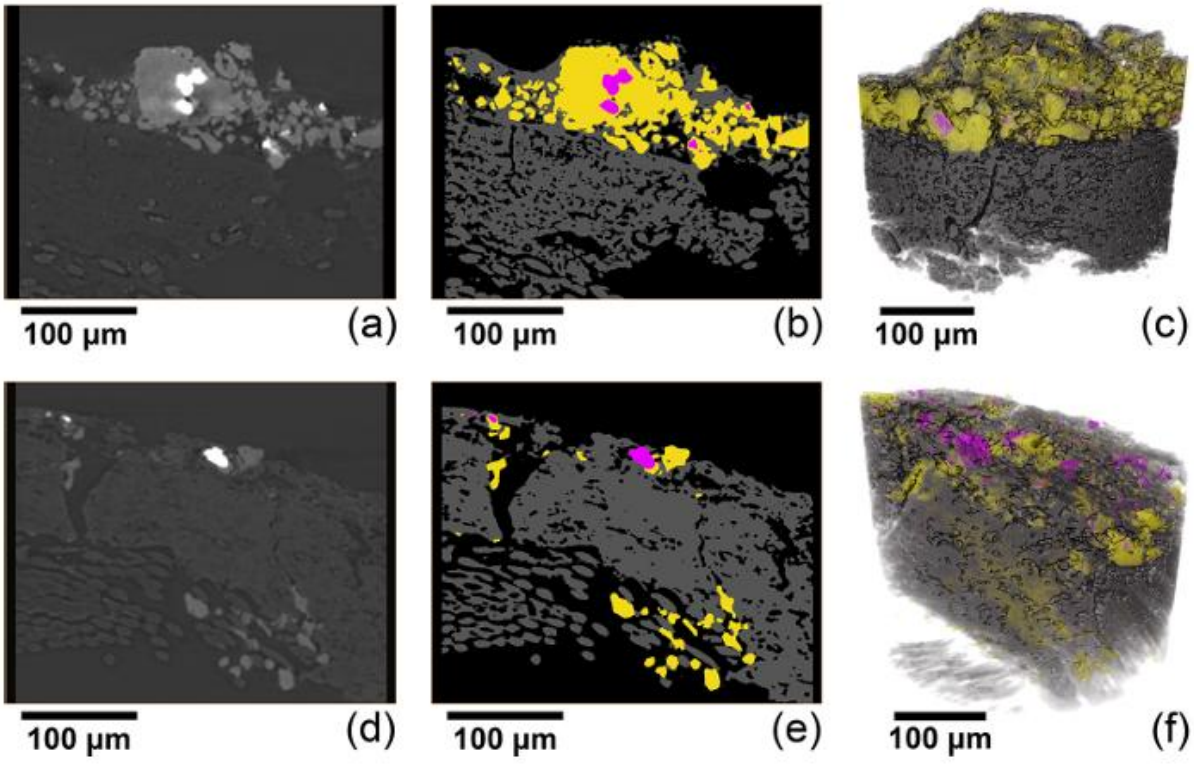

Figure 4. X-ray CT imaging at the microscale of S:Au electrodes **(a–c)** before and **(d–f)** after 1 cycle at a C/10 rate (1C = 1675 mA g_S^{-1}). In detail: **(a, d)** cross-sectional slices extracted in a plane parallel to the rotation axis (*Z* axis) and orthogonal to the electrode plane (beam attenuation represented through a grayscale); **(b, e)** corresponding four-phase segmented slices (Au: magenta, S: yellow, C/PVdF/C-cloth: gray; exterior: black); **(c, f)** four-phase segmented volume rendering (Au: magenta, S: yellow, C/PVDF/C-cloth: gray; exterior: not represented). See reference for details regarding the Experimental setup.[35]

References

(15) Z.-J. Zheng, H. Ye, Z.-P. Guo, Energy Environ. Sci. 2021, 14, 1835.
(16) Z. Li, L. Yuan, Z. Yi, Y. Sun, Y. Liu, Y. Jiang, Y. Shen, Y. Xin, Z. Zhang, Y. Huang, Adv. Energy Mater. 2014, 4, 1301473.
(17) Y.-S. Su, Y. Fu, A. Manthiram, Phys. Chem. Chem. Phys. 2012, 14, 14495.
(18) C. Liang, N. J. Dudney, J. Y. Howe, Chem. Mater. 2009, 21, 4724.
(19) K. Xi, S. Cao, X. Peng, C. Ducati, R. Vasant Kumar, A. K. Cheetham, Chem. Commun. 2013, 49, 2192.
(20) N. Moreno, A. Caballero, J. Morales, M. Agostini, J. Hassoun, Mater. Chem. Phys. 2016,

180, 82.
(21) Z. Lin, C. Liang, J. Mater. Chem. A 2015, 3, 936.
(22) J. Guo, Y. Xu, C. Wang, Nano Lett. 2011, 11, 4288.
(23) L. Carbone, T. Coneglian, M. Gobet, S. Munoz, M. Devany, S. Greenbaum, J. Hassoun, J. Power Sources 2018, 377, 26.
(24) J. Guo, J. Zhang, F. Jiang, S. Zhao, Q. Su, G. Du, Electrochim. Acta 2015, 176, 853. (25) J. Kim, D.-J. Lee, H.-G. Jung, Y.-K. Sun, J. Hassoun, B. Scrosati, Adv. Funct. Mater. 2013, 23, 1076.
(26) M. Wang, X. Xia, Y. Zhong, J. Wu, R. Xu, Z. Yao, D. Wang, W. Tang, X. Wang, J. Tu, Chem. – A Eur. J. 2019, 25, 3710.
(27) H. Shi, W. Lv, C. Zhang, D.-W. Wang, G. Ling, Y. He, F. Kang, Q.-H. Yang, Adv. Funct. Mater. 2018, 28, 1800508.
(28) G. Zhou, E. Paek, G. S. Hwang, A. Manthiram, Adv. Energy Mater. 2016, 6, 1501355.
(29) S. S. Zhang, Inorg. Chem. Front. 2015, 2, 1059.
(30) M. Inagaki, M. Toyoda, Y. Soneda, T. Morishita, Carbon N. Y. 2018, 132, 104.
(31) Z. Zhao, S. Wang, R. Liang, Z. Li, Z. Shi, G. Chen, J. Mater. Chem. A 2014, 2, 13509.
(32) H. Zhang, W. Zhao, M. Zou, Y. Wang, Y. Chen, L. Xu, H. Wu, A. Cao, Adv. Energy Mater. 2018, 8, 1800013.
(33) H. Jiang, X.-C. Liu, Y. Wu, Y. Shu, X. Gong, F.-S. Ke, H. Deng, Angew. Chemie Int. Ed. 2018, 57, 3916.
(34) A. Benítez, Á. Caballero, E. Rodríguez-Castellón, J. Morales, J. Hassoun, ChemistrySelect 2018, 3, 10371.
(35) V. Marangon, D. Di Lecce, D. Brett, P. Shearing, J. Hassoun, J. En. Chem, 2022, 64, 116.

#1 https://doi.org/10.1007/s12274-022-5364-5

Current collectors based on multiwalled carbon-nanotubes and few-layer graphene for enhancing the conversion process in scalable lithium-sulfur battery

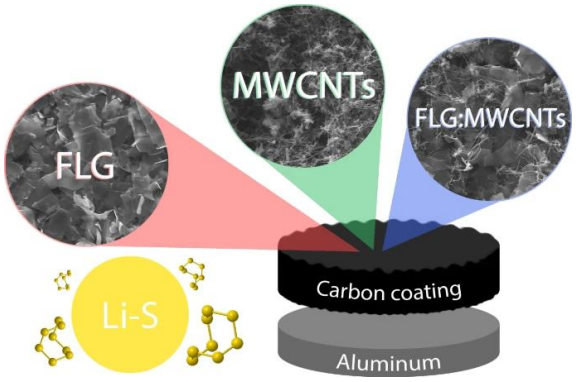

This segment of the work introduces current collectors consisting of Al substrates suitably coated by either Few Layer Graphene (FLG), MWCNTs, or a combination of them (50:50 wt.%) to optimize the Li-S battery operation. The supports were investigated in terms of morphology and structure and used in lithium cells with a composite formed by elemental sulfur including carbon black (70:30 wt.%). To further investigate the effects of the sulfur cathode composition on the lithium cell proprieties and electrochemical performance, two different electron conductor agents, namely amorphous carbon black and FLG, were used in the electrode slurry formulation. The resulting electrodes were thoroughly characterized in terms of morphology and electrochemical features in lithium cells by evaluating the reversibility, the cycling performance, and stability of the Li-S conversion process. The Li^+ diffusional proprieties through the electrode/electrolyte interphase were studied. The results suggest a crucial role of the FLG in enhancing the mechanical stability of the electrode and strongly improving the Li^+ ion diffusion. Furthermore, the data indicated an optimal cycling stability of the cells combining FLG conductive agent and MWCNTs coating on the Al support.

Experimental

- Current collectors preparation

FLG and MWCNTs (> 90% carbon basis, D x L: 110–170 nm x 5–9 μm, Sigma-Aldrich) were chosen as carbon materials to prepare three different current collectors. Slurries composed of carbon material (90 wt.%), that is, FLG, MWCNTS, or FLG:MWCNTS 50:50 wt.% mixture, and polyvinilidene fluoride (10 wt.%, Solef 6020, PVdF) polymer binder were prepared by dispersing the components in N-methyl- 2-pyrrolidone (NMP, Sigma-Aldrich) solvent. The resulting slurries were coated on aluminum foils (MTI corp., 15 μm thick) using a doctor blade tool (MTI corp.) and

adjusting the thickness in order to achieve a carbon loading of ~ 1 mg cm^{-2}. The coated aluminum foils were dried at 70 ºc until complete evaporation of the solvent and subsequently hand roll-pressed to reduce thickness and improve the coating tap density. The obtained current collectors were indicated in the text as S7 (FLG:PVdF 90:10 wt.%), S8 (MWCNTs:PVdF 90:10 wt.%), and S9 ((FLG:MWCNTs 50:50 wt.%):PVdF 90:10 wt.%). The thickness of the S7, S8, and S9 current collectors was measured using a Palmer digital thickness gauge, resulting in 40 µm, 60 µm, and 50 µm, respectively. The morphological features of the carbon-coated Al current collectors were investigated by scanning electron microscopy (SEM) through a Zeiss EVO MA10 microscope exploiting a tungsten thermionic electron source, while energy dispersive X-ray spectroscopy (EDS) was carried out on the SEM images by a X-ACT analyzer. The structure of the current collectors was studied via X-ray diffraction (XRD) by performing scans between 10º and 60º at 10 s $step^{-1}$ (step size of 0.02º) through a Bruker D8 Advance diffractometer exploiting a Cu-Kα source (8.05 keV)..

- Sulfur cathode preparation

The sulfur-carbon composite used in cathodes for lithium cell consisted of a mixture of elemental sulfur and amorphous super P carbon (SPC, Timcal) combined by the 70:30 weight ratio through melting procedure as reported previously.[36] Accordingly, elemental sulfur (≥ 99.5 %, Riedel-de Haën) and SPC were ground together and heated at 125 ºC in a silicon oil bath under continuous stirring until complete melting of sulfur and blending with SPC. Afterwards, the mixture was quenched at room temperature until solidification, and ground to achieve a fine powder. The final composite is indicated as S@SPC-73. Sulfur electrodes were prepared by doctor blade casting on the S7, S8, and S9 current collectors of slurries combining S@SPC-73, a carbon electron conductive agent, and the PVdF polymer binder by the 80:10:10 weight ratio through dispersion in NMP solvent. Two different carbon electron conductive agents were used, *i.e.*, either SPC or FLG, indicated as E1 and E2, respectively, when cited in cell or electrode configurations. The six electrode foils obtained by combining the S@SPC-73_E1 and S@SPC-73_E2 formulations with the S7, S8, and S9 current collectors were dried on a hot plate at 50 ºc for 3 h to remove the NMP solvent. Subsequently, the electrode foils were hand roll-pressed and cut into 14 mm-diameter disks (1.54 cm^2 geometric area) before being dried under vacuum overnight at 35 ºC and transferred inside an Ar-filled glovebox (MBraun, oxygen and water levels < 1 ppm). The electrodes morphology was evaluated by SEM-EDS investigation via a Zeiss EVO MA10 microscope exploiting a tungsten thermionic electron source and an X-ACT analyzer, respectively.

- Electrochemical test

CR2032 coin-type cells were assembled by stacking a S@SPC-73 electrode, a 16 mm-diameter celgard 2400 separator soaked with the electrolyte, and a 14 mm-diameter lithium disk as the anode. The electrolyte solvent was prepared by mixing 1,3-dioxolane (DOL, anhydrous, containing ca. 75 ppm BHT as inhibitor, 99.8%, Sigma-Aldrich) and 1,2-dimethoxyethane (DME, anhydrous, 99.5%, inhibitor-free, Sigma-Aldrich) with 1:1 weight ratio. Then, lithium bis(trifluoromethanesulfonyl)imide ($LiN(SO_2)_2(CF_3)_2$, LiTFSI, 99.95% trace metals basis, Sigma-Aldrich) and lithium nitrate ($LiNO_3$, 99.99% trace metals basis, Sigma-Aldrich) were dissolved as conductive salt and sacrificial agent, respectively, in the solvent mixture to achieve a concentration of 1 mol for both salts in 1 kg of solvent. The electrolyte is subsequently indicated as DOL:DME, 1 m LiTFSI, 1 m $LiNO_3$. Before employment, DOL and DME solvents were dried under molecular sieves (rods, 3 Å, size 1/16 in., Honeywell Fluka) to ensure a water content lower than 10 ppm as verified via a Karl Fischer 899 coulometer (Metrohm), while lithium salts were dried under vacuum for 2 days at 110 ºC. The subsequent electrochemical measurements were

performed on Li||S@SPC-73 cells using cathodes with a sulfur loading of ~ 2 mg cm^{-2} and an E/S ratio of 15 µl mg^{-1}. Cyclic Voltammetry (CV) was performed at the constant scan rate of 0.1 mV s^{-1} within the 1.8–2.8 V vs. Li^+/Li potential range, while electrochemical impedance spectroscopy (EIS) was carried out at the open circuit voltage (OCV) condition and during CV upon the 1st, 5th, and 10th cycle by applying an alternate voltage signal of 10 mV in the frequency range from 500 kHz to 100 mHz.. CV measurements were performed at increasing scan rates, that is, 0.05, 0.1, 0.15, 0.2, and 0.25 mV s^{-1} in the 1.8–2.8 V vs. Li^+/Li potential range to determine the Li^+ diffusion coefficient (*D*) by using the Randles–Sevcik *Eq. (1)*. CV and EIS tests were carried out by using a VersaSTAT Princeton Applied Research (PAR-AMETEK) instrument at room temperature (25 ºC). Li||S@SPC-73 cells were galvanostatically cycled at the constant current rate of C/5 (1 C = 1,675 A g^{-1}) between 1.9 and 2.8 V through a MACCOR series 4000 battery test system at room temperature (25 ºC). Additional discharge/charge cycles were performed on Li||S@SPC-73_E2_S8 cells using either a cathode sulfur loading of 5 mg cm^{-2} and an E/S ratio of 10 µl mg^{-1}, or a sulfur loading of 6.5 mg cm^{-2} with an E/S ratio of 7 µl mg^{-1}. The cells were cycled at the constant current rate of either C/5 or C/10, respectively, within the 1.7–2.8 V voltage range in a chamber with a controlled temperature of 30 ºC with a maximum fluctuation of ±0.1 ºC with respect to the set-point.

Results

The morphological and structural features of the carbon-coated Al current collectors using either FLG, MWCNTs, or the FLG:MWCNTs 50:50 wt.% (S7, S8, and S9, respectively) are reported in **Figure 1** by SEM-EDS (images in **Figure 1(a)–1(r)**) and XRD (patterns in **Figure 1(s)–1(u)**). The data recorded for the S7 (**Figure 1(a)–1(f)** and **1(s)**), S8 (**Figure 1(g)–1(l)** and **1(t)**), and S9 (**Figure 1(m)–1(r)** and **1(u)**) show substantial differences in terms of carbon particle distribution and shape at the current collector surface as well as of crystallinity. In particular, the SEM of S7 (**Figure 1(a)–1(c)**) clearly evidences the presence of FLG flakes with dimensions > 1 µm leading to a uniform coating in which the C (EDS in **Figure 1(d)**) and the F accounting for the PVdF binding agent (EDS in **Figure 1(e)**) cover the Al (EDS in **Figure 1(f)**) surface. The morphology of S8 is strongly influenced by the disordered nature of the MWCNTs that leads to a porous carbon surface (**Figure 1(g)–1(i)**), as also evidenced by the EDS elemental maps of C (**Figure 1(j)**), F (**Figure 1(k)**), and Al (**Figure 1(l)**). The combination of FLG and MWCNTs in the S9 current collector is reflected into a characteristic carbon coating (**Figure 1(m)–1(o)**) in which a predominant FLG-MWCNTs uniform layer and clusters formed by MWCNTs and PVdF (see EDS elemental maps in **Figure 1(p)–1(r)**) are interspersed onto the Al surface. The difference between the supports in terms of crystallinity is clearly evidenced by the XRD measurements performed on S7 (**Figure 1(s)**), S8 (**Figure 1(t)**), and S9 (**Figure 1(u)**). The current collectors containing FLG (i.e., S7 and S9) display a narrow and intense peak at ~ 26º typical of graphitic structures due to the compact packing of the FLG layers promoted by the experimental conditions adopted herein, while S8 shows a

broader and less intense signal characteristic of the MWCNTs structure. The substantially lower crystallinity due to MWCNTs compared to FLG in the current collectors can influence the performance of Li-S batteries. The use of low crystalline porous carbon collectors, such as GDL, has already evidenced crucial improvements compared to the conventional flat Al. In fact, GDL can efficiently host the elemental sulfur formed during charge into the widely available space in the support structure, thus enhancing the electric contact of the active material with the electrode and improving the battery performance. Therefore, MWCNTs could in principle ensure a suitable porosity of the carbon coating due to the wide spatial distribution of the nanotubes and allow sulfur infiltration, whereas the packed FLG flakes may provide mechanical robustness and flexibility.[37,38] The replacement of thick carbon current collectors such as GDL with carbon-coated aluminum supports actually represents a key factor to achieve Li-S batteries with volumetric energy density of practical interest. GDL support has a thickness as high as 454 μm, conventional aluminum exhibits a value limited to 15 μm, whilst S7, S8, and S9 carbon-coated aluminum current collectors with carbon loading of ~ 1 mg cm^{-2} exhibit thicknesses of 40, 60, and 50 μm, respectively, which are considered an adequate compromise for practical applicability and enhanced performance in Li-S cell.

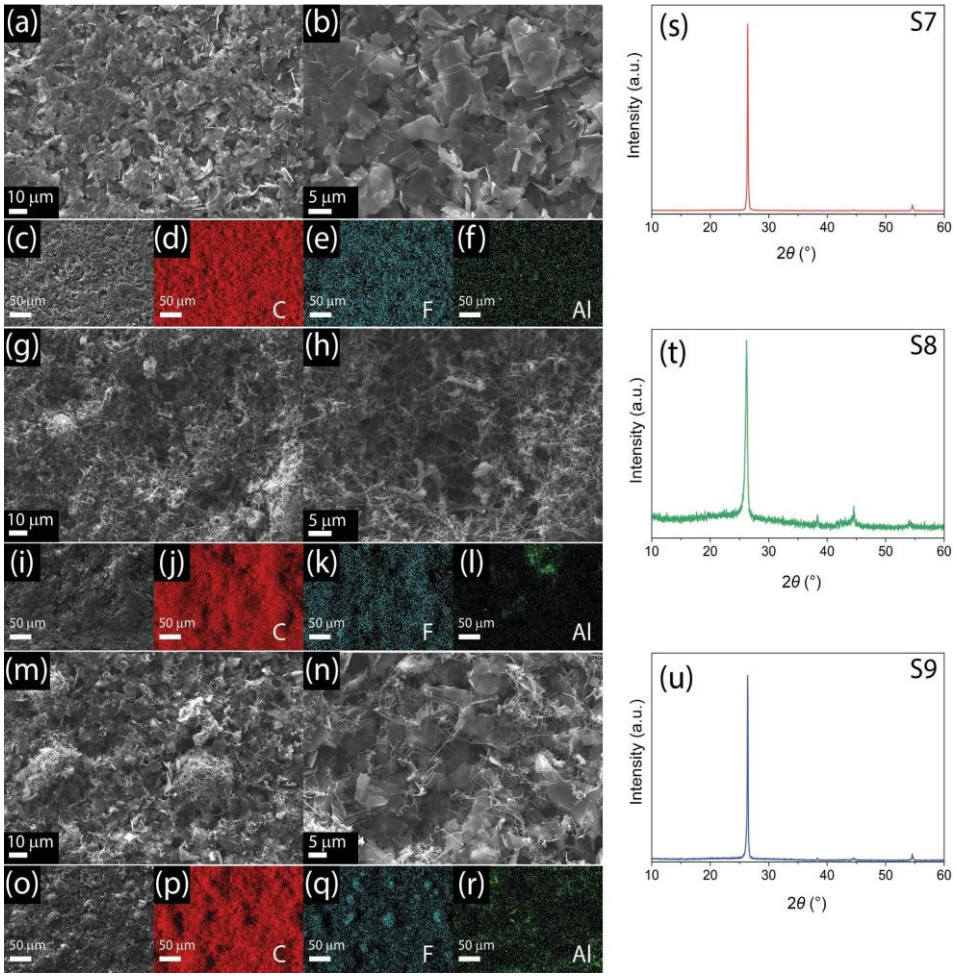

Figure 1. SEM-EDS analyses of the **(a–f)** S7, **(g–l)** S8, and **(m–r)** S9 carbon-coated aluminum current collectors; in detail: **(a–c)**, **(g–i)**, and **(m–o)** SEM images at various magnifications, and corresponding EDS elemental maps of **(d)**, **(j)**, **(p)** C, **(e)**, **(k)**, **(q)** F, and **(f)**, **(l)**, and **(r)** Al. X-ray diffractograms of the **(s)** S7, **(t)** S8, and **(u)** S9 carbon-coated aluminum current collectors. See the Experimental section for acronyms.

The influence of the various current collectors and electron conductive agents on the Li-S systems was further investigated by estimating the Li^+ diffusion coefficient (D) in the electrode/electrolyte interphase through Randles–Sevcik *Eq (1)*. The CV measurements at increasing scan rates displayed in **Figure 2** were carried out on Li||S@SPC-73_E1 (**Figure 2(a)–2(c)**) and Li|S@SPC-73_E2 (**Figure 2(d, f)**) cells with either the S7 (**Figure 2(a**, **d)**), S8 (**Figure 2(b, e)**), or S9 (**Figure 2(c, f)**) current collectors. The related voltammograms reflect the signature of the Li-S conversion process with differences depending on the used current collector and the electron conductive agent, and show the expected increase of the current peak intensity (I_p) and the overpotential by raising the scan rate. The I_p of the selected reduction and oxidation signals are plotted vs. the square root of the scan rate to obtain the corresponding $Ip/v^{1/2}$ slope by linear fit and calculate the D value (*Eq (1)*) for all the

considered states of charge . As expected, different D coefficients are obtained depending on the sulfur cathode configuration, while all the electrode formulations show similar D trends throughout the CV scans. In particular, the Li-S systems exhibit the highest coefficient in the first reduction step at, 2.25 V vs. Li^+/Li, i.e., between 5.9 x 10^{-8} and 2.3 x 10^{-7} cm^2 s^{-1}, that decreases to value between 6.9 x 10^{-9} and 1.3 x 10^{-7} cm^2 s^{-1} in the subsequent discharge step at 1.95 V vs. Li^+/Li. This trend is coherent with the prevalent presence of soluble long-chain polysulfides such as Li_2S_8 and Li_2S_6 during the initial discharge step at 2.25 V vs. Li^+/Li characterized by high ionic mobility which allows fast diffusion of the Li^+, subsequently hindered by the abundance of the solid insulating short-chain polysulfides (Li_2S_x, $1 \leq x \leq 4$) achieved with the ongoing of the discharge at 1.95 V vs. Li^+/Li. The S@SPC-73_E2_S9 electrode shows the highest D coefficient with values ranging between 2.3 x 10^{-7} and 1.1 x 10^{-7} cm^2 s^{-1}. Relevantly, all S@SPC-73 electrodes provide D values of the order of 10^{-8}–10^{-7} cm^2 s^{-1}, except for S@SPC-73_E1_S7 that shows the lowest values of 6.9 x 10^{-9}–5.9 x 10^{-8} cm^2 s^{-1}, likely due to unfavorable kinetics related to the materials combination, which may need additional investigations. Beneficial effects on the Li^+ diffusion may derive from the use of MWCNTs in the support due to the increased porosity compared to the flat FLG. This feature likely leads to better electrode/electrolyte contact and enhanced hosting ability of the solution in the electrode. The study of the Li^+ diffusional characteristics plays an essential role, particularly for challenging systems such as the Li-S battery which involves insulating species such as S and Li_2S in the electrode/electrolyte interface. Therefore, the choice of the optimal support and electronic conductor is based herein on the maximum D value achieved and the best capacity retention of the cells upon 150 cycles. The combination of these parameters represents in fact the most relevant indication on the effect of the current collector and conductive agent on the cell performances. Despite the S@SPC-73_E1_S9 electrode ensures the highest steady state capacity of 770 mAh g^{-1} in lithium cell, the corresponding D_{max} is among the lowest ones, that is, 7.7 x 10^{-8} cm^2 s^{-1} (**Figure 2(a)**). Instead, the S@SPC-73_E2_S8 and S@SPC-73_E2_S9 cathodes reveal the highest D_{max}, that is, 1.9 x 10^{-7} and 2.3 x 10^{-7} cm^2 s^{-1}, respectively, whilst only the E2_S8 combination ensures a considerable final capacity of 725 mAh g^{-1} and a good retention of 68% with respect to the pristine value over 150 cycles (**Figure 3(b)**). Moreover, the S@SPC-73_E2_S7 electrode has a D_{max} of 8.0 x 10^{-8} cm^2 s^{-1} (**Figure 3(b)**) which is far lower with respect to S@SPC-73_E2_S8 and S@SPC-73_E2_S9, likely due to the above mentioned excessive presence of FLG in the cathode formulation that can slow down the lithium ions diffusion at the electrode/electrolyte interface.

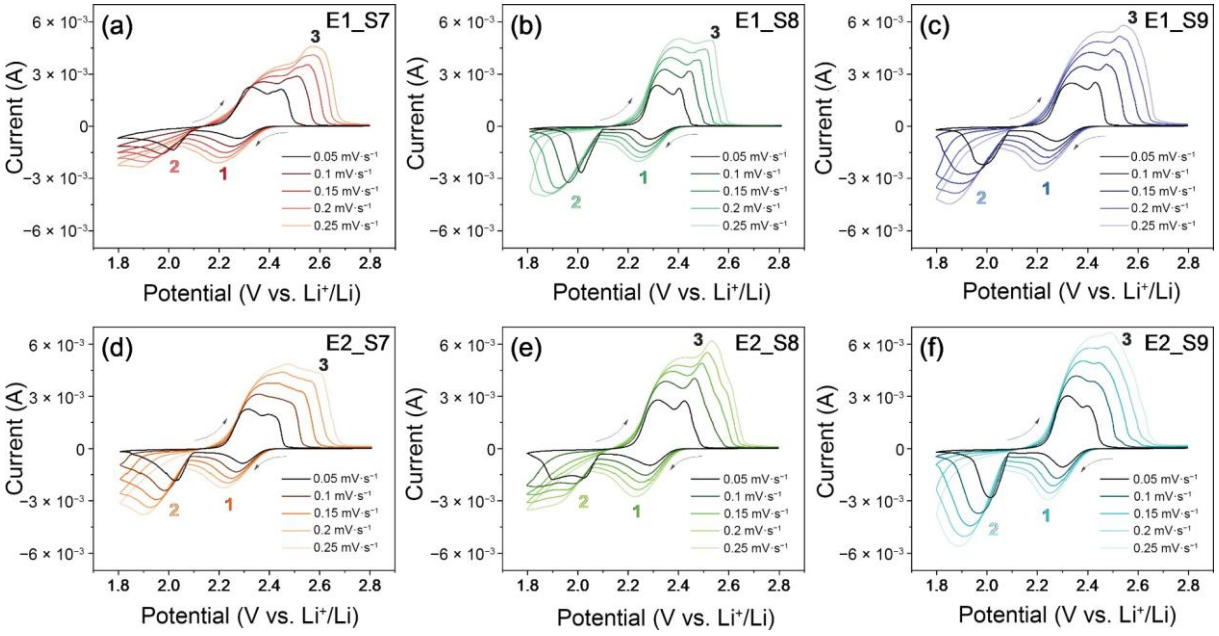

Figure 2. CV measurements related to Li|DOL:DME, 1 m LiTFSI, 1 m $LiNO_3$|S@SPC-73 cells with cathode formulations involving either **(a–c)** E1 or (**d–f)** E2 conductive agents and **(a, d)** S7, **(b, e)** S8, or **(c, f)** S9 carbon-coated Al current collectors (insets describe the cathode combinations). Voltammograms recorded at 0.05, 0.1, 0.15, 0.2, and 0.25 mV s^{-1} increasing scan rates between 1.8 and 2.8 V vs. Li^+/Li. cathode sulfur loading: 2 mg cm^{-2}; E/S ratio: 15 µl mg^{-1}. The numbers in inset indicate the peak considered for the calculation of the D through Randles–Sevcik equation (*Eq (1)*).

Galvanostatic discharge/charge cycling tests were carried out hereafter at the constant current rate of C/5 (1 C = 1.675 A g^{-1}) on Li|S@SPC-73 cells exploiting a sulfur loading of ~ 2 mg cm^{-2} and an E/S ratio of 15 µl mg^{-1}. **Figure 3** shows the voltage profiles (**Figure 3(a, c)**, and **3(e)**) and capacity trends (Figs. 3(b), 3(d), and 3(f)) of lithium cells using S@SPC-73_E1 electrodes with either the S7 (**Figure 3(a, b)**), S8 (**Figure 3(c, d)**), or S9 (**Figure 3(e, f)**) current collectors. The selected voltage profiles (**Figure 3(a, c, e)**) reveal for all the cells the evolution of the double-step Li-S conversion process identified by two discharge plateaus at ~ 2.3 and ~ 2.1 V reversed in two charge plateaus centered at 2.3 and 2.4 V, in agreement with the voltammograms of **Figure 2**. The voltage signatures also reveal a low polarization that hardly increases during the subsequent 150 runs, thus suggesting an optimized and efficient electrochemical process throughout the discharge/charge cycles taken into account. Further information is provided by the cycling trends in **Figure 3(b, d**, **f)** that allow a more detailed comparison of the various Li|S@SPC-73_E1 cells in terms of electrochemical stability. The tests indicate a first cycle capacity of 1130, 995, and 1058 mAh g^{-1} for the S@SPC-73_E1

electrodes with either the S7 (**Figure 3(b)**), S8 (**Figure 3(d)**), or S9 (**Figure 3(f)**) current collectors, respectively. The pristine capacity drastically decreases during the initial 40–50 cycles, and newly increases to stabilize at respective values of ~ 740 (**Figure 3(b)**), ~ 700 (**Figure 3(d)**), and ~ 810 mAh g^{-1} (**Figure 3(f)**). This behavior suggests a slow, but effective activation with consolidation of the electrode/electrolyte interphase, involving a partial loss of active material during the early stages of the test, subsequently leading to favorable structural rearrangements of the electrode structure, better electric contact of sulfur with the cathode, and enhancement of the cycling performance.[39,40] Therefore, the initial capacity values can be hardly associated with the final capacity retention which is instead strongly influenced by the electrode composition. In turn, the activation ensures satisfactory steady state capacity values and a retention of 64%, 66%, and 73% with respect to the initial one upon 150 cycles (**Figure 3(b, d, f)**, respectively). The cells subsequently operate with a satisfactory coulombic efficiency that progressively reaches 97%. The S@SPC-73_E2 electrodes were investigated by galvanostatic cycling in **Figure 4** using the same experimental setup previously adopted for the S@SPC-73_E1 ones. Hence, the voltage profiles of the Li|S@SPC-73_E2 cells using either S7 (**Figure 4(a)**), S8 (**Figure 4(c)**), or S9 (**Figure 4(e)**) show the proper evolution of the reversible conversion of Li and S to lithium long-chain polysulfides at 2.3 and 2.1 V during discharge, and back to Li and S at 2.3 and 2.4 V during charge, with a low overvoltage. The cycling trends in **Figure 4(b, d, f)** reveal initial capacity values of 1129, 1067, and 999 mAh g^{-1} for the cell using S7 (**Figure 4(b)**), S8 (**Figure 4(d)**), and S9 (**Figure 3(f)**) supports, respectively, that decrease during the early stages of the test, increase afterwards to steady-state values of 780, 790, and 620 mAh g^{-1}, and subsequently stabilize leading to a retention of 62%, 68%, and 62% with respect to the initial value after 150 cycles. As already observed for Li|S@SPC-73_E1 cells (**Figure 3**), Li|S@SPC-73_E2 ones also show a slight irreversibility during the first cycle, while the final coulombic efficiency notably approaches 98% upon 150 cycles. In summary, both the Li|S@SPC-73_E1 (**Figure 3**) and Li|S@SPC- 73_E2 (**Figure 4**) cells demonstrate promising cycling behavior depending on the carbon coating on the aluminum substrate. On the other hand, these data suggest the need for a careful tuning of the FLG loading when concomitantly used as electron conductor (E2) and as carbon coating on the aluminum substrate (S7 and S9). The use of FLG as the conductive agent and the MWCNTs as the carbon coating on Al in the S@SPC-73_E2_S8 electrode appears a suitable compromise for allowing optimal morphology, good mechanical stability, fast diffusion, high capacity values, and acceptable retention. The energy density of each electrode is presented in

Table 1.2.1 with respect to the average voltage of 2.2 V (**Figure 3** and **Figure 4**), the residual capacity value after 150 cycles, and the overall mass of the electrodes including the carbons, sulfur, and PVdF. The table evidence that the electrodes S@SPC- 73_E1_S9 and S@SPC-73_E2_S8 are characterized by the highest estimated energy values. **Table 1.2.2** sum up the electrochemical performance indicator obtained during the electrode optimization.

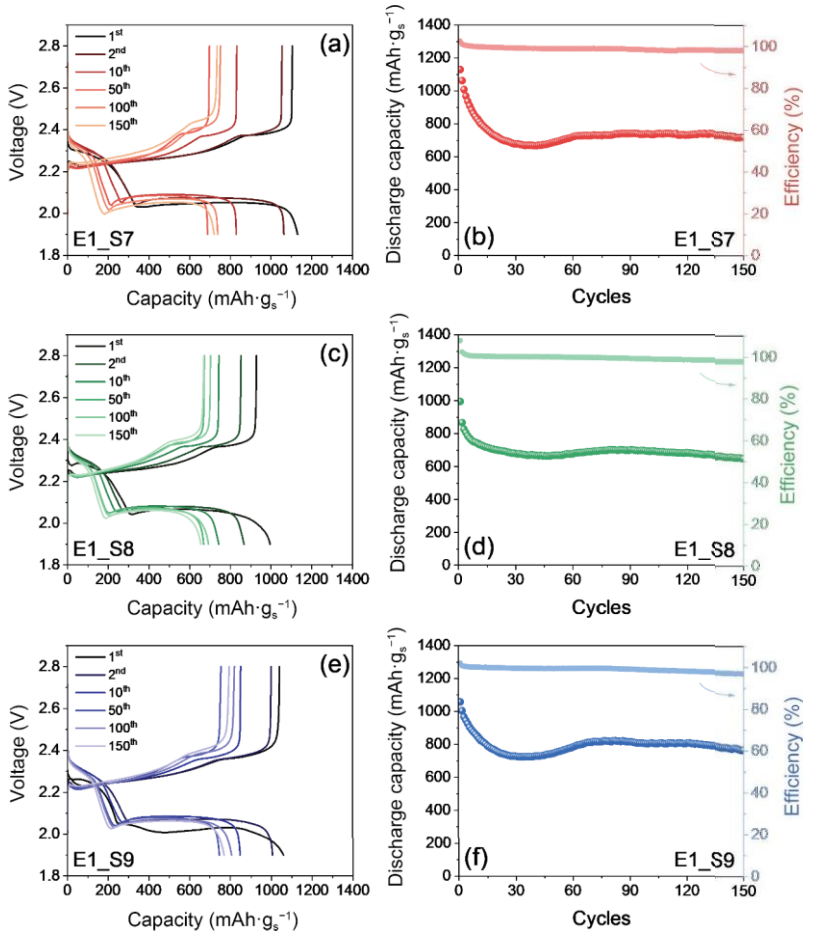

Figure 3. (a), **(c)**, **(e)** Voltage profiles and **(b)**, **(d)**, **(f)** cycling trend (right y-axes show coulombic efficiency) of galvanostatic tests performed on Li|DOL:DME, 1 m LiTFSI, 1 m $LiNO_3$|S@SPC-73_E1 cells with either the **(a**, **b)** S7, **(c, d)** S8, or **(e, f)** S9 carbon-coated Al current collectors (insets describe the various cathode combinations) at current rate of C/5 between 1.9 and 2.8 V. Sulfur loading: 1.5–2 mg cm^{-2} (electrode geometric area: 1.54 cm^2); E/S ratio: 15 µl mg^{-1}.

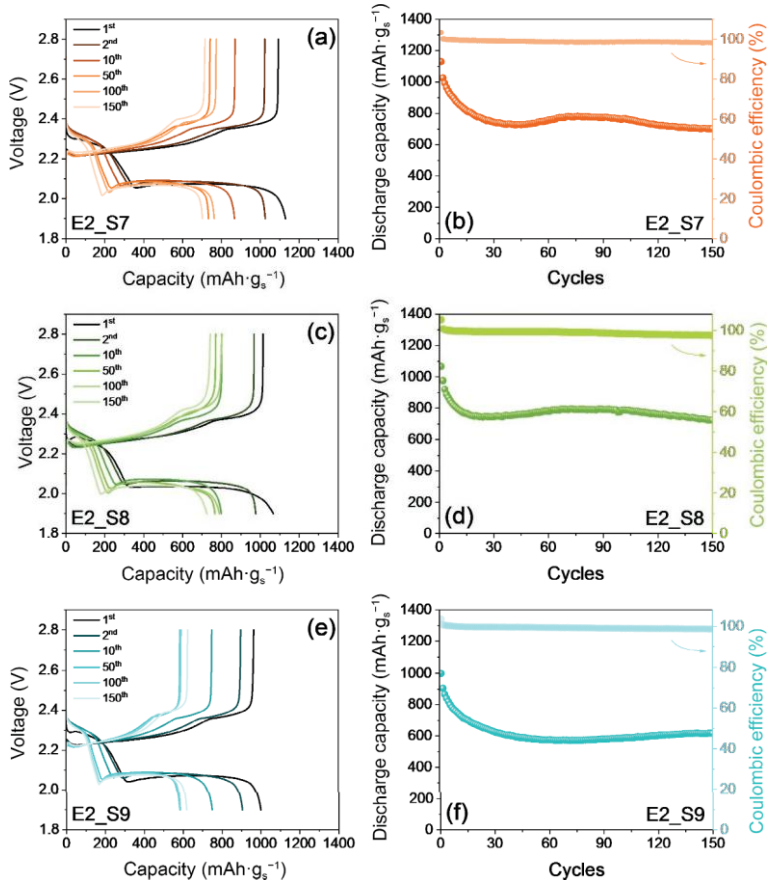

Figure 4. (a), **(c)**, **(e)** Voltage profiles and **(b)**, **(d)**, **(f)** cycling trend (right y-axes show coulombic efficiency) of galvanostatic tests performed on Li|DOL:DME, 1 m LiTFSI, 1 m $LiNO_3$|S@SPC-73_E2 cells with either the **(a**, **b)** S7, **(c, d)** S8, or **(e, f)** S9 carbon-coated Al current collectors (insets describe the various cathode combinations) at current rate of C/5 between 1.9 and 2.8 V. Sulfur loading: 1.5–2 mg cm^{-2} (electrode geometric area: 1.54 cm^2); E/S ratio: 15 µl mg^{-1}.

Table 1.2.1 Overall Energy density of the S@SPC-73 electrodes in lithium sulfur cell

Electrode	Residual Capacity (mAh)	Sulfur weight (mg)	Electrode Weight (mg) (S+Carbon+PVdF)	Electrode Energy Density (Wh kg^{-1})
S@SPC-73_E1_S7	1.9	2.7	5.4	361
S@SPC-73_E1_S8	1.7	2.6	5.0	332
S@SPC-73_E1_S9	2.2	2.9	5.1	431
S@SPC-73_E2_S7	1.9	2.7	5.3	350
S@SPC-73_E2_S8	2.4	3.3	5.9	399
S@SPC-73_E2_S9	2.0	3.2	5.5	356

Table 1.2.2 Performance of the S@SPC-73 electrodes in lithium cell.†

S@SPC-73_	D_{max} ($cm^2\ s^{-1}$)	Residual capacity ($mAh\ g_S^{-1}$)	Capacity retention (%)
E1_S7	5.9×10^{-8}	720	64
E1_S8	1.2×10^{-7}	655	66
E1_S9	7.7×10^{-8}	769	73
E2_S7	8.0×10^{-8}	701	62
E2_S8	1.9×10^{-7}	725	68
E2_S9	2.3×10^{-7}	618	62

†Maximum Li^+ diffusion coefficients (D_{max}), residual capacity upon 150 discharge/charge cycles and corresponding capacity retention delivered by the S@SPC-73 electrodes in lithium cell using the various configurations of this work. See Figure 5 for the corresponding histogram representations.

Therefore, the S@SPC-73_E2_S8 cathode was selected among the various formulations for the additional cycling tests in lithium cell with sulfur loading increased to 5 mg cm^{-2} and E/S ratio decreased to 10 µl mg^{-1} at C/5 (**Figure 5(c, d)**). A further test under more challenging condition is performed using the same electrode in a lithium cell with sulfur loading raised up to 6.5 mg cm^{-2} and E/S ratio limited to 7 µl mg^{-1} at C/10 (**Figure 5(e, f)**). The related voltage profiles (**Figure 5(c, e)**) show for both the measurements a relevant slope of the discharge plateaus evolving between 2.0 and 1.7 V at the first cycle, and suggest a partially hindered kinetics that greatly improve in the subsequent cycles by the ongoing of the activation. Hence, the subsequent profiles display well defined double discharge plateaus between 2.3 and 1.9 V and merged charge steps evolving from 2.3 to 2.4 V ascribed to the reversible Li-S conversion process. The corresponding capacity trends (**Figure 5(d, f)**) well highlight the progressive enhancement of the cycling behavior during the first 5–10 cycles as the discharge capacity increases from initial values of 380 mAh g^{-1} at C/5 (**Figure 5(d)**) and 550 mAh g^{-1} at C/10 (**Figure 5(f)**) to maximum values of 720 and 760 mAh g^{-1}. At the end of the test, the cells cycled at C/5 and C/10 deliver capacities of 555 and 430 mAh g^{-1}, with a retention of 77% and 65%, respectively, with respect to the maximum achieved values. Both cells demonstrate a coulombic efficiency approaching 99% after the first cycles, despite sporadic falls possibly ascribed to small dendrites or minor electrode detachment. Relevantly, the Li-S systems deliver promising areal capacities (additional right y-axes in **Figure 5(d, f)**) referred to the geometric

electrode area of 1.54 cm^2. Indeed, the cell cycled at C/5 has a maximum value of 3.6 mAh cm^{-2} and approaches 3 mAh cm^{-2} at the steady state, while values of ~ 5 and ~ 4 mAh cm^{-2} are achieved at C/10, respectively. Therefore, the above tests suggest the Li-S cells with current collector coating as suitable materials even under practical (6.5 mg cm^{-2} and 7 µl mg), operative conditions such as increased sulfur loading, limited E/S ratio, and thin layer configuration, which are certainly requested for boosting both the gravimetric and the volumetric energy densities, and finally scaling-up the battery. In this work we focus the attention on the fundamental role of the current collector by comparing bare aluminum and a thin three-dimensional carbon-coated aluminum, which enhances the Li-S performance through increased porosity and avoid, at the same time, excessive thickness, and weight of the sulfur electrode.

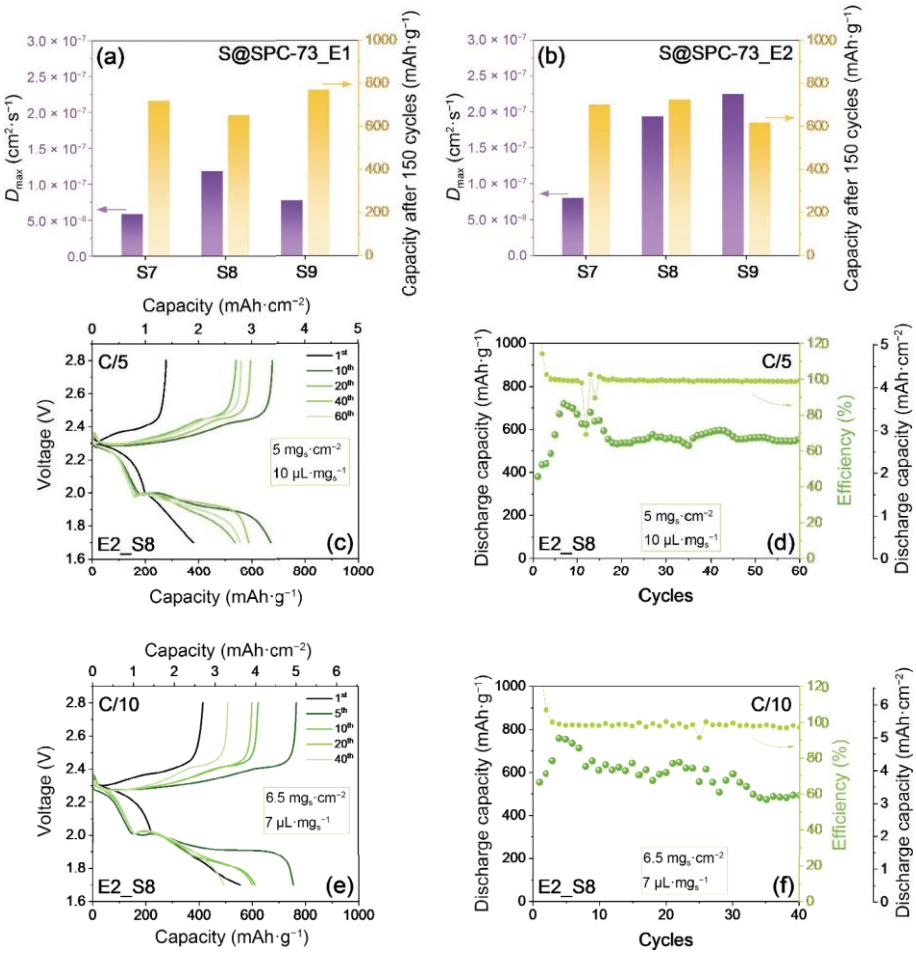

Figure 5. (**a, b**) comparison of the maximum D_{max} values (left *y*-axis) calculated by Randles–Sevcik equation (*Eq (1)*). **(c, e)** Voltage profiles and **(d, f)** cycling trends of Li|DOL:DME, 1 m LiTFSI, 1 m $LiNO_3$|S@SPC-73_E2_S8 cells cycled either **(c, d)** at C/5 with sulfur loading of 5 mg cm^{-2} and E/S ratio of 10 µl mg^{-1}, or **(e, f)** at C/10 with sulfur loading of 6.5 mg cm^{-2} and E/S ratio of 7 µl mg^{-1}. Electrode geometric area: 1.54 cm^2. Voltage range: 1.7–2.8 V. Tests performed at 30 ºC.

References

(36) D. Di Lecce, V. Marangon, W. Du, D. Brett, P. Shearing, J. Hassoun, J. Power Sources 2020, 472, 228424.
(37) Yuan, Z.; Peng, H. J.; Huang, J. Q.; Liu, X. Y.; Wang, D. W.;Cheng, X. B.; Zhang, Q. Adv. Funct. Mater. 2014, 24, 6105.
(38) Y. Y. Zhang; Z. Gao, N. N. Song, J. J. He, X. D. Li, Mater. Today Energy 2018,9, 319
(39) V. Marangon, D. Di Lecce, F. Orsatti, D. Brett, P. Shearing, J. Hassoun, Sustain. Energy Fuels 2020, 4, 2907.
(40)V. Marangon, D. Di Lecce, D. Brett, P. Shearing, J. Hassoun, J. Energy Chem. 2022, 64, 116.

1.3 On the electrolyte choice

Since not disclosed in the previous section, herein we discuss about electrolytes to drive safe and efficient Li-S battery operation, requiring optimal compatibility with lithium metal and chemical stability towards the LiPS intermediates. In this regard, electrolytes commonly used for LIB, based on carbonate solvents as diethyl carbonate (DEC) and ethylene carbonate (EC) cannot be considered for application in Li-S batteries, due to the marked reactivity with LiPS that lead to their deterioration (**Figure 1**).[41]

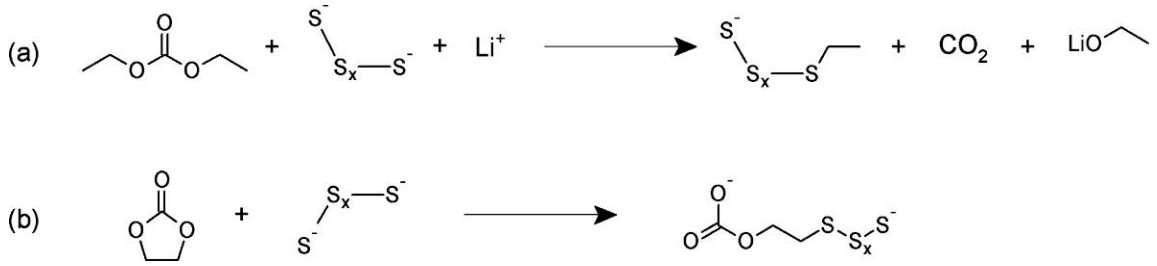

Figure 1. Proposed reactions between polysulfides and either **(a)** DEC or **(b)** EC solvents.[41]

Ethers were indicated as good candidate for application in Li-S batteries due to their higher stability towards the polysulfide intermediates.[42] Furthermore, the limited electrochemical stability window of these solvents (oxidation at around 4.0 V *vs* Li^+/Li) is compatible with Li-S battery operation (< 3.0 V *vs* Li^+/Li), while prevents their application in high-voltage lithium-ion batteries.[43] Nowadays, the binary mixture of DOL (**Figure 2a**) and DME (**Figure 2b**) combined by the 1:1 volume ratio is considered as the baseline electrolyte solvent for Li-S battery due to low viscosity, suitable stability towards both lithium and polysulfides, and compatibility with lithium salts.[44,45] In particular, lithium bis(trifluoromethanesulfonyl)imide (LiTFSI, $LiN(SO_2)_2(CF_3)_2$), lithium bis(fluorosulfonyl)imide (LiFSI, $LiN(SO_2)_2F_2$) and lithium

trifluoromethanesulfonate (lithium triflate, $LiSO_3CF_3$) conductive salts are commonly used in efficient electrolytes for Li-S batteries due to their high ionic conductivity and stability of the respective anions.[46] Despite the premises, a highly conductive and stable electrolyte is not sufficient to allow stable cycling of Li-S batteries due to the "shuttle" mechanism of the polysulfides and their parasitic reactions at the lithium metal anode.[47]

In this regard, a major breakthrough was achieved through the acknowledgement of the solid electrolyte interphase (SEI) concept, that is, a passivation layer that forms on the lithium surface due to partial reduction of the electrolyte components, protects the anode from undesired reactions and hinders the formation of dendrites.[48] The cleavage of the cyclic structure of the DOL solvent is reported to promote the formation of a stable SEI,[49] however, the addition of sacrificial agents to the electrolyte solution is by now a consolidated strategy to form a SEI layer through reduction on lithium surface.[50] $LiNO_3$ received particular attention since it was firstly proposed and several studies led to the understanding of its simple and effective SEI formation mechanism by reduction at the lithium surface that involves the precipitation of several LiN_xO_y species, making it nowadays the most common additive for Li-S batteries electrolytes.[51] The safety hazards linked to the use of lithium metal can be further limited by employment of low flammable electrolyte solvent. End-capped ethers (*glymes*) with $CH_3O(CH_2CH_2O)_nCH_3$ formula and low *n* value (**Figure 2c-f**) are liquid at room temperature and are characterized by higher flash point with respect to the flammable and volatile DOL and DME.[52] These solvents have suitable compatibility with the common conductive lithium salts, and lithium metal batteries combining glyme-based electrolytes and cathodes exploiting different chemistries such $LiFePO_4$, $LiCoO_2$, NMC or graphite revealed promising performances.[53]

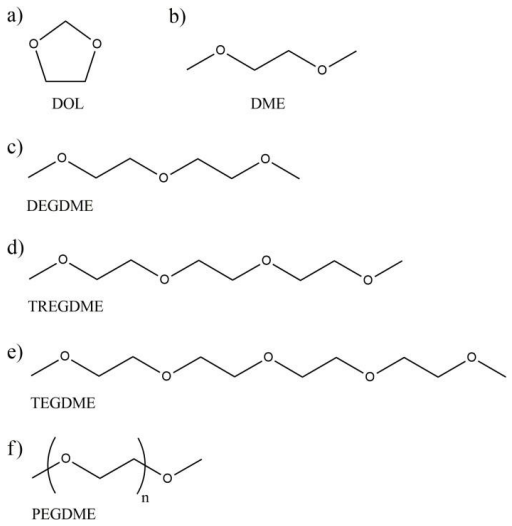

Figure 2. Molecule structures of various ether solvents employed for Li-S battery electrolytes. In particular: **(a)** DOL, **(b)** DME, **(c)** diethylene glycol dimethyl ether (DEGDME, n = 2), **(d)** triethylene glycol dimethyl ether (TREGDME, n = 3), **(e)** tetraethylene glycol dimethyl ether (TEGDME, n = 4) and **(f)** polyethylene glycol dimethyl ether (PEGDME).

Intensive work has been recently devoted to the study of the interaction between the Li^+ ions and the glyme molecules, as the study of glyme-based electrolytes exploiting high concentrations of lithium salts, usually described as solvent-in-salt solutions or solvate ionic liquids, revealed superior transport properties, high oxidative and thermal stability, and formation of an improved SEI.(54) The unique characteristics of these solvents also allow notable performance of semi-liquid Li- S batteries exploiting "catholytes", that is, lithium polysulfides(LiPS)-enriched conductive solutions which act as both cathode and electrolyte.(55) This innovative formulation prevents dissolution of sulfur from the cathode and may efficiently operate as active material with no need of solid sulfur at the positive side thank to the electrochemical activity of the dissolved polysulfides.(56) Solid polymer electrolytes are also of great interest to achieve safe rechargeable lithium batteries. In particular, solid polymer electrolytes based on polyethylene oxide (PEO) exhibit excellent thermal, mechanical and electrochemical stability, negligible volatility, efficient dendrites suppression, and their compatibility with conductive lithium salts lead to suitable Li^+ transport characteristics.(57) Nevertheless, the high molecular weight of PEO causes excessive crystallinity at room temperature that forces its application only at temperatures above 65 °C, that is, when PEO amorphous state is reached and adequate ionic conductivity (10^{-4} S cm^{-1}) is obtained.(58) Ceramic fillers such as TiO_2, SiO_2, Al_2O_3 or ZrO_2 are widely employed to promote the polymer amorphous state, however, operative temperatures around 60 °C are still needed.(59) Thus, more effort is required to optimize

solid- state polymer electrolytes, especially upon the promising results of lithium batteries exploiting both insertion and sulfur-based conversion electrodes.[60,61]

References

(41) J. Gao, M. A. Lowe, Y. Kiya, H. D. Abruña, J. Phys. Chem. C 2011, 115, 25132.
(42) C. Barchasz, J.-C. Leprêtre, S. Patoux, F. Alloin, Electrochim. Acta 2013, 89, 737.
(43) L. Wang, Y. Ye, N. Chen, Y. Huang, L. Li, F. Wu, R. Chen, Adv. Funct. Mater. 2018, 28, 1800919.
(44) K. Xu, Chem. Rev. 2004, 104, 4303.
(45) D. Aurbach, J. Power Sources 2000, 89, 206.
(46) E. Peled, S. Menkin, J. Electrochem. Soc. 2017, 164, A1703.
(47) D. Aurbach, E. Pollak, R. Elazari, G. Salitra, C. S. S. Kelley, J. Affinito, J. Electrochem. Soc. 2009, 156, A694.
(48) H. Zhang, G. G. Eshetu, X. Judez, C. Li, L. M. Rodriguez-Martínez, M. Armand, Angew. Chemie Int. Ed. 2018, 57, 15002.
(49) S. S. Zhang, Electrochim. Acta 2012, 70, 344.
(50) S. Xiong, K. Xie, Y. Diao, X. Hong, J. Power Sources 2014, 246, 840.
(51) A. Rosenman, R. Elazari, G. Salitra, E. Markevich, D. Aurbach, A. Garsuch, J. Electrochem. Soc. 2015, 162, A470.
(52) T. Tamura, T. Hachida, K. Yoshida, N. Tachikawa, K. Dokko, M. Watanabe, J. Power Sources 2010, 195, 6095.
(53) S. Seki, K. Takei, H. Miyashiro, M. Watanabe, J. Electrochem. Soc. 2011, 158, A769.
(54) Y. Gambe, Y. Sun, I. Honma, Sci. Rep. 2015, 5, 8869.
(55) D. Shanmukaraj, S. Lois, S. Fantini, F. Malbosc, M. Armand, Chem. Mater. 2018, 30, 246.
(56) L. Carbone, M. Gobet, J. Peng, M. Devany, B. Scrosati, S. Greenbaum, J. Hassoun, ACS Appl. Mater. Interfaces 2015, 7, 13859.
(57) F. Croce, G. B. Appetecchi, L. Persi, B. Scrosati, Nature 1998, 394, 456.
(58) D. Di Girolamo, S. Panero, M. A. Navarra, J. Hassoun, J. Electrochem. Soc. 2016, 163, A1175.
(59) I. Gracia, H. Ben Youcef, X. Judez, U. Oteo, H. Zhang, C. Li, L. M. Rodriguez-Martinez, M. Armand, J. Power Sources 2018, 390, 148.
(60) L. Carbone, J. Hassoun, Ionics. 2016, 22, 2341.
(61) X. Judez, H. Zhang, C. Li, G. G. Eshetu, Y. Zhang, J. A. González-Marcos, M. Armand, L. M. Rodriguez-Martinez, J. Phys. Chem. Lett. 2017, 8, 3473.

1.4 Alternatives to Lithium metal and graphite anode

The main reason for the commercial limitations of rechargeable lithium batteries lies in the reactivity of the alkali metal and in the related passivation and instability phenomena at its interface. Passivation limits the cyclability of the entire battery while instability, especially when caused by abuse or malfunctioning operations, may lead to a serious safety hazard. As discussed above, a safe use of lithium metal anode in a rechargeable LIB or Li-S battery is made possible by adopting safe electrolyte media containing sacrificial additives that form a protective SEI on the lithium surface which mitigates the parasitic "shuttle" mechanism and hinders the growth of dangerous metallic dendrites.[62] Despite the notable improvements, the reactivity of lithium metal may still pose relevant safety issues that could prevent the actual use of high-energy sulfur-based devices. Furthermore, lithium is a geo-localized element and its high price heavily affects the production of lithium batteries.[63] Concerning the anode materials, lithium titanium oxide ($Li_4Ti_5O_{12}$, LTO) is commercially employed thank to the safety content provided, allowed by relevant thermal stability and by the working voltage of 1.5 V *vs* Li^+/Li that avoids lithium plating upon charge.[64] Furthermore, tin (Sn), silicon (Si) and their oxides are naturally abundant and the electrodes based on their Li-alloys allow the exchange of multiple Li^+ ions per molar unit of metal, leading to capacity values ranging from 500 to 1000 mAh g^{-1} with respect to the limited 372 mAh g^{-1} related to graphite.[65]

#2 10.1016/j.jpowsour.2024.234059

A lithium-ion battery with cycling stability promoted by the progressive activation of a silicon oxide anode in graphene-amorphous carbon matrix

We propose a new anode configuration where nanometric SiO_2 is employed in a hydrothermal synthesis pathway which includes its partial reduction to achieve the SiO_x phases. The composite material benefits of an amorphous carbon matrix deriving from sucrose and of the addition of few-layer graphene. The FLG, which is produced via low-cost liquid-phase exfoliation of graphite, guarantees enhanced mechanical stability of the electrode and remarkable improvement of electron conductivity. The composite anode material is investigated in terms of structure, morphology, alongside thermal behavior to determine the SiO_x content. The applicability of the electrode is initially evaluated in lithium half-cell through CV and galvanostatic cycling, then, the SiO_x-based anode is combined with a $LiNi_{0.33}Co_{0.33}Mn_{0.33}O_2$ layered cathode in a Li-ion battery. Prior to application, the anode is chemically pre-lithiated via direct contact with lithium metal for short time, thus avoiding possible cell unbalancing due to the characteristic irreversible side process of the Li-alloying material at the pristine state. The full-cell demonstrates high capacity, wide rate capability, and long cycle life promoted by the progressive activation of the anode, which compensates the over-charging of the cathode during cycling. In addition, ex-situ structural and morphological studies show a notable retention of both electrodes, thus justifying the remarkable cell stability and the suitability of the new Li-ion battery.

Experimental

- Synthesis and characterization of the anodic composite material

The SiO_x-based composite material (indicated as SiO_x-CM) was synthetized according to the hydrothermal procedure reported here- after. 2.4 g of sucrose (≥99.0%, Fluka Analytical) was dissolved in 20 ml of a water/isopropanol solution (1:1 v/v) and added to a mixture of 0.350 g of fumed silica powder (SiO_2, average particles size: 0.007 μm, Sigma-Aldrich) and 0.150 g of FLG (produced via WJM method by BeDimensional S.p.A.).ref The mixture was sonicated at 50 °C for 2 h and poured into a sealed Teflon-lined stainless steel autoclave reactor, which was heated at 190 °C for 12 h through an oven and then naturally cooled at room temperature. The obtained product was retrieved from the autoclave and dried on a plate at 75 °C until complete solvent evaporation. Afterwards, the solid was annealed at 800 °C for 6 h under Ar/H2 flow (5 % H_2, 2 ml min^{-1}) using a temperature increasing rate of 10 °C min^{-1} via a tubular furnace (GHA, Carbolite). The obtained composite material was ground into an agate mortar to obtain a fine black powder. The sample structure was investigated by X-ray diffraction (XRD) through a Bruker D8 Advance instrument equipped with a Cu Kα radiation source scanning the 10°–90° 2θ range using a step size of 0.02° and rate of 10

s per step. TGA was per- formed between 25 and 1000 °C using a heating rate of 5 °C min^{-1} in dry air flow (60 ml min-1) with a Mettler-Toledo TGA 2 instrument. Morphology was investigated by SEM through a Zeiss EVO 40 relying on a LaB6 thermionic gun and by transmission electron microscopy (TEM) through a Zeiss EM910 equipped with a tungsten thermionic electron gun operating at 100 kV. The sample for TEM analyses consisted of a suspension of the SiO_x-CM in ethanol which was drop-cast onto a formvar/carbon supported copper grid (150 mesh). Energy dispersive X-ray spectroscopy (EDS) was carried out on the SEM images via a X-ACT detector associated with the SEM equipment.

- Preparation of electrodes

The electrode tapes were prepared by casting via a doctor blade tool (MTI Corp.) set at ~350 µm of slurries formed by 80 wt% active material powder, namely SiO_x-CM, , $LiNi_{0.33}Co_{0.33}Mn_{0.33}O_2$ (NCM, synthetized as reported in previous work),[66]10 wt% polyvinylidene fluoride (PVdF 6020, Solef) polymer binder, and 10 wt% SPC electron conductor dispersed in N-methyl-2-pyrrolidone (NMP, Sigma-Aldrich). The slurries were cast on copper foil (thickness of 20 µm, MTI Corp.) for SiO_x-CM, or aluminum foil (thickness of 15 µm, MTI Corp.) for NCM. The SiO_x-CM foil was dried at room temperature under air atmosphere overnight to remove the NMP solvent, while the NCM tape was heated for 3 h at 70 °C on a hot plate under a fume hood. The obtained foils were calendared using an MSK-2150 Rolling Machine (MTI Corp.) to achieve a thickness of ~80 µm and cut into discs with diameter of 14 mm (1.54 cm^2 geometric area) with a Nogami handheld punch. The electrodes were dried under vacuum for 3 h at 110 °C inside a Büchi oven and were subsequently stored inside an Ar-filled glovebox (MBraun, O_2 and H_2O contents lower than 1 ppm). The electrodes had an active material loading ranging from 2.18 to 3.12 mg cm^{-2} for SiO_x-CM and between 2.23 and 2.29 mg cm^{-2} for NCM.

- Electrochemical measurements

CR2032 coin-type cells (MTI Corp.) were assembled inside an Ar-filled glovebox by stacking a 14 mm-diameter lithium metal disc (0.25 mm thickness, MTI Corp.) as counter electrode, a 16 mm glass fiber Whatman (GF/B) disc as separator soaked with the LP-30 electrolyte (battery grade, Sigma-Aldrich, see composition below), and a SiO_x-CM or a NCM disc as working electrode. The LP-30 electrolyte consisted of a solution formed by dry EC and DMC mixed in the 1:1 v/v ratio dissolving hexafluorophosphate ($LiPF_6$) conductive salt with concentration of 1 M. The electrochemical behavior of SiOx-CM was studied through CV and EIS employing a VersaSTAT MC Princeton Applied Research (PAR-AMETEK) multichannel potentiostat. CV was performed within the 0.01–2.0 V vs. Li^+/Li potential range at a scan rate of 0.1 mV s^{-1}, while EIS spectra were collected at the open circuit voltage (OCV) condition before cycling and upon 1, 5 and 10 CV runs using an alternate voltage signal of 10 mV in the frequency range between 500 kHz and 100 mHz. The Li|SiO_x-CM half-cells were galvanostatically cycled between 0.01 and 2.0 V either at constant current rate of 50 mA g^{-1} and 120 mA g^{-1} (for Li|SiO_x-CM), or by applying various current rates increasing every 10 cycles from 20 mA g^{-1} to 40, 80, 120, and 240 mA g^{-1} before decreasing back to 20 mA g^{-1} at the 51st cycle (for both materials). The Li|NCM half-cells were cycled between 3.0 and 4.4 V at the constant rate of C/3 (1C = 278 mA g^{-1}). Full-cells were assembled by stacking a pre-lithiated SiO_x-CM anode (indicated as Li_ySiO_x-CM) and a NCM cathode separated by a 16 mm glass fiber Whatman (GF/B) disc soaked with the LP-30 solution. Chemical pre-lithiation of SiO_x-CM to achieve the Li_ySiO_x-CM configuration was performed via direct contact of the

pristine electrode surface with a lithium metal foil in presence of the LP-30 electrolyte for 10 min under a pressure of 2 kg cm^{-2}. The performance of the Li_ySiO_x-CM electrode was evaluated in first place in lithium half-cell via galvanostatic cycling between 0.01 and 2.0 V at the constant rate of 120 mA g^{-1}. The full Li_ySiO_x-CM|NCM cells have used initial negative to positive ratio (N/P) around 1.33 determined by considering the initial capacity achieved in the respective half-cells which were tested separately, i.e., 0.4939 mAh for NCM during discharge (Li-intercalation) and 0.6577 mAh for Li_ySiO_x-CM during charge (Li-dealloying/deinsertion) with active material loading of 2.23 mg cm^{-2} and 2.37 mg cm^{-2}, respectively. It is worth mentioning that an initial N/P of 1.12 can be also calculated by taking into account the first discharge (Li-alloying/insertion) of Li_ySiO_x-CM and the first charge (Li-deintercalation) of NCM, which would be in line with the discharged state of the as-assembled full-cell. However, we considered the N/P of 1.33 as the practical value corresponding to the reversible discharge of the cathode and of the full-cell, i.e., the power generation process of the battery. The electrochemical performances of the Li_ySiO_x-CM|NCM full-cell were evaluated through galvanostatic cycling in the 2.0–4.4 V voltage range either at C/3 constant rate, or by applying various rates increasing every 20 cycles from C/3 to C/2, 1C, 2C, and 3C before lowering back the current to C/3 at the 101st cycle.

Results

The structural features of SiO_x-CM are investigated by XRD, as reported in **Figure 1a**. The SiO_x-CM pattern exhibits a predominant narrow peak centered at $2\theta = 26.4°$ corresponding to graphite (002) planes originated by partial stacking of the FLG flakes, while the broad signal extending from $2\theta = 13°$ to $2\theta = 39°$ identifies the amorphous silicon oxide, and may also account for amorphous carbon derived from the annealing of the sucrose. The absence of impurities is demonstrated by the exclusive presence of carbon and silicon oxide, suggesting the feasibility of the synthesis pathway. The fraction of silicon oxide is detected through TGA and corresponding DTG performed under air flow to remove the carbon component by oxidation, as reported in **Figure 1**. The thermograph evidences an initial mass loss of 3% due to absorbed water removal, followed by a relevant step at 600 °C and a second slope between 650 and 850 °C, ascribed to the carbon in the sample. Considering the steady state region achieved over 900 °C, the TGA indicates a total C content of 65% and a SiO_x residue of 35 %. Interestingly, the first step at 600 °C can be associated with the combustion of the more exposed amorphous carbon fraction deriving from sucrose annealing, whereas the second one between 650 and 850 °C is related with the flat, low-surface area FLG flakes. The SEM images of the SiO_x-CM sample displayed in **Figure 1c** and d shows micrometric domains with size ranging from 10 to 50 μm composed of a uniform framework of amorphous carbon and flat FLG flakes, while the nanometric SiO_x particles are identified by the TEM micrographs in **Figure 1(e, f)**. The TEM images allow the discerning between SiO_x particles with size below 5 nm and the FLG flakes which reach sizes of 500 nm (**Figure 1e**), while suggesting embedment of the

SiO_x bunches in the amorphous carbon matrix (**Figure 1f**). The elements distribution in the SiO_x-CM powder is provided by the EDS maps acquired on the SEM image of **Figure 1g** and reported in **Figure 1h–j**. The mapping reveals the expected homogeneous arrangement of C (**Figure 1h**) and evidences a more relevant contribute of Si (**Figure 1i**) with respect to O (**Figure 1j**). This outcome suggests the partial reduction of SiO_2 during synthesis with formation of SiO_x oxides, and possibly elemental Si. In summary, the above reported characterization of the SiO_x-CM sample indicates suitable mixing of SiO_x nanometric particles with submicron and even micrometric domains of amorphous carbon and FLG, which are expected to buffer the volume expansion during Li–Si alloying process, increase the electrode conductivity, and promote the structural stability of the composite material.[67]

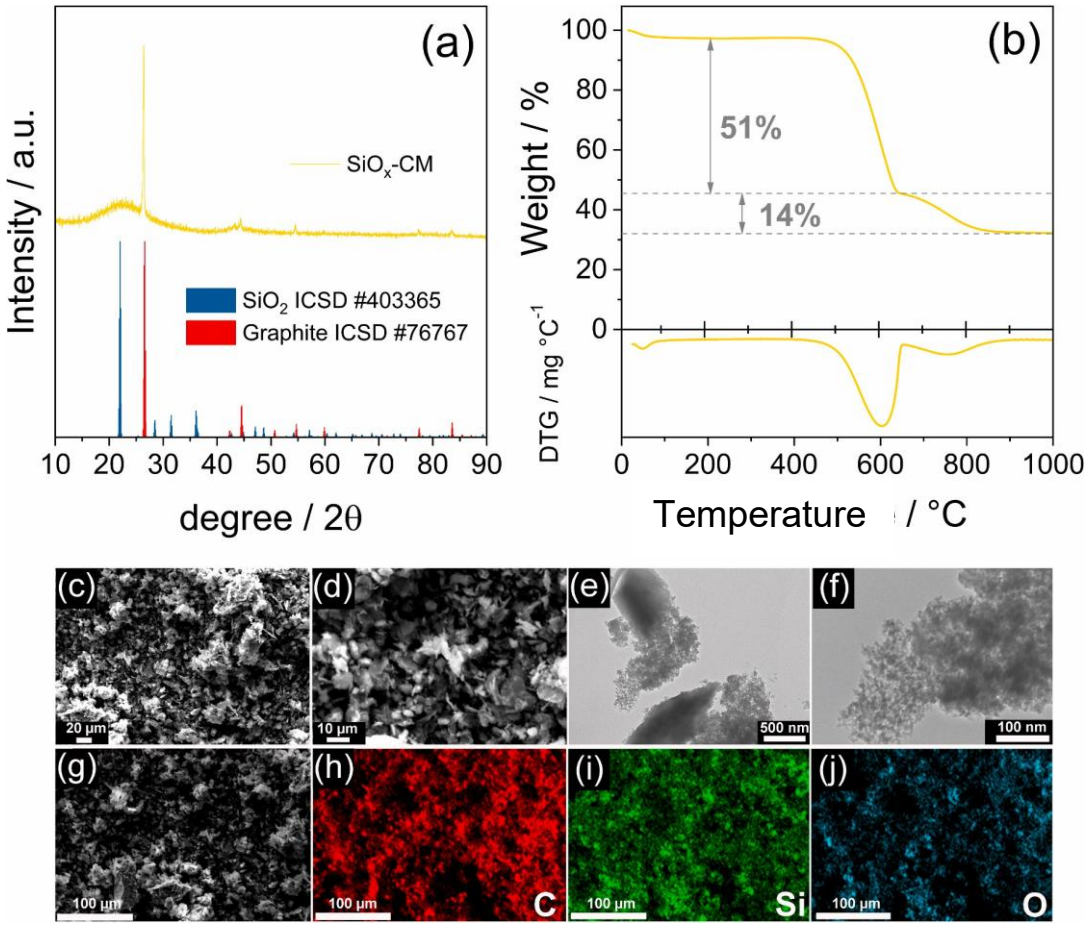

Figure 1. Physical-chemical characterization of the SiO_x-CM sample, in detail: **(a)** X-ray diffractogram, reference data for SiO_2 (blue, ICSD #403365) and graphite (red, ICSD #76767) are reported for comparison; **(b)** TGA performed under air flow with heating rate of 5 °C min^{-1} from 25 to 1000 °C (top panel) and corresponding DTG (bottom panel); **(c–j)** morphological analyses, that is, **(c, d)** SEM images recorded in secondary electrons mode at various magnifications, **(e, f)** TEM images with various magnification, **(g)** SEM image with **(h–j)** corresponding EDS elemental maps of **(h)** C, **(i)** Si and **(j)** O.

Figure 2 shows the evaluation of the electrochemical features of the SiO_x-CM electrode in

lithium half-cell by performing CV and EIS. The voltammograms of **Figure 2a** reveal during the first cathodic scan a broad wave centered at about 0.6 V vs. Li^+/Li indicating partial irreversible reduction of the electrolyte with formation of a protective SEI layer at the electrode interface.[68] Subsequently, two reduction signals are detected at 0.1 and 0.01 V vs. Li^+/Li ascribed to reduction of SiO_x with formation of lithium-silicates, partial Li-alloying with silicon, and Li insertion into the carbon matrix.[69] The first anodic scan evolves with two peaks at 0.20 and 0.25 V vs. Li^+/Li, accounting for the de-insertion of Li from the carbon matrix, and the dealloying of the Li–Si species to Li and Si.[70] The subsequent cycles (inset reports magnification) evidence the modification of the potential profiles with the definition of reduction peaks at 0.20, 0.05 and 0.01 V vs. Li^+/Li reflected during oxidation at 0.15, 0.20 and 0.25 V vs. Li^+/Li in agreement with the reversible Li–Si (de)alloying process, and Li (de)insertion in the carbon structure of the electrode.[71] In addition, the repeated CV runs reveal a decrease of cell polarization, the increase of the current peak intensity, and the improvement of the overlapping of the profiles, thus suggesting electrochemical activation of the electrode/electrolyte interphase as well as progressive stabilization of the electrode structure and of the SEI layer.[71] The observed interphase activation indicates the effectiveness of the carbon matrix achieved herein in buffering the volume variation associated to the (de)lithiation of the SiO_x/Si particles, which results in a remarkable stability of the electrode and promotes the kinetics of the electrochemical process. The EIS spectra in **Figure 2b** recorded at the OCV condition of the cell (inset) and after 1, 5 and 10 CV scans also highlight the improvement of conductivity upon cycling. The NLLS analysis of the Nyquist plots allows the evaluation of various resistive and capacitive components of the cells through the description of the spectra with an equivalent circuit.[72] Hence, the cell can be represented by the $R_e(R_nQ_n)Q_w$ circuit described as following: *i)* R_e related to the electrolyte bulk resistance obtained by high frequency intercept of the plot; *ii)* (R_nQ_n) elements (with n = 1, 2, …) accounting for the electrode/electrolyte interphase phenomena, including possible charge transfer processes and SEI formation, identified by the high-middle frequency semicircles, the total width of which allows the determination of the total interphase resistance (R_i); *iii)* Q_w constant phase element (CPE) due to the semi-infinite Warburg-type Li^+ ion diffusion represented by the tilted line at low-frequency values.[73] **Table 1.4.1** summarizes the NLLS results, and reveals an interphase resistance value of about 90 Ω at the OCV that decreases to 9 Ω after the first cycle and stabilizes around 6 Ω after 10 CV scans. Furthermore, the table shows the modification of the equivalent circuit after 1 cycle and the shrinking of the (R_nQ_n) elements. The remarkable decrease of the resistance upon cycling

and the related changes of the equivalent circuits are in line with the activation of the electrode/electrolyte inter- phase which improves the conductivity and the reaction kinetics by the ongoing of the electrochemical process. Based on the absence of the peculiar peak related to phase transition upon de-lithiation at 0.44 V, we can exclude the formation of $Li_{15}Si_4$ (crystalline) phase. Yet the amorphous phase (a-Li_xSi), which doesn't exhibit the features at 0.44 V, could still be included in the overall electrochemical activity of the composite anode. This could happen if during the synthesis step under reductive condition, some Si atoms are obtained formed the SiO_x matrix, which could buffer the Si volume expansion upon lithiation and thus posing a kinetic limitation to the $Li_{15}Si_4$ phase formation. However, these considerations are still not corroborated by experimental evidence, thus more extended work is required to fulfill this aspect.

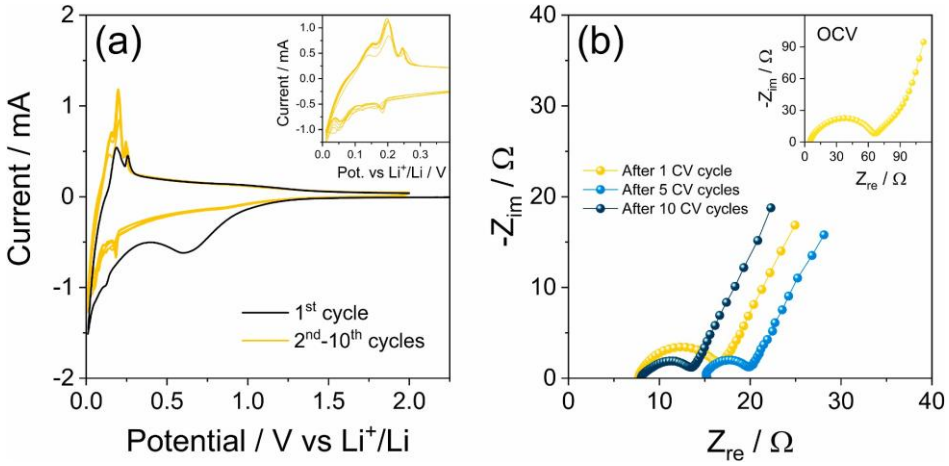

Figure 2. **(a)** CV profiles and **(b)** Nyquist plots recorded by EIS related to a Li|SiO_x-CM half-cell; CV potential range: 0.01–2.0 V vs. Li^+/Li; scan rate: 0.1 mV s^{-1}; EIS performed at the OCV cell condition (inset) and upon CV after the 1st, 5th, and 10th cycle between 500 kHz and 100 mHz; alternate voltage signal: 10 mV.

Table 1.4.1 NLLS analysis carried out on the Nyquist plots displayed in Fig 2b recorded by EIS.

Cell condition	Circuit	R_1 (Ω)	R_2 (Ω)	R_i ($\sum R_n$) (Ω)	χ^2
OCV	$R_e(R_1Q_1)(R_2Q_2)Q_w$	62.2 ± 0.5	27.6 ± 3.9	89.8 ± 3.9	2×10^{-4}
After 1 CV	$R_e(R_1Q_1)Q_w$	8.9 ± 0.1	/	8.9 ± 0.1	6×10^{-5}
After 5 CV	$R_e(R_1Q_1)Q_w$	4.9 ± 0.2	/	4.9 ± 0.2	2×10^{-4}
After 10 CV	$R_e(R_1Q_1)Q_w$	5.8 ± 0.1	/	5.8 ± 0.1	1×10^{-4}

The SiO_x-CM electrode is hereafter galvanostatically cycled in lithium half-cell, as reported in **Figure 3**. **Figure 3a** shows selected voltage profiles from a rate capability test performed by increasing the current rate every 10 cycles from 20 mA g^{-1} to 40, 80, 120 and 240 mA g^{-1}, while the corresponding cycling trend is displayed in **Figure 3b**. The voltage

profiles indicate a reversible electrochemical process centered between 0.3 and 0.4 V including various merged plateaus both in charge and discharge, due to the Li–Si (de)alloying and Li–C (de)insertion processes already described during CV discussion. The curves also show a slight decrease of delivered capacity alongside with a moderate growth of the overvoltage upon current rate increase, as expected by the raise of ohmic polarization. Indeed, the cycling trend in **Figure 3b** exhibits a maximum capacity of 370 mAh g^{-1} achieved during the first cycles at 20 mA g^{-1} and subsequent steady values of 350, 330, 310 and 270 mAh g^{-1} at 40, 80, 120 and 240 mA g^{-1}, respectively. In addition, the electrode recovers 100% of the capacity after decreasing the current rate back to 20 mA g^{-1} at the 51st cycle, thus suggesting remarkable structural retention of the electrode despite cycling at high rates. The cycling trend also evidences a progressive improvement of the delivered capacity during the initial stages of the test, in line with the activation of the electrode/electrolyte interphase observed upon CV and EIS (**Figure 2**). As above mentioned, this activation process includes formation and consolidation of the SEI layer, as well as the progressive stabilization of the electrode structure. This aspect is further evidenced in the prolonged cycling tests performed at either 50 or 120 mA g^{-1} displayed in **Figure 3c–f**. The selected voltage profiles at 50 mA g^{-1} (**Figure 3c**) and 120 mA g^{-1} (**Figure 3e**) reveal in the first discharge the partial reduction of the electrolyte with SEI film formation and the lithiation of the SiO_x particles, occurring between 1.3 and 0.3 V, as well as the typical shape ascribed to the lithium alloying with silicon and the insertion of the Li^+ into carbon below 0.3 V in agreement with the CV tests. On the other hand, the following voltage profiles exhibit at both 50 and 120 mA g^{-1} notable overlapping, constant and low polarization, as well as negligible capacity decay. Indeed, the corresponding cycling trend shows at 50 mA g^{-1} (**Figure 3d**) an initial capacity of 290 mAh g^{-1} which grows to 390 mAh g^{-1} upon activation during the initial 45 cycles and slightly decreases to 350 mAh g^{-1} after 200 cycles, while the test at 120 mA g^{-1} (**Figure 3f**) exhibits initial value of 225 mAh g^{-1}, maximum capacity of 320 mAh g^{-1} and final one of 300 mAh g^{-1}. Therefore, the data indicate a maximum delivered capacity exceeding that of graphite, an outstanding retention of 90% at 50 mA g^{-1} and 94% at 120 mA g^{-1}, and a coulombic efficiency close to 100% steadily held after the initial activation stage. The latter process, already observed during CV discussion, leads to the electrode improvement by cycling which is a favorable trend in view of the application of the anode in a balanced Li-ion battery. Overall, the good performances confirm SiO_x-CM as candidate of relevant interest for application in advanced lithium-ion systems and highlight the suitability of the synthesis pathway employed herein, which improves the dispersion of the oxide particles

within the electrode structure and ensures an efficient carbon matrix to mitigate the side effects of the volume variations upon reversible Li–Si alloying.

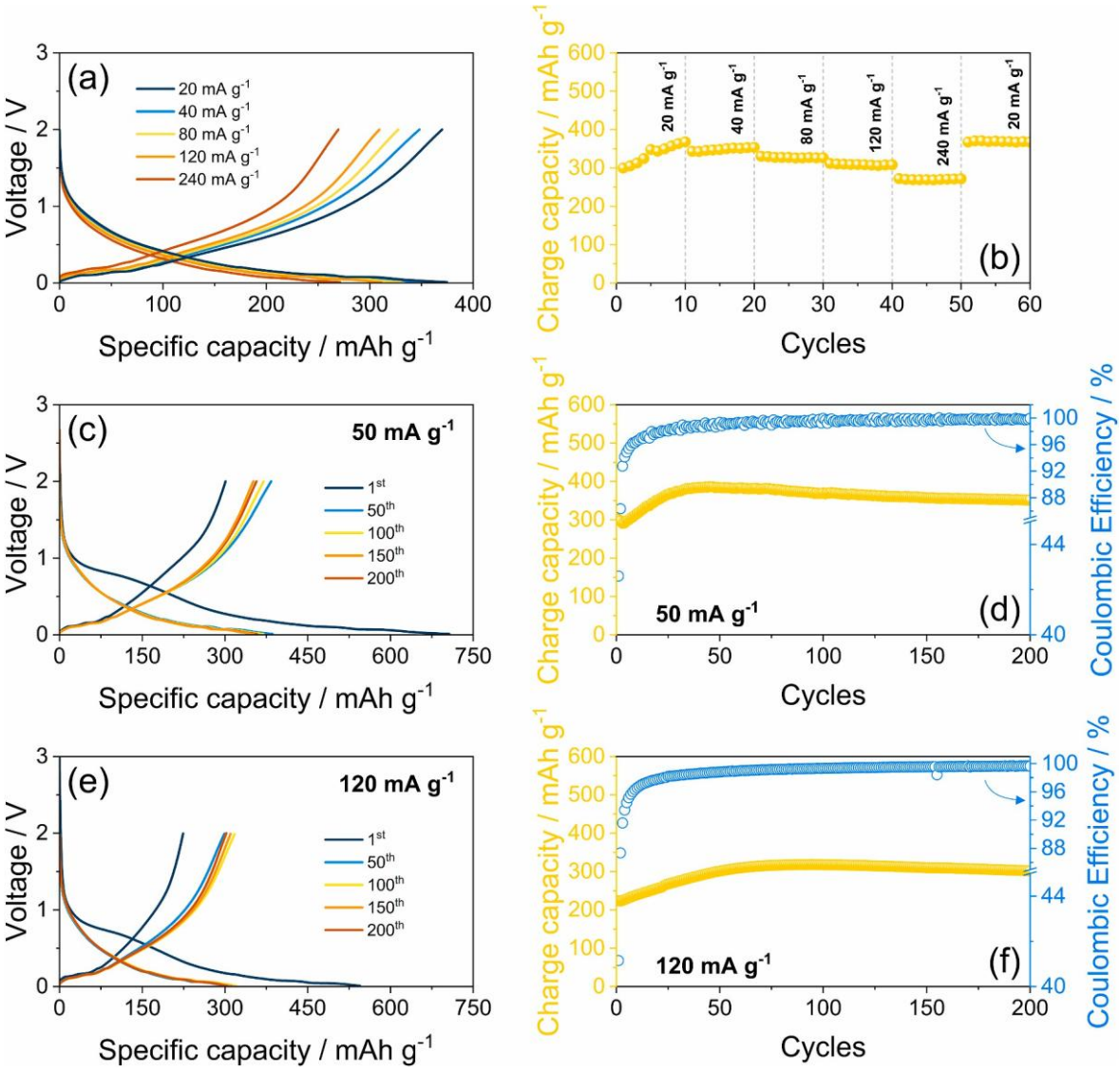

Figure 3. Galvanostatic cycling performance of a Li|SiO_x-CM half-cell, in detail: **(a, b)** rate capability test carried out at increasing current rate of 20, 40, 80, 120 and 240 mA g^{-1} before lowering back to 20 mA g^{-1} after 50 cycles in terms of **(a)** selected voltage profiles and **(b)** charge capacity trend; **(c–f)** prolonged cycling tests performed at either **(c, d)** 50 mA g^{-1} or **(e, f)** 120 mA g^{-1} current rate in terms of **(c, e)** voltage profiles and **(d, f)** corresponding charge capacity trends (right *y*-axes show Coulombic efficiency); voltage range: 0.01–2.0 V. Tests performed at 30 °C.

In order to further investigate the contribution of the various components to the capacity of the SiO_x-CM, blank electrodes using fumed silica (B1), amorphous carbon (B2), and FLG (B3) as active material are prepared and subsequently tested (these electrodes are prepared following the same route described in the Experimental Section). The electrochemical performances of these electrodes in lithium half-cells are evaluated through galvanostatic cycling at 120 mA g^{-1} in **Figure 4**. The voltage profiles at the 25th cycle of the single constituents in **Figure 4a**, namely fumed silica (B1, gray), amorphous

carbon (B2, orange), and FLG (B3, green), and the corresponding cycling trends in **Figure 4b**, evidence the actual electrochemical activity of the three materials. Indeed, the voltage profile of the Li|B3 cell shows two plateaus at ~0.2 and ~0.1 V, originating from the different intercalation types of lithium ions into the graphitic material, with a specific capacity of about 420 mAh g^{-1}. The Li|B2 cell has the typical sloping voltage ascribed to the insertion of Li^+ into the amorphous carbon centered at ~0.5 V with a capacity of 230 mAh g^{-1}. Instead, the Li|B3 cell displays a poor electrochemical response, with a specific capacity limited to 50 mAh g^{-1}, without significant contribute at the low voltage region typically ascribed to the Li-alloying reaction. This outcome suggests the predominant issue of the insulating character of pure SiO_2 in B3, which hinders the alloying process between Li and Si. On the other hand, the SiO_x-CM anode cycled in Li-cell at 120 mAh g^{-1} (**Figure 3e,f**) reveals an initial capacity of 210 mAh g^{-1}, in line with the ratio between SiO_2 (35%), amorphous C (51%) and FLG (14%) detected by TGA (**Figure 1**), and the capacity above achieved by the single components at the same current in Fig. S4 (i.e., 230, 420 and 50 mAh g^{-1}, respectively). However, the SiO_x-CM anode capacity progressively increases to reach a value exceeding 300 mAh g^{-1}, thus indicating the above-mentioned activation of the silica in the composite, which is even more relevant at a current of 50 mA g^{-1} with a maximum capacity approaching 400 mAh g^{-1} (**Figure 3c,d**).

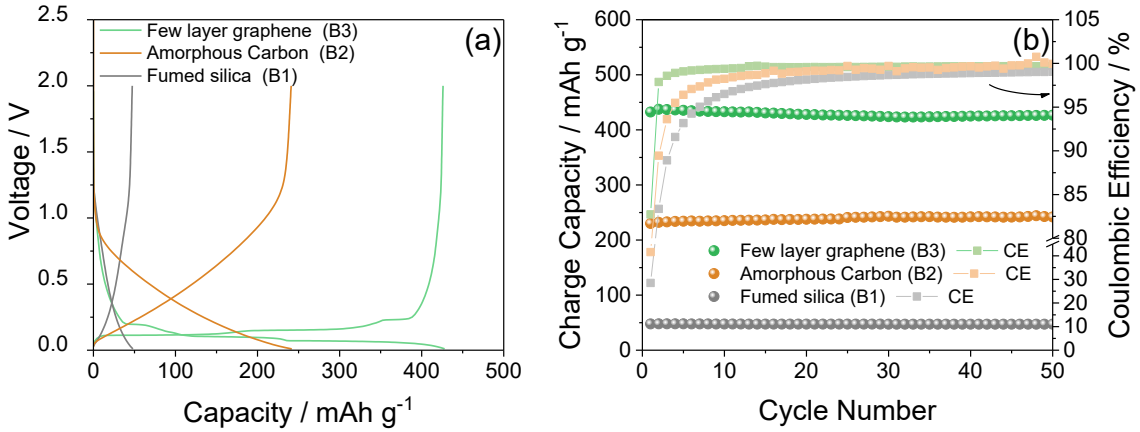

Figure 4. (a) Selected voltage profiles (25th) related to galvanostatic cycling measurements performed on: Li|B1 (gray), Li|B2 (orange), Li|B3 (green) half-cells at constant rate of 120 mA g^{-1}, between 0.01 and 2.0 V, and **(b)** capacity trends (right *y*-axes show coulombic efficiency). Galvanostatic tests performed at 30 °C. Active material loading: 0.65 (B1), 2.29 (B2), and 1.61 (B3) mg cm^{-2}.

Therefore, we have selected the $LiNi_{0.33}Co_{0.33}Mn_{0.33}O_2$ cathode (indicated as NCM) to achieve a full-cell using the SiO_x-CM anode. Prior to cell assembling, the SiO_x-CM electrode is subject to chemical pre-lithiation process through direct contact with a lithium foil soaked with the electrolyte for 10 min to obtain the activated Li_ySiO_x-CM phase, where y represents a sacrificial lithium ions fraction sufficient for compensating the

irreversible capacity during the first cycle of the anode.[74] In fact, this rapid pre-lithiation process increases the anode reversibility during the first cycle and allows a suitable Li^+ ions exchange within the full cell, thus preventing the loss of the Li-ion battery balance during cycling. The above direct chemical reduction promotes a fast and efficient activation of the material for application in a Li-ion cell, thus it can be scalable for other electrochemical energy storage devices such as those using sulfur or oxygen cathode. The N/P ratio to be used in the full Li_y-SiO_x-CM||NCM cell is preliminarily determined by analyzing the cycling performances in lithium half-cell of NCM and Li_ySiO_x-CM electrodes, prepared separately. **Figure 5a** displays the first voltage profile obtained from the above Li||NCM and the Li||Li_y-SiO_x-CM half-cells galvanostatically cycled at C/3 (1C = 278 mA g^{-1}) and 120 mA g^{-1}, respect achieved for anode (**Figure 5a, b**) and cathode (**Figure 5c, d**) allow the construction of the histogram evolution of the N/P displayed in **Figure 6b** which shows the increase from 1.33 at the first cycle to 1.58, 2.11 and 2.29 after 10, 50 and 100 cycles. The increase of the N/P ratio of the full cell upon operation is expected to stabilize the cell voltage into a steady state condition and enable the maximum capacity of the Li_ySiO_x-CM anode. An optimal N/P ratio achieved by cycling can in fact allow a sufficient Li-reservoir for the electrochemical process, and avoid possible anode depletion with consequent decrease of the cell efficiency NCM SiO_x-CM. The chart displays a capacity of 0.4939 mAh upon Li-intercalation in NCM and 0.6577 mAh upon Li-dealloying from Li_ySiO_x-CM, that lead to the determination of a practical N/P of 1.33. Furthermore, the cycling evolution of the above cells reported in **Figure 5** reveals the almost constancy of the cathode capacity, and a remarkable increase of the anode one by the ongoing of the test, due to the progressive electro- chemical activation of the Li_ySiO_x-CM, as discussed both during CV (**Figure 2**) and galvanostatic study (**Figure 3**). This particularly favorable condition actually leads to notable stability of the Li-ion cell, due to the complete absence of anode deterioration or dendrite formation. The electrochemical performance of the Li_ySiO_x-CM|NCM cell, combining fresh pre-lithiated anode and layered cathode having the same mass loadings and a geometric surface area (i.e., 1.54 cm^2) of those in **Figure 5**, are evaluated through galvanostatic cycling at the constant current rate of C/3 (1C = 278 mA g^{-1}). The selected voltage profiles reported in **Figure 6c** show at the first cycle a charge process evolving at about 3.7 V with a capacity of 200 mAh g^{-1} reflected into a discharge capacity of 153 mAh g^{-1}, leading to a coulombic efficiency of 76%. The partial irreversibility and low efficiency at the first cycle of the full-cell are due to the concomitant side oxidation (cathode) and reduction (anode) of the electrolyte during charging. These two irreversible reactions are almost balanced with a

rate of 1.1, calculated by taking the Li-deintercalation capacity of NCM and the Li-alloying capacity of Li_ySiO_x-CM in **Figure 5** at the first cycle. The subsequent profiles of **Figure 6c** show the progressive enhancement of the charge/discharge processes, which are centered at about 3.5 V and reflect at the steady state the combination of the NCM and Li_ySiO_x-CM reversible voltage slopes reported in **Figure 5**. The cycling trend of the Li-ion battery in **Figure 6d** highlights a charge capacity rapidly matching the discharge one, thus leading to a coulombic efficiency of 98% already after 10 cycles, that is subsequently improved and held throughout the entire test. The fast balancing of the Li_ySiO_x-CM|NCM system, including SEI formation and structural stabilization of both the electrodes, allows a remarkable cycle life of 120 cycles with initial discharge capacity of 153 mAh g^{-1} that slightly increases to 157 mAh g^{-1} and exhibits a final value of 141 mAh g^{-1}, resulting in a retention approaching 90%. The excellent cell stability can be certainly ascribed to the optimal cell balance in terms of N/P ratio, which is further promoted by the self-activating trend of the anode, and the progressive improvement of its Li-reservoir role as demonstrated by the histogram in **Figure 6b**. Considering a steady state capacity of 147 mAh g^{-1} (60^{th} cycle) and an average working potential of 3.7 V, the battery is associated to a theoretical energy density of almost 545 Wh kg^{-1} which may correspond to a practical value of 182 Wh kg^{-1} with a correction factor of 1/3 to take into account the inactive parts of the cell (e.g., case, electrolyte and current collectors).[75] The good performances of the Li_ySiO_x-CM|NCM battery are further sup- ported by the rate capability test displayed in **Figure 6e,f**, carried out by increasing the current rate every 20 cycles from C/3 to C/2, 1C, 2C and 3C. The related voltage profiles (**Figure 6e**) show the expected increase of overvoltage associated to the rise of the ohmic-drop by the increase of the current. Nevertheless, the corresponding cycling trend (**Figure 6f**) evidences satisfactory discharge capacity with values of 158, 145, 123, 104 and 91 mAh g^{-1} at C/3, C/2, 1C, 2C and 3C, respectively, with a notable recovering of the 84% of the capacity when the current rate is lowered back to C/3 after 100 cycles. Thus, the SiO_x-CM composite proposed herein gives rise to a Li-ion full system which relies on a fast pre-lithiation procedure of the anode, ensuring high capacity, long life, and suitable operation at high current rates.

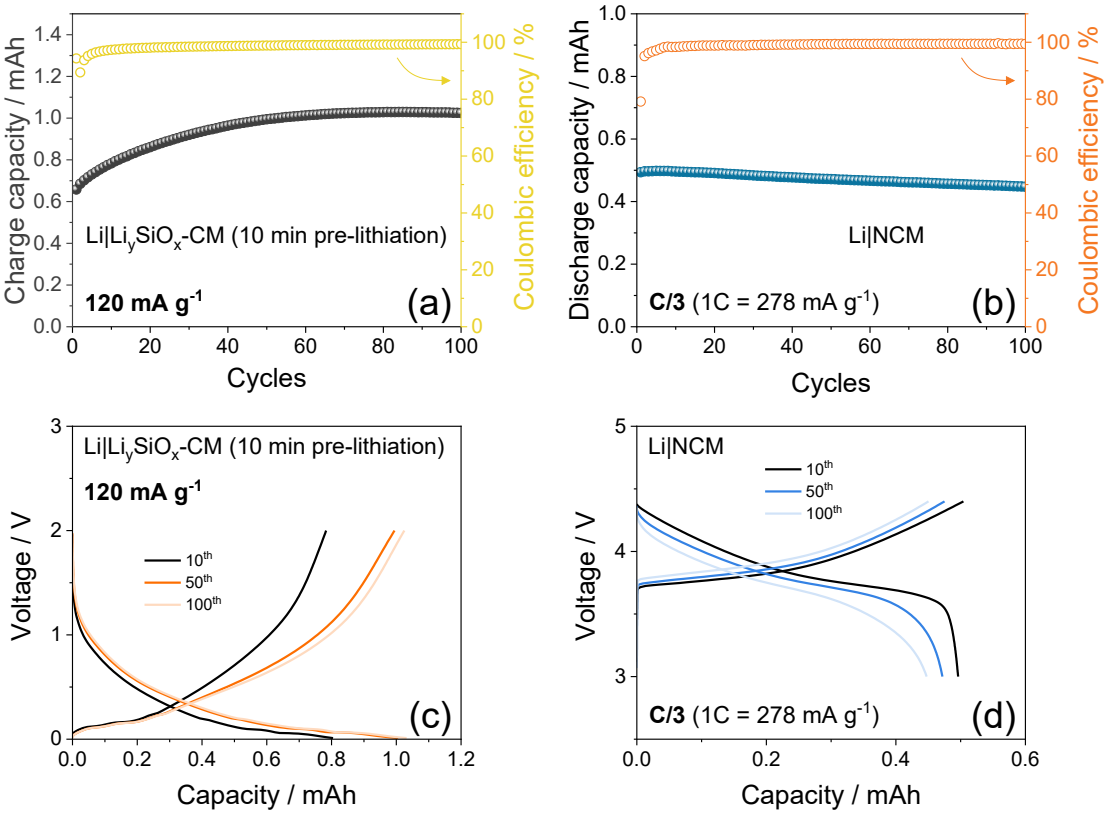

Figure 5. (a, b) Capacity trends (right *y*-axes show coulombic efficiency) and **(c, d)** selected voltage profiles related to galvanostatic cycling measurements performed on: **(a, c)** Li|LiySiOx-CM half-cell at constant rate of 120 mA g^{-1} between 0.01 and 2.0 V and **(b, d)** Li|NCM half-cell at constant rate of C/3 (1C = 278 mA g^{-1}) between 3.0 and 4.4 V. Galvanostatic tests performed at 30 °C.

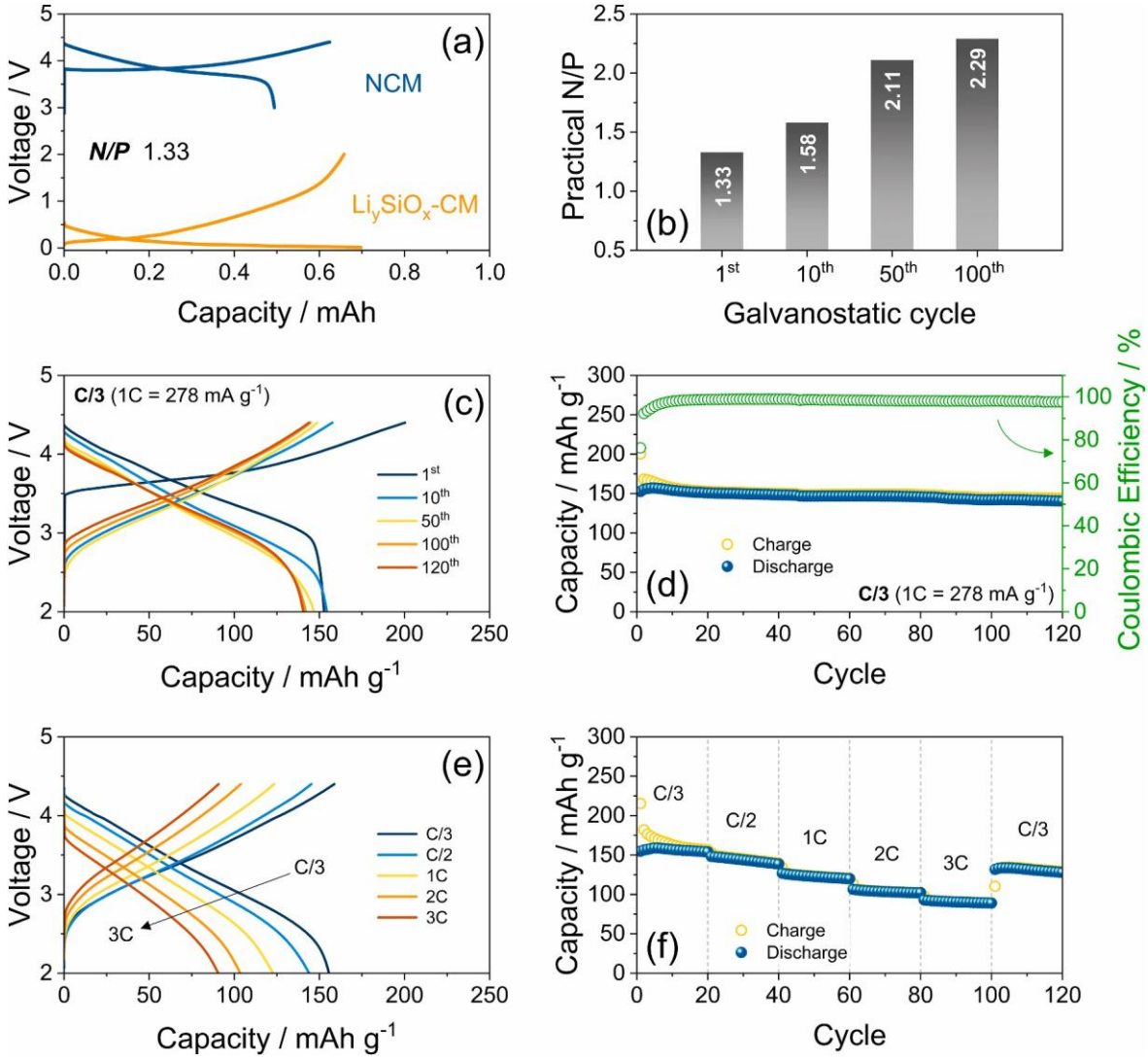

Figure 6. (a) Voltage profiles related to the first cycle of lithium half-cells cycled with SiO_x-CM (orange) or NCM (blue) electrodes120 mA g^{-1} between 0.01 and 2.0 V for SiO_x-CM or at C/3 (1C = 278 mA g^{-1}) between 3.0 and 4.4 V for NCM; **(b)** histogram representation of the practical N/P ratio between SiO_x-CM and NCM capacity evaluated at the 1st, 10th, 50th, and 100th cycle of the active half-cells. **(c–f)** Cycling performance of the Li_ySiO_x-CM|NCM full-cell, in detail: **(c, d)** prolonged test at constant current of C/3 in terms of **(c)** selected voltage profiles and **(d)** cycles trend (right *y*-axis shows Coulombic efficiency); **(e, f)** rate capability test at increasing C-rates of C/3, C/2, 1C, 2C, and 3C before lowering back to C/3 after 100 cycles in terms of **(e)** selected voltage profiles and **(f)** cycles trend. Voltage range: 2.0–4.4 V. Anode pre-lithiation time: 10 min.

References

(62) N. Takami, H. Inagaki, T. Kishi, Y. Harada, Y. Fujita, K. Hoshina, J. Electrochem. Soc. 2009, 156, A128.
(63) L. Liu, F. Xie, J. Lyu, T. Zhao, T. Li, B. G. Choi, J. Power Sources 2016, 321, 11.
(64) D. Aurbach, E. Pollak, R. Elazari, G. Salitra, C. S. S. Kelley, J. Affinito, J. Electrochem. Soc. 2009, 156, A694.
(65) A. Y. S. Eng, V. Kumar, Y. Zhang, J. Luo, W. Wang, Y. Sun, W. Li, Z. W. Seh, Adv. Energy Mater. 2021, 11, 2003493.
(66) D. Di Lecce, P. Andreotti, M. Boni, G. Gasparro, G. Rizzati, J.Y. Hwang, Y.K. Sun, J, ACS Sustain. Chem. Eng. 6 (2018) 3225.

(67) V. Marangon, E. Barcaro, L. Minnetti, W. Brehm, F. Bonaccorso, V. Pellegrini, J. Hassoun, Nano Res. 16 (2023) 8433.
(68) V. Marangon, Y. Tominaga, J. Hassoun, J. Power Sources 449 (2020) 227508,
(69) G.A. Elia, J. Hassoun, Chemelectrochem 4 (2017) 2164.
(70) L. Sbrascini, A. Staffolani, L. Bottoni, H. Darjazi, L. Minnetti, M. Minicucci, F. Nobili, ACS Appl. Mater. Interfaces 14 (2022) 33257.
(71) Q. Sun, B. Zhang, Z.-W. Fu, Appl. Surf. Sci. 254 (2008) 3774.
(72) P. Verma, P. Maire, P. Nov´ak, Electrochim. Acta 55 (2010) 6332.
(73) D. Aurbach, Y. Talyosef, B. Markovsky, E. Markevich, E. Zinigrad, L. Asraf, J. S. Gnanaraj, H.-J. Kim, Acta 50 (2004) 247.
(74) D. Munao, M. Valvo, J. Van Erven, E.M. Kelder, J. Hassoun, S. Panero, J. Mater. Chem. 22 (2012) 1556.
(75) H. Fujimoto, T. Yamaki, K. Shimoda, S. Fujinami, T. Nakatani, G. Kano, M. Kawasaki, Z. Ogumi, T. Abe, J. Electrochem. Soc. 169 (2022) 070507.

1.5 Presentation of the next research outlines

Up to now we initially deal with suitable current collectors for enhancing the conversion process in Li-S battery, and afterwards we briefly discussed glyme-based electrolyte for Li-S systems. Next, we demonstrated experimentally that the conventional graphite-based anode can be replaced by adopting SiO_x-CM which can be opportunely exploited as advanced anode in Li-ion setup. The next sections will deal with similar electrodes (cathodes and anodes) tested in Li-ion, Na-ion, Li-ion-Sulfur, and Li-ion-Oxygen configuration, highlighting their versatility in electrochemical systems leveraging *conversion*-based cathodes. These cathodes are considered low-cost alternative to currently widely-adopted batteries, are environmentally friendly, and boast (theoretically) high energy and power density. The use of safe electrolytes has been pursued by implementing, whenever possible, either non-flammable liquid-electrolyte or polymeric-electrolyte, which are expected to ensure higher safety content due to their solid nature. The results collected in this Thesis show that these new cell chemistries can be practically implemented whenever using non-metallic anode, enabling novel and more efficient battery which may ensure appropriate energy and power density, moderate environmental impact of the raw materials, and equal power supply and distribution across our modern society. **Chapter 2** proposes various strategies to achieve performance of practical interest from sulfur-based batteries, posing focus on the Li-S system and especially on the cathode composition. Section *2.1* deals with the investigation of a novel sulfur-tin-manganese oxide composite, for application in lithium and Li-ion batteries, synthetized either with a scalable method and using a low content of electrochemically inactive Sn conductive nanoparticles and polysulfide retaining agent MnO_2. Herein, an advanced Li-ion-Sulfur full-cell is developed using the SiOx-CM anode. In section *2.2*, by including MWCNTs in limited amount, the S:MWCNTs composite is investigated using modified glyme electrolytes including TEGDME and DOL as co-solvent. Section 2.3 deals with a catholyte and the metal/metal-oxide sulfur cathode, exploited in a high-power setup thanks to the exclusive reaction of long LiPS. Section 2.4 illustrates some recent results regarding Li-ion battery leveraging conversion cathode beyond sulfur, that is a Li-ion-Oxygen full-cell using non-flammable and thermally stable PEGDME based electrolyte and lithiated tin-carbon (Sn-C) nanocomposite. **Chapter 3** focuses on the study and application of polymer (PEGDME and PEO) and glyme-based electrolytes (TEGDME) dissolving opportune salts for Li-ion, Li-S, Li-O_2, and Na-S battery. Prior to application in a battery, the chemical and electrochemical properties of the solutions are evaluated in terms of thermal stability, ionic conductivity, Li^+ (or Na^+) ions

transport number and stripping/deposition overvoltage, electrochemical stability window, and electrode/electrolyte interphase resistance. The characterization is carried out by employing thermogravimetric analyses (TGA), chronoamperometry, EIS, galvanostatic measurements, linear sweep voltammetry (LSV) and CV. Section 3.1 reports the study of PEGDME dissolving LiTFSI and $LiNO_3$ for application using LFP, Sulfur, and Oxygen cathodes. The membrane is synthetized by using crystalline polyethylene glycol dimethyl ether (PEGDME, average molecular weight of 2000 g mol^{-1}), LiTFSI, $LiNO_3$ and SiO_2 as ceramic filler. The relatively low molecular weight of the selected crystalline and plasticized PEGDME allows Li^+ ions conductivity properties suitable for battery applications already at 30 °C, while the operative temperature usually related to standard polymer electrolytes based heavy polyethylene oxide (PEO) exceeds 65 °C. This new solid electrolyte configuration demonstrates excellent performance at 30 °C in Li battery when combined with an olivine-structured $LiFePO_4$ cathode, and its application in Li-S and Li-O_2 cell at the same low temperature reveals the formation of a suitable electrode/electrolyte interphase and fine cycling behavior. *Section 3.2* deals with the Membrane-Electrode-Assembly procedure of LFP and PEO-based polymer, yielding a easily scalable and direct solution to enhance the interfacial contact within electrode and membrane, resulting in enhanced electrochemical proprieties. The system has been scaled up to single-layer pouch-cell. Section 3.3 reports safe electrolyte enabling room-temperature operation of Na-S battery, which is a sub-niche of the Li-S system. The investigation suggested that slight changes in the electrolyte additives concentration can imply excessive passivation of the electrode and thus hamper electrochemical activity. Two target electrolytes enabled stable Na-S conversion process. **Chapter 4** concern full Na-ion cell assembled using a biphasic P2/P3 layered-oxide cathode and alloying-based anode, investigated using either carbonate or glyme-based electrolytes. Section *4.1* regard the activation of Sn-C anode to get Na_x(Sn-C) anode for direct application is sodium-ion battery (NIB), while *Section 4.2* demonstrates enhanced electrochemical stability of the same system studied using a glyme-based electrolyte. *Section 4.2* corroborates the versatility of the SiO_x-CM anode, which is investigated for SIB application with a P2/P3 cathode recently developed at the University of Ferrara.

Chapter 2.

Conversion Cathodes in Lithium Environment

2.1 Exploiting Sulfur-based cathode in lithium-ion battery

The demand for Li-ion batteries (LIBs) is expected to rise relentlessly due to their applications as fundamental power sources in a vast range of technologies, ranging from portable electronics to electric vehicles, and as essential stationary energy storage systems. The latter application is foreseen considering that the installed grid-scale battery storage capacity, which stood to ~28 GW at the end of 2022, is expected to expand to 35-fold within 2030 to nearly 970 GW in the Net Zero Scenario.[1] On the other hand, materials availability and cost have been identified as key factors for triggering a sustainable development with controlled economic, environmental and geopolitical impact.[2] Therefore, suitable alternatives to common LIBs with increased energy density compared to the typical 150–300 Wh kg^{-1} range, and with electrodes based on abundant, easily accessible, and highly performing materials are needed to actually promote a step forward.[3-6] Elemental sulfur (S_8) can electrochemically react with lithium delivering a theoretical capacity of 1675 mAh g_S^{-1}, according to the reversible redox reactions $S_8+16Li^++16e^- \leftrightarrows 8Li_2S$.[7] Energy storage systems based on Li-S electrochemistry may be particularly entangled, since it involves the formation of various intermediate anions and radicals, depending on the nature and physical state (solid or liquid) of the electrolyte, salt concentration, electrode morphology, and active material content.[7-10] S_8 is almost an insulator and can undergo a series of compositional and structural rearrangements in the Li−S system leading to the formation of soluble polysulfides (Li_2S_x with $4 \leq x \leq 8$) with significant changes in the cathode morphology, thus posing great practical challenges and drawbacks such as modest rate capability, rapid capacity fading, low material utilization, and poor mechanical stability.[8,11,12] Suitable current collectors, conductive matrixes, and additives in the electrodes and/or the electrolytes are requested to boost the cell performances, and ensure appropriate power and energy density.[14-17] Another limiting issue of the Li-S system is represented by the Li-metal anode which can degrade the electrolyte unless a stable solid-electrolyte-interphase (SEI) is formed, thus hampering the long-term cycling of the battery.[18,19] Soluble polysulfides can also diffuse from the cathode to the Li anode to directly react and precipitate, or can travel back to the cathode to be newly oxidized through a shuttle reaction without any charge accumulation. This undesired process can typically lead to material loss, promote dendrite formation, and limit both material utilization and cell efficiency.[20]

#3 10.1002/cssc.202400615

Scalable Li-ion Battery with Metal/Metal Oxide Sulfur Cathode and Lithiated Silicon Oxide/Carbon Anode

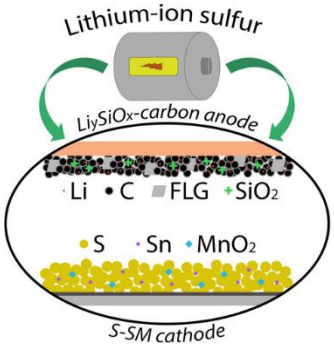

In this section we report a Li-ion sulfur cell with enhanced cathode and anode materials into a rational combination ensuring, at the same time, high-capacity, long cycle life and possible scalability. The sulfur cathode is characterized by a reinforced polysulfide control achieved by including MnO_2, and a rate capability favored by nanometric Sn particles, whilst the electrode conductivity and thin configuration are ensured by including FLG in the cathodic slurry, and MWCNTs in the current collector.[14-16] The Sn nanoparticles are introduced to act as the conductive framework in order to replace carbon additives, which should be employed by relevant amount for ensuring good conductivity.

enhanced carbons usually require complex synthesis procedures and present a high specific volume that may affect the overall energy density. Instead, metal nanoparticles can be tuned with a limited concentration thanks to their outstanding conducting character as previously demonstrated.[14] In addition, both Sn and MnO_2 are abundant and non-toxic materials, thus representing a rational choice for combination with the environmentally friendly sulfur to ensure remarkable conductivity and lithium polysulfide retention, respectively, even with concentration limited to 5 wt % each in the sulfur-based cathode composite. Thus, the scalability of the new S:Sn:MnO_2 composite, indicated as S-SM in the text, resides in a simple synthesis which foresees mixing at mild temperature S, Sn and MnO_2, thus avoiding chemical reactions or the use of solvents, and relies on mechanical grinding/milling to achieve the final powder. Therefore, the S-SM composite is initially investigated in terms of structure, morphology, thermal behavior, and electrochemical proprieties in lithium half-cell. Remarkably, the increase of the sulfur loading from 2 to ~6 mg cm^{-2} and the concomitant decrease of the E/S ratio from 10 to 5 µL mg^{-1} only partially affect the half-cell performance. We provide chemical and electrochemical pre-lithiation of the material to achieve a Li_ySiO_x-CM phase, suitable for application in full-cell in combination with the S-SM cathode. Prior to application, the pristine anode and its lithiated version are studied in half-cells using the electrolyte typically employed in the

Li−S system formed by 1,3-dioxolane (DOL) and 1,2-dimethoxyethane (DME) solvents, lithium bis(trifluoromethanesulfonyl)imide (LiTFSI) conducting salt, and $LiNO_3$ passivating additive.[15] The full-cells are subsequently assembled with sulfur loading exceeding 1 mg cm^{-2}, an E/S ratio of 15 μL mg^{-1}, and a N/P ratio below 1.2. The cells revealed remarkable cycle life, high efficiency, and moderate retention, even when tested in challenging conditions exploiting a sulfur loading approaching 3 mg cm^{-2} and E/S ratio limited to 8 μL mg^{-1}. We believe that the results reported herein may boost the development of full-cells to achieve prototypes of practical interest, upon further optimization of sulfur loading as well as of E/S and N/P ratios.

Experimental

- Synthesis of the S-SM Composite

Elemental sulfur (≥99.5 %, Riedel-de Haën), Sn (nanopowder, <150 nm particle size, ≥99 % trace metals basis, Sigma-Aldrich), and MnO_2 (≥99 %, ReagentPlus) were mixed in the 90 : 5 : 5 *w/w* ratio and heated at 125 °C under magnetic stirring in a silicon oil bath until complete melting of sulfur and uniform mixing with Sn and MnO_2. The value of 125 °C was chosen to allow sulfur melting, which begins slightly over 110 °C in standard condition, and avoid at the same time its possible evaporation which may occur at higher temperatures and decrease the sulfur content in the composite. The mixture was subsequently quenched at room temperature until the complete solidification, and ground in an agate mortar to obtain a fine grey powder. The S-SM amount produced by our simple physical mixing-based preparation pathway exceeded 5 g at laboratory scale.

- Synthesis of SiO_x-CM

SiO_x-CM was synthetized as reported in our previous work presented in the precedent section. In brief, the synthesis involved a hydrothermal step and a subsequent annealing in Ar/H_2 of a mixture of sucrose, FLG, and SiO_2. The sucrose was used as the source of amorphous carbon in the final composite in combination with FLG to promote the contribute of the SiO_x to the electrochemical process by partial Li-(de)alloying, as well as to act as active materials for the Li-(de)insertion and Li-(de)intercalation.

- Materials characterization

The S-SM structure was investigated by XRD through a Bruker D8 Advance instrument equipped with a Cu Kα radiation source (8.05 keV) scanning the 10°−50° 2θ range using a step size of 0.02° and a rate of 10 s $step^{-1}$. TGA was performed in a Mettler-Toledo TGA 2 instrument (Mettler-Toledo, Columbus, OH, USA) under dry N_2 (for S-SM) or dry air (for SiO_x-CM) flow of 50 ml min^{-1}, heating the samples from 25 to 400 or 1000 °C, respectively, with rate of 5 °C min^{-1}. The morphology of S-SM powder was detected through SEM using a Zeiss EVO 40 relying on a LaB_6 thermionic gun in backscattered electrons mode, and by TEM through a Zeiss EM910 equipped with a tungsten thermionic electron gun operating at 100 kV. The sample for TEM analyses consisted of a suspension of S-SM powder in ethanol which was drop-cast onto a formvar/carbon supported copper grid (150 mesh). EDS elemental maps were

collected on the SEM backscattered electrons images via a X-ACT system associated with the SEM equipment. FTIR spectra were recorded via a Bruker Vertex V70 instrument set up in transmittance mode.

- Electrodes preparation

The electrodes tapes were prepared by casting process with a doctor blade tool (MTI Corp.) set at ~300 μm of slurries formed by 80 wt % active material powder, namely S-SM, S or SiO_x-CM, 10 wt % polyvinylidene fluoride (PVdF 6020, Solef) polymer binder, and 10 wt % FLG in the cathodic slurry, or 10 wt % carbon black in the anodic slurry (super P carbon, SPC, Timcal) as electron conductor dispersed in N-methyl-2-pyrrolidone (NMP, Sigma-Aldrich). The slurries were cast on MWCNTs-coated aluminum foil (thickness of 60 μm, prepared according to our previous work)[16] for S-SM and S or copper foil (thickness of 20 μm, MTI Corp.) for SiO_x-CM.[35] The tapes were heated for 2 hours at 50 °C on a hot plate under a fume hood (air atmosphere) to remove the NMP solvent. The obtained foils were calendared at the 70 % with respect to the initial thickness using an MSK-2150 Rolling Machine (MTI Corp.) to achieve a final thickness of ~100 μm, and cut into discs with diameter of 14 mm (1.54 cm^2 geometric area) with a Nogami handheld punch. The SiO_x-CM electrodes were dried under vacuum for 3 h at 110 °C, while the S-SM and S control electrodes were dried under vacuum overnight at 30 °C inside a Büchi oven, and subsequently stored inside an Ar-filled glovebox (MBraun, O_2 and H_2O contents lower than 1 ppm). The electrodes had an active material loading ranging from 1.2 to 5.8 mg cm^{-2} for S-SM and S (control) and between 1.3 and 6.3 mg cm^{-2} for SiO_x-CM (note that all active material loadings are repeated in the figure panels where the electrodes are subjected to cycling tests).

- Cell assembly and electrolyte preparation

CR2032 coin-type cells (MTI Corp.) were assembled inside an Ar-filled glovebox by stacking a 14 mm-diameter lithium metal disc (0.25 mm thickness, MTI Corp.) as counter electrode, an 18 mm-diameter monolayer microporous membrane (Celgard 2500) as separator soaked with electrolyte (see composition below), and a S-SM, S (control) or SiO_x-CM disc as working electrode. The electrolyte consisted of a solution formed by DOL (anhydrous, contains ca. 75 ppm BHT as inhibitor, 99.8 %, Sigma-Aldrich) and DME (anhydrous, 99.5 %, inhibitor-free, Sigma-Aldrich) mixed in the 1 : 1 weight ratio, and dissolving LiTFSI ($LiN(SO_2)_2(CF_3)_2$, 99.95 % trace metals basis, Sigma-Aldrich) as conducting salt and lithium nitrate ($LiNO_3$, 99.99 % trace metals basis, Sigma-Aldrich) as passivating agent in the solvents mixture with a 1 mol $kg_{solvent}^{-1}$ concentration for each salt. Before using, DOL and DME solvents were preserved under molecular sieves (rods, 3 Å, size 1/16 inch, Honeywell Fluka) until a H_2O content lower than 10 ppm was achieved as determined by a Karl Fischer 899 Coulometer (Metrohm), while LiTFSI and $LiNO_3$ were dried for 2 days under vacuum at 110 °C. A catholyte containing lithium polysulfide (Li_2S_8) for UV-vis analyses was prepared by adding 0.5 wt % of Li_2S_8 to the above described electrolyte solution. UV-vis analyses were carried out on the above catholyte reference, and on catholyte solutions aged for 1 hour in contact with 20 mg of Sn or 20 mg of Sn:MnO_2 1 : 1 *w*/*w* powders in the 500–750 nm wavelength region, in order to check the Li-PS retention ability of the metal and the metal/metal oxide mixture. The absorption spectra were collected with a V-570 UV-vis Spectrophotometer (Jasco Inc.) at room temperature against a DOL:DME 1 : 1 *w*/*w* reference solution.

- Electrochemical measurements and ex-situ investigation

The electrochemical process of S-SM was studied through CV and EIS employing a VersaSTAT MC Princeton Applied Research (PAR-AMETEK) multichannel potentiostat. CV was performed within the 1.8–2.8 V *vs*. Li^+/Li potential range at a scan rate of 0.1 mV s^{-1}, while EIS spectra were collected at the OCV condition before cycling and after 1, 5 and 10 CV runs using an alternate voltage signal of 10 mV in the frequency range between 500 kHz and 0.1 Hz. The Li|S-SM half-cells were galvanostatically cycled in the 1.7–2.8 V and 1.6–2.8 V voltage ranges, respectively, at constant current rates of either C/3 or 1 C (1 C=1675 mA g_S^{-1}), or by applying current rates increasing every 5 cycles from C/10 to C/8, C/5, C/3, C/2, 1 C, and 2 C, before lowering back to C/10 after 35 cycles, in the 1.7–2.8 V (1 C and 2 C) and 1.8–2.8 V (lower rates) voltage ranges, employing an E/S ratio of 10 µL mg^{-1}. For comparison, a Li−S half-cell using the S control electrode (sulfur loading of 2.65 mg cm^{-2}) was galvanostatically cycled between 1.7 and 2.8 V at the constant current rate of C/3 by employing an E/S ratio of 10 µl mg^{-1}. An additional Li|S-SM half-cell for N/P ratio study was assembled and cycled at a current rate of C/5 in the 1.9–2.8 V voltage range, using an E/S ratio of 15 µL mg^{-1}. The Li|SiO_x-CM half-cells were filled with 50 µL of electrolyte using one 18 mm-diameter monolayer microporous membrane (Celgard 2500) as separator, and studied via galvanostatic cycling between 0.01 and 2.0 V at constant current of 120 mA g^{-1}. Li-ion sulfur full-cells were assembled by coupling chemically or electrochemically lithiated Li_ySiO_x-CM anodes and S-SM cathode, separated by an 18 mm-diameter monolayer microporous membrane (Celgard 2500) soaked with either 15 µL mg_S^{-1} or 8 µL mg_S^{-1} (the latter exclusively for high active material loading) of electrolyte. The chemical lithiation of SiO_x-CM to achieve the Li_ySiO_x-CM state was performed via direct contact of the pristine electrode surface with a lithium metal foil wet with the electrolyte for 14 or 24 hours under a pressure of 2 kg cm^{-2}. Afterwards, the electrode was removed from the lithium foil, dried for 60 minutes under vacuum, and studied in lithium half-cell and full-cell using the S-SM cathode. The electrochemical lithiation to achieve Li_ySiO_x-CM was performed in lithium half-cell (CR2032 coin-type cell, MTI Corp.) using the SiO_x-CM electrode and 50 µL of electrolyte soaking an 18 mm-diameter monolayer microporous membrane (Celgard 2500) through either 9 or 5 (the latter exclusively for high active material loading) discharge/charge cycles at constant current of 20 mA g^{-1} in the 0.01–2.0 V voltage range, and a final full discharge held at 0.01 V to achieve the lithiated condition. Then, the Li_ySiO_x-CM electrode was recovered from the above cell in the fully discharged state, dried under vacuum for 60 minutes and employed. Galvanostatic cycling tests were performed on the full-cells within 0.1 and 2.8 V at current rates of C/5 and C/10, or within 0 and 2.8 V at C/20 (1 C=1675 mA g_S^{-1}). All the galvanostatic cycling tests were carried out by a MACCOR series 4000 battery tests instrument in a chamber set at 30 °C, with maximum fluctuation of ±0.1 °C. *Ex-situ* SEM was performed on the electrodes with relatively low active material loading, retrieved from the full Li_ySiO_x-CM|S-SM cells after cycling, using a Zeiss Gemini FESEM 460 relying on a LaB_6 thermionic gun in secondary electrons mode. Before SEM, the retrieved electrodes were dried under vacuum for 1 hour.

Results

Structure, morphology and composition of the S-SM material are depicted in **Figure1**.

The XRD pattern between 10° and 50° of 2θ in **Figure 1a** reveals the exclusive presence of orthorhombic sulfur (S_8, ICSD #27840), manganese dioxide (β-MnO_2, ICSD

#73716), and tin (β-Sn, ICSD #40038) without any additional reflection. This response likely excludes the formation of crystalline by-products or impurities, which is mainly due to the mild temperature of 125 °C used for the synthesis (see Experimental section for details). The actual amount of sulfur in the S-SM material is detected through thermogravimetric analysis (TGA) under N_2 and the resulting curve is reported in **Figure 1b**. The figure exhibits a sulfur content as high as 90 % into the composite, which is expected to facilitate the tuning of the active material loading in the electrodes for increasing the energy density of the cells. Furthermore, this synthetic pathway may be reasonably scaled-up to achieve practical production, since it involves mild heating and mechanical milling/grinding in a solvent-free environment. The differential curve (DTG, **Figure 1b**) associated with the TGA analysis evidences a weight loss related to sulfur evaporation evolving through a single peak centered at 315 °C. It is worth noting that residual weight corresponds to Sn and MnO_2 fractions which are inert under the experimental constrains. The ability of Sn and MnO_2 in retaining lithium polysulfides (Li-PS) is qualitatively evaluated by UV-vis measurements in **Figure 1c**. The better polysulfide retention ability of MnO_2 is confirmed by UV-vis measurements performed on reference Li_2S_8 solution, and on solutions held in contact with Sn and Sn:MnO_2 1:1 *w/w* (**Figure 1c**). Indeed, the analysis shows the characteristic signal of Li-PS species in the visible region between 750 and 500 nm with a relevant intensity for the reference solution, while an attenuated signal is observed for the one held in contact with nanometric Sn, which almost vanishes for the solution aged with Sn:MnO_2 1:1 *w/w*. The Li-PS retention ability may be influenced by the intrinsic interactions between Sn and MnO_2 and Li_2S_x species, as well as by the morphology of the sample.

The LiPS control mechanism by MnO_2 relies on mediating LiPS redox through insoluble thiosulfate species in a two-step process, as reported in literature work. The thiosulfate groups are first created *in situ* by oxidation of initially formed soluble LiPS species on the surface of MnO_2. As reduction proceeds, the surface thiosulfate groups are proposed to anchor newly formed soluble 'higher' polysulfides by catenating them to form polythionates and converting them to insoluble 'lower' polysulfides.[15a] Other results related to numerical simulation suggested that the S and Li atoms in Li_2S_6 and Li_2S_4 preferentially bind with Mn or O atoms at the MnO_2 structure (110).[15b] Hence, the electron microscopy in **Figure 1d–j** enables to investigate the morphological features of S-SM powder. The TEM images reported in **Figure 1d and e** show substantial differences between primary micrometric and nanometric domains. The amorphous or defined flake-like particles with micron or sub-micron size can be attributed either to S or MnO_2. It is worth mentioning that the nanometric size observed

for the Sn particles is particularly suggested for possibly increasing the electron conductivity by shortening the ion-diffusion path, thus improving the kinetics of the Li-S electrochemical processes.[14] In addition, the SEM image (**Figure 1f**) indicates that the S-SM particles are aggregated in the composite to form clusters with size ranging from 1 µm or smaller to about few dozen µm. These macroscopic aggregates can avoid possible electrolyte degradation, which may be instead promoted by dispersed nanometric particles.[21] Furthermore, the EDS performed on the above SEM (**Figure 1g–j**) indicates a well uniform distribution of sulfur (**Figure 1g**) and MnO_2 (**Figure 1i and j**), while Sn exhibits the dispersion of isolated nanometric particles alternated with micrometric clusters in the active material matrix.

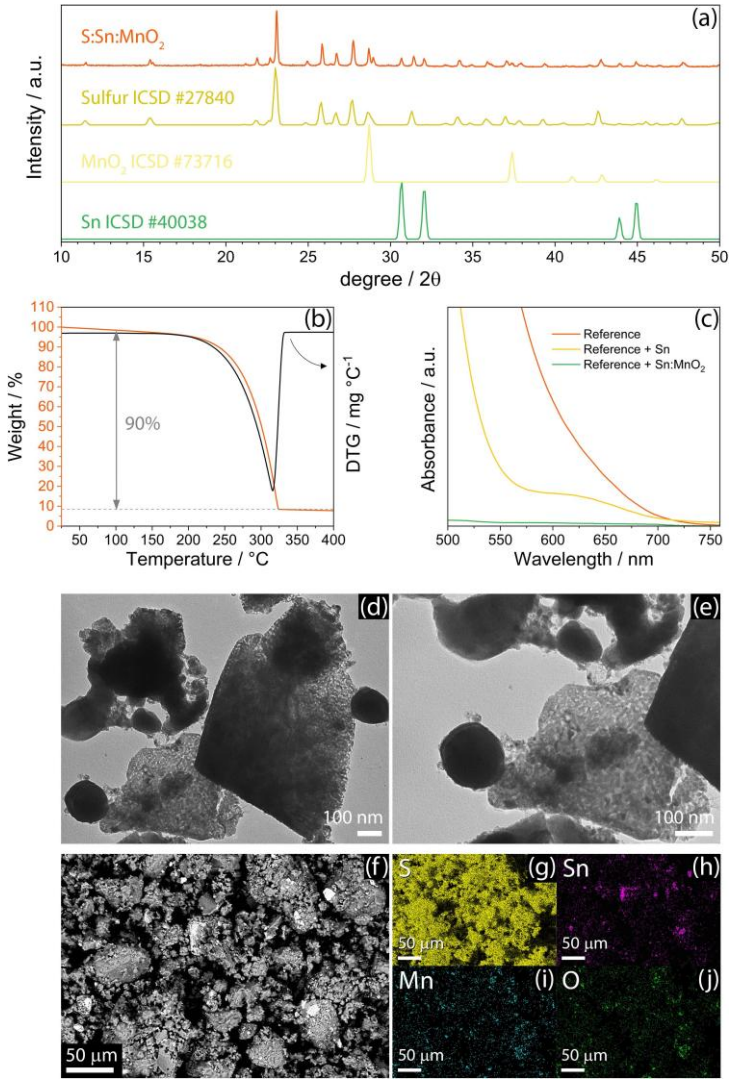

Figure 1. Physical-chemical characterization of the S-SM powder. **(a)** X-ray diffractograms for the S-SM sample (orange). Reference data for sulfur (S_8, ICSD #27840, dark yellow), manganese dioxide (β-MnO_2, ICSD#73716, light yellow), and tin (β-Sn, ICSD #40038, green), are reported for comparison. **(b)** TGA performed under dry N_2 flow with heating rate of 5 °C min^{-1} from 25 to 400 °C, and corresponding DTG. (**c**) UV-vis measurements performed on DOL:DME, 1 mol kg^{-1} LiTFSI, 1 mol kg^{-1} $LiNO_3$, 0.5 wt % Li_2S_8 solutions, without any powder addition (reference, red), with Sn (yellow) or Sn:MnO_2 1:1 *w/w* (green). **(d, e)** TEM images of the S-SM powder at various magnifications. **(f)** SEM image of S-SM powder

acquired in backscattered electrons mode, and corresponding EDS elemental maps of (**g**) sulfur (yellow), (**h**) tin (purple), (**i**) manganese (cyan), and (**j**) oxygen (green).

Prior to application in full-cell, the S-SM composite is electrochemically investigated in lithium half-cell and the results are reported in **Figure 2**. The CV in **Figure 2a** displays during the first cycle a reversible conversion process, evolving by two reduction peaks at about 2.2 and 1.9 V *vs.* Li^+/Li during the cathodic scan, and a double oxidation signal extending from 2.3 to 2.6 V *vs.* Li^+/Li during the subsequent anodic scan. This response matches the multi-step electrochemical process between lithium and sulfur, which leads to the formation of polysulfides of various chain-length by the ongoing of discharge, and their conversion back upon charge.[22] In addition, the CV signature excludes additional contribution to the electrochemical process of the Li-(de)-insertion reaction of MnO_2, as indicated in literature.[23] The decrease of the peak intensity in the CV of **Figure 2a** can be attributed to possible changes of the lithium ion diffusion coefficient,[24] or partial loss of active material during cycling, which is particularly relevant in the conventional liquid ether-based electrolyte that typically favors the dissolution and diffusion of the polysulfide intermediates. Nonetheless, the voltammograms present notable overlapping after the first cycles, thus indicating the stabilization of the interphase and remarkable reversibility of the Li-S conversion process after the initial stage. On the other hand, the kinetics of the electrochemical conversion may slow-down both by the decrease of Li^+ diffusion coefficient and by the limitation of the polysulfide anions mobility at the electrode/electrolyte interphase, due to electrolyte viscosity change promoted by Li-PS dissolution. EIS is performed at the open circuit voltage condition upon cell assembly (OCV), and after 1, 5 and 10 CV runs, and the related Nyquist plots are displayed in **Figure 2b**. The plots are analyzed by NLLS fitting method to obtain the corresponding equivalent circuits formed by resistive (R) and constant phase elements (CPE, Q), identified by the $R_e(R_iQ_i)Q_w$ model in **Table 2.1.1**. Relevantly, the OCV plot in **Figure 2b** shows an almost vertical low-frequency line attributed to the cell geometric capacity into quasi-blocking electrode setup (Q_g in the corresponding equivalent circuit of **Table 2.1.1**). This response modifies in the subsequent Nyquist plots to a line tilted at about 45°, which is typical of a Warburg-type semi-infinite Li^+ diffusion. Furthermore, **Table 2.1.1** reveals a general increase of total interphase resistance of the S-SM electrode (R_{tot}, given by the sum of the R_i elements) from $78.6 \pm 3.6\ \Omega$ at the OCV to around $75.3 \pm 0.3\ \Omega$ after 1 CV run, and to $97.2 \pm 0.9\ \Omega$ after 10 cycles. The rise of the cell impedance can in part justify the slight peak-current decrease discussed above in the corresponding CV of **Figure 2a**. The electrochemical performances of the S-SM electrode are also investigated through galvanostatic tests in half-cell at current rates increasing from C/10 (1 C = 1.675 Ags^{-1}) to C/8,

C/5, C/3, C/2, 1 C and 2 C (**Figure 2c and d**). The cycling trend depicted in **Figure 2c** for the test at increasing current rates shows a steady-state discharge capacity taken at the 3rd cycle for each C-rate of 769, 756, 715, 670, 627, and 585 mAh g_S^{-1} at C/10, C/8, C/5, C/3, C/2 and 1 C respectively. The delivered capacity drops below 200 mAh g_S^{-1} at 2 C, thus suggesting this C-rate as the limiting value for the cell application within the thin-film configuration adopted in this work, in which a carbon coated Al collector with thickness of ~60 µm or lower is used. The cell recovers the relevant capacity value of 818 mAh g_S^{-1} when the C-rate is lowered back to C/10, thus indicating an excellent stability of the electrode by switching from high to low currents. The decrease of the cell capacity by increasing the current from C/10 to 1 C may be attributed to the rise of the discharge/charge polarization observed in the corresponding voltage profiles of **Figure 2d**, mainly due to kinetic limits and ohmic-drops affecting the voltage plateaus evolving both at ~2.3 and ~2.1 V. On the other hand, a further increase of the current to 2 C turns into the deactivation of the electrochemical process related to the formation of short-chain polysulfide at low voltages due to excessive polarization, and into a concomitant drop of the delivered capacity to a value reflecting a partial Li-S conversion to long-chain polysulfide only (i.e., Li_2S_8).

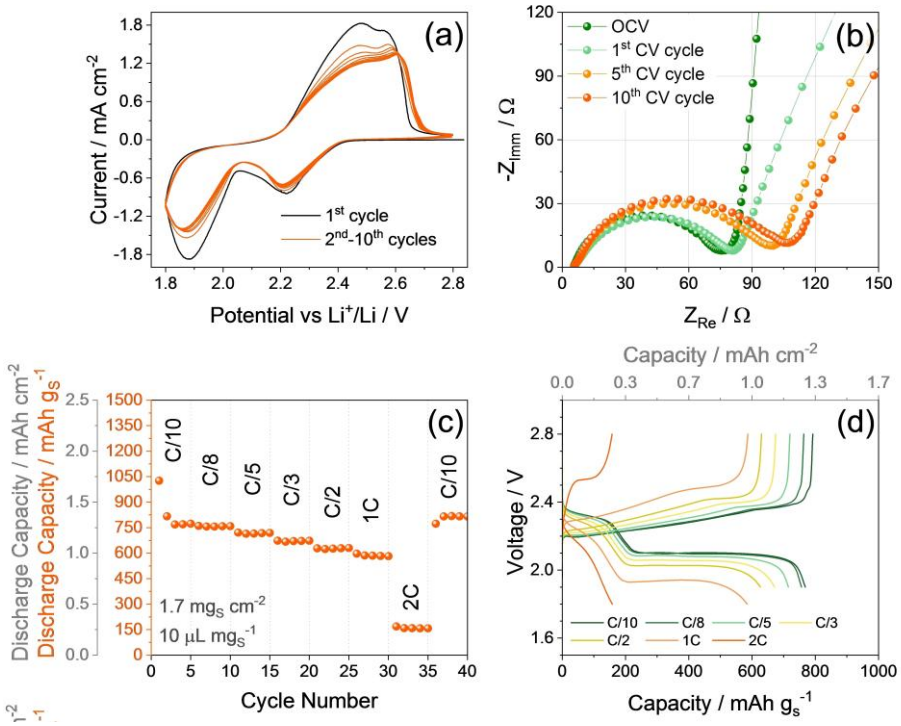

Figure 2. Electrochemical characterization of the S-SM material in lithium half-cells using the DOL:DME, 1 mol kg^{-1} LiTFSI, 1 mol kg^{-1} $LiNO_3$ electrolyte. **(a)** CV profiles, **(b)** Nyquist plot recorded by EIS. CV potential range: 1.8–2.8 V *vs.* Li^+/Li, scan rate 0.1 mV s^{-1}. EIS performed between 500 kHz and 100 mHz; voltage signal: 10 mV. **(c, d)** Rate capability test (1 C= 1675 mAg_S^{-1}), in terms of (**c**) discharge capacity trend *vs.* cycle number (additional left *y*-axis exhibits areal capacity), and (**d**) voltage profiles of the 3rd cycle for each current rate (top *x*-axis shows areal capacity).

Table 2.1.1. NLLS analysis carried out on the Nyquist plots displayed in Figure 2b. The analysis is performed on the impedance spectra acquired on the Li |S-SM half-cell at the OCV, and after 1, 5, and 10 CV runs.

Cell condition	Circuit	R_1 (Ω)	R_2 (Ω)	R_i ($\sum R_n$) (Ω)	χ^2
OCV	$R_e(R_1Q_1)(R_2Q_2)Q_g$	64.6 ± 1.4	14.0 ± 2.2	78.6 ± 3.6	4×10^{-5}
After 1 CV	$R_e(R_1Q_1)Q_w$	75.3 ± 0.3	/	75.3 ± 0.3	1×10^{-4}
After 5 CV	$R_e(R_1Q_1)Q_w$	90.6 ± 0.6	/	90.6 ± 0.6	2×10^{-4}
After 10 CV	$R_e(R_1Q_1)Q_w$	97.2 ± 0.9	/	97.2 ± 0.9	3×10^{-4}

Figure 3 exemplifies the features of the chemically and electrochemically lithiated Li_ySiO_x-CM anodes in lithium half-cells and shows their subsequent combination in Li-ion full-cells using the S-SM cathode. The charge (de-lithiation) profiles in half-cell of Li_ySiO_x-CM chemically lithiated (purple) and electro-chemically lithiated (red) reported in **Figure 3a** reveal the expected shape evolving mainly below 1.2 V, and a delivered capacity exceeding 2.0 mAh which is suitable for allowing the full discharge (Li-S conversion) of a S-SM cathode with a sulfur loading of ~1.2 mg_S cm^{-2}, such as in the example reported in yellow in the same panel for comparison. Furthermore, the cycling trends in half-cell of the S-SM (**Figure 3b**) and of the electrochemically lithiated Li_ySiO_x-CM (**Figure 3c**) allow the rough estimation of the N/P ratio in a full-cell that combines the two electrodes. Indeed, Li_ySiO_x-CM |S-SM full-cells using chemically and electrochemically lithiated anodes are assembled with an initial N/P ratio of ~1.05 and ~1.12, respectively, calculated by considering the half-cell capacity of S-SM discharge (i.e., 2.02 mAh) and Li_ySiO_x-CM charge (i.e., 2.12 and 2.26 mAh) in **Figure 3a**. On the other hand, we can predict that these N/P ratios may rise-up by comparing with the examples of the half-cells exploiting S-SM (**Figure 3b**) and Li_ySiO_x-CM (**Figure 3c**), as the anode undergoes progressive interphase improvement and its capacity increases.[25] The voltage profiles of the cycling test performed at C/5 (1 C =1675 mA g_S^{-1}) on a full-cell combining S-SM and electrochemically lithiated Li_ySiO_x-CM is reported in **Figure 3d**, while the corresponding capacity trend and respective CE are displayed in **Figure 3e**. The voltage profile of the first cycle (black curve in **Figure 3d**) appears as the combination between the double-plateau associated with the multi-step conversion process of sulfur with lithium, and the sloped curve ascribed to the Li^+ (de)alloying/(de)insertion reaction of the SiO_x-CM. Indeed, the cell exhibits two broad discharge plateaus centered around 2 V and 1.7 V, reversed into a merged charge profile evolving between 1.2 V and 2.4 V, with an initial reversible capacity of 1045 mAh g_S^{-1}. The corresponding cycling trend (**Figure 3e**) shows an immediate drop of the capacity from 1050 to 980 mAh g_S^{-1}, and subsequently a progressive decrease to 380 mAh g_S^{-1} upon 400 cycles, with CE exceeding 95 % after the first run. The observed

capacity decay is likely ascribed both to the incomplete de-alloying of the Li-Si phases during discharge at the anode upon repeated cycles and to the loss of active material, i.e. sulfur, due to deposition of Li-PS at the anode side. A very similar voltage shape is observed for the full-cell using the chemically lithiated Li_ySiO_x-CM (**Figure 3f**), however with a higher discharge capacity during the first cycle, i. e., 1170 $mAh\,g_S^{-1}$. In addition, the corresponding cycling trend (**Figure 3g**) shows a more relevant loss during the initial cycles, while a slightly higher efficiency and stability upon prolonged test, with a final capacity of 450 $mAhg_S^{-1}$ after 400 cycles. Despite the final capacities delivered by the full Li-ion sulfur cells of 380 and 450 $mAhg_S^{-1}$, respectively, correspond to a retention limited to about 40 %, it is worth considering that they still represent considerable values if compared to those of commercial Li-ion cells using the common insertion/intercala-tion cathodes and the graphite anode. Therefore, the Li-ion-sulfur cells we propose herein are a first-look to a proof-of-concept system that might represent, upon extended optimization, a competitive energy storage strategy based on the challenging Li-S conversion mechanism while relying on sustainable materials and a non-reactive anode. These results are certainly encouraging, in particular by considering the long cycling evolution, the absence of relevant signs of dendrites, and the possible scalability of the cell using the chemically lithiated Li_ySiO_x-CM. Furthermore, the practical energy density of the cell is *estimated to initially exceed 500 Wh* kg^{-1}. However, the capacity decay observed by long-term cycling in **Figure 3**, and the corresponding limitation of the practical energy density, suggest the necessity of additional improvement for scaling-up the system, such as a better tuning of the N/P ratio and the increase of the active material loading to achieve more appealing areal capacity values.

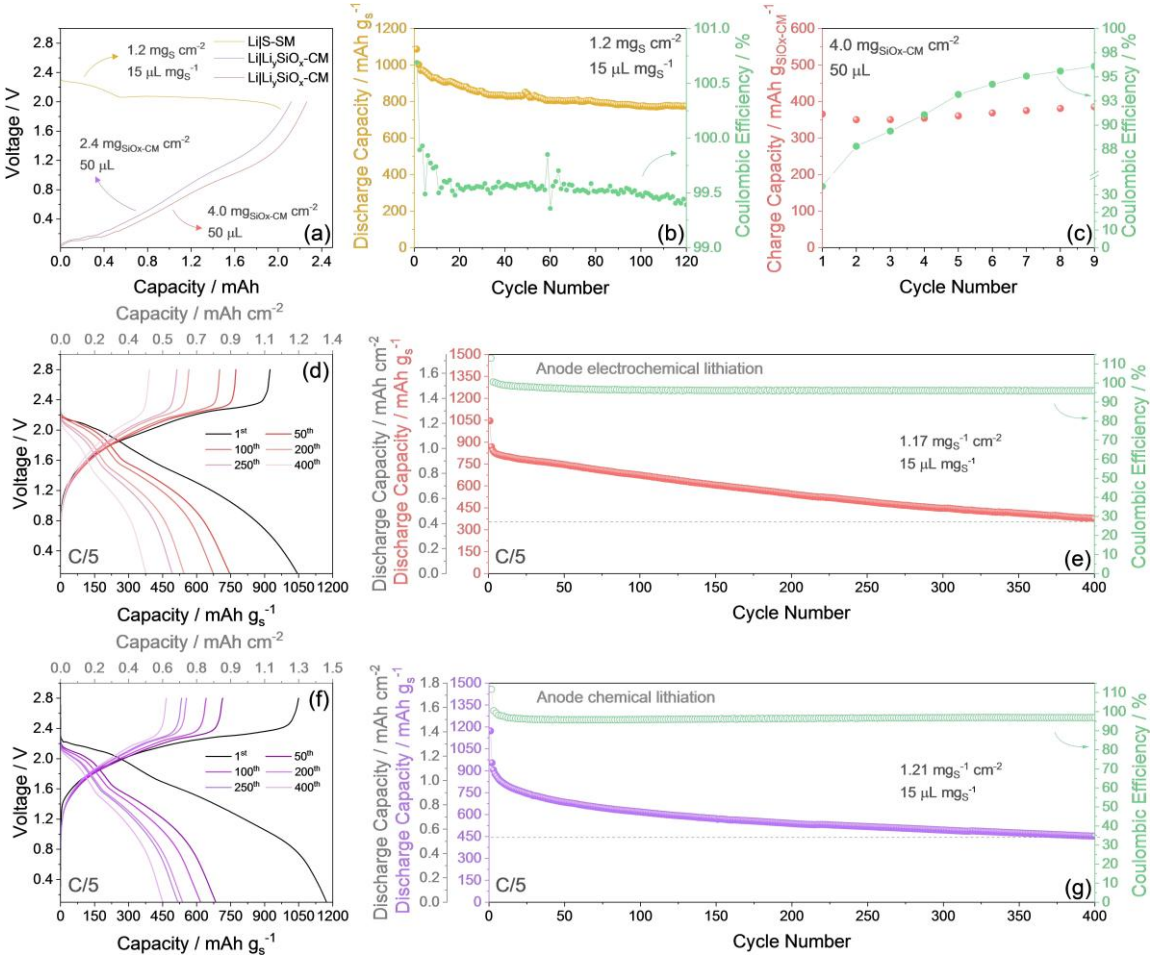

Figure 3. (a–c) Examples of chemical and electrochemical lithiation of a Li_ySiO_x-CM anode for determining the N/P ratio of a full-cell with S-SM cathode. **(a)** Charge (de-lithiation) profiles in lithium half-cells until 2.0 V of Li_ySiO_x-CM chemically lithiated for 14 h (purple) and electrochemically lithiated (red), respectively at 120 mAg^{-1} and 20 mAg^{-1}, and discharge profile of S-SM (yellow) in lithium half-cell at C/5 until 1.9 V. **(b)** Cycling trend of S-SM in lithium half-cell at C/5 between 1.9 and 2.8 V (right *y*-axis displays CE). **(c)** Cycling trend of the electrochemical lithiation of Li_ySiO_x-CM in lithium half-cell at 20 mAg^{-1} between 0.01 and 2.0 V (right *y*-axis displays CE). **(d–g)** Galvanostatic cycling performance of the Li_ySiO_x-CM S-SM full cell at C/5 in the voltage range of 0.1–2.8 V. **(d)** Test performed using the electrochemically lithiated Li_ySiO_x-CM in terms of selected voltage profiles (top *x*-axis shows areal capacity), and **(e)** corresponding cycling trend. **(f)** Test performed using the chemically lithiated Li_ySiO_x-CM in terms of selected voltage profiles (top *x*-axis shows areal capacity), and **(g)** corresponding cycling trend.

Figure 4 shows the *ex-situ* SEM images of the S-SM and Li_ySiO_x-CM electrodes after 400 cycles in the full-cells illustrated in **Figure 3d–g**, performed to evaluate the morphological changes in response to prolonged galvanostatic cycling. The SEM micrographs related to the S-SM cathode in **Figure 4a and b** show a still compact electrode morphology, where the micrometric FLG flakes are homogeneously dispersed in the MWCNTs network of the current collector substrate, while MnO_2 and Sn particles can be hardly observed in line with their notably low contents adopted herein (i.e., 5 wt% each in the sulfur composite).[26] In this regard, the bright spots observed in the surface may indicate the deposition of

poorly conducting products such as Li_2S upon cycling.[27] Interestingly, the agglomerated sulfur already observed in the pristine composite (**Figure 1f**) almost vanishes from surface of the cycled electrode, which is in line with a massive dissolution and operation as a catholyte of the active material upon prolonged cycling, as demonstrated in previous work.[28] The *ex-situ* SEM images of Li_ySiO_x-CM anodes (**Figure 4c–f**) show at the lower magnifications a more compact and flat surface for the electrochemically lithiated electrode (Figure 4c) than the chemically lithiated one (**Figure 4e**), possibly due to the physical stress promoted by pressing the latter during the pre-treatment (see Experimental). On the other hand, a higher magnification of the image reveals the presence of submicrometric precipitates in the electrochemically lithiated anode (**Figure 4b**) while the chemically lithiated one presents an amorphous deposit (**Figure 4f**). This difference may suggest a characteristic behavior of the deposition of the Li-PS on the anode surface depending on the type of lithiation pathway adopted, which would also justify the different performance achieved by the cells in **Figure 3**. It is worth mentioning that the influence of the lithiation mechanism of SiO_x-CM on the performance of the Li-ion sulfur can be also investigated with *ad hoc* studies focusing on the actual chemistry of the anode/electrolyte interphase.

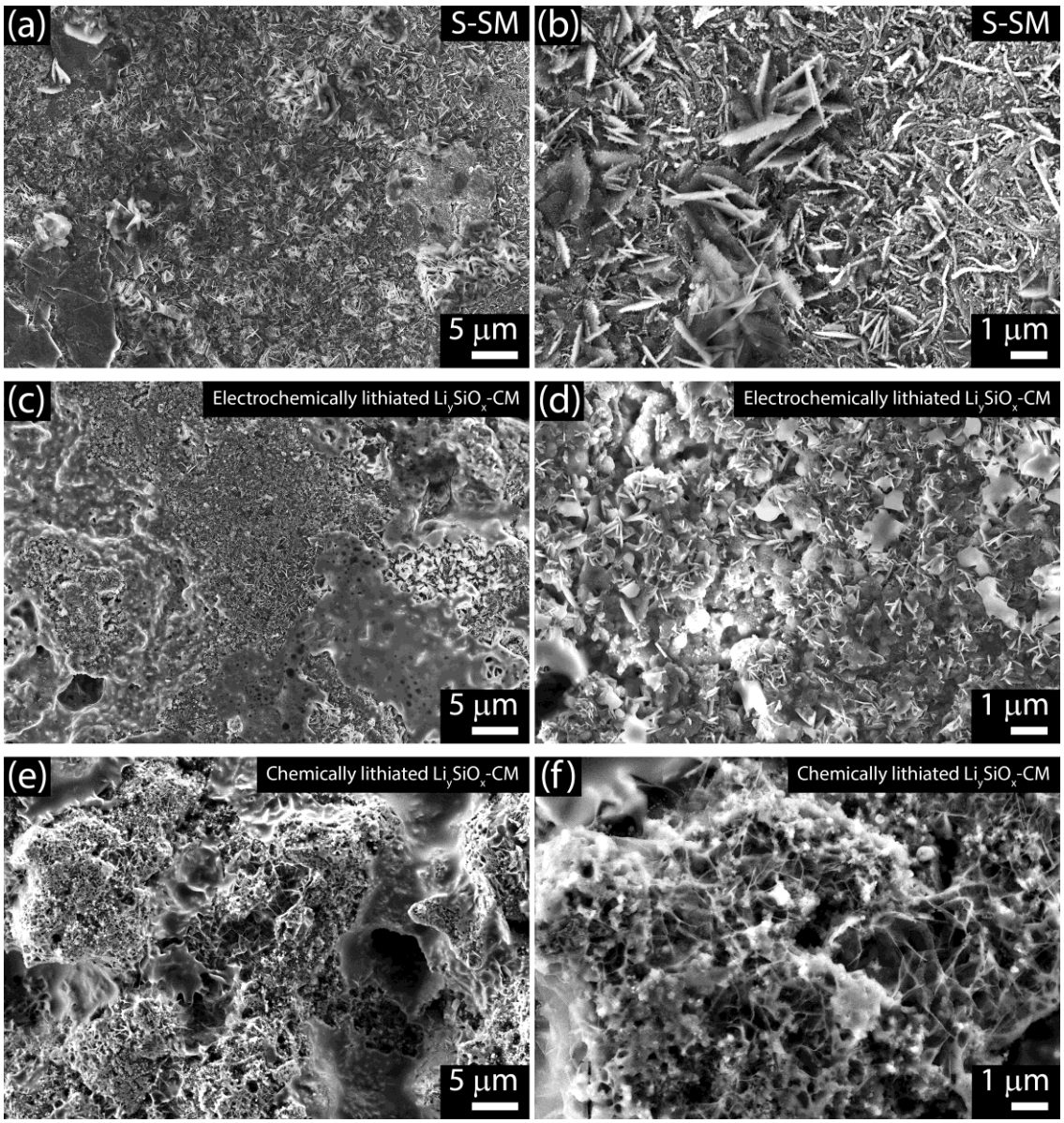

Figure 4. *Ex-situ* SEM performed on the electrodes extracted from full Li_ySiO_x-CM S-SM cells after 400 galvanostatic cycles (see corresponding cells in Figure 3d–g). **(a, b)** S-SM cathode (from test in Figure 5d and e) and **(c–f)** Li_ySiO_x-CM anode, either upon **(c, d)** electrochemical lithiation or **(e, f)** chemical lithiation.

The combination of the electrochemically lithiated Li_ySiO_x-CM anode with the S-SM cathode in full-cell is further tested by exploiting more challenging conditions, namely, active material loadings of 6.30 mg cm^{-2} for the pristine SiO_x-CM and 2.90 mg cm^{-2} for S-SM, as well as an E/S ratio limited to 8 µL mg^{-1}, as reported in **Figure 5a,b**. The selected voltage profiles and corresponding capacity trend in **Figure 5a,b**, respectively, recorded at decreasing rates of C/5, C/10 and C/20, display an initial capacity approaching 500 mAh g_S^{-1} and final value of 340 mAh g_S^{-1} after 280 cycles. The data indicate that the gradual lowering of the current rate upon cycling leads to an increase of capacity retention. Interestingly, the capacity decay experienced by the cell between 1st and 2nd cycle from 490 to 420 mAh g_S^{-1}

is far less relevant than those observed for the previous full-cells (compare with **Figure 3d-g**), which is likely due to the decreased E/S ratio that hinders excessive dissolution of the Li-PS, despite it limits, at the same time, the delivered capacity. In addition, the relevant capacity retention is achieved even with a decrease of the CE, which shows values around 98 % that drop to 93 % at C/ 10 and, subsequently, to 84 % at C/20. This behavior is ascribed to the low cycling rates which trigger both partial electrolyte degradation and excessive dissolution and consequent diffusion of the Li-PS from the relatively high loaded cathode resulting in the promotion of partial loss of active material. Nonetheless, the full Li_ySiO_x-CM| S-SM cell exploiting challenging conditions displays promising performance also promoted by proper electrochemical lithiation of the highly loaded anode, which was obtained through a limited number of cycles with respect to the tests displayed in **Figure 3d-g**, i. e., 5 full charge/discharge runs instead of 9, as represented in **Figure 5c** in terms of voltage profiles (top panel) and areal capacity trend (bottom panel). Indeed, the comparison in **Figure 5d** of the full-cells presented herein reveals a capacity retention for the high-loaded full-cell as high as 70 % after about 280 cycles, while the ones previously investigated exhibit values between 43 and 45 % at the same cycle number. These latest results fulfill the purpose of this work by demonstrating the effectiveness of our simple approach in achieving a promising full Li-ion sulfur cell exploiting a sulfur loading approaching 3 mg cm^{-2}, despite they also evidence the need of *ad hoc* improvements across the whole system, from the composition of electrodes and electrolyte for hindering the issues of Li-PS to the cycling conditions.

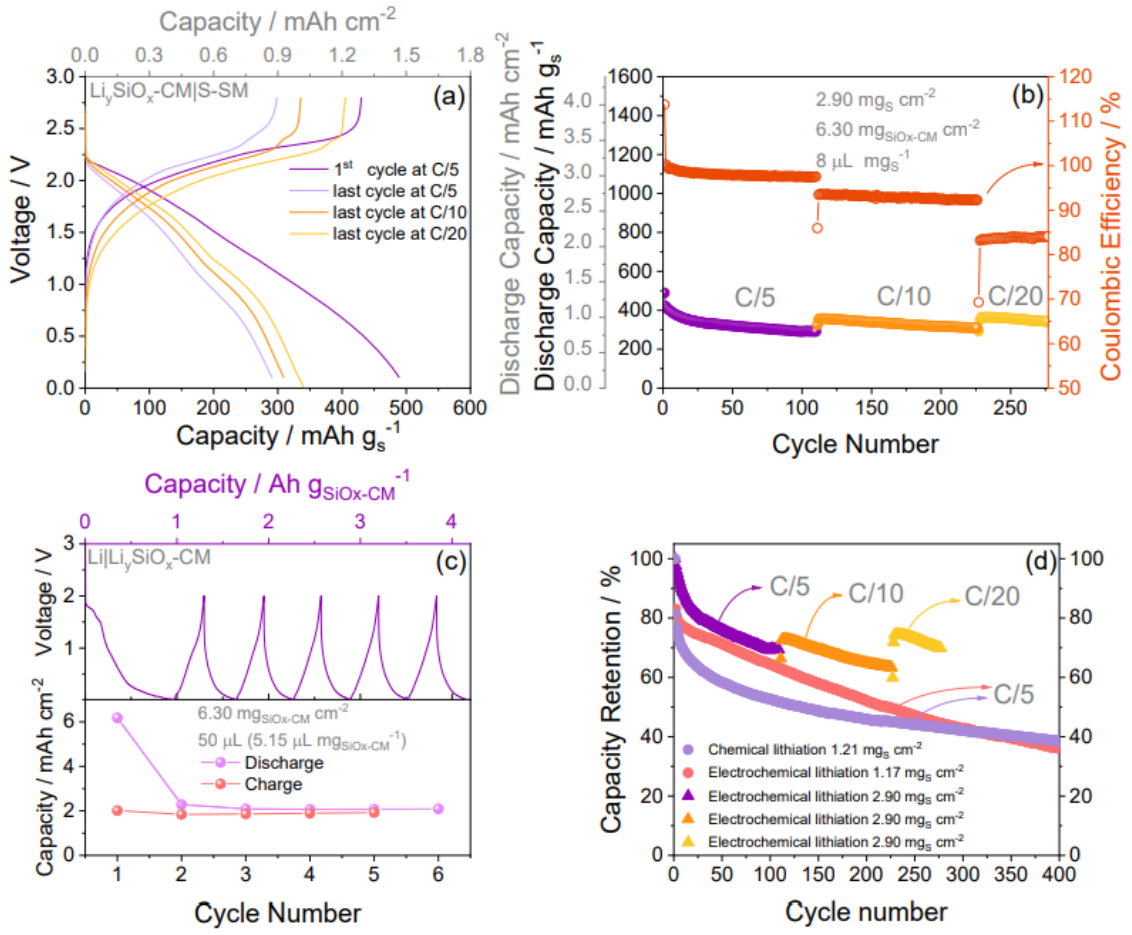

Figure 5. (a, b) Galvanostatic cycling test of a Li_ySiO_x-CM|S-SM battery including an electrochemically lithiated Li_ySiO_x-CM anode with active material loading of 6.30 mg cm^{-2} , a S-SM cathode with sulfur loading of 2.90 mg cm^{-2} and E/S ratio of 8 µl mg^{-1} : **(a)** selected voltage profiles recorded at C/5 (cycles 1-110), C/10 (cycles 111-226), and C/20 (cycles 227-277), voltage ranges: 0.1 – 2.8 V for C/5 and C/10, and 0 – 2.8 V for C/20; **(b)** corresponding cycling trend (right y-axis shows CE, additional left y-axis displays areal capacity). **(c)** Electrochemical lithiation of a SiO_x-CM electrode (active material loading: 6.30 mg cm^{-2}) in lithium half-cell cycled at 20 mA g^{-1} in the 0.01 – 2.0 V voltage range in terms of voltage profiles (top panel) and capacity trend (bottom panel). **(d)** Comparison in terms of capacity retention plot of the full Li_ySiO_x-CM|S-SM cells.

References

(1) IEA (2023), Tracking Clean Energy Progress 2023, IEA, Paris, Licence: CC BY 4.0, 2023.
(2) A. Manthiram, J. L. Lutkenhaus, Y. Fu, P. Bai, B. G. Kim, S. W. Lee, E. Okonkwo, R. M. Penner, One Earth 2022, 5, 203.
(3) A. Manthiram, J. B. Goodenough, Nat. Energy 2021, 6, 323.
(4) M. S. Whittingham, Chem. Rev. 2004, 104, 4271.
(5) J. B. Goodenough, K.-S. Park, J. Am. Chem. Soc. 2013, 135, 1167.
(6) A. Manthiram, Nat. Commun. 2020, 11, 1550.
(7) G. Li, S. Wang, Y. Zhang, M. Li, Z. Chen, J. Lu, Adv. Mater. 2018, 30, 1705590.
(8) A. Manthiram, Y. Fu, S.-H. Chung, C. Zu, Y.-S. Su, Chem. Rev. 2014, 114, 11751.
(9) J. Hassoun, B. Scrosati, Angew. Chem. Int. Ed. 2010, 49, 2371–2374.
(10) J. Hassoun, B. Scrosati, Adv. Mater. 2010, 22, 5198.
(11) R. Xu, I. Belharouak, X. Zhang, R. Chamoun, C. Yu, Y. Ren, A. Nie, R. Shahbazian-

Yassar, J. Lu, J. C. M. Li, K. Amine, ACS Appl. Mater. Interfaces 2014, 6, 21938.
(12) M. Cuisinier, C. Hart, M. Balasubramanian, A. Garsuch, L. F. Nazar, Adv. Energy Mater. 2015, 5, 1401801.
(13) L. Carbone, S. G. Greenbaum, J. Hassoun, Sustain. Energy Fuels 2017, 1, 228–247.
(14) V. Marangon, D. Di Lecce, F. Orsatti, D. J. L. Brett, P. R. Shearing, J. Hassoun, Sustain. Energy Fuels 2020, 4, 2907–2923.
(15) V. Marangon, E. Scaduti, V. F. Vinci, J. Hassoun, ChemElectroChem 2022, 9, e202200374.
(15a) Liang, X., Hart, C., Pang, Q., *Nat Commun* **6**, 5682 (2015).
(15b) F.Liang, Q.Deng, S.Ning, H.He, N.Wang, Y.Zhu, J.Zhu, Adv. Sci.2024, 11, 2403391.
(16) V. Marangon, E. Barcaro, L. Minnetti, W. Brehm, F. Bonaccorso, V. Pellegrini, J. Hassoun, Nano Res. 2023, 16, 8433–8447.
(17) S. Li, Z. Luo, L. Li, J. Hu, G. Zou, H. Hou, X. Ji, Energy Storage Mater. 2020, 32, 306–319.
(18) J. Castillo, J. A. Coca-Clemente, J. Rikarte, A. Sáenz de Buruaga, A. Santiago, C. Li, APL Mater. 2023, 11, 010901.
(19) D. Lin, Y. Liu, Y. Cui, Nat. Nanotechnol. 2017, 12, 194.
(20) L. Carbone, M. Gobet, J. Peng, M. Devany, B. Scrosati, S. Greenbaum, J. Hassoun, ACS Appl. Mater. Interfaces 2015, 7, 13859.
(21) D. Di Lecce, V. Marangon, H.-G. Jung, Y. Tominaga, S. Greenbaum, J. Hassoun, Green Chem. 2022, 24, 1021.
(22) D. Aurbach, Y. Talyosef, B. Markovsky, E. Markevich, E. Zinigrad, L. Asraf, J. S. Gnanaraj, H.-J. Kim, Electrochim. Acta 2004, 50, 247.
(23) A. Bhargav, J. He, A. Gupta, A. Manthiram, Joule 2020, 4, 285.
(24) M. Liu, F. Ma, Z. Ge, Z. Zeng, Q. Wu, H. Yan, Y. Wu, S. Lei, Y. Zhu, S. Cheng, J. Xie, Sci. China Chem. 2023, 67, 724.

2.2 Sulfur-carbon composite cathode for lithium battery

As discussed in section *2.1*, simple approaches involving coating of molten sulfur on carbon appeared to be suitable for achieving materials with satisfactory performances in lithium cell, and at the same time modest expected cost which may favor the economical sustainability of the Li/S battery and hence its large-scale diffusion.[25] Literature works demonstrated that the low electronic conductivity of the sulfur due to its insulating character represents the rate-determining step, which controls the cell polarization and hence the specific capacity and the energy density.[26] However, relatively high fractions of inert carbon matrices used for ensuring satisfactory electron conductivity actually affect both gravimetric and volumetric energy densities of the composite.[27] Li–S battery is certainly the most appealing postlithium-ion system of choice for powering the next generation of electric devices due to its relevant energy density which can exceed 450 W h kg^{-1}.[25-28] The present-state Li–S cell involves electrolytes based on solution of various salts in dioxolane (DOL) and dimethoxyethane (DME), characterized by high ionic conductivity and Li^+ transference number.[29,30] Despite these favorable characteristics, DOL:DME solutions have

relevant flammability and can favor dendrite growth at the Li metal surface, as well as excessive mobility and reactivity of the lithium polysulfides formed during the electrochemical process, thus posing serious concerns on the Li–S cell safety and large-scale diffusion.[31] Therefore, the development of new electrolyte media has been recognized as a priority in the optimization of the Li–S cell,[32] and glymes with $n \geq 2$ in the $-(CH_2CH_2O)_n-$ molecular formula have been indicated as the most suitable solvents for alternative and safe solutions. [33] The glyme-based solutions have been indicated to limit the depletion of the electrolyte at the lithium electrode surface and promote homogeneous lithium deposition, thus providing a regular electrode/electrolyte interphase and mitigating the formation of lithium dendrites. This favorable process has been attributed to the relatively long ether chain of glymes that improves the stability toward radical species formed during the Li–S conversion process and, at the same time, enhances the lithium transport across the electrolyte bulk through the chelation of the Li^+ ions by the glyme molecules allowing an efficient interchain hopping mechanism. [34] Further steps toward practical configurations of the Li–S battery are the increase of active material in the sulfur cathode for achieving adequate gravimetric energy density [35,36] and the limitation of electrode thickness and of the electrolyte volume to get a satisfactory volumetric energy density.[37,38] In this regard, thin-layer current collectors suitable for Li–S battery application have been developed atbthye beginning of the Thesis by coating aluminum with various carbons, including MWCNTs, graphene flakes formed by limited number of layers. These new supports have been used as the current collectors in Li–S cells achieving volumetric energy density comparable to Li-ion ones (i.e., 500 W h L^{-1}) and much higher gravimetric energy (480 W h kg^{-1}). In these cells, the use of the most diffused electrolyte based on DOL:DME, LiTFSI salt, and $LiNO_3$ additive was adopted to form a protective film on the lithium metal surface and limit the direct reaction of the dissolved polysulfides (particularly Li_2S_8) with the alkali metal at the anode side (i.e., the shuttle reaction). Despite this strategy is suitable for boosting the cells, they are still affected by issues ascribed to the flammable nature of the electrolyte and the formation of dendrites at the metal surface.

#4 10.1021/acsaem.3c01966

Towards Sustainable Li-S Battery Using Scalable Cathode and Safe Glyme-based Electrolyte

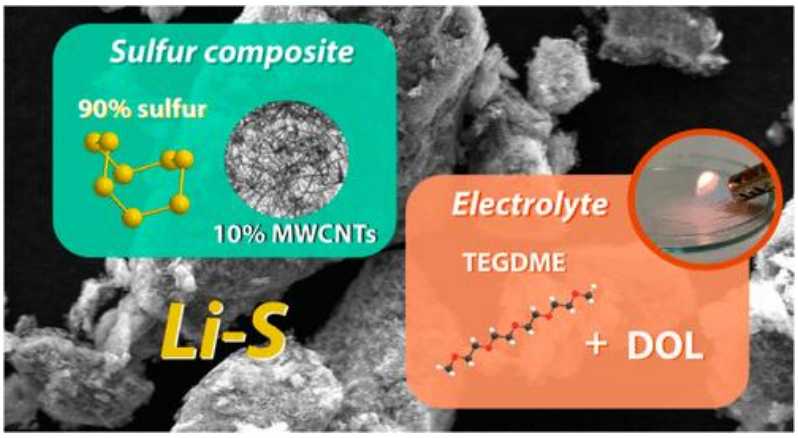

In this research we studied of TEGDME-based solutions and a sulfur-MWCNTs composite including 90 wt% of active material cast on a low-thickness MWCNTs-coated Al support (S8) to obtain Li-S cells characterized both by suitable energy density and remarkable safety content. The already known high viscosity of TEGDME (3.3–3.7 mPa s). [40] may represent a non-negligible limit hindering the thin-layer cell application, particularly in view of the relatively low wettability of the laminated sulfur electrode using carbon-coated Al-support. [41] This relevant issue can be mitigated by preparing binary solutions of TEGDME and a cosolvent with lower viscosity such as DOL (0.6 mPa s), [42] hence allowing cell operation with limited charge-transfer resistance. [43] We developed electrolytes predominantly including TEGDME with a limited fraction of DOL, i.e., either 5, 10, or 15 wt %. The main advantage of the TEGDME-/DOL-based electrolyte compared to that of the DME-/DOL-based one is the negligible flammability of the former rather than the high flammability of the latter. This aspect represents a very important factor for allowing diffusion of the Li-S battery. Furthermore, the combination of TEGDME and DOL is expected to reciprocally compensate the respective drawback of the two solvents, that is, the high viscosity of the former and the relevant flammability and low stability toward the Li_2S_x intermediates of the latter. Indeed, the TEGDME/DOL solutions can rely on the high chemical stability of the glyme molecule and advantageously exploit the low viscosity and the film-forming ability of the cyclic ether, [44] thus providing a suitable and safe environment for proper operation of the Li–S cell. The electrolytes have been investigated in terms of conductivity and interphase chemical stability by using EIS. Furthermore, the electrochemical stability window was determined by CV and linear scan voltammetry (LSV), the lithium transference number by chronoamperometry and EIS, and

the thermal behavior through TGA. At the same time, structure, morphology, and thermal stability of the sulfur composite have been determined via XRD, electron microscopy, and TGA, respectively, before being used for cathode preparation. The sulfur electrode has been preliminarily cycled in a Li cell using a DOL:DME-control electrolyte, prior to testing alongside the glyme-based solutions in Li-S batteries. Therefore, our novel approach provides the full characterization in parallel of a nonflammable electrolyte and of a sulfur cathode prepared with facile synthesis pathways including environmentally friendly materials and their application in a safe Li-S cell. The results of this study can promote the development at the large scale of Li–S batteries with enhanced performances and low economic impact due to the limited cost of sulfur and glymes compared to that of the electrode and electrolyte typically employed in the Li-ion batteries. [45,46]

Experimental

- Glyme Electrolyte Preparation and Characterization

The precursor electrolyte was prepared in an Ar-filled glovebox (MBraun, H_2O and O_2 below 1 ppm) by dissolving lithium bis(trifluoromethanesulfonyl)imide (LiTFSI, $LiN(SO_2)_2(CF_3)_2$, 99.95% trace metal basis, Sigma-Aldrich) and lithium nitrate ($LiNO_3$, 99.99% trace metal basis, Sigma-Aldrich) in TEGDME ($CH_3(OCH_2CH_2)_4OCH_3$, ≥ 99%, Sigma-Aldrich) with a concentration of 1 mol $kg_{solvent}^{-1}$ for each salt. Subsequently, three solutions were obtained by adding 1,3-dioxolane (DOL, anhydrous, contains ca. 75 ppm of BHT as the inhibitor, 99.8%, Sigma-Aldrich) in various concentrations to the precursor electrolyte, that is, 5, 10, and 15 wt % with respect to the mass of the initial solution. The electrolytes are indicated in the text as TE-5%, TE-10%, and TE-15%, respectively, and **Table 2.2.1** summarizes acronyms and the corresponding compositions.

Table 2.2.1
Electrolyte Acronyms and their corresponding compositions

TE-5%	TEGDME, 1 mol kg^{-1} LiTFSI, 1 mol kg^{-1} $LiNO_3$ + 5% DOL
TE-10%	TEGDME, 1 mol kg^{-1} LiTFSI, 1 mol kg^{-1} $LiNO_3$ + 10% DOL
TE-15%	TEGDME, 1 mol kg^{-1} LiTFSI, 1 mol kg^{-1} $LiNO_3$ + 15% DOL

Prior to use, a Karl Fischer 899 Coulometer (Metrohm) was employed to verify the water content below 10 ppm of TEGDME and DOL, which was achieved upon prolonged storage at room temperature of the solvents with molecular sieves (rods, 3 Å, size 1/16 in., Honeywell Fluka) previously dried under vacuum at 280 °C for 5 days, while LiTFSI and $LiNO_3$ were dried under vacuum for 2 days at 110 °C. TGA of the electrolytes was performed through a Mettler-Toledo TGA 2 instrument by running temperature scans in the 25–800 °C range at 5 °C min^{-1} with a N_2 flow of 50 ml min^{-1}. Fourier transform infrared (FT-IR) spectra of the solutions were recorded via a Bruker Vertex V70 instrument set up in the transmittance mode. Electrochemical measurements were carried out on either CR2032 coin-type cells (MTI Corp.) using electrodes with 14 mm diameter or T-type Swagelok cells using electrodes with 10 mm diameter assembled in an Ar-filled glovebox. The ionic conductivity of the solutions was evaluated by running EIS measurements at various temperatures on stainless-steel|electrolyte|stainless-steel symmetrical coin cells where the solution was held by an

O-ring (23–5FEP-2–50, CS Hyde) with an internal diameter of 10 mm. The O-ring thickness of 127 μm allowed us to fix the cell constant at 0.016 cm^{-1}. The EIS spectra were recorded in the 500 kHz–100 Hz frequency range using an alternate voltage signal of 10 mV, while the cell temperature was controlled by a Julabo F12 instrument. The ionic conductivity data were used to calculate the activation energy of the electrolytes via the Arrhenius *Eq (2)*. The Li^+ transference number (t^+) of the electrolytes was estimated through the Bruce–Vincent–Evans method using Li|Li symmetrical cells where the 14 mm-diameter Li electrodes were separated by two glass-fiber Whatman GF/B 16 mm-diameter discs. Accordingly, the cells were subjected to chronoamperometry tests by applying a potential signal (ΔV) of 30 mV for 90 min, while Nyquist plots were recorded via EIS before and after polarization in the 500 kHz–100 mHz frequency range using a 10 mV alternate voltage signal. The chronoamperometry and EIS outcomes were thus used in *Eq (5)*. Lithium stripping-deposition tests were performed exploiting a current of 0.1 mA cm^{-2} for galvanostatic charge/discharge processes of Li|Li symmetrical T-cells where one glass-fiber Whatman GF/B 10 mm-diameter disc separated the Li electrodes. The electrolyte stability upon aging was investigated on Li|Li symmetrical cells with one glass-fiber Whatman GF/A 16 mm-diameter disc as the separator by running EIS between 500 kHz and 100 mHz with a 10 mV alternate voltage signal every 2 h for the first 14 h after assembly and subsequently on daily basis for 18 days. The electrochemical stability window (ESW) of the solutions was determined using Li cells that employed a SPC-based working electrode separated from the 14 mm-diameter lithium anode by a glass-fiber Whatman GF/A 16 mm-diameter disc. The SPC-based cathodes were prepared by dispersing SPC (80 wt %) and PVdF binding polymer in NMP to obtain a viscous slurry, which was cast on either Al or Cu foils with the aid of a doctor blade tool (MTI Corp.). The electrode tapes were dried on a hot plate at 70 °C for 3 h and cut into 14 mm-diameter discs, which were dried under vacuum at 110 °C for 3 h before being transferred in an Ar-filled glovebox. Anodic and cathodic regions of the ESW were investigated by performing either LSV on Li|SPC-Al cells from the open-circuit voltage (OCV) condition to 5 V vs Li^+/Li or CV between 0.01 and 2.0 V vs Li^+/Li on Li|SPC-Cu cells. Both LSV and CV data were acquired at a 0.1 mV s^{-1} scan rate. The NLLS analyses allowed us to describe the Li cell through an equivalent circuit composed of resistive (R) and constant-phase (Q) capacitive elements. In particular, the high-frequency intercept of the plot with the real axis is associated with the electrolyte resistance (R_e); the amplitude of the high-medium frequency semicircle measures the interphase resistance R_i which includes contributes of the passivation film and charge transfers and is arranged in parallel with the Q_i capacitance in the (R_iQ_i) element, while the low-frequency semicircles (R_wQ_w) or tilted lines (Q_w), respectively, represent either the finite-length or semiinfinite Warburg-type Li^+ diffusion. Only fitting results with a χ^2 value of the order of 10^{-4} or lower were considered suitable. Voltammetry and EIS measurements were performed by using a VersaSTAT MC Princeton Applied Research (PAR-AMETEK) instrument, while the galvanostatic cycling data were recorded through a MACCOR series 4000 battery test system.

- Sulfur Composite Synthesis and Characterization

Elemental sulfur (≥99.5%, Riedel-de Haën) and MWCNTs (>90% carbon basis, D × L: 110–170 nm × 5–9 μm, Sigma-Aldrich) were mixed in the 90:10 w/w ratio and heated at 125 °C under magnetic stirring with a silicon oil bath until melting of sulfur and uniform mixing with MWCNTs. The viscose mixture was subsequently quenched at room temperature until solidification and ground in an agate mortar to obtain a fine powder. The composite is indicated in the text as S:MWCNTs 90:10 w/w. XRD

patterns of S:MWCNTs 90:10 w/w and bare MWCNTs were acquired using a Bruker D8 Advance equipped with a Cu Kα source (8.05 keV) by performing scans over the 10–90° 2θ range with a step size of 0.02° and a rate of 10 s $step^{-1}$. TGA was performed via a Mettler-Toledo TGA 2 instrument between 25 and 1000 °C under a N_2 flow of 50 mL min^{-1} at 5 °C min^{-1}. SEM images were captured by a Zeiss EVO 40 microscope using a LaB_6 thermionic electron gun in both secondary electrons and backscattered electrons mode. EDS elemental maps were recorded on the SEM backscattered electrons images through a X-ACT detector associated with the microscope. Transmission electron microscopy (TEM) images were acquired with a Zeiss EM 910 microscope equipped with a tungsten thermoionic electron gun working at 100 kV.

- Electrode preparation

The cathode current collector was prepared forming a slurry composed by 90 wt % MWCNTs and 10 wt % PVdF dispersed in NMP was cast on a bare aluminum foil (thickness of 15 μm, MTI Corp.) with the aid of a doctor blade tool (MTI Corp.). The cathodic support was dried at room temperature, and the final MWCNTs loading was ∼1.3 mg cm^{-2}. The sulfur electrodes were prepared by using the MWCNTs-coated aluminum support. The electrode was obtained via doctor blade casting of a slurry composed by 80% S:MWCNTs 90:10 w/w, 10% poly(vinylidene fluoride-co-hexafluoropropylene) (PVdF-HFP, Kynar Flex 2801) as the polymer binder, and 10% FLG as conductive carbon dispersed in tetrahydrofuran (THF,Sigma-Aldrich) through 1 h of magnetic stirring. The electrode tape was dried at room temperature, calendared with a MSK-2150 rolling machine (MTI Corp.) with final thickness of 100 μm, cut into discs with a diameter of 14 mm (geometrical area: 1.54 cm^2), and dried overnight at 30 °C under vacuum before being transferred in an Ar-filled glovebox. The final sulfur loading on the electrodes ranged between 1.7 and 5.2 mg cm^{-2}.

- Electrochemical test

CR2032 coin-type cells (MTI Corp.) were assembled in an Ar atmosphere by stacking a 14 mm-diameter lithium disc, an 18 mm-diameter Celgard 2400 separator soaked with the electrolyte (see volume below), and a sulfur cathode. A control electrolyte was prepared by mixing DOL and 1,2-dimethoxyethane (DME, anhydrous, 99.5%, inhibitor-free, Sigma-Aldrich) solvents in the 1:1 w/w ratio and dissolving LiTFSI and $LiNO_3$ both in a concentration of 1 mol $kg_{solvent}^{-1}$. Analogously to the other solvents, DME water content lower than 10 ppm was achieved via prolonged storage under dry molecular sieves (rods, 3 Å, size 1/16 in., Honeywell Fluka) and confirmed prior to use by a Karl Fischer 899 Coulometer (Metrohm). The sulfur electrode was initially tested in a Li cell using the DOL:DME-control electrolyte. In particular, galvanostatic cycling measurements were performed through constant current rates of either C/5 or C/3 (1C = 1.675 A g^{-1}) between 1.7 and 2.8 V for a sulfur loading of 2.2–2.3 mg cm^{-2} using an E/S ratio of 10 μl mg^{-1}, while cathodes with a sulfur loading of 5.2 mg cm^{-2} were employed for galvanostatic tests at C/10 in the 1.7–2.8 V voltage range using an E/S ratio of 6 μl mg^{-1}. Rate capability tests were also carried out exploiting a sulfur loading of 2.2 mg cm^{-2} and an E/S ratio of 10 μl mg^{-1} by increasing current rate every 5 cycles from C/10 to C/8, C/5, C/3, and C/2 and decreasing back to C/10 after 25 cycles. A voltage range from 1.8 to 2.8 V was used from C/10 to C/3, while limits of 1.7 and 2.8 V were exploited for C/2. CV tests were performed via potential scans between 1.8 and 2.8 V vs Li^+/Li at a scan rate of 0.1 mV s^{-1} through a VersaSTAT MC Princeton Applied Research (PAR-AMETEK) instrument. The S:MWCNTs 90:10 w/w cathode was subsequently tested in a Li cell using the TE-5%, TE-10%, and TE-15%

electrolytes via galvanostatic cycling measurements at C/5 constant rate (sulfur loading: 1.7–2.1 mg cm^{-2} and E/S ratio: 15 µl mg^{-1}) between 1.7 and 2.8 V. Rate capability measurements were also performed at increasing rates of C/20, C/10, C/8, C/5, C/3, and C/2 before decreasing the current back at C/20 after 30 cycles (sulfur loading: ∼2.0 mg cm^{-2} and E/S ratio: 15 µl mg^{-1}). The tests were carried out between 1.8 and 2.8 V from C/20 to C/8 and between 1.7 and 2.8 V from C/5 to C/2. The galvanostatic cycling measurements were all carried out with a MACCOR series 4000 battery test system.

Results

Notably, none of the solutions presents ignition processes after direct flame exposure for 5 s, thus confirming the enhanced safety with respect to the conventional DOL:DME-control electrolyte, which shows instead immediate fire development. The physical–chemical properties of the TE-5%, TE-10%, and TE-15% electrolytes are evaluated in **Figure 1**. The TGA (**Figure 1a**) and corresponding differential curves (DTG, Figure 1b) show for all electrolytes a first weight decrease at 150 °C with intensity growing alongside DOL concentration, likely due to the partial volatilization of the cyclic ether.(40) The evaporation of TEGDME solvent takes place around 200 °C;(40) however, the related weight loss is centered at 197 °C for TE-5%, 210 °C for TE-10%, and 263 °C for TE-15%. These discrepancies can be ascribed to the modification of the solvation environment caused by the increasing concentration of DOL, which may lead to formation of a cosolvent and influence the structure, as well as thermal behavior, of the solvent–salt complexes within the solution.(41) The DTG curves further support the formation of specific salt–solvent complexes depending on the DOL content, in view of the differences observed in the multipeak profile between 250 and 400 °C, associated with weight losses due to solvent removal from crystallized-salt structures. In addition, the thermal analysis reveals at about 430 °C the weight decrease ascribed to LiTFSI degradation.(42) It is worth noting that residual weight exhibited by the electrolytes at the end of the test can be attributed to $LiNO_3$.(43) Indeed, TE-15% shows conductivity approaching 3×10^{-3} S cm^{-1} around 50 °C exceeding the one related to TE-5% and TE-10% of 2×10^{-3} S cm^{-1}, while similar values are observed at room temperature (∼25 °C) near 1.5×10^{-3} S cm^{-1}. Relevantly, at temperature as low as −3 °C, the TE-5%, TE-10%, and TE-15% solutions still exhibit conductivities of 8×10^{-4}, 6×10^{-4}, and 7×10^{-4} S cm^{-1}, that is, suitable values to promote efficient operation in Li batteries. Furthermore, all the solutions show a linear conductivity trend with slope increasing in concomitance with the DOL concentration raise. The Arrhenius equation (*Eq (2)*) allows the estimation of the activation energy (E_a), which identifies the energy barrier limiting the Li^+ diffusion in the electrolyte.(44) The calculated values are represented in the histogram of **Figure 1d**, which reveals the increase of E_a from TE-5% (5.1×10^{-2} eV) to TE-10% (7.6×10^{-2} eV) and TE-15% (8.5×10^{-2} eV). The

increase of E_a by raising the content of the DOL in the solvent mixture may in part contrast with the expected viscosity and ion friction decreases that can, in principle, increase the Li^+ mobility. On the other hand, this behavior may be justified by the variation of dielectric constant (ε) of the mixture due to the lower ε for DOL (7.1)[40] compared to TEGDME (7.8),[40] the chain-structure of which can efficiently promote the ion-pair dissociation and mobility due to the relevant content of oxygen atoms suitable for the Li^+ coordination into Li–glyme complexes. Hence, the weighted average dielectric constant (ε_w) of the solvent mixtures, calculated in **Figure 1e** considering the TEGDME:DOL ratio, decreases from 7.77 for TE-5% to 7.74 for TE-10% and to 7.71 for TE-15%. This trend agrees with that of E_a discussed previously, evidencing the complex influence of DOL on the glyme-based electrolyte properties, although the reduction of viscosity can increase the conductivity at the higher temperatures as observed herein. The Li^+ transport features of the solutions are subsequently evaluated in a Li symmetrical cell for estimation of the Li^+ transference number (t^+) using the Bruce–Vincent–Evans equation (*Eq (5)*). **Table 2.2.2** summarizes the parameters used for calculation obtained from the chronoamperometric curve. The obtained values are displayed in **Figure 1f** as histogram columns. The solutions present t^+ values between 0.50 and 0.55 which suggest fast Li^+ transport, although a decreasing trend is observed by the increase of DOL concentration in line with the increment of E_a. Additional information about the salt dissolution in the electrolytes is provided by the corresponding FT-IR spectra in **Figure 1g**. The solutions show slight differences, whereas shifts are observed for the bands related to pure LiTFSI. In particular, the S–N–S stretching observed at 810, 773, and 774 cm^{-1} and the SO_2 group asymmetric stretching at 1200 cm^{-1} move to lower wavenumbers, indicating the dissociation of the salt. Further proof of LiTFSI dissolution is given by the variation of the relative intensities with shift to higher wavenumbers of the peaks at 1350 and 1320 cm^{-1} accounting for CF_3 asymmetric stretching. On the other hand, the increase in relative intensity of the signal near 1650 cm^{-1} attributed to LiTFSI by the DOL concentration raising may suggest a higher ion-pair association degree for TE-15% and TE-10% compared to TE-5%, in agreement with the respective lower values of ε_w discussed above.

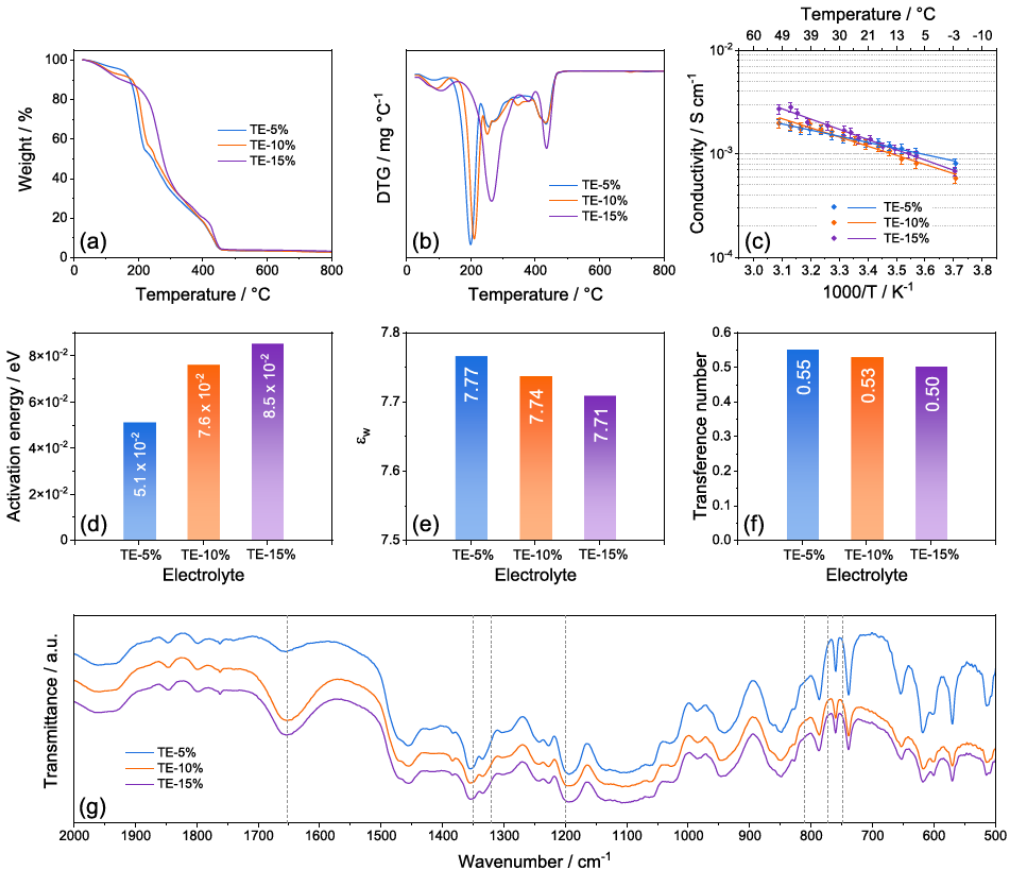

Figure 1. (a) TGA and **(b)** corresponding DTG curves of the electrolytes acquired under N_2 flow between 25 and 800 °C at the 5 °C min^{-1} rate; **(c)** ionic conductivity trends of the electrolytes reporting in addition the linear fit for each electrolyte; **(d)** histogram representation of the activation energy values calculated using the Arrhenius equation (*Eq (2)*) on the ionic conductivity trends in panel **(c)**; **(e)** histogram representation of the weighted average dielectric constants (ε_w) calculated considering the electrolytes solvents ratio and the ε values of pure DOL (7.1)[40] and TEGDME (7.8)[40]; **(f)** histogram representation of the Li^+ transference number (t^+) of the electrolytes determined through Bruce-Vincent-Evans method (*Eq (5)*); **(g)** FT-IR spectra of the TE-5%, TE-10% and TE-15% solutions. See Table 2.2.1 for electrolyte acronyms.

Table 2.2.2 Parameters used in eq. 2 to evaluate Li^+ Transference Number (t^+) through the Bruce-Vincent-Evans Method

Cell condition	R_0 (Ω)	R_{SS} (Ω)	I_0 (A)	I_{SS} (A)	t^+
TE-5%	61.4	59.5	2.31×10^{-4}	1.63×10^{-4}	0.55
TE-10%	46.8	45.2	2.75×10^{-4}	1.85×10^{-4}	0.53
TE-15%	54.5	45.2	3.09×10^{-4}	2.29×10^{-4}	0.50

The stability of the electrolytes in the Li cell is investigated in **Figure 2** by monitoring the electrode/electrolyte interphase resistance upon cell aging (**Figure 2a**), evaluation of the ESW (**Figure 2b–d**), and Li stripping-deposition ability (**Figure 2e**). **Figure 2a** shows the electrode/electrolyte interphase resistance (R_i) trends obtained by the NLLS analyses. The EIS spectra of the symmetrical Li|Li cells are plotted through the $R_e(R_iQ_i)(R_wQ_w)$ equivalent circuit. The results reveal initial R_i values of 85 Ω for TE-5%, 84 Ω for TE-

10%, and 50 Ω for TE-15%, which raises upon cells aging to reach respective values of 154, 129, and 86 Ω after 18 days. The progressive increase and sporadic decreases of the interphase resistance are associated with growth and partial dissolution of the SEI on the lithium surface, leading to stabilization of the passivation layer and protection of the alkali metal.[47] Interestingly, TE-5% exhibits generally higher values and lower stability of R_i, followed by TE-10% and TE-15%, thus suggesting that the DOL can lead to a favorable SEI upon the statical storage.[48] **Figure 2b–d** displays the voltammograms recorded via CV between 0.01 and 2.0 V vs. Li^+/Li (cathodic scan) and LSV from OCV condition to 5.0 V vs. Li^+/Li (anodic scan) on Li|SPC cells to determine the ESW of TE-5% (**Figure 2b**), TE-10% (**Figure 2c**), and TE-15% (**Figure 2d**). The CV profiles of the cathodic scan show for all the solutions a sharp signal at 1.5 V vs Li+/Li during the first cycle ascribed to $LiNO_3$ reduction, followed by a potential shoulder below 1.0 V vs. Li^+/Li and a final signal at 0.01 V vs Li^+/Li accounting for partial electrolyte decomposition, Li insertion in the carbon matrix, and possible beginning of the Li electrodeposition. The subsequent cycles reveal low polarization of the reversible (de)insertion of Li in the carbon-based electrode, with notable stability suggested by the overlapping of the profiles. Therefore, the similar CV responses indicate only a marginal effect of DOL on the electrolyte cathodic stability. On the other hand, the LSV curves evidence that DOL addition leads to a different anodic stability, which is considered as the potential for which a non-negligible current of 30 μA is measured. The lower anodic stability triggered by DOL addition to TEGDME is actually expected due to the higher reactivity of the ether ring of the former compared to the glyme chain of the latter.[49] Nevertheless, all the electrolytes provide ESWs extending from 0 to around 4.4 V vs. Li^+/Li, that is, a well sufficient span to host the Li–S electrochemical process.[50] The lithium stripping-deposition profiles reported in **Figure 2e** are acquired from Li|Li cells to evaluate the overvoltage related to Li^+ exchange through the electrolytes, which reflects the resistance of the interphase under dynamic conditions. During the initial cycles, all the solutions present a square-shape overvoltage with values approaching 40 mV, despite a slightly higher polarization being observed for TE-15% with respect to the other solutions. This may be attributed to the reactivity of the cyclic ether on the Li surface to form the SEI layer,[51] which would lead to a more relevant overvoltage in TE-15% than in TE-5% and TE-10% at the beginning of the test due to the higher content of DOL in the solution. The polarization decreases after 7 days of test due to a partial SEI dissolution, and the overvoltage reaches values of 20, 23, and 27 mV for TE-15%, TE-10%, and TE-5%, respectively, at the beginning of the 8^{th} day. Despite the small differences, the more remarked polarization decrease for TE-15% with respect to TE-10%

and TE-5% may account for a higher solubilization degree of the SEI possibly promoted by the lowered viscosity of the solvent mixture. On the other hand, the slight increase and stabilization of the overvoltage to values of ~30 mV observed for all the solutions in the second half of testing are in line with the consolidation of a suitable SEI layer.

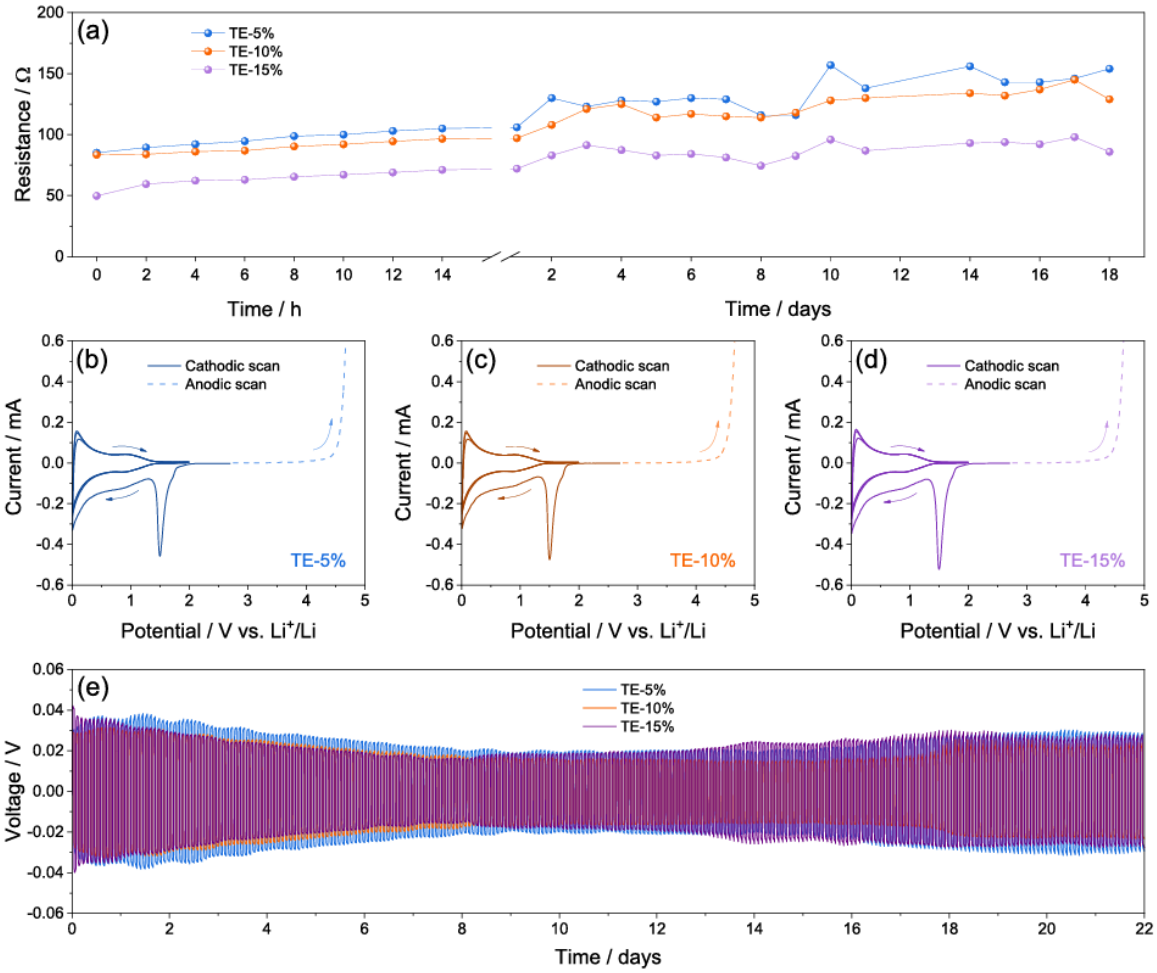

Figure 2. (a) Interphase resistance trends related to Li|Li cells using either TE-5%, TE-10% or TE15% aged for 18 days, **(b, d)** ESW evaluation of the **(b)** TE-5%, **(c)** TE-10% and **(d)** TE-15% electrolytes performed via CV in the cathodic region (0.01 – 2.0 V vs. Li+/Li) and LSV in the anodic one (from OCV to 5.0 V vs. Li+/Li) at the scan rate of 0.1 mV s-1; **(e)** Lithium stripping-deposition tests performed on Li|Li cells using either TE-5%, TE-10% or TE-15%. See Table 2.2.1 for electrolyte acronyms.

The S:MWCNTs 90:10 w/w composite powder is investigated in **Figure 3** in terms of structure, thermal behavior, and morphology by XRD (**Figure 3a**), TGA (**Figure 3b**), and SEM-EDS/TEM (**Figure 3c–i**), respectively. The X-ray diffractogram of the composite in **Figure 3**a shows the crystalline signature of orthorhombic sulfur according to the reference data (ICSD #27840 shown for comparison). The same figure reports the pattern of MWCNTs powder included in the electrode formulation and clearly reveals the graphitic character of this carbon (ICSD #76767 shown for comparison) with a main peak around 26°, which is instead observed as a broad wave extending from about 16–35° in the

composite. The absence of additional signals accounting for undesired species excludes byproducts possibly formed during material synthesis which can lead to side reactivity during the Li–S conversion process, and confirms the suitability of the sulfur–carbon melt-mix process conducted at mild temperature. The success of the sulfur composite preparation is further confirmed by TGA and the corresponding DTG in **Figure 3b**, which reveals a sole weight loss between 200 and 380 °C accounting for the sulfur evaporation with a ratio of 90% of the total mass, exactly corresponding to the predicted amount.[52] The SEM images acquired in secondary electron mode in **Figure 3c,d** show large sulfur clusters ranging from 10 to 100 μm (**Figure 3c**) formed by submicrometric primary particles covered by a thin layer of MWCNTs (**Figure 3d**). The uniform coverage of MWCNTs is highlighted by the SEM image recorded in backscattered electron mode in Figure 3e and by the corresponding EDS elemental mapping of sulfur and carbon in **Figure 3f,g**, respectively, which remark the efficient disposition of MWCNTs around the sulfur particles. Additional insight into the MWCNTs morphology and disposition in the S:MWCNTs 90:10 w/w composite is provided by the TEM images in **Figure 3h,i**. The micrographs evidence an entangled view of the system, which depicts a network of carbon across the sulfur clusters composed by connected nanotubes with micrometric length and thickness below 100 nm. Despite the relatively low ratio used herein, the conductive carbon net of the MWCNTs is expected to facilitate the electron pathway during electrochemical conversion, leading to satisfactory performance of the Li–S cell. On the other hand, the micrometric features of the composite can lower the impact of the side processes associated with the electrolyte decomposition on the overall reversibility of the main electrochemical reaction, and the high amount of the sulfur may ensure a high practical capacity and scalability of the composite material.[53]

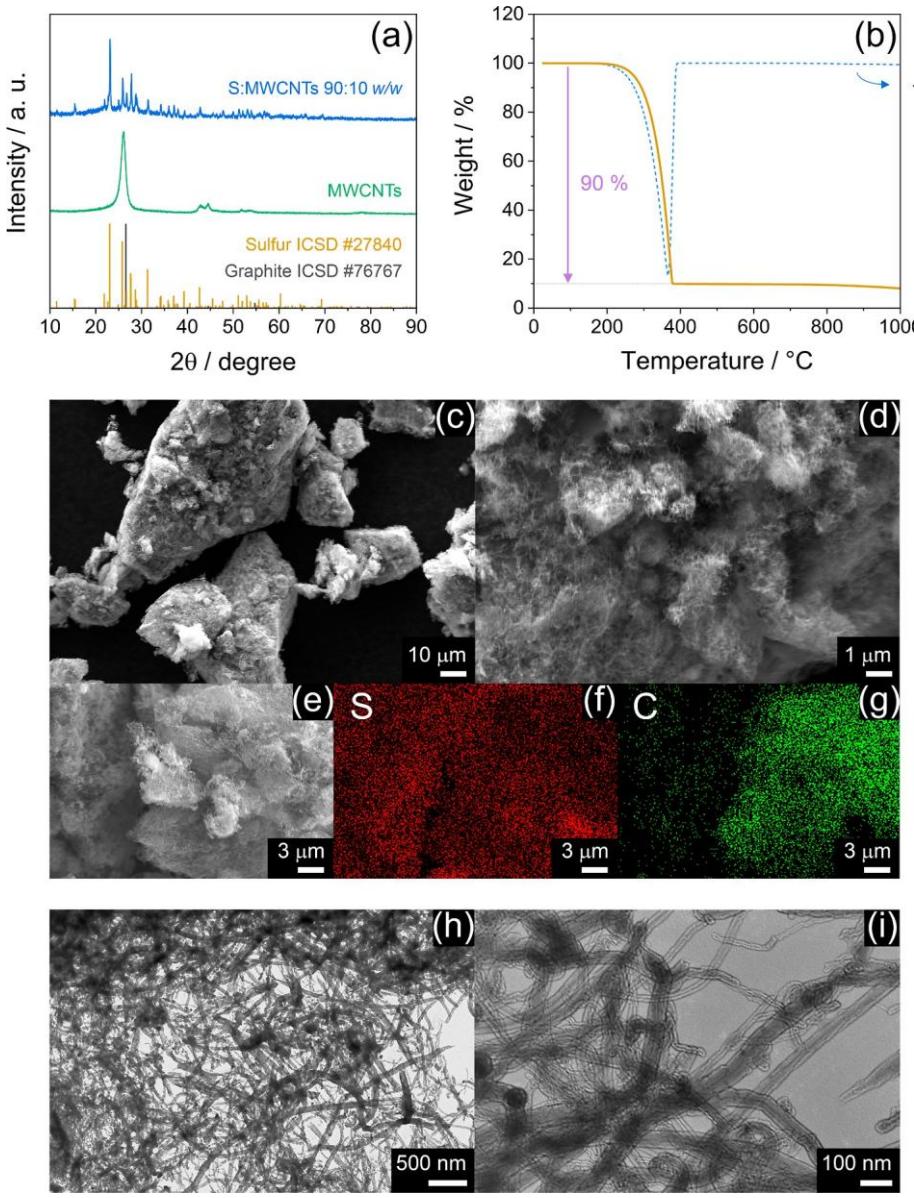

Figure 3. Physical-chemical characterization of the S:MWCNTs 90:10 w/w composite. In detail: **(a)** XRD of the composite and bare MWCNTs, reference data for sulfur (ICSD #27840) and graphite (ICSD #76767) are reported for comparison; **(b)** TGA and corresponding DTG (right y-axis) performed under N_2 flow between 25 and 1000 °C at the 5 °C min-1 rate; (c, d) SEM images at various magnification recorded in secondary electrons mode; **(e)** SEM picture acquired in backscattered electrons mode and **(f, g)** corresponding elemental maps of **(f)** sulfur and **(g)** carbon; **(e, f)** TEM images at various magnifications.

The S:MWCNTs 90:10 w/w composite is subsequently included in a cathode and cycled in a lithium cell using the DOL:DME-control electrolyte, as reported in **Figure 4**. The voltage profiles of the rate capability test displayed in **Figure 4a,b** show the typical signature of the Li–S conversion process, where two galvanostatic discharge plateaus at 2.3 and 2.1 V are reflected during subsequent charge in two merging steps at 2.3 and 2.4 V.[54] The discharge plateau at the higher voltage (i.e., 2.3 V) actually accounts for the initial conversion of Li and S to long chain polysulfides such as Li_2S_8, instead the one at the

lower voltage (~2.1 V) reflects the complex equilibrium including intermediate radical species during which the polysulfides are shortened to form Li_2S_4, Li_2S_2, and possibly Li_2S by subsequent reductions.[55] During the charge process, the oxidation back of the Li_2S_x polysulfides occurs with a different pathway compared to the discharge process since the two steps discussed above are almost convoluted.[56] As expected by the raising of C-rate from C/10 to C/3, the overvoltage between discharge and charge processes increases leading to a modest decrease of the delivered capacity; instead, the current of C/2 almost completely hinders the proper development of the low-voltage discharge plateau. Indeed, the corresponding discharge capacity trend (**Figure 4b**) evidences an initial value of 1100 mA h g^{-1} at C/10 and subsequent steady-state capacities of 976, 915, 833, 720, and 163 mA h g^{-1} at C/10, C/8, C/5, C/3, and C/2, respectively. Thus, a satisfactory rate capability is achieved by the S:MWCNTs 90:10 w/w from C/10 to C/3, as also suggested by the final capacity recovering at 922 mA h g^{-1} by lowering back the current at C/10 in the last five cycles, that is, 84% of the initial capacity and 94% compared to the steady state at the same C-rate. Instead, the very modest capacity of the cell at C/2 can be expected due to the relatively high amount of the active sulfur compared to electrochemically inactive elements such as the conductive carbon both in the composite and in the support, as well as by the laminated configuration of the electrode which can lead in turns to a relevant volumetric energy density. [57]

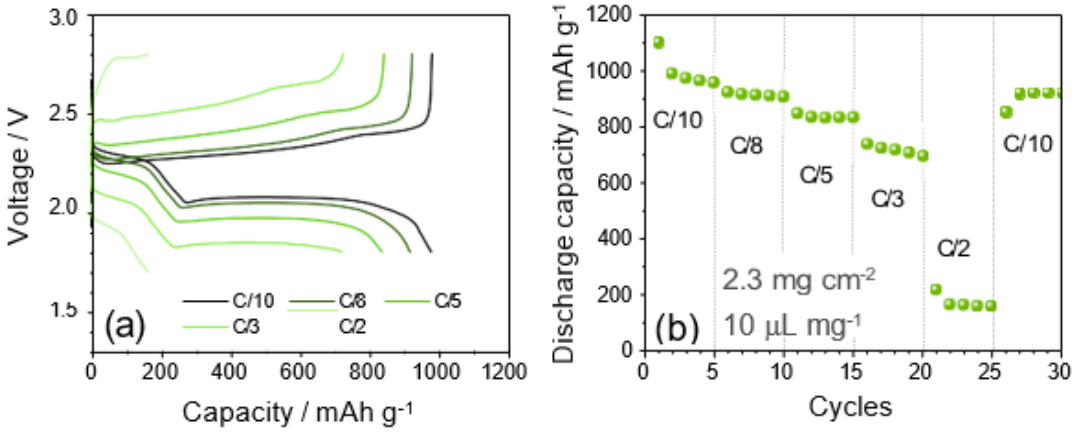

Figure 4. Galvanostatic cycling of Li cells using the S:MWCNTs 90:10 w/w electrode and the DOL:DME-control electrolyte with sulfur loading of 2.2–2.3 mg cm^{-2} and E/S ratio of 10 µL mg^{-1}. In particular: **(a)** voltage profiles and the **(b)** corresponding capacity trend related to the rate capability test.

Li–S cells using the S:MWCNTs 90:10 w/w electrode with TE-5%, TE-10%, and TE-15% electrolytes are cycled at the constant current rate of C/5 and reported in **Figure 5**. The voltage profiles in **Figure 5a–c** show that at the first cycle for all the cells, excessive polarization hinders the low-voltage discharge plateau. The above absence of the low-voltage plateau in TE-5% (**Figure 5a**), its partial development in TE-10% (**Figure 5b**), and its presence in TE-15% (**Figure 5c**) account for the enhancement of the liquid–solid conversion from soluble long-chain LiPS to short-chain ones promoted by the decrease of viscosity of the electrolyte by DOL addition.[58] On the other hand, all the cells present progressive activation of the Li–S conversion process indicated by the occurrence of the low-voltage discharge step upon cycling. Different activations depending on DOL concentration are evidenced by the cycling trends in **Figure 5d**. The figure displays an increase of the delivered cell capacity during the initial stage from 140 to 360 mAh g^{-1} for TE-5%, from 220 to 530 mAh g^{-1} for TE-10%, and from 270 to 570 mAh g^{-1} for TE-15%. Interestingly, the capacity growth speed decreases from TE-5% to TE-15%, thus suggesting a faster cell activation for lower DOL concentration. Despite the fact that decreasing viscosity from TE-5% to TE-15% can in principle allow a faster wetting of the sulfur electrode and facilitate the electrochemical process, the initial activation appears to be mostly controlled by E_a and ε_w values. In fact, **Figure 5d** evidences a capacity growth speed decreasing from TE-5% to TE-15%. This outcome may indicate that the activation speed is intimately correlated with the Li^+ transport properties of the solution, which are relevantly influenced by E_a and ε_w. Therefore, the progressively slower activation from TE-5% to TE-15% is reasonably explained by the respective decreases in E_a and ε_w (**Figure 1**).

However, the low concentration of the cosolvent in TE-5% limits the discharge capacity of the cell to a maximum of 420 mAh g^{-1} and promotes the discharge/charge overvoltage, leading to a sudden deactivation of the electrochemical process after 117 cycles with capacity below 100 mAh g^{-1} (**Figure 5d**). On the other hand, TE-15% allows in the cell a stable, steady-state capacity between 500 and 550 mAh g^{-1}, although a gradual deactivation occurs after 100 cycles to a final capacity of 250 mAh g^{-1} (**Figure 5d**). The cell using TE-10% reveals a fluctuation of the capacity between 400 and 580 mAh g^{-1} and a decrease limited to 406 mAh g^{-1} after 130 cycles (**Figure 5d**). Interestingly, all the cells have a Coulombic efficiency exceeding 96% during the whole test, except the one with TE-5% showing efficiency decrease to 82% in correspondence to conversion deactivation. The fluctuations of the discharge capacity observed in **Figure 5d** may be due to complex interplay during cycling between TEGDME, DOL, the formed cosolvents, and the Li_2S_x intermediates, depending on the TEGDME:DOL ratio. Hence, TE-10% presents the most relevant fluctuations with the most improved cycle life, thus suggesting that the addition of 10 wt % DOL particularly acts on the polysulfides solvation and nature. On the other hand, TE-5% and TE-15% appear to mainly affect the reaction kinetics and the film formation, in particular during the final stages of the cycling tests. Indeed, TE-5% exhibits stable discharge capacity in line with the beneficial effects of the glyme solvent which guarantees an efficient Li_+ exchange, but the excessive viscosity of the solution limits both capacity value and cycle life. Furthermore, TE-15% delivers higher capacity, thanks to the limited viscosity, but the continuous depletion of DOL likely causes irregular and excessive SEI that shortens the cycle life. Hence, the data of **Figure 5** evidence a complex interplay between DOL and TEGDME in the Li–S cell. The relevant amount of DOL in TE-15% mitigates the solution viscosity but slows the speed of the Li–S activation. At the same time, the DOL leads in the TE-15% cell to the higher steady-state capacity, however, with excessive SEI growth affecting the cycle life as evidenced by the capacity deactivation after 110 cycles. In spite, the low DOL content in TE-5% ensures a fast activation to the cell likely due to the enhanced Li^+ exchange allowed by the lower E_a and ε_w (see **Figure 1**) but limits the discharge capacity and leads to cell failure after 117 cycles due to the excessive polarization raise attributed to the relevant viscosity of the solution. The TE-10% appears to be the most promising compromise since the corresponding Li–S cell shows the longer cycle life likely ascribed to the optimal proportion between TEGDME and DOL, despite the fluctuation of the capacity during cycling, which may be assessed by improving the cathode configuration. In summary, the tuning of the amount of DOL cosolvent in the viscous glyme-based electrolytes investigated herein may pave the way toward optimized

compositions where low flammability, negligible toxicity, and performance are thoroughly balanced to achieve safe and scalable Li–S batteries. Certainly, further dedicated studies are necessary in order to achieve the optimal combinations of cosolvents and ad hoc concentrations of additives.

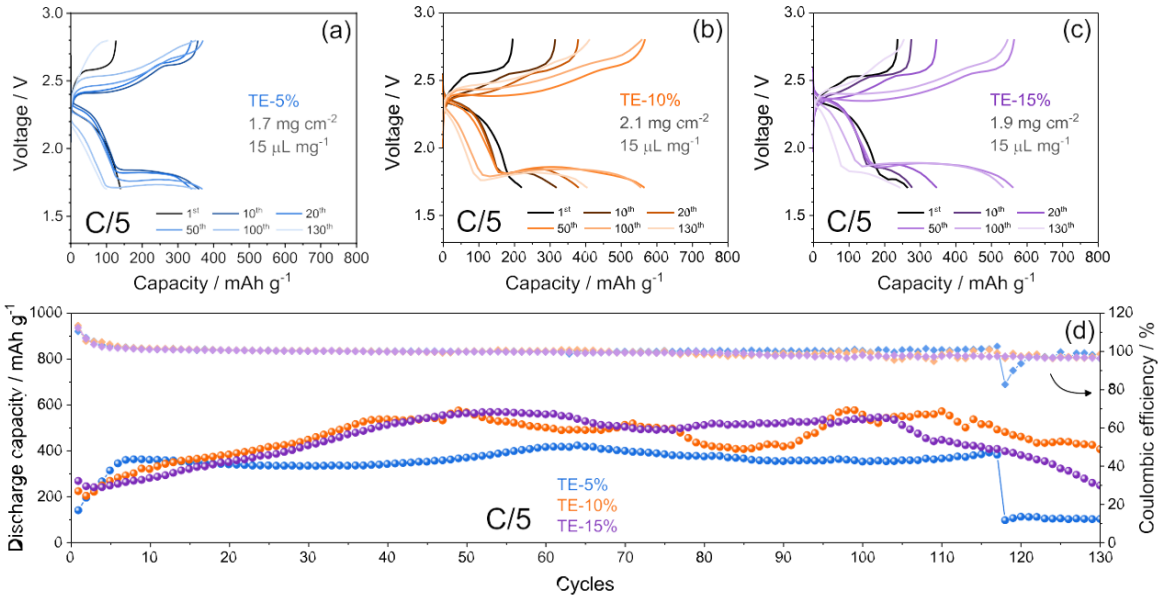

Figure 5. (a–c) Voltage profiles and **(d)** cycling trends (right *y*-axis shows Coulombic efficiency) of Li–S cells galvanostatically cycled at C/5 constant rate using either the **(a)** TE-5%, **(b)** TE-10%, or **(c)** TE-15% electrolyte and the S:MWCNTs 90:10 w/w electrode. Sulfur loading: 1.7–2.1 mg cm^{-2}; E/S ratio: 15 µl mg^{-1}; voltage range: 1.7–2.8 V.

References

(25) Ishino, Y.; Takahashi, K.; Murata, W.; Umebayashi, Y.; Tsuzuki, S.; Watanabe, M.; Kamaya, M.; Seki, Energy Technol. 2019, 7 (12), 1900197.
(26) Lu, H.; Yuan, Y.; Hou, Z.; Lai, Y.; Zhang, K.; Liu, Y.. RSC Adv. 2016, 6 (22), 18186.
(27) Agostini, M.; Xiong, S.; Matic, A.; Hassoun, J. Chem. Mater. 2015, 27 (13), 4604.
(28) Marangon, V.; Di Lecce, D.; Minnetti, L.; Hassoun, J. ChemElectroChem 2021, 8 (20), 3971.
(29) Marangon, V.; Minnetti, L.; Barcaro, E.; Hassoun, J. Chem.Eur. J. 2023, 29, No. e202301345.
(30) Cheng, Q.; Chen, Z.-X.; Li, X.-Y.; Hou, L.-P.; Bi, C.-X.; Zhang, X.-Q.; Huang, J.-Q.; Li, B.-Q. Constructing a 700 Wh kg-1-Level Rechargeable Lithium-Sulfur Pouch Cell. J. Energy Chem. 2023, 76, 181.
(33) Pang, Q.; Liang, X.; Kwok, C. Y.; Kulisch, J.; Nazar, L. F. A Comprehensive Approach toward Stable Lithium-Sulfur Batteries with High Volumetric Energy Density. Adv. Energy Mater. 2017, 7 (6), 1601630.
(34) Shen, Z.; Zhang, W.; Mao, S.; Li, S.; Wang, X.; Lu, Y. Tailored Electrolytes Enabling Practical Lithium-Sulfur Full Batteries via Interfacial Protection. ACS Energy Lett. 2021, 6 (8), 2673.
(35) Marangon, V.; Barcaro, E.; Minnetti, L.; Brehm, W.; Bonaccorso, F.; Pellegrini, V.; Hassoun, J.. Nano Res. 2023, 16 (6), 8433.
(36) Brehm, W.; Marangon, V.; Panda, J.; Thorat, S. B.; del Rio Castillo, A. E.; Bonaccorso, F.; Pellegrini, V.; Hassoun, J. Energy Fuels 2022, 36 (16), 9321.
(37)Li, W.;Yao,H.;Yan,K.;Zheng,G.;Liang,Z.;Chiang,Y.-M.;Cui, Y. Nat. Commun. 2015, 6 (1), 7436.
(38) Arbizzani, C.; Gabrielli, G.; Mastragostino, M. J. Power Sources 2011, 196 (10), 4801.
(39) Guo,F.;Hase,W.;Ozaki,Y.;Konno,Y.;Inatsuki,M.; Nishimura, K.; Hashimoto, N.; Fujita, O.

Exp. Therm. Fluid Sci. 2019, 109, 109858.
(40) Balakrishnan, P. G.; Ramesh, R.; Prem Kumar, T. J. Power Sources 2006, 155 (2), 401.
(41) Wu, Y.; Wang, W.; Ming, J.; Li, M.; Xie, L.; He, X.; Wang, J.; Liang, S.; Wu, Y. An Adv. Funct. Mater. 2019, 29 (1), 1805978.
(42) Marangon, V.; Scaduti, E.; Vinci, V. F.; Hassoun, J. ChemElectroChem 2022, 9 (11), No. e202200374.
(43) Feng, J.; Zheng, D.; Yin, R.; Niu, X.; Xu, X.; Meng, S.; Ma, S.; Shi, W.; Wu, F.; Liu, W.; Cao, X.. Small Struct. 2023, 4, 2200340. 0.82
(44) Liu, W.; Niu, X.; Feng, J.; Yin, R.; Ma, S.; Que, W.; Dai, J.; Tang, J.; Wu,F.; Shi, W.;Liu,X.;Cao,X.. ACS Appl. Mater. Interfaces 2023, 15 (12), 15344.
(45) Liu, W.; Que,W.;Yin, R.; Dai, J.; Zheng, D.; Feng, J.; Xu, X.; Wu, F.; Shi, W.; Liu, X.; Cao, X. Appl. Catal., B 2023, 328, 122488.
(46) Wang, W.; Cao, Z.; Elia, G. A.; Wu, Y.; Wahyudi, W.; Abou Hamad,E.;Emwas,A. H.;Cavallo,L.;Li,L.-J.;Ming, J. ACS Energy Lett. 2018, 3 (12), 2899.
(47) Ming, J.; Li, M.; Kumar, P.; Li, L.-J. ACS Nano 2016, 10 (6), 6037.
(48) Ming, J.; Li, M.; Kumar, P.; Lu, A.-Y.; Wahyudi, W.; Li, L.-J. ACS Energy Lett. 2016, 1 (3), 529.
(49) Tang, S.; Zhao, H. RSC Adv. 2014, 4 (22), 11251.
(50) Ruiz Holgado, M. E. F. de; Schaefer, C. R. de; Arancibia, E. L. Chem. Eng. Data 2002, 47 (2), 144.
(51) Park, C.; Kanduč, M.; Chudoba, R.; Ronneburg, A.; Risse, S.; Ballauff, M.; Dzubiella, J.. Power Sources 2018, 373, 70.
(52) Barchasz, C.; Lepretre, J.-C.; Patoux, S.; Alloin, F.. J. Electrochem. Soc. 2013, 160 (3), A430−A436.
(53) Aurbach, D.; Pollak, E.; Elazari, R.; Salitra, G.; Kelley, C. S. S.; Affinito, . J. Electrochem. Soc. 2009, 156 (8), A694.
(54) Carbone, L.; Gobet, M.; Peng, J.; Devany, M.; Scrosati, B.; Greenbaum, S.; Hassoun, J. ACS Appl. Mater. Interfaces 2015, 7 (25), 13859−13865.
(55) Shimizu, K.; Freitas, A. A.; Atkin, R.; Warr, G. G.; FitzGerald, P. A.; Doi, H.; Saito, S.; Ueno, K.; Umebayashi, Y.; Watanabe, M.; Canongia Lopes, J. N.. Phys. Chem. Chem. Phys. 2015, 17 (34), 22321−22335.
(56) Marangon,V.;Hernandez-Rentero,C.;Levchenko,S.;Bianchini, G.; Spagnolo, D.; Caballero, A.; Morales, J.; Hassoun, J. ACS Appl. Energy Mater. 2020, 3 (12), 12263−12275.
(57) Xu, K.. Chem. Rev. 2004, 104 (10), 4303.
(58) Riadigos, C. F.; Iglesias, R.; Rivas, M. A.; Iglesias, T. P.. J. Chem. Thermodyn. 2011, 43 (3), 275−283.

2.3 Catholyte and Sulfur/metal-metal oxide composite cathode

The study carried out in the previous section 2.1 and *2.2* demonstrated the suitability of a sulfur-tin-manganese-oxide and sulfur-carbon nanocomposite supported on a carbon-coated Al (S8) for application in lithium battery as well as lithium-ion-sulfur systems leveraging Li_ySiO_x-C anode. As mentioned in the Introduction, the concept of *catholyte* consists in the dissolution of lithium polysulfides into the electrolyte solution. The employing of a catholyte in a semi-liquid Li-S battery may lead to various benefits, that is, the formation of a stable SEI, the buffering of sulfur dissolution from the sulfur cathode, mitigation of volume changes due to the conversion process between sulfur and lithium, and Li-S batteries employing dissolved LiPS as active material demonstrated remarkable electrochemical performances and stable cycle life.(59) Thus, this section explores the application of glyme-based catholyte dissolving a high amount of Li_2S_8, a conductive lithium salt and the protective agent $LiNO_3$, in a semi-liquid Li-S battery exploiting a carbon-based electrode at the cathode side with presence of solid sulfur. Higy power driving from electricity may be satisfied by the present the Li-ion battery based on (de)intercalation chemistry, which can deliver a fraction of its capacity at about 3.5 V with a power level of 10 kW kg^{-1}.(60) Sulfur can electrochemically react with lithium between 2 and 3 V vs. Li^+/Li, forming soluble polysulfides trough the mechanism $S_8 + 4Li \leftrightarrows 2Li_2S_4$ with a theoretical capacity of 419 mAh g^{-1}.(61) The dissolved nature of the formed products can greatly enhance the kinetics, and therefore the power of the cell to a value as high as 50 kW kg^{-1}.(62) However, the excess of dissolved lithium salts may limit the power density due to the formation of neutral couples avoiding the lithium transport.(63) Furthermore, the actual applicability of the battery requires a high practical capacity, which can be achieved by increasing the active material loading.(64) This goal may be achieved by exploiting compact sulfur-based cathodes, including metal or metal oxides in the electrode formulation to boost the power and energy density.(65)

A High-Power Lithium-Sulfur Battery combining Catholyte and Composite Cathode

Hereafter, we exploit a synergic strategy combining the reaction of a dissolved lithium-deficient polysulfide with formula $Li_{1.5}S_8$ used as catholyte, and a sulfur electrode loaded with Sn and MnO_2. This characteristic setup is exploited within a voltage range suitable for limiting the process to soluble LiPS, thus achieving a high-power cell.

Experimental

- Catholyte preparation

The liquid catholyte was prepared by dissolving into a sealable bottle elemental sulfur (2.244 g, 0.07 mol, ≥99.5 %, Riedel-de-Haën) and Li_2S (0.322 g, 0.07 mol, 99.98%, Sigma-Aldrich) in 11 ml (9.548 g) of dioxolane (DOL anhydrous, contains ca. 75 ppm BHT as inhibitor, 99.8%, Sigma-Aldrich) and 11 ml (9.66 g) of dimethoxymethane (DME anhydrous, 99.5%, inhibitor-free, Sigma-Aldrich). After sealing the bottle an orange suspension was achieved, which was stirred for 6 h at 70 °C and for two days at room temperature to obtain a precursor looking intense red at the end of the process. The temperature was checked with the aid of a thermocouple, and maximum fluctuation of ± 2.0 °C was experienced. The used amounts of Li_2S and S was selected get to the Li-deficient catholyte with a stoichiometry of $Li_{1.5}S_8$ instead the common one (Li_2S_8). The sulfur content in 10 µL of catholyte is 0.878 mg, corresponding to a ratio with respect of the catholyte weight of 7.14 %. Before using, the solvents were dried under molecular sieves (rods, 3 Å, size 1/16 inch, Honeywell Fluka) until the water content was below 10 ppm, as tested through 899 Karl Fischer Coulometer (Metrohm). Either lithium bis(trifluoromethanesulfonyl)imide (LiTFSI, $LiN(SO_2)_2(CF_3)_2$, 99.95% trace metals basis, Sigma-Aldrich) or $LiNO_3$ (99.99% trace metals basis, Sigma-Aldrich) were dissolved in the precursor by stirring for 12 h at room temperature, to get a concentration of 1 mol of each salt in 1 kg of DOL:DME solvent. Before employment, LiTFSI and $LiNO_3$ were dried for 2 days under vacuum at 110 °C. A control electrolyte consisted of a solution formed by DOL and DME solvents mixed in the 1:1 weight ratio, LiTFSI and $LiNO_3$ in a 1 mol $kg_{solvent}^{-1}$ concentration for each salt. The catholyte and control electrolyte have been prepared inside an Ar-filled glovebox (MBraun, O_2 and H_2O content below 1 ppm).

- Electrochemical characterization

The electrochemical features of catholyte solution were studied in CR2032 coin-type cells (MTI Corp.) assembled in an Ar-filled glovebox. The ionic conductivity was investigated by means of electrochemical impedance spectroscopy (EIS) in the 500 kHz – 100 Hz frequency range through an alternate voltage signal of 10 mV on blocking-electrode stainless-steel|catholyte solution|stainless-steel symmetrical cells containing one O-rings (23-5FEP-2-50, CS Hyde, internal diameter of 10 mm) holding the catholyte with thickness of 127 µm allowed, to fix the cell constant at 0.016 cm^{-1}. The temperature of the cell ranged from 0 up to 64.1 °C and was controlled via a F 12 Julabo instrument (double-checked with a thermocouple). The Li^+ transference number (t_{Li+}) was evaluated by applying the Bruce-Vincent-Evans method (see ref 10 in Manuscript). A symmetrical cell with Li|catholyte|Li configuration was prepared by stacking two 14 mm-diameter lithium discs (0.25 mm thickness, MTI Corp.) separated

by an 18 mm-diameter Celgard 2500 monolayer microporous membrane disc soaked with 50 µL of catholyte solution. A chronoamperometry test was carried out on the cell by applying a voltage (ΔV) of 0.03 V for 90 min, and EIS was performed before and after polarization using the 500 kHz – 100 mHz frequency range and an alternate voltage signal of 10 mV. The voltage, current, and resistance values were used in *Eq (5)* to calculate t_{Li+}. The identical cell configuration was used to investigate the lithium/catholyte interphase stability upon aging at room temperature, by performing EIS measurements every 2 h for the first 14 h since assembly and during the following 14 days, using the 500 kHz – 100 mHz frequency range and an alternate voltage signal of 10 mV. Carbon electrodes were prepared through doctor blade casting over a gas diffusion layer foil (GDL ELAT 1400, 454 µm thickness) of a slurry obtained by dispersing carbon black (90%, Super P carbon, Timcal) and polyvinylidene fluoride (10%, PVdF, Solef 6020) polymer binder in *N*-methyl-2-pyrrolidone (NMP, Sigma-Aldrich). The wet foil was dried on a hot plate at 70°C, cut into 14 mm diameter discs, dried for 3 h at 110°C under vacuum inside a Büchi oven, and subsequently stored inside an Ar-filled glovebox. The electrochemical stability window of catholyte solution was determined by LSV measurements on Li|50 µL catholyte solution|Carbon cells from the open circuit voltage (OCV) to 5.0 or 0.01 V *vs.* Li^+/Li at 0.1 mV s^{-1}. The cells used a 14 mm-diameter lithium disc separated from a 14 mm-diameter carbon electrode by one 18 mm-diameter membrane (Celgard 2500). The electrochemical process was studied through CV, which was performed within 2.1 − 2.8 V *vs.* Li^+/Li at a scan rate of 0.1 mV s^{-1}. Other CV measurements were performed using the same cell configuration and scanning the potential at increasing rates, namely, 5, 6, 7, 8, 9, and 10 mV s^{-1} (3 cycles for each scan rate) in the 1.4 – 3.2 V *vs.* Li^+/Li potential range to determine the Li^+ diffusion coefficient D_{Li+} by using the Randles–Sevcik *Eq (1)*. Prior to this measurement, the cell was subject to LSV from the cell OCV to 3.2 V *vs.* Li^+/Li, using a scan rate of 5 mV s^{-1}. CV and EIS tests were carried out by using a VersaSTAT MC Princeton Applied Research (PAR-AMETEK) instrument at room temperature (25 °C). The cells were assembled by stacking a lithium disc (14 mm in diameter and 0.25 mm in thickness) and: (*i*) a carbon electrode, employed for the CV carried out at the single scan rate of 0.1 mV s^{-1}, as well as for all EIS measurements, (*ii*) a S:Sn:MnO_2 based electrode (read below for preparation details) used for the CV carried out at increasing scan rate. All the working (positive) electrodes were soaked with 66 µL of catholyte, and separated from the Li (negative electrode) by one 18 mm-diameter membrane (Celgard 2500). Lithium stripping/deposition tests were carried out either on Li|50 µL catholyte |Li or Li|50 µL DOL:DME 1:1, 1m $LiNO_3$, 1m LiTFSI|Li symmetrical cells through galvanostatic cycling measurements, applying a constant current of 2.0 mA cm^{-2} and setting a step time of 2 h for both charge (stripping) and discharge (deposition) processes. Additional high-current Li-stripping/deposition test was carried out on Li|50 µL catholyte|Li by applying various currents, namely 10, 20, 40, 60, and 100 mA cm^{-2}, before lowering back to 10 mA cm^{-2}, and setting a step time of 2 h for both charge and discharge (first and currents were applied for 8 and 6 days, respectively, while higher currents were applied for 4 days). The cells were assembled by stacking two 14 mm-diameter Li discs separated by one 18 mm-diameter membrane (Celgard 2500). The stripping/deposition measurements were carried out using a MACCOR series 4000 battery test system, in a chamber set at 30 °C, with maximum fluctuation of ±0.1 °C. Prior to the test, the cells were rested for 2 h. The fitting allows to describe the Nyquist spectra in terms of equivalent circuits, identified by the $R_e(R_iQ_i)Q$ model, including resistive (*R*) and capacitive (*Q*) elements. Specifically, R_e represents the electrolyte resistance and is indicated by the high-frequency intercept of the plot, (R_iQ_i) elements are associated to the high-medium frequency semicircle, and Q is the contribute due to constant phase elements, often identified by Q_w, indicating

the semi-infinite Warburg-type Li^+ ions diffusion which is observed as a tilted line at low frequency.

- Sulfur-based electrodes

The active materials were synthetized through a solvent-free procedure.[66-68] In brief, Sulfur, Sn, and/or MnO_2 were mixed, heated at 125 °C under magnetic stirring until complete melting of S, quenched at room temperature and grounded to obtain fine powders. The cathode tapes were obtained through casting process with a doctor blade tool set at ~500 μm of slurries formed by (round brackets indicates the weight ratio of the components) 80 wt.% active material powder, namely: *(i)* S:MnO_2 (80:20), *(ii)* S:Sn (80:20), and *(iii)* S:Sn:MnO_2 (90:5:5), 10 wt.% PVdF polymer binder, and 10 wt.% FLG as electron conductor, dispersed in NMP. The slurries were cast on GDL foils, which were heated at 70 °C on a hot plate to remove the NMP solvent. Afterwards the tapes were cut with the aid of a 14 mm-diameter punch (1.54 cm^2 geometric area), and the electrodes were dried overnight at 30 °C under vacuum inside a Büchi oven, before being stored inside an Ar-filled glovebox. The S loading in the electrodes ranged from 0.7 to 2.7 mg cm^{-2}.

- Application in lithium cell

The catholyte solution was initially tested in CR2032 coin-type lithium cells exploiting the cathodes reported above. The typical cell was assembled by stacking a 14 mm-diameter sulfur-based electrode and 14 mm lithium disc (0.25 mm thickness) separated by 18 mm-diameter membrane (Celgard 2500) soaking 66 μL of catholyte solution (containing 5.8 mg of S). The overall active material content in the cells was calculated by adding the sulfur content of the catholyte to the one in the electrode, and was made explicit in each figure caption in which the two S-sources were employed. The cells were galvanostatically cycled in the 2.1 − 2.8 V voltage range at C/2. The S:Sn:MnO_2 electrode was cycled within 2.1 − 2.8 V at C/10, C/5, C/3, C/2, and 1C, within 1.5 − 3.0 V at 5 C, 6 C, 7 C, 8 C, and 9 C, and within 0.5 − 3.5 V at 10 C, 20 C, 30 C, 40 C, and 50 C. The galvanostatic cycling measurements were performed via a MACCOR series 4000 battery test system, in a chamber set at 30 °C with maximum fluctuation of ±0.1 °C. Prior to the galvanostatic tests, the cells were rested for 2 h inside the chamber, and the first step of the test always consisted in a stabilization charge run (formation cycle) at 0.1 C to 2.8 V. The estimation of the specific discharge power and energy refers to the content of sulfur in each cell. The 1 C rate (419 mA g_S^{-1}) was calculated considering the 4-electrons electrochemical conversion of sulfur (S_8 + 4 Li → 2 Li_2S_4). **Figure 2a** shows the Nyquist plot related to EIS spectra collected at various temperatures, namely from 0.0 °C to 64.5 °C, to determine the ionic conductivity of the catholyte solution reported in **Figure 1a**. A stainless-steel|catholyte solution|stainless-steel coin cell configuration was used. The bulk resistance was calculated from the corresponding EIS spectra through NLLS fitting, and the ionic conductivity was calculated based on the *Eq (3)*. The EIS spectra recorded to investigate the aging of the lithium/catholyte interphase are reported in **Figure 2b**, while **Figure 2c** depicts the corresponding interphase resistance trend with respect to time. The results of the NLLS fitting are reported in **Table 2.3.1**.

Results

The ionic conductivity over the temperature $\sigma(T)$ of the catholyte is investigated by EIS in **Figure 1a**, and related Nyquist plots are shown in **Figure 2a**. The $\sigma(T)$ exhibits a Vogel–Tamman–Fulcher (VTF) trend according to *Eq (4)*. **Table 2.3.1** summarizes the results of the VTF plot. The catholyte solution shows a conductivity ranging from 1.4×10^{-3} S cm^{-1} at 0.0 °C to 3.7×10^{-3} S cm^{-1} at 64.5 °C, namely values having the same order of magnitude of typical Li–S electrolytes, suitable for both high and low temperature application.[69] The data achieved by plotting the conductivity using *Eq (4)* gives rise to a σ_∞ of 4.4×10^{-3} S cm^{-1}, that is the same order of magnitude of typical LIB liquid electrolytes.[70] The obtained T_0 value of 264.6 K indicates a glass transition point (T_g) for the catholyte of 234.6 K, while the fitting results account for E_a of 1.25×10^{-5} eV, which is a small value expected to promote fast ion conduction.

Table 2.3.1. Ionic conductivity at infinite temperature (σ_∞), activation energy for ion conduction (E_a), and temperature of zero configurational entropy (T_0) for the catholyte according to VTF *Eq (4)* for the conductivity trend of Figure 1a

σ_∞ (S cm^{-1})	E_a (eV)	T_0 (K)
4.4×10^{-3}	1.25×10^{-5}	234.6

The actual charge transfer occurring in the Li-cell is correlated with the net Li^+ flow through the catholyte solution, while the ionic conductivity is attributed to the mobility of all the charge carriers. Hence, the Li^+ transference number, namely the fraction of charge carried by the lithium ion (t^+), is evaluated through the Bruce–Vincent–Evans *Eq (5)*, where I_{ss} (107×10^{-6} A) and I_0 (142×10^{-6} A) are the current values at the steady and the initial state in the chronoamperometry of the symmetrical lithium cell using the catholyte in **Figure 1b**, while R_0 (14.7 Ω) and R_{ss} (9.0 Ω) are respectively the interphase resistance values before and after cell polarization (ΔV = 30 mV) in the corresponding Nyquist plots (inset of **Figure 1b**). The achieved t^+ (0.73) indicates that the charge is predominantly carried by the small Li^+ rather than the larger NO_3^- and $TFSI^-$ ions. **Figure 2b** depicts the Nyquist plots of the symmetrical lithium cell aged over time to achieve the chemical stability of the catholyte (see **Table 2.3.2** for analysis). The plots reveal a response characterized by high-to-middle frequency semicircles due to the interphase, and low-frequency finite-length Warburg element accounting for Li^+ diffusion in non-blocking configuration. The trend of the interphase resistance over time in **Figure 2c** shows an initial value of 70 Ω increasing to 107 Ω in 14 h. Subsequently, the resistance gradually decreases over 6 days until 66 Ω, and fluctuates between 72 and 82 Ω, due to partial

dissolution and consolidation of the SEI. The lower steady state resistance and better stability compared to other catholytes[71,72] suggest the Li-deficient formulation used herein to form a more effective SEI.[73] The electrochemical stability window is determined through LSV in anodic and cathodic regions of lithium cells using the catholyte and a carbon substrate as the working electrode. The voltammogram in **Figure 1c** reveals a complex behavior characterized by several peaks, suggesting various electrochemical processes. The cathodic scan indicates a small peak at 2.3 V *vs.* Li^+/Li due to the conversion by reduction of $Li_{1.5}S_8$ to Li_2S_8, and a massive peak at 1.9 V *vs.* Li^+/Li related to the conversion of the formed Li_2S_8 to short chain sulfides (*i.e.*, Li_2S_2 and Li_2S).[74] Subsequently, the NO_3^- reduction begins at 1.75 V with a current peak centered at 1.6 V *vs.* Li^+/Li, whilst the next peaks around 1.0 V and below until 0 V *vs.* Li^+/Li suggest solvent reduction (*i.e.*, DOL:DME).[74] The anodic scan indicates oxidation of $Li_{1.5}S_8$ to S_8 occurring by a single narrow current peak at 2.5 V, also observed by charging from the cell open-circuit-voltage (OCV) up to 2.8 V prior to CV (**Figure 2**), and a subsequent current decrease and fluctuation around a few μA cm^{-2} until 3.9 V, upon which a huge current threshold indicates solvent oxidation.[75] The voltammogram in **Figure 1d** shows the reversible process of the catholyte solution between 2.1 and 2.8 V vs. Li^+/Li, which is a restricted range to achieve only the soluble fraction of the Li–S reaction products. The curve depicts a reduction peak centered at about 2.2 V vs. Li^+/Li during the first cycle (orange line), shifting to ∼2.3 V and overlapping during the subsequent cycles (purple line) upon cell activation, while the oxidation peaks steadily evolve at 2.45 V vs. Li^+/Li. The excellent reversibility and fast kinetics of the electrochemical process are demonstrated by the almost complete reproducibility of the peaks after the first cycle with a difference limited to 150 mV between charge and discharge, where the full reversibility at room temperature thermodynamically foresees a difference of 59 mV. The interphase stability is investigated in **Figure 1e** by comparing Li-stripping/deposition tests in symmetrical cells at 2 mA cm^{-2} for 2 h (charge/discharge capacity 4 mAh cm^{-2}) of the catholyte and a control solution (DOL:DME 1 mol kg^{-1} LiTFSI, 1 mol kg^{-1} $LiNO_3$). The voltage profiles exhibit for both solutions an overvoltage decreasing during the initial days, where the reference solution stabilizes at ∼50 mV after the 10^{th} day, whilst the catholyte reaches almost the same value after 16 days (the inset shows the curves evolution within the 8^{th} and 20^{th} day). After the above stabilization due to the gradual consolidation of the SEI, a significant polarization increase up to ∼200 mV is experienced, indicating its possible thickening upon cycling.[75-76] Subsequently, the overvoltage progressively decreases back to a value of 80 mV at the end of the test prolonged for over 90 days (see magnifications in

Figure 2f), with a stabilization time of ~16 days for the control electrolyte and ~44 days for the catholyte.

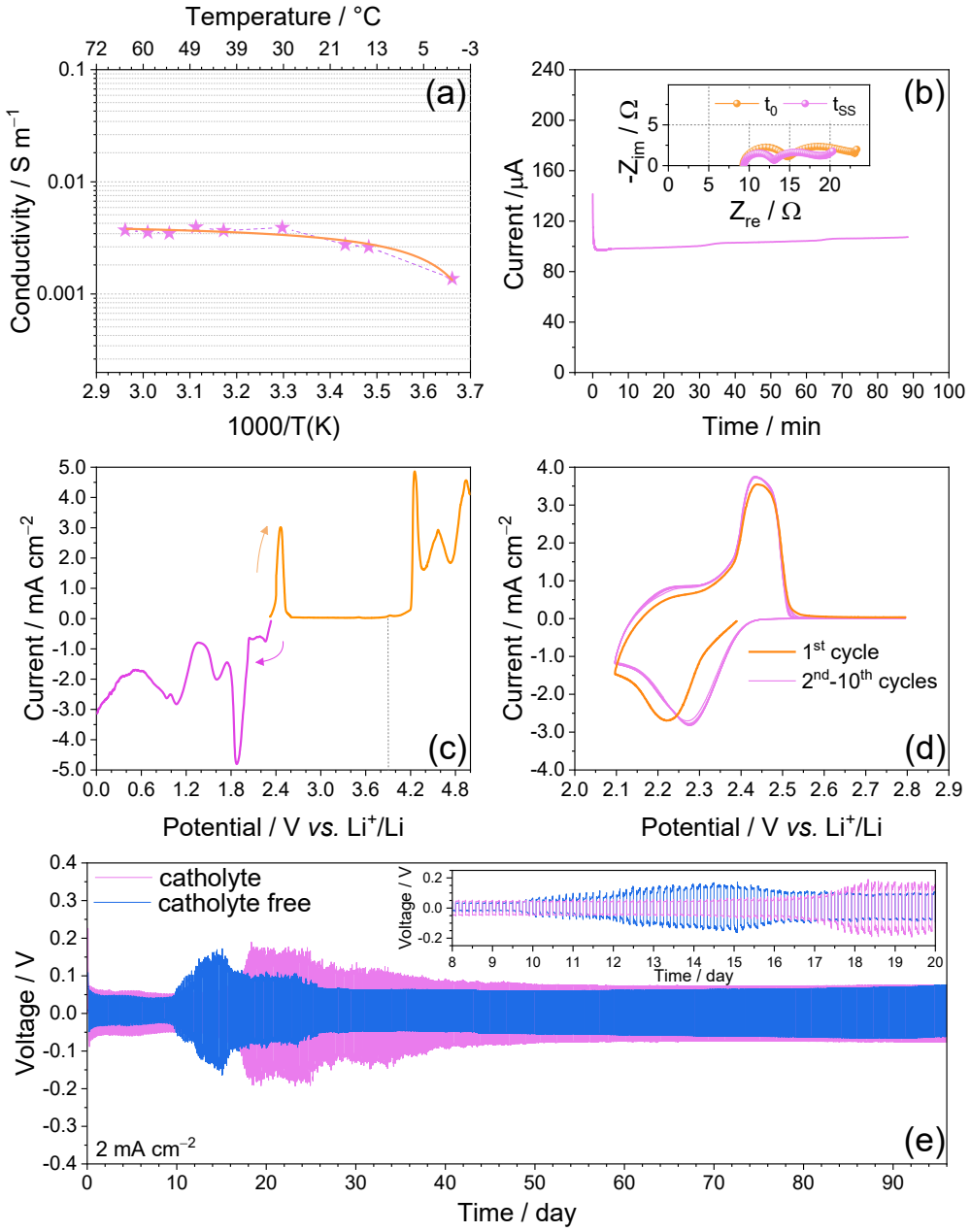

Figure 1. Electrochemical characterization of the catholyte. **(a)** ionic conductivity over temperature (corresponding Nyquist plots in Figure 2); **(b)** chronoamperometry recorded in symmetrical Li-cell (inset reports corresponding Nyquist plots acquired before and after polarization) to evaluate the Li^+ transference number through Bruce-Vincent- Evans method (see *Eq (5)* and Table 2.4.2); EIS frequency range: 500 kHz – 100 mHz; alternate voltage signal: 10 mV; **(c)** electrochemical stability window determined by LSV from OCV to 0.01 V *vs.* Li^+/Li and to 5 V *vs.* Li^+/Li carried out in Li-cell with carbon electrode; scan rate: 0.1 mV s^{-1}; **(d)** CV profiles in a potential range of 2.1 – 2.8 V *vs.* Li^+/Li, scan rate 0.1 mV s^{-1}; **(e)** Li stripping/deposition test in symmetrical Li-cell using either the catholyte (pink) or a control electrolyte (i.e., DOL:DME, 1 mol kg^{-1} LiTFSI, 1 mol kg^{-1} $LiNO_3$, orange) at constant current rate of 2.0 mA cm^{-2}, step time: 2 h (inset shows magnification in the 8th – 20th day range).

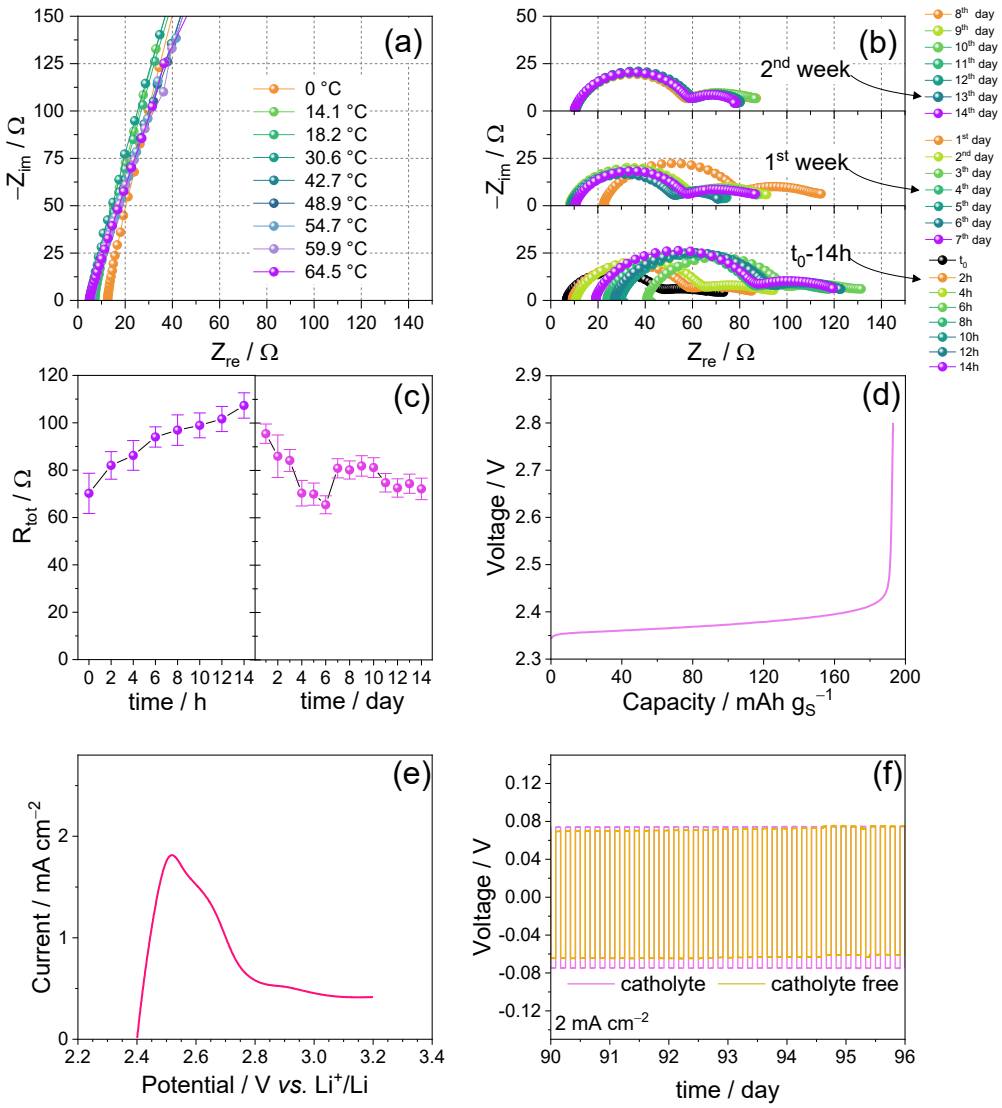

Figure 2. Electrochemical characterization of the catholyte, in detail: **(a)** Nyquist plots related with EIS measurements performed at various temperatures on a stainless-steel|catholyte solution|stainless-steel symmetrical cell to evaluate the ionic conductivity (see Figure 1a), **(b)** Nyquist plots recorded through EIS regularly measured upon aging of a Li|catholyte|Li; **(c)** Resistance trend *vs.* time achieved by regularly carrying out EIS during aging of a Li|catholyte|Li symmetrical cell, **(d)** galvanostatic charge profile of Li|catholyte solution|Carbon cell recorded at C/10 (1 C = 419 mA g_S^{-1}), antecedent to CV (see Figure 1d); **(e)** LSV carried out prior to CV in Figure 2e; **(f)** insight of the stripping/deposition within the 90th and 96th day (test reported in Figure 1e).

Various sulfur composites previously characterized, that is, S:MnO_2, S:Sn, and S:Sn:MnO_2,[66-68] are prepared and combined with the catholyte to achieve loading up to 6 mg_S cm^{-2} and cycled in a Li-cell within voltage limits allowing the exploitation of soluble polysulfides. The results in **Figure 3** show for the cell with S:Sn:MnO2 the highest discharge voltage and capacity (2.35 V and 240 mAh g_S^{-1}) values. **Figure 3** displays the galvanostatic cycling results of Li-S cells exploiting the catholyte and three sulfur-based cathodes, namely S:MnO_2, S:Sn, and S:Sn:MnO_2.The aim of this test, carried out at C/2 (1 C = 419 mA g_S^{-1}) within the 2.1 – 2.8 V voltage range, is to determine the most suitable trade-off among the materials based on the delivered specific capacity, sulfur content in the cathodic active material, and voltage profiles stability.

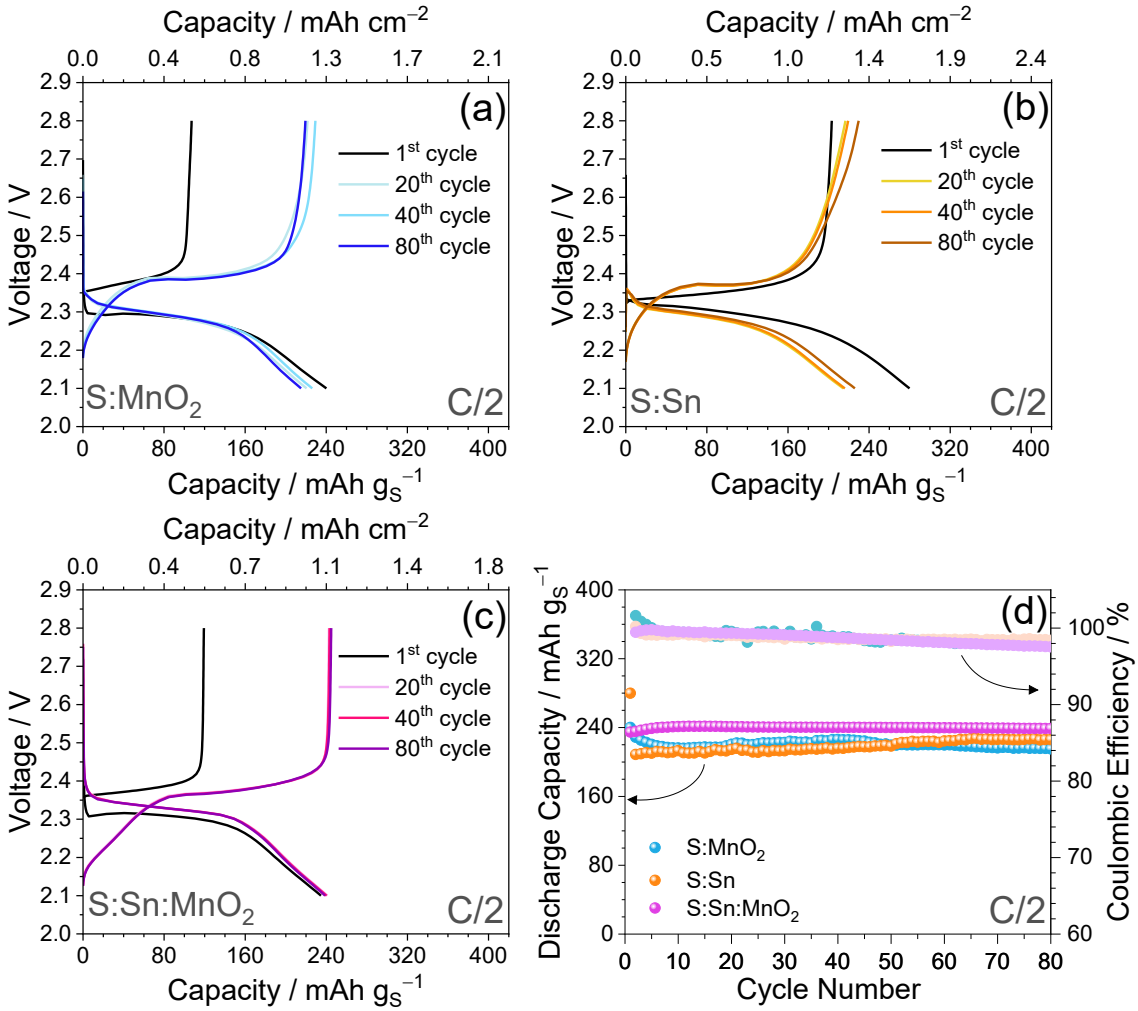

Figure 3. Galvanostatic cycling performance of the catholyte in lithium half-cell exploiting various sulfur-based cathode. In detail: **(a)** selected voltage profiles of Li|catholyte|S:MnO_2 (80:20 *w:w)*, **(b)** selected voltage profiles of Li|catholyte|S:Sn (80:20 *w:w*); **(c)** selected voltage profiles of Li|catholyte|S:Sn:MnO_2 (90:5:5 *w:w*) (top *x*-axes display the areal capacity); **(d)** capacity trends comparison upon 80 charge/discharge runs (right *y*-axis shows Coulombic Efficiency). All cells were cycled at the constant rate of C/2 (1C = 419 mA g_S^{-1}) between 2.1 – 2.8 V. Each cathode was soaked with 66 µL of catholyte. Electrodes geometric area: 1.54 cm^2. Overall sulfur loading between 4.5 and 6.0 mg cm^{-2}.

Therefore, S:Sn:MnO_2 is selected as the preferred choice for subsequent investigations with the catholyte in **Figure 4, 5 and 6**. The rate capability of this Li-cell is studied at: (i) C/10, C/5, C/3, C/2, and 1C between 2.1 and 2.8 V (**Figure 5a**); (ii) 5C, 6C, 7C, 8C and 9C between 1.5 and 3.0 V (**Figure 5b**); (iii) 10C, 20C, 30C, 40C and 50C between 0.5 and 3.5 V (**Figure 5c**). The comparison of the related discharge capacity trends in **Figure 5d** indicates that the cell can even operate at an extremely high current rate of 50C, which corresponds to a specific value of ~21 A g_S^{-1} or ~120 mA cm^{-2}. The cell delivers a discharge capacity ranging from 305 mAh g_S^{-1} at C/10 to 25 mAh g_S^{-1} at 50C, with the values decreasing upon current increase, as expected by the rising ohmic-drop. The capacity values correspond to a Li_xS_8 polysulfide with $3.2 \leq x \leq 2.4$ from C/10 to 1C, $1.2 \leq x \leq 0.6$ from 5C to 9C, and $0.6 \leq x \leq 0.1$ from 10C to 50C, as reported in **Figure 5**. The composition Li_2S_4 upon galvanostatic discharge of the liquid polysulfide is reached only in the theoretical case at very low current, such as the one reported in panel (a) of **Figure 4**. Instead, polysulfides having lower Li content are achieved by increasing the c-rate, such as Li_xS_8 with $3.2 \leq x \leq 2.4$ from C/10 to 1 C (panel b), $1.2 \leq x \leq 0.6$ from 5 C to 9 C (panel c), and $0.6 \leq x \leq 0.1$ from 10 C to 50 C (panel d). In addition, **Figure 6a–c** summarizes the specific current (either in terms of mA g_S^{-1} or mA cm^{-2}) and discharge capacity upon rate capability tests. A Li|catholyte|S:Sn:MnO_2 cell is also subjected to CV at increasing scan rates (**Figure 5e**) to get D_{Li+} by Randles–Sevcik *Eq (1)* where Ip is the CV peak current, z is the number of exchanged electrons (z = 1 for each peak, respectively at 2.0 and 2.8 V vs. Li^+/Li), F is the Faraday constant (96 485 C mol^{-1}), A is the electrode geometric area (1.54 cm^2), C is the estimated concentration of Li^+ in the sulfur electrode volume (mol dm^{-3}), ν is the CV scan rate (mV s^{-1}), R is the gas constant (8.31451 J mol^{-1} K^{-1}), and T is the room temperature (298 K). The I_p of the reduction and oxidation signals are plotted vs. the square root of the scan rate ($\nu^{1/2}$) in **Figure 6d** to obtain the corresponding $Ip/\nu^{1/2}$ slope by linear fit and calculate the D value reported in **Table 2.3.3**. The cell exhibits a relevant diffusion coefficient, with higher value upon cathodic scan (5.8×10^{-8} cm^2 s^{-1}) than the anodic one (4.2×10^{-8} cm^2 s^{-1}). Taking into account delivered capacities, currents and working voltages of **Figure 5**, the impressive rate capability leads to energy and power densities ranging from 700 Wh kg_S^{-1} and 100 W kg_S^{-1} at C/10 to 100 Wh kg_S^{-1} and 35 kW kg_S^{-1} at 50C.

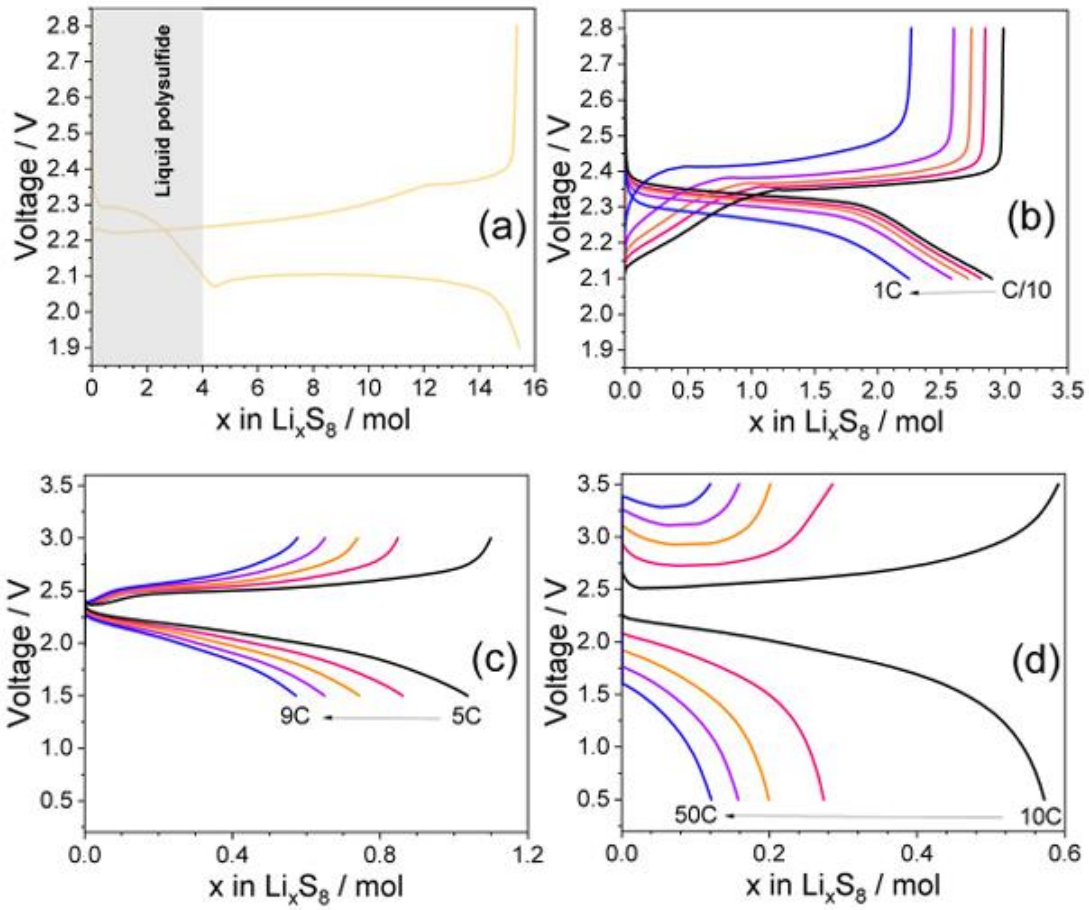

Figure 4. (a) Theoretical galvanostatic voltage profile of the Li-S cell at very low current in terms of exchanged Li moles (x) in the Li_xS_8 polysulfide formula highlighting the liquid region until Li_2S_4, and galvanostatic cycling tests of the cells reported in this work at: **(b)** C/10, C/5, C/3, C/2, and 1 C (1 C = 419 mA g_S^{-1}, S loading 6.5 mg cm^{-2}) in the 2.1 – 2.8 V voltage range; **(c)** 5 C, 6 C, 7 C, 8 C, and 9 C (S loading 5.2 mg cm^{-2}) in the 1.5 – 3.0 V voltage range; **(d)** 10 C, 20 C, 30 C, 40 C, and 50 C (S loading 5.2 mg cm^{-2}) in the 0.5 – 3.5 V voltage range.

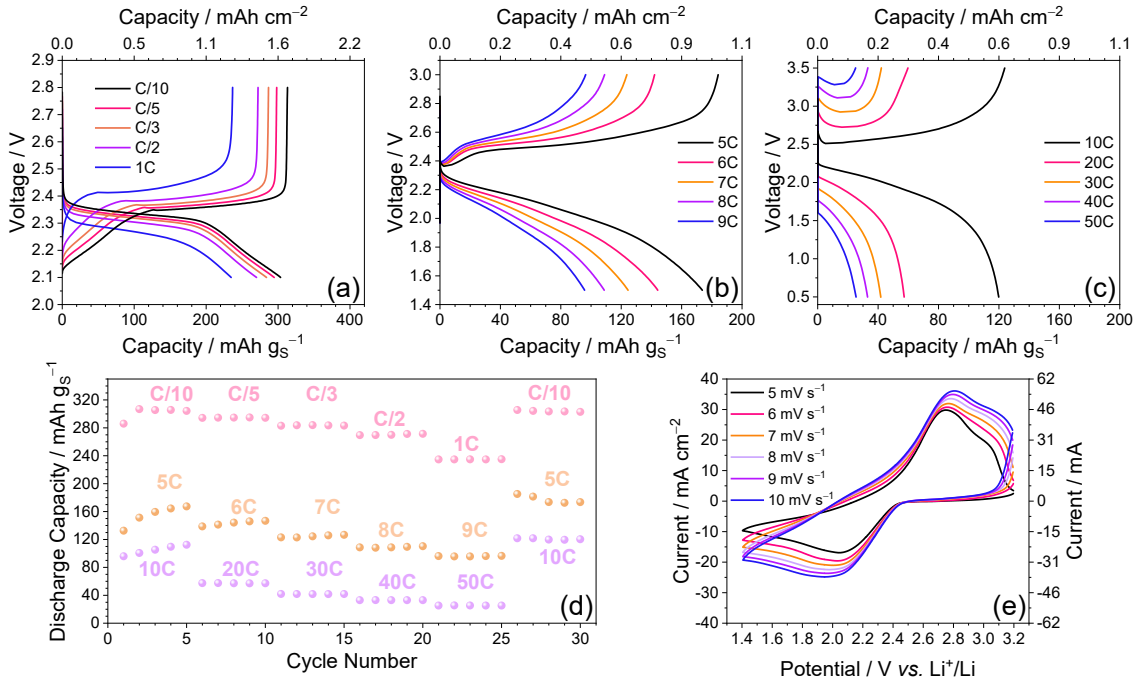

Figure 5. Rate capability and CV measurements of Li-cells combining S:Sn:MnO_2 electrode and the catholyte. Test at: **(a)** C/10, C/5, C/3, C/2, and 1 C (1 C = 419 mA g^{-1}, S loading 6.5 mg cm^{-2}) in the 2.1 – 2.8 V voltage range; **(b)** 5 C, 6 C, 7 C, 8 C, and 9 C (S loading 5.2 mg cm^{-2}) in the 1.5 – 3.0 V voltage range; **(c) 10** C, 20 C, 30 C, 40 C, and 50 C (S loading 5.2 mg cm^{-2}) in the 0.5 – 3.5 V voltage range; **(d)** discharge capacity trends *vs.* cycle number; and **(e)** CV measurement recorded at 5, 6, 7, 8, 9 and 10 mV s^{-1} increasing scan rates (3rd voltammogram for each scan rate is reported), potential range: 1.4 – 3.2 V *vs.* Li^+/Li. The data have been considered for the calculation of D_{Li+} through the Randles–Sevcik *Eq (1)*.

Figure 6 summarizes the specific current (either in terms of mA g_S^{-1} or mA cm^{-2}) and discharge capacity delivered by Li|catholyte|S:Sn:MnO_2 cells upon rate capability tests, and depicts the linear fit of the peak current intensities (I_p) plotted *vs.* the square root of the scan rate ($v^{1/2}$) related to the CV measurements performed at increasing v (see **Figure 2e** in Manuscript) to estimate the Li^+ diffusion coefficient (D_{Li+}) by using the Randles-Sevcik *Eq (1)*. The obtained D_{Li+} values are reported in **Table 2.3.3**.

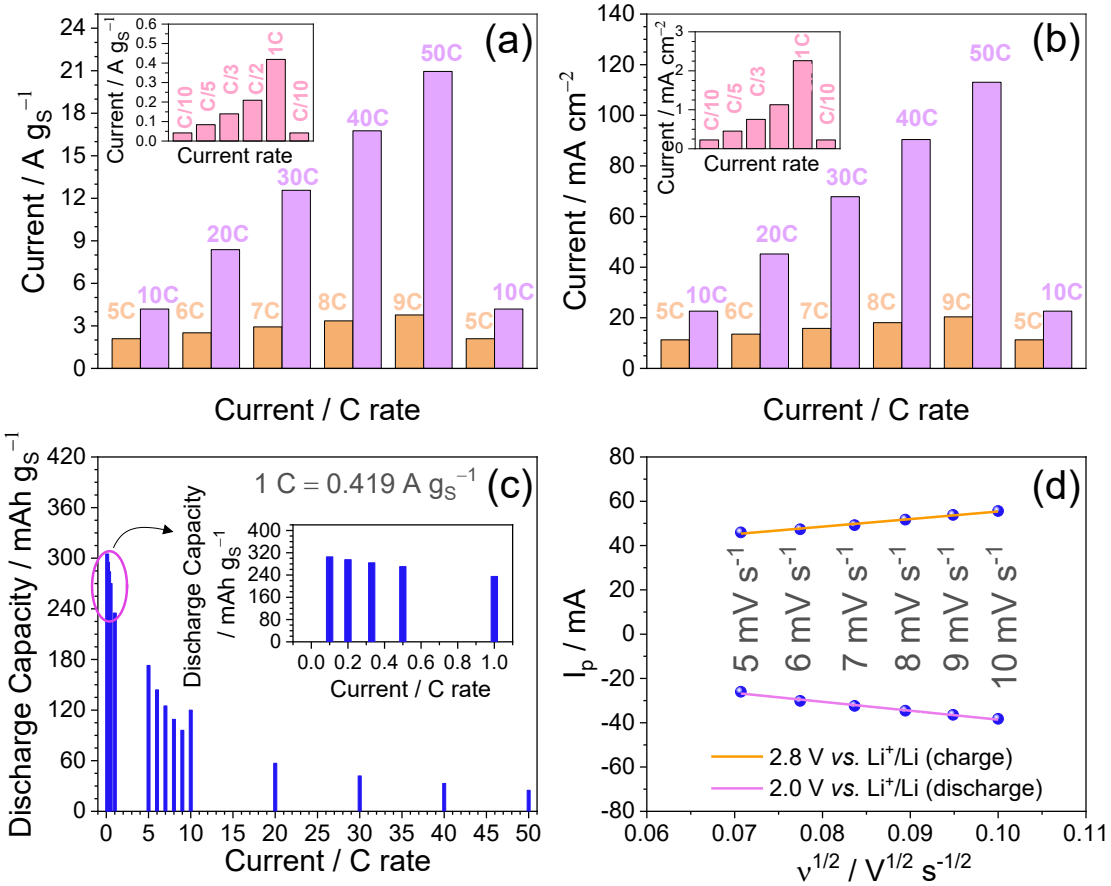

Figure 6. Rate capability tests performed in Li|catholyte|S:Sn:MnO_2 cell. In detail: **(a)** specific current (A g_S^{-1}) *vs.* current rate (C-rate); **(b)** areal current (mA cm^{-2}) *vs.* C-rate; **(c)** specific discharge capacity (taken at the 3rd discharge run for each current rate) *vs.* C-rate; **(c)** linear fits of the peak currents (I_p) vs. the root square of the scan rate ($v^{1/2}$) employed for the CV measurements reported in Figure 5. The linear fit slopes are employed to calculate the Li^+ diffusion coefficient (D_{Li+}) values through the Randles-Sevcik *Eq (1)*. See Table 2.3.3 for the actual D_{Li+} values.

Table 2.3.3. Li^+ diffusion coefficient (D) values measured through the Randles-Sevcik *Eq (1)* during CV measurements of Li|66 µL catholyte|S:Sn:MnO_2 cell.

Potential / V *vs.* Li^+/Li	D / cm^2 s^{-1}
2.0	5.8×10^{-8}
2.8	4.2×10^{-8}

With the aim of highlighting the power of the lithium cell using the catholyte with S:Sn:MnO2, **Figure 7** shows the outcomes of cycling tests performed at an extremely-high current rate of 10C and 50C. To preliminarily evaluate the contribute of the Li^+ dissolution/deposition overvoltage at elevated areal currents and capacity regimes, galvanostatic tests at 10, 20, 40, 60, and 100 mA cm^{-2} are performed for 1 h of charge/discharge in symmetrical Li-cells with the catholyte, and the resulting voltage signatures are reported in **Figure 8**. The figure indicates that the overvoltage increases concomitantly with the current up to 0.4 V at 20 mA cm^{-2} (corresponding to a C-rate between 8 and 10C) and 1.2 V at 100 mA cm^{-2} (between 40 and 50C). Considering this

result, we may estimate for a single Li metal electrode, such as the one used in the Li–S cell of **Figure 7**, a contribution to the polarization of ~0.2 V at 10C and 0.6 V at 50C. Taking into account these values, the cell cycled at 10C (4.19 A g_S^{-1}, **Figure 7a**) exploits a voltage range of 1.5–3.0 V; instead, the one cycled at 50C (20.9 A g_S^{-1}, **Figure 7b**) is cycled within a range extended to 0.5–3.5 V to achieve the reaction of the dissolved polysulfide without significant solvent decomposition. Relevantly, the cells undergo a progressive improvement which decreases the polarization and doubles the initial capacity to values of 120 mAh g_S^{-1} at 10C (**Figure 7a**) and of 70 mAh g_S^{-1} at 50C (**Figure 7b**) at the 500th cycle. This enhancement, ascribed to electrode/electrolyte interphase activation, is even more evident in **Figure 7c**, which compares the cycling trends of the two cells. The coulombic efficiency reaches value higher than 99% by 10 cycles for both cells, and reveals a value higher than 100% during the initial cycles only for the cell at the lower C-rate, in which the partial reduction of the electrolyte with protective SEI formation may be more relevant.(69) To grasp the high-power features of the Li–S conversion process, a Ragone plot in which specific power is plotted as a function of specific energy is reported in **Figure 7d**. The cells tested at 6C, 10C, and 50C respectively show a power as high as at 5, 10, and 40 kW kg_S^{-1}, delivering at the 100th discharge (plain line) an energy density of 200, 160, and 66 Wh kg_S^{-1}, which is further improved to 240, 220, and 78 Wh kg_S^{-1} at the last discharge after 500 cycles (dashed line). This impressive behavior is further evidenced by the average specific discharge power vs. cycle number reported in **Figure 7e**.

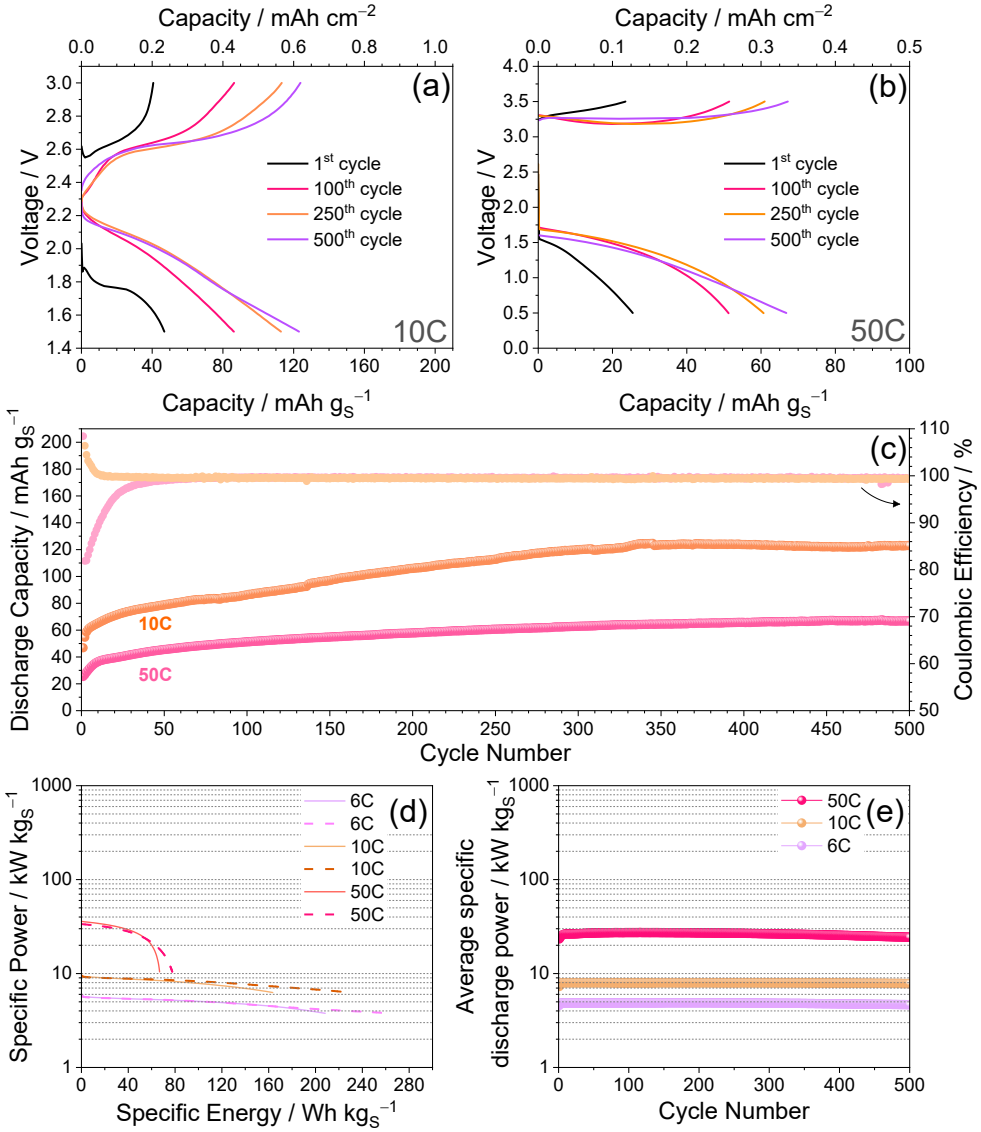

Figure 7. Galvanostatic cycling tests performed on lithium cells using the catholyte in combination with the S:Sn:MnO_2 electrode at the current rates of: **(a)** 10 C (1 C = 419 mA g^{-1}), **(b)** 50 C. Voltage ranges: 1.5 – 3.0 V for 10 C and 0.5 – 3.5 V for 50 C, sulfur loadings of 5.0 and 4.5 mg cm^{-2}, respectively; **(c)** corresponding discharge capacity *vs.* cycle number; **(d)** Ragone plot of the 100th (plain line) and 500th cycle (dashed line); **(e)** average specific discharge power *vs.* cycle number. Tests performed at 30 °C.

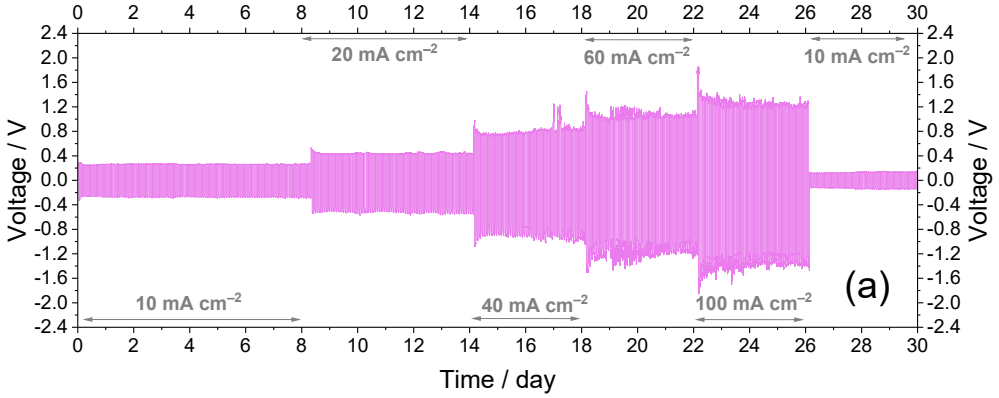

Figure 8. (a) Li-stripping/deposition test at the constant currents of 10, 20, 40, 60, and 100 mA cm^{-2}, before lowering back to 10 mA cm^{-2} after 26 days, step time: 2 h. Tests performed at 30 °C.

Reference

(59) L. Lu, X. Han, J. Li, J. Hua and M. Ouyang, J. Power Sources, 2013,226, 272–288.
(60) Y. Su, Y. Fu, B. Guo, S. Dai and A. Manthiram, Chem. – Eur. J., 2013,19, 8621–8626.
(61) H. Shin, M. Agostini, I. Belharouak, J. Hassoun and Y.-K. Sun,Carbon, 2016, 96, 125–130.
(62) C. Tan, M. D. R. Kok, S. R. Daemi, D. J. L. Brett and P. R. Shearing,Phys. Chem. Chem. Phys., 2019, 21, 4145–4154.
(63) S.-H. Chung, C.-H. Chang and A. Manthiram, J. Power Sources, 2016,334, 179–190.
(64) G. Zhou, L. Li, C. Ma, S. Wang, Y. Shi, N. Koratkar, W. Ren, F. Li and H.-M. Cheng, Nano Energy, 2015, 11, 356–365.
(65) Y. Liu, Y. Elias, J. Meng, D. Aurbach, R. Zou, D. Xia and Q. Pang,Joule, 2021, 5, 2323–2364.
(66) E. Barcaro, V. Marangon, D. Bresser and J. Hassoun, ChemSusChem,2025, 18, e202400615.
(67) V. Marangon, D. Di Lecce, F. Orsatti, D. J. L. Brett, P. R. Shearing andJ. Hassoun, Sustainable Energy Fuels, 2020, 4, 2907–2923
(68) V. Marangon, E. Scaduti, V. F. Vinci and J. Hassoun, ChemElectro-Chem, 2022, 9, e202200374.
(69) M. Agostini, D.-J. Lee, B. Scrosati, Y. K. Sun and J. Hassoun, J. PowerSources, 2014, 265, 14–19.

2.4 A Novel Li-ion-Oxygen battery

European Green Deal was launched in 2019 by the EU-commission, to achieve net-zero CO_2 emissions until 2050, and reach for first the climate-neutral condition. Key strategies to match this ambitious target involved reforming the energy policies and adapting the internal market to accommodate renewable sources.[1] Additionally, in June 2022 the EU decided a crucial restriction of the internal combustion engines by 2035.[2] Therefore, the demand for batteries to power electric vehicles have been predicted to increase by 5 times on 2030 and by 15 times on 2050, to substantially support the transition to a more sustainable transportation.[3] In this scenario, a recent work indicated that the battery demand in Europe can exceed 1.0 T Wh per year by 2030, thus outpacing the domestic production and requiring a growth rates from 31% to 68 % per year. Hence, the research suggested production capability acceleration by the stakeholders to match the demand growth post-2030, with reliable industrial policies.[4] However, the need for EVs with extended driving range triggered the request for efficient energy storage systems such as the lithium-ion (Li-ion) battery, which is currently the most widely diffused power source. These batteries rely on critical metals such as nickel, manganese, and cobalt, which pose significant environmental and economic concerns, in particular considering their limited and geographically localized availability, and the rising price due to growing demand.[5-6] Among the various systems, metal-air batteries in which the oxygen electrochemically reacts with metal having a low redox potential such as Zn, Al, Na or Li appeared the most promising candidates in terms of low cost, sustainability and high energy density.[7-10]

Non-aqueous Li-O_2 battery battery operates according to the overall reaction $2Li + O_2 \leftrightarrows Li_2O_2$, which is a multi-step process evolving at 2.9V with the impressive theoretical energy density of 3400 Wh kg^{-1} and 8050 Wh L^{-1}.[11-12] Typically, the O_2 gas is hosted *ad hoc* into a gas diffusion layer (GDL) coated with carbon-based materials, such as nanotubes, graphene, or hard carbons, and often combined with various catalysts optimized to enhance the formation of Li_2O_2 by reversible oxygen reduction reaction (ORR)/oxygen evolution reaction (OER) during cycling.[13-16] Another crucial component of the Li-O_2 battery is the electrolyte which should be lowly volatile, as well as thermally and chemically stable. Recent improvements of glymes, polymer, and ionic liquid electrolytes have played key role in facilitating and triggering the research and development of Li-O_2 battery.[17-20] Indeed, the traditional electrolytes employed in Li-ion battery, typically based on organic carbonate solvents, can easily undergo parasitic reaction and degradation against the highly reactive and nucleophile intermediates formed during Li-O_2 cell

operation, such as superoxide radicals and the peroxide itself.[20] Glyme solvents have been suggested to be particularly advantageous in Li-O_2 batteries as they can stabilize the superoxide ion by forming complexes such as ($Li^+(solvent)_n\cdots O_2^-$), thus enhancing the reversibility of the cell and mitigating the side reactions.[21] A significant limitation of the Li-O_2 cell may be represented by the use of lithium metal as the anode with possible formation of non-uniform SEI during charge and discharge cycles. This uneven SEI growth can facilitate the development of dendritic structures penetrating the separator until possible internal short circuits within the cell, with serious safety risks hindering the practical battery application.[22] The addition of sacrificial agents, such as vinylene carbonate, $LiNO_3$, or $(MgNO_3)_2$, in the electrolyte has been indicated as a potential strategy to form more stable and uniform SEI, limit dendrite growth, reduce lithium reactivity, and finally enhance the overall safety and cycle life of the cell.[23-25] The most alternative pathway to avoid the challenges associated with Li has foreseen the complete replacement of the alkali metal anode with conversion or alloying anodes, based on Fe, Cu, Sn, Sb, or Si, to achieve the Li-ion configuration using the oxygen cathode, offering enhanced safety and stability by almost suppressing the above mentioned risks.[26-31]

In this work, we investigated the performance of electrolytes based on PEGDME 250 with LiTFSI and $LiNO_3$ salts in Li-O_2 cells. The PEGDME 250 is selected due to its enhanced safety profile, including lower flammability, higher flash point, and reduced toxicity compared to glymes with lower molecular weight such as TREGDME and TEGDME, which have already shown excellent cyclability and film formation ability in Li-O_2 battery. These characteristics suggested PEGDME 250 as very promising candidate for use as a green and sustainable electrolyte solvent. Initially, the electrolytes have been analyzed using various techniques to examine their physical-chemical properties. Subsequently, a range of electrochemical measurements has been employed to investigate their conductivity, stability window, and lithium-ion transference number. Then the electrolytes have been tested in Li-O_2 cells, combining MWCNTs and FLG as the cathodic material. This cathode setup has been previously studied in combination with TEGDME-based electrolytes, providing a benchmark for comparison. Finally, Li-ion-O_2 cells has been achieved with a lithiated Sn@C anode, and studied under various currents and operating regimes to demonstrate their actual applicability upon a careful control and possible protection of the anode/electrolyte interphase. Electrochemical tests combined with ex-situ measurements on the electrodes have been also carried out to demonstrate the occurrence of the reversible OER/OER reaction and the interphase characteristics.

Experimental

- Electrolyte preparation

Two electrolyte solutions were prepared by dissolving either LiTFSI alone, or LITFSI and $LiNO_3$ (99.99% trace metals basis, Sigma-Aldrich) in PEGDME 250 (average M_n 250, Sigma-Aldrich) at a concentration of 1 mol of each salt in a 1 kg of solvent. The first electrolyte was referred in the text as PEGDME 250 LiTFSI 1 m, while the second one as PEGDME 250 LiTFSI 1 m $LiNO_3$ 1 m. Before preparing the electrolytes, LiTFSI and $LiNO_3$ salts were dried under vacuum at 110 °C for 2 days. The PEGDME 250 solvent was stored in an Ar-filled glovebox with *extra-dry* molecular sieves (0.3 nm, rods, ~1.6 mm diameter, Sigma-Aldrich) for at least one week. The *extra-dry* condition of the sieves was previously achieved by heating them under vacuum at 240 °C for 5 days. Before preparing the electrolyte, the water content of the PEGDME 250 was verified by an 899 Karl Fischer Coulometer (Metrohm) to be below 30 ppm.

- Preparation of MWCNTs/FLG and Sn@C

The cathodic material for hosting the oxygen of the Li-O_2 cells was prepared as follow: commercial MWCNTs (>90% carbon basis, D × L: 110–170 nm × 5–9 µm, Sigma–Aldrich) and FLG were combined into a 50:50 weight ratio in tert-butanol/distilled

water (6:4 weight ratio), stirred, and sonicated at 50 °C to promote liquid-phase exfoliation of FLG and separation of carbon nanotubes, dried at 65 °C, and finally annealed under nitrogen at 750 °C for activation. Nanometric Sn and sucrose were combined in water, heated at 50 °C under magnetic stirring until full evaporation, annealed in a tube furnace at 700 °C for 3 hours under an Ar/H_2 (5% H_2) atmosphere, and then cooled to room temperature and grinded. The Sn to C weight ratio into the final composite was of approximately 1:2.

- Electrode preparation

Electrodes for voltammetry tests were prepared by dispersing SP Carbon (SPC, Timcal) and PVdF binder in 80:20 weight ratio in N-Methyl-2-pyrrolidone (NMP, Sigma-Aldrich) to get a slurry, which was cast either on Al or Cu foils with a doctor blade tool (MTI Corp.). The cathode for Li-O_2 and Li-ion-O_2 cells was prepared by dispersing MWCNTs/FLG 50:50 material and PVdF binder with 80:20 weight ratio in NMP to form a viscous slurry, which was cast onto a GDL (36 BB, Sigracet) using the doctor blade. The anode for Li-ion-O_2 cells was prepared by dispersing Sn@C, SPC, and PVdF binder in a 70:10:20 weight ratio in NMP to achieve a slurry, which was cast on Cu foil. All prepared electrode tapes were dried on hot plate at 70 °C for 3 hours, and cut into discs with diameters of either 10, 14 mm, or 16 mm (geometric area: 0.79, 1.54, and 2.00 cm^2, respectively). Before transfer to argon-filled glove box (MBraun), all electrodes were further dried under vacuum at 110 °C for 3 hours.

- Physical-chemical tests of the electrolytes

TGA was carried out over the temperature range of 25-1000 °C, under N_2 flow with a heating rate of 5 °C min^{-1} using a TGA 2 Mettler-Toledo instrument and placing the samples (~8 mg) inside alumina-based pans. Differential scanning calorimetry (DSC) was performed using a DSC250 from TA Instruments. Approximately 5 mg of the electrolyte was hermetically sealed in an aluminum pan inside an Ar-filled glovebox. Initially, the samples were heated to 100 °C with a rate of 5 °C min^{-1} and held for 5 minutes. Then, the samples were cooled to −150 °C at a rate of −5 °C min^{-1} and held for 5 minutes. Measurements were subsequently taken by heating the samples from -150 °C to 100 °C at a rate of 5 °C min^{-1}. FT-IR spectra of solutions were recorded using a Bruker Alpha II spectrometer equipped with an ATR (attenuated total reflection) accessory and a diamond crystal tip. Measurement was conducted inside an Ar-filled glovebox to avoid moisture and oxygen interference. Each spectrum was collected over a range of 500 cm^{-1} to 2000 cm^{-1} with a resolution of 2 cm^{-1} and with 24 scans per sample. The ATR crystal was cleaned with isopropanol between measurements to prevent cross-contamination. Fourier transform Raman (FT-Raman) spectra were recorded using a Bruker MultiRAM FT-Raman spectrometer equipped with a Nd laser source (1064 nm excitation wavelength). Measurements were performed under ambient conditions. Each spectrum was collected with a laser power of 400 mW, using a spectral range of 500–3500 cm^{-1}. The instrument was configured with a liquid nitrogen-cooled Ge detector. Each sample spectrum was obtained by averaging 100 scans with a resolution of 4 cm^{-1} to achieve an optimal signal-to-noise ratio. X-ray photoelectron spectroscopy (XPS) measurements were conducted on lithium foils soaked in electrolytes for 48 hours in an Ar-filled glovebox to promote SEI film formation. The foils were then dried under vacuum for 24 hours to remove residual electrolyte. Sample transfer to the XPS instrument was achieved using a dedicated transfer chamber to prevent atmospheric exposure. Measurements were taken under vacuum using a PHI 5000 VersaProbe III scanning XPS Microprobe, equipped

with monochromatic Al Kα source at binding energy of 1486.6 eV. Experimental conditions included an X-ray beam size of 100 μm, 25 W power, and an acceleration voltage of 15 kV. Spectra were analyzed using Casa XPS software (version 2.3.26). These several processes were practically hindered by our the Li-O_2 cell setup (i.e., a top-meshed 2032 coin cells inside sealed glass chambers filled with pure oxygen as described subsequently). However, we are trying to set up an new experimental tool of practical interest to allow the separation of a cycled Li anode from a Li-O_2 sealed cell to perform the related XPS analysis, and the results will be illustrated in future work.

- Electrochemical tests on the electrolytes

All electrochemical tests of the electrolytes were conducted using either CR2032 coin cells (MTI corp.) or T-cells (Swagelok-type, 10 mm-diameter) assembled inside an Ar-filled glovebox (MBraun), where H_2O and O_2 levels were maintained below 0.5 ppm. The ionic conductivity of the solutions was measured through electrochemical impedance spectroscopy (EIS) conducted at various temperatures using stainless-steel | electrolyte | stainless-steel symmetrical coin cell, with an O-ring (23-5FEP-2-50, CS Hyde) having external diameter of 16 mm and internal diameter of 8 mm to hold the solution in place. The O-ring with a thickness of 127 μm enabled to fix the cell constant at 0.0253 cm^{-1}. The EIS spectra were obtained over a frequency range from 100 kHz to 1000 Hz using an alternate voltage of 10 mV, while the cell temperature was controlled by a Julabo F12 instrument. The t^+ of the electrolytes was measured using the Bruce–Vincent–Evans method. A chronoamperometric test was carried out by applying 30 mV for 90 minutes to a symmetrical Li | electrolyte | Li T-cell, where the 2 Li disks with a diameter of 10 mm were separated by 10 glass fiber disks (Whatman GF/A) with diameter of 10 mm soaking the electrolyte. EIS was performed both before and after polarization, using a 10 mV signal over a frequency range from 500 kHz to 100 mHz. The t_+ values were subsequently calculated using *Eq (5)*. Lithium stripping-deposition tests were conducted at the constant current of 0.1 mA cm^{-2} for over 1 h of charge/discharge cycles in a Li | Li symmetrical coin cells, in which a glass fiber separator with diameter of 16 mm (Whatman GF/B), soaked by the electrolyte, separated 2 Li disks with a diameter of 14 mm. Subsequently, the same cells underwent additional stripping-deposition tests, in which charging and discharging were conducted at constant currents of 0.2 mA cm^{-2}, 0.45 mA cm^{-2}, and 0.8 mA cm^{-2} for 1 hour over 24 cycles for each current. The anodic and cathodic regions of the electrochemical stability window were investigated by performing LSV on Li | SPC-Al cell from the open-circuit voltage (OCV) to 5 V *vs.* Li^+/Li, and CV on Li | SPC-Cu cell between 0.01 and 2.0 V *vs.* Li^+/Li. Both LSV and CV were performed at a scan rate of 0.1 mV s^{-1} in T-cells using carbon electrode and Li disk separated by 2 glass fiber disks (Whatman GF/B) soaking the electrolyte, and an additional Li-reference disk, all with a diameter of 10 mm. The Li/electrolyte interphase resistance during aging was analyzed by performing EIS on symmetrical coin cell using two Li disks with a diameter of 14 mm separated by a glass fiber disk (Whatman GF/B) soaking the electrolyte with a diameter of 16 mm. EIS measurements were conducted over a frequency range from 500 kHz to 100 mHz with a 10 mV alternate voltage signal. Measurements were taken every 20 minutes during the first hour after cell assembly, hourly for the initial 24 hours, and then every 24 hours for a duration of 32 days.

- Electrochemical tests on the Li-O_2 and Li-ion-O_2 cellsThe electrochemical tests of Li-O_2 and Li-ion-O_2 cells were carried out using top-meshed CR2032 coin cells (MTI corp.) placed inside sealed glass chambers filled with pure oxygen. The

MWCNTs/FLG 50:50 cathode had a diameter of 16 mm, while the anode diameter measured 14 mm, and the two electrodes were separated by two glass fiber disks (Whatman GF/B) with a diameter of 18 mm or 16 mm soaking the electrolyte. The Li-O_2 cells were cycled at constant current rate of 0.66 mA (0.33 mA cm^{-2}) with cell capacity limited by time to 1 mAh (0.5 mAh cm^{-2}) within a maximum voltage range of 1.5 – 4.8 V for Li-O_2 using either PEGDME LiTFSI 1 m or PEGDME LiTFSI 1 m $LiNO_3$ 1 m electrolytes. The Li-O_2 cells have been also subjected to CV within 1.5 – 4.3 V *vs.* Li^+/Li potential range using a scan rate of 0.05 mV s^{-1}, and to full discharge/charge test at 100 mA $g_{cathode}^{-1}$ within the 1.8−4.5 V voltage range for 1 cycle. MWCNTs/FLG 50:50 electrodes were retrieved from the above cells at the OCV condition and upon full discharge and full charge, washed with diethylene glycol dimethyl ether (DEGDME, 99% Signa Aldrich), and subsequently subjected to *ex-situ* XRD study through a Bruker D8 Advance instrument equipped with a Cu Kα radiation source scanning the 30° – 50° 2θ with step size of 0.02° and rate of 10 s $step^{-1}$. The Li-ion-O_2 full cells were cycled at constant current rate of 0.66 mA (0.33 mA cm^{-2}) with cell capacity limited by time to 0.5 mAh (0.25 mAh cm^{-2}) within a maximum voltage range of 0.1 – 4.8 V using PEGDME LiTFSI 1 m $LiNO_3$ 1 m electrolyte. Prior to use in Li-ion-O_2 cell, the Sn@C anode was pre-lithiated chemically by *ex-situ* capillary contact of the electrode with a lithium foil for 14 h under a pressure of 120 g cm^{-2} in presence of commercial electrolyte (LP30, Sigma Aldrich battery grade) formed by ethylene carbonate (EC), dimethyl carbonate (DMC) in a 1:1 volume ratio dissolving 1 M of lithium hexafluoro phosphate ($LiPF_6$). Subsequently the treated anode, indicated as $Li_xSn@C$, was thoroughly washed with DMC and dried under vacuum. This process ensured the anode to act as the Li-reservoir suitable for Li-ion-O_2 cell application (31). The Li-ion-O_2 cell using the PEGDME 250 LiTFSI 1 m $LiNO_3$ 1 m electrolyte, MWCNTs/FLG 50:50 as cathode support, and pre-lithiated $Li_xSn@C$ as anode has been subjected to galvanodynamic polarization measurement with current ranging from 0 to 6 mA cm^{-2}, using a step of 0.05 mA cm^{-2} for 5 s, subsequent galvanostatic charging to 5 V, EIS tests before and upon the polarization, and further galvanostatic cycling at a current rate of 1, 2, and 3 mA cm^{-2} with voltage ranging from 0 to 5.0 V and charge/discharge time limited to 7.5 min. Furthermore, the Li-ion O_2 cell has been subjected to a galvanostatic rate capability test by setting 30 minutes of charge/discharge time, and varying the current from 0.1, to 0.2 and 0.5 mA cm^{-2} within maximum voltage limit of 4.5 V and minimum of 0.01 V. All electrodes loadings (i.e., mg cm^{-2} of active material) are indicated in the figure caption of corresponding tests. Cells with the configuration Li| PEGDME 250 LiTFSI 1 m $LiNO_3$ 1 m | $Li_xSn@C$ have also been assembled under either Ar or O_2 atmospheres, and monitored in terms of potential, EIS, and XRD evolution over 240 h to study the effects of oxygen permeation into the electrolyte. The $Li_xSn@C$ electrodes retrieved from the aged cells were washed with diethylene glycol dimethyl ether (DEGDME, 99% Signa Aldrich) before XRD measurements.

- Instruments for electrochemical tests

EIS, chronoamperometry, LSV, CV, and galvanodynamic polarization were conducted using a VersaSTAT MC instrument from Princeton Applied Research (PAR-AMETEK), while lithium stripping-deposition and galvanostatic cycling were performed using a MACCOR Series 4000 battery test system.

Results

The physical-chemical characteristics of the electrolytes studied in this work are summarized in **Figure 1** with reference to the PEGDME 250 solvent. **Figure 1a** displays the TGA curves (top panels) and corresponding DTG (bottom panels) conducted under an N_2 atmosphere between 25°C and 1000°C for pure PEGDME 250 solvent (black), PEGDME 250 LiTFSI 1 m (red), and PEGDME 250 LiTFSI 1 m $LiNO_3$ 1 m (blue) electrolytes. The comparison reveals significant differences in evaporation kinetics between the pure PEGDME 250 and the electrolytes. Indeed, the solvent begins weight loss at 65 °C and its full evaporation ends at 308 °C, with a DTG peak centered at 270 °C. In contrast, the TGA curve of PEGDME 250 LiTFSI 1 m shows multiple stages of weight loss, starting at 70 °C with an initial DTG peak at 250 °C, mainly attributed to solvent evaporation. The rate of weight loss slows between 270 °C and 340 °C, likely due to solvent removal from coordination structures formed by the strong interactions between the oxygen groups in the ether-based chain and Li^+ ions.[32-33] A second significant weight loss occurs at higher temperature until 500 °C, with a DTG peak at 406 °C and residual weight of 1.5% further decreasing to 0.4% at 1000 °C. This response corresponds to the degradation of the LiTFSI salt, as confirmed by the TGA of pure LiTFSI in **Figure 2**. Similarly, the TGA curve of PEGDME 250 LiTFSI 1 m $LiNO_3$ 1 m reveals multiple stages of weight loss beginning at 72 °C, with a DTG peak at 214 °C as the solvent evaporates. Relevantly, the weight loss rate slows earlier at 240 °C in this solution, due to the higher amount of Li^+-glyme coordination structures triggered by the concomitant presence of two salts. As observed in the previous sample, a second significant weight loss starts at 370 °C and ends around 500 °C with a residual weight of 2.3 %, further decreasing to 0.65 % at 1000 °C. It is worth mentioning that the degradation of $LiNO_3$ salt does not occur around 600 °C, as instead expected by the TGA curve of the pure salt in **Figure 2**. Rather, $LiNO_3$ starts degradation over 800 °C due the above mentioned interaction of Li^+ with the glyme chains,[32] as suggested by the weight loss from 1.7 % to 0.65 % between 800 °C and 1000 °C with slight DTG peak at 870 °C. **Figure 1b** shows DSC plot of PEGDME 250 solvent (black, bottom panel), PEGDME 250 LiTFSI 1 m (red, middle panel), and PEGDME 250 LiTFSI 1 m $LiNO_3$ 1 m (blue, top panel) electrolytes between −150 °C and 100 °C. The DSC plot of pure PEGDME 250 displays an exothermic hump between −74 °C and −63 °C, likely ascribed to crystal reorganization due to the presence of stabilizers such as di-butyl phthalate (DBP) in the commercial glymes, or to other order-disorder rearrangements.[34] Furthermore, the glass transition of the pure solvent may be suggested around −53 °C.[35] A double melting signal is observed between −50 °C and −28 °C with

peaks at −43 °C and −35 °C, possibly ascribed to crystalline heterogeneity promoted by partial melting and reorganization into different structures during the initial thermal treatment of the sample.[36] The DSC of PEGDME 250 LiTFSI 1 m displays a shift of the glass transition down to −88 °C. The double melting peak observed for pure PEGDME 250 merges into a single one at −54 °C with a lower magnitude or enthalpy, thus suggesting that LiTFSI can hinder the above mentioned crystalline heterogeneity, and facilitate the electrolyte melting at a lower temperature.[37-38] The DSC of PEGDME 250 LiTFSI 1 m $LiNO_3$ 1 m shows almost merged peaks for glass transition and melting, and indicates that the two phase changes may occur almost simultaneously between −102 °C and −75 °C. Hence, the glass transition occurs at approximately −90 °C similarly to the $LiNO_3$-free electrolyte, while the melting substantially shifts to −87 °C and strongly decreases in magnitude likely due to the doubled concentration of Li^+ ions and the presence of two different anions. **Figure 1c** reports the FT-IR spectra of PEGDME 250 solvent (black), PEGDME 250 with LiTFSI 1 m (red), and PEGDME 250 with LiTFSI 1 m and $LiNO_3$ 1 m (blue). The FT-IR of the two electrolytes reveal additional peaks compared with PEGDME 250 solvent, all ascribed to the LiTFSI salt: the peak centered at 1351 cm^{-1} is associated with the asymmetrical stretching of the CF_3 group,[39,40] the signal at 1186 cm^{-1} is due to asymmetrical stretching of the SO_2 group, while the one at 1056 cm^{-1} is related with asymmetrical stretching of the S-N-S bond.[41,42] Furthermore, the peak at 1133 cm^{-1} of the SO_2 symmetrical stretching merges with the solvent one at 1025 cm^{-1}. The PEGDME 250 LiTFSI 1 m $LiNO_3$ 1 m electrolyte shows further peaks at 1420 cm^{-1} and 827 cm^{-1} due to asymmetrical stretching and out-of-plane deformation mode of the NO_3^- group, respectively, while the peak at 1300 cm^{-1} of NO_3^- symmetrical stretching merges with the solvent one at 1305 cm^{-1}.[43]

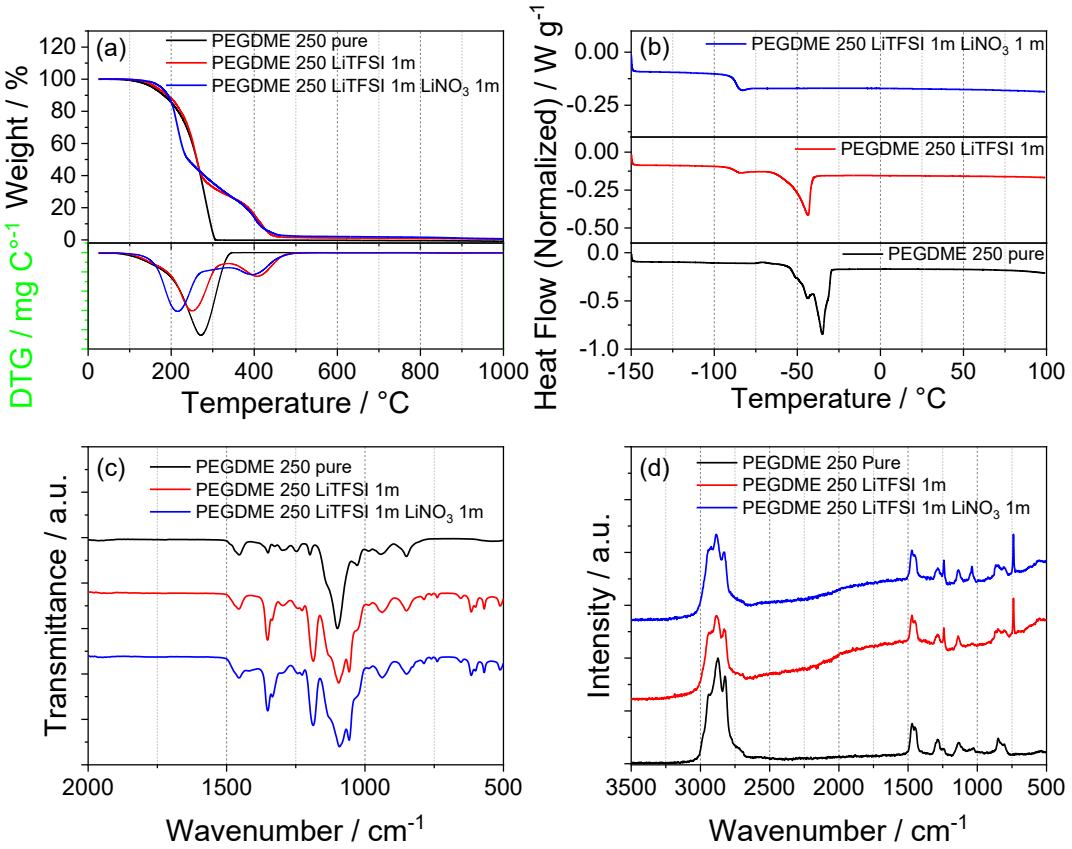

Figure 1. Physical-chemical characterization of pure PEGDME 250 solvent (black), PEGDME 250 LiTFSI 1 m (red) and PEGDME 250 LiTFSI 1 m $LiNO_3$ 1 m (blue) electrolytes, in detail: **(a)** TGA and corresponding DTG curves acquired under N_2 flow between 25 °C and 1000 °C at the 5 °C min^{-1} rate, **(b)** DSC thermograms acquired between −150 and 100 °C at 5°C min^{-1} rate, and **(c)** FT-IR and **(d)** FT-Raman spectra.

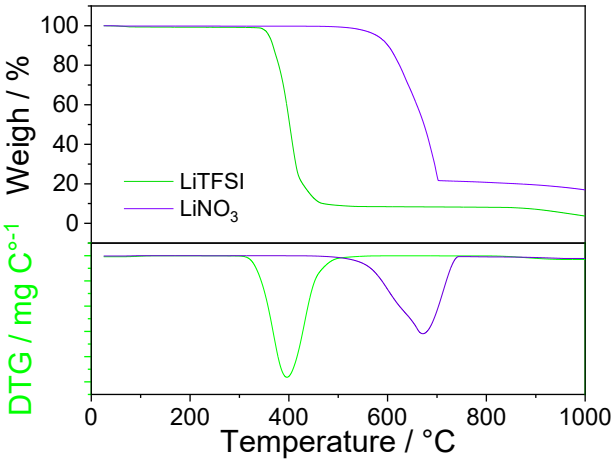

Figure 2. TGA and corresponding DTG curves acquired under N_2 flow between 25 °C and 1000 °C at the 5 °C min^{-1} rate for LiTSI (green) and $LiNO_3$ (violet) salts.

The presence of these peaks suggests actual dissolution of the salts included in the studied electrolytes. **Figure 1d** shows the FT-Raman spectra of the electrolytes and the pure solvent, allowing the identification of characteristic features ascribed to each composition. Both electrolytes reveal peaks associated with the LiTFSI salt, such as that centered at

1240 cm^{-1} due to symmetrical stretching of the -CF_3 group, and at 738 cm^{-1} due to symmetrical stretching of the S-N-S bond as well as bending of the -CF_3 group. In addition, the FT-Raman spectrum of PEGDME 250 LiTFSI 1 m $LiNO_3$ 1 m shows a peak at 1040 cm^{-1} due to symmetrical vibration of the NO_3^- group, accounting for the salt-solvent interactions. **Figure 3** examines by XPS the composition of the SEI film formed on the surface of lithium foils soaked for 2 days in PEGDME 250 LiTFSI 1 m (red) and PEGDME 250 LiTFSI 1 m $LiNO_3$ 1 m (blue) electrolytes. The corresponding survey spectra in **Figure 3a** highlight a SEI predominantly composed of carbon, oxygen, fluorine, sulfur, nitrogen, and lithium, attributed to degradation and/or precipitation at the metal surface of the electrolytes' components such as PEGDME (mainly C and O) and salts (F, S, N and Li). These outcomes suggest a complex interaction of the electrolytes with the lithium leading to SEI formation. Deconvoluted XPS spectra presented in **Figures 3b-g** provide detailed insights on SEI composition by identifying the contributions of individual elements. The C 1s spectra (**Figure 3b**) display peaks at 293.5 eV corresponding to the -CF_3 group, at 287.4 eV associated with Li_2CO_3,[44-46] and at approximately 285 eV due to -C-C- bonds. Relevantly, the peak at 286 eV linked with R-O-R and R-O-Li bonds is observed only in the sample containing $LiNO_3$ salt, thus suggesting the latter to partially limit the solvent degradation from ether to carbonate at the lithium surface. Analogously, the O 1s spectra (**Figure 3c**) reveal a peak at 533.6 eV of R-O-R and R-O-Li only for the sample containing $LiNO_3$, consistently with the results of the C 1s spectra. On the other hand, peaks respectively at 531.2 eV and 528.5 eV in the O 1s spectra indicate the presence of Li_2CO_3 and Li_2O in the SEI for both electrolytes. [47-49]The F 1s spectra (**Figure 3d**) include a peak at 689.4 eV related with the -CF_3 group in line with the C 1s identification,[50] and another one at 685.1 eV associated with LiF (32,59) likely formed by LiTFSI decomposition at the lithium surface. The convoluted N 1s signal (**Figure 3e**) reveals two distinct peaks, the first at 397.4 eV ascribed to negatively charged nitrogen species such as Li_3N (N^{3-}). and the second at 399.7 eV attributed to various nitrogen-oxygen compounds (LiN_xO_y).[51,52] The latter peak is more pronounced in the spectrum of the $LiNO_3$-added electrolyte, as indeed expected by the additional nitrogen source of the sacrificial agent, whereas the nitrogen contributions in the other electrolyte originate only from the LiTFSI. The two peaks at 169.4 eV and 167.9 eV in the S 2p spectra (**Figure 3f**) can be attributed to the S $2p_{3/2}$ and S $2p_{1/2}$ doublet of the -SO_2- group, while the one at ~161 eV corresponds to Li_2S, all peaks suggesting the degradation of the LiTFSI salt.[53,54] The Li 1s spectra (**Figure 3g**) feature a peak at approximately 53 eV, which can be attributed to Li_2O, Li-O-R, and Li_2S species, more relevantly in the electrolyte containing

$LiNO_3$ that stabilizes Li-O-R species as mentioned above.[55-57] The XPS results highlight that the SEI is predominantly composed of inorganic species, shaped by the decomposition products of the electrolytes and their interactions with lithium. On the other hand, the addition of $LiNO_3$ favors the presence of organic species such as R-O-R and Li-O-R, mainly due to the concomitant side chemical reduction or precipitation of this sacrificial salt at the lithium metal interphase which relevantly modifies the SEI layer composition. This process ultimately contributes to a better stability of the lithium interface, thus suggesting its significant role in SEI formation and stability. It is worth mentioning that these results may be different if an electrochemically SEI is formed progressively upon cycling. Yet, this aspect was not disclosed in this work and will be an object of future investigation.

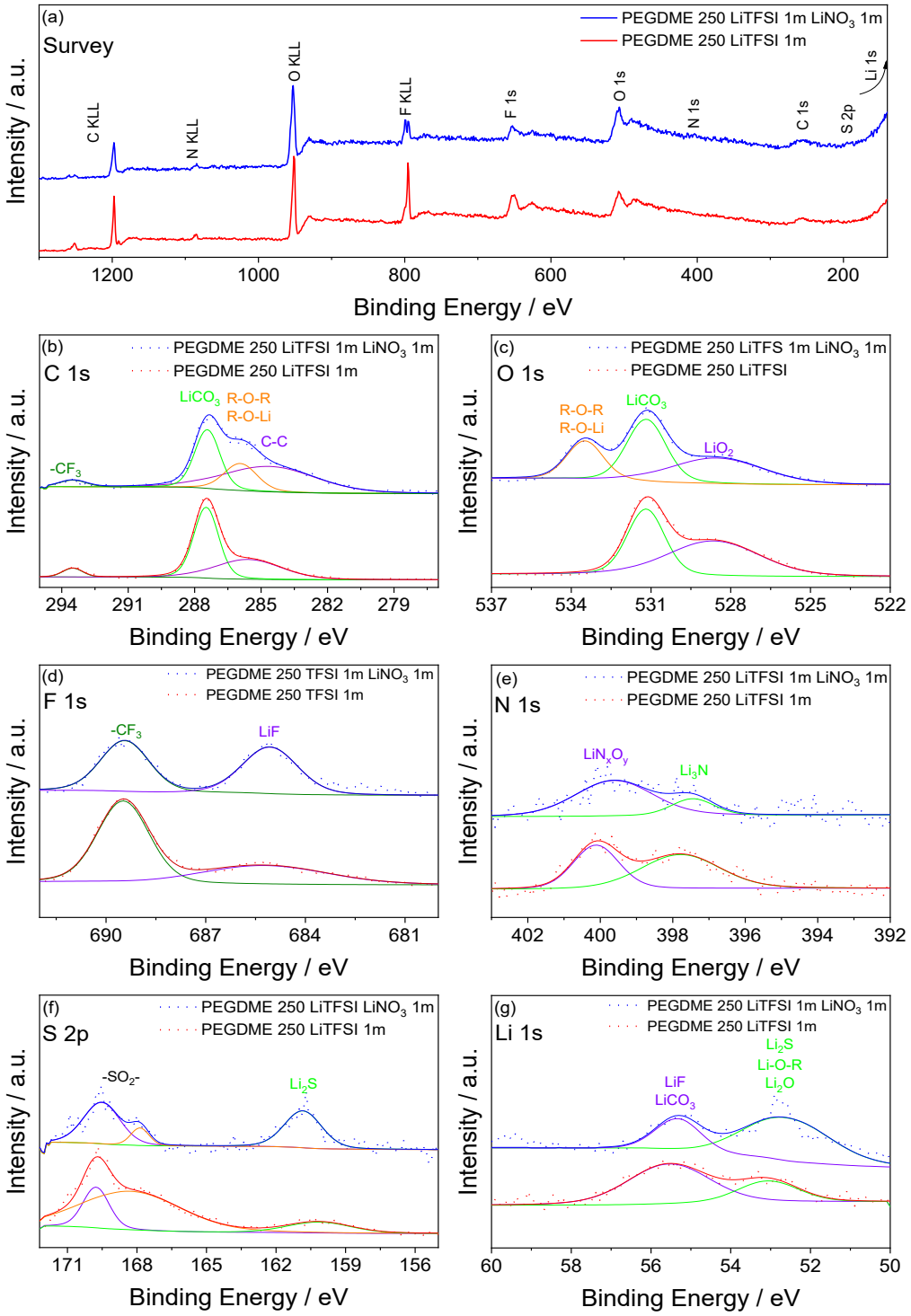

Figure 3. Spectroscopic characterization of the SEI, in detail: **(a)** XPS survey spectra of the surface of lithium metal foils soaked in PEGDME 250 LiTFSI 1 m (red) PEGDME 250 LiTFSI $LiNO_3$ 1 m (blue) electrolytes for 2 days, and deconvoluted XPS spectra of **(b)** C 1s, **(c)** O 1s, **(d)** F 1s, **(e)** N 1s, **(f)** S 2p and **(g)** Li 1s.

Figure 4 summarizes the electrochemical characteristics of the electrolytes investigated by meaning of various techniques. The conductivity plots over the temperature achieved by EIS are shown in **Figure 4a**. The PEGDME 250 LiTFSI 1 m has a conductivity of 1.91×10^{-3} S cm^{-1} at 84.7 °C, which is higher compared to that of PEGDME 250 LiTFSI 1

m $LiNO_3$ 1 m at the same temperature (1.55×10^{-3} S cm^{-1}). Cooling down leads to conductivity decrease in the former electrolyte, whereas the conductivity of the latter remains almost constant, and the two solutions reach the same value of 1.5×10^{-3} S cm^{-1} at 70.5 °C. Beyond this point, the conductivity of the electrolyte containing LiTFSI progressively decreases to reach 1.34×10^{-4} S cm^{-1} at −7.4 °C, instead the electrolyte containing both LiTFSI and $LiNO_3$ exhibits a slight increase to 1.71×10^{-3} S cm^{-1} at 57.7 °C and a subsequent gradual decrease until 3.69×10^{-4} S cm^{-1} at −7.4 °C. Notably, the conductivity of the electrolyte containing both salts remains always higher than that of PEGDME LiTFSI 1 m below 70.5 °C. It is worth mentioning that the conductivity plot of PEGDME 250 LiTFSI can be adequately described by Arrhenius-type behavior, whereas the second electrolyte requires the application of the Vogel–Tamman–Fulcher (VTF) theory to explain the conductivity trend (37,38,43,64). The electrolytes are subsequently examined in symmetrical Li | Li cell to determine t^+ using the Bruce-Vincent-Evans method (*Eq (5)*). The achieved values for the $LiNO_3$-free solution (t^+ = 0.58) and $LiNO_3$-added one (t^+ = 0.59) differ only within the experimental error range (**Figure 4a** inset), thus suggesting that the presence of NO_3^- does not reduce the current transported by Li^+ expected by the equation $t^+ = \sum_i \frac{q^+}{q^i}$, where q^+ represents the charge carried by Li^+, where q^i is the one carried by all the ions, that is, Li^+, NO^-, and $TFSI^-$ in the solution containing $LiNO_3$, or excursively by Li^+ and $TFSI^-$ in the bare solution. Likely, this issue is avoided in this work since the $LiNO_3$ mainly precipitates from the electrolyte bulk to the electrode surface to form the protective SEI layer, thus holding similar t^+ values for the two electrolytes, and possibly analogue ionic conductivity and viscosity. Furthermore, the t_+ values are consistent with those reported for other glyme-type electrolytes, indicating these solutions as suitable candidates for application in lithium batteries. The electrochemical stability of the electrolytes is evaluated in **Figure 4b** by conducting prolonged lithium stripping and deposition experiments through galvanostatic cycling using a current of 0.1 mA cm^{-2} in symmetrical Li | Li configuration. The cell with PEGDME 250 LiTFSI 1 m electrolyte (red) shows polarization decrease from an initial value of 28.8 mV to 16.5 mV during the initial 500 hours of cycling, and subsequent stabilization upon 1000 hour of test. This trend suggests a consolidation of the SEI layer, resulting in steady performance over extended cycling. The cell using PEGDME 250 LiTFSI 1 m $LiNO_3$ 1 m solution has initial polarization of 30 mV, i.e., slightly higher value compared to the $LiNO_3$-free electrolyte, which decreases to 28.1 mV and fluctuates by increasing to 33.1 mV before dropping to 30.5 mV, further rising to 33.7 mV and stabilizing at 22.1 mV after approximately 900

hours. These fluctuations can be attributed to partial dissolution, growth, and subsequent stabilization of the SEI layer, as promoted by the presence of $LiNO_3$ in this electrolyte which may actually trigger the SEI formation dynamics. Furthermore, the higher polarization observed for the cell containing $LiNO_3$-added solution may be associated with the more complex SEI composition, as already suggested by XPS analysis. On the other hand, a more robust and protective SEI could in principle improve the long-term stability of the cell and prevent possible dendrite formation at the lithium metal surface. The electrochemical stability window is investigated in lithium cells with SPC working electrode both for PEGDME 250 LiTFSI 1 m electrolyte (**Figure 4c**) and PEGDME 250 LiTFSI 1 m $LiNO_3$ 1 m electrolyte (**Figure 4d**) using LSV for the anodic region and CV for the cathodic one (see experimental section for details). The LSV of PEGDME 250 LiTFSI 1 m solution reveals an initial peak at 3.8 V *vs.* Li^+/Li, attributed to possible oxidation of PEGDME 250 stabilizer (DBP) already mentioned during DSC discussion. Subsequently, a main peak starting at 4.8 V *vs.* Li^+/Li indicates the ultimate degradation of the electrolyte through oxidative decomposition, i.e., a value which is considered the anodic stability limit. The CV of the same electrolyte in **Figure 4c** shows during the first cathodic scan a broad reductive wave around 1 V *vs.* Li^+/Li likely due to Li-insertion into the disordered CSP matrix, a peak at 0.5 V *vs.* Li^+/Li ascribed to the irreversible reduction of the electrolyte with SEI formation,[57,58] and the typical sharp signal near 0 V *vs.* Li^+/Li due to the beginning of lithium plating onto the working electrode. The subsequent anodic scan reveals a peak at ~0.1 V *vs.* Li^+/Li due to the dissolution of previously plated Li by stripping from the electrode surface and a small peak at around 1 V *vs.* Li^+/Li ascribed to Li de-insertion from the carbonaceous matrix. During the 2nd cycle the reduction peak at 0.5 V *vs.* Li^+/Li decreases, and it vanishes during the subsequent cycles suggesting the gradual consolidation of a protective SEI layer that avoids further electrolyte degradation. In addition, the other mentioned peaks reversibly evolve with slight shift and a lower magnitude. Hence, these data indicate that the PEGDME 250 LiTFSI 1 m electrolyte has an electrochemical stability window extending from 0 V to 4.8 V *vs.* Li^+/Li, with a side degradation at ~3.8 V *vs.* Li^+/Li which could potentially affect the cell performance unless a favorable SEI is formed. The LSV of the cell using the PEGDME 250 LiTFSI 1 m $LiNO_3$ 1 m electrolyte (**Figure 4d**) reveals that the peak attributed to DBP oxidation almost disappears, thus suggesting its possible direct reaction with $LiNO_3$ which deactivates the related anodic signal. The main anodic peak is observed at 4.6 V versus Li^+/Li, indicating a lower onset of oxidative decomposition of the $LiNO_3$-added electrolyte compared with the PEGDME 250 LiTFSI 1 m one. Whilst lowering the oxidative decomposition potential

might initially appear detrimental, it is important to point out that $LiNO_3$ is intentionally added to the electrolyte as a sacrificial agent which decomposes preferentially to facilitate the formation of a robust and effective SEI, ultimately improving the overall stability and of the cell. On the other hand, the missing irreversible oxidation at 3.8 V Li^+/Li represents a further, non negligible, advantage of the $LiNO_3$-added solution. The CV in **Figure 4d** shows a distinct peak at 1.3 V *vs.* Li^+/Li during the first cathodic scan with PEGDME 250 LiTFSI 1 m $LiNO_3$ 1 m electrolyte, which is attributed to the irreversible reduction of the sacrificial additive. The broad wave from 1.1 to 0.2 V *vs.* Li^+/Li observed by further lowering the potential includes partial reduction of the electrolyte and Li insertion into the amorphous SPC. The last cathodic peak at ~0 V *vs.* Li^+/Li consists with the above-mentioned Li deposition, however with less extend compared to the $LiNO_3$-free electrolyte due to the formation of more resistive SEI.[59,60] During the subsequent anodic scan, a peak is observed at approximately 0.1 V versus Li^+/Li as the Li strips away from the electrode, and a small signal appears around 1 V *vs.* Li^+/Li due to Li de-insertion from SPC. Interestingly, the electrolyte degradation peaks disappear already at the second cathodic scan, and the CV proceeds only with reversible Li (de)insertion at ~1 V and stripping/deposition at ~0 V Li^+/Li, without significant shift. This outcome suggests the formation of fully passivating SEI already during the initial cycle, which is achieved only after the 2nd one in the $LiNO_3$-free electrolyte. The chemical stability of the electrolyte in contact with metallic Li is evaluated by monitoring the time evolution of electrode/electrolyte interphase resistance in symmetrical cells. The resistance value plotted *vs.* time in **Figure 4e** are achieved through NLLS fitting of the corresponding EIS spectra. The EIS response of PEGDME 250 LiTFSI 1 m electrolyte is modelled using the $R_e(R_1Q_1)(R_2Q_2)(R_3Q_3)$ equivalent circuit, including the electrolyte resistance (R_e) at high frequency, and a series of resistances with constant phase elements (R_iQ_i) reflecting the complexity of the interfacial processes, where SEI and charge transference locate at medium frequencies while diffusion occurs at low frequency. The total resistance sharply increases from an initial value of 62.2 Ω to 165 Ω upon six hours, which suggests significant changes at the electrode/electrolyte interface as the SEI begins formation. A more gradual, whilst continuous, resistance growth is observed subsequently with values reaching 213 Ω after 24 hours, 241 Ω upon 2 days, and 322 Ω over the whole test of 32 days. Occasional fluctuations with minor resistance decrease are attributed to partial dissolution, reorganization or morphology changes of the SEI layer into a dynamic process extending over time, and possibly leading to final electrode/electrolyte interface stabilization. Instead, the EIS data of the cells with the PEGDME 250 LiTFSI 1 m $LiNO_3$ 1

m electrolyte are more accurately modelled using the simpler $R_e(R_1Q_1)(R_2Q_2)$ equivalent circuit, suggesting a different interfacial structure and SEI formation kinetics. The cell displays a resistance of 74.5 Ω at the OCV that reaches 93.5 Ω after six hours, 124 Ω after 24 hours, and 147 Ω upon 72 hours, i.e., relevantly lower values compared to the $LiNO_3$-free solution.

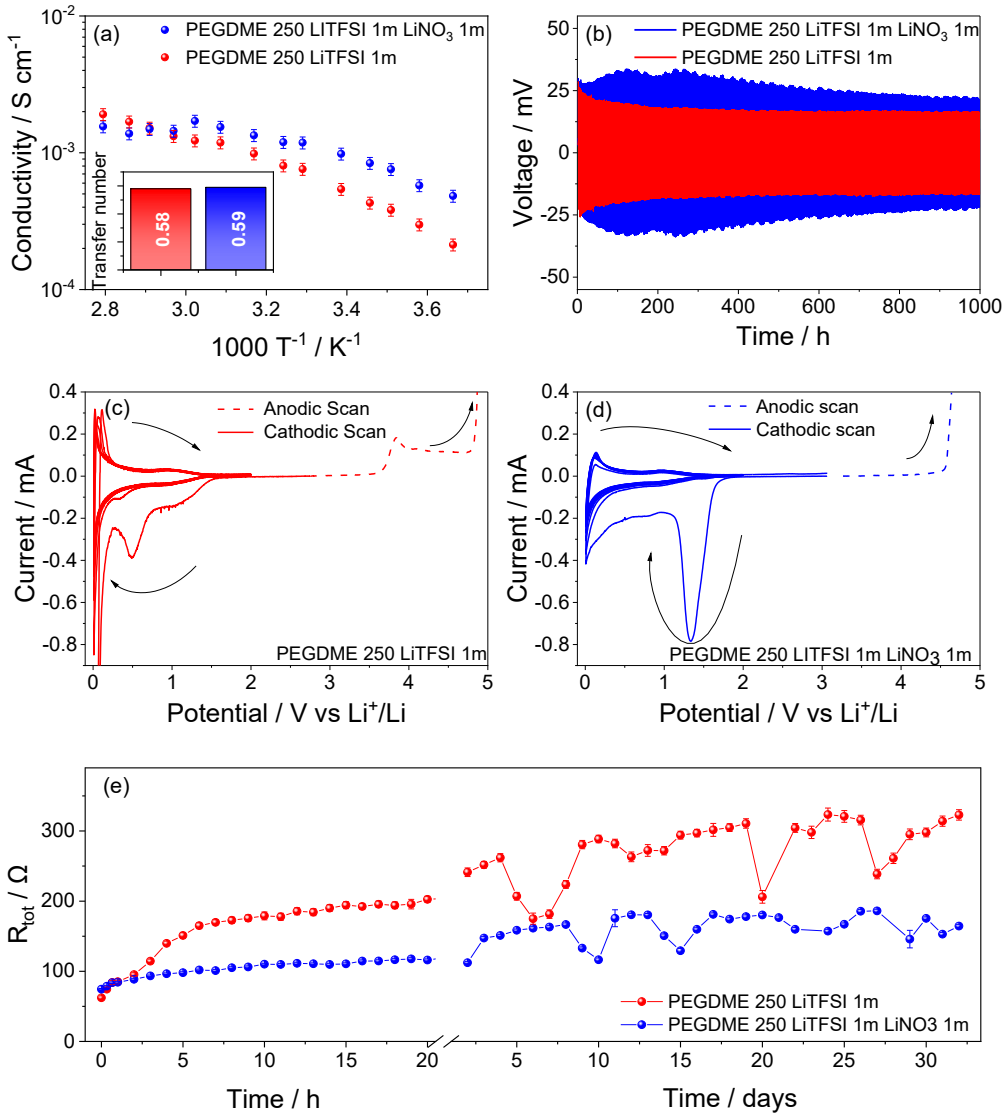

Figure 4. Electrochemical characterization of PEGDME 250 LiTFSI 1 m (red) and PEGDME 250 LiTFSI 1 m $LiNO_3$ 1 m (blue) electrolytes, in detail: **(a)** conductivity trends *vs.* temperature and t_+ values (inset), **(b)** lithium stripping/deposition test performed on Li | Li symmetrical cells, by applying a current of 0.1 mA cm^{-2}, step time 1 h, **(c, d)** electrochemical stability window determined by means of CV in the cathodic region (solid line) and LSV in the anodic one (dashed line) in lithium cells with **(c)** PEGDME 250 LiTFSI 1 m, and **(d)** PEGDME 250 LiTFSI 1 m $LiNO_3$ 1 m, using SPC-Cu working electrode from 0.01 V to 3 V *vs.* Li^+/Li for the cathodic region, and SPC-Al working electrode from OCV to 5 V *vs.* Li^+/Li for the anodic region at a scan rate of 0.1 mV s^{-1}, **(e)** trend of the interphase resistance *vs.* time related to Li | Li cells.

According to the current value and the capacity limit adopted in the following galvanostatic test in full-cell, in the test reported in **Figure 5** (i.e., 0.33 mA cm^{-2}, and 0.5

mAh cm^{-2}, respectively), the lithium contribution to the overall polarization is estimated to be of the order of 0.2 V, as demonstrated by the stripping/deposition tests at various capacity an current regimes displayed.

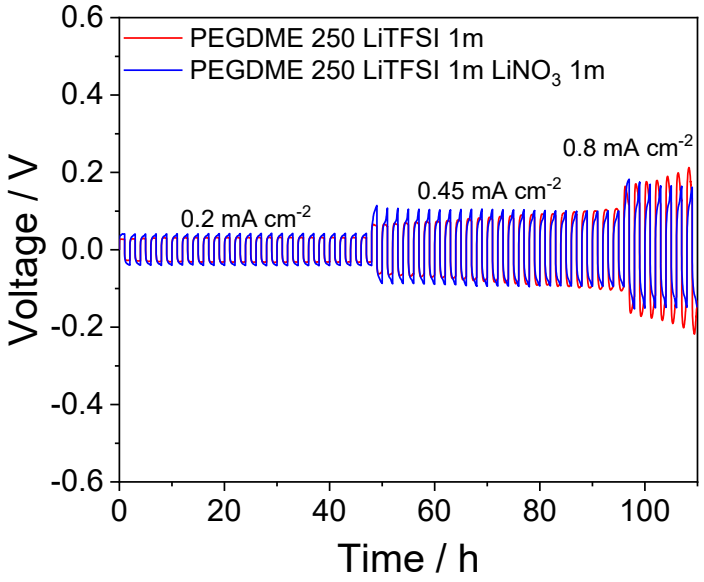

Figure 5. Lithium stripping/deposition test performed on Li | Li symmetrical cells, by applying a current of 0.2 mA cm^{-2}, 0.45 mA cm^{-2}, and 0.8 mA cm^{-2}, step time 1 h, to the cells containing PEGDME 250 LiTFSI 1 m (red) and PEGDME 250 LiTFSI 1 m $LiNO_3$ 1 m (blue) electrolytes.

Figure 6 shows lithium cells exploiting the Li| PEGDME 250 LiTFSI 1 m $LiNO_3$ 1 m |Li_xSn@C configuration under Ar (black) or O_2 (blue) atmospheres. **Figure 6a** reveals a steady state potential of 0.45 V *vs.* Li^+/Li for the former, while a continuous change accounting for Li_xSn@C dealloying process prolonged for 240 h for the latter due to the direct reaction of the lithiated material with the permeated oxygen into the electrolyte. This direct reaction leads to the growth of a passivation oxide layer which depresses the XRD diffraction of the residual, non lithiated Sn@C as evidenced by the XRD patterns of the electrodes recovered from the aged cells in Figure 5b. The evolution of the EIS of the two interphases (Ar and O_2) at the beginning of the test (**Figure 6c**) and upon 240 h of aging (**Figure 6d**) depicts for both cells an increase of the resistance, more remarkably for the latter cell (under O_2, R_{tot} from 60 to 698 Ω) than the former (under Ar, R_{tot} from 169 to 517 Ω), and additionally with change of the related equivalent circuit (**Table 2.4.1**, $R_{tot} = R_1 + R_2$).

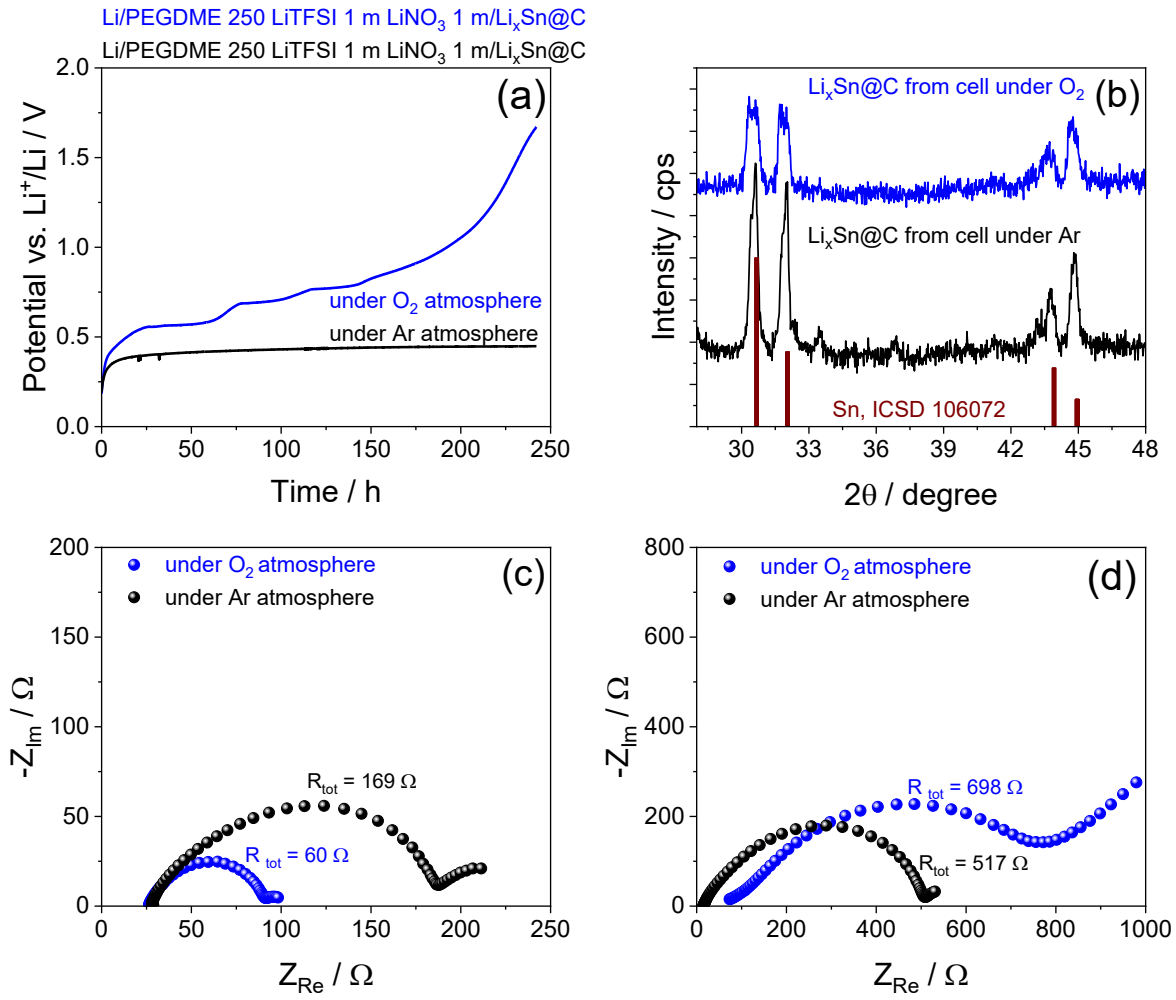

Figure 6. Evolution of Li| PEGDME 250 LiTFSI 1 m $LiNO_3$ 1 m |Li_xSn@C cells under Ar (black) or O_2 (blue) atmosphere. **(a)** Potential trends over 240 h of aging. **(b)** XRD diffraction patterns of the Li_xSn@C electrodes recovered from the aged cells. **(c, d)** Evolution of the EIS Nyquist plots of the two interphases **(c)** at the beginning of the test and **(d)** upon 240 h of aging.

Table 2.4.1. NLLS analyses of the Nyquist Plots recorded by EIS for Li| PEGDME 250 LiTFSI 1 m $LiNO_3$ 1 m |Li_xSn@C cells under Ar or O_2 atmospheres upon 240 h of aging, reported in Figure 6.

Condition	Circuit	R_e	R_1	R_2	χ^2
Under Ar					
OCV	$R_e(R_1Q_1)Q_2$	27.0±0.3	169.3±2.1	/	4.3×10^{-4}
240 h	$R_e(R_1Q_1)Q_2$	14.5±0.3	516.9±4.9	/	9.0×10^{-4}
Under O_2					
OCV	$R_e(R_1Q_1)Q_2$	23.4±1.3	60.3±1.2	/	1.2×10^{-4}
240 h	$R_e(R_1Q_1)\ (R_1Q_1)Q_3$	44.6±4.6	153.2±4.6	544.3±25.3	1.6×10^{-5}

Figure 7 shows the practical evaluation of the Li-ion-O_2 cell using the PEGDME 250 LiTFSI 1 m $LiNO_3$ electrolyte, i.e., the one with the better performances according to our findings with the MWCNTs/FLG 50:50 cathode and the Li_xSn@C as anode, by exploiting polarization tests, EIS, and galvanostatic cycling at increasing current rates. The **Figure 6a**

shows the polarization curves until a current as high as 6 mA cm^{-2}, repeated for three times upon galvanostatic charge of the full cell after each test. The first polarization curve (dark blue) reveals two main plateaus, a shorter one centered at 2 V with a power peak of 2 W g^{-1}, and a longer one evolving from 1.5 to lower voltages involving a higher power of 3 W g^{-1}. After the first polarization test, the cell is charged again (voltage profile in **Figure 7b**), verified by EIS to have a small resistance from 10 to ~20 Ω (figure inset and **Table 2.4.2**), and subjected to a second polarization run with the within same condition as for the previous one. Surprisingly, the polarization curve changes shape (**Figure 7a**, blue), the first region at voltages over 2 V extends, and the second one below 2 V shrinks, thus triggering a higher power peak at about 4 W g^{-1}. These modifications, as well as a similar shape observed upon third test within the same conditions, indicate the stability of the Li-ion oxygen cell and its remarkable power. It is worth mentioning that this good behavior may be triggered by favorable interfacial modifications upon cycling, and by the presence of the $LiNO_3$ which may act as a redox mediator in the low voltage region. The relevant performance of this Li-ion-O_2 full-cell is further demonstrated by galvanostatic cycling tests performed by applying current rates increasing from 1 to 3 mA cm^{-2}, and a constant time limit to increase concomitantly delivered capacity and power (see experimental section). **Figure 7c** shows a steady state voltage signature (2^{nd} cycle), however with non-negligible polarization as expected by the ohmic drop promoted by the high current. On the other hand, the corresponding cycling trends in **Figure 7d** evidences a remarkable stability for the cell at 1 mA cm^{-2}, which delivers a capacity of 150 mAh g^{-1} for 80 cycles with efficiency of 100 %, before losing the performance. Relevant, however with a shorter cycle life, are the cells cycled at 2 and 3 mA cm^{-2}, which deliver 300 and 450 mAh g^{-1} for 30 and 15 cycles, respectively, due to the more demanding anode exploitation mentioned above. Despite the cycle life is still shortened by reaction of the O_2 diffused into the electrolyte with the lithiated anode, the improved performances reported herein for the Li-ion version of the oxygen cell indicate the system as very promising and safe battery for next generation energy storage applications. Another rate capability test is subsequently performed by increasing the discharge/charge time to 30 min and ranging the current from 0.1 to 0.5 mA cm^{-2}, to exploit the lower polarization region and reduce the voltage gap of the Li-ion oxygen cell using PEGDME 250 LiTFSI 1 m $LiNO_3$ electrolyte. The voltage profiles of **Figure 7e** indicate that the cell operates by holding the discharge plateau over 2.2 V with specific capacity of 43 mAh g^{-1}, and energy density of 95 Wh kg^{-1} at 0.1 mA cm^{-2}, whilst the working voltage is 2 V with specific capacity of 86 mAh g^{-1} and energy density of 172 Wh kg^{-1} at 0.2 mA cm^{-2}, over 3 repeated cycles (**Figure 7f**). Instead, the

cell cycled at 0.5 mA cm^{-2} operates similarly to those cycled at 1, 2 and 3 mAh cm^{-2} (compare **Figure 7e** and **Figure 7c**), within a wide voltage ranging from 0.5 to 4.5 V, with a specific capacity of 216 mAh g^{-1} and average energy of ~500 Wh kg^{-1}. Despite the significant polarization at the higher currents, the performances of the Li-ion oxygen cell reported in this work match the ones of the typical Li-ion battery, however without using metals at the cathode side with a very low economic impact. It is worth mentioning that polarization and voltage profile changes of the Li-ion oxygen dell may be promoted by oxygen permeation into the electrolyte and direct reaction with the anode as mentioned above, and demonstrated by **Figure 6**. Indeed, the OCV potential evolutions for lithium cells exploiting the configuration Li| PEGDME 250 LiTFSI 1 m $LiNO_3$ 1 m |Li_xSn@C under Ar (black line) or O_2 (blue line) atmosphere reported in **Figure 6** reveal a steady state value of 0.45 V *vs.* Li^+/Li for the former, while a continuous change accounting for Li_xSn@C dealloying process prolonged for 240 h for the latter. The potential modification of the cell under O_2 without any current flow certainly confirms the direct reaction of the lithiated Sn@C with the oxygen permeated into the electrolyte (i.e., a *short-circuit*-like reaction). This direct reaction leads also to the growth of a passivation oxide layer which covers the anode material and depresses the XRD diffraction of the residual, non lithiated Sn@C as evidenced by the XRD patterns of the electrodes recovered from the aged cells in **Figure 6b**. This issue is also evidenced by the EIS evolution of the two interphases with Nyquist plots of the two cells at the beginning of the test (**Figure 6c**) and upon 240 h of aging (**Figure 6d**) in Ar (black) and O_2 (blue) environments. The plots reveal for both cells an increase of the impedance as promoted by the SEI growth, however with a more remarkable magnitude for the latter cell (under O_2 R_{tot} increases from 60 to 698 Ω) than the former (under Ar R_{tot} increases from 169 to 517 Ω), in addition with change of the related equivalent circuit (see **Table 2.4.1**, where R_{tot} of the interphase is represented by $R_1 + R_2$).

Table 2.4.2. NLLS analysis carried out on the Nyquist plots reported as inset of Figure 7b. The impedance spectra were acquired on a Li_xSn@C | PEGDME 250 LiTFSI 1 m $LiNO_3$ 1 m | MWCNTs:FLG full-cell, at the OCV and after the first and second galvanodynamic polarization runs.

Condition	Equivalent circuit	R	χ^2
OCV	$R_e(RQ)Q_w$	10.1 ± 0.3	2 x 10^{-5}
After 1st run	$R_e(RQ)Q_w$	18.7 ± 0.4	3 x 10^{-5}
After 2nd run	$R_e(RQ)Q_w$	22.3 ± 1.5	3 x 10^{-4}

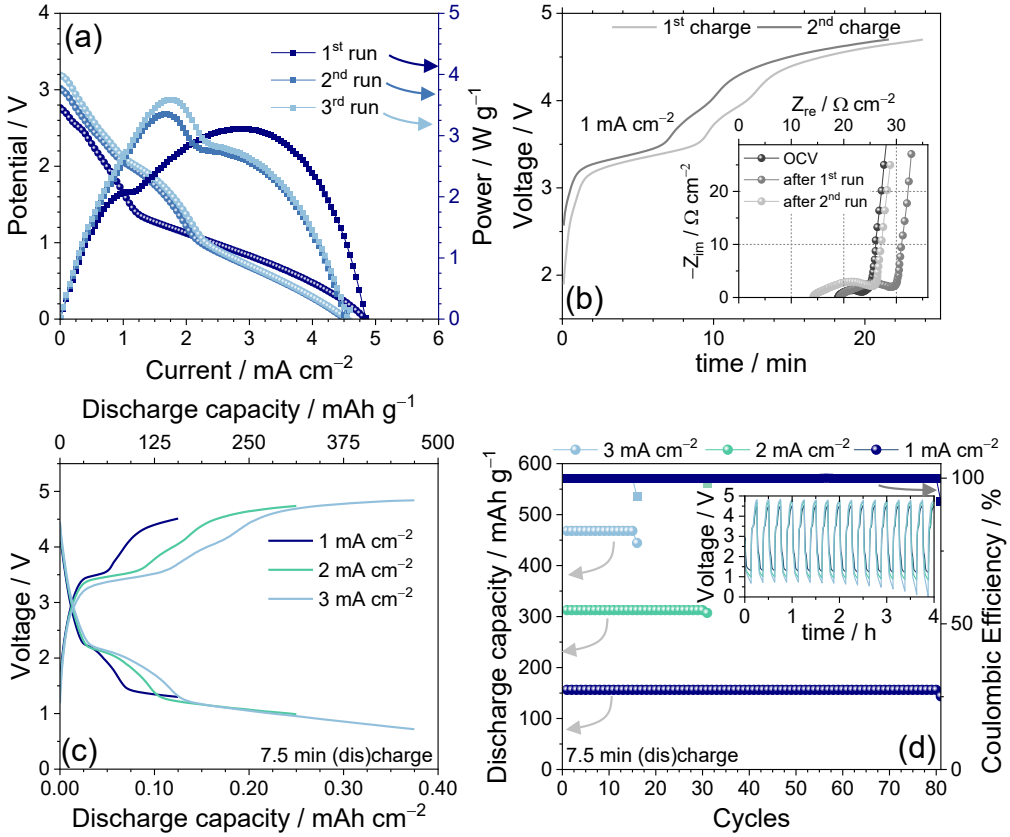

Figure 7. Practical evaluation of Li-ion-O_2 battery operating parameters using the PEGDME 250 LiTFSI 1 m $LiNO_3$ electrolyte, MWCNTs/FLG 50:50 as cathode support, and pre-lithiated Li_xSn@C as anode: **(a)** polarization plot obtained by means of galvanodynamic polarization measurement (current range 0 – 6 mA cm^{-2}, step: 0.05 mA cm^{-2}, 5 s), **(b)** voltage profile of the galvanostatic charge occurred between the 1st – 2nd and 2nd – 3rd run (Nyquist plot are reported as inset), **(c)** 2nd voltage profile of three Li-ion-O_2 full-cells investigated by applying a current rate of 1, 2, and 3 mA cm^{-2} for 7.5 min, and **(d)** corresponding discharge capacity trends *vs.* cycle number (coulombic efficiency in right-hand side *y*-axis, inset shows the voltage profiles *vs.* time trends), voltage range: 0 – 5.0 V, cathode geometric area: 2.0 cm^2, loading: 1.0 ± 0.2 mg cm^{-2} of MWCNTs/FLG 50:50, anode geometric area: 1.54 cm^2, loading: 6.4 ± 0.2 mg cm^{-2} of Sn@C.

References

(1) J.B. Skjærseth, Towards a European Green Deal: Int Environ Agreem 21 (2021) 25–41. h
(2) G. Goppelt, ATZelectronics Worldwide 17 (2022) 36–41.
(3) J. Piątek, T.M. Budnyak, S. Monti, G. Barcaro, R. Gueret, E.S. Grape, A. Jaworski, A.K. Inge, B.V.M. Rodrigues, A. Slabon, ACS Sustain Chem Eng 9 (2021) 9770–9778.
(4) S. Link, L. Schneider, A. Stephan, L. Weymann, P. Plötz, Nat Energy 10 (2025) 526–534. https://doi.org/10.1038/s41560-025-01722-y.
(5) R.E. Ciez, J.F. Whitacre, Nat Sustain 2 (2019) 148–156.
(6) K. Turcheniuk, D. Bondarev, V. Singhal, G. Yushin, , Nature 559 (2018)
(7) X. Bai, Y. Sun, X. Li, R. He, Z. Liu, J. Pan, J. Zhang, , Electrochemical Energy Reviews 7 (2024) 33.
(8) Y. Li, J. Lu, ACS Energy Lett 2 (2017) 1370–1377. https://doi.org/10.1021/acsenergylett.7b00119.
(9) Md.A. Rahman, X. Wang, C. Wenz, J Electrochem Soc 160 (2013) A1759–A1771.
(10) J. Hassoun, K. Kimura, Y. Tominaga, Adv Sustain Syst (2025).
(11) L. Carbone, S.G. Greenbaum, J. Hassoun ustain Energy Fuels 1 (2017) 228–247.
(12) C.O. Laoire, S. Mukerjee, K.M. Abraham, E.J. Plichta, M.A. Hendrickson, Journal of Physical Chemistry C 113 (2009) 20127–20134.

(13) J. Liu, Z. Wang, J. Zhu, J Power Sources 306 (2016) 559–566.
(14) S. Levchenko, V. Marangon, S. Bellani, L. Pasquale, F. Bonaccorso, V. Pellegrini, J. Hassoun, ACS Appl Mater Interfaces 15 (2023) 39218–39233.
(15) S. Levchenko, G. Valente, J. Hassoun, Adv Sustain Syst (2024). h
(16) L. Carbone, P.T. Moro, M. Gobet, S. Munoz, M. Devany, S.G. Greenbaum, J. Hassoun, Appl Mater Interfaces 10 (2018) 16367–16375
(17) B. Kumar, J. Kumar, R. Leese, J.P. Fellner, S.J. Rodrigues, K.M. Abraham J Electrochem Soc 157 (2010) A50.
(18) L. Cecchetto, M. Salomon, B. Scrosati, F. Croce, , J Power Sources 213 (2012) 233–238.
(19) H.-G. Jung, J. Hassoun, J.-B. Park, Y.-K. Sun, B. Scrosati, , Nat Chem 4 (2012) 579–585.
(20) J. Hassoun, F. Croce, M. Armand, B. Scrosati, Angewandte Chemie - International Edition 50 (2011) 2999–3002.
(21) C.O. Laoire, S. Mukerjee, K.M. Abraham, E.J. Plichta, M.A. Hendrickson, , The Journal of Physical Chemistry C 114 (2010) 9178–9186.
(22) P.G. Bruce, S.A. Freunberger, L.J. Hardwick, J.-M. Tarascon, Nat Mater 11 (2012) 19–29.
(23) J. Ming, Z. Cao, Y. Wu, W. Wahyudi, W. Wang, X. Guo, L. Cavallo, J.-Y. Hwang, A. Shamim, L.-J. Li, Y.-K. Sun, H.N. Alshareef, ACS Energy Lett 4 (2019) 2613–2622. h
(24) S. Xiong, K. Xie, Y. Diao, X. Hong, Electrochim Acta 83 (2012) 78–86.
(25) S.H. Lee, J. Hwang, J. Ming, Z. Cao, H.A. Nguyen, H. Jung, J. Kim, Y. Sun, , Adv Energy Mater 10 (2020).
(26) B. Wang, T. Xu, S. Huang, D. Kong, X. Li, Y. Wang, J Mater Chem A Mater 9 (2021) 6070–6088. h
(27) D. Cao, Q. Zhang, A.M. Hafez, Y. Jiao, Y. Ma, H. Li, Z. Cheng, C. Niu, H. Zhu, , Small Methods 3 (2019) 1800539.
(28) Z. Huang, C. Zhang, W. Lv, G. Zhou, Y. Zhang, Y. Deng, H. Wu, F. Kang, Q.-H. Yang, J Mater Chem A Mater 7 (2019) 727–732.
(29) W. Chen, R. V. Salvatierra, M. Ren, J. Chen, M.G. Stanford, J.M. Tour, Advanced Materials 32 (2020) 2002850.
(30) G. Li, H. Li, Y. Wang, D. Xiong, S. Wang, Y. Yan, S. Chen, B. Tian, Y. Shi, ACS Appl Mater Interfaces 13 (2021) 56109–56115.
(31) J. Hassoun, H.-G. Jung, D.-J. Lee, J.-B. Park, K. Amine, Y.-K. Sun, B. Scrosati, Nano Lett 12 (2012) 5775–5779
(32) V. Marangon, C. Hernandez-Rentero, S. Levchenko, G. Bianchini, D. Spagnolo, A. Caballero, J. Morales, J. Hassoun, ACS Appl Energy Mater 3 (2020) 12263–12275.
(33) J.-B. Park, J. Hassoun, H.-G. Jung, H.-S. Kim, C.S. Yoon, I.-H. Oh, B. Scrosati, Y.-K. Sun, Lett 13 (2013) 2971–2975.
(34) D. Di Lecce, V. Marangon, H.-G. Jung, Y. Tominaga, S. Greenbaum, J. Hassoun, Green Chemistry 24 (2022) 1021–1048.
(35) W.A. Henderson, f Physical Chemistry B 110 (2006) 13177–13183.
(36) W.A. Henderson, F. McKenna, M.A. Khan, N.R. Brooks, V.G. Young Jr., R. Frech, GChemistry of Materials 17 (2005) 2284–2289.
(37) V. Marangon, L. Minnetti, E. Barcaro, J. Hassoun, Batteries, Chemistry - A European Journal 29 (2023).
(38) W. Ghder Soliman, Ch. Swathi, T. Yasasvi, B. Keerthi Priya, D. Akhila Reddy, , Mater Today Proc 42 (2021) 429–435.
(39) A. Bartolotta, G. Carini, G. D'Angelo, M. Federico, V. Romano, G. Di Marco, , Macromol Chem Phys 224 (2023).
(40) C.A. Gracia-Fernández, S. Gómez-Barreiro, J. López-Beceiro, S. Naya, R. Artiaga, by DSC, J Mater Res 27 (2012) 1379–1382.
(41) L. Balo, H. Gupta, S.K. Singh, V.K. Singh, A.K. Tripathi, N. Srivastava, R.K. Tiwari, R. Mishra, D. Meghnani, R.K. Singh, Journal of Solid State Electrochemistry 23 (2019) 2507–2518. h
(42) K.P. Barteau, M. Wolffs, N.A. Lynd, G.H. Fredrickson, E.J. Kramer, C.J. Hawker, Macromolecules 46 (2013) 8988–8994
(43) D.H.C. Wong, A. Vitale, D. Devaux, A. Taylor, A.A. Pandya, D.T. Hallinan, J.L. Thelen, S.J. Mecham, S.F. Lux, A.M. Lapides, N.P. Balsara, J.M. Desimone, Chemistry of Materials 27 (2015) 597–603.
(44) I. Rey, J.C. Lassègues, J. Grondin, L. Servant, , Electrochim Acta 43 (1998) 1505–1510.

(45) V.S. Patil, K. Vithya, M. Premalatha, B. Sundaresan, Macromol Symp 387 (2019).
(46) D. Brouillette, D.E. Irish, N.J. Taylor, G. Perron, M. Odziemkowski, J.E. Desnoyers, , Physical Chemistry Chemical Physics 4 (2002) 6063–6071.
(47) R.E. Miller, R.R. Getty, K.L. Treuil, G.E. Leroi, , J Chem Phys 51 (1969) 1385–1389.
(48) G.M. Veith, J. Nanda, L.H. Delmau, N.J. Dudney, J Phys Chem Lett 3 (2012) 1242–1247.
(49) Ó. Vargas, Á. Caballero, J. Morales, E. Rodríguez-CastellónACS Appl Mater Interfaces 6 (2014) 3290–3298.
(50) D. Di Lecce, V. Marangon, A. Benítez, Á. Caballero, J. Morales, E. Rodríguez-Castellón, J. HassounJ Power Sources 412 (2019) 575–585.
(51) A. Schechter, D. Aurbach, H. Cohen, Langmuir 15 (1999) 3334–3342.
(52) D. Ensling, M. Stjerndahl, A. Nytén, T. Gustafsson, J.O. Thomas, J. Mater. Chem. 19 (2009) 82–88.
(53) Q. Liu, A. Cresce, M. Schroeder, K. Xu, D. Mu, B. Wu, L. Shi, F. Wu, Energy Storage Mater 17 (2019) 366–373.
(54) M. Tułodziecki, J.-M. Tarascon, P.-L. Taberna, C. Guéry, , Electrochem Commun 77 (2017) 128–132.
(55) R. Demir-Cakan, M. Morcrette, Gangulibabu, A. Guéguen, R. Dedryvère, J.-M. Tarascon, Environ Sci 6 (2013) 176.
(56) M. Agostini, S. Xiong, A. Matic, J. Hassoun, Chemistry of Materials 27 (2015) 4604–4611.
(57) K.P.C. Yao, D.G. Kwabi, R.A. Quinlan, A.N. Mansour, A. Grimaud, Y.-L. Lee, Y.-C. Lu, Y. Shao-Horn, J Electrochem Soc 160 (2013) A824–A831.

Chapter 3.

Polymers and glyme electrolytes for Lithium and Sodium battery

3.1 A versatile polymer electrolyte for lithium-ion, lithium-sulfur, and lithium-oxygen battery

Lithium-metal batteries (LMB) have been shown since late 1990s to be the most energetic rechargeable systems due to the extremely high gravimetric capacity of Li (3861 mA h g^{-1}) delivered at the lowest redox potential among the anodes (−3.04 V vs. standard hydrogen electrode).[1-4] Much effort has been devoted to stabilizing the lithium metal, including the formation of suitable SEI layers with high ionic conductivity, low electrochemical reactivity and relevant chemical stability.[5] However, the high energy content of Li metal can promote a relevant reactivity with large part of the liquid organic electrolytes leading to mechanical, chemical, and electrochemical instability of the SEI with final LMB failure.[6, 7] The most suitable approach for an efficient use of Li in rechargeable battery involved the use of solid electrolytes, either polymeric or inorganic, instead of liquid ones in view of their mechanical stability and low flammability.[3, 8] In particular, cells using polymer electrolytes based on poly(ethylene oxide) (PEO) with chemical formula $-(CH_2CH_2O)_n-$ and high molecular weight (>600 000 Da) demonstrated the most promising features in terms of scalability and practical applicability.[9-11] However, the mainly crystalline state at room temperature of high-molecular-weight PEO hinders suitable ionic conductivity for battery application, that is achieved only at temperature higher than 60 °C over which the polymer becomes predominantly amorphous.[12] Relevantly, a LMB using PEO-based electrolyte and $LiFePO_4$ (LFP) cathode with energy density higher than 100 W h kg^{-1} operating from 60 to 80 °C has been successfully launched onto the market as lithium metal polymer (LMP®) battery by the Bolloré Group (France).[13] A similar cell stability and scalability can be achieved at a temperature lower than 60 °C using the same Li-LFP configuration mentioned above, in which the PEO-based electrolyte is replaced by a solid poly(ethylene glycol)dimethyl ether (PEGDME) with low molecular weight (e. g.,<5000 Da) for allowing suitable ionic conductivity and operative condition.[14] Recent results demonstrated the crucial role of PEGDME-based polymer electrolytes in stabilizing the electrochemical performance of lithium batteries using layered oxide-based cathodes such as $LiNi_{0.85}Co_{0.1}Mn_{0.05}O_2$.[15] Following this trend, the energy density of the LMB can be remarkably increased by using cathodes with

different chemistry rather than the olivine-structured LFP which relies on Li-(de)insertion electrochemical process.[16, 17] Li-S and Li-O_2 batteries, based on the Li conversion reaction, have been suggested as the most promising candidates for increasing the energy density of the LMBs to values exceeding 300 W h kg^{-1}.[18] However, these triggering energy storage systems, mainly developed using liquid electrolyte, still suffer by the same severe issues affecting the LMB, that is, SEI instability, Li dendrites formation and cell failure with safety limits.[19, 20] These emerging LMBs have additional critical issues that may affect the anode side, mainly related with the formation of reactive and nucleophilic intermediates during the electrochemical process, such as lithium polysulfides (Li_2S_x with $2 \leq x \leq 8$) in the Li-S battery or lithium peroxide (Li_2O_2) and superoxide (LiO_2) in the Li-O_2 one.[21-26] The use of polymer electrolyte, in analogy with the above reported LMB with insertion cathode, has been indicated as an adequate pathway to mitigate the issues of the lithium metal, in particular using the sulfur cathode.[27-30]

#7 10.1002/chem.202301345

Room-Temperature Solid-State Polymer Electrolyte in Li-$LiFePO_4$, Li-S and Li-O_2 Batteries

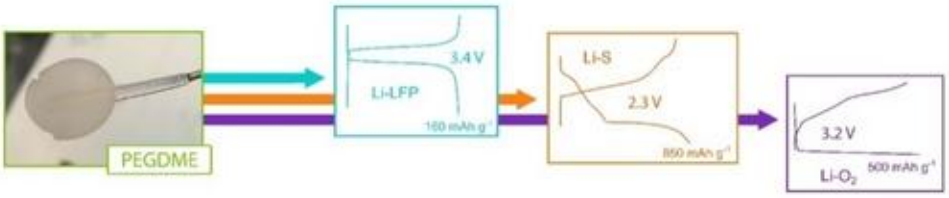

In this work we developed a composite polymer electrolyte (CPE) based on crystalline PEGDME including LiTFSI and $LiNO_3$ salts, and SiO_2 ceramic filler (indicated as PEGDME_CPE), treated with a liquid analogue solution of tetra(ethylene glycol)dimethyl ether (TEGDME_LE) subsequently removed to get a self-standing plasticized polymer electrolyte (indicated subsequently as PEGDME_PCPE). A preliminary analysis has been conducted on the liquid TEGDME_LE solution by EIS, chronoamperometry, LSV, and CV. Furthermore, galvanostatic cycling on lithium metal cells with the liquid configuration have been performed exploiting LFP, sulfur, and oxygen cathodes. Subsequently, the PEGDME_PCPE electrolyte is characterized in terms of conductivity, lithium transference number, electrochemical and chemical stability using the techniques listed above. Polymeric Li cells using PEGDME_PCPE stacked with LFP, S and O_2 cathodes have been assembled and galvanostatically cycled at room temperature to evaluate the applicability of the system. The results reported herein may allow the development of LMBs exploiting the solid polymer configuration, characterized by a relevant safety and high energy content for energy storage applications.

Experimental

- Electrolytes preparation

  The liquid electrolyte plasticizing agent was prepared in an Ar-filled glovebox (MBraun, H_2O and O_2 levels under 1 ppm) by dissolving lithium bis(trifluoromethanesulfonyl)imide (LiTFSI, $LiN(SO_2)_2(CF_3)_2$, 99.95 % trace metal basis, Sigma-Aldrich) conductive salt and lithium nitrate ($LiNO_3$, 99.99 % trace metal basis, Sigma-Aldrich) additive in tetra(ethylene glycol)dimethyl ether (TEGDME, $CH_3(OCH_2CH_2)_4OCH_3$, ≥99 %, Sigma-Aldrich) with a concentration of 1 mol $kg_{solvent}^{-1}$ for each salt. Before using, LiTFSI and $LiNO_3$ were dried under vacuum at 110 °C for 2 days, while TEGDME was stored under dry molecular sieves (rods, 3 Å, size 1/16 in., Honeywell Fluka) to achieve a water content lower than 10 ppm as verified by a Karl Fischer 899 Coulometer (Metrohm). The TEGDME-solution is indicated in the text as TEGDME_LE. The composite polymer electrolyte (CPE) precursor was prepared according with a previous paper.14 PEGDME (average molecular weight 2000 g mol^{-1}, Sigma-Aldrich) was initially mixed with LiTFSI and $LiNO_3$ to achieve a concentration of 1 mol kg_{PEGDME}^{-1} for each salt, afterwards, fumed silica powder (SiO_2, average particle size: 0.007 μm, Sigma-Aldrich) was added to the polymer-salts mixture by a 10 % weight ratio. The components were dispersed/dissolved in acetonitrile (ACN, CH_3CN, Sigma-Aldrich) and magnetically stirred for two days to obtain a viscous slurry, which was cast on a plastic foil (23-5FEP-2-50, CS Hyde) by doctor blade (MTI Corporation) technique. Upon several drying steps performed under vacuum, the membrane was introduced in an Ar-filled glovebox and stored at 25 °C for about 20 days to achieve complete solidification. Subsequently, the polymer electrolyte was cut into membranes with diameter of either 10 or 18 mm, which were soaked for two days with an excess of TEGDME_LE to allow uniform wetting, and subsequently dried under vacuum for 5 h to remove the liquid excess and obtain a new plasticized composite polymer electrolyte (PCPE) indicated in the text as PEGDME_PCPE.

- Electrolyte characterization

  TGA of TEGDME_LE and PEGDME_PCPE were carried out by a Mettler-Toledo TGA 2 instrument in the 25–800 °C temperature range using a heating rate of 5 °C min^{-1} under a N_2 flow of 50 ml min^{-1}. FTIR spectra of TEGDME_LE, PEGDME_CPE and PEGDME_PCPE were acquired using a Bruker Vertex V70 instrument set up in the transmittance mode. The electrochemical properties of TEGDME_LE and PEGDME_PCPE were evaluated in CR2032 coin-type cells (MTI Corporation) with various configuration assembled in an Ar-filled glovebox. The ionic conductivity was investigated by performing EIS at various temperatures in the 500 kHz – 100 Hz frequency range through an alternate voltage signal of 10 mV on blocking-electrode stainless-steel|electrolyte|stainless-steel symmetrical cells using either one O-ring (23-5FEP-2–50, CS Hyde, internal diameter of 10 mm) filled with TEGDME_LE, or two O-rings holding a 10 mm-diameter PEGDME_PCPE membrane. The O-ring thickness of 127 μm allowed to fix the cell constant at 0.016 cm^{-1} for TEGDME_LE and 0.032 cm^{-1} for PEGDME_PCPE. The temperature of the cells was controlled via a F12 Julabo instrument. The Li+-transference number was evaluated by applying the Bruce–Vincent–Evans method. Symmetrical cells with Li|electrolyte|Li configuration were prepared by using two 14 mm-diameter lithium discs separated either by four 16 mm-diameter glass fiber Whatman GF/A discs soaked with TEGDME_LE or by two O-rings holding a 10 mm-diameter PEGDME_PCPE membrane. A chronoamperometry test was carried

out on the cells by applying a voltage (ΔV) of 30 mV for 90 min, and EIS was performed before and after polarization using the 500 kHz–100 mHz frequency range and an alternate voltage signal of 10 mV. Carbon-based electrodes were prepared by doctor blade casting on either Al or Cu foils of a slurry obtained by dispersing carbon black (80 %, Super P carbon, Timcal) and polyvinilidene fluoride (20 %, PVdF, Solef 6020) polymer binder in NMP (Sigma-Aldrich). The slurries were dried on hot plates at 70 °C to remove the NMP solvent, cut into discs with diameter of either 14 mm or 10 mm and dried under vacuum at 110 °C for 3 h before being transferred in an Ar-filled glovebox. The electrochemical stability window of the electrolytes was determined by CV measurements on Li|electrolyte|SPC-Cu cells between 0.01 and 2.0 V vs. L^i+/Li at 0.1 mV s^{-1} and by LSV on Li|electrolyte|SPC-Al cells from the open circuit voltage (OCV) to 5.0 V vs. Li^+/Li at 0.1 mV s^{-1}. The Li|SPC cells used either a 14 mm-diameter lithium disc separated from a 14 mm-diameter SPC electrode by two 16 mm-diameter glass fiber Whatman GF/A discs soaked with TEGDME_LE, or a 14 mm lithium disc separated from a 10 mm-diameter SPC electrode by two O-rings holding a 10 mm-diameter PEGDME_PCPE membrane. Lithium stripping/deposition tests were carried out on Li|electrolyte|Li symmetrical cells through galvanostatic cycling measurements using a constant current of 0.1 mA cm^{-2} and setting a step time of 1 h for both charge and discharge processes. The cells were assembled by stacking two 14 mm-diameter lithium discs separated either by two 16 mm-diameter glass fiber Whatman GF/A discs soaked with TEGDME_LE or by two O-rings holding a 10 mm-diameter PEGDME_PCPE membrane. The same cell configurations were adopted to investigate the electrolytes stability upon aging in contact with lithium metal by performing EIS measurements on Li|electrolyte|Li cells every 2 h for the first 14 h since assembly and subsequently every day for about 30 days. The voltammetry and EIS tests were performed via a VersaSTAT MC Princeton Applied Research (PAR-AMETEK) instrument, while the galvanostatic cycling measurements were carried out using a MACCOR series 4000 battery test system.

- Electrolytes application

  The cathodes used in lithium cell employed various active materials, in detail: i) LFP with a carbon content of about 5 % was developed by Advanced Lithium Electrochemistry (Aleees Taiwan, model A1100); ii) a sulfur-carbon composite, which was prepared by mixing elemental sulfur (≥99.5 %, Riedel-de Haën) with SPC by the 70 : 30 weight ratio, followed by heating at 125 °C under magnetic stirring with the aid of a silicon oil bath until complete melting of sulfur and blending with SPC, subsequent quenching at room temperature and grinding of the final composite indicated in the text as S@SPC-73;55 iii) multiwalled carbon nanotubes (MWCNTs, >90 % carbon basis, D×L: 110–170 nm×5–9 µm, Sigma-Aldrich), which were annealed at 750 °C for 12 h under N_2 flow to achieve the N_2@MWCNTs. The electrode slurries were prepared by dispersing in NMP solvent the following mixtures: i) LFP/SPC/PVdF 80 : 10 : 10 wt . %; ii) S@SPC-73/SPC/PVdF 80 : 10 : 10 wt%; iii) N_2@MWCNTs/PVdF 80 : 20 wt%. The slurries were cast via doctor blade technique on either a carbon-coated Al foil (thickness of 20 µm, MTI Corporation) for LFP, a porous carbon-cloth ELAT 1400 gas diffusion layer (GDL, MTI Corporation) for S@SPC-73, or a 39BC GDL (SiGracet) for N_2@MWCNTs. The LFP and N_2@MWCNTs electrode tapes were dried on a hot plate for 3 h at 70 °C and cut into 14 mm-diameter (LFP) and 16 mm-diameter (N_2@MWCNTs) discs which were dried for 3 h at 110 °C under vacuum before being transferred in an Ar-filled glovebox, while the S@SPC-73 tape was dried at room temperature until complete evaporation of NMP and cut into 14 mm-diameter

discs which were dried at 35 °C overnight under vacuum before transfer. The final active material loadings of the cathodes were between 4.3 and 4.8 mg cm^{-2} for LFP (electrode geometric area: 1.54 cm^2), between 1.3 and 1.4 mg_S cm^{-2} for S@SPC-73 (electrode geometric area: 1.54 cm^2), and of 0.9 mg_{MWCNTs} cm^{-2} for N_2@MWCNTs (electrode geometric area: 2.01 cm^2). The electrolytes were tested in CR2032 coin-type lithium cells using a 14 mm-diameter lithium disc as anode, one of the cathodes described above, and different electrolyte/separator combinations, in particular: Li|TEGDME_LE|cathode cells employed i) one 16 mm-diameter glass fiber Whatman GF/B disc as separator for LFP, ii) one 16 mm-diameter Celgard 2400 separator soaked with the electrolyte by the 15 µl mg^{-1} electrolyte/sulfur (E/S) ratio for S@SPC-73, and iii) two 18 mm-diameter glass fiber Whatman GF/A discs for N_2@MWCNTs; on the other hand, Li|PEGDME_PCPE|cathode cells employed a 18 mm-diameter PEGDME_PCPE membrane separating Li anode and cathode. Regular CR2032 coin-type cells were used for Li-LFP and Li-S cells, while top-meshed CR2032 cells (MTI Corporation) inserted in pure O_2-filled glass tubes were used to achieve the Li-O_2 cells. Li-LFP cells were galvanostatically cycled between 2.7 and 3.9 V at either C/5 or C/10 (1C = 170 mA g_{LFP}^{-1}) whether using TEGDME_LE or PEGDME PCPE, respectively. Cycling tests were performed on Li-S cells at C/10 (1C = 1675 mA g_S^{-1}) in the 1.9–2.8 V voltage range for Li|TEGDME_LE|S@SPC-73 configuration, while one activation cycle at C/20 between 1.6 and 2.8 V followed by prolonged cycling at C/20 in the 1.7–2.8 V voltage range was employed for Li|PEGDME_PCPE|S@SPC-73 configuration. Finally, Li-O_2 cells were cycled in the 1.5–4.8 V voltage range at the constant rate of 100 mA g_{MWCNTs}^{-1} by setting a step time of 5 h for both discharge and charge to limit the cell capacity at 500 mA h g_{MWCNTs}^{-1}. The galvanostatic cycling measurements were performed through a MACCOR series 4000 battery test system setting room temperature at 30 °C with a maximum fluctuation of ±0.1 °C.

Results

Prior to studying the PEGDME_PCPE, the liquid analogue TEGDME_LE is electrochemically characterized in **Figure 1**. The ionic conductivity trend reported vs. the temperature in **Figure 1a** shows the typical VTF behavior, already observed for liquid glyme-based electrolytes, in particular at low temperatures. Accordingly, **Table 3.1.1** summarizes the results of the VTF plot for the TEGDME_LE.

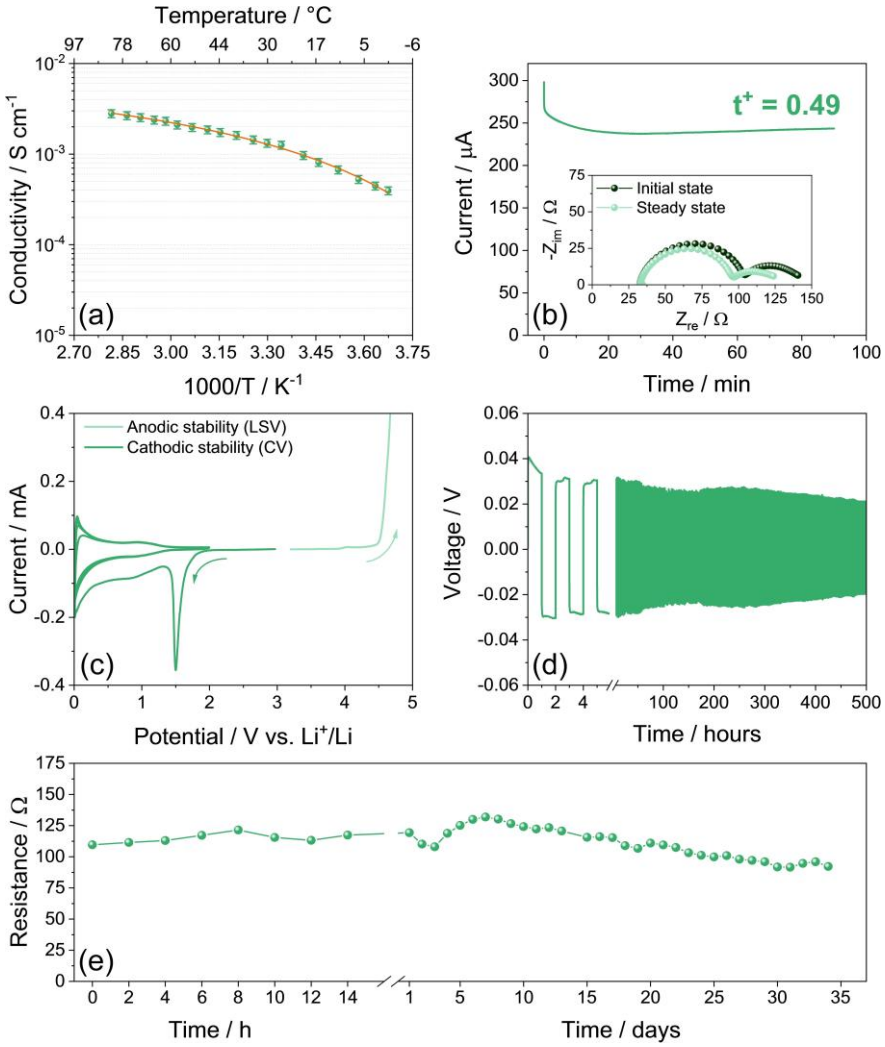

Figure 1. Electrochemical characterization of TEGDME_LE. **(a)** Ionic conductivity plot; **(b)** Chronoamperometry curve recorded on a Li||Li symmetrical cell and related Nyquist plots acquired before and after polarization (inset) used to evaluate the electrolyte Li^+-transference number by the Bruce–Vincent–Evans method *Eq (5)*; EIS frequency range: 500 kHz–100 mHz; alternate voltage signal: 10 mV; **(c)** Electrochemical stability window determined either by CV between 0.01 and 2.0 V vs. Li^+/Li and by LSV from cell OCV potential to 5 V vs. Li^+/Li carried out on Li||SPC cells; scan rate: 0.1 mV s

Table 3.1.1 Ionic conductivity at infinite temperature (σ_∞), activation energy for ion conduction (E_a), and temperature of zero configurational entropy (T_0) for the PEGDME_LE according to VTF *Eq (4)* used for the conductivity trend of Figure 1a.

Electrolyte	σ_∞ (S cm^{-1})	E_a (eV)	T_0 (K)
TEGDME_LE	$9.9\times10^{-3} \pm 0.1\times10^{-3}$	$14.3\times10^{-3} \pm 1.7\times10^{-3}$	221.2 ± 3.9

The liquid electrolyte shows a conductivity ranging from 3×10^{-4} S cm^{-1} at 0 °C to 3×10^{-3} S cm^{-1} at 80 °C, with a value at room temperature approaching 10^{-3} S cm^{-1}, all suitable values for battery application.[31-33] The chronoamperometry and Nyquist plots recorded before and after polarization of a Li|TEGDME_LE|Li symmetrical cell in **Figure 1b** allow the evaluation of the Li^+-transference number (t^+) through the Bruce–Vincent–Evans

method *Eq (5)*. The result reported in **Table 3.1.2** indicates a t^+ of 0.49, which can ensure a fast charge transfer at the electrode/electrolyte interphase of the cell. The CV and LSV performed on Li|TEGDME_LE|SPC cells reported in **Figure 1c** show a sharp peak centered at 1.5 V vs. Li^+/Li related to the reduction of $LiNO_3$ and a wave around 0.8 V vs. Li^+/Li ascribed to the reductive decomposition of the TEGDME with formation of a SEI layer.[34-36] The tests also reveal a reversible process between 0.1 and 0 V vs. Li^+/Li associated with the Li-(de)insertion into the SPC, as well as a relevant increase of the oxidative current due to the decomposition of the solution at about 4.2 V vs. Li^+/Li, thus suggesting an electrochemical stability window of TEGDME_LE extending from 0 to 4.2 V vs. Li^+/Li. The Li stripping/deposition test performed on a Li|TEGDME_LE|Li symmetrical cell in **Figure 1d** suggests a low overvoltage, with steady state value of 0.02 V after 500 h, achieved upon gradual decrease of the polarization (overvoltage) due to partial dissolution and stabilization of the passivation layer at the electrode/electrolyte interphase. **Figure 1e** shows the resistance trend of the Li/TEGDME_LE interphase determined by EIS during aging for 35 days of a cell with symmetrical configuration without any current flow. The curves are evaluated with equivalent circuits including the electrolyte resistance as high-frequency intercept of the plot with the real axis (R_e) in series with resistances and constant phase elements accounting for the electrode/electrolyte interphase semicircle at medium-high frequency (R_iQ_i), and the Warburg-type finite-length diffusion at low frequency (R_wQ_w). The trend indicates interphase resistance values seldom exceeding 125 Ω and decreasing to 92 Ω after 35 days due to the above mentioned partial dissolution of the SEI, thus suggesting a relevant chemical stability of the TEGDME_LE and its adequateness for application in Li-metal battery.

Table 3.1.2 Parameters used in *Eq (5)* according to Bruce–Vincent–Evans method to calculate the PEGDME_LE Li^+ transference number (t^+). See Figure 1 for chronoamperometric curve and Nyquist plots.

Electrolyte	i_0 (A)	i_{ss} (A)	R_0 (Ω)	R_{ss} (Ω)	t^+
TEGDME_LE	2.98×10^{-4}	2.43×10^{-4}	71.8	64.1	0.49

Subsequently, the TEGDME_LE is tested in various Li cells differing by the cathode chemistry as reported in **Figure 2** in order to verify its suitability. The voltage profiles of the Li|TEGDME_LE|LFP cell cycled at C/5 (1C = 170 mA g_{LFP}^{-1}) between 2.7 and 3.9 V in **Figure 2a** reveal the typical flat, two-phase profile related with lithium (de)insertion into the $LiFePO_4$ olivine, centered at about 3.5 V and evolving with a remarkable

reversibility and very low overvoltage. The cell delivers a capacity of 155 mA h g_{LFP}^{-1}, which is nearly the 94 % of the theoretical value of the used material, and retains almost 99 % of the initial capacity with efficiency approaching 100 % over the whole cycling test as reported in the trend of **Figure 2b**. This relevant performance is in line with the results reported in the literature for similar electrolytes using the liquid glyme, and confirms the remarkable potentiality of TEGDME_LE for Li-metal battery application. Furthermore, the Li|TEGDME_LE|S@SPC-73 cell cycled at C/10 (1C=1675 mA g_S^{-1}) between 1.9 and 2.8 V reported in **Figure 2c** shows a voltage profile fully consistent with the Li-S system.[55] Indeed, the figure displays the evolution of a double plateau at 2.4 and 2.1 V leading to a capacity of the order of 1400 mA h g_S^{-1} due to the reversible conversion reaction $16Li+S_8 \leftrightarrows 8Li_2S$, which involves the formation of various soluble polysulfides having chemical formula Li_2S_x with $2 \leq x \leq 8$.[38,39] The above reaction appears stable over the cycles taken into account, with a retention approaching 90 % and an efficiency exceeding 98 % at the steady state (trend in **Figure 2d**). The performance in terms of voltage profiles of the Li-O_2 cell using the TEGDME_LE cycled at 100 mA g_{MWCNTs}^{-1} is reported in **Figure 2e**. The test is carried out by limiting the charge and discharge time to 5 h, which is reflected into a constant specific capacity of 500 mA h g^{-1} with respect to the MWCNTs mass on the GDL support. Furthermore, the cycling procedure foresees an additional voltage cutoff at 1.5 V during discharge and 4.8 V during charge. This setup is usually implemented for Li-O_2 cells in order to limit the formation of the insulating Li_2O_2 during the ORR at about 2.7 V, and mitigate the increase of the cell resistance and polarization. **Figure 2e** shows an OER evolving below 4.7 V, while the corresponding cycling trend in **Figure 2f** evidences a constant capacity of 500 mA h g_{MWCNTs}^{-1} delivered over 30 cycles with an efficiency of 100 %. Hence, all the tests reported in **Figure 2** suggest the TEGDME_LE as adequate media for several configuration of rechargeable energy storage systems using the lithium metal, differing by the cathode chemistry and the electrochemical responses.

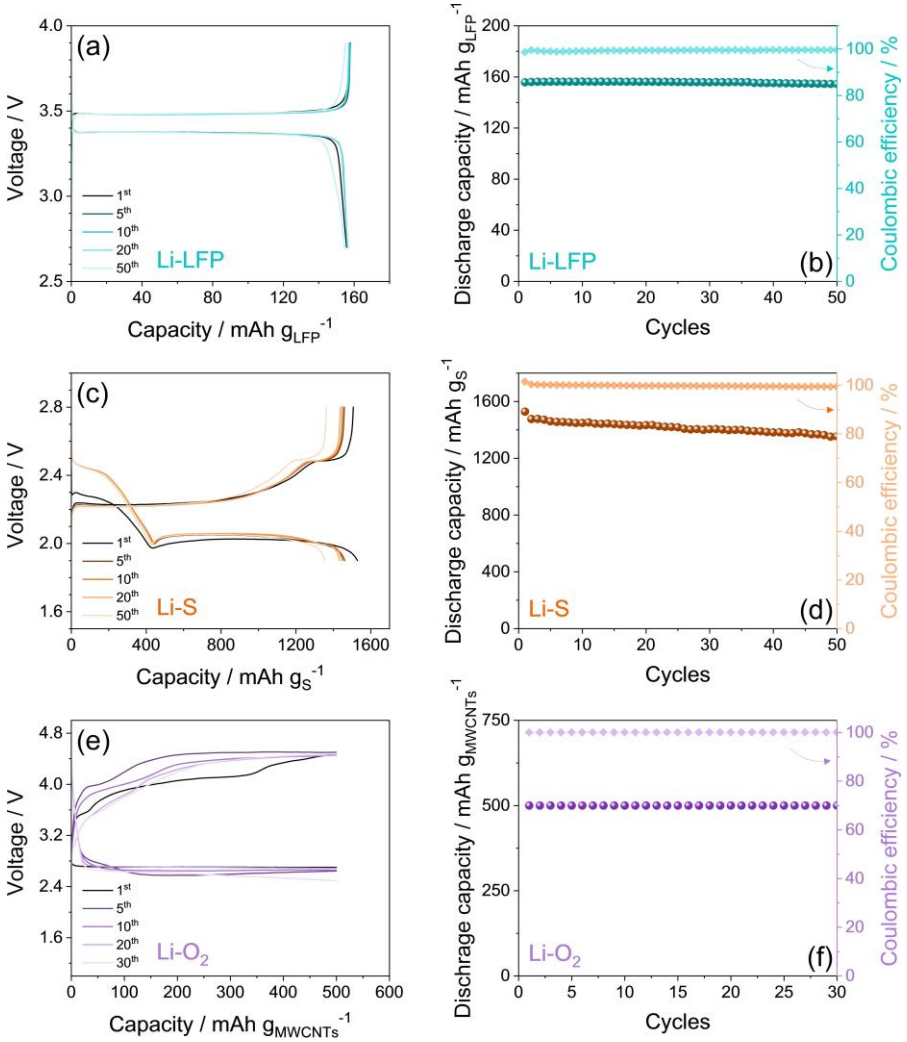

Figure 2. (a), **(c)**, **(e)** Voltage profiles and **(b)**, **(d)**, **(f)** corresponding cycling trends (coulombic efficiency is reported on right *y*-axes) of lithium cells using TEGDME_LE and various cathode chemistries, in detail: **(a)**, **(b)** a Li-LFP cell cycled at the constant current rate of C/5 (1C=170 mA g_{LFP}^{-1}) between 2.7 and 3.9 V; **(c)**, **(d)** a Li-S cell using the S@SPC-73 cathode cycled at C/10 (1C=1675 mA g_S^{-1}) between 1.9 and 2.8 V (E/S ratio: 15 µl mg_S^{-1}); **(e)**, **(f)** a Li-O_2 cell using the N_2@MWCNTs cathode cycled at the constant current of 100 mA g_{MWCNTs}^{-1} (MWCNTs loading: ~0.9 mg cm^{-2}) between 1.5 and 4.8 V by setting a step time of 5 h for both discharge and charge processes to limit the capacity to 500 mA h g_{MWCNTs}^{-1}.

The TEGDME_LE is hereafter used to plasticize a solid polymer membrane based on crystalline PEGDME including the same salts and SiO_2 ceramic filler (PEGDME_CPE) developed previously,[14] to achieve the self-standing polymer electrolyte (PEGDME_PCPE) characterized in **Figure 3**. The photograph of **Figure 3a** remarks the solid nature of PEGDME_PCPE after complete vacuum removal of the TEGDME_LE, and the slight transparency of the membrane suggests the plasticized nature which allows its direct use without further treatment in Li-metal cell operating at room temperature. The TGA and corresponding DTG in **Figure 3b** show for PEGDME_PCPE a thermal behavior accounting for the removal by evaporation of both TEGDME fraction below 290 °C (green line) and PEGDME around 400 °C (blue line). The complexity of the DTG profiles

observed between 200 and 400 °C reflects weight losses ascribed to solvated salts, solvent-salt and solvent-ceramic complexes, while the peaks at temperature exceeding 400 °C are associated with the LiTFSI salt decomposition. In addition, the higher residual weight observed at 800 °C for PEGDME_PCPE compared to TEGDME_LE is due to the presence of the SiO_2 ceramic filler in the former. Overall, the TGA suggests relevant thermal stability of the PEGDME_PCPE, extended over 200 °C which is a key requirement for allowing sufficient safety level, in particular for electrolytes designed for the use in lithium-metal batteries. A further investigation of the electrolyte features is given by the FTIR spectra reported in **Figure 3c** for TEGDME_LE (green line), PEGDME_CPE (orange line), and PEGDME_PCPE (blue line). In order to verify the salt dissolution in the polymer electrolyte, which is one of the most important features for allowing ion conduction, the characteristic FTIR bands expected for pure LiTFSI, that is, at 749, 773 and 810 cm^{-1} related to symmetric S−N−S stretching, at 1200 cm^{-1} due to SO_2 asymmetric stretching, and at 1320 and 1350 cm^{-1} for CF_3 asymmetric stretching, are reported as dashed lines in **Figure 3c**. The spectra clearly demonstrate for the liquid solution (green line), the composite polymer (orange line) and for the plasticized polymer (blue line) that the LiTFSI dissociates, as indicated by the shifts in the vibrational wavenumbers of the $TFSI^-$ anion from 810, 773, and 749 cm^{-1} to lower values. Furthermore, the increase of the relative peak intensities at 1350 and 1320 cm^{-1} compared to the one expected for pure LiTFSI, and the shift of the signal at 1200 cm^{-1} to lower wavenumbers, are fully consistent with a completely dissociated LiTFSI in the PEGDME_PCPE.[70] On the other hand, the similarity between the FTIR spectra of the PEGDME_PCPE and the TEGDME_LE suggests the conductive nature of the former, and its possible use as an electrolyte membrane in a lithium-metal battery.

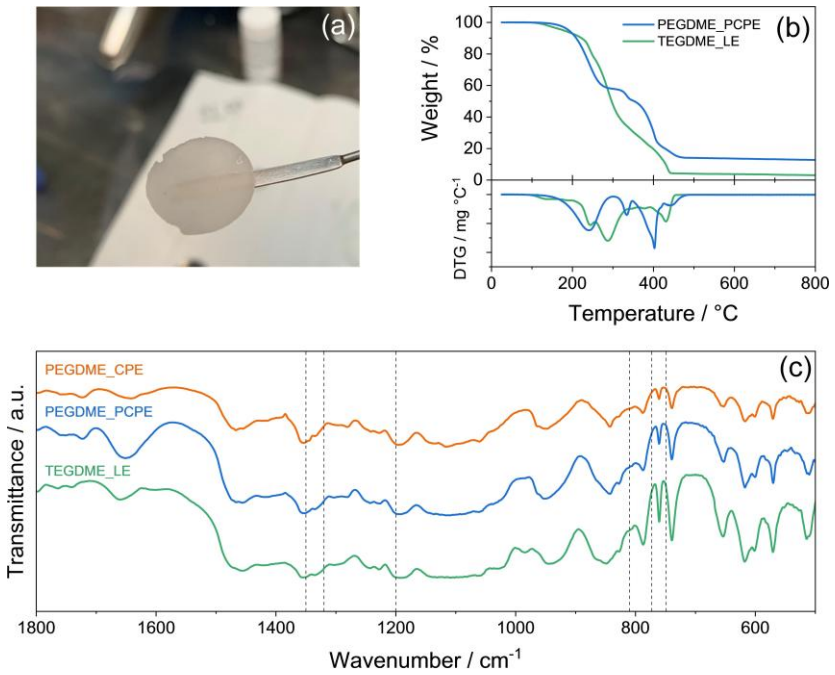

Figure 3. (a) Photograph of a PEGDME_PCPE membrane with diameter of 18 mm. **(b)** TGA (top) and corresponding DTG (bottom) of TEGDME_LE and PEGDME_PCPE recorded in the 25–800 °C temperature range at a heating rate of 5 °C min^{-1} under N_2 flow. **(c)** FTIR spectra of TEGDME_LE, PEGDME_CPE, and PEGDME_PCPE.

The PEGDME_PCPE is studied in **Figure 4** in terms of ionic conductivity, Li+-transference number, electrochemical stability window, overvoltage and chemical stability in lithium cell. Analogously to TEGDME_LE, also PEGDME_PCPE reveals a conductivity trend over the temperature (**Figure 4a**) according to the VTF model. The comparison of the data achieved by plotting the conductivity trends using *Eq (4)* for PEGDME_PCPE (**Table 3.1.3**) and TEGDME_LE (**Table 3.1.1**) gives raise to similar conductivity at infinite temperature (σ_∞) around 10^{-2} S cm^{-1}, which is in line with the same nature of PEGDME and TEGDME used as the solvent for the two electrolytes. The values of T_0 obtained for PEGDME_PCPE (204.1 K) and TEGDME_LE (221.2 K) allow the estimation of the glass transition point (T_g) of the two media, that is, 234 K for the liquid electrolyte and 251 K for the solid one. It is worth mentioning that the T_g for PEGDME_PCPE is in line with that characteristic of the solid PEGDME material, thus further accounting for the mainly polymeric nature of the plasticized membrane.[73] Furthermore, the data indicate a higher activation energy for Li^+ ions motion (E_a) in the polymer membrane (32.1 eV) with respect to the liquid solution (14.3 eV), as indeed expected by the higher viscosity and different transport mechanism in the former electrolyte compared to the latter one. This difference is reflected in the value of the Li^+-transference number calculated in **Figure 4b** using chronoamperometry and EIS in Li|PEGDME_PCPE|Li cell. Indeed, the related data reported in **Table 3.1.4** allow the determination from *Eq (5)* of a t^+ of 0.31 for PEGDME_PCPE, which is lower than that of

TEGDME_LE (compare with **Figure 1b** and **Table 3.1.2**), but still sufficient for battery application.[78] The transference number of PEGDME_PCPE is lower than the one of TEGDME_LE due to its solid frame which may hinder the lithium ion transport and diffusion more relevantly than the liquid. Hence, the electrolyte maintains its solid nature despite the partial inclusion of TEGDME_LE in the polymer structure as a plasticizer, thus allowing higher safety level but lower performances compared to the liquid.[78] The electrochemical stability window of the polymer electrolyte is determined by CV and LSV on Li|PEGDME_PCPE|SPC cells in **Figure 4c**. The figure evidences the same peaks revealed for TEGDME_LE (compare with **Figure 1c**) accounting for the reduction of $LiNO_3$, formation of the SEI,[(41-47)] and Li-(de)insertion in SPC during cathodic scan with remarkable stability and reversibility of the latter processe as suggested by the overlapping profiles. Moreover, the figure shows the electrolyte decomposition by oxidation during the anodic sweep, which occurs at a higher potential in the polymer electrolyte with respect to the liquid one, that is, at about 4.5 V vs. Li^+/Li. The Li stripping/deposition test in **Figure 4d** performed in Li|PEGDME_PCPE|Li cell reveals a low overpotential limited to 0.08 V at room temperature that decreases to 0.05 V at the end of the test due to partial SEI dissolution,48 which is a key characteristic for allowing the proper LMB operation. **Figure 4e** shows the trend of the resistance over the aging time of the symmetrical cell achieved by EIS. The data reveal an initial resistance value of about 150 Ω, progressively increasing to ∼350 Ω in 14 h and to ∼400 Ω in 10 days as the SEI is formed and consolidated, and then decreasing to about 310 Ω due to SEI partial dissolution.[(14)] It is worth mentioning that PEGDME_PCPE is characterized by higher steady state resistance compared to TEGDME_LE, that is, of about 310 Ω rather than 100 Ω, respectively. The higher electrode/electrolyte resistance of PEGDME_PCPE compared to TEGDME_LE is in line with the higher E_a and the lower t^+ in the former compared to the latter, which in turn hinder the kinetics of the charge transfer process.[(12)] Furthermore, **Figure 4e** indicates that the resistance value remains stable, with minor fluctuations over one month of aging, thus suggesting the formation of a favorable SEI at the electrode/electrolyte interphase which can promote the use of PEGDME_PCPE in LMB.[(39)]

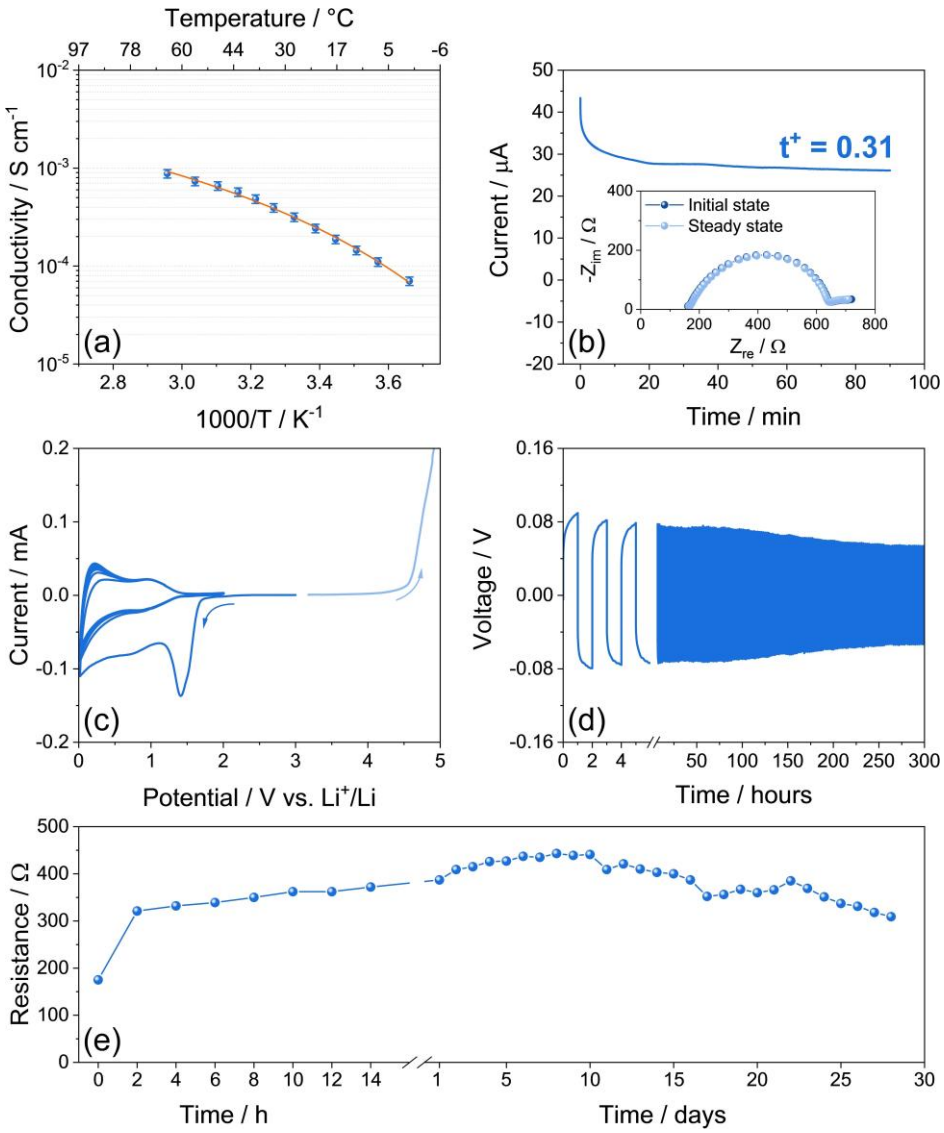

Figure 4. Electrochemical characterization of PEGDME_PCPE. **(a)** Ionic conductivity plot. **(b)** Chronoamperometry curve recorded on a Li|Li symmetrical cell and related Nyquist plots acquired before and after polarization (inset) used to evaluate the electrolyte Li^+-transference number by the Bruce–Vincent–Evans method (*Eq (5)* and Table 3.1.4); EIS frequency range: 500 kHz–100 mHz; alternate voltage signal: 10 mV: **(c)** Electrochemical stability window determined either by CV between 0.01 and 2.0 V vs. Li^+/Li and by LSV from cell OCV potential to 5 V vs. Li^+/Li carried out on Li|SPC cells; scan rate: 0.1 mV s^{-1}. **(d)** Li stripping/deposition test performed on a Li|Li symmetrical cell using a constant current rate of 0.1 mA cm^{-2}. **(e)** Resistance trend vs. time achieved by regularly measuring EIS during aging of a Li|Li symmetrical cell in the 500 kHz–100 mHz frequency range by applying an alternate voltage signal of 10 mV.

Table 3.1.3 Ionic conductivity at infinite temperature (σ_∞), activation energy for ion conduction (E_a), and temperature of zero configurational entropy (T_0) for the PEGDME_PCPE according to VTF *Eq (4)* used for the conductivity trend of Figure 4a.

Electrolyte	σ_∞ (S cm^{-1})	E_a (eV)	T_0 (K)
PEGDME_PCPE	$14.9\times10^{-3} \pm 0.1\times10^{-3}$	$32.1\times10^{-3} \pm 6.3\times10^{-3}$	204.1 ± 7.1

Table 3.1.4 Parameters used in *Eq (5)* according to Bruce–Vincent–Evans method to calculate the PEGDME_PCPE Li^+-transference number (t^+). See Figure 4 for chronoamperometric curve and Nyquist plots.

Electrolyte	i_0 (A)	i_{ss} (A)	R_0 (Ω)	R_{ss} (Ω)	t^+
PEGDME_PCPE	4.34×10^{-5}	2.61×10^{-5}	486	478	0.31

The polymer electrolyte is used in **Figure 5** in Li|PEGDME_PCPE|LFP cell cycled at C/10 (1C=170 mA g_{LFP}^{-1}) between 2.7 and 3.9 V (Figure 5a,b), Li|PEGDME_PCPE|S@SPC-73 cell cycled at C/20 (1C=1675 mA g_S^{-1}) between 1.6 and 2.8 V for one activation cycle and in the 1.7–2.8 V range during subsequent ones (**Figure 5c,d**), and Li|PEGDME_PCPE|O_2 cell cycled at the constant current of 100 mA g_{MWCNTs}^{-1} by setting a charge/discharge time of 5 h to limit the capacity at 500 mA h g_{MWCNTs}^{-1} between 1.5 and 4.8 V (**Figure 5e,f**). The voltage signature of the Li|PEGDME_PCPE|LFP cell in Figure 5a reveals an initial cycle with a higher charge polarization, and lower discharge capacity compared to the analogue cell using the liquid electrolyte (compare with **Figure 2a**). Subsequently, the polarization of the cell using PEGDME_PCPE decreases and the capacity increases, to reach similar values compared the cell using TEGDME_LE, that is, a capacity of about 150 mA h g^{-1} and a polarization below 0.15 V in line with an efficient Li-(de)insertion process into the $LiFePO_4$ olivine. The improvement of the cell is even more evident in **Figure 5b** which reports the cycling trend, and shows a capacity progressively increasing from about 115 mA h g_{LFP}^{-1} at the initial cycle to about 150 mA h g_{LFP}^{-1}, and an efficiency approaching 100 % at the steady state. This behavior, already observed in lithium cells using analogue PEO-based electrolytes and LFP cast including PVdF binder, is typically ascribed to the increase of the electrode/electrolyte interphase ionic conductivity upon the progressive wetting of the electrode during operation, and to the formation of a favorable blend between the polymer electrolyte and the binder allowing a faster motion of the Li^+ ions compared to the pristine state.[9,12] The voltage profile of the Li|PEGDME_PCPE|S@SPC-73 cell reported in **Figure 5c** depicts during the first cycle a similar signature to the one with the liquid electrolyte (compare with **Figure 2c**), reflecting the reversible conversion reaction between Li and S, although a lower capacity of about 1200 mA h g_S^{-1} and higher polarization are observed. This difference may account for the above mentioned slower kinetics of the charge transfer for the Li-S cell using the polymer electrolyte compared to the liquid one, despite a lower discharge cutoff (1.7 V rather than 1.9 V) and cycling rate (C/20 instead of C/10) are used in the former compared to the latter. It is worth mentioning that the first discharge in the polymer cell is performed at a

lower cutoff with respect to the following cycles, that is, 1.6 V, in order to allow the consolidation of adequate SEI at the electrode/electrolyte interphase.[39] The voltage profiles of **Figure 5c** evolve with a capacity progressively decreasing, in line with the increase of the cell resistance from ~200 to about 400 Ω already observed in the first stages in **Figure 4e**, and subsequently stabilizing at ~400 mA h g_S^{-1}. The corresponding cycling trend in **Figure 5d** is characterized by an efficiency approaching 100 % at the end of the test, and accounts for the formation of a suitable electrode/electrolyte interphase in the polymer Li-S cell. It is worth mentioning that the decrease of the Li-S cell capacity may be ascribed to a partial loss of the active material dissolved in the polymer matrix due to the limited diffusion of the Li_2S_x species, which in turns can contribute to the formation of a suitable interphase and allow safe cycling without polysulfides shuttle.[27] On the other hand, the voltage profiles of the polymer Li|PEGDME_PCPE|O_2 cell reported in **Figure 5e** shows relevant differences compared to the liquid cell of **Figure 2e**. The first discharge process reflecting the ORR occurs at a lower voltage using PEGDME_PCPE (2.5 V) compared to TEGDME_LE (2.7 V), thus suggesting a higher polarization. Furthermore, the first discharge delivers 500 mA h g_{MWCNTs}^{-1} which is the capacity expected by the adopted time limit, while the subsequent charge (OER) appears incomplete and leads to a capacity of about 180 mA h g_{MWCNTs}^{-1} with very low efficiency (~35 %) considered in this case as charge/discharge ratio for better visualization, as also evidenced in the corresponding trend of **Figure 5f**. After the first cycle, the charge capacity progressively increases, and the efficiency improves to values approaching 90 % at the 14th cycle. This behavior reflects a slower kinetics of the OER in the polymer Li-O_2 cell compared to the liquid one, and suggests the need for further tuning of the electrode/electrolyte interphase to increase the wettability, and the use of a catalyst to fasten the reaction in the three-phases (solid/polymer/gas) system. Nevertheless, the stable discharge capacity trend observed in **Figure 5f** represents a promising preliminary result for the development of a safe and high capacity Li-O_2 polymer cell.

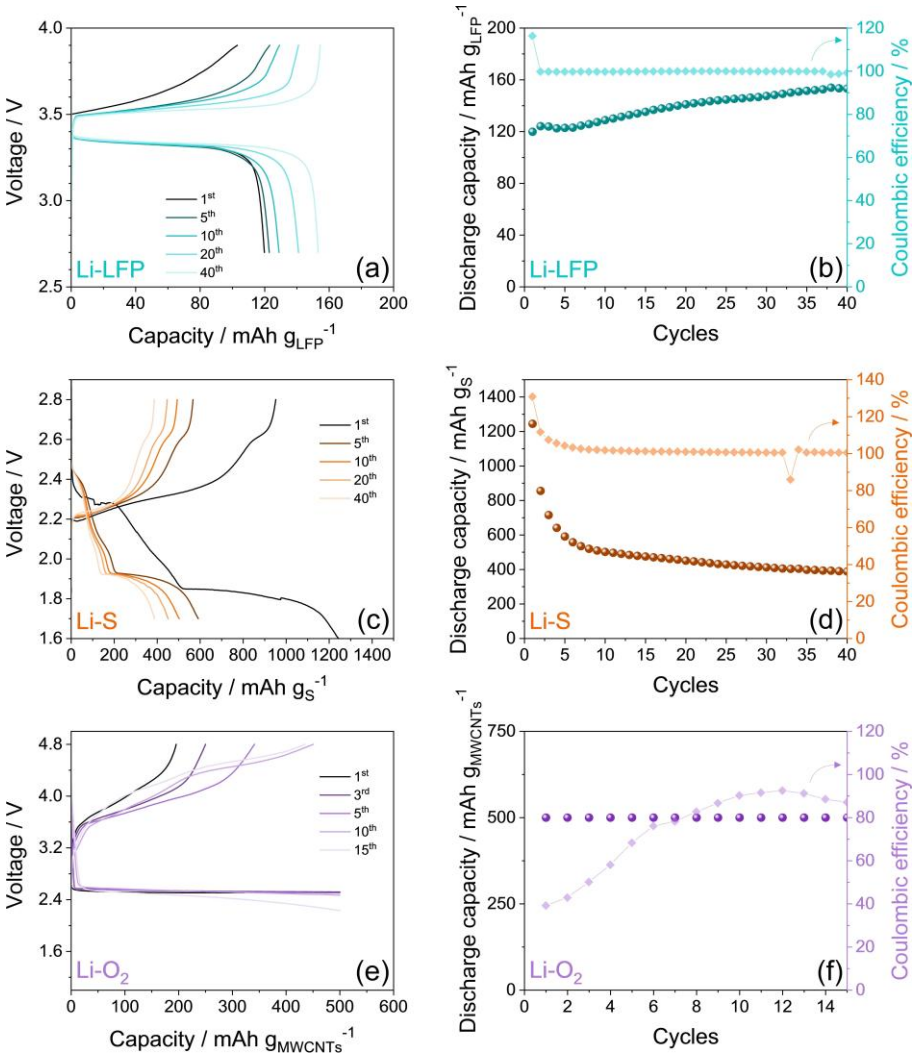

Figure 5. (a), **(c)**, **(e)** Voltage profiles and **(b)**, **(d)**, **(f)** corresponding cycling trends (coulombic efficiency is reported on right *y*-axes) of lithium cells using PEGDME_PCPE and various cathode chemistries, in detail: **(a)**, **(b)** a Li-LFP cell cycled at the constant current rate of C/10 (1C=170 mA g_{LFP}^{-1}) between 2.7 and 3.9 V; **(c)**, **(d)** a Li-S cell using the S@SPC-73 cathode cycled at C/10 (1C=1675 mA g_S^{-1}) between 1.7 and 2.8 V after one activation cycle at C/20 in the 1.6–2.8 V voltage range; **(e)**, **(f)** a Li-O_2 cell using the N_2@MWCNTs cathode cycled at the constant current of 100 mA g_{MWCNTs}^{-1} (MWCNTs loading: ~0.9 mg cm^{-2}) between 1.5 and 4.8 V by setting a step time of 5 h for both discharge and charge processes to limit the capacity to 500 mA h g_{MWCNTs}^{-1}.

References

(1) W. Xu, J. Wang, F. Ding, X. Chen, E. Nasybulin, Y. Zhang, J.-G. Zhang,Energy Environ. Sci. 2014, 7, 513.

(2) A. Varzi, K. Thanner, R. Scipioni, D. Di Lecce, J. Hassoun, S. Dörfler, H.Altheus, S. Kaskel, C. Prehal, S. A. Freunberger, J. Power Sources 2020,480, 228803.

(3) D. Lin, Y. Liu, Y. Cui, Nat. Nanotechnol. 2017, 12, 194.

(4) Y. Wang, B. Liu, Q. Li, S. Cartmell, S. Ferrara, Z. D. Deng, J. Xiao, J. PowerSources 2015, 286, 330.

(5) M. L. Meyerson, J. K. Sheavly, A. Dolocan, M. P. Griffin, A. H. Pandit, R.Rodriguez, R. M. Stephens, D. A. Vanden Bout, A. Heller, C. B. Mullins, JMater Chem A Mater 2019, 7, 14882.

(6) J. B. Goodenough, Y. Kim, Chem. Mater. 2010, 22, 587.

(7) D. Aurbach, E. Zinigrad, Y. Cohen, H. Teller, Solid State Ion 2002, 148,405.

(8) C. Li, S. Zhang, X. Miao, C. Wang, C. Wang, Z. Zhang, R. Wang, L. Yin,Batter Supercaps 2022, 5, e202100288.
(9) G. B. Appetecchi, F. Croce, J. Hassoun, B. Scrosati, M. Salomon, F. Cassel,J. Power Sources 2003, 114, 105.(10) W. Lyu, G. He, T. Liu, ChemistryOpen 2020, 9, 713.
(11) R. Lei, Y. Yang, C. Yu, Y. Xu, Y. Li, J. Li, Sustain. Energy Fuels 2021, 5,1538.
(12) G. B. Appetecchi, J. Hassoun, B. Scrosati, F. Croce, F.
Cassel, M. Salomon,J. Power Sources 2003, 124, 246.
(13) I. Gracia, M. Armand, D. Shanmukaraj in Solid Electrolytes for AdvancedApplications Springer International, Cham, 2019, pp. 347–373, Eds. R.Murugan, W. Weppner.
(14) V. Marangon, Y. Tominaga, J. Hassoun, J. Power Sources 2020, 449,227508.
(15) H. Huo, M. Jiang, B. Mogwitz, J. Sann, Y. Yusim, T. Zuo, Y. Moryson, P.Minnmann, F. H. Richter, C. Veer Singh, J. Janek, Angew. Chem. Int. Ed.2023, 62, e202218044
(16) S. Brutti, J. Hassoun, B. Scrosati, C.-Y. Lin, H. Wu, H.-W. Hsieh, J. PowerSources 2012, 217, 72.
(17) Y. Wang, P. He, H. Zhou, Energy Environ. Sci. 2011, 4, 805.
(18) L. Carbone, S. G. Greenbaum, J. Hassoun, Sustain. Energy Fuels 2017, 1,228.
(19) H.-J. Peng, J.-Q. Huang, X.-B. Cheng, Q. Zhang, Adv. Energy Mater. 2017,7, 1700260.
(20) L. Grande, E. Paillard, J. Hassoun, J.-B. Park, Y.-J. Lee, Y.-K. Sun, S.Passerini, B. Scrosati, Adv. Mater. 2015, 27, 784.
(21) S. Drvarič Talian, J. Moškon, R. Dominko, M. Gaberšček, ACS Appl. Mater.Interfaces 2017, 9, 29760.
(22) L. Zhou, D. L. Danilov, R. Eichel, P. H. L. Notten, Adv. Energy Mater. 2021,11, 2001304.
(23) C. Li, Z. Xi, D. Guo, X. Chen, L. Yin, Small 2017, 14, 1701986.
(24) R. Black, S. H. Oh, J.-H. Lee, T. Yim, B. Adams, L. F. Nazar, J. Am. Chem.Soc. 2012, 134, 2902.
(25) J. Herranz, A. Garsuch, H. A. Gasteiger, J. Phys. Chem. C 2012, 116, 19084.
(26) P. Hartmann, D. Grübl, H. Sommer, J. Janek, W. G. Bessler, P. Adelhelm, J.Phys. Chem. C 2014, 118, 1461.
(27) V. Marangon, D. Di Lecce, L. Minnetti, J. Hassoun, ChemElectroChem2021, 8, 3971.
(28) J. Hassoun, B. Scrosati, Adv. Mater. 2010, 22, 5198.
(29) G. Ma, F. Huang, Z. Wen, Q. Wang, X. Hong, J. Jin, X. Wu, J Mater Chem AMater 2016, 4, 16968.
(30) S. S. Jeong, Y. T. Lim, Y. J. Choi, G. B. Cho, K. W. Kim, H. J. Ahn, K. K. Cho,J. Power Sources 2007, 174, 745.
(31) M. Agostini, J. Hassoun, Sci. Rep. 2015, 5, 7591.
(32) G. A. Elia, J. Hassoun, Sci. Rep. 2015, 5, 12307.
(33) Q. Wang, Z. Wen, J. Jin, J. Guo, X. Huang, J. Yang, C. Chen, Chem.Commun. 2016, 52, 1637.
(34) M. Liu, D. Zhou, H. R. Jiang, Y. X. Ren, F. Y. Kang, T. S. Zhao, Nano Energy2016, 28, 97.
(35) Y. T. Kim, E. S. Smotkin, Solid State Ion 2002, 149, 29.
(36) H. Horie, T. Abe, T. Kinoshita, Y. Shimoida, World Electric Vehicle Journal2008, 2, 25.
(37) D. Di Lecce, R. Verrelli, J. Hassoun, Green Chem. 2017, 19, 3442.
(38) P. J. Carvalho, C. H. G. Fonseca, M.-L. C. J. Moita, Â. F. S. Santos, J. A. P.Coutinho, J. Chem. Eng. Data 2015, 60, 3721.
(39) D. Di Lecce, V. Marangon, H.-G. Jung, Y. Tominaga, S. Greenbaum, J.Hassoun, Green Chem. 2022, 24, 1021

3.2 Toward new paradigm for polymer-electrode setup

Lithium battery using PEO-based solid electrolyte has been widely studied in several literature works,[1,2] and even employed in electric vehicles with cell operating at the solid-polymeric state above 70 °C.[3] However, limiting factors including possible dendrite formation, weak mechanical features, restricted electrochemical stability window, and modest Li^+ transference number (t_{Li+}) hindered in part further development of this cell.[4]
On the other hand, the polymer cell can in principle allow the safe use of the lithium metal, which has a specific capacity as high as 3800 mAh g^{-1} and a redox potential as negative as −3 V vs. SHE.[5,6] These appealing features renewed the interest on high-energy lithium metal cells exploiting the polymer setup, and triggered the research for more stable and performing membranes.(7) In this regard, the ones using PEO with molecular weight (MW) from 600,000 to 5,000,000 Da appeared as the most promising, since they are mechanically stable at temperature ranging from 50 to 100 °C in particular if ceramic additives such as Al_2O_3,[9] ZrO_2,[10] and SiO_2[11,12] are exploited. In addition, ceramics with nanometric size can promote membrane amorphization and favor by their polarity the Grotthuss-type Li^+ transport within the PEO-chains, thus lowering the operative temperature, increasing the t_{Li+}, and promoting the alkali ions' conduction.[2] Literature works focusing on the liquid electrolyte indicated the use of additives such as $LiNO_3$ as suitable strategy for allowing further stabilization of the SEI at the Li anode, and promote cell operation, in particular using a sulfur cathode.[13-16] PEO-based membranes can certainly facilitate the system scalability due to the higher strength compared to PEGDME and allow the preparation of batteries using roll-to-roll techniques.[3] Beside these considerations, polymer electrolytes are usually considered safer than typical liquid ones, thanks to their solid-state nature that can avoid electrolyte leakage from the cell case, the high melting/boiling points and/or decomposition temperature that ensure modest volatility, and the low flammability which reduces, but doesn't fully exclude, the risk of ignition.[18-24] These aspects are really appealing, especially when highly reactive metal anodes are exploited.

#8 10.1002/batt.202400542

Polymeric Lithium Battery using Membrane Electrode Assembly

In memory of Professor Bruno Scrosati (August 1937 – November 2024), who was an excellent professor and scientist, leading the electrochemistry and the battery fields worldwide.

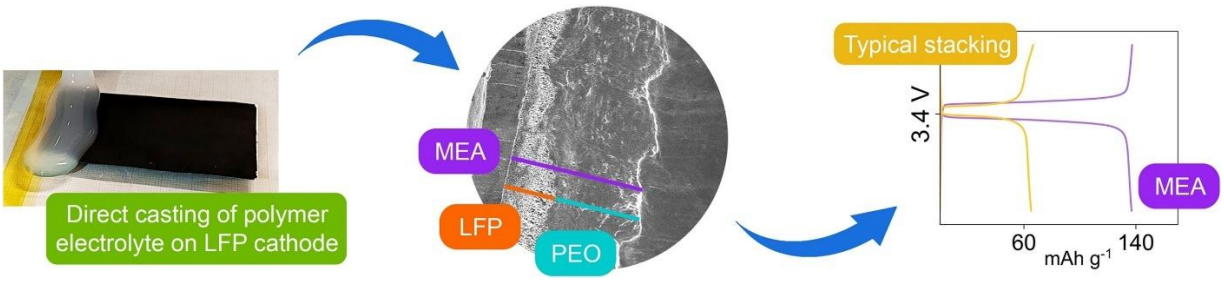

Membrane electrode assembly (MEA) with PEO-based electrolyte and $LiFePO_4$ electrode operates in polymer lithium cell at 70 °C. The cell delivers 155 mAh g^{-1} at 3.4 V for over 100 cycles without signs of decay. The all-in-one approach is suited for scaling up polymer lithium cells with high cathode loading to the pouch cell configuration. In this work, we have investigated a membrane with adequate conductivity above 50 °C, using a PEO with MW of 600,000 Da and the LiTFSI salt, including the $LiNO_3$ additive. In analogy to fuel cell systems,[25-27] the membrane is included into a MEA formed by casting the polymer electrolyte onto the LFP cathode, to achieve an *all-in-one* cathode/electrolyte tape. The direct casting of the polymer electrolyte on the cathode ensures better interface contact and stacking symmetry with respect to the typical membrane-electrode alignment during cell assembly, reduces the manufacturing steps from electrode and electrolyte preparation to final Li-cell achievement, and facilitates advanced battery configurations such as the pouch-cell one thanks to the direct realization of high-surface cathode/electrolyte tapes. In this study, electron microscopy sheds light on the remarkable contact between cathode and electrolyte, which allows shorter wetting time, higher capacity, and higher energy density with respect to the typical configuration as demonstrated by the extensive and multi-technique characterization adopted herein. The inclusion of abundant and inexpensive SiO_2 in the solid electrolyte leads to the decrease of crystallinity degree and melting point of the polymeric membrane, improves thermal stability of the *all-in-one* cathode/electrolyte tape the Li-stripping/deposition ability at various areal capacity (0.1 and 1.0 mAh cm^{-2}), and enhances the Li-interphase features of the membrane, finally promoting the cell safety. Moreover, the MEA setup ensures remarkable performance in

Li-metal battery even under restricted electrolyte content that matches the practical lithium-ion batteries requests, i. e., between 2.0 and 3.0 $mg_{electrolyte}$ for mg of active material.[28] Repeated heating-cooling thermal cycles are proven as viable strategy to enhance the polymer charge transport proprieties as demonstrated by ionic conductivity measurements and *ad-hoc* galvanostatic cycling protocols. Finally, the *all-in-one* setup is particularly adequate for Li-metal pouch-cell with promising performance in terms of delivered capacity and cycle life. Therefore, the approach used in this work may be suitable for achieving high energy polymer battery, which is currently classified from an industrial point of view at the level of *intermediate technology readiness*, with excellent processability, good electrochemical performances, and relevant safety content.[29]

Experimental

- Preparation of the Solid-State Polymer Electrolyte

The polymer electrolyte was prepared by wet-mixing and doctor blade casting. PEO (average MW 600,000 Da, Sigma-Aldrich), LiTFSI ($LiN(SO_2)_2(CF_3)_2$, 99.95 % trace metals basis, Sigma-Aldrich) conducting salt, and lithium nitrate ($LiNO_3$, 99.99 % trace metals basis, Sigma-Aldrich) passivating agent were mixed into a 1 mol kg_{PEO}^{-1} concentration for each salt, and fumed silica powder (SiO_2, average particles size: 0.007 μm, Sigma-Aldrich) was added as 10 % weight ratio with respect to the PEO-salts mixture. The components were mixed for 1 h inside a bottle by magnetic stirring, then 37.5 ml of acetonitrile (ACN, CH_3CN, Sigma-Aldrich) were added into a ratio of 5 ml ACN to 1 g of PEO-salts-SiO_2 mixture, and left stirring for 2 days to obtain a viscous and homogeneous slurry. A polymeric membrane was obtained by casting the slurry on a plastic foil (23-5FEP-2-50, CS Hyde) via a doctor-blade tool (MTI Corp.) set at ~1000 μm, and drying for 1 h at 50 °C on a hot plate until complete solidification. All the processes were performed in ambient atmosphere. Before employment, LiTFSI and $LiNO_3$ were dried for 2 days under vacuum at 110 °C to avoid weigh errors due to moisture uptake. The solid-state polymer electrolyte was cut into discs with diameter of 14 mm (1.54 cm^2 geometric area) with a Nogami handheld punch, dried for 24 h at 70 °C under vacuum inside a Büchi oven, and stored inside an Ar-filled glovebox (MBraun, O_2 and H_2O contents lower than 1 ppm). The average thickness of the dry membrane was determined through sampling various portions using a gauge, and resulted of ~50 μm. Typically, the weight of a 14 mm-diameter disc of electrolyte corresponded to ~19 mg. The electrolyte is indicated hereafter as PEO-11. A control polymer electrolyte was prepared following the same procedure by excluding the addition of SiO_2. This electrolyte is indicated as PEO-control.

- Physical-Chemical Characterization of the Electrolyte

TGA was performed from 25 to 450 or 800 °C using a heating rate of 5 °C min^{-1} under dry N_2 flow (50 ml min^{-1}) with a Mettler-Toledo TGA 2 instrument (Mettler-Toledo, Columbus, OH, USA). The sample weight was typically ~8–10 mg. FTIR spectra were recorded via a Bruker Vertex V70 instrument set up in the transmittance mode. The structure of PEO-11, PEO 600,000, and SiO_2 was investigated by XRD through a Bruker D8 Advance instrument equipped with a Cu Kα radiation source (8.05 keV) scanning the 10 °–60 ° 2θ range using a step size of 0.02 ° and a rate of 10 s $step^{-1}$.

DSC measurements were carried out in a TA Discovery instrument under N_2 atmosphere in sealed aluminum crucibles (samples weight 10–15 mg) using a heating rate of 5 °C min^{-1} between −90 and 90 °C. Both PEO-11 and PEO-control samples were tested twice and only the second DSC run was considered. Prior to the tests, the samples were equilibrated at 40 °C for 15 min, and each temperature limit (i. e., −90 and 90 °C) was held for 10 min.

- Electrochemical Characterization of the Electrolyte

The electrochemical properties of PEO-11 were studied in CR2032 coin-type cells (MTI Corp.) with various configurations assembled in an Ar-filled glovebox. The ionic conductivity was assessed by performing EIS in the 500 kHz–100 Hz frequency range through an alternate voltage signal of 10 mV on blocking-electrode stainless-steel|PEO-11|stainless-steel symmetrical cells using one O-ring (23-5FEP-2-50, CS Hyde, internal diameter of 10 mm) holding two 10 mm-diameter PEO-11 membranes; the membranes were chosen to fit the O-ring dimension within ±2 μm. The O-ring thickness of 127 μm allowed to fix the cell constant at 0.016 cm^{-1}. The temperature of the cell, within a range from 29.9 up to 91.6 °C, was controlled via a F 12 Julabo instrument and double-checked with a thermocouple. The t_{Li+} value was evaluated by applying the Bruce-Vincent-Evans method. Accordingly, a symmetrical cell with Li|PEO-11|Li configuration was prepared by stacking two 14 mm-diameter lithium discs separated by one 14 mm-diameter PEO-11 membrane and held at 70 °C. A chronoamperometry test was carried out on the cell by applying a voltage (ΔV) of 30 mV for 90 min, and EIS was performed before and after polarization using the 500 kHz–100 mHz frequency range and an alternate voltage signal of 10 mV. Voltage, current, and resistance values were used in *Eq (5)* to get the t_{Li+}, where I_0 and I_{ss} are the current values at the initial and steady state, and R_0 and R_{ss} are the interphase resistance values before and after cell polarization, respectively, determined from the impedance spectra (read below for fitting details). A similar cell configuration was adopted to investigate the solid-state electrolyte stability upon aging at 70 and 90 °C in contact with lithium metal, by performing EIS measurements on Li|PEO-11|Li cells every 2 h for the initial 10 h upon assembly, and subsequently every day for 27 days. Carbon-based electrodes were prepared through doctor blade casting on either Al or Cu foils of a slurry obtained by dispersing carbon black (80 %, Super P carbon, SPC, Timcal) and polyvinylidene fluoride (20 %, PVdF, Solef 6020) polymer binder in N-methyl-2-pyrrolidone (NMP, Sigma-Aldrich). The slurries were dried on hot plates at 70 °C to remove the NMP solvent, cut into discs with diameter of 14 mm and dried under vacuum at 110 °C for 2 h before being transferred in an Ar-filled glovebox. The electrochemical stability window of the electrolyte was determined by CV measurements on Li|PEO-11|SPC−Cu cell between 0.01 and 2.0 V vs. Li+/Li at 0.1 mV s−1 and by LSV on Li|PEO-11|SPC−Al cell from the open circuit voltage (OCV) to 5.0 V vs. Li+/Li at 0.1 mV s−1. The Li|SPC cells used a 14 mm-diameter lithium disc separated from a 14 mm-diameter SPC electrode by one 14 mm-diameter PEO-11 membrane. Lithium stripping/deposition tests were carried out at 70 and 90 °C on Li|PEO-11|Li symmetrical cells through galvanostatic cycling measurements using a constant current of 0.1 mA cm^{-2} and setting a step time of either 1 h or 10 h for both charge (stripping) and discharge (deposition) processes. The cells were assembled by stacking two 14 mm-diameter lithium discs separated by one 14 mm-diameter PEO-11 membrane. The fitting enables to describe the Nyquist spectra in terms of equivalent circuits including resistive (R) and constant phase elements (CPE, Q), in detail: (i) Re, which is the electrolyte resistance, is indicated by the high-frequency intercept of the plot; (ii) (RiQi) associated to the high-medium frequency semicircle; (iii) Q_w, which is depicted by a low-frequency line and indicates the semi-infinite Warburg-type Li^+

diffusion. The voltammetry and EIS tests were performed via a VersaSTAT MC Princeton Applied Research (PAR-AMETEK) instrument, placing the cells inside a Büchi oven set at the appropriate temperature (double-checked through a thermocouple), with maximum fluctuation of ±0.1 °C. The stripping/deposition measurements were carried out using a MACCOR series 4000 battery test system, in a chamber set at 70 or 90 °C, with maximum fluctuation of ±0.1 °C. Note that the temperature is also reported in the corresponding panels and figure caption.

- MEA Setup and Application in Lithium Cell

The assembly based on LFP and PEO-11 is indicated in the text as MEA-LFP, and its preparation is depicted by the photographic images in **Figure 1**. Electrode tapes were prepared by casting via a doctor blade tool set at ~200 μm of slurries formed by 80 % carbon-coated LFP, having a carbon content of about 5 % developed by Advanced Lithium Electrochemistry (Aleees Taiwan, model A1100), 10 % PVdF polymer binder, and 10 % SPC electron conductor dispersed in NMP. The slurry was cast on aluminum (thickness of 15 μm, MTI Corp.) or carbon coated aluminum (Alcc, thickness of 18 μm, MTI Corp.) and dried at 70 °C on a hot plate to remove the NMP solvent. The obtained tapes were calendared using an MSK-2150 Rolling Machine (MTI Corp.) at 70 % with respect to their initial thickness, to achieve a final thickness of ~80 μm. Control Al and Alcc foils were employed to estimate the average loading of the cathode tapes, which corresponded to ~5.2 $mg_{LFP}\,cm^{-2}$ and ~7.5 $mg_{LFP}\,cm^{-2}$, respectively. A polymeric membrane was applied by casting the above described PEO-11 slurry on the electrode tapes via a doctor blade tool set at ~1000 μm. The tapes were dried at 50 °C on a hot-plate in ambient atmosphere for 30 min, and inside a Büchi oven under vacuum at 70 °C for 24 h to achieve the MEA-LFP, which was subsequently stored inside an Ar-filled glovebox and cut into discs having a diameter of 14 mm (1.54 cm^2 geometric area) using a Nogami handheld punch for cell application. Whenever the Al or the Alcc based current collectors have been employed, they have been indicated in the text and in the corresponding figure caption. The average thickness of the MEA-LFP was determined through sampling various electrodes using a gauge, and resulted to be ~140 μm. LFP control electrode was prepared using bare Al with the same procedure reported above, excluding the application of the polymeric electrolyte membrane. The PEO-11 electrolyte was tested in CR2032 coin-type lithium cells using a 14 mm-diameter lithium metal disc as anode and different cathode-electrolyte setups, in detail: (i) Li|PEO-11|LFP cell with one 14 mm-diameter PEO-11 disc as separator and one LFP control electrode, (ii) Li|MEA-LFP cells with 14 mm-diameter MEA-LFP disc, (iii) Li|MEA-LFP cells with 14 mm-diameter MEA-LFP disc and an additional 14 mm-diameter PEO-11 disc. The cells were galvanostatically cycled between 2.7 and 3.9 V at C/100, C/10, C/8, C/5, and C/3 (1 C=170 mA g_{LFP}^{-1}). The system scalability was verified by assembling Li|MEA-LFP pouch cells (either 12.8 cm^2 with 3.2 cm×4.0 cm or 8.0 cm^2 with 3.2 cm×2.5 cm) in a dry room with a dew point below −55 °C. The positive electrodes for the pouch-cells were prepared following the above reported procedure (see **Figure 1**) by coating the LFP slurry on an Alcc foil and had an active material loading between 6.3 and 6.5 mg cm^{-2} (LFP content was estimated through a control Alcc foil). Prior to pouch-cell assembly, the Li foil (200 μm, MTI corp.) was laminated with Cu (10 μm thickness, MTI Corp.), while Ni and Al tabs were exploited as current collecting tabs for the negative and positive electrode, respectively. The galvanostatic cycling measurements were performed via a MACCOR series 4000 battery test system, in a chamber set at 30, 70 or 80 °C with maximum fluctuation of ±0.1 °C. Prior to the galvanostatic tests, the cells were held for 6 h inside the chamber at the same temperature.

- Morphological Characterization

The MEA-LFP morphological features were investigated by SEM through a ZEISS Crossbeam XB340 operating with an accelerating voltage of 5 kV, employing a secondary electrons detector. The sample for cross-section image was obtained by physical cutting the MEA-LFP, and sticking the obtained piece to the side of the sample holder. Partial deformation of the tape components could not be excluded. To avoid external contamination, the samples were transferred from the glove box to the microscope with the aid of a sealed transfer box.

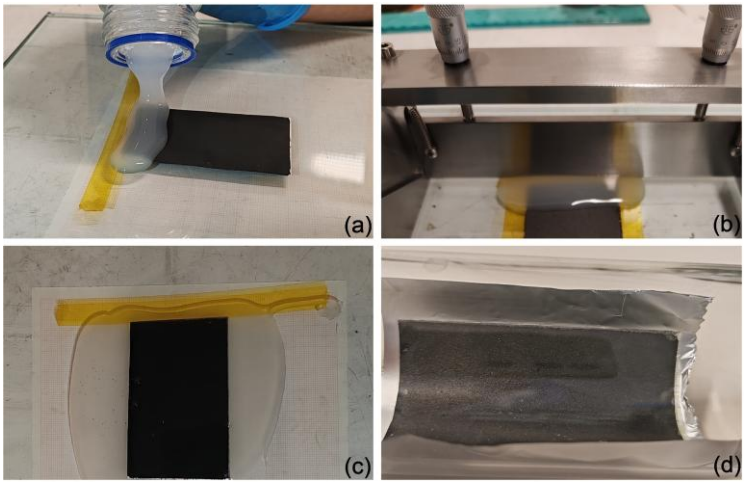

Figure 1. Photographic images of the MEA-LFP casting process, in details: **(a)** PEO-11 pouring onto a dry LFP electrode; **(b)** PEO-11 membrane application through doctor blade technique, **(c)** MEA-LFP before drying process, **(d)** MEA-LFP after drying process.

Results

Figure 2 reports the physical-chemical features of the electrolyte membrane developed in this work. The TGA and corresponding DTG in **Figure 2a and b** compare the thermal behavior of bare PEO 600,000 and PEO-11 membrane, respectively, and account for the nearly complete removal by evaporation of ACN and H_2O during the drying process of PEO-11 cast, since a weight loss as small as 0.8 % due to trapped solvent or moisture is observed up to 200 °C, while extensive PEO removal is associated with the peaks at temperature between 330 and 440 °C. Furthermore, the data reveal more complex shape for PEO-11 (**Figure 2b**) rather than PEO 600,000 (**Figure 2a**) since it shows a double peak instead of single one due to interactions between salts and PEO matrix which may shift the thermal loss of PEO from the electrolyte.[30-33] On the other hand, these peaks exemplify how salts can influence the ionic association in the polymer matrix, which is reflected into electrolyte crystallization and characteristic thermal stability.[34, 35] It is worth mentioning that additional ionic association studies may decouple experimentally the individual movements and correlations of cations, anions, and polymer chains, as well as the co-existence of multiple dynamics and transport events ruling ionic interactions, as indeed demonstrated in literature works.[36, 37] The small weight losses occurring beyond 500 °C

for PEO-11 are associated with the LiTFSI and $LiNO_3$ salts decomposition, and the residual weight observed at 800 °C is due to the presence of the SiO_2 ceramic filler.[38, 39] Therefore, the results obtained through TGA suggest suitable thermal stability of the PEO-11 extended over 330 °C, which is a key requirement for allowing safe operation of lithium-metal cells.

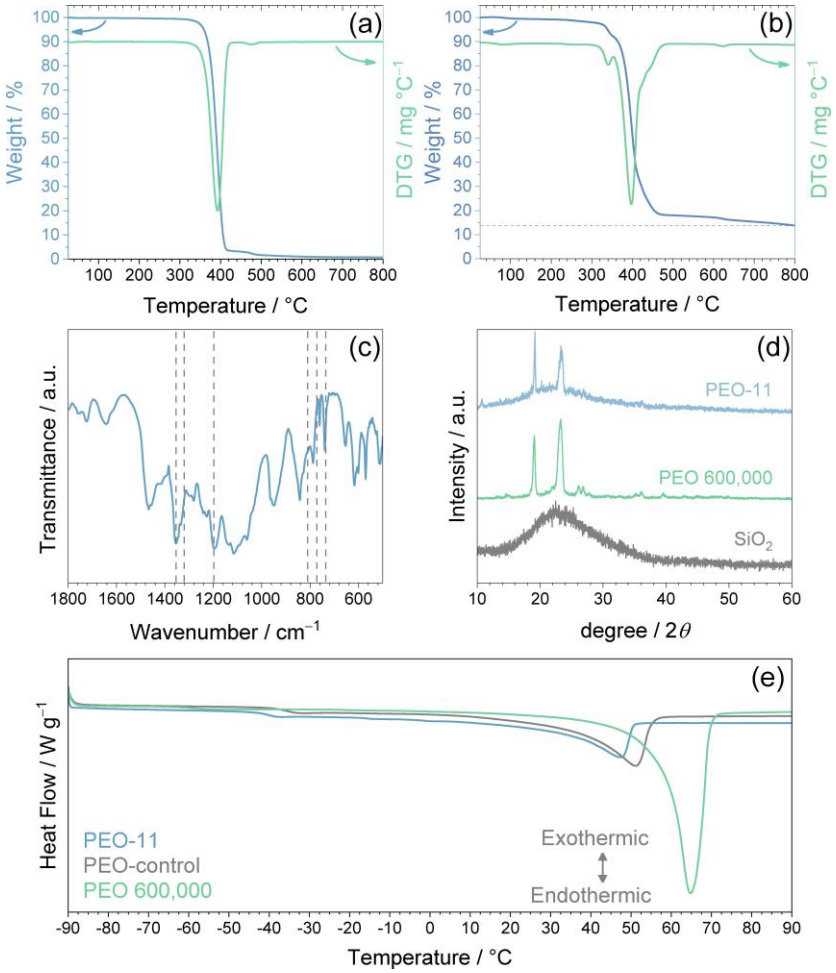

Figure 2. Brief physical-chemical characterization of the PEO-11 electrolyte: **(a–b)** TGA (blue) and corresponding DTG (green) of **(a)** PEO 600,000 powder and **(b)** PEO-11 performed under dry N_2 flow with heating rate of 5 °C min^{-1} in the 25–800 °C temperature range. **(c)** FTIR spectra of PEO-11 electrolyte; expected signals from LiTFSI are marked as dashed lines. **(d)** X-ray diffractograms for PEO-11 (blue), PEO 600,000 (green), and SiO_2 (grey). **(e)** DSC curves of PEO-11 (blue), PEO-control (gray), and PEO 600,000 powder (green).

A spectroscopic investigation of the PEO-11 is given by the FTIR spectrum reported in **Figure 2c**. To verify the actual salt dissolution in the polymer matrix, which is one of the fundamental features for allowing ion conduction, the typical FTIR bands expected for pure LiTFSI, that is, at 749, 773 and 810 cm^{-1} related to symmetric S−N−S stretching, at 1200 cm^{-1} due to SO_2 asymmetric stretching, and at 1320 and 1350 cm^{-1} for CF_3 asymmetric stretching,[40] are also reported as dashed lines in the figure. The spectra

demonstrates that the LiTFSI dissociates, as indicated by the shifts in the vibrational wavenumbers of the $TFSI^-$ anion from 810, 773, and 749 cm^{-1} to lower values.(41) Moreover, the increase of the peak intensities at 1350 and 1320 cm^{-1} compared to the one expected for pure LiTFSI, and the shift of the signal at 1200 cm^{-1} to lower wavenumbers, corroborate the complete dissociation of LiTFSI in the PEO matrix.

The structure of the polymer electrolyte has been analyzed through XRD, and the pattern between 10 ° and 60 ° is reported in **Figure 2d**. The figure confirms the presence of SiO_2, observed as a broad band between 15 and 40 °, and shows the crystallinity of the PEO-11 through two peak reflections at 19 ° and 24 °, which are also observed in the pristine PEO 600,000 powder. It is worth noting that the intensity of these two peaks is reversed in the PEO-11 membrane compared to PEO 600,000 powder, mainly due to the presence of silica that can actually modify the structure of the polymer electrolyte by the interplay within the polymer matrix as Lewis acid/base interactions.(42) Additionally, the XRD pattern of the PEO-11 does not shows any peaks of the salts as a further evidence of their complete dissolution via complexation in the polymer matrix, in accordance with the FTIR results previously discussed. DSC is carried out to assess the effect of SiO_2 on the polymer crystallinity. DSC is performed on the PEO-11 electrolyte, on a control electrolyte indicated as PEO-control which includes exclusively the lithium salts, and on the PEO 600,000 powder. Thus, **Figure 2e** shows the DSC thermal curves, while **Table 3.2.1** reports the values of the parameters obtained by the tests. Prior to measurements, the samples are equilibrated at 40 °C to exclude possible effects of the corresponding thermal history.(29, 43) The thermograms in **Figure 2e** evidence in first place the decrease of melting temperature of the polymer (T_m, **Table 3.2.1**) as promoted by addition of the lithium salts from 65.0 °C (PEO 600,000) to 51.5 °C (PEO-control electrolyte), and further to 45.4 °C by including the SiO_2 filler (PEO-11 electrolyte). On the other hand, the effect of SiO_2 in inhibiting the crystallinity degree (χ_{crys}) within the PEO structure is estimated in **Table 3.2.1** through the following relationship:

$$\Delta_{crys} \approx \Delta H_m^{sample} / \Delta\Delta H_m^{PEO} \times 100$$

where the melting enthalpy of the samples (ΔH_m, **Table 3.2.1**) is determined by integration of the area subtended to the melting peak. The analyses display the decrease of χ_{crys} from 44.7 % for PEO-control to 23.9 % for PEO-11, and reveal in addition a lower glass-transition temperature (T_g, **Table 3.2.1**) of PEO-11 with respect to PEO-control, i.e., −40.0 °C and −34.1 °C, respectively, which is expected to improve the flexibility of the polymer chains and promote segmental and rotational modes, thus favoring ionic transport within PEO-11. (29, 36, 37)

Table 3.2.1. Parameters obtained from DSC tests of pristine PEO 600,000 powder, PEO-control and PEO-11 electrolytes.

Sample	T_g (°C)	ΔH_m (J g^{-1})	T_m (°C)	χ_{crys} (%)
PEO 600,000	−58.2	135.6	65.0	/
PEO-control	−34.1	60.6	51.5	44.7
PEO-11	−40.0	32.4	45.4	23.9

The PEO-11 electrochemical behavior is studied in **Figure 3** in terms of ionic conductivity over temperature, Li^+-transference number, chemical stability in lithium cell, electrochemical stability window, and overpotential during lithium stripping and deposition. The PEO-11 ionic conductivity trend over the temperature (**Figure 3a**) shows the typical Vogel-Tamman-Fulcher (VTF) trend. Accordingly, the conductivity is plotted using the VTF *Eq (4)*.

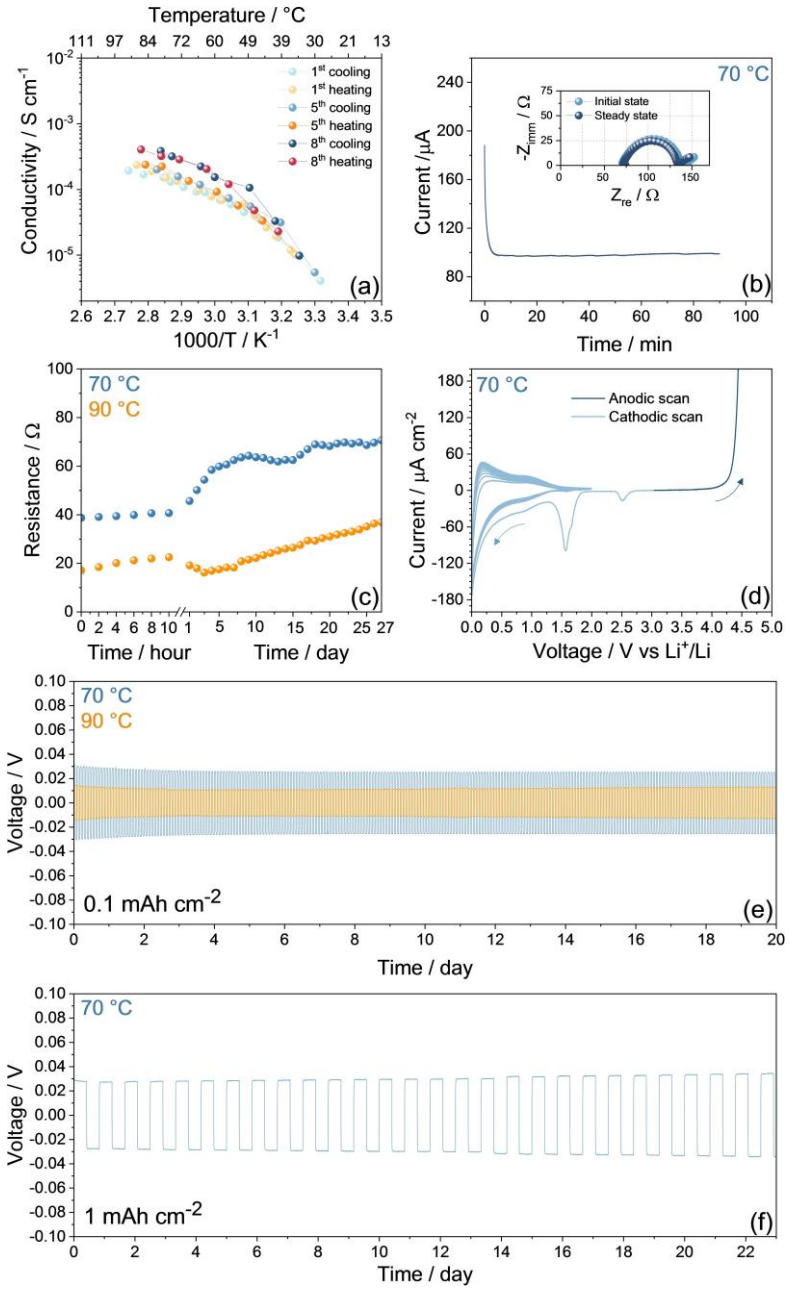

Figure 3. Electrochemical characterization of the PEO-11 electrolyte. In detail: **(a)** ionic conductivity plots over temperature; **(b)** chronoamperometry curve recorded in a Li|Li symmetrical cell (inset reports corresponding Nyquist plots acquired before and after polarization) used to evaluate the polymer Li^+-transference number through Bruce-Vincent-Evans method (see *Eq (5)* and Table 3.2.2); EIS frequency range: 500 kHz–100 mHz; alternate voltage signal: 10 mV; **(c)** resistance vs. time trends achieved by EIS measurements upon aging of Li|Li symmetrical cells in the 500 kHz–100 mHz frequency range, applying an alternate voltage signal of 10 mV, **(d)** electrochemical stability window determined either by CV between 0.01 and 2.0 V vs. Li^+/Li or by LSV from cell OCV to 5.0 V vs. Li^+/Li carried out in Li|PEO-11|SPC cells; scan rate: 0.1 mV s^{-1}; **(e, f)** Li stripping/deposition tests performed on Li|PEO-11|Li cells using the constant current rate of 0.1 mA cm^{-2} and step time of either (e) 1 h (0.1 mAh cm^{-2}) or (f) 10 h (1 mAh cm^{-2}).

Table 3.2.2 summarizes the results of the VTF plot for the PEO-11. The polymeric electrolyte shows a conductivity ranging from 3.8×10^{-6} S cm^{-1} at 29.9 °C to 4.8×10^{-4} S cm^{-1} at 91.6 °C, with values increasing over subsequent heating-cooling cycles, as

observed in similar electrolytes.[45] The electrolyte resistance is determined by the intercept of the tilted line with the Z_{re} axis through the R_eQ equivalent circuit exploited in the NLLS fitting. The data achieved by plotting some representative conductivity trends, namely 1st, 5th, and 8th cooling/heating cycle using VTF *Eq (4)* give raise to conductivity at infinite temperature (σ_∞) between 1.8×10^{-3} and 1.3×10^{-4} S cm^{-1}, namely one order of magnitude smaller than liquid and plasticized solid-state electrolytes.(20) The values of T_0 obtained for PEO-11 (between 221.2 and 296.4 K) allow the estimation of the T_g value of the electrolyte, that evolves upon cooling/heating processes from 251 K (1st cooling run) up to 326 K (8th heating run). Despite the latter value seems to be particularly high for a PEO-based electrolyte, and likely affected by error, it appears in line with the results which indicate at the 8th heating run an electrolyte conductivity of ~10^{-4} S cm^{-1} starting from 49.0 °C. It is worth noting that the T_g values estimated from the VTF fitting for PEO-11 differs of about 18 K from the T_g determined experimentally through DSC (i. e., 233 K, **Table 3.2.1**), likely due to approximations in the application of the VTF *Eq (4)*. Furthermore, the fitting results account for an activation energy for Li^+ ions motion (E_a), progressively changing upon consecutive heating/cooling cycles of the PEO-11, from 2.9×10^{-4} eV (1st cooling) to 7.5×10^{-5} eV (8th heating). The initial value is in line with other polymer electrolytes, as indeed expected by the higher viscosity and different transport mechanism of this electrolyte compared to typical liquid ones,(44-49) while the results related with the 8th run suggest a decrease of about one order of magnitude of E_a that may actually rise the ionic conductivity. The value of the t_{Li+} at 70 °C, calculated in **Figure 3b** through chronoamperometry and EIS are obtained by applying the Bruce-Vincent-Evans equation (*Eq (5)*) This equation is used without any correction since the bulk resistance change appears negligible (see Nyquist plots in the inset of **Figure 3b**).(50) Indeed, the related data reported in **Table 3.2.3** allow the determination of a t_{Li+} of 0.39 for PEO-11, which is lower than that of typical liquid electrolytes, but still suitable for battery and in line with other literature results.(30,51) **Figure 3c** shows the trend of the resistance over the aging time of the symmetrical lithium cells achieved by EIS. The data reveal an initial resistance value of 17 and 38 Ω at 90 and 70 °C, respectively, slightly increasing to 23 and 46 Ω in 10 h. Subsequently, the interphase resistance at 90 °C displays a decrease from the 1st to the 3rd day to 16 Ω, meanwhile the opposite trend is observed at 70 °C since the interphase resistance reaches 54 Ω within the same time interval. As the SEI is formed and consolidated, the interphase resistance at 70 °C fluctuates around 70 Ω, possibly due to partial dissolution and stabilization, while the trend at 90 °C shows a progressive increase up to 37 Ω after 27 days. It is worth noting that the PEO-11 is

characterized by higher steady state resistance at 70 °C than 90 °C, however it shows a better stability over aging time at the lower temperature, thus suggesting the formation of a more effective SEI at the electrode/electrolyte interphase which can promote efficient use in lithium-metal battery. On the contrary, the behavior at 90 °C can originate from a slight and progressive decomposition of the membrane at the lithium interphase promoted by the high temperature, despite detailed studies may be needed to properly assess this aspect. Furthermore, the higher electrode/electrolyte resistance of PEO-11 at 70 °C is in line with the relatively low t_{Li+} in this electrolyte, which could in turn partially hinder the kinetics of the charge transfer process, in particular at low temperatures.(52) The electrochemical stability window of the PEO-11 is determined by CV and LSV at 70 °C using Li|PEO-11|SPC cells in **Figure 3d**. The figure shows a peak centred at 1.5 V vs. Li^+/Li related with the reduction of the $LiNO_3$, and a broad wave around 0.75 V vs. Li^+/Li ascribed to the reductive decomposition of the polymer with the formation of SEI layer.(53-55) Moreover, the test reveals reversible processes between 0.1 and 0 V vs. Li^+/Li associated with the Li-(de)insertion into the SPC (CV), as well as a relevant increase of the current at about 4.0 V vs. Li^+/Li (LSV) due to the complete oxidation of the PEO to carbonyl groups and volatile degradation products, thus suggesting an electrochemical stability window extending from 0 to 4.0 V.[56] It is worth mentioning that the anodic stability limit is established by taking into account an oxidative current threshold of 5 μA cm^{-2}, which is widely accepted and suggested as suitable value to achieve a reliable response in polymer electrolyte.(57) The Li stripping/deposition test in **Figure 3e** performed in Li|PEO-11|Li cell evidences a modest and stable overpotential of 0.03 V upon 480 hours (20 days) of cycling at 70 °C, and a value below 0.02 V at 90 °C, which is a key characteristic for allowing the proper lithium metal battery operation. Despite the polarization is lower at 90 °C, the better aging-stability observed at 70 °C (see **Figure 3c**) suggests the latter as preferrable value for the galvanostatic cycling measurements rather than the former one. On the other hand, the selected temperature can be considered also adequate in practical solid-state battery modules.(58) A further indication of the Li/electrolyte interface suitability is provided by the additional Li stripping/deposition test performed adopting challenging conditions, that is, by setting a step time between charge and discharge of 10 h to achieve a capacity of 1 mAh cm^{-2}. Notably, the Li/Li cell shows stable cycling over 23 days with initial polarization as low as 0.030 V that mildly increases to 0.034 V towards the final stages of the test, thus confirming the improved interphase formed by PEO-11 at the Li surface despite the intensive extraction/plating of Li.

Table 3.2.2 Ionic conductivity at infinite temperature (σ_∞), activation energy for ion conduction (E_a), and temperature of zero configurational entropy (T_0) for the PEO-11 according to VTF *Eq (4)* used for the conductivity trend of Figure 3a.

Electrolyte condition	σ_∞ (S cm^{-1})	E_a (eV)	T_0 (K)
1st cooling	$1.2\times10^{-3} \pm 2.5\times10^{-4}$	$2.9\times10^{-4} \pm 3.3\times10^{-4}$	221.2 ± 4.2
1st heating	$1.8\times10^{-3} \pm 2.0\times10^{-3}$	$1.0\times10^{-3} \pm 5.4\times10^{-4}$	223.5 ± 22.4
5th cooling	$3.9\times10^{-4} \pm 2.2\times10^{-4}$	$4.1\times10^{-4} \pm 1.4\times10^{-4}$	251.8 ± 12.0
5th heating	$2.6\times10^{-4} \pm 2.4\times10^{-4}$	$2.3\times10^{-4} \pm 1.5\times10^{-4}$	272.7 ± 19.0
8th cooling	$6.5\times10^{-4} \pm 7.5\times10^{-4}$	$3.0\times10^{-4} \pm 2.1\times10^{-4}$	265.4 ± 20.9
8th heating	$1.3\times10^{-4} \pm 3.2\times10^{-4}$	$7.5\times10^{-5} \pm 2.1\times10^{-5}$	296.4 ± 5.0

Table 3.2.3 Parameters used in *Eq (5)* according to Bruce-Vincent-Evans method to calculate the PEO-11 Li^+ transference number (t_{Li+}). See Figure 2 for chronoamperometric curve and respective inset for Nyquist plots.

Electrolyte	Initial current (I_0) (A)	Steady state current (I_{ss}) (A)	Initial resistance (R_0) (Ω)	Steady state resistance (R_{ss}) (Ω)	t_{Li+}
PEO-11	188.1×10^{-6}	98.8×10^{-6}	32.5	30.7	0.39

Prior to the galvanostatic cycling testing, the polymer weight with respect to electrode and the morphological features of the MEA-LFP are determined by TGA and SEM, respectively, as reported in **Figure 4**. **Figure 4a** reports the TGA (top panel) and corresponding DTG (bottom panel) of the samples, and shows for the MEA-LFP a thermal behavior accounting for the almost total removal by evaporation of ACN and H_2O during the drying process, since a weight loss as small as 0.7 % is experienced up to 200 °C, while the peaks at temperature corresponding to 290 and 380 °C are associated with PEO loss, in partial agreement with the TGA reported in **Figure 2b**. Despite these peaks hold the same shape as for the bare polymer electrolyte, the loss of the PEO-11 directly cast on the electrode tapes (either on Al or Alcc foils) is observed at lower temperature. This response may be related with the incremented exposure of the surface area of the MEA-LFP compared to bare PEO-11 due to the presence of the porous LFP electrode as the support for the electrolyte casting in the former rather than the flat plastic substrate employed for the latter. The top panel of **Figure 4a** reveals for the MEA-LFP cast on Alcc a polymer content of 52 % while the one exploiting bare Al is characterized by a higher polymer content of 60 %. This difference may be rationalized taking into account that both tapes

have almost the same final thickness (~140 μm), instead the MEA-LFP cast on Al has a lower active material loading than the one on Alcc (i. e., 5.2 and 7.5 $mg_{LFP}\,cm^{-2}$, respectively), thus a higher polymer content. Repeated measurements along the membranes indicate further slight difference in thickness, which are however neglected since they are within the experimental error of the tests.

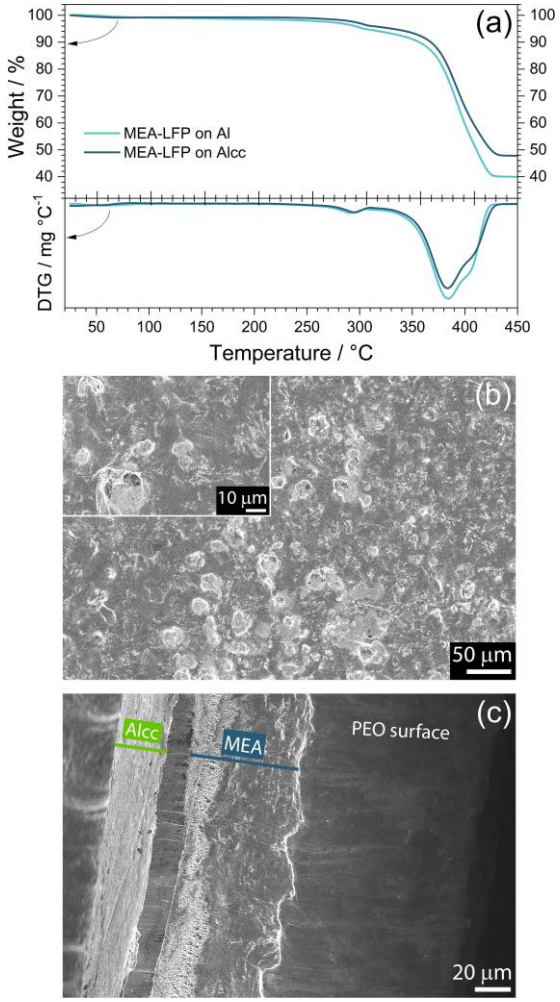

Figure 4. (a) TGA (top panel) of the MEA-LFP tapes cast on bare Al (light blue) or Alcc (dark blue) performed under dry N_2 flow with heating rate of 5 °C min^{-1} from 25 to 450 °C, and corresponding DTG (bottom panel). **(b)** SEM images of the MEA-LFP taken from top-view (inset reports higher magnification). **(c)** SEM image of the MEA-LFP taken from the cross-section view.

Figure 4b shows the surface morphology of the MEA-LFP cast on Alcc, instead **Figure 4c** reveals the cross-sectional features of the same tape taken ad hoc to verify the actual electrode/electrolyte stacking. **Figure 4b** depicts a surface fully covered by PEO-11 without any sign of exposed LFP portions, thus suggesting a uniform distribution of the electrolyte, which is a key requirement for avoiding short-circuits in the Li-cell using the MEA-LFP. Both panel and its inset, showing a higher magnification, clearly indicate the presence of bright domains possibly attributed to small clusters with enhanced amorphous degree. This setup may actually favor the efficient Li^+ conduction in the electrolyte, that

mainly relies on chain segmental motion within the polymer's amorphous regions promoting a fast ion transport.[59,60] **Figure 4c** sheds light on the lateral-morphology of the MEA-LFP tape, which gives precious information on the effectiveness of the MEA-LFP preparation process, despite a partial deformation of the stack by cutting the assembly cannot be completely excluded. The right-to-left view of the cross-section image reveals, respectively, the Alcc support with a thickness of ~20 μm roughly in line with the supplier specification, and the MEA-LFP with overall extent of ~90 μm which may be roughly divided into two portions, i.e., at the left LFP and at the right PEO-11 membrane. This stacking suggests a regular distribution of LFP and polymer electrolyte, and a uniform bulk of the membrane, notwithstanding the partially patchy aspect seen in **Figure 4b**.

The polymer electrolyte is used in **Figure 5** either in a typical Li|PEO-11|LFP or in a Li|MEA-LFP cell configuration (both LFP cathodes cast on bare Al), cycled at C/8 between 2.7 and 3.9 V at 70 °C. The enhancement of the cell performance exploiting the all-in-one cathode/electrolyte tape (i.e. Li|MEA-LFP) compared to the simple components stacking (i.e. Li|PEO-11|LFP) is evidenced in **Figure 5a**, which displays the related capacity trends. The Li|PEO-11|LFP cell shows an initial capacity as low as 12 mAh g^{-1}, with a value progressively increasing to 66 mAh g^{-1} upon 35 cycles. Instead, the Li|MEA-LFP cell initially delivers about 62 mAh g^{-1}, and the capacity increases to a value as high as 136 mAh g^{-1} within the same cycling interval. Progressive increase of the delivered capacity has been already observed in literature for lithium cells exploiting PEO-based electrolytes and LFP electrodes including PVdF binder into their formulation.[52,61] This trend is usually ascribed to increase of the electrode/electrolyte interphase conductivity upon the ongoing active material wetting promoted by charge/discharge runs, with formation of a favorable blend between the polymer electrolyte and the binder, leading to faster motion of the Li^+ ions than the pristine state of the cell.[52,61] Herein, this aspect is further supported by the data of the polymer electrolyte directly cast on the cathode which shows an enhancement of the cell performance, thus evidencing how the MEA setup can ensure a better contact and blending of the electrode/electrolyte components. **Figure 5a** also displays a Coulombic Efficiency approaching 100 % at the steady state for both cell configurations. The voltage signatures of Li|PEO-11|LFP and Li|MEA-LFP cells in **Figure 5b** reveal a first cycle with more notable hampering of the electrochemical process for the former setup rather than the latter, reflected into a lower discharge capacity of the Li-cell with typical configuration compared to the one exploiting the MEA setup, namely 12 rather than 62 mAh g^{-1}. Subsequently, the polarization of the cells decreases and the discharge capacity increases, triggering the plateau slightly below 3.45 V related with the

$LiFePO_4 \leftrightarrows Li^+ + FePO_4$ electrochemical Li-(de)insertion reversible process, which evolves at the 15th cycle with a capacity of 20 mAh g^{-1} for the Li|PEO-11|LFP cell and 75 mAh g^{-1} for the Li|MEA-LFP one in **Figure 5c**. The capacity respectively reaches values of 66 and 136 mAh g^{-1} at the 35th cycle as the cells polarization further shrinks in **Figure 5d**, thus suggesting the MEA setup as preferential solution to facilitate the battery assembling and boost its performances when a polymeric electrolyte is exploited, in particular using relatively high active material loading.

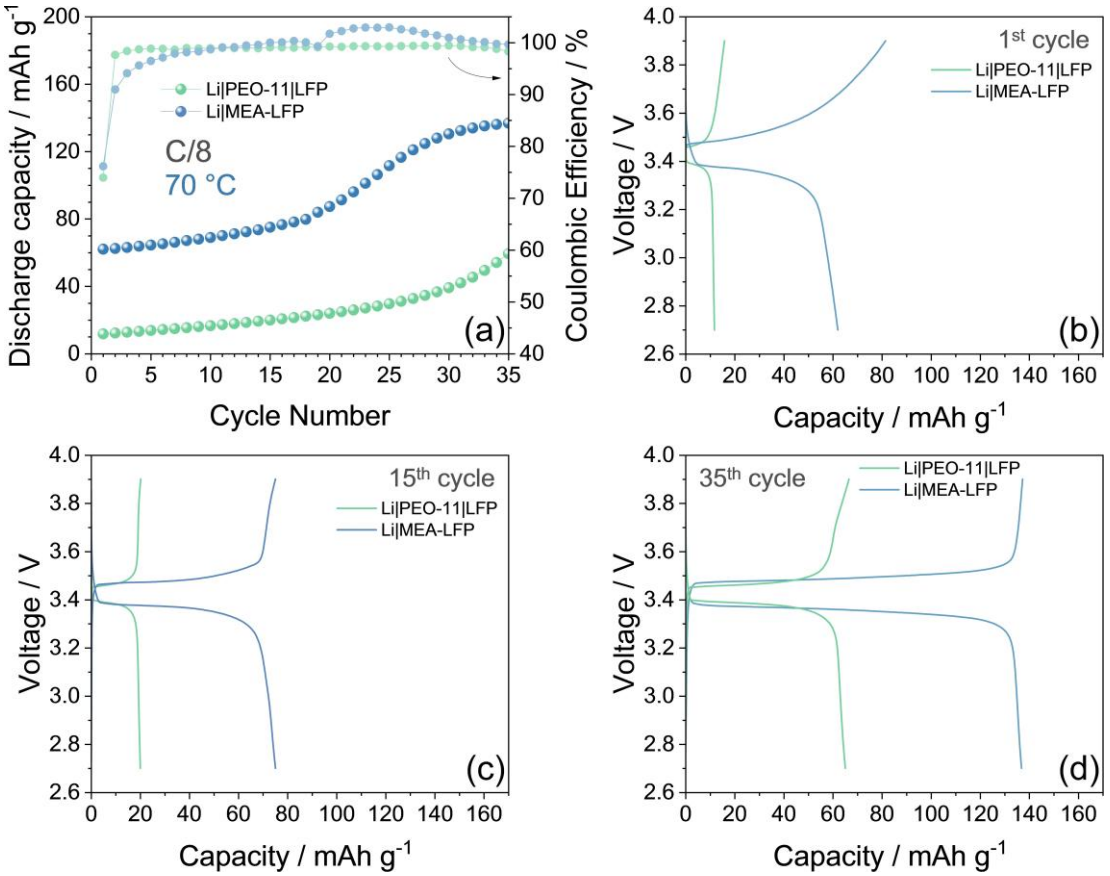

Figure 5. Galvanostatic cycling performance of the PEO-11 electrolyte in lithium cell with either Li|PEO-11|LFP (green) or Li|MEA-LFP (blue) setup using Al current collector. In detail: **(a)** capacity trends comparison upon 35 charge/discharge cycles (right y-axis shows Coulombic Efficiency); comparison between the voltage profiles during **(b)** 1st cycle; **(c)** 15th cycle; **(d)** 35th cycle. Both cells cycled at the constant C-rate of C/8 (1 C=170 mA g_{LFP}^{-1}) between 2.7 and 3.9 V. Electrodes geometric area: 1.54 cm^2.

A further improvement, especially in terms of cycling under high C-rates, may be achieved by the using Alcc rather than Al current collector. Thus, the Li|MEA-LFP cell using Al is subjected to galvanostatic cycling test at C/8, instead the one using the Alcc is cycled at the higher current of C/3, concomitantly with an increased active material loading, and the results are reported in **Figure 6**. The tests show different activation shapes for the two cells, not only driven by the choice of the current collector but also by the active material loading and employed current rate, which remarkably change the cycling trend. Indeed, the voltage profiles in **Figure 6a** shows at C/8 a shape analogous to the one reported above,

with initial reversible capacity around 70 mAh g^{-1} progressively increasing and greatly stabilizing to a value 155 mAh g^{-1} after 50 cycles, which is remarkably held without any further profile modification over 100 charge/discharge runs. The stable cycling is also evidenced by the plateaus at about 3.4 V during discharge and 3.5 V during charge, which are partially hampered only at the beginning of the measurements. This evolution is also reflected in the cycling trend reported in **Figure 6b**, where the cell displays an increase in terms of delivered capacity upon cycling and excellent cycling stability, with Coulombic Efficiency over 99.5 % upon the activation stage, thus highlighting an efficient Li-(de)insertion process into the LFP olivine structure. Despite the use of Alcc, the voltage profiles of the test carried out at C/3 in **Figure 6c** shows the electrochemical process evolving upon cycling with a less pronounced enhancement of the voltage plateau, as likely ascribed to diffusion limits not related with the electrode/electrolyte interphase but rather with the limitation of the Li^+ ions transport within the electrolyte bulk leading to notable ohmic overpotential at high currents.(52) This aspect is confirmed by the slope of the voltage profiles observed in **Figure 6c** at C/3, which appears more relevant compared with the ones of the test performed at C/8 (compare with **Figure 6a**). Nevertheless, the cycling trend depicted in **Figure 6d** indicates a continuous increase of the delivered capacity, expected from the improvement of the electrode/electrolyte interphase, from around 40 mAh g^{-1} at the 1st cycle to 80 mAh g^{-1} upon 100 cycles, in line with the incomplete development of discharge plateau observed in **Figure 6c**. The data reported above suggest possible improvement of the cycling response at high C-rates by better tuning some key parameters such as the active material to polymer ratio, internal pressure of the cell, electrode morphology (in terms of porosity and particles size), polymer viscosity, and casting process (wet or dry), to finally achieve MEAs well performing both at low and high currents.(62) On the other hand, the promising electrochemical responses of the Li|MEA-LFP cell, both in terms of delivered capacity trend and voltage signature evolution, as well as the alternative preparation process which foresees a notable processability and casting options, and offers interesting preliminary insights for achieving high-performance and safe energy storage systems.

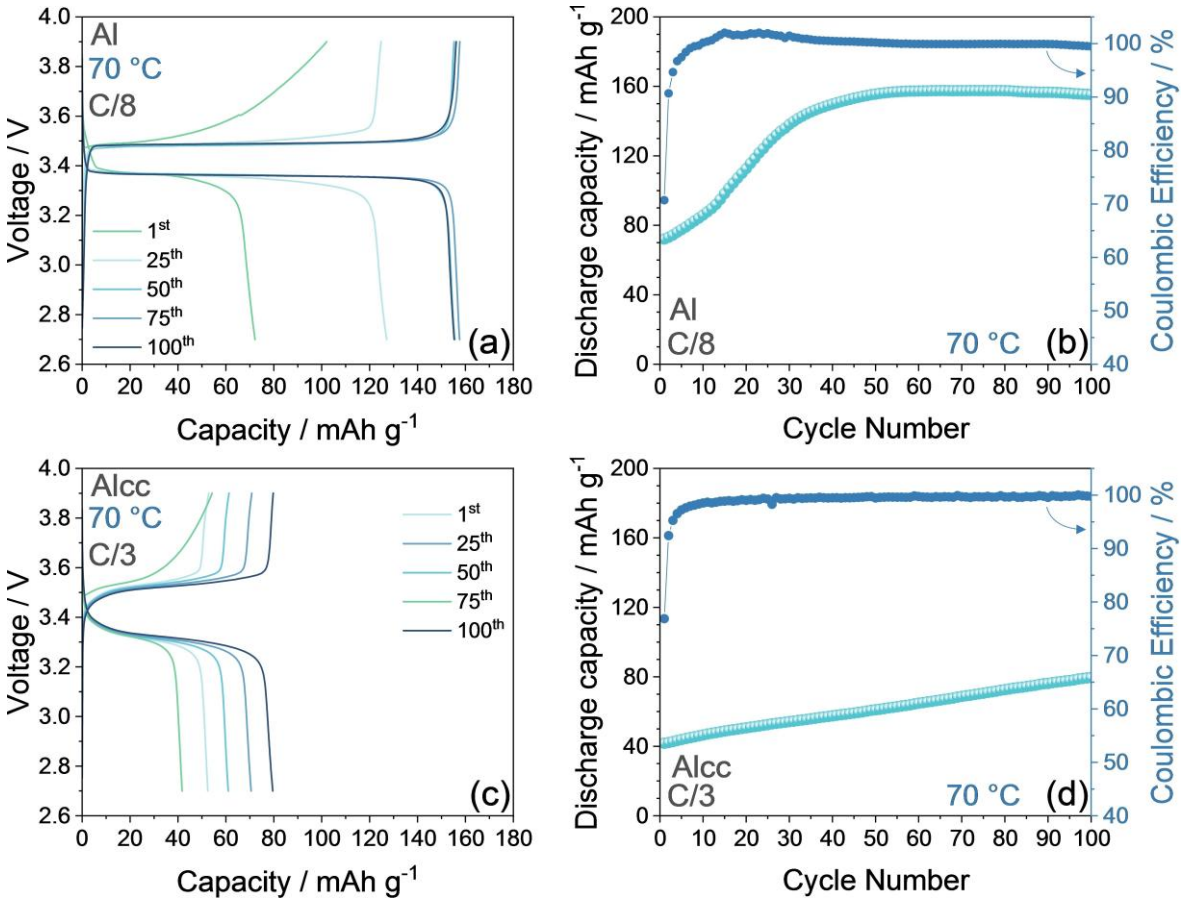

Figure 6. Galvanostatic cycling performance of the Li|MEA-LFP cells. (a) Selected voltage profiles and (b) corresponding cycling trend (right *y*-axis shows Coulombic Efficiency) at C/8 (1 C=170 mA g_{LFP}^{-1}) for a cell using Al current collector. (c) Selected voltage profiles and (d) corresponding cycling trend (right *y*-axis shows Coulombic Efficiency) at C/3 for a cell using Alcc current collector. Voltage range of 2.7–3.9 V. Electrodes geometric area: 1.54 cm^2.

The scalability of the MEA-LFP system is evaluated by applying the Li|MEA-LFP configuration in pouch-cells. **Figure 7** shows photographic images illustrating the procedure adopted to achieve the above cells with electrode geometric area of either 12.8 or 8.0 cm^2 and active material loading between 6.3 and 6.5 mgLFP cm^{-2}. Thus, a pouch-cell with 12.8 cm^2 area and active material loading of 6.3 mg_{LFP} cm^{-2} is tested at C/100 and C/10 at 30 °C, and subsequently at C/10 at 70 °C as reported in **Figure 8**. **Figure 8a** and **Figure 8b** shows the voltage profiles and cycling trend, respectively, related to the galvanostatic cycling performed at C/100 at 30 °C. Despite the relevantly low C-rate adopted to achieve acceptable electrochemical activity from the polymeric cell at the lower temperature, the figure shows a delivered capacity still limited to about 50 mAh g^{-1} as expected by the poor conductivity of the PEO-11 electrolyte, that is, below 10^{-5} S cm^{-1} at 30 °C (see **Figure 3**). Furthermore, the subsequent voltage profile in **Figure 8c**, recorded at current increased to C/10 at the same temperature, depicts extremely polarized charge and discharge processes of the LFP cathode with associated capacity below 5 mAh g^{-1}. The

performances obtained at 30 °C are relevantly enhanced when the temperature is increased to 70 °C, as evidenced by the selected voltage profile recorded at C/10 (**Figure 8d**) which reveals a capacity of 80 mAh g^{-1} (~0.4 mAh cm^{-2}). This result further demonstrates that such temperature is sufficient to trigger a partially amorphous state of the PEO-11 electrolyte, and allow the operation of the Li|MEA-LFP pouch-cell. In addition, a pouch-cell with electrode geometric area of 8.0 cm^2 and active material loading of 6.5 mg_{LFP} cm^{-2} tested at C/5 and 80 °C (**Figure 8e and f**) shows a life extending over 40 cycles, with stable delivered capacity around 60 mAh g^{-1} (~0.3 mAh cm^{-2}) gradually increasing over operation. Despite these results indicate the need for further improvement of the delivered capacity, the cycling ability of the pouch-cells demonstrates the potentiality of the MEA-LFP concept for application in advanced and scalable Li-metal cell configurations.

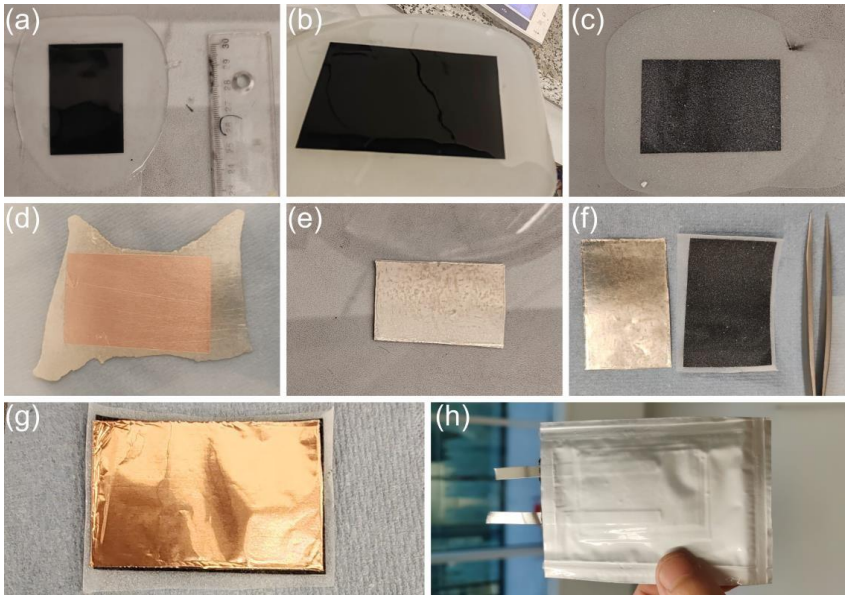

Figure 7. Photographic images illustrating the procedure to achieve Li|MEA-LFP pouch-cells, in particular: **(a-c)** casting and drying of the PEO-11 electrolyte on the LFP cathode to obtain the MEA-LFP junction; **(d-f)** preparation of the lithium anode on a copper current collector with geometric area adjusted to match that of the LFP cathode; **(g)** stacking of the electrodes and **(h)** final pouch-cell.

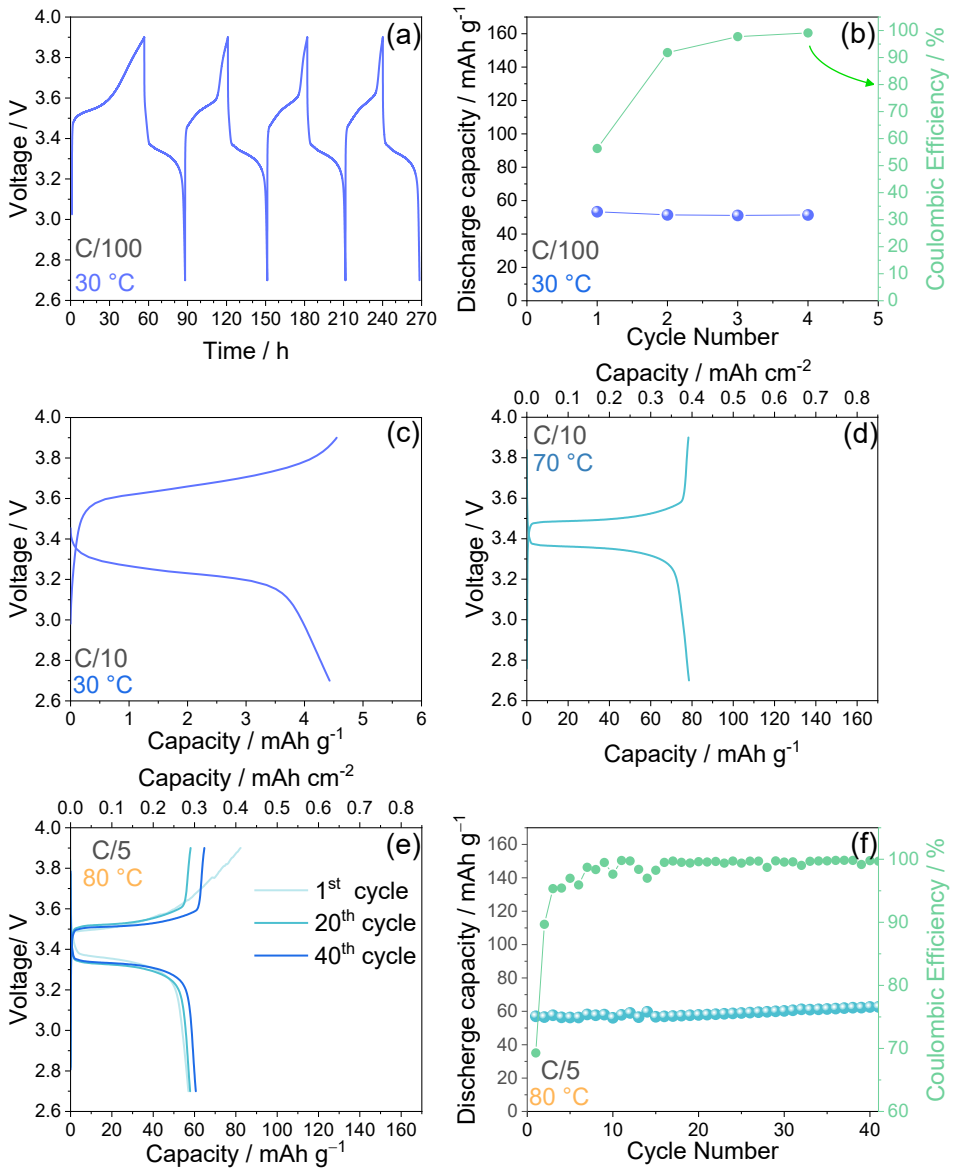

Figure 8. Galvanostatic cycling performance of the Li|MEA-LFP pouch-cells, in detail: **(a-d)** cycling performance of a pouch-cell with 12.8 cm^2 electrodes area and 6.3 mg_{LFP} cm^{-2} in terms of **(a, c, d)** voltage profiles recorded at **(a)** C/100 at 30 °C, **(c)** C/10 at 30 °C and **(d)** C/10 at 70 °C (top x-axis shows areal capacity), and **(b)** discharge capacity trend of the cycling at C/100 (right y-axis reports the Coulombic Efficiency); **(e, f)** cycling performance of a pouch-cell with 8.0 cm^2 electrodes area and 6.5 mgLFP cm^{-2} in terms of **(e)** voltage profiles (top x-axis shows areal capacity) and **(f)** discharge capacity trend (right y-axis reports the Coulombic Efficiency) recorded at C/5 at 80 °C. All tests ran within the 2.7 – 3.9 V voltage range.

References

(1) J. Serra Moreno, M. Armand, M. B. Berman, S. G. Greenbaum, B. Scrosati, S. Panero, J Power Sources 2014, 248, 695–702.
(2) F. Croce, G. B. Appetecchi, L. Persi, B. Scrosati, Nature 1998, 394, 456– 458.
(3) A. Varzi, K. Thanner, R. Scipioni, D. Di Lecce, J. Hassoun, S. Dörfler, H. Altheus, S. Kaskel, C. Prehal, S. A. Freunberger, J Power Sources 2020, 480, 228803.
(4) G. B. Appetecchi, F. Croce, J. Hassoun, B. Scrosati, M. Salomon, F. Cassel, J Power Sources 2003, 114, 105–112.

(5) X. Ren, L. Zou, X. Cao, M. H. Engelhard, W. Liu, S. D. Burton, H. Lee, C. Niu, B. E. Matthews, Z. Zhu, C. Wang, B. W. Arey, J. Xiao, J. Liu, J.-G. Zhang, W. Xu, Joule 2019, 3, 1662–1676.
(6) P. K. Choubey, K. S. Chung, M. S. Kim, J. C. Lee, R. R. Srivastava, Minerals Engineering 2017, 110, 104–121.
(7) F. Croce, M. L. Focarete, J. Hassoun, I. Meschini, B. Scrosati, Energy Environ Sci 2011, 4, 921–927.
(8) D. Devaux, R. Bouchet, D. Glé, R. Denoyel, Solid State Ion 2012, 227, 119–127.
(9) B. W. Zewde, S. Admassie, J. Zimmermann, C. S. Isfort, B. Scrosati, J. Hassoun, ChemSusChem 2013, 6, 1400–1405.
(10) G. Derrien, J. Hassoun, S. Sacchetti, S. Panero, Solid State Ion 2009, 180, 1267–1271.
(11) R. Lei, Y. Yang, C. Yu, Y. Xu, Y. Li, J. Li, Sustain Energy Fuels 2021, 5, 1538–1547.
(12) D. Lin, W. Liu, Y. Liu, H. R. Lee, P. C. Hsu, K. Liu, Y. Cui, Nano Lett 2016, 16, 459–465.
(13) S. S. Zhang, J Electrochem Soc 2012, 159, A920–A923.
(14) S. S. Zhang, J Power Sources 2016, 322, 99–105.
(15) E. Yoo, Y. Qiao, H. Zhou, J Mater Chem A Mater 2019, 7, 18318–18323.
(16) S. Xiong, K. Xie, Y. Diao, X. Hong, Electrochim Acta 2012, 83, 78–86.
(17) V. Marangon, Y. Tominaga, J. Hassoun, J Power Sources 2020, 449, 227508.
(18) S. S. Jeong, Y. T. Lim, Y. J. Choi, G. B. Cho, K. W. Kim, H. J. Ahn, K. K. Cho, J Power Sources 2007, 174, 745–750.
(19) V. Marangon, D. Di Lecce, L. Minnetti, J. Hassoun, ChemElectroChem 2021, 8, 3971–3981.
(20) V. Marangon, L. Minnetti, E. Barcaro, J. Hassoun, Chemistry – A European Journal 2023, 29, e202301345.
(21) H. Cavers, P. Molaiyan, M. Abdollahifar, U. Lassi, A. Kwade, Adv Energy Mater 2022, 12, 2200147.
(22) X. Liu, C. Zhang, S. Gao, S. Cai, Q. Wang, J. Liu, Z. Liu, Mater Chem Phys 2020, 239, 122014.
(23) H. Yang, W. Tian, X. Chen, Z. Li, P. Liu, Q. Wang, X. Nie, Q. Wang, L. Jiao, Batter Supercaps 2024, DOI 10.1002/batt.202400383.
(24) Q. Zhao, S. Stalin, C. Z. Zhao, L. A. Archer, Nat Rev Mater 2020, 5, 229– 252.
(25) X. Cheng, Z. Shi, N. Glass, L. Zhang, J. Zhang, D. Song, Z. S. Liu, H. Wang, J. Shen, J Power Sources 2007, 165, 739–756.
(26) F. Croce, J. Hassoun, C. Tizzani, B. Scrosati, Electrochem commun 2006, 8, 1125–1131.
(27) J. Hassoun, F. Croce, C. Tizzani, B. Scrosati, Electrochem commun 2007, 9, 2045–2050.
(28) J. T. Frith, M. J. Lacey, U. Ulissi, Nat Commun 2023, 14, 420.
(29) M. Wetjen, M. A. Navarra, S. Panero, S. Passerini, B. Scrosati, J. Hassoun, ChemSusChem 2013, 6, 1037–1043.
(30) J. Evans, C. A. Vincent, P. G. Bruce, Polymer (Guildf) 1987, 28, 2324–2328.
(31) B. Boukamp, Solid State Ion 1986, 18–19, 136–140.
(32) B. Boukamp, Solid State Ion 1986, 20, 31–44.
(33) S. Brutti, J. Hassoun, B. Scrosati, C.-Y. Lin, H. Wu, H.-W. Hsieh, J Power Sources 2012, 217, 72–76.
(34) D. A. Jokhakar, D. Puthusseri, P. Manikandan, Z. Li, J. Moon, H.-J. Weng, V. G. Pol, Sustain Energy Fuels 2020, 4, 2229–2235.
(35) G. Abels, I. Bardenhagen, J. Schwenzel, F. Langer, J Electrochem Soc 2022, 169, 020560.

(36) V. Bocharova, A. P. Sokolov, Macromolecules 2020, 53, 4141–4157.
(37) A. Ghosh, S. Samanta, S. Ge, A. P. Sokolov, K. S. Schweizer, Macro- molecules 2022, 55, 2345–2357.
(38) V. Marangon, C. Hernandez-Rentero, S. Levchenko, G. Bianchini, D. Spagnolo, A. Caballero, J. Morales, J. Hassoun, ACS Appl Energy Mater 2020, 3, 12263–12275.
(39) J. Xie, Solid State Ion 2004, 175, 755–758.
(40) D. H. C. Wong, A. Vitale, D. Devaux, A. Taylor, A. A. Pandya, D. T. Hallinan, J. L. Thelen, S. J. Mecham, S. F. Lux, A. M. Lapides, P. R. Resnick,
T. J. Meyer, R. M. Kostecki, N. P. Balsara, J. M. DeSimone, Chem. Mater.
2015, 27, 597–603.
(41) I. Rey, J. C. Lassègues, J. Grondin, L. Servant, Electrochim Acta 1998, 43, 1505–1510.
(42) N. Meng, X. Zhu, F. Lian, Particuology 2022, 60, 14–36.
(43) M. Volel, M. Armand, W. Gorecki, Macromolecules 2004, 37, 8373–8380.
(44) G. A. Elia, U. Ulissi, S. Jeong, S. Passerini, J. Hassoun, Energy Environ Sci
2016, 9, 3210–3220.
(45) B. W. Zewde, L. Carbone, S. Greenbaum, J. Hassoun, Solid State Ion
2018, 317, 97–102.
(46) M. Nojabaee, J. Popovic, J. Maier, J Mater Chem A Mater 2019, 7, 13331– 13338.
(47) D. Di Lecce, V. Marangon, H.-G. Jung, Y. Tominaga, S. Greenbaum, J. Hassoun, Green Chem. 2022, 24, 1021–1048.
(48) W. A. Henderson, J Phys Chem B 2006, 110, 13177–13183.
(49) T. Tamura, K. Yoshida, T. Hachida, M. Tsuchiya, M. Nakamura, Y. Kazue,
N. Tachikawa, K. Dokko, M. Watanabe, Chem Lett 2010, 39, 753–755.
(50) S. Bublil, G. Peta, M. Fayena-Greenstein, H. Alon-Yehezkel, O. Raskin, Y. Elias, D. Aurbach, J Electrochem Soc 2022, 169, 110523.
(51) J. Popovic, D. Höfler, J. P. Melchior, A. Münchinger, B. List, J. Maier, J Phys Chem Lett 2018, 9, 5116–5120.
(52) G. B. Appetecchi, J. Hassoun, B. Scrosati, F. Croce, F. Cassel, M. Salomon,
J Power Sources 2003, 124, 246–253.
(53) S. S. Zhang, J Power Sources 2006, 162, 1379–1394.
(54) S. S. Zhang, Electrochim Acta 2012, 70, 344–348.
(55) A. Rosenman, R. Elazari, G. Salitra, E. Markevich, D. Aurbach, A. Garsuch,
J Electrochem Soc 2015, 162, A470–A473.
(56) S. Wei, S. Inoue, D. Di Lecce, Z. Li, Y. Tominaga, J. Hassoun,
ChemElectroChem 2020, 7, 2376–2388.
(57) L. Herbers, J. Minář, S. Stuckenberg, V. Küpers, D. Berghus, S. Nowak, M. Winter, P. Bieker, Advanced Energy and Sustainability Research 2023, 4, 2300153.
(58) A. K. Thakur, R. Prabakaran, M. R. Elkadeem, S. W. Sharshir, M. Arıcı, C. Wang, W. Zhao, J.-Y. Hwang, R. Saidur, J Energy Storage 2020, 32, 101771.
(59) W. A. Henderson, Macromolecules 2007, 40, 4963–4971.
(60) Y. T. Kim, E. S. Smotkin, Solid State Ion 2002, 149, 29–37.
(61) J. Cheng, G. Hou, Q. Sun, Z. Liang, X. Xu, J. Guo, L. Dai, D. Li, X. Nie, Z. Zeng, P. Si, L. Ci, Solid State Ion 2020, 345, 115156.
(62) L. Zhu, P. Zhu, Q. Fang, M. Jing, X. Shen, L. Yang, Electrochim Acta 2018,
292, 718–726.

3.3 Glyme-based electrolyte for Na-S battery

The LIB has been established as the technology of choice to fulfill the challenging requests of energy storage, due to the advantages of the Li-intercalation electrodes in terms of reversibility and specific energy density which exceeds 250 Wh kg^{-1}.[1-4] Despite the undeniable advantages, the materials used in LIB electrodes such as cobalt, nickel, manganese, copper, and lithium itself, are now posing serious concerns due to the expected decrease in availability and increase in cost.[5, 6] In this complex scenario, sodium-based batteries are drawing increasing interest in view of the wide availability of the alkali metal and the remarkable energy content promoted by its low redox potential of −2.71 V versus SHE.[7-9] Among the various proposed sodium batteries, the Na–S one appeared the most appealing since it holds at the same time several bonuses, including the use of abundant, environmentally friendly, and low-cost materials, and the relevant theoretical energy density of the cell.[7] Indeed, the electrochemical conversion process between Na and S, summarized by the $16Na + S_8 \leftrightarrows 8Na_2S$ reaction, may lead to an energy density as high as 1274 Wh kg^{-1}.[10, 11] Despite the notable expectation, the Na–S battery suffers from severe issues concerning the solubility of the high-order polysulfides such as Na_2S_8 and Na_2S_6 which can migrate by diffusion to the anode, reduce on its surface, and move back to the cathode to be newly oxidized within a shuttle process preventing the actual energy storage and shortening the cell life.[12, 13] The remarkable insulant character of Na_2S alongside its detrimental deposition in the cell, and the relatively low reversibility of the charge-transfer process can further limit the possible application of this intriguing technology.[12, 14] Great efforts to overcome these issues concerned all the cell components, including cathode,[15-19] anode,[20-22] interlayer,[12, 23] and electrolyte,[24-29] with the aim of achieving a practical configuration of the Na–S battery. Nevertheless, the very limited benchmarking of the Na–S cell, and in particular of the electrolyte, hindered the actual evaluation of the various proposed breakthroughs. Recent reports have focused on the effects of the various solvents, conductive salts, and Na-protective additives on the Na/electrolyte interphase, however, only limited attention has been devoted to the influence of the single components and their concomitant effects on the electrochemical performance of the cell.[30-36] Indeed, further knowledge is still required to figure out the role of the sacrificial agent in allowing the use of the reactive metal anode in the Na–S battery. Beneficial effects on cell performance and efficiency have been attributed to the $NaNO_3$ additive, while a comprehensive study on its actual role is still needed.[37, 38] Moreover, FEC has been proposed due to its passivation ability upon reduction with the alkali metals,[39, 40] however with a focus on SIB rather than

Na–S ones for which the appropriate concentration, reactivity, and role of this important sacrificial agent need considerable clarification. In this Section, we discuss recent results regarding safe electrolyte for room-temperature Sodium-Sulfur battery. The research outcomes have been presented at the ELLIPSE (ELectroLyte and Interfaces in PoSt-Li BattEry) Conference held in Ulm (Germany, 15-16/09/2025).

#9 10.1002/adsu.202400268

Effective Liquid Electrolytes for Enabling Room-Temperature Sodium-Sulfur Batteries

We propose herein a step forward for the understanding of the role of the various electrolyte constituents on the Na–S electrode/electrolyte interphase in view of possible benchmarking. For this matter, tetraethylene glycol dimethyl ether (TEGDME) is hereafter selected as the favorite solvent to ensure suitable ions exchange and low flammability of the solutions, and two common slats, i.e., $NaClO_4$ or $NaCF_3SO_3$, are chosen as the most adequate for electrolyte preparation. The electrochemical properties of the solutions are thoroughly studied to shed light on the differences deriving from the choice of the conductive salt, while the effect of the FEC addition is subsequently investigated. Electrolytes containing either 0.5, 1, 2, or 3% in weight of FEC are screened in terms of physical-chemical and electrochemical features. Relevantly, a benchmark sulfur electrode exploiting 70 wt.% of active material in the composite is used to assess the electrochemical performance of the electrolytes in Na–S battery, and the most promising solutions are verified using an optimized, yet still scalable, sulfur electrode. The detailed study proposed in this work can allow the optimization of cells with reproducible outcomes beginning from the electrolyte and therefore facilitate the achievement of advanced Na–S battery configurations characterized by potentially scalable performances.

Experimental

- Electrolytes Preparation

  TEGDME ($CH_3(OCH_2CH_2)_4OCH_3$, ≥ 99%, Sigma-Aldrich) was selected as solvent to prepare two electrolytes, one dissolving $NaClO_4$ (ACS reagent, ≥ 98.0%, Sigma-Aldrich) conducting salt with concentration of 1 mol $kg_{solvent}^{-1}$ (1m), and the other dissolving $NaCF_3SO_3$ (98%, Sigma-Aldrich) conducting salt with concentration of 1m. The solutions were indicated in the text as TE-Cl and TE-F, respectively. A set of 8 electrolytes was prepared by adding various concentrations of FEC (≥ 99%, acid < 200 ppm, anhydrous, Sigma-Aldrich) as passivating agents, that was, 0.5%, 1%, 2%, and 3% with respect to the electrolyte weight. The 8 electrolytes were indicated in text as TE-Cl_0.5%, TE-Cl_1%, TE-Cl_2%, TE-Cl_3%, TE-F_0.5%, TE-F_1%, TE-F_2% and TE-F_3%. **Table 3.3.1** summarizes the acronyms used for the electrolytes and the corresponding compositions. Before use, TEGDME and FEC solvents were stored under molecular sieves (rods, 3 Å, size 1/16 in., Honeywell Fluka) to achieve a water content below 10 ppm as measured by a Karl Fischer 899 Coulometer (Metrohm), while $NaClO_4$ and $NaCF_3SO_3$ were dried under vacuum at 110 °C for two days. All the electrolytes were prepared and stored in an Ar-filled glovebox (MBraun) with H_2O and O_2 levels lower than 1 ppm.

- Electrolytes Characterization

  TGA of solvents, salts, and electrolytes were performed by temperature scans in the 25-800 °C range under a N_2 flow of 50 ml min^{-1} with a rate of 5 °C min^{-1} via a

Mettler-Toledo TGA 2 instrument. Ionic conductivity was evaluated for TE-Cl and TE-F by performing EIS at various temperatures in the 500 kHz–100 Hz frequency range using a 10 mV alternate voltage signal in CR2032 coin-type cells (coin-cells, MTI Corp.) having the stainless-steel|electrolyte|stainless-steel configuration, where the electrolyte was held by an O-ring (23-5FEP-2-50, CS Hyde) with internal diameter of 10 mm, thickness of 127 μm, and cell constant of 0.016 cm^{-1}. The cell temperature was controlled through a Julabo F12 instrument. Symmetrical Na|Na coin-cells employing Na metal electrodes with a diameter of 14 mm separated by a 16 mm-diameter glass-fiber (Whatman GF/B) disc soaked with either TE-Cl or TE-F were prepared to evaluate the Na^+ transference number (t^+) of the two solutions through the Bruce–Vincent–Evans method. The above tests consisted of a chronoamperometric step performed on the cells by applying a voltage of 30 mV (ΔV) for 90 min, alongside EIS measurements carried out before and after polarization in the 500 kHz–100 mHz frequency range using a 10 mV alternate voltage signal. The initial and the steady state currents, as well as the interphase resistance values obtained from the fitting of the EIS spectra (see method below), were used in *Eq (5)* to calculate t^+, where i_0 and i_{ss} were the current values at the initial and steady state, respectively, and R_0 and R_{ss} were the interphase resistances before and after cell polarization, respectively. The ESW of the electrolytes was determined by performing voltammetry measurements on coin cells exploiting Na 14 mm-diameter anode and carbon-based cathode separated by a 16 mm-diameter glass-fiber (Whatman GF/B) disc. The carbon-based electrodes were prepared by doctor blade (MTI Corp.) casting on either Al or Cu foil (MTI Corp.) of a slurry composed of SPC (Timcal) at the 80 wt.% and PVdF binding agent at the 20 wt.% dispersed in NMP. The electrodes were indicated as SPC-Cu and SPC-Al, respectively. The electrode tapes were dried on a hot plate at 70 °C, cut into discs with a 14 mm diameter, and dried under vacuum at 110 °C for 3 h before being transferred in the Ar-filled glovebox. CV measurements were carried out on Na|SPC-Cu cells in the 0.01–2.0 V versus Na^+/Na potential range at a rate of 0.1 mV s^{-1} to evaluate the cathodic stability, while the anodic one was determined by an LSV run performed on Na|SPC-Al cells from the OCV condition to 5 V versus Na^+/Na at 0.1 mV s^{-1}. Sodium stripping/deposition stability was investigated by galvanostatic cycling tests on Na|Na symmetrical cells applying a current of 0.1 mA cm^{-2}: a step time of 1 h was set for both nominal charge and discharge for coin-cells using 14 mm-diameter Na electrodes separated by two glass-fiber Whatman GF/B 18 mm-discs, while a step time of 10 h was exploited for Swagelok T-type cells using 10 mm Na electrodes separated by three glass-fiber (Whatman GF/B) 10 mm-diameter discs. The stability of the electrolytes upon aging in contact with Na metal was studied via EIS measurements performed in the 500 kHz–100 mHz frequency range through an alternate voltage signal of 10 mV on Na|Na symmetrical coin-cells using 14 mm-diameter Na electrodes separated by a glass-fiber (Whatman GF/B) 16 mm-diameter disc. The EIS tests were carried out every 2 h during the first 14 h after assembling and subsequently every day for 23 days. All the voltammetry and EIS measurements were carried out using a VersaSTAT MC Princeton Applied Research (PAR-AMETEK) instrument, while the galvanostatic cycling data were acquired via a MACCOR 4000 battery test system. All the Nyquist plots recorded by EIS were fitted via NLLS method using the Boukamp software, which allowed the description of the spectra with equivalent circuits that include resistive (R) and capacitive (Q) elements. The fitting led to the identification of i) R_e, which was the electrolyte resistance indicated by the high-frequency intercept of the plot; ii) R_i, which defines the electrode/electrolyte interphase resistance measured by the amplitude of the semicircle in the high-medium frequency region including various

convoluted contributions, and is arranged in parallel with the Q_l capacitive element in (R_lQ_l); iii) the (R_wQ_w) and Q_w elements, which identify either the finite-length or semi-infinite Warburg-type Na^+ diffusion through either a semicircle or a tilted line, respectively, in the low-frequency region. FTIR spectra of the electrolytes were obtained using a Bruker Vertex V70 instrument set up in the transmittance mode. SEM was performed via a Zeiss Gemini microscope (accelerating voltage of 5 kV) ex situ on Na electrodes retrieved after 1 month of aging from symmetrical Na|Na coin-cells assembled using 10 mm-diameter sodium electrodes and one 16 mm-diameter separator (Whatman GF/B) soaked with the electrolyte. Before SEM measurements, the Na electrodes were washed with 300 µl of diethylene glycol dimethyl ether (DEGDME, anhydrous, 99.5%, Sigma-Aldrich) and subsequently dried under vacuum for 10 min. The DEGDME solvent was dried under molecular sieves (rods, 3 Å, size 1/16 in., Merck) before use. XPS was performed on Na samples exposed to either TE-Cl, TE-F, TE-Cl_3% or TE-F_3%. Accordingly, Na|Na coin-cells were assembled using 10 mm-diameter sodium electrodes separated by one glass-fiber (Whatman GF/B) 16 mm-diameter disc and aged for 23 days. Subsequently, the cells were disassembled in an Ar-filled glovebox and the Na samples were retrieved, washed with 300 µl of TEGDME, dried under vacuum for 1 h, and transferred to the XPS instrument with a sealed chamber. The XPS measurements were carried out through a Kratos Axis Ultra^{DLD} spectrometer (Kratos Analytical Ltd.) with a monochromated Al K_α X-ray source ($h\nu$ = 1486.6 eV) operating at 20 mA and 15 kV. The wide scans were collected over an analysis area of 300 × 700 µm^2 at a photoelectron pass energy of 160 eV and energy step of 1 eV, while high-resolution spectra were collected at a photoelectron pass energy of 20 eV and an energy step of 0.1 eV. Differential electrical charging effects on the surface of the sample were neutralized during the measurements of all specimens. The spectra were referenced to the adventitious C 1s peak at 284.8 eV. The spectra were analyzed with the CasaXPS software (Casa Software Ltd., version 2.3.24), and the residual background was eliminated by the Shirley method.

- **Na–S Cells Testing**

Elemental sulfur (≥ 99.5%, Riedel-de Haën) and SPC were mixed in the 70:30 weight ratio, heated at 125 °C under magnetic stirring with the aid of a silicon oil bath until complete melting of sulfur, cooled at room temperature until solidification of the mixture, and finally ground in an agate mortar to obtain a fine powder. The sulfur-carbon composite was indicated in the text as S:SPC 70:30 *w/w*. The sulfur cathode was prepared by doctor blade casting on aluminum foil (MTI Corp., 15 µm thick) of a slurry composed by 80 wt.% of S:SPC 70:30 *w/w*, 10 wt.% of FLG as electron conductive agent and structural enhancer, and 10 wt.% of PVdF, dispersed in NMP solvent. The electrode tape was dried at room temperature until complete evaporation of NMP, calendared through an MSK-2150 rolling machine (MTI Corp.) to a final thickness of ≈80 µm, cut into 14 mm-diameter discs and dried under vacuum at 30 °C overnight before being transferred in the Ar-filled glovebox. The final sulfur loading achieved on the cathode surface ranged between 1.7 and 2.0 mg cm^{-2} (electrode geometric area: 1.54 cm^2). CR2032 coin-cells were prepared by stacking a S:SPC 70:30 *w/w* cathode, a 18 mm-diameter glass-fiber separator (Whatman GF/B) soaked with 200 µl of electrolyte, and a 14 mm-diameter sodium anode (Na–S cells). Galvanostatic cycling tests were performed on the Na–S cells by using a constant current rate of C/20 (1C = 1675 mA g^{-1}) in the 1.4–2.6 V voltage range setting a safety step-time of 20 h for charge process in order to switch to discharge if the theoretical capacity (i.e., 1675 mAh g$_S^{-1}$) was reached. The galvanostatic cycling tests were carried out via a MACCOR 4000 battery test system

setting the room temperature at 30 °C with a maximum fluctuation of ± 0.1 °C.

Results

The physical-chemical and electrochemical characteristics of the bare electrolytes intended as the ones dissolving either $NaClO_4$ (TE-Cl) or $NaCF_3SO_3$ (TE-F) without FEC addition are evaluated in **Figure 1** (all electrolytes acronyms and compositions are reported in **Table 3.3.1** for readers convenience). The TGA of the solutions performed under N_2 flow (**Figure 1a**) and the related differential (DTG) curves display for both the electrolytes the main weight loss above 200 °C attributed to the TEGDME solvent evaporation, and an additional minor change at 245 °C likely due to the removal of crystallization solvent from salts complexes.[42-44] The salts degradation is observed at 530 °C for $NaClO_4$ in TE-Cl and 510 °C for $NaCF_3SO_3$ in TE-F. The ionic conductivity trends of TE-Cl and TE-F are investigated in the Arrhenius plots in **Figure 1b**. The two electrolytes show similar conductivity in the 10–74 °C interval, with values increasing from 6.1×10^{-4} to 1.7×10^{-3} S cm^{-1} for TE-Cl and from 5.2×10^{-4} to 1.2×10^{-3} S cm^{-1} for TE-F, although a notable difference is observed between 10 °C and −3 °C. Indeed, TE-Cl holds the quasi-linear variation with a remarkable final value of 5.0×10^{-4} S cm^{-1}, while TE-F conductivity abruptly decreases to 5.7×10^{-5} S cm^{-1}. This discrepancy is due to the efficient dissolution of $NaClO_4$ in TE-Cl even at lower temperatures, and the formation of lowly conductive crystalline phases including solvated $NaCF_3SO_3$ in TE-F at temperatures lower than 10 °C as suggested by the literature,[47] despite further effects ascribed to ion association with the formation of neutral couples without charge transport cannot be excluded.[37] On the other hand, both the solutions exhibit conductivity values suitable for battery application in the temperature range from 10 to 74 °C, while TE-Cl may be also suited for low-temperature operation. The ion mobility in TE-Cl and TE-F is further evaluated by determining the Na^+ transference number (t^+) at room temperature using the Bruce–Vincent–Evans method. Accordingly, t^+ is calculated with *Eq (5)* using the parameters in **Table 3.3.2** which are achieved by performing chronoamperometric tests on Na|Na cells and NLLS-fitting of the EIS Nyquist plots recorded before and after polarization. **Figure 1c** reveals relatively high t_+ values for both solutions and suggests enhanced mobility of the Na^+ ions in line with the results achieved for similar glyme-based solutions, despite the Bruce–Vincent–Evans method may lead to overestimated values in particular in the liquid electrolytes. Furthermore, the lower t+ value obtained for TE-Cl (0.74) compared with TE-F (0.80) indicates a faster ion mobility in the latter compared to the former, likely due to the different nature of the two salts. The ESW of TE-Cl and TE-F is determined with CV in the cathodic region (0.01–2.0 V versus Na^+/Na) and linear sweep voltammetry in the

anodic one (between OCV and 5.0 V versus Na^+/Na). **Figure 1d,e** shows the corresponding voltammograms revealing for both TE-Cl (**Figure 1d**) and TE-F (**Figure 1e**) a first reduction process at ≈0.7 V versus Na^+/Na, accounting for partial electrolyte reduction with the formation of a passivation layer or SEI. Reversible deposition/dissolution of Na ions between 0.05 and 0.08 V versus Na^+/Na and (de)insertion slightly below 1.0 V versus Na^+/Na can be also observed during the first cycle, as well as in the subsequent overlapping ones. On the other hand, the two solutions show different anodic stability, which is taken as the potential value over which a non-negligible oxidation current of 30 μA is detected. Hence, TE-Cl exhibits electrolyte oxidation at 4.42 V versus Na^+/Na while TE-F shows the same behavior already at 2.98 V versus Na^+/Na. These values greatly influence the application range of the solutions since TE-Cl may be actually employed in Na batteries using phosphates- or layered oxide-based cathodes working above 3 V, while TE-F would be hardly suitable due to excessive side-reaction. Nevertheless, the application in Na–S battery can be still considered both for TE-Cl and TE-F due to the operating voltage centered at ≈2.0 V of the electrochemical conversion process between Na and S. With the aim of further testing the electrochemical stability, **Figure 1f** reports the sodium stripping/deposition tests carried out on Na|Na cells through galvanostatic cycling using a current of 0.1 mA cm^{-2}, and setting a step time of 1 h for charge and discharge. The results display the absence of sodium dendrites formation over 500 h of cycling and a low overvoltage, although significant differences between the solutions are observed. TE-Cl exhibits initial overvoltage of 9 mV which rapidly stabilizes at a steady state of 10 mV, and grows in the final stages to a maximum of 14 mV. Instead, TE-F shows a constant polarization slightly exceeding 3 mV for the whole testing time. These data are in line with the higher t_+ in TE-F than TE-Cl shown in **Figure 1c**, and further suggest a faster Na^+ transfer kinetics at room temperature leading to a lower polarization in the former compared to the latter. On the other hand, the increase of the overvoltage in TE-Cl at the end of the test can be ascribed to a slight growth of the passivation layer and the charge transfer resistance, possibly promoted by the relatively high density of $NaClO_4$ solution compared to other salts. The stripping-deposition test in **Figure 1g** performed with a step time extended to 10 h evidences for TE-F a nearly constant square-shape overvoltage of 7 mV over 90 h of cycling, while an increasing slope is observed for TE-Cl with initial value of ≈17 mV growing to ≈25 mV at the end of the test. This behavior supports the formation of a thicker SEI layer on the Na electrodes which may increase the electrode/electrolyte interphase resistance when TE-Cl is employed rather than TE-F.

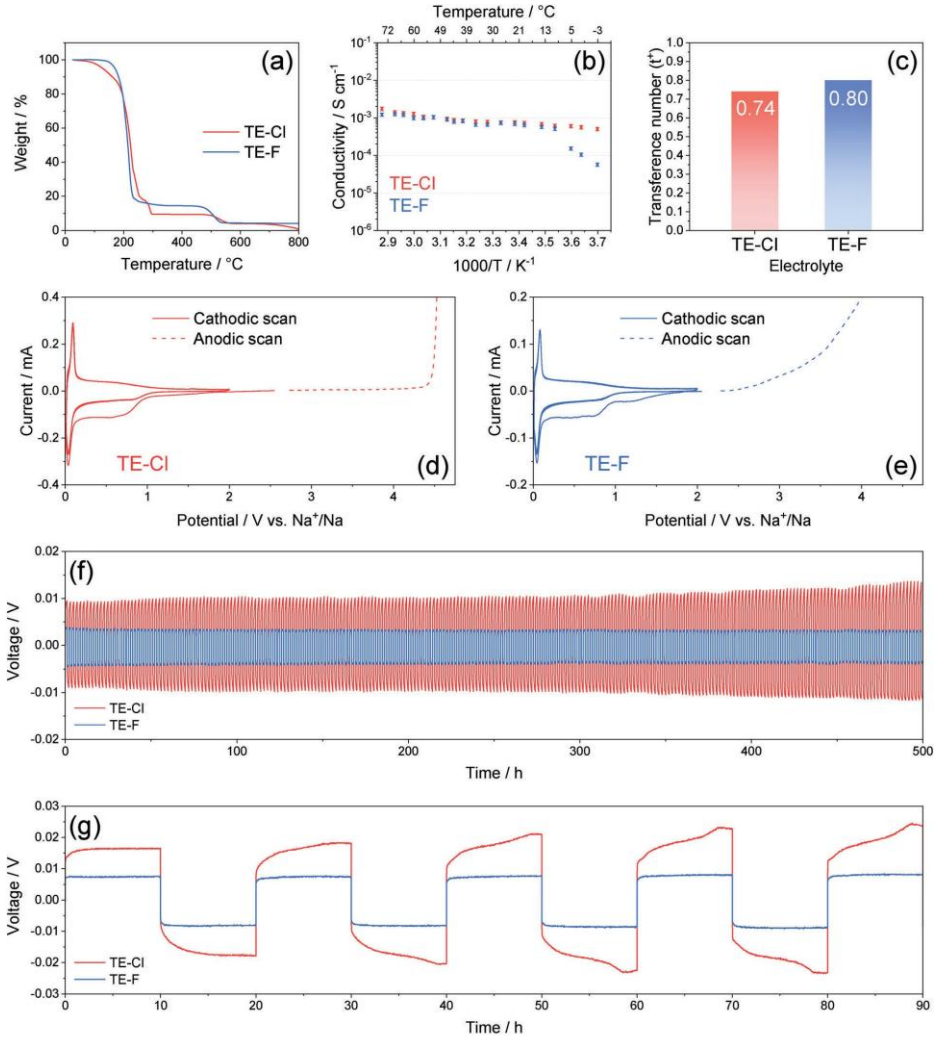

Figure 1. Characterization of TE-Cl and TE-F: **(a)** TGA performed under N_2 flow in the 25–800 °C temperature range; **(b)** Arrhenius plots reporting ionic conductivity trends determined by EIS at various temperatures, frequency range: 500 kHz–100 Hz; alternate voltage signal: 10 mV; **(c)** histogram representation of the t_+ values; **(d, e)** ESWs of **(d)** TE-Cl and **(e)** TE-F evaluated by CV in the 0.01–2.0 V versus Na+/Na potential range and LSV from the OCV condition to 5.0 V versus Na^+/Na; scan rate: 0.1 mV s^{-1}; **(f, g)** Na stripping/deposition tests achieved by applying a constant current rate of 0.1 mA cm^{-2} with step time of either **(f)** 1 h or **(g)** 10 h for charge and discharge.

Table 3.3.1. Acronyms and compositions of the investigated electrolytes.

Electrolyte acronym	Composition
TE-Cl	TEGDME, 1m $NaClO_4$
TE-Cl_0.5%	TEGDME, 1m $NaClO_4$ + 0.5% FEC
TE-Cl_1%	TEGDME, 1m $NaClO_4$ + 1% FEC
TE-Cl_2%	TEGDME, 1m $NaClO_4$ + 2% FEC
TE-Cl_3%	TEGDME, 1m $NaClO_4$ + 3% FEC
TE-F	TEGDME, 1m $NaCF_3SO_3$
TE-F_0.5%	TEGDME, 1m $NaCF_3SO_3$ + 0.5% FEC
TE-F_1%	TEGDME, 1m $NaCF_3SO_3$ + 1% FEC
TE-F_2%	TEGDME, 1m $NaCF_3SO_3$ + 2% FEC
TE-F_3%	TEGDME, 1m $NaCF_3SO_3$ + 3% FEC

Table 3.3.2. Parameters used in *Eq (5)* to calculate the t_+ values for TE-Cl and TE-F through the Bruce–Vincent–Evans method.

Electrolyte	Initial current (I_0) [A]	Steady-state current (I_{ss}) [A]	Initial resistance (R_0) [Ω]	Steady-state resistance (R_{ss}) [Ω]	t^+
TE-Cl	1.26×10^{-3}	9.25×10^{-4}	0.52	0.81	0.74
TE-F	6.20×10^{-4}	5.00×10^{-4}	1.14	1.12	0.80

The FEC-doped electrolytes are investigated by TGA performed in **Figure 2a** for the solutions using $NaClO_4$ (i.e., TE-Cl_0.5% - TE-Cl_3%) and in **Figure 2b** for the ones dissolving $NaCF_3SO_3$ (i.e., TE-F_0.5% - TE-F_3%). The outcomes indicate for the TE-Cl family (**Figure 2a**) an initial weight loss beginning over 100 °C, with variations centered near 200 °C and between 220 and 240 °C. Despite the above weight losses being coherent with TEGDME and FEC evaporation, the solutions exhibit a complex response not linearly associated with the FEC content. This behavior might suggest the partial formation of a co-solvent between TEGDME and FEC, and the corresponding solvent-salt complexes, which would also explain the relevant weight loss in the FEC region at 200 °C, in contrast with the low additive amount ranging from 0.5 to 3%. Subsequently, the TE-Cl derivatives show weight losses at ≈280 °C due to the TEGDME-$NaClO_4$ crystallization solvent evaporation, and at 530 °C upon $NaClO_4$ degradation, in agreement with the TGA of TE-Cl discussed in **Figure 1**. On the other hand, the TGA curves of the FEC-doped TE-F (**Figure 2b**) display one main weight loss starting above 100 °C and centered at ≈200 °C due to the solvent and possible co-solvent removal, a barely detectable step over 250 °C related to solvent loss from TEGDME-$NaCF_3SO_3$ complexes, as well as a final one at 510 °C attributed to $NaCF_3SO_3$ degradation. As already observed for TE-Cl family, the data suggest that low amounts of FEC can modify the thermal response and the solvation complexes also for the TE-F electrolytes which hold, at the same time, a suitable thermal stability. Na stripping/deposition measurements performed with a charge/discharge step time of 1 h are reported for the FEC-doped TE-Cl (**Figure 2c**) and TE-F (**Figure 2d**), alongside with the performance of bare solutions to facilitate the comparison. The data clearly indicate that the FEC remarkably raises the cell overvoltage due to the growth of a resistive SEI triggered by the additive reduction at the Na surface. The figure also shows a notable change of the polarization during time, depending on the FEC amount and the employed conductive salt. In particular, the cell using TE-Cl_0.5% presents an initial polarization below 0.2 V which rapidly decreases after 100 h of cycling, and stabilizes below 0.1 V until the end of the test, while that employing TE-Cl_1% shows a similar

behavior however with a slight polarization increase between 250 and 300 h of cycling to ≈0.2 V, and a rapid decrease after 300 h to a value of ≈0.03 V. Meanwhile, the cells with TE-Cl_2% and TE-Cl_3% maintain a constant overvoltage between 0.15 and 0.2 V over the whole test. The decrease of the Na|Na cell polarization can be related to a partial dissolution of the native SEI occurring during repeated cycling, which is reasonably affected by the amount of FEC and possibly avoided with additive concentration ≥ 2% in the presence of $NaClO_4$. This behavior is expected to relevantly impact the Na cells' performance, since a partial dissolution of the native passivation layer may certainly lead to a less resistive electrode/electrolyte interphase, however it may provide a relatively weak protection of the Na surface. The cells using FEC-doped TE-F electrolytes exhibit a similar process, although the dissolution occurs earlier than the analog TE-Cl solutions (compare Fi**gure 2d** with **Figure 2c**), and can be avoided only by increasing the FEC content up to 3%. Indeed, the cell using TE-F_0.5% shows rapid decrease of the polarization from 0.16 to 0.05 V already after 30 h of cycling and a second gradual drop after 60 h leading to a minimum value of 0.013 V. On the other hand, the overvoltage of the cell with TE-F_1% gradually drops from 0.20 to 0.13 V during the initial 85 h, and then rapidly to 0.027 V until the end of the test, while the one with TE-F_2% passes from 0.23 to 0.18 V in 250 h, and then abruptly to a final value of 0.042 V. Instead, the cell using TE-F_3% displays a constant polarization between 0.15 and 0.20 V during the whole cycling test. Therefore, the partial dissolution of the SEI seems to have a different time-constant, depending either on the salt nature or on the FEC content. Nevertheless, the passivation of Na and its polarization is certainly increased by FEC, which promotes a further side process in addition to the one already observed for $NaClO_4$ and $NaCF_3SO_3$ with far lower overvoltage. Additional insight into the Na stripping/deposition is achieved by prolonging the charge/discharge time to 10 h in cells using FEC-doped TE-Cl (**Figure 2e**) and TE-F (**Figure 2f**). The cells using the TE-Cl family reveal a characteristic overvoltage evolving through a reversible double wave with a slight stabilization after the first cycle, while a similar but less pronounced shape is observed for the ones using the TE-F family. The cell with TE-F_0.5% shows lower overvoltage compared to the one with TE-Cl_0.5%, and evolves according to a slowly polarized square signal already after 2 cycles. The cell using TE-F_1% appears similar yet more polarized than the one with TE-F_0.5%, and forms the square wave after 3 cycles, while the cells employing TE-F_2% and TE-F_3% maintain the double wave-shape during the whole cycling. These data confirm the relevant role of the FEC additive in promoting the formation of the passivation layer and influencing the Na extraction/deposition mechanism. The latter aspect seems

particularly pronounced when cells using the FEC-added solutions (**Figure 2e,f**) are compared with the bare electrolytes (**Figure 1g**) in which the exclusive contributes of the conductive salt and the solvent are expected.[58, 59] In addition, the trends of **Figure 2e,f** indicate once more the higher solubility of the SEI formed at the Na surface in the TE-F solutions compared to TE-Cl ones, despite the presence of FEC. **Figure 2g** summarizes by histograms the related anodic stability (the values for TE-Cl and TE-F precursors are included for comparison). Hence, TE-Cl family stands up 4.5 V versus Na^+/Na, instead the TE-F one displays oxidation already between 3.8 and 4.1 V versus Na^+/Na. Furthermore, the data indicate that FEC addition slightly enhances the anodic stability of the TEGDME-$NaClO_4$ solution, and it strongly improves (≈1 V) the TEGDME-$NaCF_3SO_3$ one. This beneficial effect of FEC was recently observed for Li-based systems as well,[61] and it is likely due to the formation of a stable cathode electrolyte interphase that protects the positive electrode and hinders the decomposition of the electrolyte at high voltages. Herein, the addition of FEC to the TEGDME-$NaCF_3SO_3$ electrolyte seemingly promotes an enhanced CEI compared to the exclusive use of the conducting salt, thanks to a synergy between $NaCF_3SO_3$ and the fluorinated carbonate that allows increased anodic stability. **Figure 2h** reports the interphase resistance trends of the FEC-doped TE-Cl solutions upon aging in Na|Na cells, with value obtained from the NLLS analyses The FEC-added electrolytes exhibit relevantly higher interphase resistance than the bare TE-Cl, with values at the OCV from 840 to 2600 Ω, sharply rising between 1500 and 6400 Ω already after 2 h of aging due to a relevant SEI growth. Surprisingly, TE-Cl_0.5% presents the highest resistance (≈6000 Ω), and TE-Cl_1% displays remarkable values (from 3000 to 4000 Ω) from 2 h until the end of the test. Instead, TE-Cl_2% and TE-Cl_3% exhibit initial resistances of 1060 and 840 Ω, respectively, which progressively grow to 5100 and 6900 Ω in 23 days. These data suggest the fast formation of a resistive SEI in the solutions with lower FEC content (TE-Cl_0.5% and TE-Cl_1%), and a slowed down growth of the film in those with higher additive amount (TE-Cl_2% and TE-Cl_3%). Moreover, TE-Cl_1% reveals after 23 days the lowest interphase resistance (≈ 4000 Ω) with the most stable trend, suggesting a suitable compromise for Na-cell application. Except for the initial 2 h of test, the TE-F electrolytes added by FEC show a rather different behavior than TF-Cl ones, as demonstrated by the trends of the interphase resistance in **Figure 2i** which is based on the NLLS, and the analysis reveals a fast initial resistance increase from 690–960 to1160–1360 Ω, accounting for the relevant reduction of the electrolytes occurring in 2 h, and the subsequent progressive raise leading to values between 1700 and 2700 Ω. It is worth mentioning that the highest resistance is achieved after 23 days in the cell using TE-

F_0.5%, whilst the lowest value is related to the one using TE-F_3%.

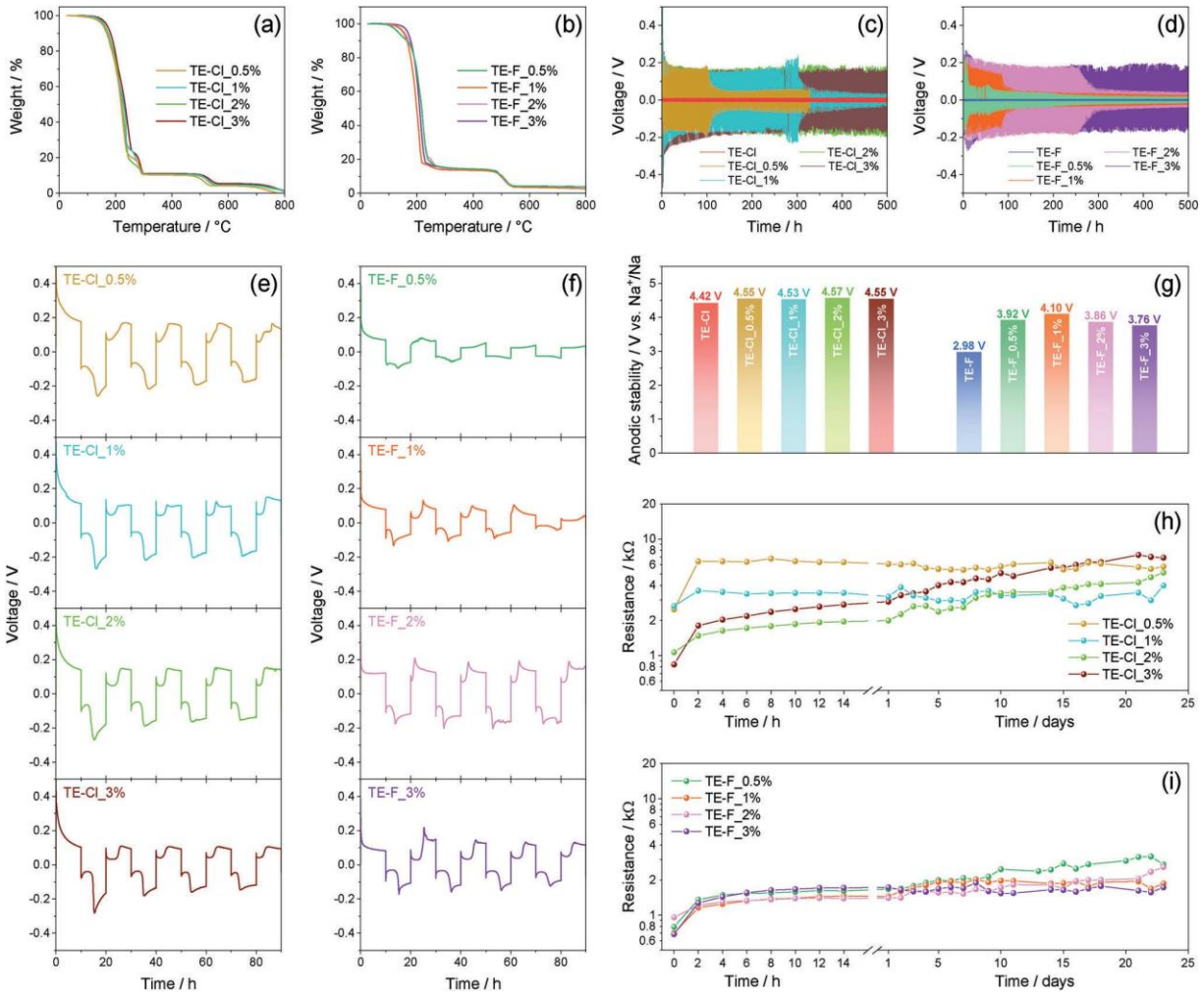

Figure 2. Characterization of the FEC-doped electrolytes (see Table 3.3.1 for compositions): **(a, b)** TGA of the electrolytes dissolving either **(a)** $NaClO_4$ or **(b)** $NaCF_3SO_3$ performed under N_2 flow in the 25–800 °C temperature range; **(c–f)** Na stripping/deposition tests achieved by applying a constant current of 0.1 mA cm^{-2} with step time of either c,d) 1 h or **(e,f)** 10 h for charge and discharge on Na|Na cells using electrolytes dissolving **(c, e)** $NaClO_4$ or **(d, f)** $NaCF_3SO_3$; **(g)** histogram representation of the anodic stability values measured by LSV, scan rate: 0.1 mV s^{-1}; **(h, i)** resistance trend versus time obtained through EIS carried out upon aging of Na|Na cells using electrolytes with **(h)** $NaClO_4$ or **(i)** $NaCF_3SO_3$.

Figure 3 reports a detailed investigation carried out by FTIR spectroscopy on the electrolytes to provide further insights into their composition, as well as by ex situ SEM performed on Na electrodes aged in contact with the TEGDME-based solutions for 1 month to observe the morphological features of the SEI in dependence of the electrolyte composition. As deduced from the FTIR spectra in **Figure 3a**, both the TEGDME-$NaCF_3SO_3$-based and the TEGDME-$NaClO_4$-based electrolyte solutions reveal the

expected combination of signatures due to the solvent and the respective conducting salt. Indeed, $NaCF_3SO_3$ is identified by signals at 638 and 1033 cm^{-1} corresponding to the symmetric SO_3 vibration and stretching, respectively, as well as by peaks at 755 and 1225 cm^{-1} related to the CF^3 band stretching,[62] while the NaClO4 contribution is revealed by the vibrational mode of $ClO4^-$ at 624 cm^{-1}.[63] On the other hand, the FEC is observed by signals with intensity increasing in concomitance to its concentration in the solutions, that is, at 727 and 767 cm^{-1} due to the O─C─O ring breathing mode,[61] at 1647 cm^{-1}, which is usually observed for CF-containing species,[64] and at 1833 cm^{-1}, identifying the C═O vibrational mode.[65] Interestingly, a minor peak is observed at 1722 cm^{-1}, with a detectable intensity only for TE-F_2%, TE-Cl_0.5%, and TE-Cl_3%, which may be attributed to carbonate species deriving from FEC side reactions within the solutions.[66, 67] The effects of the composition of the solutions on the properties of the passivation film on the Na electrode are investigated by SEM in **Figure 3b–u**. The sodium sample treated with TE-Cl (**Figure 3b,c**) presents an irregular surface characterized by indented micrometric agglomerates across the electrode surface, indicating a poor passivation ability of the bare combination of the TEGDME solvent and the $NaClO_4$ conducting salt. Remarkably, the addition of a limited amount of FEC in TE-Cl_0.5% is sufficient to form a thin SEI layer on Na, despite the presence of multiple cracks and nanometric agglomerates on the surface observed in the corresponding micrographs (**Figure 3d,e**). Following this trend, the treatment with TE-Cl_1% leads to an SEI with a characteristic morphology, where the homogeneous layer shows porous regions approaching sizes of ≈10 μm (**Figure 3f,g**). The further increase of the FEC concentration in TE-Cl_2% and TE-Cl_3% thickens the SEI layer, leading to the formation of submicrometric clusters scattered around the electrode surface for the former (**Figure 3h,i**), and to the complete coverage of Na for the latter (**Figure 3j,k**), likely suggesting an excessive electrode passivation. The sodium samples aged in contact with the TEGDME-$NaCF_3SO_3$-based solutions display a similar growth trend as for the previous ones, however with a considerably different morphology of the corresponding SEIs. Indeed, TE-F leads to an irregular disposition on the Na surface of spherical aggregates with sizes of <1 μm (**Figure 3l,m**), while Na passivation is observed upon aging with TE-F_0.5% where the SEI displays deep cracks until the metal surface (**Figure 3n,o**). The increase of the FEC content in TE F_1% causes a uniform coverage of the Na surface through an SEI with heterogeneous morphology (**Figure 3p,q**), which undergoes an abrupt thickening and partial cracking when the FEC content is further increased in TE-F_2% (**Figure 3r,s**). This trend is consistent with the SEM data acquired for TE-F_3%, where the further thickening of the passivation film leads to the formation of

submicrometric crystal-like structures scattered around the electrode surface (**Figure 3t,u**). Notably, the SEM analyses reported in **Figure 3** indicate the relevant or likely excessive Na passivation upon contact with solutions having FEC concentration ≥2%, as indeed hypothesized in the discussion of **Figure 2**. On the other hand, the mild passivation promoted by the solutions with FEC concentration of either 0.5% or 1% can facilitate the Na^+ ions diffusion toward the sodium electrode, while excessive passivation is expected to prevent an adequate operation of the metallic anode and depress the Na–S cell response.

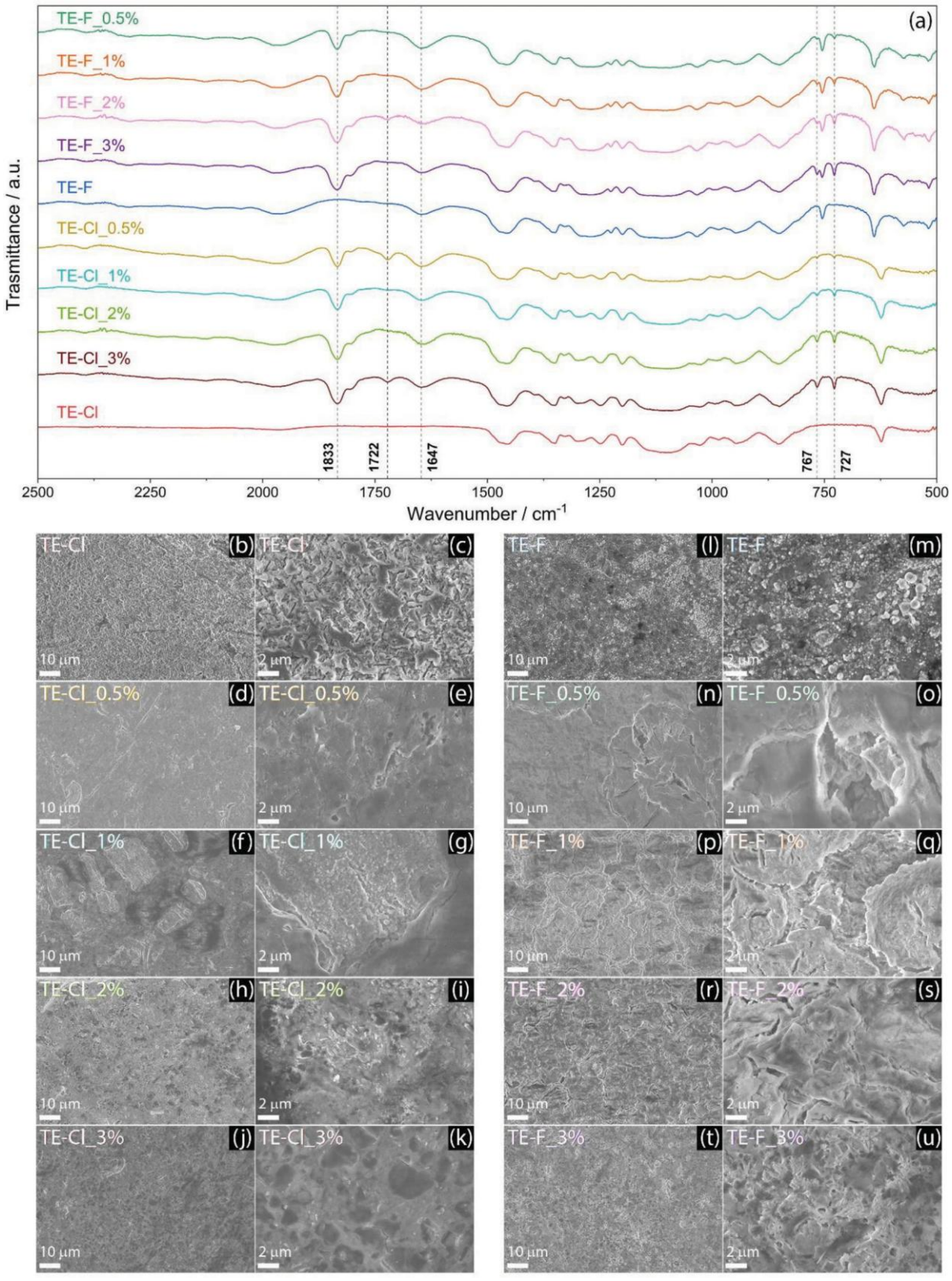

Figure 3. (a) FTIR spectra of the TEGDME-based electrolytes; **(b–u)** SEM images at various magnifications of Na electrodes aged in contact with **(b, c)** TE-Cl, **(d, e)** TE-Cl_0.5%, **(f, g)** TE-Cl_1%, **(h, i)** TE-Cl_2%, **(j, k)** TE-Cl_3%, **(l, m)** TE-F, **(n, o)** TE-F_0.5%, **(p, q)** TE-F_1%, **(r, s)** TE-F_2% and **(t, u)** TE-F_3% in Na|Na cells. See Table 3.3.1 for electrolyte acronyms.

The composition of the passivation film formed on the Na surface in the bare electrolytes and the ones modified with FEC addition is investigated through XPS in **Figure 4**. The Na samples are retrieved from Na|Na cells aged for more than 20 days with either TE-Cl, TE-F, TE-Cl_3%, or TE-F_3% (see Experimental section for details). The survey spectra related to TE-Cl and TE-F in **Figure 4a** share the Na, C, and O signals, and also reveal the expected differences due to $NaClO_4$ and $NaCF_3SO_3$ reduction products, respectively. TE-Cl exhibits signals in Cl 2p regions,[68] while peaks in the F 1s, F KLL, and S 2p peaks are detected for TE-F.[69, 70] Some detail on the SEI composition is obtained from the corresponding high-resolution spectra reported in **Figure 4b–j**. The Na 1s signal ascribed to the formation of NaCl and NaF precipitates at the Na surface as well as due to the metal itself appears at (1071.5 ± 0.2) eV for both TE-Cl (**Figure 4b**) and TE-F (**Figure 4f**).[31] In addition, contributes of the C─C, C─O, and C═O bonds due to the reduction of the TEGDME solvent to carbonates and organic species are deducted from the C 1s signals at (284.8 ± 0.2), (286.3 ± 0.2) and (287.5 ± 0.2) eV for TE-Cl (**Figure 4c**) and TE-F (**Figure 4g**).[31] Further contributes at (289.0 ± 0.2) and (293.9 ± 0.2) eV ascribed to O─C═O and C-F bonds, respectively, are observed only for TE-F (**Figure 4g**) as indeed expected from the fluorinated salt.[70] Interestingly, the O─C═O signal suggests in TE-F the formation of a characteristic SEI with a significant amount of organic fraction upon glyme reduction in the presence of $NaCF_3SO_3$.[70] The O 1s region shows for TE-Cl (**Figure 4d**) and TE-F (**Figure 4h**) composite peaks, that are deconvoluted into the Na KLL Auger peak at ≈536 eV, the contribution at ≈531 eV accounting for Na─O interactions in sodium-ethers, oligomers, carbonates, and oxides,[31, 70] and another peak between 532 and 533 eV confirming the presence of C─O bonds[31] as well as Cl─O ones.[71] The Cl 2p signals for TE-Cl (**Figure 4e**) consist of two 2p3/2/2p1/2 doublets at 208.5/210.1 and 206.3/207.9 eV of ClO4 and ClO3 groups, respectively, due to the salt deposition and reduction at the Na-interphase.[68, 72] On the other hand, TE-F displays the typical signals in the F 1s (**Figure 4i**) and S 2p (**Figure 4j**) regions due to C─F (688.6 ± 0.2 eV), Na─F (683.8 ± 0.2 eV) and S─O (2p3/2/2p1/2 doublet at 169.2/170.4 eV) interactions deriving from $NaCF_3SO_3$ decomposition.[73, 74] The role of FEC on the SEI composition is evaluated in **Figure 4k**, which reports the survey spectra of Na samples from sodium symmetrical cells using TE-Cl_3% and TE-F_3%. As expected, TE-Cl_3% reveals the presence of weak F KLL and F 1s signals ascribed to FEC, and a slight decrease of the Cl 2p wave intensity. Therefore, the XPS data reveal the concomitant contributes of the TEGDME solvent, the salts (i.e., either $NaClO_4$ and $NaCF_3SO_3$), and the FEC additive to the by-products forming the passivation layer covering the Na surface. These products lead to unique SEI compositions, with

atomic percentages extracted from the XPS and reported in **Table 3.3.3**. The SEI layers deriving from TE-F and TE-F_3% show almost the same composition in terms of Na, C, O, and F, with the exception of S which greatly decreases from 3.1% in TE-F to 1.7% in TE-F_3%. On the other hand, a decrease of Na, C, and Cl, a great increase of O, alongside the presence of F can be observed by comparing TE-Cl and TE-Cl_3%, thus suggesting the preferential formation in the outer layers of inorganic species, such as sodium carbonates and chlorates. The XPS outcomes appear in line with the different properties observed in Na-Na symmetrical cells, and evidence a relevant dependence of the SEI composition on the electrolyte formulation which is expected to affect the electrochemical performance of Na–S cells.

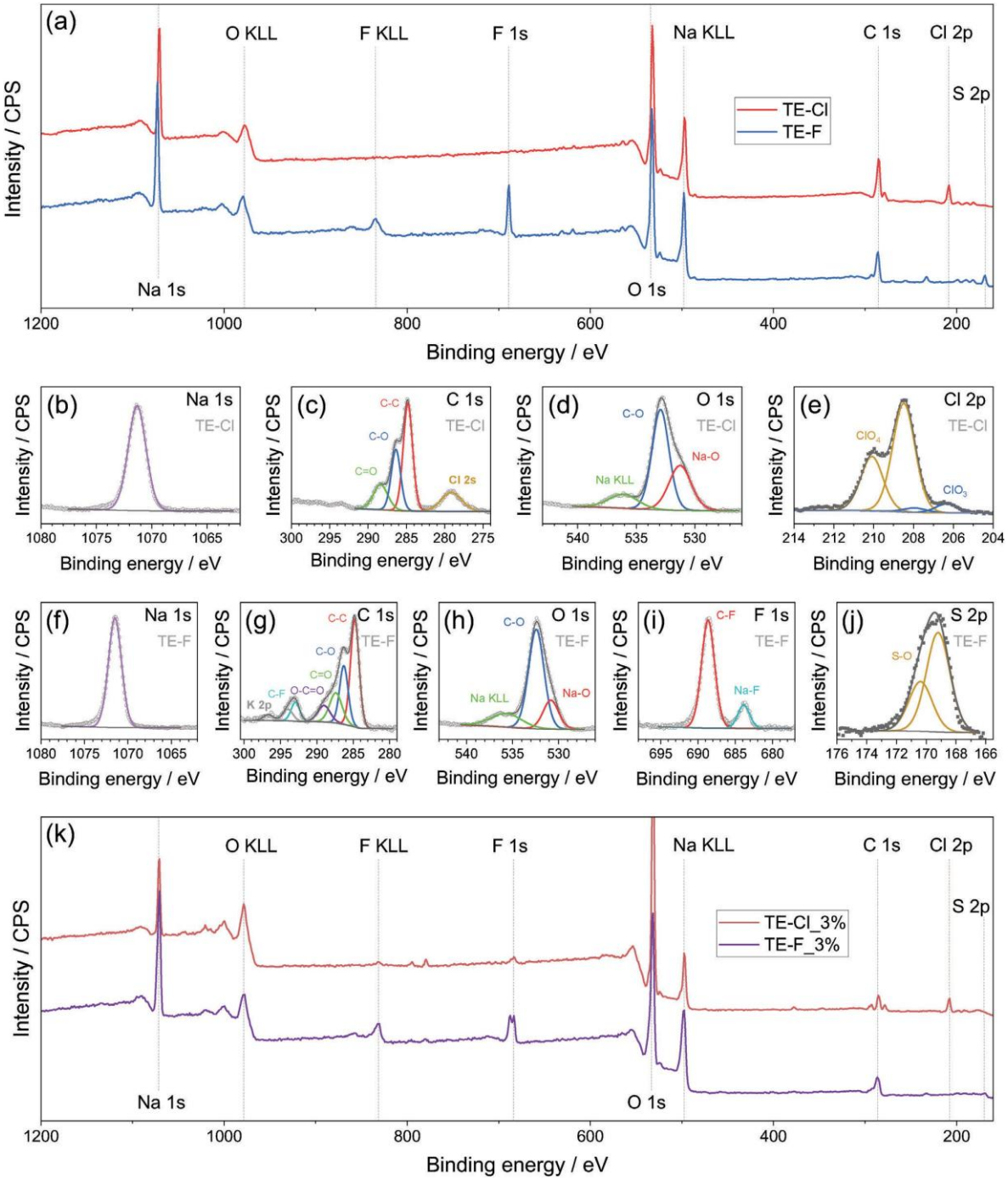

Figure 4. XPS analyses of sodium electrodes retrieved from Na|Na cells using TE-Cl, TE-F, TE-Cl_3% or TE-F_3%. In detail: **(a)** survey spectra related to TE-Cl and TE-F; b–e) high-resolution spectra recorded in **(b)** Na 1s, **(c)** C 1s, **(d)** O 1s and **(e)** Cl 2p regions for TE-Cl; **(f–j)** high-resolution spectra recorded in **(f)** Na 1s, **(g)** C 1s, **(h)** O 1s, **(i)** F 1s and **(j)** S 2p regions for TE-F; **(k)** survey spectra related to TE-Cl_3% and TE-F_3%. See Table 3.3.1 for electrolyte acronyms.

Table 3.3.3. Atomic percent compositions recorded through XPS on the surface of Na samples collected from Na-cells using either TE-Cl, TE-F, TE-Cl_3% or TE-F_3%. See Figure 4 for related XPS spectra, the Experimental section for sodium treatment, and Table 3.3.1 for electrolyte acronyms.

Electrolyte	Na [%]	C [%]	O [%]	Cl [%]	F [%]	S [%]
TE-Cl	11.2	41.5	41.6	5.7	0	0
TE-F	14.8	31.0	40.5	0	10.6	3.1
TE-Cl_3%	7.4	15.2	71.4	3.9	2.1	0
TE-F_3%	15.2	30.3	41.9	0	10.8	1.7

The two electrolyte sets are hereafter tested in Na–S cells at the constant current rate of C/20 (1C = 1675 mA g^{-1}) between 1.4 and 2.6 V as reported in **Figures 5** (TE-Cl set) **and 6** (TE-F set) using a sulfur-Super P carbon black (S:SPC) 70:30 w/w cathodic composite cast on bare aluminum. **Figure 5a** shows the voltage-time profile during the first cycle of Na–S cells using the TE-Cl set, and indicates remarkable differences promoted by the FEC addition to the electrolyte. Hence, the voltage of the cell using the bare TE-Cl shows two discharge plateaus at 2.25 and 1.72 V with slopes accounting respectively for the formation of high-order polysulfides Na_2S_x ($4 \leq x \leq 8$) and short-order ones ($2 \leq x \leq 4$) upon conversion reaction between Na and S. Subsequently, two charge steps at 1.95 and 2.32 V upon oxidation of the polysulfides are observed, the latter of which proceeds without any end until the time cut-off of 20 h adopted as protection. This behavior clearly indicates a severe polysulfide shuttle process, which is typically promoted by a poorly protected Na surface, favoring a continuous reaction of the soluble Na_2S_x species with the metal anode. On the other hand, the shuttle reaction is somehow mitigated in the second cycle (**Figure 5b**) and progressively vanishes upon several cycles (see 30th cycle in **Figure 5c**). The addition of FEC even at very low concentration almost fully hinders the shuttle reaction, and remarkably allows the completion of the charging process already at the first cycle, as shown in **Figure 5a** for the cells using TE-Cl_0.5%, TE-Cl_1%, TE-Cl_2% and TE-Cl_3%. Furthermore, the curves related to the first cycle show the occurrence of an additional discharge plateau at ≈1.95 V, the magnitude of which increases by raising the FEC content due to the electrochemical reduction of the additive. It is worth mentioning that the shape of the charge profile of the Na–S cell may also reflect a contribution of the FEC to the plateaus related to the oxidation of the polysulfides, thus possibly suggesting a role of the additive on the kinetics of the Na–S process. The second cycle (**Figure 5b**) evidences for the FEC-doped solutions a well-defined multi-step discharge/charge process, the shape of which depends on the additive content, while the TE-Cl precursor shows partial deactivation of the high-voltage discharge step. After 30 cycles (**Figure 5c**), the Na–S conversion process is almost fully hindered in the cells using TE-Cl_2% and TE-

Cl_3%, instead, the ones using TE-Cl_0.5% and TE-Cl_1% still reveal a reversible reaction with acceptable magnitude. These results, in combination with the features of the electrolytes in Na-metal cells discussed in **Figures 2 and 3**, indicate that the excessive SEI growth and consequent resistance increase for TE-Cl_2% and TE-Cl_3% may limit the evolution of the Na–S electrochemical process. **Figure 5d** shows the discharge capacity and coulombic efficiency trends over cycling for the various Na–S cells discussed above. The cell using TE-Cl exhibits an initial capacity slightly below 400 mAh g^{-1}, that subsequently decreases to 200 and reaches ≈130 mAh g^{-1} at the steady state, with very modest values of the coulombic efficiency (40–60%) and final failure possibly due to dendrites formation. The low efficiency is clearly ascribed to the above-discussed shuttle process affecting the cell with the bare electrolyte (see top-side panels a, b, c in **Figure 5**), which finally leads to irregularities of the SEI promoting in principle the metal dendrites on the Na surface. On the other hand, the addition of FEC is reflected in the increase of the first cycle capacity to ≈700, 800, 900, and 1000 mAh g^{-1} for the cells with TE-Cl_0.5%, TE-Cl_1%, TE-Cl_2%, and TE-Cl_3%, respectively. This initial capacity increase is due to the contribution of the FEC redox reaction, which progressively vanishes during the subsequent cycles. Besides the side action of the additive, the Na–S cells using the doped electrolytes reveal a remarkable increase of the coulombic efficiency to values approaching 90% as the shuttle process is mitigated. The cells using TE-Cl_0.5% and TE-Cl_1% reveal suitable capacity trends with steady-state values of 180 and 240 mAh g^{-1}, respectively, despite only the latter exhibiting cycle life over 100 cycles, notable retention (238 mAh g^{-1} at the end of the test), and constant coulombic efficiency exceeding 90%. Instead, the cells using TE-Cl_2% and TE-Cl_3% show a fast drop of the discharge capacity to 40 mAh g^{-1} only after 30 cycles, despite a coulombic efficiency approaching 90%. These discrepancies may be ascribed to a less effective SEI in TE-Cl_0.5%, an excessive film growth in TE-Cl_2% and TE-Cl_3%, and possibly to an optimal condition in TE-Cl_1%. Hence, a relevant growth of the passivation layer using TE-Cl_2% and TE-Cl_3% can certainly prevent the dendrites formation, however, it may strongly increase the interphase resistance and limit the Na–S conversion process. Instead, an insufficient protection of Na due to the relatively low FEC content in TE-Cl_0.5% can promote partial polysulfide shuttle, thus decreasing the cell efficiency, leading to the loss of active material and lowering the Na–S cell capacity.

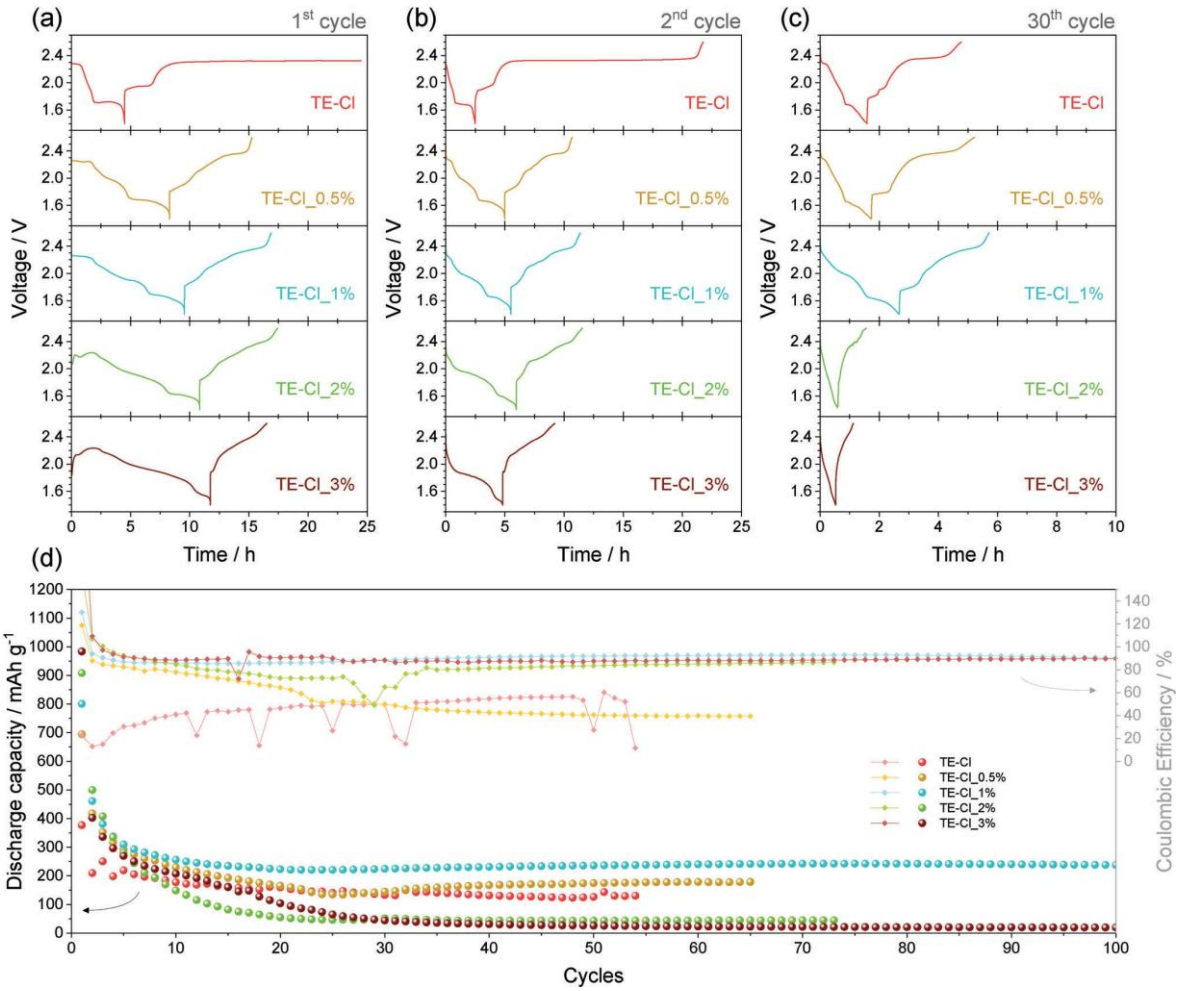

Figure 5. Galvanostatic cycling tests performed on Na–S cells using electrolytes dissolving $NaClO_4$ (see Table 3.3.1 for compositions): **(a–c)** voltage profiles versus time of the **(a)** 1st , **(b)** 2nd, and **(c)** 30th cycle, and **(d)** corresponding capacity trends versus cycle number with right y-axis reporting coulombic efficiency; constant current rate: C/20 (1C = 1675 mA gs^{-1}); voltage range: 1.4–2.6 V.

The Na–S cells using TE-F-based solutions show in **Figure 6** analog performances to those with TE-Cl-based electrolytes discussed in **Figure 5**. The cell using bare TE-F exhibits at the first cycle (**Figure 6a** top panel) the two plateaus during discharge attributed to the formation of sodium polysulfides, reversed into a double-step charge due to their electrochemical oxidation with a prolonged high-voltage plateau ascribed to the polysulfides shuttle, however less extended than the one observed for the bare TE-Cl (compare with **Figure 5a**, top panel). The latter process is in part limited during subsequent cycles upon the consolidation of the SEI (**Figure 6b,c**). The addition of FEC leads to the expected mitigation of the shuttle process and the concomitant appearance of new redox steps both in charge and in discharge (**Figure 6a**), with magnitude raising from TE-F_0.5% to TE-F_1% and TE-F_2%, despite TE-F_2% and TE-F_3% show similar first discharge. The voltage profiles during the subsequent cycles (**Figure 6b,c**) show for cells using TE-F_2% and TE-F_3% the progressive deactivation of the Na–S conversion due to

excessive passivation of Na (see **Figure 3**), while TE-F_0.5% and TE-F_1% lead to a well reversible evolution of the discharge/charge Na–S plateaus. Similarly to TE-Cl solutions, **Figure 6d** shows low efficiency and failure due to dendrite growth for the cell using bare TE-F electrolyte, with the most enhanced cycling behavior, efficiency, and capacity retention for the TE-F_0.5% and TE-F_1%, and a fast capacity decay despite the high efficiency for TE-F_2% and TE-F_3%. Also in the case of TE-F electrolyte, the addition of the FEC promotes the first cycle capacity from 400 mAh g^{-1} (TE-F) to a maximum approaching 1000 mAh g^{-1} (TE-F_2% and TE-F_3%). Furthermore, the cell using bare TE-F reveals a steady-state capacity of ≈100 mAh g^{-1} with occasional drops due to dendrites, and a columbic efficiency as low as ≈60% as the shuttle process runs, thus confirming the poor characteristics of the SEI. Meanwhile, the cells using TE-F_2% and TE-F_3% exhibit efficiency increased between 80 and 90%, however with rapid capacity decrease suggesting the hindering of the reaction between Na and S due to a sluggish electrode/electrolyte interphase. Relevantly, TE-F_0.5% and TE-F_1% show cycle life extended over 100 cycles, with steady-state capacity of 220 and 260 mAh g^{-1}, respectively, and coulombic efficiency exceeding 80%. It is worth mentioning that the efficiency of the latter cells decreases to values between 60 and 70% at the end of the test possibly due to a partial dissolution of the SEI at the Na surface. Hence, the cell using TE-F_0.5% (**Figure 6d**) reveals a longer cycle life with respect to the one using TE-Cl_0.5% (**Figure 5d**), thus suggesting a more stable interphase in the former than in the latter, which is possibly promoted by an optimized interplay between the FEC additive and $NaCF_3SO_3$ salt compared to $NaClO_4$ one in this specific concentration. On the other hand, the slightly enhanced capacity of TE-F_1% (**Figure 6d**) with respect to TE-Cl_1% (**Figure 5d**) associated with a lower coulombic efficiency indicates for the Na–S cell using the former electrolyte a less resistive but more soluble SEI, in line with the electrolytes' properties studied in **Figures 1 and 2**. Therefore, the data recorded in **Figures 5 and 6** indicate the addition of 1% of FEC to the TE-Cl and TE-F as the most suitable condition to achieve, at the same time, long cycle life, enhanced capacity, and acceptable coulombic efficiency of the Na–S cell.

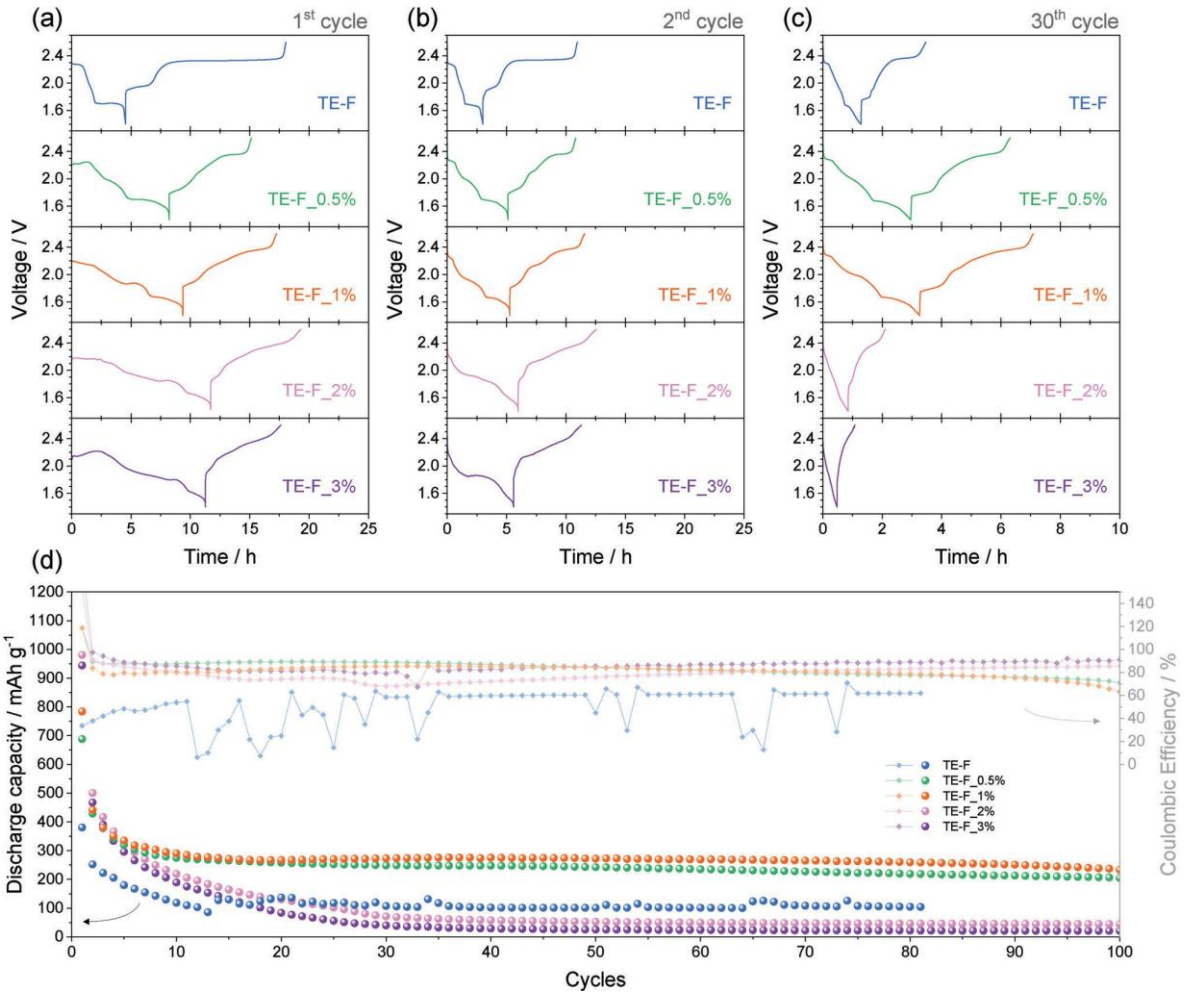

Figure 6. Galvanostatic cycling tests performed on Na–S cells using electrolytes dissolving $NaCF_3SO_3$ (see Table 3.3.1 for compositions): **(a–c)** voltage profiles versus time of the **(a)** 1st, **(b)** 2nd, and **(c)** 30th cycle, and **(d)** corresponding capacity trend versus cycle number with right *y*-axis reporting coulombic efficiency; constant current rate: C/20 (1C = 1675 mA g_S^{-1}); voltage range: 1.4–2.6 V.

References

(1) C. P. Grey, D. S. Hall, Nat. Commun. 2020, 11, 6279.
(2) D. Di Lecce, R. Verrelli, J. Hassoun, Green Chem. 2017, 12, 3442.
(3) S. T. Myung, F. Maglia, K. J. Park, C. S. Yoon, P. Lamp, S. J. Kim, Y. K. Sun, ACS Energy Lett. 2017, 2, 196.
(4) J. Wang, L. Liao, H. R. Lee, F. Shi, W. Huang, J. Zhao, A. Pei, J. Tang, X. Zheng, W. Chen, Y. Cui, Nano Energy 2019, 61, 404.
(5) G. Calvo, A. Valero, Environ. Dev 2022, 41, 100640.
(6) A. Valero, A. Valero, G. Calvo, A. Ortego, Renew. Sustain. Energy Rev. 2018, 23, 178.
(7) D. Kundu, E. Talaie, V. Duffort, L. F. Nazar, Angew. Chem., Int. Ed. 2015, 54, 3431.
(8) J. Y. Hwang, S. T. Myung, Y. K. Sun, Chem. Soc. Rev. 2017, 46, 3529.
(9) X. Dou, I. Hasa, D. Saurel, C. Vaalma, L. Wu, D. Buchholz, D. Bresser, S. Komaba, S. Passerini, Mater. Today 2019, 23, 87.
(10) Z. Yan, L. Zhao, Y. Wang, Z. Zhu, S. Chou, Adv. Funct. Mater. 2022, 32, 2205622.
(11) Y. Wang, B. Zhang, W. Lai, Y. Xu, S. Chou, H. Liu, S. Dou, Adv. Energy Mater. 2017, 7, 1602829.
(12) X. Yu, A. Manthiram, ChemElectroChem 2014, 1, 1275.
(13) C. Ye, Y. Jiao, D. Chao, T. Ling, J. Shan, B. Zhang, Q. Gu, K. Davey, H. Wang, S. Qiao, Adv. Mater. 2020, 32, 1907557.

(14) S. Xin, Y. X. Yin, Y. G. Guo, L. J. Wan, Adv. Mater. 2014, 26, 1261.
(15) Q. Guo, S. Sun, K. Kim, H. Zhang, X. Liu, C. Yan, H. Xia, Carbon Energy 2021, 3, 440.
(16) J. Mou, T. Liu, Y. Li, W. Zhang, M. Li, Y. Xu, J. Huang, M. Liu, J. Mater. Chem. A 2020, 8, 24590.
(17) W. Lai, H. Wang, L. Zheng, Q. Jiang, Z. Yan, L. Wang, H. Yoshikawa, D. Matsumura, Q. Sun, Y. Wang, Q. Gu, J. Wang, H. Liu, S. Chou, S. Dou, Angew. Chem. Int. Ed. 2020, 52, 22171.
(18) C. Ye, H. Jin, J. Shan, Y. Jiao, H. Li, Q. Gu, K. Davey, H. Wang, S. Z. Qiao, Nat. Commun. 2021, 12, 7195.
(19) W. Tang, W. Zhong, Y. Wu, Y. Qi, B. Guo, D. Liu, S. J. Bao, M. Xu, Chem. Eng. J. 2020, 325, 124978.
(20) D. J. Lee, J. W. Park, I. Hasa, Y. K. Sun, B. Scrosati, J. Hassoun, J. Mater. Chem. A 2013, 1, 5256.
(21) M. Kohl, F. Borrmann, H. Althues, S. Kaskel, Adv. Energy Mater. 2016, 6, 1502185.
(22) S. Liu, S. Tang, X. Zhang, A. Wang, Q. H. Yang, J. Luo, Nano Lett. 2017, 17, 5862.
(23) Z. Huang, S. Wang, X. Guo, J. Safaei, Y. Lei, W. Lai, X. Zhang, B. Sun, D. Shanmukaraj, M. Armand, T. Rojo, G. Wang, Adv. Mater. Technol. 2023, 8, 2202147.
(24) D. Di Lecce, L. Minnetti, D. Polidoro, V. Marangon, J. Hassoun, Ionics 2019, 25, 3129.
(25) D. Guo, J. Wang, T. Lai, G. Henkelman, A. Manthiram, Adv. Mater. 2023, 35, 230084.
(26) Y. X. Ren, H. R. Jiang, T. S. Zhao, L. Zeng, C. Xiong, J. Power Sources 2018, 326, 304.
(27) S. Wei, S. Xu, A. Agrawral, S. Choudhury, Y. Lu, Z. Tu, L. Ma, L. A. Archer, Nat. Commun. 2016, 7, 11722.
(28) J. Wu, J. Liu, Z. Lu, K. Lin, Y. Q. Lyu, B. Li, F. Ciucci, J. K. Kim, Energy Storage Mater. 2019, 23, 8.
(29) J. Ma, M. Wang, H. Zhang, Z. Shang, L. Fu, W. Zhang, B. Song, K. Lu, Adv. Funct. Mater. 2023, 33, 2214430.
(30) Z. W. Seh, J. Sun, Y. Sun, Y. Cui, ACS Cent. Sci. 2015, 1, 449.
(31) L. Lutz, D. Alves Dalla Corte, M. Tang, E. Salager, M. Deschamps, A. Grimaud, L. Johnson, P. G. Bruce, J. M. Tarascon, Chem. Mater. 2017, 22, 6066.
(32) S. Sarkar, M. J. Lefler, B. S. Vishnugopi, R. B. Nuwayhid, C. T. Love, R. Carter, P. P. Mukherjee, Cell Rep. Phys. Sci. 2023, 4, 101356.
(33) C. Li, H. Xu, L. Ni, B. Qin, Y. Ma, H. Jiang, G. Xu, J. Zhao, G. Cui, Adv. Energy Mater. 2023, 13, 2301758.
(34) X. Zhang, S. Zhang, J. Lu, F. Tang, K. Dong, Z. Yu, A. Hilger, M. Osenberg, H. Markötter, F. Wilde, S. Zhang, J. Zhao, G. Xu, I. Manke, F. Sun, G. Cui, Adv. Funct. Mater. 2024, 2402253.
(35) B. Qin, Y. Ma, C. Li, H. Xu, J. Li, B. Xie, X. Du, S. Dong, G. Xu, G. Cui, Energy Storage Mater. 2023, 61, 102891.
(36) H. Xu, C. Li, L. Ni, X. Du, B. Xie, J. Wang, Z. Cui, L. Du, W. Deng, J. Zhao, J. Ju, G. Xu, G. Cui, Energy Storage Mater. 2024, 70, 103445.
(37) L. Carbone, S. Munoz, M. Gobet, M. Devany, S. Greenbaum, J. Hassoun, Electrochim. Acta 2017, 231, 223.
(38) A. Ghosh, A. Kumar, A. Roy, M. R. Panda, M. Kar, D. R. MacFarlane, S. Mitra, ACS Appl. Mater. Interfaces 2019, 11, 14101.
(39) Y. Lee, J. Lee, J. Lee, K. Kim, A. Cha, S. Kang, T. Wi, S. J. Kang, H. W. Lee, N. S. Choi, ACS Appl. Mater. Interfaces 2018, 10, 15270.
(40) A. Nimkar, N. Shpigel, F. Malchik, S. Bublil, T. Fan, T. R. Penki, M. N. Tsubery, D. Aurbach, ACS Appl. Mater. Interfaces 2021, 13, 46478.
(41) D. Di Lecce, V. Marangon, H. G. Jung, Y. Tominaga, S. Greenbaum, J. Hassoun, Green Chem. 2022, 24, 1021.
(42) Y. Ugata, K. Shigenobu, R. Tatara, K. Ueno, M. Watanabe, K. Dokko, Phys. Chem. Chem. Phys. 2021, 23, 21419.
(43) R. Tatara, Y. Okamoto, Y. Ugata, K. Ueno, M. Watanabe, K. Dokko, Electrochemistry 2021, 82, 590.
(44) Z. Tian, Y. Zou, G. Liu, Y. Wang, J. Yin, J. Ming, H. N. Alshareef, Adv. Sci. 2022, 2, 2201207.
(45) B. Boukamp, Solid State Ion 1986, 20, 31.

(46) B. Boukamp, Solid State Ion 1986, 18–12, 136.
(47) V. Marangon, Y. Tominaga, J. Hassoun, J. Power Sources 2020, 442, 227508.
(48) J. Evans, C. A. Vincent, P. G. Bruce, Polymer (Guildf) 1987, 28, 2324.
(49) D. Morales, R. E. Ruther, J. Nanda, S. Greenbaum, Electrochim. Acta 2019, 304, 239.
(50) L. G. Chagas, S. Jeong, I. Hasa, S. Passerini, ACS Appl. Mater. Inter- faces 2019, 11, 22278.
(51) D. Di Lecce, D. Campanella, J. Hassoun, J. Phys. Chem. C 2018, 122, 23925.
(52) Y. Fang, J. Zhang, L. Xiao, X. Ai, Y. Cao, H. Yang, Adv. Sci. 2017, 4, 1600392.
(53) V. H. Nguyen, M. Le Nguyen, H. P. Tran, V. M. Tran, N. T. Tran, M. L. P. Le, J. Solid State Electrochem. 2021, 25, 767.
(54) H. Ryu, T. Kim, K. Kim, J. H. Ahn, T. Nam, G. Wang, H. J. Ahn, J. Power Sources 2011, 126, 5186.
(55) A. Kumar, A. Ghosh, A. Ghosh, A. Ahuja, A. Sengupta, M. Forsyth, D. R. MacFarlane, S. Mitra, Energy Storage Mater. 2021, 42, 608.
(56) E. Park, J. Park, K. Lee, Y. Zhao, T. Zhou, G. Park, M. G. Jeong, M. Choi, D. J. Yoo, H. G. Jung, A. Coskun, J. W. Choi, ACS Energy Lett. 2023, 8, 179. (57) K. Westman, R. Dugas, P. Jankowski, W. Wieczorek, G. Gachot, M. Morcrette, E. Irisarri, A. Ponrouch, M. R. Palacín, J. M. Tarascon, P. Johansson, ACS Appl. Energy Mater. 2018, 1, 2671.
(58) Y. Liu, R. Jiang, H. Xiang, Z. Huang, Y. Yu, Electrochim. Acta 2022, 425, 140746.
(59) J. Ma, X. Feng, Y. Wu, Y. Wang, P. Liu, K. Shang, H. Jiang, X. Hou, D. Mitlin, H. Xiang, J. Energy Chem. 2023, 77, 290.
(60) L. O. Vogt, M. El Kazzi, E. Jämstorp Berg, S. Pérez Villar, P. Novák, C. Villevieille, Chem. Mater. 2015, 27, 1210.
(61) Q. Ren, Q. Wang, L. Su, G. Liu, Y. Song, X. Shangguan, F. Li, J. Mater. Chem. A 2024, 12, 1072.
(62) N. C. Su, S. A. M. Noor, M. F. Roslee, N. S. Mohamed, A. Ahmad, M. Z. A. Yahya, Ionics 2019, 25, 541.
(63) Y. L. Ni'mah, M. Y. Cheng, J. H. Cheng, J. Rick, B. J. Hwang, J. Power Sources 2015, 278, 375.
(64) V. Marangon, E. Barcaro, E. Scaduti, F. Adami, F. Bonaccorso, V. Pellegrini, J. Hassoun, ACS Appl. Energy Mater. 2023, 6, 11560.
(65) I. A. Profatilova, C. Stock, A. Schmitz, S. Passerini, M. Winter, J. Power Sources 2013, 222, 140.
(66) E. Markevich, G. Salitra, M. Afri, Y. Talyosef, D. Aurbach, J. Elec- trochem. Soc. 2020, 167, 070509.
(67) H. Kuwata, H. Sonoki, M. Matsui, Y. Matsuda, N. Imanishi, Electro- chemistry 2016, 84, 854.
(68) G. G. Eshetu, T. Diemant, M. Hekmatfar, S. Grugeon, R. J. Behm, S. Laruelle, M. Armand, S. Passerini, Nano Energy 2019, 55, 327.
(69) D. Di Lecce, V. Marangon, M. Isaacs, R. Palgrave, P. R. Shearing, J. Hassoun, Small Methods 2021, 5, 2100596.
(70) S. Kim, Y. Jung, J. Park, M. Hong, H. R. Byon, Bull. Korean Chem. Soc. 2021, 42, 1519.
(71) A. V. Naumkin, A. Kraut-Vass, S. W. Gaarenstroom, C. J. Powell, "NIST X-ray Photoelectron Spectroscopy Database, NIST Standard Reference Database Number 20, National Institute of Standards and Technology, Gaithersburg MD, 20899 (2000)"
(72) E. Sahadeo, J. Song, K. Gaskell, N. Kim, G. Rubloff, S. B. Lee, Phys. Chem. Chem. Phys. 2018, 20, 2517.
(73) S. Kondou, Y. Sakashita, A. Morinaga, Y. Katayama, K. Dokko, M. Watanabe, K. Ueno, ACS Appl. Mater. Interfaces 2023, 15, 11741

Chapter 4.

Na-ion battery

4.1 On the anode choice

Na-ion battery so far appeared as the less expensive and more accessible analogue of the most widely diffused Li-ion one, based on the ions exchange by a rocking-chair mechanism .[1,2] However, the exploitation of such an intriguing reaction, which can efficiently move the lithium ions from cathode to anode for storing energy and back to get power, appeared relevantly more complex in the sodium environment than lithium (3,4). Indeed, one of the most diffused and efficient cathodes for Na-cell is represented by the transition-metal layered oxide that can be sodium deficient or sodium rich, with O2, P2, P3 or P3' structures. [5-10] This variety of configurations typically requires a sodium metal anode to compensate the alkali metal content into the cathode structure. [11] On the other side, olivine-type electrodes have represented so far the cheapest, still well-performing, cathode for actual application in Li-ion batteries due to the modest economic and environmental impact. [12,13] However, the synthetic pathways for achieving the sodium analogue of these electrodes typically lead to the predominant formation of the electrochemically inactive maricite structure instead of the olivine triphylite one.[14-16] Hence, electrochemical de-lithiation from Li-based olivines can be used for removing the alkali metal from the polyanionic framework, to finally get a version of the cathode host framework, which can operate reversibly when coupled in sodium metal battery.[17] Therefore, a balanced Na-ion battery using at the cathode side either layered oxides or electrochemically converted olivines mandatory foresees the adequate pre-storing of Na reservoir in anodes, in analogy to what already adopted for Li-ion cells, in particular using the Li-alloying electrodes.[18-21] Among the alloying materials suitable for this activation process, Si, Sn and Sb revealed the most promising features both in lithium[22-28] and in sodium batteries.[29-35] The study of pre-sodiation of both cathode and anode acquired relevant importance for Na-ion batteries, due to the above mentioned sodium deficiency at the cathode side and initial irreversibility due to solid electrolyte interphase (SEI) formation at the anode side.[36] In these regards, different strategies have been adopted for the pre-sodiation of electrodes, including electrochemical activation of anode and cathode ,[16,36,37] chemical or mechanochemical treatments,[38-40] as well as the use of sacrificial Na salts as the additives.[41-43] Relevantly, the high conductivity of metallic Sn and Sb can allow either the typical electrochemical sodiation by charging/discharging in half cell to retrieve the electrode for full-cell application,[27] or a more scalable and appealing pathway in which the Na-metal alloy is directly achieved by mechanochemical treatments.[44]

Chemical approach to achieve sodiated alloying anode for direct application in Na-ion battery

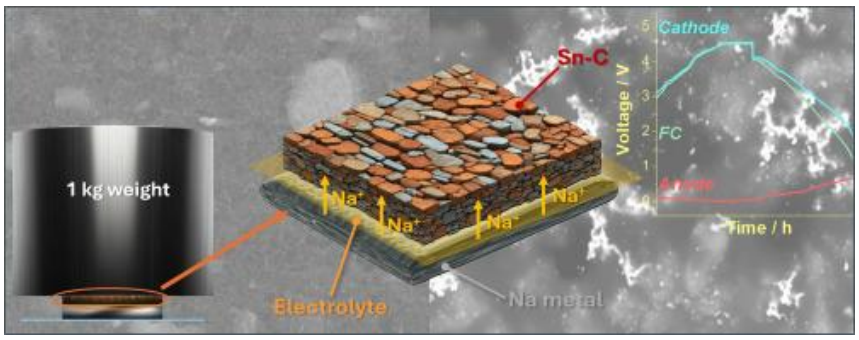

Experimental

Sn-C was synthetized as reported in literature.[45] In brief, resorcinol was mixed with formaldehyde and sodium carbonate as catalyst to obtain a dark orange hydrogel, which was aged, ground, washed with water and then immersed in tert-butyl alcohol and filtered. Afterwards, the particles were mixed overnight with the organometallic tin source tributylphenyltin (TBPT), recovered, placed in an oven under Ar-H_2 flux, and heated at 700 °C for 2 h. NCAM was synthetized through a co-precipitation method, according to previous works,[46] by dissolving nitrate precursors of Al, Co, Ni, and Mn in deionized water to obtain a solution with a Al/Co/Ni/Mn molar ratio of 1:2:2:4.5. The corresponding hydroxide was precipitated from the solution using NaOH, filtered, washed with deionized water, and dried. This precursor was mixed with NaOH in 1:1 molar ratio, calcinated at 500 °C, grinded, pelletized, calcinated again at 1000 °C in a dry air flow, rinsed with deionized water, and dried under vacuum at 100 °C overnight. The electrode slurries were prepared by dispersing the active material (either NCAM or Sn-C), PVdF binder, and carbon black (Super P carbon, Timcal), mixed by the 8:1:1 wt% ratio in NMP, and then stirred at room temperature until homogenization (about 2 h). The obtained slurries were cast by a doctor blade tool on either aluminum (thickness of 20 µm, MTI Corporation) for NCAM or scratched copper foils (thickness of 30 µm, MTI Corporation) for Sn-C and subsequently dried for 3 h on a hot plate at 70 °C, cut into disks of 10 mm-diameter, and dried again for 3 h at 110 °C under vacuum to remove possible traces of water and NMP solvent. Prior to vacuum drying, NCAM electrodes were pressed with a hydraulic press (Silfradent) for 30 s at 110 bar, while the SnC tape was calendared by using an MSK-2150 Rolling Machine (MTI Corp.) to achieve a thickness within the range of 100−110 µm. Carbon/PVdF electrodes coated on scratched Cu foil, labelled SPC-Cu, were prepared to determine the electrolyte cathodic stability. These single bond SPC-Cu electrodes were achieved by doctor blade casting procedure described above, using carbon black (Super P carbon, Timecal) and PVdF binder in the 80:20 wt. % ratio, cut into 10 mm disks, and dried at 110 °C for 3 h under vacuum. Sn-C electrodes were sodiated via capillary contact between the material and sodium metal inside an Ar-filled glove box: the Sn-C electrode was placed in contact with a sodium metal disk wetted with a 1 M solution of sodium perchlorate ($NaClO_4$) dissolved in propylene carbonate (PC, battery grade, Sigma-Aldrich) with 3 % in weight of fluoroethylene carbonate (FEC, battery grade, Solvionic) and placed in between two Petri dishes. Subsequently, a 1 kg weight was stacked on the electrode and the system was allowed to chemically react

until the target time was reached (1 h, 2 h, 6 h, 10 h, and14 h). The final active material loading of Sn-C electrodes employed in the capillary sodiation studies was about 2.0 mg cm^{-2}, as normalized to the electrode geometric area (0.785 cm^2). It is worth mentioning that the activation time of the Sn-C electrodes in this work may be subjected to ad hoc modulation according to the active material loading, pressure, electrode, and electrolyte composition adopted during the process. Two-electrode Swagelok T-type sodium half-cells were assembled by stacking a 10mm-diameter working electrode (either pristine or sodiated Sn-C anode, or NCAM cathode), a 10mm-diameter sodium metal disk (Sigma Aldrich, 99 %) as counter electrode, and a 10 mm-diameter glass fiber (Whatman GF/B) disk as separator. A three-electrode Swagelok T-type sodium cell was prepared using a 10 mm-diameter SPC-Cu working electrode, a 10 mm-diameter sodium metal counter electrode, a 10 mm-diameter glass fiber (Whatman GF/B) disk as the separator, and an additional 10 mm sodium metal disk as reference electrode. Three-electrode Swagelok T-type full-cells were assembled by stacking a NCAM cathode, a 2 h sodiated Sn-C anode, one glass fiber (Whatman GF/B) disk as the separator, and an additional sodium metal disk as the reference electrode placed at the top side of the T-cell. Optimized setup CR2032 coin-type full-cells (MTI Corporation) were assembled by using a 10 mm-diameter NCAM cathode, a 10 mm-diameter Sn-C anode activated for 30 min, and a 16 mm-diameter glass fiber (Whatman GF/B) disk as the separator (the active material loading of the electrodes is reported in the respective figure caption whenever a full-cell is reported). All the full-cells were prepared by using negative to positive (N/P) capacity ratios of 1.1, as determined by considering mass loadings and specific capacities of the two electrodes. In every cell configuration, 1 M solution of $NaClO_4$ in PC + 3 % wt FEC was used as electrolyte. The sodiated Sn-C electrodes were used without any other treatment before assembling the cells. All cells were assembled and sealed inside an Ar-filled glovebox (MBraun, O2 and H2O content lower than 1 ppm). XRD patterns of the pristine and activated Sn-C electrodes, leaned on a glass sample holder and sealed with Kapton tape, were collected through a Bruker D8 Advance instrument using a Cu Kα source and a graphite monochromator of the diffracted beam by performing scans in the 2θ range from 27° to 47° at a rate of 4 s $step^{-1}$ with a step size of 0.02°. SEM images of the pristine and sodiated (14 h) Sn-C electrodes and EDS spectra were collected through a Zeiss Sigma 300 FE-SEM (5 keV beam) equipped with Bruker QUANTAX EDS detector. Raman spectroscopy was performed on micrometric Sn powder (< 45 μm particle size, 99.8 % trace metal basis, Sigma-Aldrich), pristine, and sodiated Sn-C electrodes, by using a Czerny-Turner spectrometer (iHR320 Horiba Scientific) equipped with a diffraction grating of 1800 grooves mm−1 and a laser source with λ = 532 mm. Before the analysis, all the electrodes, recovered after chemical process, were washed with dimethyl carbonate (DMC) solvent and dried under vacuum for 30 min. For Raman analysis all the samples were placed into a sealed sample holder in Ar atmosphere. The activated Sn-C electrodes were cycled in two-electrode Na|Sn-C half-cells at the constant current of 15 mA g^{-1} in the voltage range of 0.01 – 2.0 V for the capillary sodiation process study. Full Sn-C|NCAM coin-type cells were cycled at the constant current rate of 120 mA g_{cat}^{-1} in the following voltage ranges: 1.0 – 4.1 V, 1.0 – 4.0 V, 1.5 – 4.5 V by adopting the CCCV mode at 4.5 V until a residual current value of 12 mA g_{cat}^{-1} was reached. A rate capability test was conducted on an additional Sn-C|NCAM coin-type full-cell by increasing the current from 1 C (considered in this work as 50 mA g_{cat}^{-1} for convenience) to 2 C, 3 C, 4 C, and 5 C every 5 cycles and lowering back to 1 C after 25 cycles in the 1.0 – 4.0 V voltage range. Long-term galvanostatic cycling was conducted on the same cell at the constant current of 200 mA g_{cat}^{-1} in the 1.0 – 4.0 V voltage range, by adopting

the CCCV mode at 4.0 V until a residual current value of 50 mA g_{cat}^{-1} was reached. EIS measurements were carried out on the three-electrode Sn-C|NCAM T-type cell at the OCV condition and after 1, 8, and 10 galvanostatic cycles by superimposing an alternate voltage signal of 30 mV in the 500 kHz – 100 mHz frequency range (1 V bias voltage). The charge/discharge cycling tests were performed by a MACCOR series 4000 battery test system, while the EIS measurements were carried out by using a VersaSTAT MC Princeton Applied Research (PAR, AMETEK) instrument. All the data were recorded at room temperature (25 °C). Ex-situ SEM images of pristine and cycled Sn-C and NCAM electrodes were collected as above described.

Results

In order to minimize the relevant irreversible capacity of Na-alloying electrodes, such as in Sn-C during the first cycle, that limits their direct use in full Na-ion cell without the proper treatment,[17] we originally exploit here a strategy consisting of capillary contact between the electrode and sodium metal wet by the electrolyte, in order to obtain a chemical partial pre-sodiation. The cycling response and the structural features are reported in **Figure 1**. The related galvanostatic tests are performed at a current of 15 mA g^{-1} between 0.01 and 2.0 V on electrodes contacted with Na for various times to assess the actual chemical sodiation degree vs. contact time. **Figure 1a** shows the obtained voltage profiles as a function of the percent state of charge (SoC%). The SoC% values are calculated for each cell as the percent ratio of the first discharge (Na-alloying) capacity to the first charge (Na-dealloying) reversible capacity. Magnification of the low SoC% region is reported in the inset. The discharge capacity of the cell using the pristine Sn-C (0 h of sodiation) shows an irreversibility exceeding by 250 % the reversible value, thus indicating SoC% of 250 %. This relevant side capacity is mainly due to the concomitant electrolyte decomposition and electrode structural re-organization during first discharge, which is a characteristic of this type of electrodes.[17] As the time of contact between Na metal and Sn-C increases, the SoC% shrinks to reach 170 % for 1 h of sodiation, and less than 5 % for 14 h of sodiation, thus suggesting the gradual suppression of the irreversible capacity, and the concomitant increase of reversible Na storage into the Sn-C structure by progressive chemical alloying. This behavior is also evidenced in **Figure 1b**, which shows that the values of the first discharge capacity decrease upon chemical activation time by approximately following an exponential function (dashed line). On the other hand, the effectiveness of Na-Sn alloying is demonstrated by the XRD patterns of the sodiated Sn-C samples reported in **Figure 1c**, that reveal the gradual disappearance of the metallic Sn reflections at 2θ of 30.5°, 31.9°,43.8°, and 44.8° (reference ICSD #106072), and the concomitant formation of weak signals attributed to a Na_xSn_y alloy at 2θ between 31.5° and 35°.[17] This response well suggests the tunability of the chemical sodiation process adopted in this work for possible

application of the alloying electrode in combination with a vast array of cathodes, that may require different sodiation degree, such as layered oxides,[10] olivines,[16] and Na-conversion materials.[52]

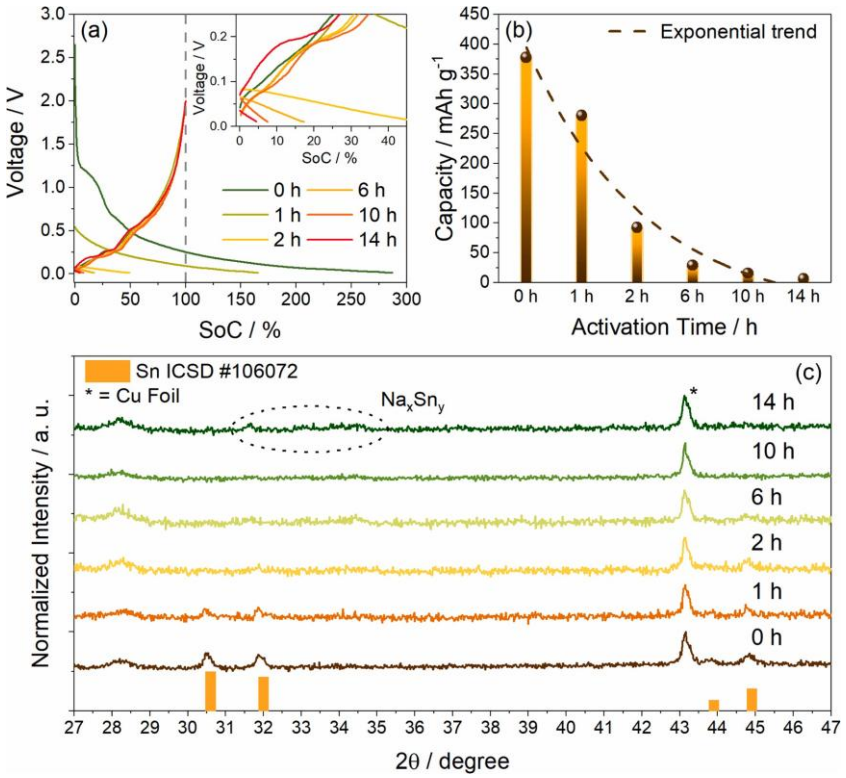

Figure 1. Electrochemical and structural characterization of Sn-C samples with different sodiation times. **(a)** Voltage profiles as a function of SoC%, corresponding to the degree of sodiation, with magnification of the low SoC% region in the inset. Tests performed by using a constant current of 15 mA g^{-1} in the 0.01 – 2.0 V voltage range. **(b)** First discharge (Na-alloying) capacity values at corresponding sodiation time with related exponential trend (dashed line). **(c)** XRD patterns of sodiated Sn-C samples compared to corresponding reference diffractogram of Sn (ICSD #106072).

Figure 2 depicts the structural and morphological changes of the Sn-C electrodes upon 14 h of sodiation described above, exploited by Raman spectroscopy and SEM/EDS. Prior to the analysis on electrodes, a Raman spectrum of micrometric Sn powder is collected in order to achieve a reference for metallic tin signals, which are centered at about 143 and 211 cm^{-1}. The Raman spectra recorded for pristine, and sodiated Sn-C (**Figure 2a**) indicate the presence of two strong bands at 1350 and 1600 cm^{-1}, due to D and G vibrations of the carbon matrix. Nevertheless, the pristine electrode (brown line) shows a weak peak around 200 cm^{-1} (indexed with asterisk) ascribed to the vibrational transition of Sn, while in the sodiated sample (green line) this peak almost vanishes. Furthermore, the magnified region between 150 and 800 cm^{-1}reveals for the sodiated sample two additional indexed peaks, possibly ascribed to residual $NaClO_4$ salt and product of the SEI formed at the Sn-C surface after the direct reaction with Na metal.[53,54] On the other hand, the SEM images at

different magnifications of the pristine Sn-C (**Figure 2b–d**) and of the sodiated one (**Figure 2i–k**) depict changes of the typical submicrometric agglomerated morphology principally occurring at the material surface. These changes are in part evidenced by the rise of bright spots, highlighted by blue circles and arrows in **Figure 2j**, likely accounting for the presence of sodium at the activated Sn-C surface. The EDS elemental maps collected on the SEM of the bare Sn-C in **Figure 2d** show the expected presence of C (**Figure 2e**) and Sn (**Figure 2f**) components of the active material, Cu (**Figure 2h**) of the support, and F (**Figure 2g**) of the polymeric binder used to form the electrode tape. Instead, F is missing in the maps collected on the SEM of the sodiated electrode of **Figure 2k** while Cu is weakened (**Figure 2o**), likely due to the surface covering by SEI. Furthermore, Na is detected (**Figure 2n**) alongside with C (**Figure 2l**) and Sn (**Figure 2m**), thus accounting for the Sn-C sodiation.

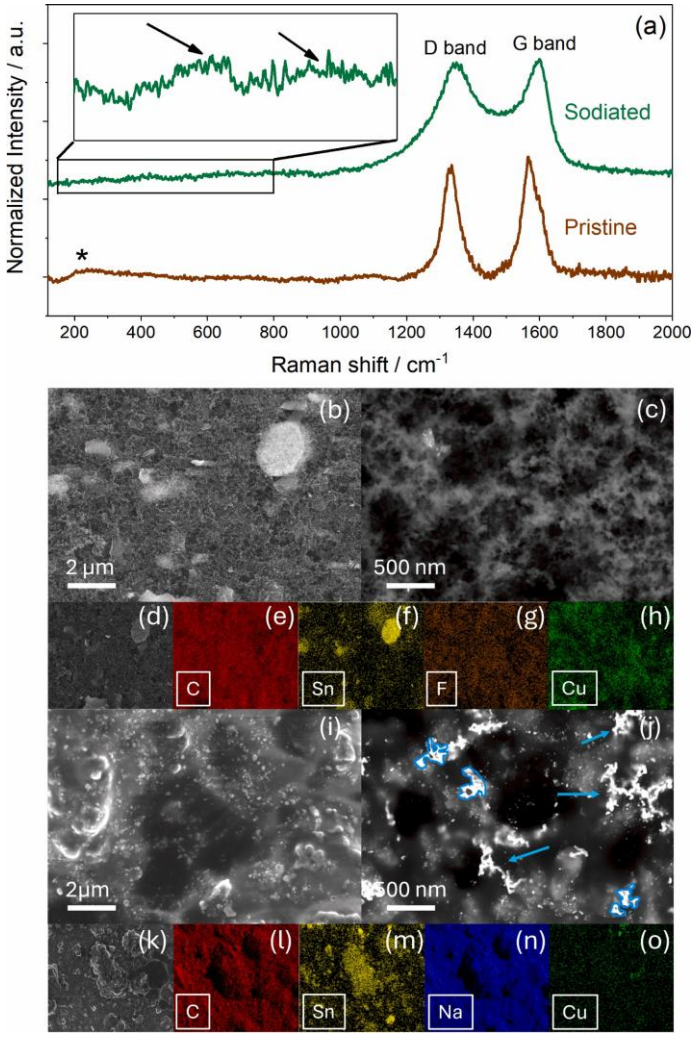

Figure 2. Characterization of the pristine and sodiated (14 h) Sn-C electrodes. **(a)** Raman spectra recorded in the 150 – 2000 cm^{-1} range. Indexed peaks identify specific transitions identifications. SEM images at different magnifications of **(b-d)** pristine and **(i-k)** sodiated electrodes. In details: **(c, j)** backscattered electrons images. SEM-EDS elemental maps of **(e, l)** C, **(f, m)** Sn, **(h, o)** Cu, **(g)** F, and **(n)** Na for **(e-h)** pristine and **(l-o)** sodiated

electrodes.

Figure 3 shows the galvanostatic cycling of three different Sn-C|NCAM full-cells at a constant current increased up to 120 mA g^{-1} instead of 15 mA g_{cat}^{-1} (**Figure 3**), and within various voltage setups adopted to limit the electrolyte decomposition and increase the cell efficiency and cycle life. **Figure 3a–c** shows the voltage profiles of the cells cycled in the 1.5 – 4.5 V with an additional constant voltage step at 4.5 V until a current value of 12 mA g^{-1} is reached (CCCV mode), 1.0 – 4.1 V, and 1.0 – 4.0 V voltage ranges, respectively, while **Figure 3d** depicts the cycling trends and coulombic efficiency of the three cells. It is worth noting that a 30 min activation rather than a longer step, such as that previously adopted for the preliminary full-cell, is carried out on the Sn-C anode due to the loading effect on the activation time already mentioned. The voltage profiles of the three cells reveal the combination of anode and cathode features, with the partial de-sodiation of Na-deficient NCAM and of the concomitant sodiation of Sn-C. The cell cycled up to 4.5 V (**Figure 3a**) presents the higher maximum capacity of about 130 mAh g^{-1}, despite a low coulombic efficiency under 95 % in the initial cycles which decreases to 75 % after 100 cycles, leading to a rapid capacity fade to 20 mAh g^{-1} already after 50 cycles (green dots in **Figure 3d**). This behavior may be ascribed to the above-mentioned parasitic reactions of the electrolyte at low potential at the anode side, which can reach value approaching 0 V as triggered by the relatively high voltage of the full cell and the CCCV mode.[53] To limit this drawback, the CCCV mode is avoided and the upper voltage cut-off lowered to 4.1 V (**Figure 3b**), and subsequently to 4.0 V (**Figure 3c**). The corresponding cells reveal a lower maximum capacity of about 110 mAh g^{-1} and 101 mAh g^{-1}, respectively, compared to the one cycled at a higher cutoff, however with an increase of coulombic efficiency and stability. Indeed, both cells show a coulombic efficiency higher than 98 % for the whole test, with a capacity retention of 48 % for the cell up to 4.1 V (orange dots in **Figure 3d**) and of 57 % for the cell up to 4.0 V (blue dots in **Figure 3d**). Therefore, the obtained results suggest the narrowing of the voltage window and the use of high current rates as suitable setup to limit the parasitic reactions and increase the efficiency and stability of the resulting full-cell.

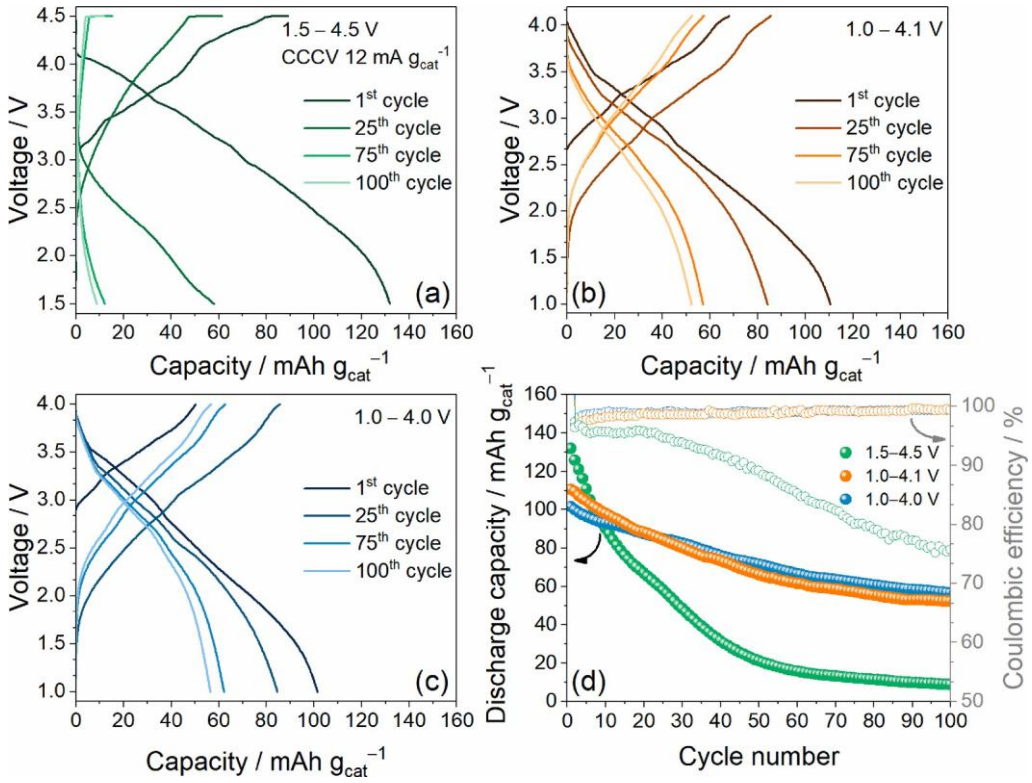

Figure 3. Galvanostatic cycling tests of Sn-C|NCAM full-cells adopting different voltage ranges at the constant current rate of 120 mA g^{-1}. In detail: **(a-c)** selected voltage profiles, and **(d)** discharge capacity trends reporting coulombic efficiencies on right-hand side y-axis. Voltage ranges: 1.5 – 4.5 V with an additional constant voltage step at 4.5 V (CCCV mode) until a final current of 12 mA g^{-1} (green); 1.0 – 4.1 V (orange); 1.0 – 4.0 V (blue). Electrodes loading (NCAM and Sn-C, respectively): 3.73 mg cm^{-2} and 5.53 mg cm^{-2} (green), 2.0 mg cm^{-2} and 4.0 mg cm^{-2} (orange), 2.1 mg cm^{-2} and 3.4 mg cm^{-2} (blue). Sn-C activated for 30 min timeframe.

The galvanostatic performance of the optimized Sn-C|NCAM full-cell are reported in **Figure 4**. Initially, the rate capability of the cell is evaluated in terms of voltage profiles (**Figure 4a**) and the cycling trend (**Figure 4b**) by increasing the current from 1 C to 5 C (1 C = 50 mA g^{-1}) in the 1.0 – 4.0 V voltage range, which is the one providing the best performance in **Figure 3**. The profiles of **Figure 4a** suggest an increase of the ohmic polarization by raising the current which leads to the decrease of capacity from 120 mAh g^{-1} at 1 C to a still relevant value of 80 mAh g^{-1} at 5 C. On the other hand, the cycling trend of **Figure 4b** depicts that the initial capacity is almost completely recovered by decreasing the current back to 1 C (~ 108 mAh g^{-1}) after the whole test, and that the increase of the current raises the coulombic efficiency over 98 % since the parasitic reactions are mitigated as mentioned above.[38, 39] This aspect suggests again the use of high current instead of the low one to trigger the capacity retention of the full-cell.[40] Nevertheless, the trend of **Figure 4b** suggests a good rate capability and stability of the optimized cell configuration upon the stress caused by raising the currents.

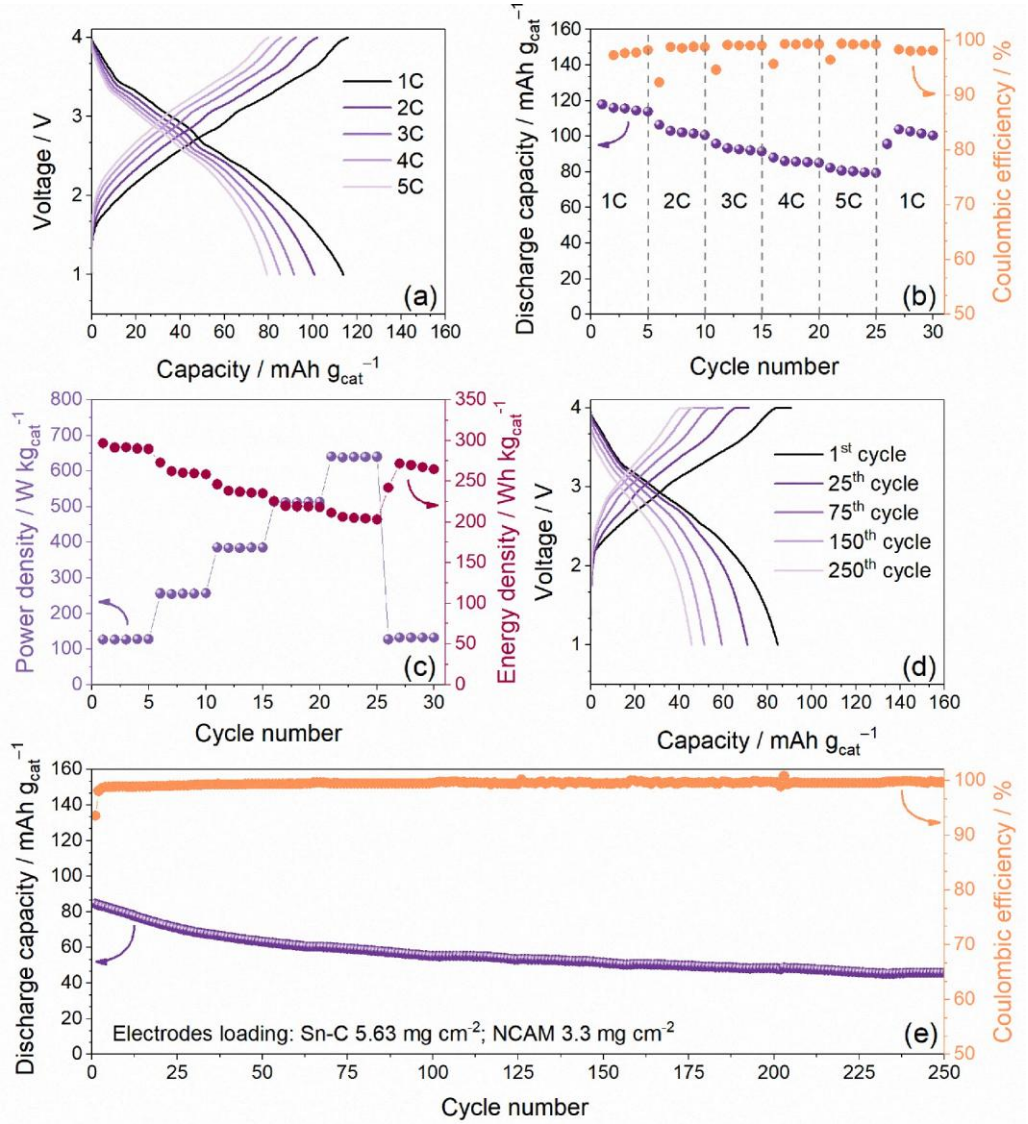

Figure 4. Electrochemical performance of optimized Sn-C|NCAM full-cell. Rate capability test in terms of **(a)** selected voltage profiles (5th for each current rate) and **(b)** discharge capacity trend reporting coulombic efficiencies on right-hand side y-axis (1C = 50 mA g^{-1}). Voltage range 1.0 – 4.0 V. **(c)** Trend of power density and energy density obtained from the rate capability test results. Long-term cycling test at the constant current of 200 mA g^{-1} in terms of (d) selected voltage profiles and **(e)** discharge capacity trend reporting coulombic efficiencies on right-hand side y-axis started after the rate capability test. Voltage range 1.0 – 4.0 V with an additional constant voltage step at 4.0 V (CCCV mode) until a final current of 50 mA g^{-1}. Sn-C activated for 30 min timeframe.

Gravimetric energy density and power density (**Figure 4c**) are calculated from the rate capability test integrating the capacity or the current as a function of the cell voltage, respectively, and normalizing by the mass of the cathode active material (the average discharge voltage was employed for the power density). The cell reveals an initial energy density at 1 C of about 300 Wh kg$_{cat}^{-1}$, which decreases as the current increases, whilst the power density raises concomitantly to reach a maximum value of about 650 W kg$_{cat}^{-1}$ at 5C.

These high values can actually reflect lower, but still relevant, gravimetric energy and power densities of the entire Na-ion battery, as normalized to the whole mass including anode, electrolyte, and other inactive components (e.g. current collectors, separator, cell casing). Relevantly, our full-cell holds the promising energy density of 205 Wh kg_{cat}^{-1} even at a current as high as 250 mA g^{-1}. These outcomes suggest the use of the chemically sodiated alloying Sn-C anode to improve the energy density of the Na-ion full-cell. With the aim of further studying the lifespan, a long term cycling test of the Sn-C|NCAM full-cell is carried out at the constant current rate of 200 mA g^{-1} in the 1.0 – 4.0 V voltage range, with an additional constant voltage step at 4.0 V until a final current of 50 mA g^{-1}. The voltage profiles (**Figure 4d**) show the well-defined combination of anode and cathode features, and a maximum capacity of 85 mAh g^{-1}, in agreement with the rate capability test. The cell also depicts a coulombic efficiency approaching 100 % after initial cycles, and a capacity retention of 55 % after 250 charge/discharge runs (**Figure 4e**), thus confirming the key role of the electrolyte stability and the anode chemical activation to get a relevant performance of the Na-ion full-cell. Eventual scale-up of the system could rely on roll-to-roll systems, as already suggested in literature work illustrating similar procedures in Li-ion systems.[41,42] Yet, this strategy should target maximum safety, thus relying on nonflammable and not hazardous solvents. Future studies will cover this aspect.

References

(1) B. Scrosati, J. Garche, J. Power Sources 195 (2010) 2419–2430.
(2) D. Di Lecce, R. Verrelli, J. Hassoun, Green Chem. 19 (2017) 3442–3467.
(3) N. Yabuuchi, K. Kubota, M. Dahbi, S. Komaba, Chem. Rev. 114 (2014) 11636–11682.
(4) I. Hasa, J. Hassoun, S. Passerini, , Nano Res. 10 (2017) 3942–3969.
(5) K. Kubota, N. Yabuuchi, H. Yoshida, M. Dahbi, S. Komaba, MRS Bull. 39 (2014) 416–422.
(6) S. Komaba, N. Yabuuchi, T. Nakayama, A. Ogata, T. Ishikawa, I. Nakai Inorg. Chem. 51 (2012) 6211–6220.
(7) N. Yabuuchi, R. Hara, M. Kajiyama, K. Kubota, T. Ishigaki, A. Hoshikawa, S. Komaba, , Adv. Energy Mater. 4 (2014) 1301453.
(8) H. Yoshida, N. Yabuuchi, K. Kubota, I. Ikeuchi, A. Garsuch, M. Schulz-Dobrick, S. Komaba, Chem. Comm. 50 (2014) 3677–3680.
(9) M.H. Han, E. Gonzalo, G. Singh, T. Rojo, Energy Environ. Sci. 8 (2015), 81-102
(10) D. Di Lecce, D. Campanella, J. Hassoun J. Phys. Chem. C 122 (2018) 23925–23933.
(11) D. Di Lecce, S. Levchenko, F. Iacoviello, D.J.L. Brett, P.R. Shearing, J. Hassoun, ChemSusChem. 12 (2019) 3550–3561.
(12) Y.M. Xin, Int. J. Electrochem. Sci. 16 (6) (2021) 210655.
(13) V. Marangon, L. Minnetti, E. Barcaro, Chem. Eur. J. 29 (2023) e202301345.
(14) C. Tealdi, J. Heath, M.S. Islam, J. Mater. Chem. A Mater. 4 (2016) 6998–7004.
(15) S. Qiao, Int. J. Electrochem. Sci. 14 (2019) 11616–11629.
(16) L. Minnetti, L. Sbrascini, A. Staffolani, V. Marangon, F. Nobili, J. Hassoun,
(17) I. Hasa, J. Hassoun, Y.K. Sun, B. Scrosati, Chemphyschem. 15 (2014) 2152–2155.
(18) M. Marinaro, M. Weinberger, M. Wohlfahrt-Mehrens, Electrochim. Acta 206 (2016) 99–107.
(19) E. Barcaro, V. Marangon, M. Mutarelli, J. Hassoun,. Power Sources 595 (2024) 234059.

(20) M. Haruta, T. Moriyasu, A. Tomita, T. Takenaka, T. Doi, M. Inaba, J. Electrochem. Soc. 165 (2018) A1874–A1879.
(21) L. Minnetti, V. Marangon, P. Andreotti, A. Staffolani, F. Nobili, J. Hassoun, Electrochim. Acta 452 (2023) 142263.
(22) A.R. Kamali, D.J. Fray, Rev. Adv. Mater. Sci. 27 (2011) 14–24.
(23) S.M. Oh, S.T. Myung, M.W. Jang, B. Scrosati, J. Hassoun, Y.K. Sun, Phys. Chem. Chem. Phys. 15 (2013) 3827.
(24) C.M. Park, S. Yoon, S.I. Lee, J.H. Kim, J.H. Jung, H.J. Sohn, , J. Electrochem. Soc. 154 (2007) A917–A920.
(25) M. He, K. Kravchyk, M. Walter, M.V. Kovalenko, , Nano Lett. 14 (2014) 1255–1262.
(26) J. Hassoun, G. Derrien, S. Panero, B. Scrosati, Electrochim. Acta 54 (2009) 4441–4444.
(27) I. Hasa, S. Passerini, J. Hassoun, cathode, RSC Adv. 5 (2015) 48928.
(28) L. Sbrascini, A. Staffolani, L. Bottoni, H. Darjazi, L. Minnetti, M. Minicucci, F. Nobili, ACS Appl. Mater. Interfaces 14 (2022) 33257–33273.
(29) D.Y.W. Yu, P.V. Prikhodchenko, C.W. Mason, S.K. Batabyal, J. Gun, S. Sladkevich, A.G. Medvedev, O. Lev, Nat. Commun. 4 (2013) 2922.
(30) S. Komaba, Y. Matsuura, T. Ishikawa, N. Yabuuchi, W. Murata, S. Kuze, , Electrochem. commun. 21 (2012) 65–68.
(31) B. Zhang, G. Rousse, D. Foix, R. Dugas, D.A.D. Corte, J.M. Tarascon, Adv. Mater. 28 (2016) 9824–9830.
(32) Y.C. Lu, C. Ma, J. Alvarado, T. Kidera, N. Dimov, Y.S. Meng, S. Okada,. Power Sources 284 (2015) 287–295.
(33) H. Zhu, Z. Jia, Y. Chen, N. Weadock, J. Wan, O. Vaaland, X. Han, T. Li, L. Hu, Nano Lett. 13 (2013) 3093–3100.
(34) L.D. Ellis, T.D. Hatchard, M.N. Obrovac, J. Electrochem. Soc. 159 (2012). A1801–A1805.
(35) G. Liu, Z. Sun, X. Shi, X. Wang, L. Shao, Y. Liang, X. Lu, J. Liu, Z. Guo, Adv. Mater. 35 (2023) 2305551.
(36) S. Lin, H. Zhang, C. Shu, W. Hua, X. Wang, Y. Zhao, J. Luo, Z. Tang, Y. Wu, W. Tang, Adv. Funct. Mater. 34 (2024) 2409628.
(37) N. Qin, Y. Sun, C. Hu, S. Liu, Z. Luo, X. Cao, S. Liang, G. Fang, J. Energy Chem. 77 (2023) 310–316.
(38) Y. Niu, Y. Guo, Y. Yin, S. Zhang, T. Wang, P. Wang, S. Xin, Y. Guo, Adv. Mater. 32 (2020) 2001419.
(39) J.H. Jo, J.U. Choi, Y.J. Park, J.K. Ko, H. Yashiro, S.T. Myung, Energy Storage Mater. 32 (2020) 281–289.
(40) L. Sbrascini, A. Sarapulova, C. Gauckler, L. Gehrlein, F. Jeschull, T. Akçay, R. Monig, M. Marinaro, F. Nobili, S. Dsoke, , Batter. Supercaps. 7 (2024) e202400207.
(41) H. J. Kim, S. Choi, S. J. Lee, M. W. Seo, J. G. Lee, E. Deniz, Y. J. Lee, E. K. Kim and J. W. Choi, *Nano Lett.*, 2016, 16, 282–288
(42) Z. Huang, Z. Deng, Y. Zhong, M. Xu, Sida Li, X. Liu, Y. Zhou, K. Huang, Y. Shen, Y. Huang, Carbon Energy, 2022, 6, 1107-1132

#11 10.1016/j.jpowsour.2025.239124

Highly-cyclable Na-ion battery exploiting a nanostructured tin-carbon anode, layered oxide P3/P2 cathode and a glyme based electrolyte

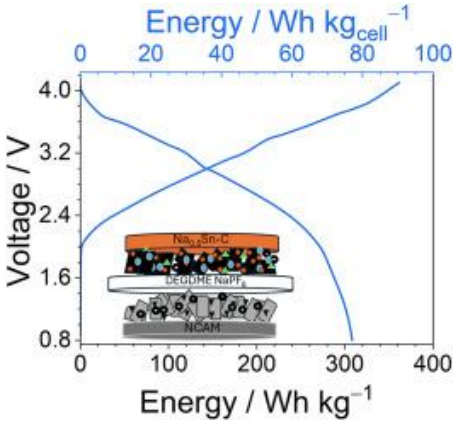

A highly-cyclable Na-ion full-cell is realized by rationally combining enhanced cathode, anode and electrolyte materials to ensure a high capacity retention and stable galvanostatic cycling. The P2/P3-mixed layered-oxide cathode benefits from the incorporation of a small amount of Al^{3+} in the structure, which reinforces the stability toward the characteristic phase transitions of this class of materials. [41-43] Our approach can enable the realization of practical SIBs adopting P3/P2 class of layered-oxide cathodes, thus paving the way for further studies on this topic. Typical cathodes that deliver higher reversible capacity, such as those having O3 structure (i.e., the most diffused structure of Li-layered oxide cathode), are preferred since they can allow easier setup of the systems, in spite of pre-treatments may be still requested for allowing high cell efficiency. [44-48] However, the O3-type cathodes can face some problems, such as the poor symmetry of the crystal structure that may influence the electrochemical response of the native structure, since Na-ions diffuse through face-shared interstitial tetrahedral sites, while multiple phase transitions from O3 to O′3, P3, P′3, and P3″ can trigger an adverse effect on the cycling performance. [49,50] Moreover, the sodium extraction from the O3-phase can generate an increasing number of prismatic vacancies, resulting in the sliding of crystallite layers and culminating in the formation of thermodynamically stable P3-type phase. [51] On the other hand, P2-class cathode typically benefits from a larger Na layer spacing compared to the others, which can enhance the transport proprieties of Na^+, the rate performance, and the cycling stability of the electrode.[52] However, the large fraction of empty Na^+ ion sites in P2 layered materials can lead to inadequate Coulombic efficiency during the first charge/discharge cycle, with related issues on Na full-cell balancing. Hence, the synergic combination of the fast Na^+-ions diffusion of the P2-type material with the appropriate cycling stability

exhibited by P3-type ones appeared to us of particular interest to enhance the electrochemical performance of the biphasic cathode. [(53), (54), (55), (56)] Meanwhile, we demonstrated that chemical-sodiation can suitably allow the development of Na-ion energy storage systems using Na-deficient cathode, since the sodium content of the anode can be tuned by optimizing and controlling the sodiation procedure. We expect these findings to trigger renewed interest on mixed layered structured cathodes, often excessively overlooked in the past due to the lack of Na within their structure. The anode relies on nanometric tin particles incorporated into a buffering and highly-conductive carbon matrix. [(57)] The related slurry has been prepared by using CMC, which is a fluorine-free binder that allows for the aqueous processing to reduce manufacturing costs and increase the environmental compatibility.[(38)] In addition, the use of glyme-based electrolyte is suggested as a chemically stable alternative to the conventional carbonate-based solutions. The electrodes have been initially investigated in sodium half-cells to assess their performance in the proposed electrolyte medium, and then in full sodium-ion cells to determine the energy content, interphase properties, and electrochemical behavior. Finally, a thorough overview of the structural and morphological evolution of the electrodes upon cycling is provided by ex situ X-ray diffraction and scanning electron microscopy.

Experimental

- Electrode materials

The $Na_{0.48}Al_{0.03}Co_{0.18}Ni_{0.18}Mn_{0.47}O_2$ (NCAM) cathode material consisting of 79 vol% P3-type (space group R3m, No. 16) and 21 vol% P2-type (space group P63/mmc, No. 194) structures was synthesized through a co-precipitation route and calcination at 1000 °C following an optimized method reported in previous works.[(42,43)] The vol% was obtained from the Rietfeld refinement carried out in the above cited literature works. The tin-carbon (Sn-C) anode with a Sn to C weight ratio of 35:65 was synthetized as via resorcinol-formaldehyde jellification, impregnation with an organometallic tin precursor, and annealing under Ar/H_2 (95/5 vol%) at 700 °C.[(58)]

- Electrode preparation

The electrode slurries were prepared in a mortar by dispersing the active material powder, either NCAM or Sn-C, carbon black (Super P carbon, SPC, Timcal), and either polyvinylidene fluoride (PVdF 6020, Solef) or CMC (average molecular weight 700 000, Sigma-Aldrich) as binder for the cathode and anode tapes, respectively. The three components were mixed in the 8:1:1 wt% ratio and dispersed either in N-methyl-2-pyrrolidone (NMP, Sigma-Aldrich) for the cathode, or in deionized H_2O for the anode achieving a 2.5 wt% CMC solution. The obtained slurries were cast by a doctor blade tool on either aluminum foil (thickness of 15 µm, MTI Corporation) for NCAM or copper foil (thickness of 10 µm, MTI Corporation) for Sn-C and subsequently dried at 70 °C inside a climatic chamber equipped with a peristaltic pump. The tapes were subsequently calendared by using an MSK-2150 Rolling Machine (MTI Corp.) to achieve thickness values within the range from 80 to 100 µm for the anode (about 60 % of the initial thickness) and in the range from 70 to 90 µm for the cathode (about 70 %

of the initial thickness). Afterwards, the tapes were cut into discs of 10 and 14 mm-diameter (electrode geometric area of 0.785 and 1.54 cm^2, respectively) and dried for 2 h at 110 °C under vacuum inside a Büchi oven to remove possible traces of H_2O and NMP before transfer in an Ar-filled glovebox (MBraun, H_2O and O_2 below 0.5 ppm). Additional slurries of anode and cathode were prepared with the same procedure as above, however with different thickness. Therefore, the active material loading ranged within 3.5 and 7.6 $mg_{Sn\text{-}C}$ cm^{-2} and within 1.5 and 11.5 mg_{NCAM} cm^{-2}. The specific values are indicated in the corresponding figure panels. After drying and calendaring, the electrode tape was cut into discs of 10 mm-diameter and later employed for the electrolyte electrochemical stability test. The sodiated state of the Sn-C electrodes $(Na_xSn\text{-}C)_{minutes}$ was obtained inside an Ar-filled glove box via capillary contact between the pristine Sn-C electrode and sodium metal by applying a weight of 0.2 kg at the electrode surface for a certain time. Prior to the contact, the sodium metal foil was soaked with the electrolyte solution, that is, sodium hexafluorophosphate as the conducting salt ($NaPF_6$, 99.9 % trace metals basis, anhydrous, battery grade, Sigma-Aldrich) dissolved in diethylene glycol dimethyl ether (DEGDME, $CH_3(OCH_2CH_2)_2OCH_3$, Sigma-Aldrich) in a 1 mol_{salt} $dm_{solvent}^{-3}$ (1 M concentration). Prior to use, DEGDME was stored in dry molecular sieves (0.3 nm, rods, ∼1.6 mm diameter, Sigma- Aldrich) for one week to remove H_2O, the content of which was verified to be below 10 ppm by an 899 Karl Fischer Coulometer (Metrohm). Three sodiation times were evaluated, that is, 15, 27 and 30 min, and the obtained electrodes have been indicated as $(Na_xSn\text{-}C)_{15min}$, $(Na_xSn\text{-}C)_{27min}$ and $(Na_xSn\text{-}C)_{30min}$.

- Material characterization

XRD was performed by scanning the 10°–60° 2θ range on the pristine Sn-C anode with step size of 0.02° and rate of 10 s $step^{-1}$, using a Bruker D8 Advance instrument equipped with a Cu Kα radiation source (8.05 keV). TGA was performed on the pristine CMC powder, and the aqueous CMC solution between 25 and 800 °C, with a heating rate of 5 °C min^{-1} by a Mettler-Toledo TGA 2 instrument (Mettler-Toledo, Columbus, OH, USA) under a dry air flow.

- Na half-cells characterization

Three-electrode Swagelok-type T-cells using 10 mm-diameter electrodes and CR2032 coin-type cells (MTI Corp.) using 14 mm-diameter electrodes were assembled inside an Ar-filled glovebox by stacking a sodium metal disc (99.9 % trace metal basis, Sigma-Aldrich) as counter/reference electrode, a 10 or 16 mm glass fiber (Whatman GF/B) disc as separator soaked with the DEGDME 1 M $NaPF_6$ electrolyte (50 µl and 200 µl for coin- and Swagelok-type cells, respectively), and either Sn-C, $(Na_xSn\text{-}C)_{min}$, or NCAM as working electrode. The electrochemical processes and the electrode/electrolyte interphases of Sn-C and NCAM were investigated through CV and EIS in three-electrode Swagelok-type T-cells employing a VersaSTAT MC Princeton Applied Research (PAR-AMETEK) multichannel potentiostat. CV was performed within the 0.01–2.0 V vs. Na^+/Na and 1.2–4.2 V vs. Na^+/Na potential ranges for Sn-C and NCAM, respectively, at a scan rate of 0.1 mV s^{-1}, while EIS measurements were collected at the OCV condition before cycling, and upon 1 and 5 CV runs, using an alternate voltage signal of 10 mV in the frequency range between 500 kHz and 100 mHz. Rate capability test on the pristine Sn-C anode was performed by galvanostatic cycling in Na half-cell between 0.01 and 2.0 V, applying specific currents increasing every 10 cycles from 0.05 A g^{-1} to 0.10, 0.20, 0.30, 0.60, and 1.2 A g^{-1}, before decreasing it back to 0.05 A g^{-1} at the 61st cycle. The chemical pre-sodiation of the anode was investigated by galvanostatic cycling $Na||(Na_xSn\text{-}C)_{min}$ half-cells between 0.01 and 2.0 V at the constant current rate of 0.05 A g^{-1}, the sodiation degree

(x) related to the 27 min sodiation protocol was estimated through galvanostatic and potentiostatic methods. The galvanostatic test was carried out in 2-electrode cell, by applying a current of 0.05 A g^{-1} from the OCV of the Na||$(Na_xSn\text{-}C)_{27min}$ cell to 2.0 V. The potentiostatic test was a coulometry performed in 3-electrode cell by holding the potential at 0.5 V vs. Na^+/Na for 5 h and 20 min, acquiring the current each 3 s. To assess the Na-plating risk window, the 2-electrode half-cell used to estimate the sodiation degree was galvanostatically discharged using a current of 0.05 A g−1 held for 8 h. Na||NCAM half-cells were galvanostatically cycled either in the 1.4–4.2 V voltage range at the constant current rate of 0.05 A g^{-1}, or limiting the voltage window between 1.4 and 4.0 V at a constant specific current of either 0.05 A g^{-1} or 0.1 A g^{-1}. All the galvanostatic cycling tests were carried out in CR2032 coin-type cells using a MACCOR series 4000 battery tests instrument either at 25 or 30 °C (see specific values in the corresponding figure captions).

- Full-cells characterization

$(Na_xSn\text{-}C)_{27min}$||NCAM full-cells were assembled by using a negative to positive ratio (N/P) between 1.1 and 1.2, as determined by considering the initial capacity achieved by the electrodes in the respective Na half-cells, e.g., 1.19 mAh cm^{-2} for NCAM during discharge (Na-intercalation) and 1.53 mAh cm^{-2} for $(Na_xSn\text{-}C)_{27min}$ during charge (Na-dealloying), with active material mass loadings of 7.5 mg cm^{-2} and 6.2 mg cm^{-2}, respectively. The full-cells were assembled by stacking one $(Na_xSn\text{-}C)_{27min}$ electrode, one glass fiber (Whatman GF/B) disc as separator soaked with the DEGDME 1 M $NaPF_6$ electrolyte (50 µl) and one NCAM electrode. The specific capacity, as well as the specific current, is referred to the cathode active material mass. The $(Na_xSn\text{-}C)_{27min}$ and NCAM capacity values for the N/P determination were evaluated by galvanostatic cycling of the corresponding Na half-cells either between 0.01 and 2.0 V at 0.05 A g^{-1} for $(Na_xSn\text{-}C)_{27min}$, or between 1.4 and 4.4 V at 0.05 A g^{-1} for NCAM. The electrochemical performance of the $(Na_xSn\text{-}C)_{27min}$||NCAM full-cell was evaluated through galvanostatic cycling in the 0.8–4.2 V voltage range either at the 0.05 A g^{-1} or 0.10 A g^{-1} constant current rate (referred to the NCAM mass), or in the restricted 0.8–4.0 V and 0.8–3.9 V voltage ranges at 0.05 A g^{-1}. For the latter test, a potentiostatic step was adopted at 3.9 V at the end of every charge until the current decreased to 0.0125 A g^{-1}. The rate capability test was carried out in the 0.8–4.1 V voltage range by applying specific currents increasing every 5 cycles from 0.05 A g−1 to 0.10, 0.15, 0.20, and 0.25 A g^{-1} before lowering it back to 0.05 A g^{-1} at the 26^{th} cycle. The energy density of this test was reported considering either the cathode active material content (NCAM) or both anode plus cathode (namely NCAM and Sn-C). The current rate capability test was carried out without using potentiostatic steps. An additional normalization of the energy density (Wh kg^{-1}) of the full-cells has been carried out by taking into account full electrode masses and stack with separator/electrolyte for possibly enabling preliminary benchmarking of the laboratory-scale cells. EIS spectra were collected using an alternate voltage signal with an amplitude of 10 mV between 500 kHz and 20 mHz at the OCV and in the discharged state after the rate capability test. After the above test, the full-cell was also subjected to CV within the 0.8–4.2 V vs. Na^+/Na potential range using a scan rate of 0.1 mV s^{-1}. All the galvanostatic cycling of the full-cells were carried out in CR2032 coin-type cells, while the rate capability test combined with EIS, SEM and CV was carried out in a 3-electrode Swagelok-type T-cell. The galvanostatic cycling tests were performed using a MACCOR series 4000 battery tests instrument either at 25 or 30 °C (see specific values in the corresponding figure captions). The EIS and CV tests employed a VersaSTAT MC Princeton Applied Research (PAR-AMETEK).

- Ex situ analyses

The $(Na_xSn\text{-}C)_{27min}$ and NCAM electrodes were investigated by XRD after 100 galvanostatic charge/discharge cycles in $(Na_xSn\text{-}C)_{27min}$||NCAM full-cells at 0.05 A g^{-1} in the 0.8–4.0 V voltage range. The XRD data were acquired in the 10°–80° 2θ range through a Bruker D8 Advance instrument equipped with a Cu Kα radiation source using a step size of 0.02° and rate of 10 s per step. SEM of a $(Na_xSn\text{-}C)_{27min}$ electrode retrieved from a cycled full-cell was performed using a ZEISS Crossbeam XB340 microscope operating with an accelerating voltage of 5 kV in secondary electrons mode. To avoid external contamination, the electrode was transferred from the Ar-filled glove box to the microscope with the aid of a sealed transfer box. Prior to all the ex situ analyses, the cells were recovered at the discharged state and disassembled inside the Ar-filled glove box, and the retrieved electrodes were washed with a few drops of DEGDME and dried under vacuum at room temperature. The $(Na_xSn\text{-}C)_{27min}$ electrode morphology and elemental distribution were investigated by means of SEM-EDS using a Zeiss EVO 40 relying on a LaB_6 thermionic gun in secondary electrons mode operating at 5 kV. EDS elemental maps were collected on the SEM secondary electrons images via an X-ACT system associated with the SEM equipment.

Results

As mentioned above, the Sn-C electrode is achieved by using water as casting-solvent and CMC as binder in order to lower the overall price and mitigate possible health/environmental issues caused by fluorinated binders and organic solvent (38). Therefore, a thorough investigation is certainly requested in addition to that previously reported in literature to check the stability of the nanostructured Sn-C in the new environment (58). Initially, the thermal proprieties of the CMC binder are investigated through TGA upon heating from 25 °C to 800 °C under dry air flow, either in the pristine state (i.e., material powder) or in the H_2O 2.5% CMC solution used for the slurry preparation. The thermograms and respective derivate curves are reported in **Figure 1a**, which shows for the dry CMC three main oxidation/decomposition steps indicated by the derivative peaks centered a 280 °C, 310 °C, and 400 °C, while the process at 120 °C is attributed to the loss of trapped water/moisture within the CMC structure. The same test carried out on the aqueous CMC solution displays the expected weight loss at 120 °C due to the removal of the water, until reaching ~2.5 % of the initial weight, that is, a value matching the nominal CMC content. Interestingly, the water removal occurs through various steps, indicating the formation of solvation structures with the CMC. The stability of the nanometric Sn particles toward possible oxidation to SnO_2, triggered by water during electrode preparation and drying, is assessed via XRD.

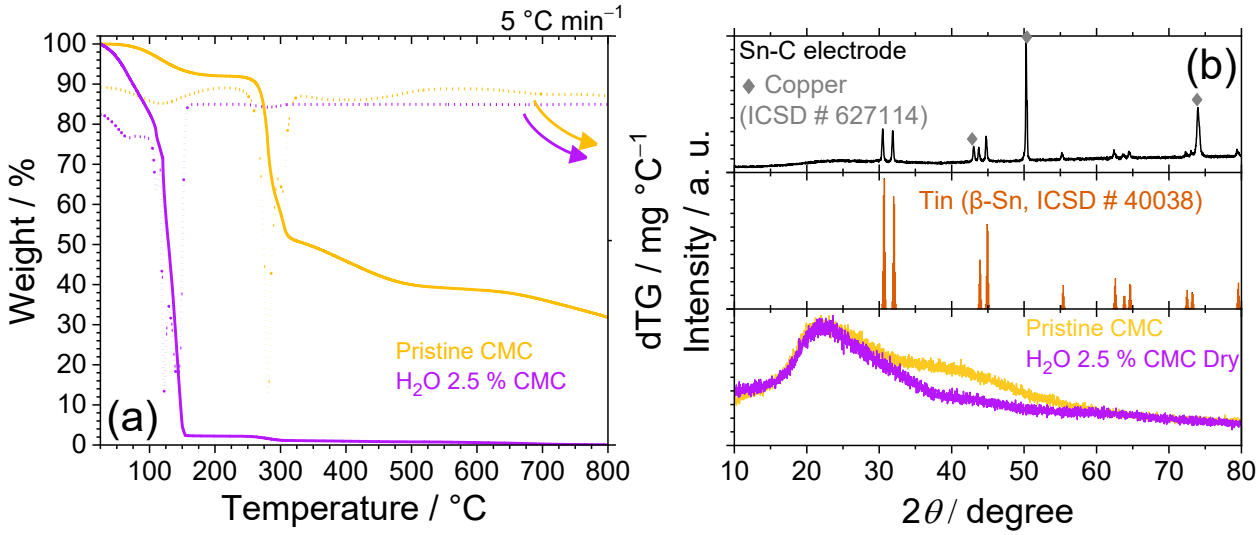

Figure 1. Physicochemical features of the Sn-C electrode and CMC binder, in detail: **(a)** TGA of pristine CMC and H_2O 2.5 % CMC binder solution, and corresponding DTG curves (dotted lines); **(b)** X-ray diffractograms of the Sn-C electrode and CMC binder at the pristine state and after drying the H_2O solution, reference data for Sn (β-Sn, ICSD # 40038) and Cu (ICSD # 627114) are reported for comparison.

The diffractogram of the dry Sn-C electrode in **Figure 1b** indicates the absence of additional phases, beside the ones related to Sn and to the Cu current collector (reference data from ICSD #4038 and #627114, respectively). These outcomes indicate the relevant stability of the active material during water processing, while the broad wave detected between 20 and 30° originates from the carbon matrix hosting the nanometric Sn particles, and possibly from the amorphous CMC binder whose diffractogram is also reported for better comparison in **Figure 1b** (61,62).

Figure 2 reports the electrochemical response of the Sn-C electrode in Na half-cell achieved by performing CV and EIS. The voltammograms in **Figure 2a** reveal during the first cathodic scan a current onset below 0.6 V *vs.* Na^+/Na, due to the beginning of Na-Sn alloy formation and the concomitant insertion of Na into the amorphous carbon matrix until 0.01 V *vs.* Na^+/Na (63). This voltametric wave appears partially irreversible, mostly due to the side reduction of the electrolyte which typically leads to the formation of a protective SEI layer at the electrode surface (64). A different kinetics for the oxidation processes compared to reduction one is indicated by the first anodic scan, which shows a more resolved signal evolving by a series of peaks extending from 0.15 to 0.66 V *vs.* Na^+/Na due to the Na-Sn de-alloying below 0.5 V and *vs.* Na^+/Na the de-insertion of Na from the carbon at higher values (65). The signal related to the irreversible electrolyte reduction remarkably decreases at the second cathodic scan, and almost fully vanishes during the subsequent cycles which exhibit exclusively a voltage slope with onset below

0.4 V *vs.* Na^+/Na. Instead, the anodic profiles show the above discussed oxidation peaks, which appear well defined between 0.1 and 0.7 *vs.* Na^+/Na during the whole CV test. These results substantially differ from previous literature on Sn-based anodes for SIBs, which reported the presence of one or more additional peaks upon the cathodic scan in the region between 0.1 and 0.8 V *vs.* Na^+/ Na, thus suggesting possible influence of the binder nature, the characteristic electrode structure and its morphology on the Na–Sn alloying kinetics (66–69). By the ongoing of CV, the current intensity raises for the anodic process at 0.21 V *vs.* Na^+/Na, fluctuates for the one at 0.28 V *vs.* Na^+/Na, while decreases for the processes over 0.5 V *vs.* Na^+/Na. The modification in current response of the Na–Sn de-alloying processes indicates the variation of the corresponding kinetics likely due to the consolidation of the SEI layer and stabilization/rearrangement of the hosting carbon matrix upon repeated cycling, which favor the low-voltage processes (< 0.5 V *vs.* Na^+/Na) and limit the cell polarization (64). In addition, the improvement of the profiles overlapping upon repeated scans suggests the progressive stabilization of the electrochemical process, thus indicating the effectiveness of the Sn-C nanostructure in buffering the volume variations associated to the Na–Sn (de)alloying to avoid structural degradation of the electrode.

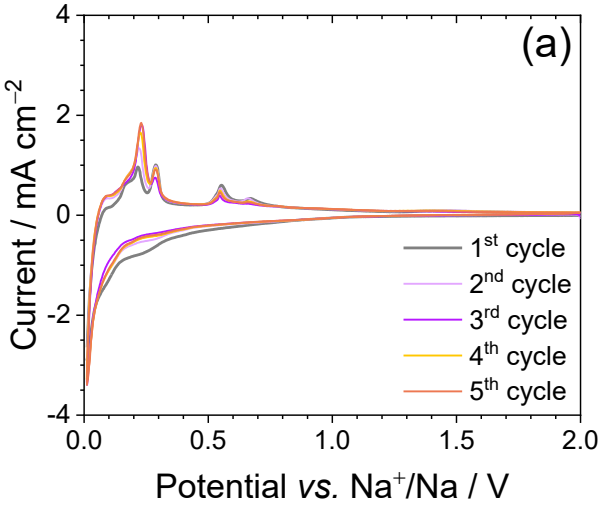

Figure 2. (a) CV profiles of Na||Sn-C half-cell; CV potential range: 0.01 – 2.0 V *vs.* Na^+/Na, scan rate: 0.1 mV s^{-1}, temperature: 25 °C.

Figure 3 summarizes the galvanostatic cycling performances of the Sn-C electrode in sodium half-cell. A rate capability test is initially performed by increasing the current every 10 cycles from 0.05 A g^{-1} to 0.10, 0.20, 0.30, 0.60, and 1.20 A g^{-1}, with selected voltage profiles in **Figure 3a** and the corresponding charge capacity trend in **Figure 3b**. The voltage profile after 10 cycles at the same current reveals an efficiency approaching 100%, and a reversible electrochemical process centered between 0.2 and 0.8 V, evolving

by a single sloped profile during discharge and various merged plateaus during charge, as already observed during the CV (compare **Figure 3a** with **Figure 2a**). The curves of **Figure 3a** also show a moderate decrease in terms of delivered capacity alongside a slight increase of the overpotential upon current increase, due to the increasing ohmic polarization. Indeed, the charge capacity *vs.* cycle number trend displayed in Figure 3b exhibits a maximum capacity of 212 mAh g^{-1} achieved at 0.05 A g^{-1}, and values of 166, 137, 80, 50, and 32 mAh g^{-1} at 0.10, 0.20, 0.30, 0.60, and 1.20 A g^{-1}, respectively. In addition, the electrode recovers 89.6% of the initial capacity after decreasing the current rate back to 0.05 A g^{-1} at the 61st cycle, thus suggesting remarkable structural stability upon cycling at high currents. The trend of **Figure 3b** also evidences a progressive improvement of the delivered capacity during the initial stages of the test, which is accompanied by an increase of the Coulombic efficiency from 61.5 % at the first cycle to a value around 99 % upon 10 galvanostatic cycles. This activation process is likely justified by the progressive improvement of the electrode/electrolyte interphase previously observed by CV and EIS. On the other hand, a fast enhancement of the cell efficiency is crucial to avoid a relevant consumption of the cyclable Na, which may potentially undermine the performance of the full-cell especially in presence of a sodium-deficient cathode such as the one adopted in this study ($Na_{0.48}Al_{0.03}Co_{0.18}Ni_{0.18}Mn_{0.47}O_2$, or NCAM) (42). Taking into account this limitation, the pre-sodiation of the Sn-C anode through direct contact with sodium metal, *i.e.*, chemical sodiation, is selected as viable method to ensure a sufficient sodium reservoir in the full-cell setup using the NCAM cathode (70). The control of the contact time between Sn-C and Na metal, the applied pressure, and the content of active material in the electrode play fundamental role during pre-sodiation. The above conditions are crucial for regulating the sodium content into the anode, which must provide a sufficient amount of cyclable Na to balance the full-cell, and avoid at the same time an excess that can trigger undesired metal plating at the anode surface during charge (70). Other pre-sodiation strategies not considered in this work rely on the use of sacrificial salts and/or additives within the cell, however with additional processing steps that may lead to gas evolution upon cell operation (26,71–75). Therefore, the chemical sodiation of the Sn-C electrode is evaluated herein by tuning the contact time, as evidenced by **Figure 3c** which shows the voltage profile at the first (left-hand side) and 150th (right-hand side) cycles of Na half-cells studied at 0.05 A g^{-1} using Sn-C electrodes chemically sodiated for either 15, 27, or 30 min. The data indicate for the pre-treated electrodes the absence of the irreversible shape typically ascribed to the electrolyte reduction, and evidence a higher capacity upon charge compared to pristine Sn-C, that is, around 250 – 260 mAh g^{-1} instead

of 212 mAh g^{-1}. These outcomes suggest an effective pre-sodiation triggered by the contact time, and possible over-sodiation at the electrode surface due to the excess charge capacity, which appears not detrimental for the anode stability as demonstrated by the corresponding cycling trend in **Figure 3d** (76). It is worth mentioning that the cell using the $(Na_xSn\text{-}C)_{15}$ still delivers around 200 mAh g^{-1} during first discharge, thus indicating an insufficient sodiation degree achieved using 15 min of contact to get a suitable balancing of the full-cell with the Na-deficient NCAM. On the other hand, the cell using $(Na_xSn\text{-}C)_{30}$ shows less than 20 mAh g^{-1} during first discharge, thus reaching almost full sodiation of the Sn-C in 30 min of contact with Na. The latter excessive sodiation may lead to alkali metal deposition during Na-ion full-cell charging, although it may represent a viable pathway in view of a possible application in Na metal-free sulfur-based full-cells (63). On the other hand, the $(Na_xSn\text{-}C)_{27min}$ delivers 90 mAh g^{-1}, which is expected to counterbalance the NCAM capacity even considering its Na-deficiency. Therefore, we may indicate 27 min as the most adequate timeframe within our pre-sodiation conditions to achieve efficient Na-ion cell. The trend in **Figure 3d** evidences for the cells using the pre-sodiated electrodes a retention ranging from 70 % to 76 % over 150 cycles, which is also demonstrated by the voltage profile of the last cycle in **Figure 3c** (right-hand panel). Furthermore, the pre-sodiated electrodes show a faster interphase activation compared to the pristine Sn-C electrode, since the related Na half-cells reach a Coulombic efficiency higher than 99% far faster (compare **Figure 3b** and **Figure 3d**).

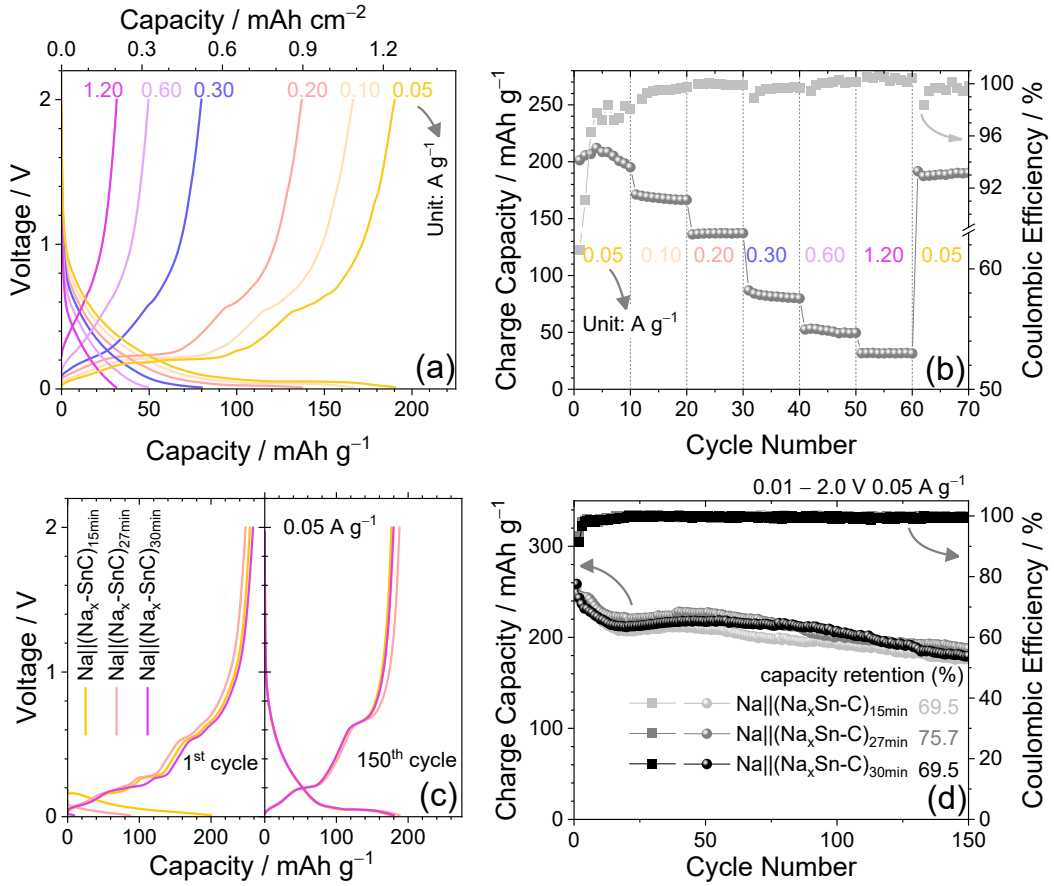

Figure 3. (a, b) Galvanostatic cycling performance upon rate capability test of Na||Sn-C half-cell in terms of **(a)** selected voltage profiles (10th cycle for each current rate) and **(b)** corresponding charge capacity *vs.* cycle number trend; **(c, d)** galvanostatic cycling performance of Na||(Na$_x$Sn-C)$_{min}$ half-cells tested at 0.05 A g^{-1} using Sn-C electrodes chemically sodiated for either 15, 27, or 30 min reported in terms of **(c)** 1st (left-hand panel) and 150th (right-hand panel) voltage profile and **(d)** corresponding charge capacity *vs.* cycle number trends. Right *y*-axes in panels **(b)** and **(d)** reports Coulombic efficiency; voltage range: 0.01 – 2.0 V; electrode geometric area: 1.54 cm^2; active material mass loading: 6.0 – 6.8 ± 0.1 mg cm^{-2}. Temperature: 25 °C.

The chemical sodiation triggered by mechanical contact between Na foil and the electrode wet by the electrolyte allows a rapid and efficient activation of the material, for application in Na-ion batteries leveraging alloying negative electrodes (70,77). The development of new battery configurations that exploit pre-sodiation by capillary diffusion requires an adequate tuning of the contacting time, to have a Na-inventory in the anode sufficient to fully allow the electrochemical reaction at the cathode. The activation protocol for the Sn-C electrode with contact time of 27 min is selected as suitable for Na-ion cell application, and therefore investigated hereafter electrochemically by means of galvanostatic and potentiostatic techniques, and morphologically using *ex-situ* SEM-EDS analysis to determine the actual Na content in the (Na$_x$Sn-C)$_{27min}$ electrode. **Figure 4a** indicates a delivered capacity upon galvanostatic charge of the Na||(Na$_x$Sn-C)$_{27min}$ cell using a current of 0.05 A g^{-1} between the OCV and 2.0 V corresponding to 268.0 mAh g^{-1}, in accordance

with the result presented in **Figure 3** within the experimental error. On the other hand, **Figure 4b** shows the potentiostatic polarization (coulometry) extended to a timeframe comparable with that of the previous galvanostatic experiment. Hence, a sodiation degree in $(Na_xSn\text{-}C)_{27min}$ of x = 0.5 is calculated by taking into account the overall extracted capacity (ε = 2.828 C), the Faraday constant (F = 96485 C mol^{-1}), the mass of Sn-C in the electrode (m = 2.872×10^{-3} g), and its molar weight using the $Sn_{0.35}C_{0.65}$ chemical formula ($M_{Sn\text{-}C}$ = 49.355 g mol^{-1}), using the relation: $x = \frac{\varepsilon \times M_{Sn-C}}{F \times m}$. The plating-risk window analysis represents a key-factor which determines the safety level of the anode in a Na-ion device safety features (78,79). To assess this aspect for the $(Na_{0.50}Sn\text{-}C)_{27min}$ electrode, the half-cell of **Figure 4a** is over-discharged for 8 h using a current of 0.05 A g^{-1} without imposing any voltage limit, and the result reported in **Figure 4c** (inset shows a magnification of the onset for Na-nucleation). This test suggests that the anode has a tolerance of 13 mAh g^{-1} over its theoretical capacity (*i.e.*, 271 mAh g^{-1} for $Sn_{0.35}C_{0.65}$) before Na-plating, thus allowing the estimation of ± 5 % of possible N/P fluctuation without compromising the safe Na-ion full-cell operation. Importantly, the Na distribution across the electrode upon chemical sodiation is accounted by means of SEM-EDS analysis in **Figure 4d-g**. The elemental maps distributions of Na and Sn, respectively reported in **Figure 4d** and **Figure 4e**, suggest that the sodiation protocol related to 27 min yields to uniform $(Na_{0.50}Sn\text{-}C)_{27min}$ electrode, without relevant clusters of metallic Na or considerable damage to the electrode morphology. To further verify the sodiation degree (x), the atomic ratio of Na and Sn in the $(Na_xSn\text{-}C)_{27min}$ electrode is accounted by sampling EDS spectrum in various portions (some representative spots spectra are reported in **Figure 4f** and **Figure 4g**). Remarkably, x is estimated to range from 0.67 to 0.36, with average value of 0.52 which agrees with the coulometry estimation of **Figure 4b**, despite the error derived from the presence of Na in the CMC binder, as well in possible electrolyte salt residue.

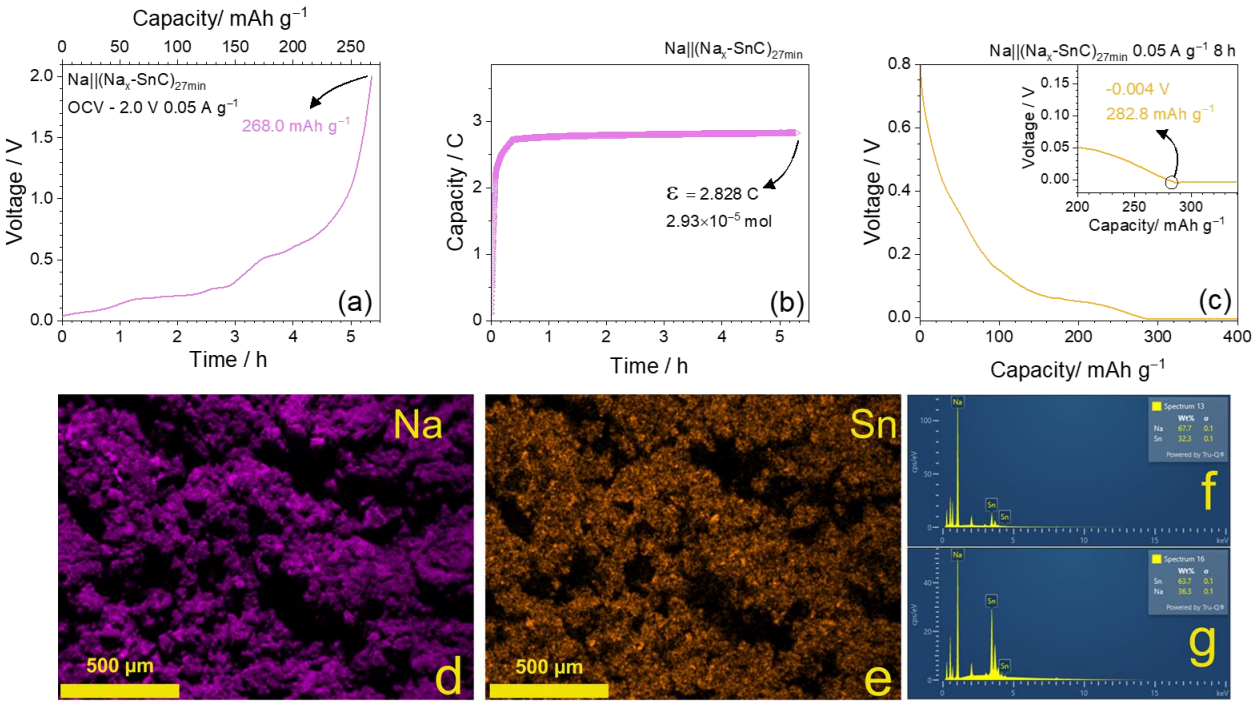

Figure 4. Estimation of Na content across the $(Na_xSn\text{-}C)_{27min}$ electrode through electrochemical methods and SEM-EDS investigation, and determination of its Na-plating window, in detail: **(a)** galvanostatic charge of $Na||(Na_xSn\text{-}C)_{27min}$ half-cell reported in terms of first charge profile (6.112 ± 0.1 mg of Sn-C, 14 mm electrode); **(b)** coulometry test (chrono coulometry at 0.5 V *vs.* Na^+/Na, 1 point collected each 3 s, 5 h and 20 min timeframe) to assess the sodiation degree *x* in $(Na_xSn\text{-}C)_{27min}$ electrode (2.872 ± 0.1 mg of Sn-C, 10 mm electrode, test carried out in T-cell); **(c)** plating test carried out using the half-cell of panel (a) to assess the allowed fluctuation of the N/P ratio before Na-plating; **(d, e)** SEM-EDS elemental maps distribution, related respectively to Na and Sn, and **(f, g)** related EDS spectra.

The NCAM cathodes were prepared and studied in previous work using a carbonate-based electrolyte (42), which offered relevant stability towards oxidation and allowed for the investigation of high-voltage features of the electrochemical process (80). Lately, great attention has been devoted to glyme-based electrolytes relying on solvents with $CH_3(OCH_2CH_2)_nOCH_3$ as the general formula due to their relevant Na^+ solvation capability and transport properties, as well as adequate viscosity and dielectric constant particularly for low *n* values that ensure high Na^+ conductivity (12). However, their stability towards oxidation is usually limited to potential values below 4.5 V *vs.* Na^+/Na, which can hinder their application in batteries using high voltage cathodes. Herein, the DEGDME 1 M $NaPF_6$ electrolyte solution is exploited due to the promising performance demonstrated in other systems (81–83), although a thorough investigation to assess its compatibility with the NCAM cathode is still needed. Therefore, the electrochemical process and electrode/electrolyte interphase of the of NCAM in DEGDME 1 M $NaPF_6$, as well as its cycling response in Na half-cells are investigated by CV, EIS, and galvanostatic cycling, and the results are reported in **Figure 5**. The voltammetry curves (**Figure 5a**) reveal a

reversible electrochemical Na^+ (de)intercalation process, characterized by several peaks occurring within the 1.2 − 4.2 V *vs.* Na^+/Na potential range. It is worth mentioning that the first anodic scan (black curve in **Figure 5a**) starts from a potential of about 3.1 V *vs.* Na^+/Na, i.e., a high value indicating for the pristine NCAM material a partially charged state, which is in line with the sodium content below 0.5 equivalents in its stoichiometry. As the voltammetry scan begins, a first couple of oxidation peaks appears at about 3.2 and 3.4 V *vs.* Na^+/Na, as attributed to the Ni^{4+}/Ni^{2+} couple, followed by two merged peaks at 3.7 and 3.8 V *vs.* Na^+/Na ascribed to the Co^{4+}/Co^{3+} couple, and by a current increase with an onset at 4.1 V *vs.* Na^+/Na, likely due to possible phase transition including a partial electrolyte oxidation (43,84). The first cathodic scan shows the partial reversibility of the latter process, with reduction signal slightly below 4.1 V *vs.* Na^+/Na, and the two reversible peaks ascribed Co^{4+}/Co^{3+} couple merged at ~ 3.7 V *vs.* Na^+/Na, and those associated to the Ni^{4+}/Ni^{2+} couple at 3.3 and 3.2 V *vs.* Na^+/Na, all with a very modest polarization and remarkable symmetry compared to the oxidation ones. By the ongoing of the first cathodic scan, the CV reveals the appearance of reduction waves approximately at 2.7 V, 2.3 V, and below 2 V *vs.* Na^+/Na associated to the Mn^{4+}/Mn^{3+} redox process, which are reversed during the second and the subsequent anodic scans into a single broad peak extended from 1.8 to 2.9 V *vs.* Na^+/Na (43,84). In spite of a minor signal decrease above 4.1 V, all the described oxidation and reduction signals are almost fully reproduced in the course of the whole CV test, with more defined peaks compared to those observed in previous work using carbonate electrolyte (13,42,85). Hence, the CV response of **Figure 5a** suggests that the kinetics associated with the ion motion within the solid-state electrode layers can be promoted into a more efficient way by the glyme-based electrolyte rather than the carbonate-based one. Furthermore, the almost full overlapping of the voltammograms during the whole test suggests a relevant reversibility in the glyme-based electrolyte of the NCAM electrochemical process, which can proceed without significant modification or gliding of the layers into the material, and with minor structural reorganization due to sodium vacancy ordering. The electrode/electrolyte interphase changes during CV are monitored by performing EIS, as illustrated by the corresponding Nyquist plots in the inset of **Figure 4a**. The data reflect the contribution of several resistive and pseudocapacitive elements, arranged in the equivalent circuit depicted in **Table 4.1.2** along with the corresponding NLLS fitting results. The various elements account for the electrolyte resistance at high frequencies, the interphase resistance including the Na^+ diffusion across the SEI and the charge transfer processes at intermediate frequencies, as well as the Na^+ diffusion within the NCAM lattice at low frequencies. The NLLS results show a relatively

low electrode/electrolyte interphase resistance at the OCV, that is, 151 Ω, which decreases to 112 Ω upon discharge to 1.2 V *vs.* Na^+/Na due to the concomitant increase of the NCAM conductivity promoted by full-sodiation. The resistance increases back to 166 Ω at the discharged state after 5 cycles is in part due to NCAM de-sodiation with conductivity decrease, and in part due to the marginal electrode passivation induced by the partial electrolyte oxidation or minor phase change at 4.2 V *vs.* Na^+/Na as discussed during CV (41). The latter irreversible processes may be strongly limited by decreasing the charge voltage cutoff or by increasing the employed current, as demonstrated by the galvanostatic cycling tests performed on Na||NCAM cells hereafter. Initially, the galvanostatic performance of the Na||NCAM cell is investigated in the 1.4 – 4.2 V voltage range at 0.05 A g^{-1} as reported in **Figure 5b** in terms of voltage profiles and in **Figure 5c** in terms of discharge capacity *vs.* cycle number trend. In line with the CV, the voltage profiles show an initial short charge (gray line) evolving through the series of plateaus described above from 3.2 to 4.1 V, and the side plateau at 4.2 V at the end of the charge possibly due to the partially irreversible process. The initial charge with a capacity of about 60 mAh g^{-1} is reflected during the first discharge into multistep discharge with an overall capacity of 115 mAh g^{-1}, accounting for the Na-deficiency of the NCAM, while the subsequent charge and discharge proceed reversibly with a slight increase of capacity upon cycling to 123 mAh g^{-1} at the 69th cycle, and an efficiency approaching 99 % (se corresponding cycling trend in **Figure 4c**). The latter capacity value is indeed selected to achieve the discharge capacity retention, which resulted in 78 % after 300 cycles. The excellent performance of the NCAM in the glyme-based solution within the experimental setup adopted herein represents a step forward compared to the one previously achieved by NCAM in carbonate-based one, where a higher capacity achieved by increasing the voltage cutoff was retained for only 60% over 100 cycles due to the formation of insulating side products at the electrode/electrolyte interphase (41). As mentioned above, a further improvement of the capacity retention may be achieved by lowering the charge cutoff to 4.0 V or by increasing the current, although expectedly a lower capacity may be achieved due to the limited exploitation of the NCAM electrochemical process. Accordingly, further galvanostatic tests are performed, limiting the voltage range to 1.4 – 4.0 V and using specific currents of either 0.05 or 0.1 A g^{-1} (**Figure 5d-f)**. The voltage profiles of the cells show similar features to those discussed previously in **Figure 5b** without relevant signs of electrolyte decomposition; however, with a lower capacity due to the lower voltage cutoff and/or higher current. Indeed, the cells cycled at 0.05 A g^{-1} (**Figure 5d**) show an initial charge capacity of ~ 50 mAh g^{-1} and a reversible one of ~115 mAh g^{-1}, while the one

cycled at the higher current of 0.1 A g^{-1} (**Figure 5e**) evidences a similar initial charge capacity and a reversible one of 96 mAh g^{-1}. Both cells proceed without any capacity fade over 100 cycles, with an average Coulombic efficiency ranging between 99.5% and 99.6% (see the capacity and efficiency trends in **Figure 5f**), thus suggesting essentially the absence of irreversible reactions.

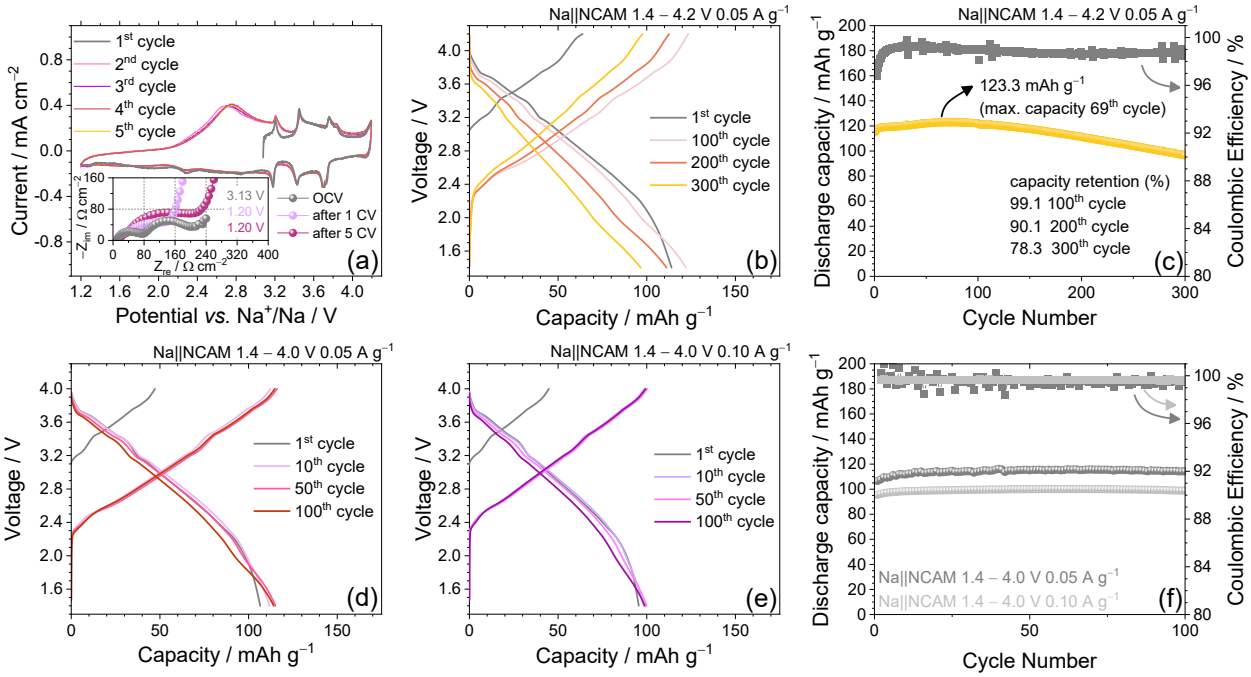

Figure 5. Electrochemical response of the Na||NCAM half-cells, in detail: **(a)** CV profiles recorded between 1.2 and 4.2 V *vs.* Na^+/Na, inset shows Nyquist plot recorded by EIS during CV (test carried out at 25 °C); **(b, c)** selected voltage profiles **(b)** and discharge capacity trend **(c)**, with coulombic efficiency reported in right *y*-axis, related to galvanostatic cycling tests performed between 1.4 and 4.2 V at a specific current of 0.05 A g^{-1}. **(d, e, f)** Selected voltage profiles related to galvanostatic cycling tests performed between 1.4 and 4.0 V at a current of **(d)** 0.05 A g^{-1} and **(e)** 0.05 A g^{-1} and **(f)** related discharge capacity trend **(**coulombic efficiency reported in right *y*-axis). Active material loading: 4.8 – 6.0 ± 0.1 mg cm^{-2}, CV scan rate: 0.1 mV s^{-1}; EIS performed at the OCV cell condition and upon CV after the 1st and 5th cycle between 500 kHz and 100 mHz, alternating voltage signal with an amplitude of 10 mV. The galvanostatic tests were performed at 30 °C.

Table 4.1.2 NLLS analysis carried out on the Nyquist plots displayed as inset in Figure 5a recorded on a three-electrode Na||NCAM half-cell at the OCV and after 1 and 5 CV runs.

Cell condition	**Circuit**	**R_1 (Ω)**	**R_2 (Ω)**	**$R_I=\sum R_n$ (Ω)**	**χ^2**
OCV	$R_e(R_1Q_1)(R_2Q_2)Q_w$	47.4 ± 1.1	103.6 ± 13.1	151.0 ± 14.2	4×10^{-4}
After 1 CV	$R_e(R_1Q_1)(R_2Q_2)Q_w$	21.5 ± 2.9	90.5 ± 8.3	112.0 ± 11.2	3×10^{-4}
After 5 CV	$R_e(R_1Q_1)(R_2Q_2)Q_w$	14.4 ± 2.1	152.2 ± 7.5	166.6 ± 9.6	4×10^{-4}

3.3 Full Na-ion battery

Recently, only few reports have reported SIBs exploiting Na-deficient cathodes and

alloying anodes, mainly due to the challenges associated with these active materials (31,86). Herein, we concomitantly overcome the Na-deficiency of the NCAM and the initial irreversibility of the Sn-C by rationally balancing the sodium content into a $(Na_xSn\text{-}C)_{27min}$ electrode, to ensure an N/P ratio between 1.1 – 1.2. Accordingly, **Figure 6** reports the results related to galvanostatic cycling of full $(Na_xSn\text{-}C)_{27min}$||NCAM cells (see representative scheme in **Figure 6a**) under various conditions, as well as the *ex situ* XRD analysis carried out on the electrodes after cycling. In line with the outcomes of anode and cathode observed in the above-reported investigation, a first test is carried out by cycling the full-cells in the 0.8 – 4.2 V voltage range either at 0.05 A g^{-1} or at 0.1 A g^{-1} with results are displayed in **Figure 6b** and **Figure 6c** in terms of selected voltage profiles, and in **Figure 6d** in terms of comparison of discharge capacity *vs.* cycle number, respectively. The full-cells reveal both at 0.05 A g^{-1} (**Figure 5b**) and at 0.1 A g^{-1} (**Figure 5c**) a sloped voltage shape, resulting from the combination of the anode and cathode ones, with maximum discharge capacity respectively of 115 mAh g^{-1} and 110 mAh g^{-1}, retained for ~85% over 100th cycle with average efficiency exceeding 99 % (**Figure 5d**). This stable behavior indicates an optimal cell balance, with only slight influence of the applied current on the cell. It is worth mentioning that literature works indicated further improvement of the cell performance by adopting *ad hoc* designed formation cycles (87,88). To further promote the stability, the full-cells are galvanostatically cycled in the restricted voltage ranges of 0.8 – 4.0 V and 0.8 – 3.9 V, using a current rate of 0.05 A g^{-1} as displayed in **Figure 6e**,**f** in terms of voltage profiles and in **Figure 6g**,**h** in terms of discharge capacity *vs.* cycle number trend. Lowering the charge cutoff does not significantly affect the cell capacity, which stabilizes around 115 mAh g^{-1} in both cases, as also promoted by the additional potentiostatic step adopted in the case of the cell charged at the lowest voltage cutoff (see experimental section for further details). The voltage profiles of **Figure 6e** and **Figure 6f** reveal slight increase of the charge/discharge polarization during cycling, although the typical voltage shape of NCAM remains almost unaltered, thus suggesting the retention of the corresponding electrochemical activity. Relevantly, the cell cycled using 4.0 V as the charge cutoff retains about 85 % of the initial maximum capacity upon 100 (dis)charge runs, similarly to that charged up to 4.2 V, while the one exploiting 3.9 V cutoff retains 95 % over the same cycling interval. This retention improvement may be ascribed to the high and stable efficiency in view of a mitigated electrolyte decomposition at the cathode side, as already discussed in the half-cells study in **Figure 4f**, although a still observed capacity decrease upon cycling indicates the need for further optimizations both in terms of cycling conditions and electrolyte composition. The structural features of

NCAM and $(Na_xSn\text{-}C)_{27min}$ upon 100 cycles is checked by *ex-situ* XRD on the full-cell cycled between 0.8 and 4.0 V of **Figure 6e,g** and the acquired patterns are reported in **Figure 6i.** The figure evidences the structural retention for the NCAM cathode, as all the main peaks of the mixed P2/P3 layered oxide hold their position after cycling, due to the enhanced stability toward phase transition favored by the presence of Al^{3+} (41). Instead, the $(Na_xSn\text{-}C)_{27min}$ structure after galvanostatic cycling appears different compared to the spectra of the pristine Sn-C reported in **Figure 1b**. Indeed, the XRD pattern in **Figure 6i** shows less intense peaks for elemental Sn and signals related to the $NaSn_2$ phase at 12° and 36°, thus indicating partial de-alloying upon full-cell discharge. This outcome suggests partial anode exploitation potentially affecting the capacity retention in the full-cell, which can be addressed by further tuning N/P ratio and by improving the testing procedures.

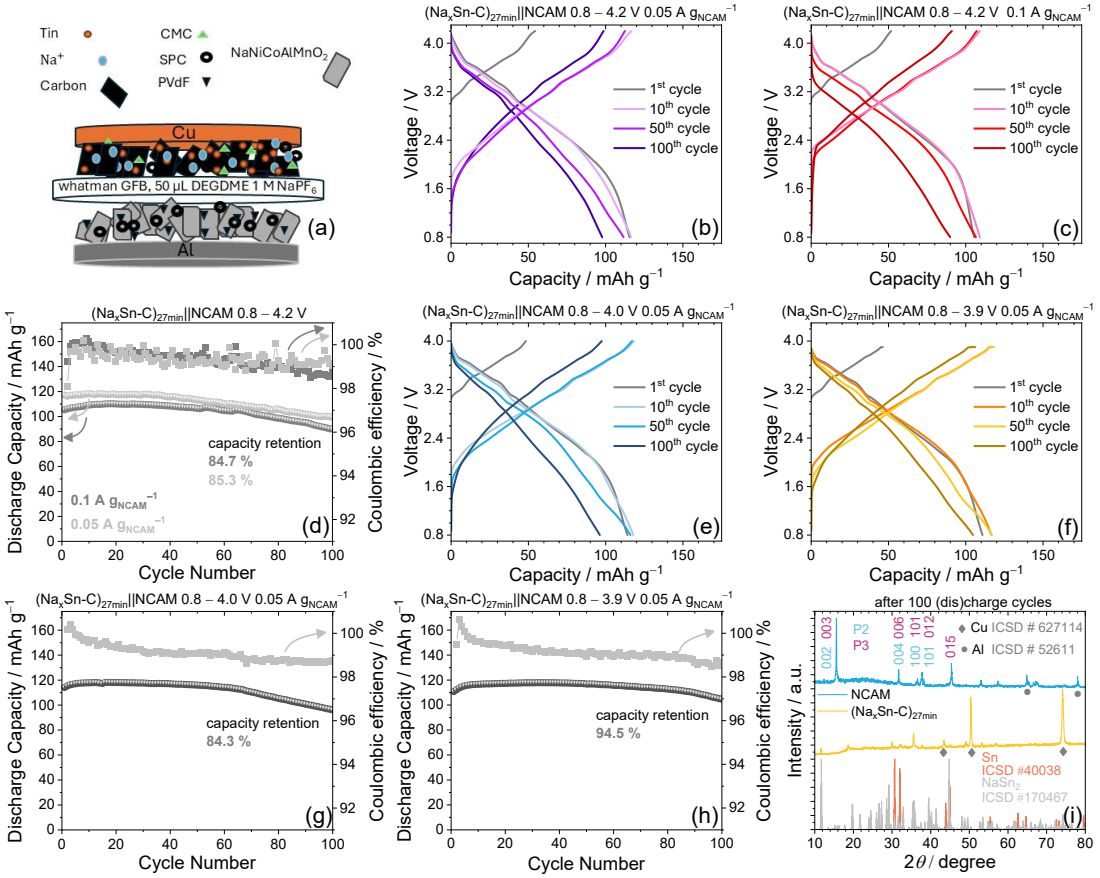

Figure 6. (a) Schematic representation of the sodium-ion battery configuration; **(b-h)** galvanostatic cycling performance of $(Na_xSn\text{-}C)_{27min}$||NCAM full-cells at various conditions reported in the figure caption, in detail:, **(b, c, e, f)** selected voltage profiles and **(d, g, h)** corresponding discharge capacity *vs.* cycle number trends (coulombic efficiency in right-hand side *y*-axes); **(i)** *ex situ* X-ray diffractograms of $(Na_xSn\text{-}C)_{27min}$ and NCAM electrodes after 100 cycles between 0.8 and 4.0 V. Electrode geometric area: 1.54 cm^2; active material loading: 5.3 – 6.8 ± 0.1 mg_{NCAM} cm^{-2}, 3.5 – 4.5 ± 0.1 $mg_{Sn\text{-}C}$ cm^{-2}; N/P ratio between 1.1 and 1.2. Temperature for galvanostatic cycling: 30 °C.

With the aim of further investigating the $(Na_xSn\text{-}C)_{27min}$||NCAM cell in terms of energy content, **Figure 7** reports a rate capability test combined with EIS study, carried out in the

intermediate 0.8 – 4.1 V voltage range by increasing the current every 5 cycles from 0.05 A g^{-1} to 0.10, 0.15, 0.20, and 0.25 A g^{-1} before lowering back the current to 0.05 A g^{-1} at the 26th cycle. The corresponding voltage profiles (**Figure 7a**) depict the shape expected by the galvanostatic tests already discussed in **Figure 6**, with moderate polarization upon current rate increase, and a maximum capacity of ~ 120 mAh g^{-1} achieved at the lowest current. Interestingly, the cell delivers about 90 % of its maximum capacity by doubling the current from 0.05 to 0.1 A g^{-1}, and a still a relevant 78 % of the maximum value by five-fold current increase, from 0.05 to 0.25 A g^{-1}. **Figure 7b** displays the theoretical energy density values for the Na-ion cell as referred either to the NCAM cathode mass (bottom y axis) or to the overall electrode mass, namely NCAM and $(Na_xSn\text{-}C)_{27min}$ (top y-axis), estimated by taking into account the corresponding voltage profiles at the 5th cycle at each current rate of **Figure 7a**. The figure shows an energy density ranging from 250 Wh kg^{-1} to 310 Wh kg^{-1} as referred to the NCAM cathode mass, which turns into a value ranging from 115 Wh kg^{-1} to 170 Wh kg^{-1} when the overall anode plus cathode mass (NCAM and Sn-C active material) is taken into account. In addition to the normalization reported in Figure **7b** (Wh kg^{-1} of NCAM cathode and NCAM + Sn-C active materials). On the other hand, the cell shows a coulombic efficiency exceeding 99 % after the first cycle at each current, and a full capacity retention by lowering back the current to the initial value after the rate capability test (see corresponding trend in **Figure 7c**). The interphase modifications of the electrodes by full-cell cycling are investigated by the EIS Nyquist plots in **Figure 7d**, and NLLS analysis using the resistive and pseudocapacitive elements in the equivalent circuit of **Table 4.1.3**. The elements account for electrolyte resistance, and the combined Na^+ diffusion and transfer events in the two electrodes. The $(Na_xSn\text{-}C)_{27min}$||NCAM exhibits EIS responses characterized by relatively low interphase resistance at the OCV, settling at 26.6 Ω, and moderately increasing upon stabilization of the interphase at 59.5 Ω, that is a modest value accounting for the cell stability and relevant capacity retention driving from the adequate setup in terms of electrodes features. Beside the stability of the cathode above demonstrated, a further interesting proof of the integrity of the water-processed anode using the CMC binder is given by the SEM images of the $(Na_xSn\text{-}C)_{27min}$ anode retrieved from the full-cell upon cycling. The images reported in **Figure 7e,f** with different magnifications depict a uniform morphology, characterized by a rough surface reasonably due to the CMC, wrapping-up the micrometric Sn-C particles, some of which are clearly visible at higher magnification (**Figure 7f**). Moreover, few splits spotted onto the surface may suggest limited changes through the electrode caused by the volume variation upon cycling.

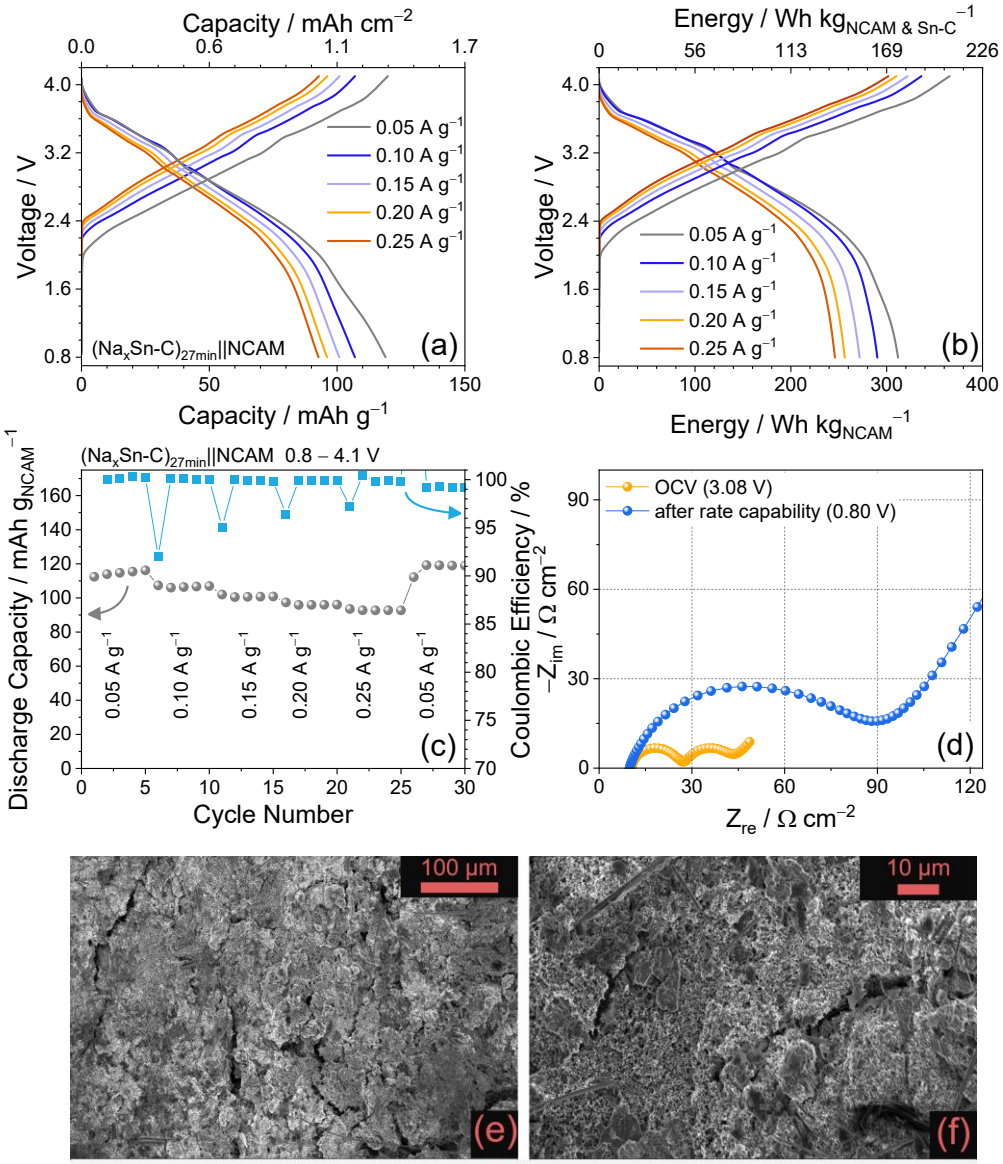

Figure 7. Galvanostatic cycling performance upon current rate capability test of (Na_xSn-C)$_{27min}$||NCAM full-cell, in detail: **(a)** selected voltage profiles (5th of each current rate explored), **(b)** charge/discharge voltage *vs.* energy density (top *x*-axis refers to both electrodes active material masses, while bottom *x*-axis refers to NCAM mass only), **(c)** capacity trend *vs.* cycle number (coulombic efficiency in right-hand side *y*-axis), **(d)** electrochemical characterization of the electrodes/electrolyte interphases through Nyquist plot recorded by EIS (data collected before cycling and after the 30th discharge), **(e, f)** SEM images at different magnification of the (Na_xSn-C)$_{27min}$ electrode retrieved from cycled full-cell. Electrodes geometric area: 0.785 cm², active material: 11.5 ± 0.1 mg$_{NCAM}$ cm^{-2}, 7.6 ± 0.1 mg$_{Sn\text{-}C}$ cm^{-2}. Active material ratio: 1.28, N/P between 1.1 – 1.2. Tests performed at 25 °C.

Table 4.1.3 NLLS analysis carried out on the Nyquist plots displayed in **Figure 6d**. The impedance spectra were acquired on the (Na_xSn-C)$_{27min}$||NCAM cell at the OCV and after the current rate capability test.

Cell condition	**Circuit**	**R_1 (Ω)**	**R_2 (Ω)**	**$R_I=\sum R_n$ (Ω)**	**χ^2**
OCV	$R_e(R_1Q_1)(R_2Q_2)Q_w$	12.5 ± 0.1	14.1 ± 1.0	26.6 ± 1.1	3×10^{-4}
After 30 cycles	$R_e(R_1Q_1)\ Q_w$	59.5 ± 1.2	/	59.5 ± 1.2	3×10^{-4}

References

(44) X. Liang, X. Song, H.H. Sun, H. Kim, M.-C. Kim, Y.-K. Sun, Commun 16 (2025) 3505.
(45) T.-Y. Yu, J. Kim, G. Oh, M.H. Alfaruqi, J.-Y. Hwang, Y.-K. Sun, Energy Storage Mater 61 (2023) 102908.
(46) Y.-J. Guo, P.-F. Wang, Y.-B. Niu, X.-D. Zhang, Q. Li, X. Yu, M. Fan, W.-P. Chen, Y. Yu, X. Liu, Q. Meng, S. Xin, Y.-X. Yin, Y.-G. Guo, Nat Commun 12 (2021) 5267.
(47) X. Yuan, Y. Guo, L. Gan, X. Yang, W. He, X. Zhang, Y. Yin, S. Xin, H. Yao, Z. Huang, Y. Guo, , Adv Funct Mater 32 (2022) 2111466.
(48) S.-M. Oh, S.-T. Myung, J.-Y. Hwang, B. Scrosati, K. Amine, Y.-K. Sun, Chemistry of Materials 26 (2014) 6165–6171
(49) S. Birgisson, T.L. Christiansen, B.B. Iversen, Chemistry of Materials 30 (2018) 6636–6645.
(50) X. Li, Y. Fan, B. Johannessen, X. Xu, K.W. See, W.K. Pang, , Batter Supercaps 7 (2024) e202300618.
(51) T. Risthaus, L. Chen, J. Wang, J. Li, D. Zhou, L. Zhang, D. Ning, X. Cao, X. Zhang, G. Schumacher, M. Winter, E. Paillard, J. Li, Chemistry of Materials 31 (2019) 5376–5383.
(52) I. Hasa, D. Buchholz, S. Passerini, B. Scrosati, J. Hassoun, Adv Energy Mater 4 (2014) 1400083.
(53) X. Chen, X. Zhou, M. Hu, J. Liang, D. Wu, J. Wei, Z. Zhou, J Mater Chem A Mater 3 (2015) 20708–20714.
(54) H.M. Mudassir, C. Xie, F. Xia, R. Fang, Q. Chen, Z. Liu, T. Dong, F. Liu, S. Hu, Z. Jian, J. Wu, J Mater Sci Technol 238 (2025) 230–237.
(55) M.M. Rahman, J. Mao, W.H. Kan, C.-J. Sun, L. Li, Y. Zhang, M. Avdeev, X.-W. Du, F. Lin, , ACS Mater Lett 1 (2019) 573–581.
(56) X. Chen, J. Song, J. Li, H. Zhang, H. Tang, J Appl Electrochem 51 (2021) 619–627.
(57) G. Derrien, J. Hassoun, S. Panero, B. Scrosati, Advanced Materials 19 (2007) 2336–2340.
(58) J. Hassoun, G. Derrien, S. Panero, B. Scrosati, Advanced Materials 20 (2008) 3169-3175.
(61) R. Dai, W. Sun, Y. Wang, , Electrochim Acta 217 (2016) 123–131.
(62) Y. Liu, F. Fan, J. Wang, Y. Liu, H. Chen, K.L. Jungjohann, Y. Xu, Y. Zhu, D. Bigio, T. Zhu, C. rs, Nano Lett 14 (2014) 3445–3452.
(63) D.-J. Lee, J.-W. Park, I. Hasa, Y.-K. Sun, B. Scrosati, J. Hassoun, J Mater Chem A Mater 1 (2013) 5256-5261.
(64) I. Hasa, J. Hassoun, S. Passerini, Nano Res 10 (2017) 3942–3969.
(65) J.M. Stratford, M. Mayo, P.K. Allan, O. Pecher, O.J. Borkiewicz, K.M. Wiaderek, K.W. Chapman, C.J. Pickard, A.J. Morris, C.P. Grey, J Am Chem Soc 139 (2017) 7273–7286
(66) J. Ni, X. Zhu, Y. Yuan, Z. Wang, Y. Li, L. Ma, A. Dai, M. Li, T. Wu, R. Shahbazian-Yassar, J. Lu, L. Li, Nat Commun 11 (2020) 1212.
(67) M. Song, C. Wang, D. Du, F. Li, J. Chen, Sci China Chem 62 (2019) 616–621.
(68) R.F. Shahzad, S. Rasul, M. Mamlouk, I. Brewis, R.A. Shakoor, A.W. Zia, Small Struct 6 (2025) 2400367..
(69) Y. Xu, Y. Zhu, Y. Liu, C. Wang, , Adv Energy Mater 3 (2013) 128–133.
(70) L. Minnetti, E. Barcaro, L. Sbrascini, F. Nobili, J. Hassoun, Mater Res Bull 191 (2025) 113546.
(71) D. Shanmukaraj, K. Kretschmer, T. Sahu, W. Bao, T. Rojo, G. Wang, M. Armand, ChemSusChem 11 (2018) 3286–3291.
(72) Y. Niu, Y. Guo, Y. Yin, S. Zhang, T. Wang, P. Wang, S. Xin, Y. Guo, High-Efficiency Cathode Sodium Compensation for Sodium-Ion Batteries, Advanced Materials 32 (2020) 2001419..
(73) J. Martinez De Ilarduya, L. Otaegui, J.M. López del Amo, M. Armand, G. Singh, J Power Sources 337 (2017) 197–203.
(74) G. Singh, B. Acebedo, M.C. Cabanas, D. Shanmukaraj, M. Armand, T. Rojo, Electrochem Commun 37 (2013) 61–63.
(75) A.J. Fernández-Ropero, M. Zarrabeitia, G. Baraldi, M. Echeverria, T. Rojo, M. Armand, D. Shanmukaraj, ACS Appl Mater Interfaces 13 (2021) 11814–11821.
(76) E. Barcaro, V. Marangon, D. Bresser, J. Hassoun, ChemSusChem 18 (2025) e202400615..
(77) X. Guo, S. Wang, J. Wang, H. Gao, Z. Huang, W. Lai, W.K. Pang, J. Qu, M.H. Nguyen, C. Yang, C. Dong, H. Liu, G. Henkelman, M. Armand, D. Aurbach, G. Wang,, Angewandte Chemie International Edition (2025) e202509929.
(78) C. Kirst, E. Zonta, A. Kunz, A. Karger, M. Düsdieker, A. Frank, V. Savvin, B. Pham, J.P. Singer, A. Jossen, Electrochim Acta 536 (2025) 146703.

(79) H. Hijazi, Z. Ye, L. Zhang, J. Deshmukh, M.B. Johnson, J.R. Dahn, M. Metzger, , J Electrochem Soc 170 (2023) 070512.
(80) Y. Huang, L. Zhao, L. Li, M. Xie, F. Wu, R. Chen, Advanced Materials 31 (2019) 1808393.
(81) J. Yang, J. Ruan, Q. Li, F. Fang, Y. Song, D. Sun, F. Wang, Adv Funct Mater 32 (2022) 2200566.
(82) A.C.S. Jensen, H. Au, S. Gärtner, M. Titirici, A.J. Drew, , Batter Supercaps 3 (2020) 1306–1310.
(83) K. Westman, R. Dugas, P. Jankowski, W. Wieczorek, G. Gachot, M. Morcrette, E. Irisarri, A. Ponrouch, M.R. Palacín, J.-M. Tarascon, P. Johansson, ACS Appl Energy Mater 1 (2018) 2671–2680.
(84) I. Hasa, D. Buchholz, S. Passerini, J. Hassoun, ACS Appl Mater Interfaces 7 (2015) 5206–5212
(85) Y. Sun, G. Åvall, S.-H. Wu, G. A. Ferrero, A. Freytag, P.B. Groszewicz, H. Wang, K.A. Mazzio, M. Bianchini, V. Baran, S. Risse, P. Adelhelm, Nat Mater 24 (2025) 1441-1449.
(86) W. Zuo, A. Innocenti, M. Zarrabeitia, D. Bresser, Y. Yang, S. Passerini, Acc Chem Res 56 (2023) 284–296.
(87) L. Merker, M. Blessing, B. Zhang, H.S. Stein, Advanced Intelligent Discovery (2025) 202500025.
(88) A. Kempf, P. Adelhelm, M. Graczyk-Zajac, , Batter Supercaps (2025) 2500340.

4.2 A composite anode for Sodium-ion battery

Hard carbon appeared of actual interest since it can be derived from numerous natural products or even wastes, by adopting adequate carbonization processes, but unfortunately are affected by low-volumetric capacity.[89-99] On the other hand, hard/amorphous carbons have gained significant attention as sustainable substrates for energy storage due to their advantageous features including disordered character, controllable porosity, and rich surface functionality, whose interplay dictates the anode electrochemical performance.[100] These materials foresee various alkali-ion storage mechanisms such as adsorption, intercalation, and pore-filling, which in overall can influence their reversible capacity and cycling stability.[101-102] Meanwhile graphite, *i.e.*, the most widespread and successful anode in LIB industry with a specific capacity of 372 mAh g^{-1} mainly evolving below 0.2 V vs. Li^+/Li, has been only marginally exploited due to its quite low capacity, modest compatibility with carbonated-based Na-aprotic electrolytes, and limited stability of binary graphite co-intercalation compounds.[103-106] In principle, graphitic character can facilitate the kinetics of the co-intercalation process since the de-solvation energy may be very low or absent. Indeed, the ability to co-intercalate solvent within the structure to form stable ternary compound was unraveled around a decade ago exploiting sodium salts in glyme-based electrolyte media.[107-108] Therefore, the employment of graphitic materials should be tuned considering their massive use in LIB systems due to Li-intercalation ability, as well as in several other fields due to high electrical and thermal conductivity.[109] In this scenario, further anode materials operating at low voltage versus Na^+/Na with adequate Na-storage ability and specific capacity appeared to us to welcome enhance the energy density in full-cell configuration, and to avoid at the same time dendrite formation. Among them, silicon oxide-carbon anodes have been selected, due to the wide interest arose from their successful application in LIB.[110-116]

A Silicon Oxide-Carbon Anode with High Reversibility for Na-ion Battery

In the last section we report the synthesis and characterization of a composite anode formed by FLG and SiO_2 embedded in AC for application in SIB. The FLG is a commercial substrate stacking tents of graphene layers that confers to the material partially graphitic character, while the AC matrix is derived by annealing a sucrose precursor dissolved in water/alcohol dispersion of FLG and SiO_2. The synthesis, previously developed by exploiting different C to SiO_2 ratio for application either in LIB or in Li-ion sulfur battery (see *Section 1.4* and *Section 2.1*), is performed through environmentally compatible hydrothermal process. The anode is characterized in terms of structure, chemical properties, morphology, and performances in Na half- and full-cell. The impact of the highly-reversible anode has been characterized by using both Cu and less expensive/heavy Al current collector, which can be advantageously employed in Na-cell. The data evidenced that both FLG and AC well contribute to the material capacity in Na-cell, while SiO_2, which is usually considered an insulator, has a non-negligible electrochemical activity when included within the carbonaceous framework. Accordingly, the composite anode has revealed reversible Na^+-storage within its structure through multiple-step electrochemical processes, involving both the crystalline/amorphous-carbon and SiO_2 components. Considering the suitable electrochemical performance, the anode has been tested in a laboratory-scale SIB using layered oxide cathode, a glyme-based electrolyte, and exploiting the favorable replacement of the Cu current collector with Al, which is expected to enhance the energy density of the system. The Na-ion cell, operating at about 3 V with high reversibility and relevant Coulombic efficiency (99.97 % mean value upon 300 cycles), has been considered suitable energy storage system for complementary applications to LIB, such as small consumer electronics.

Experimental

- Synthesis of the composite anode

The SiO_2/FLG/AC anode material, hereafter indicated as SiO_xC, was prepared by slightly modifying a synthesis previously proposed in *Section 1.4* for LIBs. Accordingly, 2.40 g of sucrose (≥ 99.0%, Fluka Analytical) were dissolved in 20 ml of a solution composed by distilled water and isopropanol (1:1 volume ratio), and added to a mixture of 0.25 g of amorphous silicon dioxide powder (SiO_2, silica, average particles size 0.007 μm, Sigma-Aldrich) and 0.25 g of FLG. The mixture was sonicated at 50 °C for 2 h, and transferred into an autoclave reactor, which was heated at 190 °C for 12 h and then cooled to room temperature. This process yielded to a brownish-hue compound, which was retrieved from the autoclave and dried on a plate at 70 °C until complete solvent evaporation. Thereafter the compound is exposed to an Ar/H_2 flow (5 % H_2, Air Liquide Italia) inside a tubular furnace, pre-conditioned at 100 °C (1 h

timeframe, temperature increase rate of 5 °C min^{-1}), then annealed at 800 °C (6 h timeframe, temperature increase rate of 10 °C min^{-1}) and finally cooled down to room temperature. The obtained material was ground into an agate mortar to obtain a fine black powder, later employed as electrochemically active material to satisfy sodium ions housing within the electrode. AC used as a blank was prepared by drying a sucrose solution at 100 °C, and annealing using the same condition adopted above for the SiO_xC composite.

- Synthesis of the $Na_{0.48}Al_{0.03}Co_{0.18}Ni_{0.18}Mn_{0.47}O_2$ cathode

The P2/P3-type layered sodium cathode, $Na_{0.48}Al_{0.03}Co_{0.18}Ni_{0.18}Mn_{0.47}O_2$ (indicated with the acronym NCAM), was synthesized through a co-precipitation route following an optimized method reported in the previous two sections. Aluminum nitrate nonahydrate ($Al(NO_3)_3 \cdot 9H_2O$, Sigma-Aldrich, ≥ 98%), cobalt(II)-nitrate hexahydrate ($Co(NO_3)_2 \cdot 6H_2O$, Sigma-Aldrich, ≥ 99.0%), nickel(II)-nitrate exahydrate ($Ni(NO_3)_2 \cdot 6H_2O$, Sigma-Aldrich, ≥ 98.5%), and manganese(II)-nitrate tetrahydrate ($Mn(NO_3)_2 \cdot 4H_2O$, Sigma-Aldrich, ≥ 97.0%) were dissolved in deionized water to form a solution observing the 1:2:2:4.5 molar ratio with respect to Al:Co:Ni:Mn. A 0.5 M NaOH aqueous solution was dropwise added to the nitrate solution to precipitate a hydroxide precursor (50 mol % excess with respect to the hydroxide). The hydroxide precursor was filtered, washed various times with deionized H_2O, and dried as below: overnight at 70 °C, then for 12 h at 120 °C in a dry air flow. Next, the precursor was mixed with sodium hydroxide (NaOH pellets, Sigma-Aldrich, ≥ 98%) in the 1:1 molar ratio. The resulting precursor was calcinated at 500 °C for 5 h in a dry air flow, then grinded in a mortar, pelletized, calcinated at 1000 °C for 6 h in a dry air flow, naturally cooled, rinsed with excess of deionized water, filtered, dried under vacuum at 100 °C, and then stored in a dry ambient.

- Material characterization

The structure of the SiO_xC powder was investigated by XRD through a Bruker D8 Advance instrument equipped with a Cu Kα radiation source scanning the 10° – 60° 2θ range using a step size of 0.02° and rate of 10 s $step^{-1}$. The composition of the material was studied by TGA performed within the 25 − 1000 °C temperature range using a heating rate of 5 °C min^{-1} in dry air flow, with a Mettler-Toledo TGA 2 instrument (Mettler-Toledo, Columbus, OH, USA). Fourier-transform infrared (FT-IR) spectra were recorded via a Bruker Vertex V70 instrument set up in transmittance mode, in a wavenumber range from 400 to 4000 cm^{-1}. The SiO_xC powder morphology was investigated by SEM through a Zeiss Gemini SEM 460 relying on a zirconium oxide coated-tungsten field emission gun, exploiting the secondary electrons mode and using in-lens objective lens, while TEM and selected area diffraction patterns (SAED) were carried out by means of Talos L120C-G2 (ThermoFisher) equipped with a LaB_6 thermionic electron gun operating at 120 kV. XPS measurements were carried out using a Specs XR50 source with an Al anode at a power of 300 W. The analyzer employed was a Specs Astraios 190 with a 2D-CMOS detector and a 3×25 mm entrance slit. All the high-resolution spectra were acquired with a pass energy of 10 eV, in normal emission conditions. All spectra were fitted first by iteratively calculating a Shirley background and then using a linear combination of Voigt single peaks (or doublets) for all signals related, except for the C 1s sp2 signal, for which a gaussian-broadened Doniach-Sunjic lineshape has been used. The components are explicitly shown in the plots and described in the legends, together with the resulting envelope function.

- Electrodes casting and characterization

The electrode tapes were prepared by casting via a doctor blade tool (MTI Corp.) of slurries formed by 80 wt.% active material powder, which was either SiO_xC or NCAM [8,9], 10 wt.% polyvinylidene fluoride (PVdF 6020, Solef) polymer binder, and 10 wt.% carbon black (super P carbon, Timcal, indicated as CSP) electron conductor, dispersed in *N*-methyl-2-pyrrolidone (NMP, Sigma-Aldrich). The slurries were cast onto Al (thickness of 20 μm, MTI Corp.) for NCAM, and either onto Cu (thickness of 10 μm, MTI Corp.) or Al for SiO_xC, and dried at 70 °C inside an oven equipped with a peristaltic pump to remove the NMP solvent. The obtained foils were calendared using an MSK-2150 Rolling Machine (MTI Corp.) to achieve a thickness of 70 % with respect to the original tapes, usually within the range of 120 − 130 μm. The tapes were cut into discs with diameters of 10 and 14 mm (0.785 and 1.54 cm^2 geometric area, respectively) using dedicated Nogami handheld punches. The electrodes were dried under vacuum for 2 hours at 110 °C inside a Büchi oven and finally stored inside an Ar-filled glovebox (MBraun, O_2 and H_2O contents lower than 1 ppm). The active material loading of the electrodes was 2.0 – 6.2 ± 0.1 mg cm^{-2} for SiO_xC and 2.3 – 5.9 ± 0.1 mg cm^{-2} for NCAM (always clarified in the figure caption whenever an electrode is tested). The above procedure was also adopted for casting on Cu the material constituents, *i.e.*, either SiO_2, FLG, or AC, dispersed in NMP solvent with CSP and PVdF (80:10:10 weight ratio, respectively), to achieve blank electrodes for sake of comparison with SiO_xC. The SiO_xC electrode morphology was investigated by SEM through a Zeiss Gemini SEM 460 relying on a zirconium oxide coated-tungsten field emission gun, exploiting the secondary electrons mode. The structure of the electrode was investigated by XRD through a Bruker D8 Advance instrument equipped with a Cu Kα radiation source scanning the 10° – 60° 2θ range using a step size of 0.02° and rate of 10 s $step^{-1}$. Either pristine or cycled electrodes tested in Na-cell using the glyme electrolyte over 100 cycles at 0.05 A g^{-1} within 0.01 – 2.0 V range were investigated.

- Electrolytes

The electrolytes used in this work are: *(i)* tetraethylene glycol dimethyl ether (TEGDME, $CH_3(OCH_2CH_2)_4OCH_3$, Sigma-Aldrich) dissolving $NaCF_3SO_3$ (98 %, Sigma-Aldrich) salt with concentration of 1 mol_{salt} $kg_{solvent}^{-1}$ (1 m), indicated in the text with the acronym TE-F, (*ii*) diethylene glycol dimethyl ether (DEGDME, $CH_3(OCH_2CH_2)_2OCH_3$, Sigma-Aldrich) dissolving sodium hexafluorophosphate ($NaPF_6$, 99.9% trace metals basis, anhydrous, battery grade, Merck) salt with concentration of 1 M, indicated in the text with the acronym DE-P. Before employment, TEGDME and DEGDME were stored under molecular sieves (rods, 3 Å, size 1/16 inch, Honeywell Fluka, dried under vacuum at 270 °C for 3 days, cooled down, and stored under Ar) until a H_2O content lower than 10 ppm was achieved as determined by a Karl Fischer 899 Coulometer (Metrohm). The $NaCF_3SO_3$ salt was dried for 2 days under vacuum at 110 °C to remove water traces and stored under Ar.

- Electrochemical characterization

CR2032 coin-type cells (MTI Corp.) and 3-electrodes T-type cells (10 mm-diameter electrodes) were assembled inside an Ar-filled glovebox (MBraun, O_2 and H_2O content lower than 1 ppm) by stacking respectively a 14 or 10 mm-diameter sodium metal disc (99.9%, Sigma-Aldrich, trace metal basis) cut from sodium pieces, roll pressed and finally punched as counter and reference electrode, a 16 or 10 mm-diameter glass fiber (Whatman GF/B) disc as separator soaked with the electrolyte (amount fixed respectively to 50 μl and 200 μl for coin-cells and T-cell), and either a SiO_xC or NCAM disc as working electrode. The adopted cell setup is indicated in each figure caption. The electrochemical features of SiO_xC were examined through CV and EIS employing a VersaSTAT MC Princeton Applied Research (PAR-AMETEK)

multichannel potentiostat at room temperature. CV was performed in 3-electrodes T-type cells within the 0.01 – 2.0 V *vs.* Na^+/Na potential range at a scan rate of 0.1 mV s^{-1}, while EIS spectra were collected at the open circuit voltage (OCV) condition before cycling and upon 1, 5 and 10 CV runs using an alternate voltage signal of 10 mV in the frequency range between 500 kHz and 100 mHz. The fitting enabled to describe the Nyquist spectra in terms of equivalent circuits including resistive (R) and constant phase elements (CPE, Q), in detail: *(i)* R_e is the electrolyte resistance, indicated by the high-frequency intercept of the plot; *(ii)* (R_iQ_i) is associated with the high-medium frequency semicircle accounting for the electrode/electrolyte interphase; *(iii)* Q_w is ascribed to the semi-infinite Warburg-type Li^+ diffusion, depicted by a low-frequency tilted line.

- Half-cells galvanostatic cycling

The Na|TE-F|SiO_xC coin-cells were galvanostatically cycled between 0.01 − 2.0 V either at constant current rate of 0.05 A g^{-1}, or by applying various current rates increasing every 10 cycles from 0.015 A g^{-1} to 0.03, 0.06, 0.09, and 0.15 A g^{-1} before decreasing back to 0.015 A g^{-1} at the 50^{th} cycle. Subsequently, the latter current was held for 60 discharge/charge runs, and the cells were subject again to the above reported current rate variations. The galvanostatic cycling tests were performed via a MACCOR series 4000 battery test systems (room temperature 25 °C, maximum fluctuation ± 1.0 °C). Prior to the galvanostatic tests, the cells were rested for 2 h. Naturally, the active material content within the electrode is accounted by considering all the SiO_xC material.

- Na-ion Full-cell exploiting NCAM cathode

The developed Na-ion full-cell configuration has been obtained by stacking NCAM cathode just after casting drying as indicated above, and a chemically sodiated Na-SiO_xC anode. Accordingly, the SiO_xC electrode (14 mm-diameter, 1.54 cm^2 geometric area) was placed in direct contact with a Na foil wetted by DE-P and pressed with 0.2 kg weight. The partially sodiated Na-SiO_xC electrode was recovered upon 3 minutes of capillary contact, which was determined as sufficient timeframe to store a Na^+ amount for ensuring a proper cell-balance. Subsequently, the Na-SiO_xC|DE-P|NCAM full-cell was galvanostatically cycled at the constant current rate of 0.05 A g^{-1} between 1.0 and 4.0 V. Current rate and capacity of the full-cell were referred to the cathode active material weight.

Results

Figure 1 reports some physical-chemical characteristics of the SiO_xC powder. The structure of the anode material is checked by means of XRD, as depicted by the pattern in **Figure 1a** which shows a major narrow peak centered at 2 θ = 26.4° corresponding to the graphite (002) planes reflection due to the partial stacking of the FLG sheets. The same diffractogram reveals a broad signal from 2 θ = 13° to 2 θ = 39° which may be attributed to non-crystalline nanometric fumed silica used for the synthesis, and the AC originating from the sucrose source as indicated by a previous report for analogue materials used in LIB. On the other hand, the latter work suggested that changing the ratio of the anode constituents doesn't influence the crystalline features of the final product, however it could

affect the sample's morphology and electrochemical response. Therefore, the weight ratio of silicon oxide and carbons within the composite anode is detected in **Figure 1b** through TGA, performed under air flow, and corresponding DTG. After the initial weight loss of 4 % due to absorbed moisture within the material below 150 °C, the data evidence a substantial decay at 560 °C and a second one between 630 and 900 °C, ascribed to the removal of carbons in the anode as CO_2 gas formed by direct combustion with the oxygen in the air flow, leading to an overall C content of 81 %, and a residue of 19 % corresponding to the SiO_x portion, both rescaled to exclude the water loss. Interestingly, if compared to a previous SiO_xC anode for LIB, the one reported herein shows a rather different composition which is tuned for SIB. Indeed, the magnitudes of the first loss associated with the more exposed amorphous carbon deriving from sucrose below 600 °C, and the second one related to the more compact FLG occurring at higher temperature, indicate for the two carbons a weight ratio of 55% and 26 % in this SiO_xC, instead of 61% and 14 % in the one developed for LIB. Furthermore, the silica residue above 800 °C is about 19 %, rather than 32 % achieved in the previous work. The lower silica amount and higher FLG content compared to the material previously designed for LIB can actually enhance the conductivity of the electrode to allow a more efficient operation in SIB. **Figure 1c** shows the FT-IR spectra of the SiO_xC powder, including the synthesis sources (*i.e.*, sucrose and SiO_2), whilst FLG is not taken into account due to its negligible contribution to the IR signal. In fact, this material has almost pure graphitic IR-response since it is prepared by exfoliation of bulk graphite crystals using high-speed solvent jet streams, without significant formation or addition of any functional group. As expected, sucrose reveals a wide signal at 3324 cm^{-1} due to the vibrational modes of O-H in intermolecular hydrogen bond from hydroxyl substituents, as well as C-H vibrational signals at 2919 cm^{-1} due to $-CH_3/-CH_2$ aliphatic groups, 1781 cm^{-1} due to C=O stretching of -COO in acetyl esters, 1693 and 1447 cm^{-1} respectively due to asymmetric and symmetric modes of O-H in carboxyl and carbonyl groups, and at 1063 cm^{-1} ascribed to the C-O, C-C, C-O-C or -C-C- stretching.[115] On the other hand, SiO_2 shows the signals of O-H hydroxyl stretching, however due to silanol groups, at 3260 cm^{-1},[116] a wave at 1638 cm^{-1} due to the H-O-H bending vibrations of adsorbed water,[117] and a signal at 1428 cm^{-1} ascribed to the O-CO-O bending in Si-O-CO-O-Si carbonates formed by CO_2 impurities.[118] Furthermore, the SiO_2 reveals the main signal at 1097 cm^{-1} ascribed to Si-O-Si stretching in siloxane groups, a shoulder at 959 cm^{-1} due to the Si-OH stretching in silanol groups, a peak at 814 cm^{-1} for the asymmetric stretching of Si-O in siloxane groups, and a marked signal a 471 cm^{-1} for the symmetric stretching of the same

groups.[119] As for the SiO_xC, the spectrum appears quite different from the ones of the precursors, since the material is synthesized in reductive condition at 800 °C (see experimental section). Hence, the FT-IR evidences for the sample the typical signal at 3007 cm^{-1} ascribed to the C-H stretching modes in aliphatic/olefinic groups or aromatic rings,[120] and others at 1876 cm^{-1} due to stretching of C=O in organic carbonates.[137] In addition, a signal at 1544 cm^{-1} is due to stretching of C=C in olefinic groups or aromatic rings,[120] while the one at 1430 cm^{-1} is ascribed to H-C-H bending in substituted aliphatic groups.[121] Finally, further vibrations appear at 1168 cm^{-1} due to stretching of C-O, C-OH and C-O-C in phenols and carboxylic acids or ethers,[122] 1076 cm^{-1} due to stretching of Si-O in siloxane groups, and at 472 cm^{-1} due to stretching of Si-O in siloxane groups.[124] For readers' convenience, **Table 4.2.1** collects the signals achieved by the FT-IR spectra. In summary, the FT-IR study suggests that the SiO_xC sample is well functionalized with various groups, mainly originating from the formulation of the precursor, and likely promoted by the synthetic process adopted herein.

The sample composition and the absence of contaminants are supported by the XPS analysis performed on the SiO_xC powder. **Figure 1d** displays the Si 2p core level spectrum, which is fitted with three components, the first of which (81%) is centered at 104.4 eV, and reflects the signal from SiO_2 where the Si is in the +4 oxidation state. Another component is centered at 105.5 eV (15%), and possibly attributed to $Si(OH)_4$ in which Si is still at +4 oxidation state, but with slightly higher binding energy.[53] The latter component well supports the FT-IR results which suggest the presence of Si-OH silanol groups, possibly promoted by absorbed water for sample exposition to the atmosphere. The third component observed at 103.3 eV (4%) may be likely attributed to Si in the +2 oxidation state, e.g., Si_2O_3, due to the partial reduction of the SiO_2 promoted by the H_2 at 800 °C during the synthesis (see experimental section for details). Furthermore, the signal recorded from O 1s in **Figure 1e** confirms the latter hypothesis by showing the same peak distribution (76%, 18% and 6%) for the components at 533.8, 534.8, and 532 eV, respectively. On the other hand, the C 1s (**Figure 1f**) reveals a predominant component at 284.6 eV (78.5%), suggesting principally sp2 nature of the carbon, and a smaller component at 285.5 eV (21.5%) due to sp3 carbon contribution.

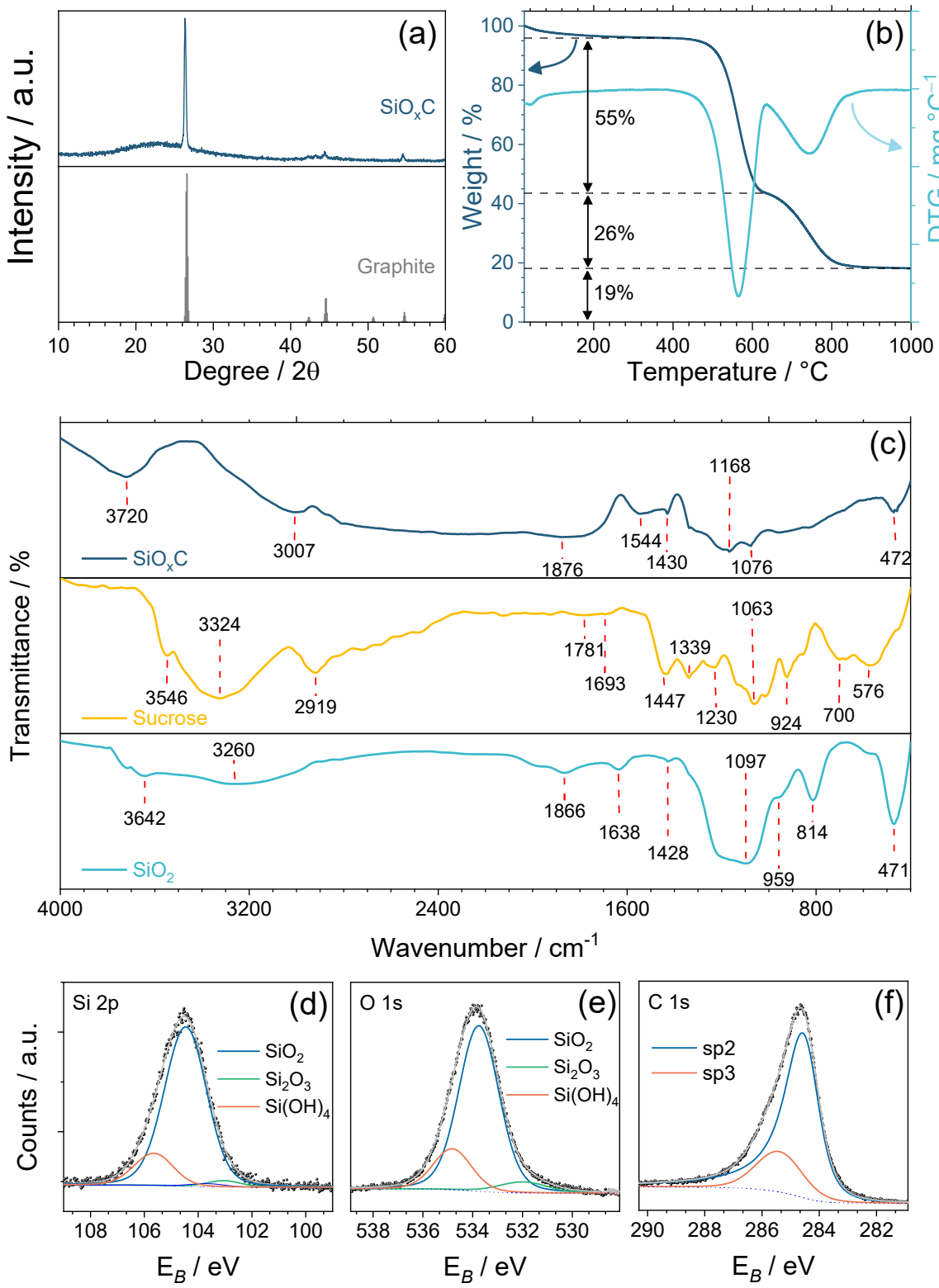

Figure 1. Physical-chemical characterization of the SiO_xC powder, in detail: **(a)** X-ray diffractograms for the SiO_xC sample, reference data for graphite (ICSD #76767) is reported for comparison; **(b)** TGA performed under dry air flow with heating rate of 5 °C min^{-1} from 25 to 1000 °C, and corresponding DTG; **(c)** FT-IR spectra acquired in transmittance mode of SiO_xC powder, sucrose, and SiO_2 from 4000 to 400 cm^{-1} wavenumber; **(d-f)** XPS core level spectra of **(d)** Si 2p, **(e)** O 1s, and **(f)** C 1s of the of SiO_xC powder.

Table 4.2.1 Signal indexing of the FT-IR spectra of SiO_xC, sucrose and SiO_2 sources reported in Figure 1c.

	Wavenumber (cm^{-1})	Assignments		Group	Ref
SiO_xC	3007	$\nu_{(C-H)}$	$-CH_3$/ $-CH_2$ / -CH	Aliphatic/olefinic groups or aromatic rings	45
	1876	$\nu_{(C=O)}$	-O-CO-O-	Organic carbonates	49
	1544	$\nu_{(C=C)}$	-C=C-	Olefinic groups or aromatic rings	50
	1430	$\delta_{(H-C-H)}$	$-CH_2$	Substituted aliphatic groups	46
	1168	$\nu_{(C-O)}$	C-OH and C-O-C	Phenols and carboxylic acids or ethers	50
	1076	$\nu_{(Si-O)}$	Si-O-Si	Siloxane groups	46
	472	$\nu_{(Si-O)}$	Si-O-Si	Siloxane groups	46
Sucrose	3324	$\nu_{(O-H)}$	-OH	Intermolecular hydrogen bond from hydroxyl substituents	45
	2919	$\nu_{(C-H)}$	$-CH_3$/ $-CH_2$	Aliphatic groups	45
	1781	$\nu_{(C=O)}$	-COO	Acetyl ester	45
	1693	$\nu_{asimm(O-H)}$	-COO	Carboxylic or carbonyl groups	45
	1447	$\nu_{simm(O-H)}$	-COO	Carboxylic or carbonyl groups	45
	1063	$\nu_{(C-O)}$ or $\nu_{(C-C)}$	C-O-C or -C-C-	Carboxylic or carbonyl groups	45
SiO_2	3260	$\nu_{(O-H)}$	-OH	Hydroxyl on silanol groups	46
	1638	$\delta_{(H-O-H)}$	H_2O	Adsorbed water	47
	1428	$\delta_{(O-CO-O)}$	Si-O-CO-O-Si	Carbonates from CO_2 impurities	48
	1097	$\nu_{(Si-O)}$	Si-O-Si	Siloxane groups	46
	959	$\nu_{(Si-OH)}$	-SiOH	Silanol groups	46
	814	$\nu_{asimm(Si-O)}$	Si-O-Si	Siloxane groups	46
	471	$\nu_{simm(Si-O)}$	Si-O-Si	Siloxane groups	46

The morphology of the SiO_xC sample is investigated by the SEM/TEM micrographs in **Figure 2**. The SEM image in **Figure 2a** shows micrometric agglomerates with a size of about 70 μm, within a matrix including smaller dispersed particles. The magnified images in **Figure 2b-d**, clearly reveal that both the agglomerates and the smaller particles are formed by an intimate mixture of FLG flakes, AC, and SiO_x. The TEM image of the FLG in **Figure 2e** evidences the stacking of the graphene layers, with resulting poly-crystallinity detected by SAED in panel inset. On the other hand, the nanometric SiO_x spherules

embedded in the AC matrix of the composite-anode powder are also detected in the TEM of **Figure 2f**. Therefore, we can describe the SiO_xC sample as an array in which carbons of different natures (FLG, AC) and SiO_x are mixed to form a heterogeneous morphology, including extended submicron matrix as well as 3D-aggregates, despite the rigorous grinding process to which the sample is subjected. The composite submicrometric/micrometric shape of the sample may hold some advantages, such as enhanced electrochemical performance in SIB, structural stability, and high conductivity. Indeed, larger particles with ionic conductivity may limit the electrolyte decomposition and depletion upon cycling, which is instead triggered by the submicron particles. On the other hand, the small particles may improve the ion conductivity of the material by shortening the Na^+-diffusion paths.[144] Furthermore, as already suggested by the TGA results, also SEM/TEM indicates a different morphology of this sample compared to previous ones, due to the different ratio of the components (namely SiO_2, FLG, and sucrose),[40] which may be more adequate to the Na-ion battery application.

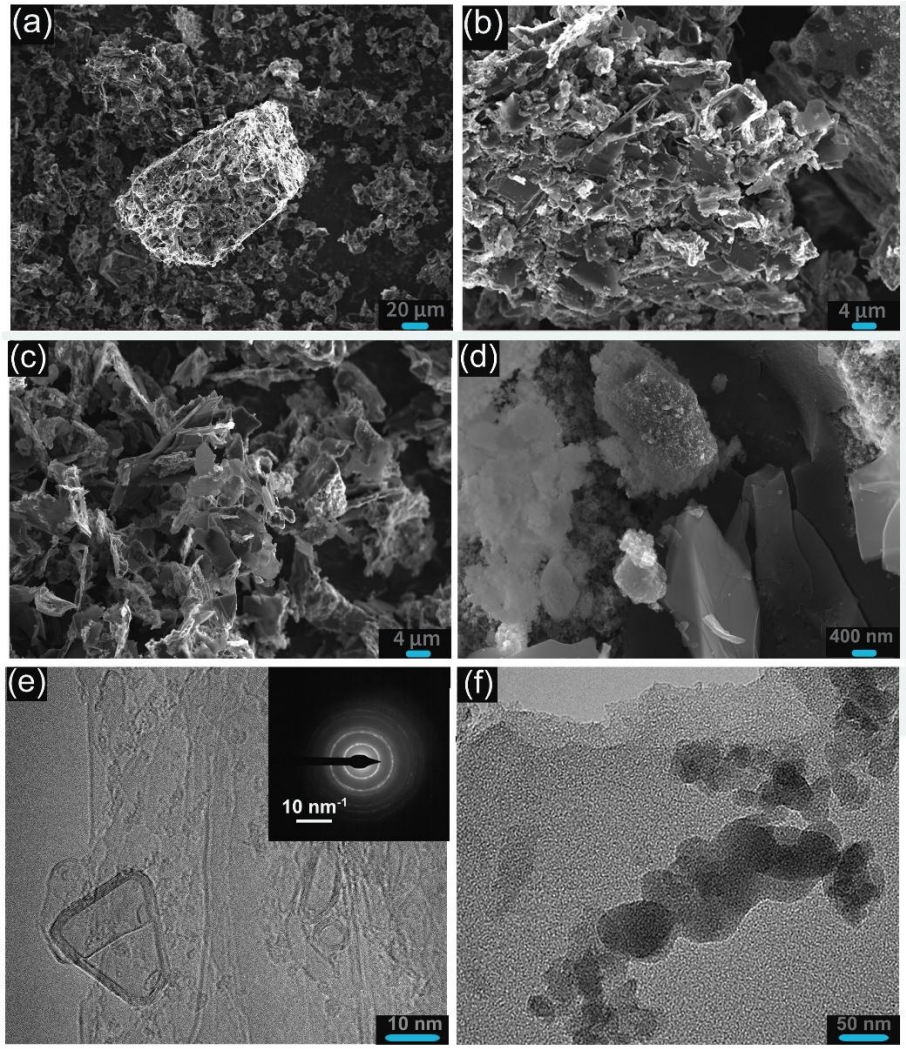

Figure 2. Morphological characteristics of the SiO_xC powder, in detail: **(a-d)** SEM images acquired in secondary electrons mode using in-lens objective lens. TEM image of **(e)** FLG

pristine powder (inset reporting its SAED) and (**f)** SiO_xC powder.

Figure 3 reports the investigation of the electrochemical features of the SiO_xC electrode cast onto either Al or Cu and studied in sodium half-cell filled with the TE-F electrolyte, achieved by CV and EIS. The voltammograms reveal during the first cathodic scan a broad wave with current onset beginning at about 1.30 V Na^+/Na, showing distinct peaks at 0.80, 0.70, 0.45, and 0.05 V *vs.* Na^+/Na, which have comparable specific current and a narrowest shape using the Cu current collector (**Figure 3b**) rather than Al (**Figure 3a**). During the second cathodic scan, the CV peaks split to 6 resolved ones, whilst the broad wave between 1.30 and 0.00 V *vs.* Na^+/Na vanishes, thus indicating partial irreversible reduction of the electrolyte with formation of the SEI at electrodes surface. This protective and conductive film is usually composed of NaF, Na_2CO_3 and/or other species within a thickness range of tenths of nm depending on the electrolyte composition and cycling experimental constrains.[145,146] The first anodic scan reveals 3 resolved peaks at 0.09, 0.49, 0.80 V *vs.* Na^+/Na, a shoulder at 0.90 V *vs.* Na^+/Na, and a low intensity wave between 0.9 and 1.30 V *vs.* Na^+/Na, which are reproduced during the second run. The subsequent cycles show a remarkable overlapping of the above-mentioned anodic and cathodic peaks that appear narrowest using Cu, with a slight current reduction and broadening of the oxidation process at about 0.80 V *vs.* Na^+/Na, a similar trend for the reduction one at 0.70 V only for the sample using Al current collector. The above slight shifts in peak position and intensity may be ascribed to structural rearrangement of the electrode as well as to the consolidation and the stabilization of the SEI by the ongoing of the CV in the glyme-based electrolyte.[147] The well reversible response of the SiO_xC electrode can be justified by the stability of its interphase with the electrolyte, demonstrated EIS spectra reported in **Figure 3c,d** recorded at the OCV condition of the half-cells and after 1, 5 and 10 CV scans. The NLLS analysis of the Nyquist plot allows the evaluation of resistive and constant phase elements (CPE) of the cells through the description of each spectrum with an equivalent circuit. Accordingly, the cell can be represented by the $R_e(R_nQ_n)Q_w$ circuit, where: *i)* R_e is the electrolyte bulk resistance obtained as high frequency intercept of the plot with the *x*-axis; *ii)* (R_nQ_n) elements (with $n = 1, 2, \ldots$) account for the electrode/electrolyte interphase phenomena, such as charge transfer and SEI formation, identified by the high-middle frequency semicircles whose overall width lead to the total interphase resistance (R_i); *iii)* Q_w is a CPE due to the semi-infinite Warburg-type Na^+ ion diffusion represented by the tilted line at low-frequency values. The NLLS fitting results of the electrode cast on Al and Cu current collector, reported respectively in **Table 4.2.1** and

Table 4.2.2, reveal similar interphases resistance at the OCV of 23.7 Ω and 14.8 Ω, respectively. As soon as the first CV cycle is completed, the resistance values diverge, the one of the electrode using Al current collector increases by almost 3 times (**Table 4.2.1**), whilst the one using the Cu shrinks by 1/3 (**Table 4.2.2**). The raising resistance of the electrodes cast on Al is most likely ascribed to possible corrosion of this current collector within reductive condition, and partial deterioration even by the action of the $CF_3SO_3^-$ anion.[130-135] Rather, the Cu current collector is much more stable, and the resistance of the electrode using it as the support decreases after the first CV mostly due to a partial dissolution of the native SEI on SiO_xC. It is worth mentioning that the lower resistances of the material using Cu rather than Al also justifies the narrowest shape of the CV peaks observed using the former current collector (also motivated by its intrinsic higher-electron conductivity). On the other hand, the resistance increases with relevantly slower magnitude to about 155 Ω upon 10 cycles for the SiO_xC electrode on Al, and to a value as low as 10 Ω during the same interval for the one on Cu as the SEI growth and finally stabilizes.

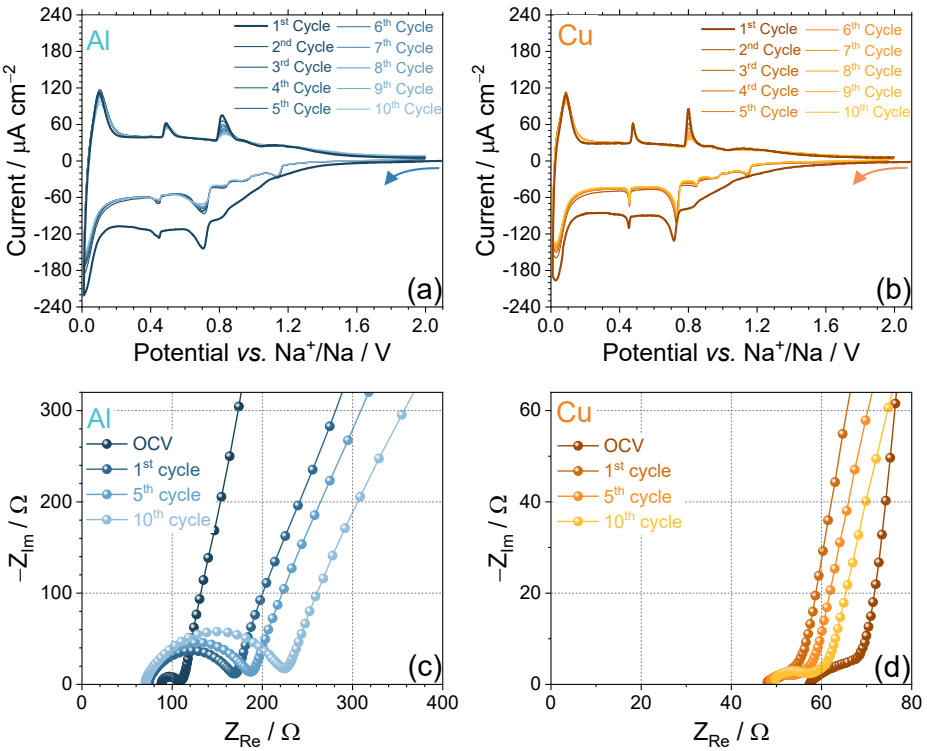

Figure 3. Electrochemical features of the SiO_xC electrode casted onto Al or Cu, in detail: **(a, b)** CV profiles, and **(c, d)** Nyquist plots recorded by EIS related to Na|TE-F|SiO_xC T-cells; CV potential range: 0.01 – 2.0 V *vs.* Na^+/Na; scan rate: 0.1 mV s^{-1}; EIS performed at the OCV cell condition and upon CV after the 1st, 5th, and 10th cycle between 500 kHz and 100 mHz; alternate voltage signal: 10 mV. Experiments performed at 25 °C.

Table 4.2.1 NLLS analysis carried out on the Nyquist plots displayed in Figure 2c. The impedance spectra were acquired on a Na|TE-F|SiO_xC cell, having the positive electrode casted onto Al, at the OCV and after 1, 5, and 10 CV runs.

Cell condition	Circuit $R_e(R_iQ_i)Q_w$	R_1 (Ω)	χ^2
OCV	$R_e(R_1Q_1)Q_w$	23.7 ± 2.2	3×10^{-5}
After 1 CV	$R_e(R_1Q_1)Q_w$	95.9 ± 0.4	4×10^{-5}
After 5 CV	$R_e(R_1Q_1)Q_w$	116.3 ± 0.5	7×10^{-5}
After 10 CV	$R_e(R_1Q_1)Q_w$	155.4 ± 0.7	7×10^{-5}

Table 4.2.2 NLLS analysis carried out on the Nyquist plots displayed in Figure 2d. The impedance spectra were acquired on a Na|TE-F|SiO_xC cell, having the positive electrode casted onto Cu, at the OCV and after 1, 5, and 10 CV runs.

Cell condition	Circuit $R_e(R_iQ_i)Q_w$	R_1 (Ω)	R_2 (Ω)	$R_I=\sum R_i$ (Ω)	χ^2
OCV	$R_e(R_1Q_1)Q_w$	14.8 ± 0.1	-	14.8 ± 0.1	3×10^{-5}
After 1 CV	$R_e(R_1Q_1)(R_2Q_2)Q_w$	4.2 ± 0.1	3.8 ± 1.6	8.0 ± 1.6	3×10^{-5}
After 5 CV	$R_e(R_1Q_1)(R_2Q_2)Q_w$	7.1 ± 0.1	2.7 ± 1.0	9.8 ± 1.0	4×10^{-5}
After 10 CV	$R_e(R_1Q_1)(R_2Q_2)Q_w$	9.6 ± 0.1	2.5 ± 1.1	12.1 ± 1.1	7×10^{-5}

Therefore, we may state that the SiO_xC electrode can actually operate in SIB with a multistep process characterized by modest polarization. Furthermore, the electrochemical process of the SiO_xC keeps its efficiency and low polarization, however with higher interphase resistance using Al current collector rather than Cu, which has instead a relevantly higher cost.[137] After the investigation of the electrochemical processes allowing the Na^+ storage within our anode, the SiO_xC electrode is galvanostatically cycled in sodium half-cell using the TE-F electrolyte, as reported in **Figure 5**. **Figure 5a,b** shows selected voltage profiles from a test performed at 0.05 A g^{-1}, while the corresponding charge capacity *vs.* cycle number and efficiency trends are displayed in **Figure 5c,d**. The first (dis)charge runs reported as insets in **Figure 5a,b** indicate initial low coulombic efficiency of SiO_xC (respectively 53 and 51 % using Al and Cu), due to the above-mentioned partial reduction of the electrolyte with SEI film formation, occurring between 1.2 and 0.2 V, in good agreement with the CV tests. Subsequently, the voltage profiles show reversible process centered at an average value of 0.4 V, where the multiple peaks described upon CV appear merged into four sloping regions both for Al and Cu current collector, i.e., 1.2 – 0.8 V (~15 and 20 mAh g^{-1} capacity contribution), 0.8 – 0.5 V (25 and 35 mAh g^{-1}), 0.5 – 0.1 V (40 and 55 mAh g^{-1}), and below 0.1 V (20 and 50 mAh g^{-1}), thus leading to an overall discharge capacity of 102 and 163 mAh g^{-1}, respectively. It is worth mentioning that charge and discharge occur with almost symmetrical profiles, with minor polarization and reversible shape as also demonstrated by the corresponding capacity and efficiency trends displayed in **Figure 5c,d**. Therefore, the cells retain the initial capacity of 100 and 160 mAh g^{-1} over 400 galvanostatic cycles for 92.7 % and 93.7 %, while the average coulombic efficiencies after the initial cycle are of 99.4 – 99.5 %, respectively for Al and Cu current collector. These data remark a notable reversibility and stability of the

above-mentioned electrochemical processes, and the relevant ability of the SiO_xC electrode for Na^+ storage.

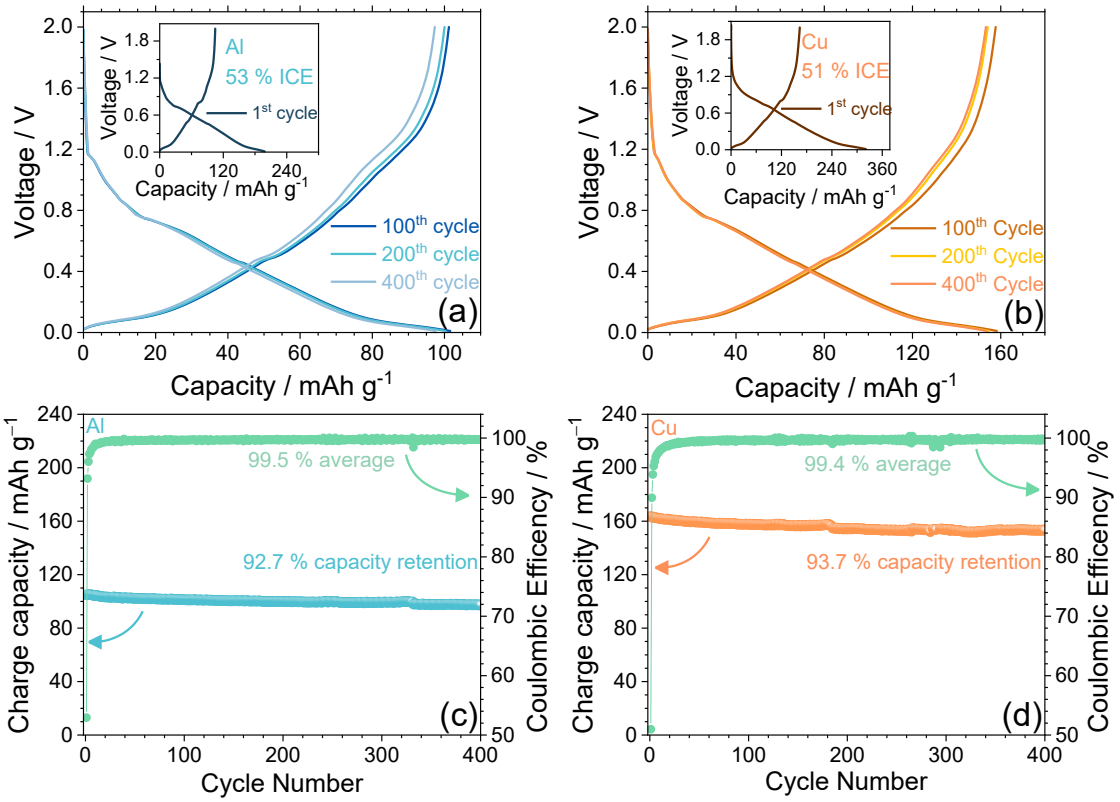

Figure 4. Galvanostatic cycling performance of Na|TE-F|SiO_xC half-cells with electrodes casted onto Al (light blue) or Cu (orange), in terms of **(a, b)** selected voltage profiles (insets report the first discharge/charge run) and **(c, d)** corresponding charge capacity trends *vs.* cycle number (coulombic efficiency in right-hand side *y*-axes), voltage range: 0.01 – 2.0 V, current rate: 0.05 A g^{-1}; electrodes geometric area: 1.54 cm^2, loading: 2.3 ± 0.1 mg_{SiOxC} cm^{-2} (Al), 2.0 ± 0.1 mg_{SiOxC} cm^{-2} (Cu). Test performed at 25 °C.

Figure 5 shows further galvanostatic cycling tests of the SiO_xC in sodium half-cells, carried out by applying currents increasing every 10 cycles to determine the rate capability of the material. The selected voltage profiles (10^{th} for each current rate) are reported in **Figure 5a,b**, and the corresponding charge capacity trend *vs.* cycle number with coulombic efficiency are displayed in Figure **5c,d**, which shows the applied current as insets. The voltage profiles reveal at the 10^{th} cycle (**Figure 5a,b**) the electrochemical process centered at ~0.45 V with more relevant specific capacity for electrodes cast on Cu rather than Al, as previously justified. On the other hand, the cells show higher capacity at the lower current of 0.015 A g^{-1} both for material cast on Al and on Cu (115 and 180 mAh g^{-1}, respectively) than at the higher one of 0.15 A g^{-1} (80 and 150 mAh g^{-1}, respectively), with a coulombic efficiency of 98.4 % at lower current and 99.8% at the higher one. Thus, we can declare that the practical 1-C rate of the SiO_xC electrode casted onto Cu, that is 0.15 A g^{-1}. The higher capacity at the lower current is associated with the lower ohmic polarization that favors the occurrence of the electrochemical process, particularly at low voltage, while the

higher efficiency at the higher current is typically ascribed to the kinetic limitation of side reactions such as electrolyte decomposition.[138] Hence, the delivered capacity decreases as current and polarization increase, the coulombic efficiency rises, whilst the pristine capacity values are restored as the current is lowered back to the lowest value upon 40 cycles.

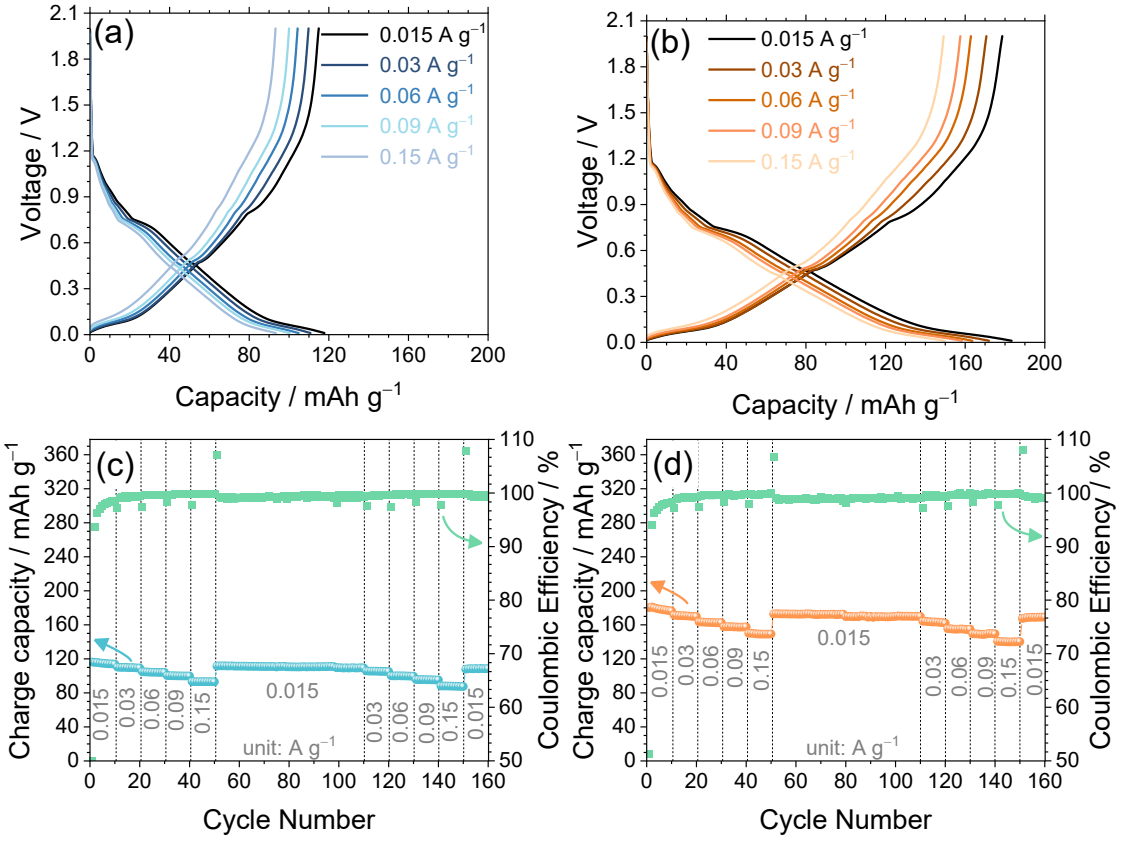

Figure 5. Galvanostatic cycling rate capability tests of Na|TE-F|SiO_xC half-cells, having electrodes casted either onto Al (blue) or Cu (orange), in terms of: **(a, b)** selected voltage profiles and **(c, d)** corresponding charge capacity trends *vs.* cycle number (coulombic efficiency in right-hand side *y*-axes), voltage range: 0.01 – 2.0 V, electrodes geometric area: 1.54 cm^2, loading: 2.3 − 2.5 ± 0.1 mg_{SiOxC} cm^{-2}, temperature: 25 °C.

Overall, our results show that the SiO_xC anode has suitable performance both when cast on Cu or Al current collectors, particularly in term of capacity retention. Despite ~ 36 % lower capacity, the latter current collector is considered the best candidate for full-cell application, since it is lighter, less expensive, and therefore technically advantageous in terms of practical energy density and cost. Furthermore, the good electrochemical performance suggests the SiO_xC as a stable anode that favorably stores Na^+ through various processes. On the other hand, the anode synthesis is environmentally compatible since it involves solvents such as alcohol and H_2O, and easily accessible materials (SiO_2, Sucrose, FLG) with a ratio optimized to avoid inactive fractions and increase the electrode conductivity. However, the good electrochemical performances of SiO_xC in Na half-cells

operating until 2 V using the in the TE-F electrolyte can be hindered in Na-ion full-cell, which instead operates until higher voltage. Previous work has in fact indicated an electrochemical stability window of the TE-F electrolyte extended up to 2.98 V *vs.* Na^+/Na before ongoing oxidative decomposition, that is an inconveniently low value to enable practical application. This issue is limited in the subsequent paragraph by improving the electrode/electrolyte interphase through using different glyme-based electrolyte, and adopting a chemical treatment of the SiO_xC electrode to compensate for the initial low-coulombic efficiency of the anode.

3.3 Na-ion full cell using the SiO_xC anode

With the aim of further exploiting the potentiality of our anode, we designed a SIB configuration exploiting the SiO_xC material cast on Al with a layered oxide NCAM electrode operating at conveniently high potential. Since TE-F electrolyte cannot stand up voltages higher than 3.8 V, we have replaced the electrolyte by using a shorter glyme (DEGDME) and a different salt ($NaPF_6$), to achieve the DE-P which is stable until a suitable threshold. Moreover, the PF_6^- anion possesses the lowest HOMO energy level among other salts,[139-140] making it more stable toward electron loss and/or decomposition. Next, the SiO_xC anode is used in a Na-ion full-cell with the DE-P and the Na-deficient NCAM cathode. The chemical pre-sodiation of the anode performed mechanically outside the full-cell leads to its balancing with a N/P ratio approaching 1, as evidenced by the voltage profiles of the two electrodes separately tested in Na half-cells in **Figure 6**. The capacities well match each other, thus enabling a stable full-cell if the active materials are balanced 1 to 1 with respect to their weight. Subsequently, the Na-SiO_xC|DE-P|NCAM full-cell is cycled at 0.05 A g^{-1} in the 1.0 – 4.0 V range. The full-cell display adequate stability and electrochemical response upon cycling (**Figure 6b**), highlighted by a first discharge capacity of 100.2 mAh g^{-1}, retained by 63.3 % after 300 cycles, and a mean coulombic efficiency corresponding to 99.97 %, allowed by the highly-reversible electrochemical activity of SiO_xC. The voltage profiles evolution upon cycling of this cell (**Figure 6c**) suggest the combination of the anode and cathode signatures, with an average working voltage centered at about 2.9 V, and almost symmetrical profiles that ensure adequate energy efficiency of this SIB. After the first cycle, the capacity is maintained at 100.2 mAh g^{-1}, then slowly decreases to 88.5 at the 50th cycle, steadily losing on average 0.123 mAh g^{-1} each cycle (**Figure 6b**). This trend indicates that the cell is properly operating thanks to N/P optimization (around 1.1), while the relatively stable cycling is promoted both from anode and cathode optimal electrochemical responses. The coulombic efficiency of the cell (**Figure 6b**) shows a steady state value ranging from 99.4 % to 100.1

%, thus further accounting for the suitability of the anode material we developed herein. The use of the chemical activation of the anode (*i.e.*, chemical pre-sodiation by capillary contact) developed in a previous work allows possible scalability of the full-cell, without any electrochemical pre-treatment which is a remarkable advantage in view of a practical application of the battery. The interphase resistance evolution was tracked by acquiring EIS spectra at the OCV condition and at the end of the 300th discharge. The obtained Nyquist plots are reported in **Figure 6d** and their NLLS analysis is displayed in **Table 4.2.3** which suggests a good stability of the interphase resistance, incrementing from 31.4 Ω at the OCV to 65.7 Ω at the end of the galvanostatic cycling test.

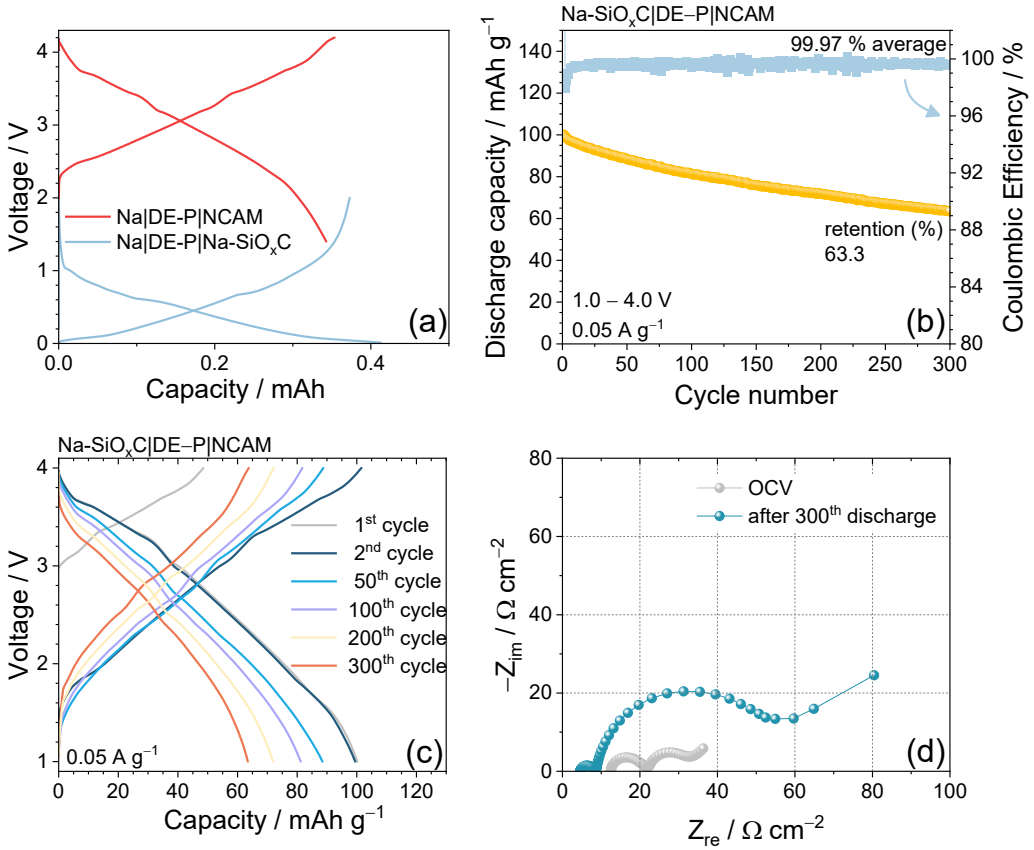

Figure 6. (a) Reversible voltage profiles of SiO_xC from 2 to 0.01 V (light blue) and NCAM from 1.4 to 4.2 V (red) in Na half -cell, performed at 0.05 A g^{-1} to analyze the voltage-capacity curves evolution; **(b, c)** galvanostatic cycling performance of the Na-SiO_xC|DE-P|NCAM full-cell, in detail: **(b)** discharge capacity trends *vs.* cycle number (coulombic efficiency in right-hand side *y*-axis), **(c)** selected voltage profiles; **(d)** Nyquist plots recorded by EIS related to the full-cell. Galvanostatic cycling carried out using a current rate of 0.05 A g^{-1} in the 1.0 – 4.0 V voltage range, active material content: 5.9 ± 0.1 mg_{NCAM} cm^{-2} and 6.2 ± 0.1 mg_{SiOxC} cm^{-2}, both electrodes casted onto Al.

Table 4.2.3 NLLS analysis carried out on the Nyquist plots displayed in Figure 6d. The impedance spectra were acquired on a Na|TE-F|SiO_xC cell at the OCV and after 300 (dis)charge runs.

Cell condition	**Circuit** $R_e(R_iQ_i)Q_w$	**R_1 (Ω)**	**R_2 (Ω)**	**R_2 (Ω)**	**χ^2**
OCV	$R_e(R_1Q_1)(R_2Q_2)Q_w$	12.6 ± 0.5	18.8 ± 1.0	31.4 ± 1.1	1×10^{-4}
After 300 cycles	$R_e(R_1Q_1)(R_2Q_2)Q_w$	5.7 ± 0.2	60 ± 5.1	65.7 ± 5.1	2×10^{-4}

References

(89) Dou, X.; Hasa, I.; Saurel, D.; Vaalma, C.; Wu, L.; Buchholz, D.; Bresser, D.; Komaba, S.; Passerini, S. Materials Today 2019, 23, 87–104.
(90) Fang, S.; Bresser, D.; Passerini, S.. Adv Energy Mater 2020, 10 (1).
(91) Chen, Y.; Li, F.; Guo, Z.; Song, Z.; Lin, Y.; Lin, W.; Zheng, L.; Huang, Z.; Hong, Z.; Titirici, M.-M. J Power Sources 2023, 557, 232534.
(92) Leng, Y.; Dong, S.; Chen, Z.; Sun, Y.; Xu, Q.; Ma, L.; He, X.; Hai, C.; Zhou, Y.. J Power Sources 2024, 613, 234826.
(93) Yang, B.; Wang, J.; Zhu, Y.; Ji, K.; Wang, C.; Ruan, D.; Xia, Y. J Power Sources 2021, 492, 229656.
(94) Zhu, H.; Shen, F.; Luo, W.; Zhu, S.; Zhao, M.; Natarajan, B.; Dai, J.; Zhou, L.; Ji, X.; Yassar, R. S.; Li, T.; Hu, L. Nano Energy 2017, 33, 37–44.
(95) Xie, L.; Tang, C.; Bi, Z.; Song, M.; Fan, Y.; Yan, C.; Li, X.; Su, F.; Zhang, Q.; Chen, C. Energy Mater 2021, 11 (38)
(96) Dou, X.; Hasa, I.; Saurel, D.; Vaalma, C.; Wu, L.; Buchholz, D.; Bresser, D.; Komaba, S.; Passerini, S. Materials Today 2019, 23, 87–104.
(97) Adam, M.; Abdalla, T.; Mohammed, M.; Bari, M. A. Al; Hossain, M. M. J Power Sources 2025, 652, 237674.
(98) Gan, S.; Huang, Y.; Hong, N.; Zhang, Y.; Xiong, B.; Zheng, Z.; He, Z.; Gao, S.; Deng, W.; Zou, G.; Hou, H.; Ji, X. Nanomicro Lett 2025, 17 (1), 325.
(99) Xu, L.; Li, Y.; Xiang, Y.; Li, C.; Zhu, H.; Li, C.; Zou, G.; Hou, H.; Ji, X. ACS Nano 2025, 19 (15), 14627–14651.
(100) Kim, H.; Hong, J.; Yoon, G.; Kim, H.; Park, K.-Y.; Park, M.-S.; Yoon, W.-S.; Kang, K.. Energy Environ Sci 2015, 8 (10), 2963–2969.
(101) Åvall, G.; A. Ferrero, G.; Janßen, K. A.; Exner, M.; Son, Y.; Adelhelm, P. Adv Energy Mater 2023, 13 (38).
(102) Son, Y.; Åvall, G.; Ferrero, G. A.; Freytag, A. I.; Escher, I.; Janßen, K. A.; Jauregui, M.; Saurel, D.; Galceran, M.; Adelhelm, P. Batter Supercaps 2024, 7 (3).
(103) Moriwake, H.; Kuwabara, A.; Fisher, C. A. J.; Ikuhara, Y. RSC Adv 2017, 7 (58), 36550–36554.
(104) Jache, B.; Adelhelm, P. Angewandte Chemie - International Edition 2014, 53 (38), 10169–10173.
(105) Hasa, I.; Dou, X.; Buchholz, D.; Shao-Horn, Y.; Hassoun, J.; Passerini, S.; Scrosati, B. J Power Sources 2016, 310, 26–31.
(106) Jain, P. K. . Mineral Processing and Extractive Metallurgy Review 2025, 1–24.
(107) Liu, Z.; Yu, Q.; Zhao, Y.; He, R.; Xu, M.; Feng, S.; Li, S.; Zhou, L.; Mai, L. Chem Soc Rev 2019, 48 (1), 285–309.
(108) Yang, Z.; Zhang, H.; Jiang, R.; Cheng, X.; Jing, C.; Luo, J.; Jia, P.; Yang, J. J Energy Storage 2025, 135, 118400.
(109) Chandra, C.; Devina, W.; Alvin, S.; Kim, J. Chemical Engineering Journal 2021, 404, 126520.
(110) Chuong, Y. N. K.; Le, P. M. L.; Vu, P. T.; Van Tran, M. Applied Physics A 2024, 130 (9), 633.
(111) Pustovalova, A. A.; Morozov, A. V.; Polivara, N. M.; Dikhtyar, Y. Y.; Nedoluzhko, A. I.; Pazhetnov, E. M.; Abakumov, A. M. Mater Res Bull 2025, 192, 113613.
(112) Chen, T.; Yan, X.; Zhang, Y.; Cao, J.; Hu, L.; Gao, W.; Li, D.; Song, W.; Zhang, J.; Xia, Y.; Xia, X.; Zhang, W.; Huang, H.. J Energy Storage 2025, 138, 118704.
(113) Luo, W.; Shi, Q.; Zhang, C.; Yi, R.; Zhao, W.; Cui, Y.; Shen, Y.; Ge, J.; Wang, C.; Huang, Y. J Mater Chem A Mater 2025, 13 (40), 34640–34647.
(114) Qiao, Y.; He, Z.; Tian, S.; Song, C.; Zhang, F.; Xia, Y. Balancing Act: J Power Sources 2025, 649, 237486.
(115) Del Rio Castillo, A. E.; Pellegrini, V.; Ansaldo, A.; Ricciardella, F.; Sun, H.; Marasco, L.; Buha, J.; Dang, Z.; Gagliani, L.; Lago, E.; Curreli, N.; Gentiluomo, S.; Palazon, F.; Prato, M.; Oropesa-Nuñez, R.; Toth, P. S.; Mantero, E.; Crugliano, M.; Gamucci, A.; Tomadin, A.; Polini, M.; Bonaccorso, F.Mater Horiz 2018, 5 (5), 890–904.
(116) Barcaro, E.; Marangon, V.; Bresser, D.; Hassoun, J. ChemSusChem 2025, 18 (1),

e202400615.
(117) Barcaro, E.; Marangon, V.; Mutarelli, M.; Hassoun, J.. J Power Sources 2024, 595, 234059.
(118) Bauer, A.; Song, J.; Vail, S.; Pan, W.; Barker, J.; Lu, Y. The Scale-up and Commercialization of Nonaqueous Na-Ion Battery Technologies. Adv Energy Mater 2018, 8 (17)..
(119) Minnetti, L.; Barcaro, E.; Sbrascini, L.; Nobili, F.; Hassoun, J.. Mater Res Bull 2025, 191, 113546.
(120) Moosavi-Nasab, M.; Taherian, A. R.; Bakhtiyari, M.; Farahnaky, A.; Askari, H. Food Bioproc Tech 2012, 5 (2), 638–647.
(121) Li, K.-M.; Jiang, J.-G.; Tian, S.-C.; Chen, X.-J.; Yan, F. The Journal of Physical Chemistry C 2014, 118 (5), 2454–2462.
(122) Freda, M.; Piluso, A.; Santucci, A.; Sassi, P. Appl Spectrosc 2005, 59 (9), 1155–1159.
(123) Danon, A.; Stair, P. C.; Weitz, E. The Journal of Physical Chemistry C 2011, 115 (23), 11540–11549.
(124) Tammer, M. G.. Colloid Polym Sci 2004, 283 (2), 235–235.
(125) Marangon, V.; Hernández-Rentero, C.; Olivares-Marín, M.; Gómez-Serrano, V.; Caballero, Á.; Morales, J.; Hassoun, J. ChemSusChem 2021, 14 (16), 3333–3343.
(126) Alfonsetti, R.; Lozzi, L.; Passacantando, M.; Picozzi, P.; Santucci, SAppl Surf Sci 1993, 70–71, 222–225.
(127) Finster, J.; Schulze, D.; Bechstedt, F.; Meisel, A. Surf Sci 1985, 152–153, 1063–1070.
(128) Paparazzo, E.; Fanfoni, M.; Severini, E.; Priori, S. Journal of Vacuum Science & Technology A: Vacuum, Surfaces, and Films 1992, 10 (4), 2892–2896
(129) Hasa, I.; Passerini, S.; Hassoun, J. RSC Adv 2015, 5 (60).
(130) Lee, B.; Paek, E.; Mitlin, D.; Lee, S. W. Rev 2019, 119 (8), 5416–5460.
(131) Seh, Z. W.; Sun, J.; Sun, Y.; Cui, Y. A ACS Cent Sci 2015, 1 (8), 449–455.
(131) Ferrero, G. A.; Åvall, G.; Janßen, K.; Son, Y.; Kravets, Y.; Sun, Y.; Adelhelm, P. Rev 2025.
(133) Tian, Z.; Zou, Y.; Liu, G.; Wang, Y.; Yin, J.; Ming, J.; Alshareef, H. N. Advanced Science 2022, 9 (22).
(134) Liu, X.; Zhao, J.; Dong, H.; Zhang, L.; Zhang, H.; Gao, Y.; Zhou, X.; Zhang, L.; Li, L.; Liu, Y.; Chou, S.; Lai, W.; Zhang, C.; Chou, S.. Adv Funct Mater 2024, 34 (37).
(135) Huang, Y.; Zhao, L.; Li, L.; Xie, M.; Wu, F.; Chen, R.. Advanced Materials 2019, 31 (21).
(136) Hassoun, J. K. K. T. Y. Cellulose-Based Electrolytes in Rechargeable Zn-Battery: An Overview. Adv Sustain Syst 2025, e00287.
(137) Bridel, J.-S.; Grugeon, S.; Laruelle, S.; Hassoun, J.; Reale, P.; Scrosati, B.; Tarascon, J.-M. J Power Sources 2010, 195 (7), 2036–2043.
(138) Marangon, V.; Barcaro, E.; De Boni, F.; Prato, M.; Bresser, D.; Hassoun, J.. Adv Sustain Syst 2024, 8 (11).
(139) Cheng, F.; Cao, M.; Li, Q.; Fang, C.; Han, J.; Huang, Y. ACS Nano 2023, 17 (18), 18608–18615.
(140) Yan, Y.; Chen, G.; Liu, W.; Qu, M.; Xie, Z.; Wang, F.. J Energy Storage 2024, 104, 114590.

Chapter 5.

Conclusions & Remarks

The work carried out in this Thesis represent a modest contribution to the fast-pace evolving energy-storage field. The core aspects pursued during these last three years comprised the development of lab-scale Li-ion, Na-ion, Li-ion-Sulfur, and Li-ion-Oxygen full-cell prototype. Moving from conventional Li-*insertion* into pure graphitic structure to SiO_x-C and Sn-C, and their successful implementation in full-cell, suggest that alternative anode material can be opportunely developed and implemented for LIB. On the other hand, good compatibility of these anodes was demonstrated in SIB, elaborating innovative devices based on Na-deficient layered-oxide cathode. Advanced chemistries beyond-*intercalation*, a prominent topic for high-energy and high-power application thanks to the *conversion* reaction of Li-ion with light chalcogens, such as O_2 and S_8 molecules, have been practically developed using non-metallic Li source at the anode, thus proving that matching conversion and intercalation in the same system is effectively possible. The approach followed is quite unconventional, since all the parts of the battery must well-match each other, from either chemical or physical point-of-view. There is a resolute conviction that these works will be considered pioneering in the next decades. Further optimization is required for these systems, which should be mainly devoted to the improvement of electrolyte formulation, due to the central role that this component plays within the battery. The safety concerns regarding the flammability of most well-performing liquid-electrolytes have been tackled by developing polymeric-electrolytes based on PEO and PEGDME, ceramic filler and suitable lithium salts, enabling more reliable Li-metal batteries using cathodes based on either intercalation or conversion reaction, which nowadays hold much promise. Related Publications are listed following the next section. The Remarks have been presented respecting the Thesis structure, while the related Publications are reported chronologically.

Remarks

(1) Current collectors using FLG, MWCNTs, or a mixture of them on Al were studied for application in Li-S battery. XRD measurements suggested a relevant graphitic crystallinity, in particular for the support using the FLG as the only coating on Al. Electrodes were prepared using the carbon-coated current collectors, a sulfur-carbon black composite, and either SPC or FLG electron conductive agent to achieve six formulations with remarkable differences in terms of morphology. CV tests performed on Li-S cells have shown fast and reversible conversion process for all the electrodes. The best tradeoff

among D_{max} and capacity retention upon cycling indicated S8-E2 as the most suitable current collector for successive high-sulfur content study. Next, areal capacities of 3.6 and 5 mAh cm^{-2} were achieved, retained for the 77% and 65% at the end of the galvanostatic test. Therefore, the proper combination of FLG and MWCNTs in the sulfur electrode formulation may lead to stable and efficient cathodes suitable for achieving Li-S batteries of practical interest.

(2) A composite anode indicated including silicon oxide in amorphous carbon and FLG framework, has been characterized in terms of physical-chemical properties and electrochemical behavior in lithium half-cell prior to application in full Li-ion battery. XRD of the SiO_x-CM powder confirmed the amorphous state of SiO_x and of the carbon derived from the organic precursor, and the crystalline structure of FLG, while TGA quantified the carbon to silicon oxide weight ratio as 65% and 35%, respectively.The Li-ion cell has been obtained by chemical pre-lithiation of the SiO_x-CM anode through direct contact with lithium metal for 10 min to achieve the Li_ySiO_x-CM phase and subsequent combination with a pristine NCM cathode. The Li_ySiO_x-CM||NCM system displayed a reversible process centered at 3.5 V, a maximum capacity of 158 mAh g_{NCM}^{-1}, rate capability up to 3C, cycle life over 120 cycles at C/3 with retention approaching 90%, and coulombic efficiency above 98% after the initial stages of the test. The remarkable performances of the Li-ion cell have been attributed to the stable and activated charge/discharge processes of the Li_ySiO_x-CM anode, which compensated by a progressive increase of the N/P possible de-lithiation or over-charging of the NCM cathode. The research outcomes have been presented at the 39th ISE Topical Meeting Conference held in Stresa (Italy, 5-9 June 2024).

(3) Li-ion sulfur cells with a remarkable cycle life have been achieved by combining a composite sulfur cathode added with Sn and MnO_2 with a pre-lithiated silicon oxide/carbon anode (Li_ySiO_x-C). The S-SM electrode exhibited in half-cell a reversible electrochemical process with maximum capacity of ~1090 mAh g_S^{-1}, CE approaching 99 %, and a rate capability extending up to 1 C. Therefore, we have proposed as alternative an electrochemically or chemically pre-lithiated Li_ySiO_x-CM anode, which can achieve in half-cell a maximum capacity of 500 mAh g^{-1} for over 400 cycles without significant decay. The Li-ion batteries demonstrated a significant performance extended over 400 cycles, a CE higher than 95 % after the initial stages, however with capacity decay leading to a final value of 380 mAhg_S^{-1} for the cell using the electrochemically lithiated anode and of 450 mAh g_S^{-1} for the cell using the chemically lithiated one. These responses have been achieved by leveraging suitable anode and cathode, with a N/P ratio from 1.02 to 1.12 set to concomitantly allow long cycle life and remarkable efficiency. The use of relatively high active material loadings (6.3 and 2.9 mgcm^{-2} for anode and cathode, respectively) and the limitation of the E/S ratio to 8 µl mg^{-1}, alongside with optimized cycling conditions, improved the capacity retention, despite *ex-situ* SEM of the electrodes upon cycling in full-cells revealed dissolution of sulfur from the cathode and partial deposition of Li-PS at the anode side. Thin-layer cathode and anode, in addition to the chemical lithiation process, may represent a step forward for facilitating the practical scaling-up of high-energy Li-ion batteries exploiting the sulfur chemistry.

(4) The TE-5%, TE-10%, and TE-15% electrolytes revealed the absence of ignition upon direct exposure to flame, thus suggesting a remarkable safety content. The suitable ionic conductivity of the electrolytes from -3 to 50 °C allowed the estimation of the activation energy for Li^+ motion, depending on the DOL content. The Li^+ transference number of the solutions decreased from 0.55 to 0.50 from TE-5% to TE-15% due to the lower dielectric constant in the latter compared to the former, which also influenced the LiTFSI dissolution. On the other hand, the increment of DOL concentration lowered the electrode/electrolyte interphase resistance in the Li cell that reached the lowest values for TE-15% upon aging. All solutions revealed a cathodic limit of 0 V vs. Li^+/Li and anodic limit decreasing from 4.41 V for TE-5%, to 4.38 V for TE-10%, and to 4.37 V for TE-15% due to the reactivity of the DOL ring. Li stripping/ deposition tests have shown modest charge/discharge over- voltage and the lowest polarization for TE-15%. A composite cathode including 90 wt% sulfur with a micrometric shape and a submicron primary arrangement of MWCNTs network revealed in a DOL:DME control-electrolyte a maximum capacity of ∼1100 mA h g^{-1}, with life extended up to 200 cycles and Coulombic efficiency ∼99%. Similar control cells with sulfur loading increased to 5.2 mg cm^{-2} and E/S ratio decreased to 6 µl mg^{-1} exhibited a maximum capacity of 500 mA h g^{-1} (4 mA h and 2.6 mA h cm^{-2}), life of 200 cycles, and Coulombic efficiency above 97%. Subsequently, the above electrode and the investigated glyme-based electrolytes are combined in a safe Li−S cell. The lowest DOL concentration (TE-5%) has allowed a fast cell activation, however, with capacity limited to 420 mA h g^{-1} and a sudden deactivation due to a polarization increase. Instead, the highest DOL content (TE-15%) promoted a capacity exceeding 550 mA h g^{-1}, however, with a gradual decrease after 100 cycles due to the excessive SEI growth. Likely, TE-10% represented an optimal compromise, showing fluctuations of the delivered capacity between 400 and 580 mA h g^{-1} and a life of 130 cycles.

(5) The specific energy achieved by Li|catholyte|SSnMnO_2 cell is comparable with that of the state-of-art LIB, while the power appears much higher and competes with that of electrochemical capacitors. We exploited high-order soluble LiPS in a cell characterized by faster kinetics and higher power, despite limited capacity, rather than the typical Li–S battery reaching low-order insoluble ones, such as Li_2S_2 and Li_2S. The data indicated a rate capability over 50C with still significant capacity, thus suggesting our approach suitable for increasing cell power.

(6) We evaluated the thermal, chemical, electrochemical, and interfacial properties of PEGDME-based electrolytes with LiTFSI and $LiNO_3$ salts and proposed their possible use in Li-O_2 battery. XPS at the solid state has highlighted the influence of $LiNO_3$ in modifying the SEI composition and improving the stability of the lithium interface. The solution with $LiNO_3$ revealed stability from 0 V to 4.6 V *vs.* Li^+/Li, beyond which decomposition occurs without any trace of the above side reaction at lower voltage. Li-stripping/deposition tests have shown polarization less than 30 mV upon 1000 h, while the Li/electrolyte interphase revealed a resistance below 150 Ω for the $LiNO_3$ added solution and above 300 Ω for the bare one upon 32 days of aging, thus suggesting the additive to promote a stable SEI. The results demonstrated that the full-cell can deliver at 2 V a power

density as high as 4 W g^{-1}, a capacity of 150 mAh g^{-1} for 80 cycles with efficiency of 100 % at 1 mA cm^{-2}, and a relevant capacity of 300 and 450 mAh g^{-1} for 30 and 15 cycles at 2 and 3 mA cm^{-2}, respectively. These results suggested the setup as suitable for environmentally compatible, safe, and low cost energy storage application.

(7) A polymer electrolyte based on solid PEGDME plasticized by a TEGDME solution has been developed and studied in lithium metal batteries operating at room temperature with $LiFePO_4$, sulfur, and oxygen cathodes. The electrolyte revealed thermal stability extending over 200 °C, and a solid structure in which the SiO_2 ceramic is well dispersed and lithium salts are efficiently dissolved. The polymer electrolyte showed a room temperature conductivity exceeding 10^{-4} S cm^{-1}, a Li^+-transference number of 0.31, electrochemical stability ranging from 0 to 4.4 V vs. Li^+/Li, a Li-stripping deposition overvoltage lower than 0.08 V, and stable electrode/electrolyte interphase with resistance lower than 400 Ω. The Li-$LiFePO_4$ polymer cell revealed initial high polarization, which subsequently decreased to reach a steady state capacity of ~150 mA h g_{LFP}^{-1} and polarization below 0.15 V, thus suggesting efficient Li-(de)insertion process into the olivine cathode. This behavior has been ascribed to an increase in the electrode/electrolyte interphase ionic conductivity through progressive wetting of the electrode, and the formation of a suitable blend between polymer electrolyte and electrode binder allowing fast Li^+ motion. The Li-S cell revealed a reversible conversion reaction between Li and S according to the overall electrochemical process $16\,Li + S_8 \leftrightarrows 8\,Li_2S$, with an initial discharge capacity of 1200 mA h g_S^{-1}, decreasing and stabilizing during the subsequent cycles to about 400 mA h g_S^{-1}. The Li-O_2 polymer cell showed a first discharge process accounting for an ORR at 2.5 V with a capacity of 500 mA h g_{MWCNTs}^{-1}, and incomplete subsequent charge (OER) with a capacity of 180 mA h g_{MWCNTs}^{-1} and low efficiency (~35 %). After the first cycle, the charge capacity progressively increased, and the efficiency improved to values approaching 90 %. This behavior was attributed to kinetics and wettability limits during ORR and OER processes, evolving in a complex solid/polymer/gas interphase that might require the use of catalysts to improve the reaction kinetics. The promising results achieved in this work, in addition to the relevant safety content of the cells, suggest the polymer electrolyte studied herein as a suitable medium for safe room temperature LMBs exploiting a vast range of cathodes and differing by energy content and characteristic electrochemical process.

(8) The use of the MEA-LFP facilitate the cell preparation and the system setup, and promote fast blending between polymer electrolyte and working electrode to achieve cells with better performances, within a shorter activation process in comparison with the typical Li-polymer cell, in which electrode and electrolyte are prepared separately, and subsequently stacked together during assembly process Our setup may boost the scaling up of efficient polymer cells using the lithium metal anode. The polymer electrolyte has shown conductivity ranging from 4.8×10^{-4} to 3.8×10−6 S cm^{-1}, depending on temperature, t_{Li+} of 0.39, suitable electrode/electrolyte interphase with resistance lower than 80 Ω either at 70 or 90 °C, electrochemical stability ranging from 0 to 4.0 V vs. Li^+/Li, and a Li stripping/deposition overvoltage lower than 0.04 and 0.02 V at 70 and 90 °C, respectively. The alternative configuration of lithium polymer cell exploiting the all-in-one cast

electrode/electrolyte process, in analogy to the MEA in fuel cell technology, revealed promising results. The MEA-LFP was characterized in terms of polymer content in the tapes through TGA, providing values ranging from 52 to 60 % with respect to total electrode weight depending on the active material loading in the electrode tape and on the adopted current collector. The SEM analysis showed a uniform and homogeneous covering of the active material by the polymeric membrane, and depicted the components blending in the MEA-LFP setup. The data highlighted an interplay between the polymer and active material, which influenced the electrochemical response of the electrode. The Li|MEA-LFP polymer cell tested at C/8 displayed an increase of the delivered capacity during the initial stages, which subsequently reached a steady value of ~155 mAh g_{LFP}^{-1} and polarization below 0.15 V. The applicability of the MEA-LFP was further tested in pouch-cells, which exhibited a maximum capacity of 80 mAh g_{-1} at C/10 and cycle life over 40 cycles at C/5 with stable trend. This strategy may be promising for various cathode chemistries differing by the energy density and characteristics of the electrochemical process, such as Li-(de)intercalation or conversion (e. g., layered materials or sulfur, respectively). Therefore, further research is currently ongoing in our laboratories to exploit these promising and challenging systems.

(9) TEGDME-based electrolytes using either $NaClO_4$ or $NaCF_3SO_3$ and various concentrations of FEC (i.e., 0.5%, 1%, 2% or 3%) as SEI film-forming agent have been thoroughly analyzed before application in Na–S cells. Modifications of the sodium stripping/deposition overvoltage shape suggested possible effects of FEC on the Na electrochemical process kinetics. The differences have been attributed to the specific chemical nature of the SEI at the Na surface, which is characterized by the predominant presence of reductive decomposition products of the conductive salts, the solvent, and the FEC. Ex-situ SEM performed on Na electrodes upon aging in contact with the electrolytes confirmed the growth of the SEI in concomitance with an increase of the FEC concentration, and notable differences in morphology depending on the composition of the electrolyte solution. The FEC-doped solutions revealed Na–S kinetics influenced by the additive through the promotion of an additional discharge process at ≈1.8 V which greatly enhanced the cell performance. In particular, the cells using TE-Cl_1% and TE-F_1% exhibited long cycle life and coulombic efficiency exceeding 90% and 80%, respectively. Hence, Na–S cells using the bare electrolytes evidenced a weak SEI and poor reaction kinetics, instead TE-Cl_1% and TE-F_1% solutions ensured stable cycling and limited increase of the interphase resistance within a potential range limited between 1.4 and 2.6 V. The galvanostatic cycling performed within 1.4 and 2.6 V with either TE-Cl_1% or TE-F_1% revealed enhanced capacity and coulombic efficiency. The data reported in this work evidenced the key importance of the thorough electrolyte investigation for determining the proper setup requested for exploiting advanced Na–S cell configuration.

(10) The pre-treatment process of a Sn-C anode for achieving its efficient operation as alloying electrode in Na-ion battery in combination with a NCAM layered cathode has been studied in detail. The treatment consisted of direct Sn-C chemical sodiation by capillary contact of the electrode with Na metal, controlling time and pressure, especially considering active material loading, to properly tune the alkali metal content in the

electrode. XRD, Raman spectroscopy, SEM/EDS analysis, and electrochemical tests have shown the achievement of different sodiation degrees in the anode by changing the activation time. These preliminary outcomes allowed the optimization of the Na_xSn-C||NCAM full-cell setup to avoid the side reactions by better tuning its balance, increasing the current rate, and narrowing the voltage window. Indeed, the optimized full-cell revealed a rate capability extended up to 250 mA g^{-1} C, with improved electrode/electrolyte interphase stability and promising maximum energy and power densities of 300 Wh kg_{cat}^{-1} and 650 W kg^{-1}. Furthermore, the cell revealed a stability increased to 250 charge/discharged cycles at 200 mA g^{-1} with a maximum capacity of 85 mAh g^{-1} and good retention. The obtained results suggested the direct chemical anode sodiation adopted as suitable approach to achieve full Na-ion battery with promising performances in terms of efficiency and stability, which is proposed for sustainable energy storage.

(11) We provided a viable pathway to achieve highly cyclable Na-ion full-cells based on layered-oxide cathode, Na-alloying anode water-processed with CMC binder, and a glyme-based electrolyte. We have concomitantly overcome two issues (i.e., Na-deficiency in NCAM and Sn-C first cycle irreversibility) by adopting chemical pre-sodiation of the alloying anode prior to the use in Na-ion full-cell. This process allowed the anode to act as the Na reservoir in an efficient full-cell using the NCAM cathode, by tuning the electrode loading, the binder nature, the electrolyte formulation, and the Na/Sn-C contacting timeframe. The full-cells, achieved by rationally combining a Sn-C anode pre-sodiated for 27 min and the NCAM cathode with a N/P ratio from 1.1 to 1.2, revealed high cycling stability, with maximum capacity around 120 mAh g^{-1}, that approached the maximum electrodes capacity achieved in half-cell. The full-cell performance has been retained between 85 % and 95 % of the maximum capacity over 100 galvanostatic (dis)charge cycles, depending on experimental constraints such as voltage cutoff from 3.9 to 4.1 V, and applied current from 0.05 to 0.25 A g^{-1}. Hence, we have estimated for our $(Na_xSn$-$C)_{27min}$||NCAM full-cell an energy density ranging from 310 to 250 Wh kg^{-1}, based on the cathode mass only, which reflected values from 175 to 141 Wh kg^{-1} considering both electrodes active material, whilst lower values considering all the cell components, including inactive ones, that may be further improved by tuning the materials for possible cell scaling-up.

(12) A negative electrode has been achieved from SiO_2, FLG, and amorphous carbon by hydrothermal treatment and exposure to Ar/H_2 flow inside a furnace for application in SIB. The CV response of the SiO_xC electrode in Na-cell revealed multiple processes, including initial reductive decomposition with SEI formation from 1.3 to 0.3 V vs. Na^+/Na, reversible Na^+-solvent co-intercalation from 1.3 to 0.7 V, Na^+-intercalation at 0.45 V, Na^+-insertion or deposition in AC nearby 0 V, and minor Na-Si alloying at about 0.05 V vs. Na^+/Na. The SiO_xC depicted in half-cell charge and discharge occurring with almost symmetrical profile for both Al and Cu, with capacity of 102 and 163 mAh g^{-1} retained over 400 cycles for 93 % and 94 %, respectively. Despite 36 % lower capacity for electrodes cast on Al, this current collector has been considered the most suitable candidate for full-cell application, since it is lighter, cheaper, and therefore advantageous in terms of

cell practical energy density and cost. Before the use in full-cell, the SiO_xC electrode was activated through chemical capillary contact treatment to achieve a Na-SiO_xC anode for SIB. Hence, the Na-SiO_xC||NCAM full-cell had average working voltage centered at about 2.9 V, with capacity ranging from 100 mAh g^{-1} to 63 mAh g^{-1} upon 300 cycles, and average coulombic efficiency exceeding 99.9 %. A higher capacity can be possibly achieved from this full-cell by further tuning the cell balance (increasing the N/P ratio to get adequate Na reservoir), or by incrementing the furnace step temperature, which is expected to enhance the specific capacity of the anode. These data suggest possible setup of the Na-ion full-cell using the SiO_xC anode, glyme-based Na-electrolyte, and NCAM cathode, in view of complementary application of SIB technology with LIB.

Related Publications

(1) V. Marangon, E. Barcaro, L. Minnetti, W. Brehm, V. Pellegrini, F. Bonaccorso, J. Hassoun, **Current collectors based on multiwalled carbon-nanotubes and few-layer graphene for enhancing the conversion process in scalable lithium-sulfur battery**, Nano Research, 16, 8433–8447 (2023), 10.1007/s12274-022-5364-5

(2) V. Marangon, L. Minnetti, E. Barcaro, J. Hassoun, **Room-Temperature Solid-State Polymer Electrolyte in Li-LiFePO$_4$, Li-S and Li-O$_2$ Batteries**, Chemistry European Journal, 29, e202301345 (2023), 10.1002/chem.202301345

(3) V. Marangon, E. Barcaro, E. Scaduti, F. Adami, F. Bonaccorso, V. Pellegrini, J. Hassoun, **Toward Sustainable Li–S Battery Using Scalable Cathode and Safe Glyme-Based Electrolyte**, ACS Applied Energy Materials, 6, 11560–11572 (2023), 10.1021/acsaem.3c01966

(4) E. Barcaro, V. Marangon, M. Mutarelli, J. Hassoun, **A lithium-ion battery with cycling stability promoted by the progressive activation of a silicon oxide anode in graphene-amorphous carbon matrix,** Journal of Power Sources, 595, 234059 (2024), 10.1016/j.jpowsour.2024.234059

(5) V. Marangon, E. Barcaro, F. De Boni, M. Prato, D. Bresser, J. Hassoun, **Effective Liquid Electrolytes for Enabling Room-Temperature Sodium–Sulfur Batteries,** Advanced Sustainable Systems, 8, 2400268 (2024), 10.1002/adsu.202400268

(6) E. Barcaro, V. Marangon, D. Bresser, J. Hassoun, **Scalable Li-Ion Battery with Metal/Metal Oxide Sulfur Cathode and Lithiated Silicon Oxide/Carbon Anode**, ChemSusChem, 18, e202400615 (2025), 10.1002/cssc.202400615

(7) E. Barcaro, V. Marangon, D. Bresser, J. Hassoun, **Polymeric Lithium Battery using Membrane Electrode Assembly**, Batteries & Supercaps, 8, e202400542 (2025), 10.1002/batt.202400542

(8) E. Barcaro, J. Hassoun, **A high-power lithium–sulfur battery combining a catholyte and a composite cathode**, Chemical Communications, 61, 4208–4211 (2025), 10.1039/d4cc06344a

(9) L. Minnetti*, E. Barcaro*, L. Sbrascini, F. Nobili, J. Hassoun, **Chemical approach to achieve sodiated alloying anode for direct application in Na-ion battery**, Materials Research Bulletin, 191, 113546 (2025). 10.1016/j.materresbull.2025.113546

(10) S. Levchenko*, E. Barcaro*, A. Comini, A. Matic, J. Hassoun, **Thermally stable electrolyte for lithium-oxygen battery and its metal-free version,** Journal of Colloids and Interphase Sciences, 706, 139622 (2026), 10.1016/j.jcis.2025.139622

(11) E. Barcaro, D. Amato, V. Marangon, D. Bresser, J. Hassoun, **Highly-Cyclable Na-Ion Battery Exploiting a Nanostructured Tin-Carbon Anode, Layered-Oxide P3/P2 Cathode and a Glyme-based Electrolyte**, Journal of Power Sources, 666, 239124 (2026), 10.1016/j.jpowsour.2025.239124

(12) E. Barcaro, D. Amato, S. Forti, C. Coletti, J. Hassoun, **A Silicon Oxide-Carbon Anode with High Reversibility for Na-ion Battery**, Energy & Fuels, 10.1021/acs.energyfuels.5c06312 (currently under proof)

*Co-first authors

Acknowledgements

This work has been principally carried out in the University of Ferrara, the Project has been funded under the National Recovery and Resilience Plan (NRRP), Mission 04 Component 2, Investment 1.5 – NextGenerationEU, Call for tender n. 3277 dated 30/12/2021, Award Number: 0001052 dated 23/06/2022. Other fundings were provided by the grant "Fondo di Ateneo per la Ricerca Scientifica, FAR 2023" University of Ferrara, "Fondo di Ateneo per la Ricerca Scientifica, FAR 2024" University of Ferrara, and the project "Accordo di Collaborazione Quadro 2015" between University of Ferrara (Department of Chemical and Pharmaceutical Sciences) and Sapienza University of Rome (Department of Chemistry). The company BeDimensional S.p.A. (Lungotorrente Secca 30R, Genova, 16163, Italy) is acknowledged for providing FLG powder. The Italian Institute of Technology is thanked for providing the XPS facility. I deeply thank all the Bachelor and Master students I supported during their Thesis work, M. Mutarelli, E. Scaduti, G. Giacomelli, F. Balboni, M. Chaieb, D. Amato, and G. Morson, thanks for all the lasting experience together, working with you taught me how to improve both scientifically and humanly. I warmly thank S. Levchenko, L. Minnetti and N. Soontornnon for the occasional collaborations, fruitful scientific discussion, and time spent together at the University of Ferrara, which enriched the content of this work.

Special Thanks to the Helmholtz Institute Ulm (HIU, Helmholtzstrasse 11, Ulm, 89081, Germany), founded in 2011 by Karlsruhe Institute of Technology and part of the Helmholtz Association, particularly to Professor D. Bresser for hosting me in his research group "Electrochemical Energy Storage Materials". Many thanks to Dr. V. Marangon, who practically taught me the basics of energy-storage-related laboratory in early 2022, during my Master Thesis, and welcomed me in HIU.

I express sincere and deepest gratitude to Professor J. Hassoun, who enlightened my scientific critical thinking, shaping my personal development and constantly keeping up the bar. I owe to him the dedication and passion for the subject, which will be held perpetually.

to the memory of my father, Michele, and to my family, Carmela and Emanuele